PRACTICAL SPECTROSCOPY SERIES VOLUME 23

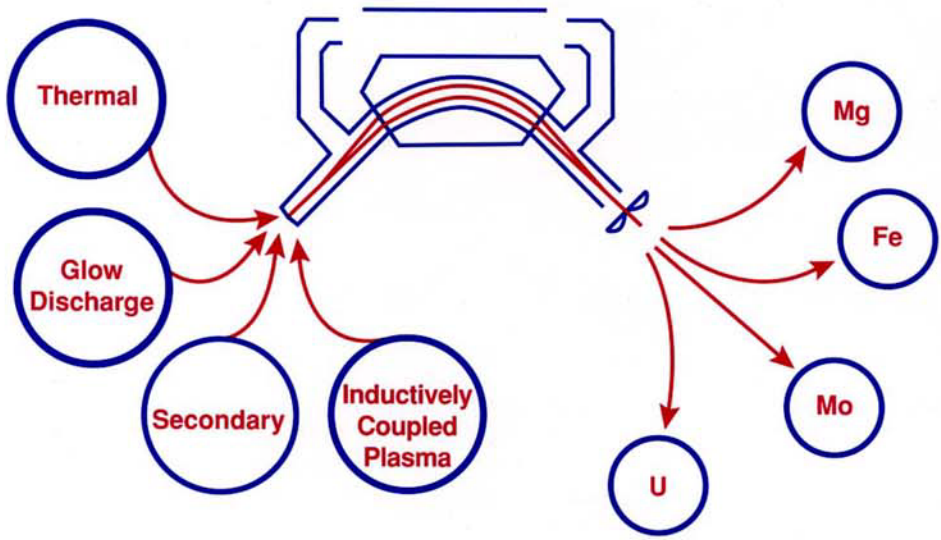

Inorganic Mass Spectrometry

Fundamentals and Applications

edited by
Christopher M. Barshick
Douglas C. Duckworth
David H. Smith

Inorganic Mass Spectrometry

Inorganic Mass Spectrometry

Fundamentals and Applications

edited by
Christopher M. Barshick
Douglas C. Duckworth
David H. Smith

Oak Ridge National Laboratory
Oak Ridge, Tennessee

MARCEL DEKKER, INC.

NEW YORK • BASEL

ISBN: 0-8247-0243-3

This book is printed on acid-free paper.

Headquarters
Marcel Dekker, Inc.
270 Madison Avenue, New York, NY 10016
tel: 212-696-9000; fax: 212-685-4540

Eastern Hemisphere Distribution
Marcel Dekker AG
Hutgasse 4, Postfach 812, CH-4001 Basel, Switzerland
tel: 41-61-261-8482; fax: 41-61-261-8896

World Wide Web
http://www.dekker.com

The publisher offers discounts on this book when ordered in bulk quantities. For more information, write to Special Sales/Professional Marketing at the headquarters address above.

Current printing (last digit):
10 9 8 7 6 5 4 3 2 1

PRINTED IN THE UNITED STATES OF AMERICA

Preface

The aim of this book is twofold: to introduce the topic of inorganic mass spectrometry to the nonpractitioner of the technique and to familiarize those conversant with it with recent developments in some of the foremost laboratories in the world. The book should be of value to industry, academia, and government laboratory staff and should appeal to both national and international audiences. It is written so that a college senior majoring in the sciences can follow the discussion but has enough technical sophistication to keep it the benchmark for books in this field for the next decade.

This book describes the fundamental operating characteristics of the most common inorganic mass spectrometers. At the heart of this discussion is a description of the various ionization sources that generate a representative analyte population for mass analysis. The initial chapters introduce the mass spectrometric hardware that separates the ionized fractions of analytes, one mass from another. The detection schemes used to measure this ion population, and the data processing systems that permit this information to be of value to the chemical analyst, are also discussed.

Modern mass spectrometers are usually one of four types: magnetic sector, quadrupole, time-of-flight, or ion trap. A brief introduction to each is provided. Classical applications are discussed to illustrate how these devices have shaped the landscape of elemental and isotopic chemical analysis.

The first two chapters were written by members of the research staff of Oak Ridge National Laboratory. Because each type of inorganic mass spectrometer has been extensively reviewed in the literature, only short discussions of the fundamentals, instrumentation, and classical applications are given. Theory is covered to an appropriate extent.

The balance of the book is composed of chapters authored by some of the leading experts in the field of inorganic mass spectrometry. The focus of this section is specialized topics, with emphasis on new developments in the field in the last 10 years. The final chapters focus on what we believe will be the future of inorganic mass spectrometry.

This book is appropriate for anyone with an interest in elemental or isotopic chemical analysis. Among the anticipated readership are those from the industrial community who are not involved in research per se, but rely heavily on inorganic mass spectrometers to make chemical measurements important to their respective industries, including semiconductors, aluminum, steel, and materials fabrication. Academics and government staff scientists will see this book as an opportunity to learn about current developments in the field without having to spend weeks sorting through the literature. Professors of graduate-school courses in mass spectrometry will find this a valuable reference for their students.

Christopher M. Barshick
Douglas C. Duckworth
David H. Smith

Contents

Contributors

Kathryn L. Ackley *University of Cincinnati, Cincinnati, Ohio*

Christopher M. Barshick *Oak Ridge National Laboratory, Oak Ridge, Tennessee*

Joseph A. Caruso *University of Cincinnati, Cincinnati, Ohio*

John N. Christensen *University of Michigan, Ann Arbor, Michigan*

Stephen S. Cristy *Lockheed Martin Energy Systems, Oak Ridge, Tennessee*

James E. Delmore *Idaho National Engineering and Environmental Laboratory, Idaho Falls, Idaho*

Douglas C. Duckworth *Oak Ridge National Laboratory, Oak Ridge, Tennessee*

John R. Eyler *University of Florida, Gainesville, Florida*

Chris M. Hall *University of Michigan, Ann Arbor, Michigan*

Alex N. Halliday *ETH Zentrum, Zürich, Switzerland*

Gary M. Hieftje *Indiana University, Bloomington, Indiana*

Der-Chuen Lee *University of Michigan, Ann Arbor, Michigan*

Xiaozhong Luo *University of Michigan, Ann Arbor, Michigan*

R. Kenneth Marcus *Clemson University, Clemson, South Carolina*

David P. Myers *Leco Corporation, St. Joseph, Michigan*

John W. Olesik *The Ohio State University, Columbus, Ohio*

Stephen J. Ray *Indiana University, Bloomington, Indiana*

Mark Rehkämper *Universitaet Muenster, Muenster, Germany*

Lee R. Riciputi *Oak Ridge National Laboratory, Oak Ridge, Tennessee*

David H. Smith *Oak Ridge National Laboratory, Oak Ridge, Tennessee*

Karen L. Sutton *University of Cincinnati, Cincinnati, Ohio*

Clifford H. Watson *University of Florida, Gainesville, Florida*

1

Thermal Ionization Mass Spectrometry

David H. Smith
Oak Ridge National Laboratory
Oak Ridge, Tennessee

1.1 INTRODUCTION

Thermal (or surface—the two terms are synonymous in this context) ionization has a long history in the measurement of isotope ratios. It has seen widespread use in the determination of atomic weights [1], age dating in geological applications [2], and in various nuclear applications [3]. Quantitative results can be obtained through the technique of isotope dilution (see Chapter 5). In this guise, it has entered fields previously closed to it, including the environment [4,5] and nutrition [6,7]. Its primary attractions are its high sensitivity for many elements and its good precision and accuracy. This topic has been the subject of several recent review articles [8,9].

In thermal ionization, ions are produced by the interaction of analyte species with a heated surface, which is usually a metal. No other source of energy is used. Most commonly, singly charged metal ions are monitored in the analysis, but this is not invariably so. If negative ions are monitored, an oxide species is often a better choice than the metal ion. Significant work in the last few years has led to new appreciation of this hitherto neglected area of research [10].

Not all elements are amenable to thermal ionization, positive or negative. It is obvious that elements whose natural state is a gas cannot be addressed by this technique. In addition, some elements are too volatile; others have a first ionization potential too high, and a few, such as mercury, display both characteristics. Generally speaking, solid elements with first ionization potentials below about 7.5 eV can be analyzed through measurement of positive ion beams. Use of silica gel

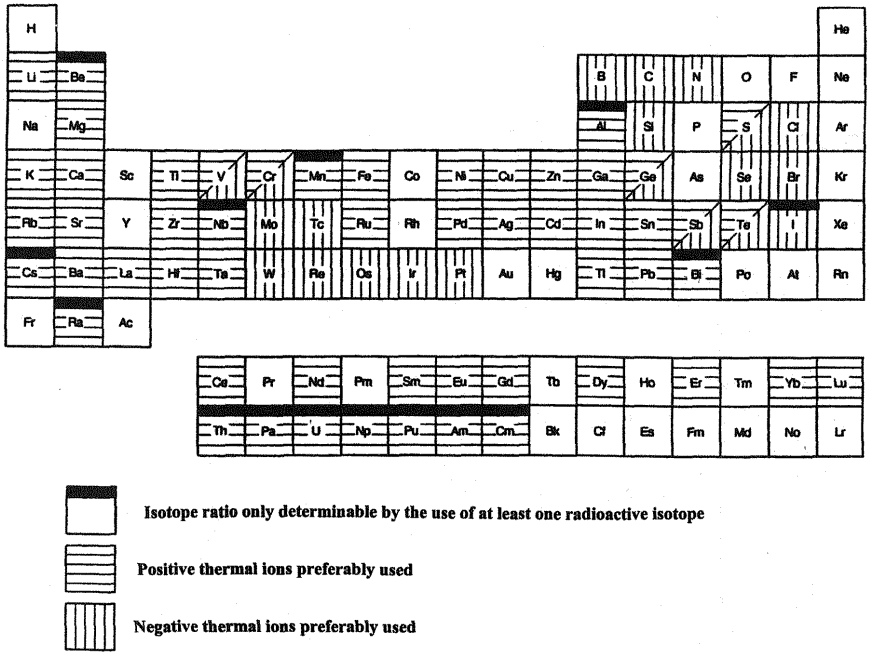

Figure 1 Elements amenable to thermal ionization, positive or negative. (From Ref. 10.)

or other ion emitters, however, extends application to elements with high first ionization potential (IP) and high volatility; for example, zinc (IP = 9.4 eV) has been successfully analyzed by using silica gel. Figure 1.1, taken from a recent review by Heumann [10], identifies for most elements which of the two ionization modes is preferable; it also identifies which elements are amenable to analysis using isotope dilution.

1.2 HISTORY

The first observation of positive ions emitted from a salt on a heated surface was reported by Gehrcke and Reichenheim in 1906 [11]. The method was first applied in mass spectrometry by Dempster in 1918 [12]. Kunsman performed pioneering studies of the mechanism and of means of controlling ion production [13,14]. Langmuir and Kingdon modified the Saha equation (which is applicable only to plasmas) to provide a theoretical understanding of the process in 1925 [15]; this topic is treated in more detail later. As greater understanding of the process was achieved, various means of expanding application of the technique were devised.

Most of these involved modifying the ionizing surface in some manner that made production of positive ions more efficient. Some involved changing the surface entirely, as in the use of silica gel [16]. Other ionization-enhancing techniques involved altering the surface to one of higher work function, as in introducing carbon into a rhenium substrate [17]. An overlayer of a material of high work function, generated through either electroplating or other means, is another method that has been successfully applied [18,19]. These topics are treated in more detail later in the chapter.

1.3 Theory

To the best of the author's knowledge, no treatment of the theory underlying thermal ionization has appeared since the description by Kaminsky over 30 years ago [20]. As his book is no longer listed in *Books in Print*, it seems desirable to include a description of it here, if only for reference. The following treatment follows that of Kaminsky. In these equations, subscripts (+) and (0) are used to refer to the state of the atom on the surface, representing, respectively, the singly charged positive ion and the atom, and subscripts (i) and (a) are used to refer to the species (ions and atoms, respectively) leaving the surface.

The theory of thermal ionization starts with the work of Langmuir and Kingdon [15], who derived an equation from first principles that describes a gas-phase atomic beam impinging on a hot metal surface; the atoms adsorb on the surface and then desorb from it, partly as atoms and partly as singly charged positive ions. The length of time the impinging species remains on the surface is called the *mean residence time*, τ_a and τ_i, for atoms and singly charged positive ions, respectively. The desorption process is described by a first-order rate law.

$$N_{tx} = N_0 \exp(-t/\tau_x) \tag{1.1}$$

where N_0 is the steady-state flux of the atomic beam impinging on the surface; the subscripts x and i represent atoms and ions, respectively; and N_{tx} is the flux of desorbing ions or atoms leaving the surface t seconds after interruption of the impinging beam. A plot of log N_{tx} versus time yields a straight line whose slope is $1/\tau_x$.

To describe the efficiency of ion formation, it is useful to define two parameters, the degree of ionization and the ionization coefficient. These are defined as follows:

$$\alpha = N_i/N_a \tag{1.2}$$

$$\beta = N_i/N \tag{1.3}$$

where α is the degree of ionization and β the ionization coefficient; N_i and N_a are the numbers of singly charged positive ions and atoms, respectively, leaving the hot surface per unit area per second; N is the flux of atoms impinging on the

surface per unit area per second. On the assumption that a steady state is achieved, the numbers of atoms impinging on the surface must equal the sum of the atoms and ions leaving:

$$N = N_a + N_i \tag{1.4}$$

Langmuir and Kingdon used Saha's original work [21], which was developed for plasmas, as a starting point to derive an expression for α in terms of experimental parameters. In the absence of an external electric field the equation is written

$$\alpha = (g_+/g_0) \exp[(\Phi - I)/kT] \tag{1.5}$$

This is the famous Saha-Langmuir equation. In it, g_+/g_0 is the ratio of the statistical weights of the ionic and atomic states, Φ is the work function of the surface, I is the first ionization potential of the element in question, k is the Boltzmann constant, and T is the absolute temperature. Note that g_+/g_0 is close to 1 for electronically complex elements; for simpler elements it can take on a variety of values depending on how many electronic states can be populated in the two species; for alkali atoms, for example, it is often ½. Attainment of thermodynamic equilibrium was assumed in the derivation of this equation, and it is applicable only to well-defined surfaces.

Much experimental effort has been expended to confirm this equation. Early work was compromised by the difficulty in obtaining a good enough vacuum. Oxygen was the primary troublemaker; oxygen bonds with most metals, forming a layer on the surface that has properties different from those of the pure metal and that interacts with the impinging atoms. Figure 1.2 illustrates the situation; it takes only a few seconds at 10^{-6} torr for a monolayer of oxygen to form on tungsten surfaces [22]. This effect has been experimentally investigated by Kawano et al. [23]. Kaminsky measured residence times of alkali atoms on clean and gas-covered tungsten surfaces and found that they were about 100 times longer on the gas-covered surface [24]. Desorption energies for the ions were also affected by gas coverage.

The Saha-Langmuir equation has been used to obtain both ionization potentials [25] and work functions [26]. Measuring ion beam intensities at several different temperatures and plotting their logarithms vs. $1/T$ yield a straight line whose slope is $(\Phi - I)/k$. If either Φ or I is known, the other is readily calculated. Hertel introduced a method of measuring ionization potentials that was independent of the work function of the surface, using instead as reference an element of known ionization potential; he applied it in the determination of the first ionization potentials of the lanthanide elements [27].

Atoms adsorbed on a metal surface exchange electrons with it and, as a result, may be desorbed as either atoms or ions. Only those ions and atoms with enough energy to break the adsorption bond will leave the surface. The strength of this bond is measured by the desorption energy, E_a and E_i, for atoms and singly

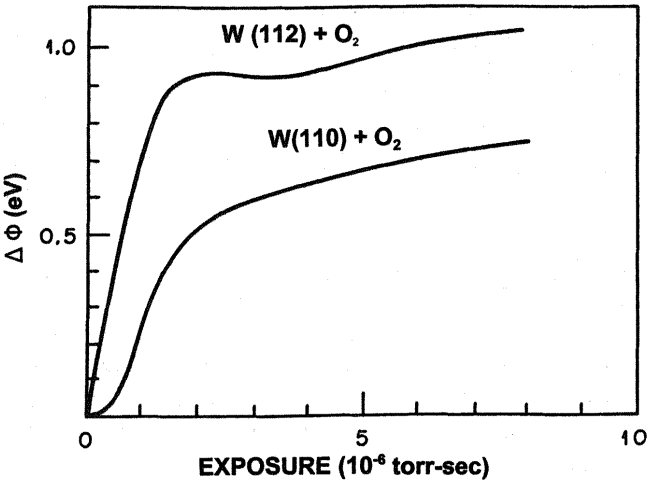

Figure 2 Change in work function of the (110) and (112) planes of tungsten exposed to oxygen at room temperature. (From Ref. 22.)

charged ions, respectively. The desorption characteristics of alkali ions have been investigated by Kaminsky [24]. Atoms are experimentally harder of access than ions, and there are only a few reports of such investigations in the literature. Hughes studied the desorption of rubidium atoms from tungsten surfaces [28], and Smith studied the desorption of uranium atoms from tungsten [29] and thorium and uranium atoms from rhenium [30].

As a free electropositive atom approaches a metal surface, there is a perturbation of the energy levels of its external electrons. This causes the allowed electronic states to spread into an energy band whose maximum is given by I_r, the first ionization potential of the element at a distance r from the surface. This maximum is shifted away from the discrete energy level occupied by the valence electron at an infinite distance from the surface upon which definition of the first ionization potential is based. The divergence of I_r and I is greatest for elements of low first ionization potential and increases the nearer the atom approaches the surface. At distances less than a critical distance ($r < r_c$), electron exchange is so rapid that it is impossible to distinguish between atomic and ionic states. At any given instant, an adsorbed atom with $r < r_c$ will either have an electron in energy state E_c, in which case it will be present as an atom, or it will not, in which case it will be present as a singly charged positive ion. From Fermi statistics, the probability that the energy state E_c is occupied is given by

$$W_0 = W(E_c) = \{1 + \exp[(E_c - \eta)/kT]\}^{-1} \tag{1.6}$$

where η is the electrochemical potential and includes both the electrostatic and chemical parts of the work involved in the transition of atom to ion. The probability that the state is not occupied is given by

$$W_+ = 1 - W(E_c) = \{1 + \exp[-(E_c - \eta)/kT]\}^{-1} \tag{1.7}$$

The charge transfer probability for an atom is proportional to the ratio of these probabilities:

$$\frac{W_+}{W_0} = A\left\{\frac{1 + \exp[(E_c - \eta)/kt}{1 + \exp[-(E_c - \eta)/kt}\right\} = A\exp[(E_c - \eta 0/kt \tag{1.8}$$

A is the ratio of statistical weights g_+/g_0 defined previously [Eq. (1.5)]. In Eq. (1.8), $E_c - \eta = \Phi - I_{rc}$ where I_{rc} is the ionization potential for the adsorbed atom at distance r_c from the surface. Each of these expressions defines the change in energy involved in the transfer of the electron to the surface. Figure 1.3 is the potential diagram for cesium adsorbed on tungsten [31].

Historically, there has been debate over whether there is an activation energy, ΔQ, involved in the transition between atomic and ionic states on the surface. From Figure 1.3 it can be seen that

$$\Delta Q = (\Phi - I_{rc}) = E_i - E_0 - (I - \Phi) \tag{1.9}$$

This equation was first derived by Dobretsov [32]. Using this equation, Eq. (1.8) can be rewritten:

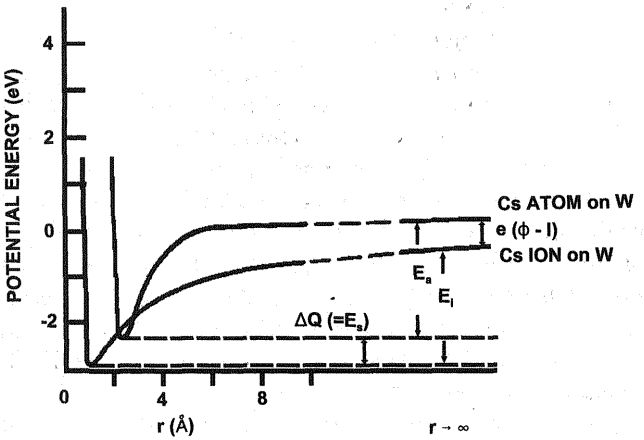

Figure 3 Potential energy diagram for the adsorption of cesium on tungsten. (From Ref. 20.)

$$W_+/W_0 = A \exp [E_i - E_a - (I - \Phi)]/kT \tag{1.10}$$

To arrive at an expression for α it is necessary to multiply the charge transfer probability by the probability of evaporation of ions and atoms. The Frenkel equation [33] expresses the probability that the kinetic energy of a given ion or atom will exceed the desorption energy:

$$W(E_x) = \omega_{0x}(E_x) \exp E_x/kT) = 1/\tau_x \tag{1.11}$$

where the subscript x is either i or a for ions and atoms, respectively; $W(E_x)$ is the desorption probability of the species; τ_x is the mean residence time for the given species; and ω_{0x} is the frequency of exchange of the electron with the surface. Kaminsky measured mean residence times of alkali metals on tungsten surfaces [24]; they are on the order of 10^{-12} second. To obtain an expression for the degree of ionization, α, Eqs. (1.10) and (1.11) are multiplied together:

$$\alpha = \frac{N_i}{N_a} = \frac{W_+ W(E_i)}{W_0 W(E_a)} = A \exp [(\Phi - I)/kT)] \tag{1.12}$$

This equation, which relates the Frenkel equation [Eq. (1.11)], the Saha-Langmuir equation [Eq. (1.5)], and the ratio of charge transfer probabilities, makes possible a detailed study of the thermal ionization process.

There is some doubt about the validity of Eq. (1.9). It assumes that the atomic and ionic states of an adsorbed atom on a hot surface are distinguishable; as shown in Figure 1.3, ΔQ should be nonzero if this is so. If, on the other hand, $\Delta Q = 0$, this equation reduces to

$$E_a - E_i = (I - \Phi) \tag{1.13}$$

Available experimental evidence, though scanty, suggests that ΔQ is within experimental error of 0, at least for some elements [30].

To summarize the surface ionization phenomenon, an atom on a hot filament surface exchanges an electron with it at rates of 10^{10}–10^{14} sec^{-1} [34]. The adsorbed species will desorb as an atom or a singly charged positive ion; the probability is controlled by the desorption energies of the two species. It is important to note that the Saha-Langmuir equation applies only to an atomic beam impinging on a hot surface; it does not apply to the single-filament situation. It is easy to see why: As the temperature is raised, the element in question evaporates from the surface at a progressively faster rate, an effect not addressed by the equation. To illustrate this point, the author has over the decades analyzed over 30 elements by positive thermal ionization using single filaments; in all cases but those of the most refractory elements (e.g., Th), there is a temperature that if exceeded will lead to evaporation so fast and complete that it is impossible to recover and get a good analysis; this phenomenon has also been reported by Heumann for iron [35]. Such observations are not predicted by the equation.

The Saha-Langmuir equation also does not apply to situations in which chemical as well as physical processes occur at the ionizing filament. An instance of this is the double- or triple-filament arrangement common in thermal ionization, in which procedures that ensure stable ion emission cause species other than gas-phase atoms to impinge on the ionizer. An example of this is uranium; the loading procedure includes heating the filament to dull red heat in air for a few seconds. The uranium is almost always loaded in a weak nitric acid solution, which means uranium is present in oxide form. The heating step is an oxidative one, presumably taking uranium to its highest oxidation state. Because uranium oxides are more volatile than the metal, this procedure ensures that almost all the uranium evaporates as either UO or UO_2, which in turn means interaction with the ionizer must break the U-O bond as well as produce U^+. This is not the situation described by the Saha-Langmuir equation [15].

Despite these caveats, the Saha-Langmuir equation is useful in predicting order-of-magnitude estimates of ionization efficiency and in comparing ionization efficiencies of two or more elements. For example, the ionization efficiencies of Pu, U, and Th calculated from the equation are relatively correct, approximately corresponding to experimentally observed behavior, which is roughly an order of magnitude decrease in efficiency with each step in going from Pu to U to Th.

1.4 INSTRUMENTATION

Most isotope ratio measurements have been performed using sector mass spectrometers. Some work has been reported, notably by Heumann [35], in which a quadrupole-based system was used. Instruments used for measurement of isotope ratios are most often dedicated to that purpose. In most instances only a relatively small mass range needs to be monitored, just enough to encompass the isotopes of the analyte element. Without the ability to scan the entire elemental mass range [usually from m/z = 6 (Li) through m/z = 238 (U) for elemental analysis], mass spectrometers designed to measure isotope ratios cannot readily be adapted for other purposes. See Chapter 2 for a discussion of instrumentation required for elemental analysis of solid materials and Chapter 3 for a treatment of the instrumenation needed for elemental analysis of solutions.

1.4.1 Filament Considerations

The filament material most commonly used in thermal ionization is rhenium. There are several properties that dictate its choice. It has a high enough melting point (3180°C) that it can withstand the temperatures required for efficient ionization (up to about 2200°C). It has the highest work function of any metal with a high enough melting point; like all metals, its work function varies with the crystal

face in question and ranges from about 5.0 eV to about 5.8 eV, with 5.4 eV the average for the polycrystalline material [36]. Platinum has a higher work function (5.7 eV) than rhenium, but its melting point is too low (1772°C) for it to be useful as filament material in many applications. In addition to its high work function, rhenium has mechanical properties that make it attractive as filament material. For example, unlike tungsten, it retains its ductility after heating or spot welding. Another advantage important in many applications is that rhenium metal is available in high purity (>99.999%). The advent of zone refining led to large improvements in purity; prior to that, it was extremely difficult to analyze thorium using rhenium filaments because thoria-lined furnaces were used in annealing the metal. Aside from rhenium, the two most commonly used metals for filaments are tungsten and tantalum. The work functions for these elements are about 1 eV lower than rhenium's, so in general ion emission is lower. Tantalum has seen widespread use as an evaporator filament in multifilament configurations; work function is irrelevant, it is less costly than rhenium, and the relatively low temperatures required of evaporators make demands on purity less stringent. There are also special applications in which use of rhenium is inappropriate; an obvious instance is an application in which rhenium is itself the analyte element.

There are two filament configurations used in thermal ionization: single-filament and multifilament; multifilament configurations can have two or three individual filaments. All these configurations are illustrated in Fig. 1.4. The choice

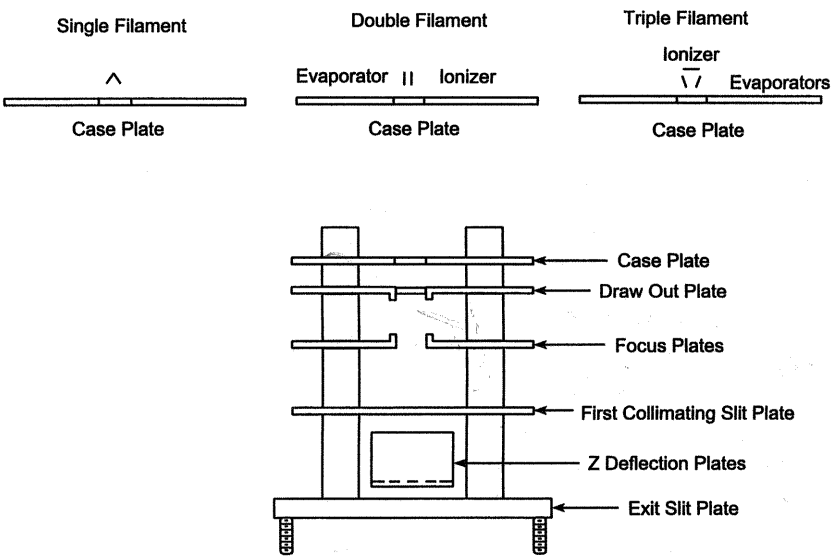

Figure 4 Ion source configurations used in thermal ionization mass spectrometry.

between them is made on the basis of the needs of the experiment. Multifilament configurations are most common. There can be either two or three filaments, but the principle of operation is identical for each. The sample is loaded on a side filament, which is often made of tantalum rather than the more expensive rhenium. The sample is evaporated from the side filament at a temperature that depends on the volatility of the element undergoing analysis. This vapor, which is not necessarily atomic, impinges on the ionizing filament, which is almost invariably made of rhenium and maintained at a constant high temperature; 2100°C is common. Ions generated at this surface are subjected to the extraction field of the ion source, are accelerated, and undergo mass analysis. The temperature required for the evaporating filament is substantially lower than that required for ionization when only a single filament is used; for uranium, for example, the two temperatures are 1500°C for the evaporator and 1700–1800°C for single-filament ionization. Sample size is usually in the microgram range when Faraday cup detection is used; as a result, such detectors are common in multifilament systems.

It is necessary to obtain stable emission from the evaporator if results of high quality are desired. In general, each element requires a different procedure, although of course some elements behave similarly. Samples and standards are treated as much alike as possible to ensure that data are taken on that portion of the fractionation curve for which calibration is valid; this topic is treated in greater detail later.

In the single-filament configuration, the same surface serves both to evaporate and to ionize the sample. It is more efficient than multifilament configurations

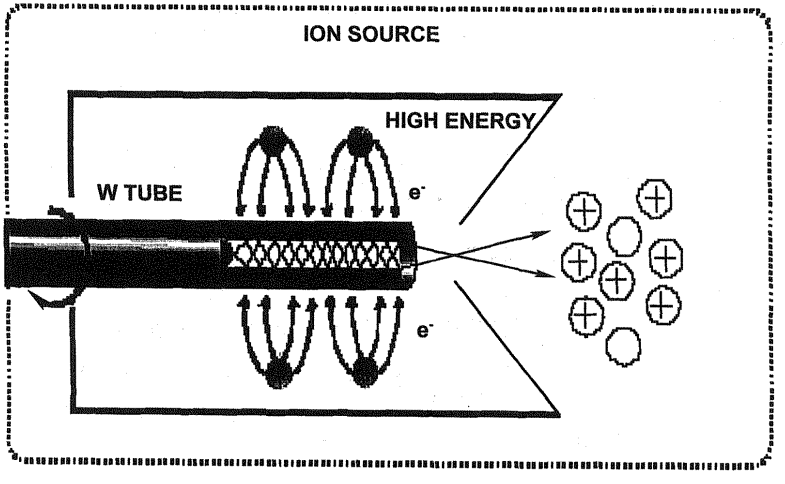

Figure 5 Drawing of new high-efficiency ion source. (From Ref. 37.)

when ions collected are compared to atoms loaded; the value of this ratio is, of course, element-dependent. For many elements, samples of 1 nanogram or less can be routinely analyzed provided a pulse-counting detection system is employed.

A new thermal ionization source developed by Olivares and coworkers at Los Alamos National Laboratory is much more efficient at production of ions than the more conventional filament configurations described previously [37]. Designed originally for use in isotope separators, it has been modified for use in isotope ratio measurements using a quadrupole mass spectrometer. Called a *thermal ionization cavity*, it is designed around a tungsten tube that contains the sample and is heated by electron bombardment. A drawing of this source is given in Fig. 1.5. Because of the amount of heat generated the source must be water-cooled, making it more complex than conventional designs. Ionization efficiencies are very high in comparison to those of normal thermal ionization sources. Efficiency for europium is 72%, for uranium 8%, and for thorium 2%, all figures an order of magnitude or more better than single-filament results. Typical precision for isotope ratio measurements is quoted as $\pm 0.1\%$.

1.4.2 Collectors

The two most common types of detection systems used in isotope ratio measurements are Faraday cups and pulse-counting electron multipliers. Multipliers are occasionally used in current-integration mode but are not as precise as Faraday cups or as sensitive as pulse counting; there seems to be no compelling need for this mode of operation in thermal ionization. All these collectors, of course, are used in many different kinds of mass spectrometry. Faraday cups give better precision and require more sample than pulse counting; choice of collector is often dictated by the demands of the experiment (or, of course, by available equipment). Each type of collector has its strengths and weaknesses. Constructing a Faraday cup that is quiet and linear is not a simple task. Pulse counting, in which each ion is counted as it arrives at the collector, requires fast electronics that must be very quiet; typical background counting rates in good systems are about one count a minute, approximately the cosmic ray background. An example of a pulse-counting detection system is shown schematically in Fig. 1.6. Multipliers are operated at negative potential for detection of positive ions; 2–4 kV is typical in pulse-counting applications. Each dynode is successively nearer ground than its predecessor, so the potential gradient across the detector causes secondary electrons to travel through it from the first dynode to the last; transit times of 1 nsec or so are typical. Ions strike the first dynode of an electron multiplier; each such impact generates two or more electrons, resulting in amplification of the original signal. The electron cascade passes from one dynode to the next, each stage effecting amplification of the original signal, with the pulse from the last dynode

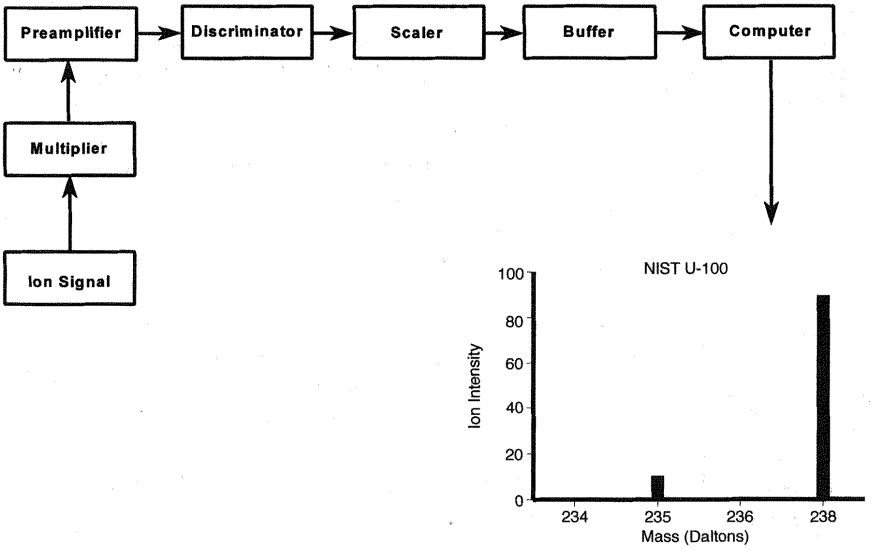

Figure 6 Schematic diagram of a pulse-counting detection system.

being the output of the device. Multipliers used in pulse counting usually have 14 to 17 dynodes. Typical gains for pulse-counting multipliers are on the order of 10^6–10^8, far greater than when current integration is used. The signal pulse from the multiplier then goes through a preamplifier, with gains of 10 to 30 being typical. A discriminator is used to screen out dark-current noise from the multiplier. The situation is depicted in Fig. 1.7. There will always be some residual noise in any pulse-counting system, some of which is caused by cosmic rays. After the discriminator, the signal passes to a scaler, which accumulates the counts in one channel (or whatever term is used to describe the minimum time unit of the data system); the number of bits in the scaler, together with the dwell time, determines the maximum count rate the system can handle without overloading. The single number of counts accumulated in the scaler is then passed to a buffer, where it is stored until it is transferred to the computer. There is a period after the arrival of an ion in which the counting system is paralyzed; this is called the *dead time* and is about 10 nsec in fast systems. Any ions arriving during this interval will not be registered; a spuriously low number of counts will result. The dead time varies with individual multipliers and must be measured in some way. The appropriate correction is then applied to the count rate; this has the effect of putting an upper limit on the count rate that must not be exceeded if the best results are desired. Conversion efficiency at the first dynode of multipliers is dependent on the velocity of the ions striking it [38]. It is also dependent on chemical species

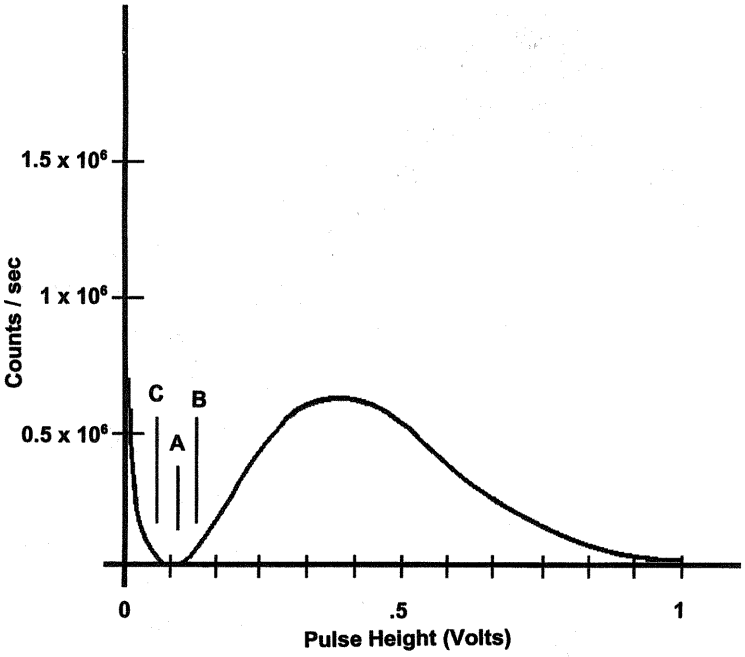

Figure 7 Operation of a discriminator.

[39] and ionic mass [40]. This matter has been discussed in some detail by Hayes and Schoeller [41].

Because instability in beam intensity is a primary cause of imprecision in isotope ratio measurements, it is a big advantage to monitor all isotopes of interest simultaneously. Commercial instruments are available with multicollector arrays that effect this [42,43], a drawing of one of these is given in Fig. 1.8 [43]. Note that the axial collector is recessed behind the focal curve. Since the ion beam spreads after crossing the focal point, the result is that a smaller fraction of the beam is intercepted by the axial collector than by the others. This fact must be addressed when calibrating the instrument. Multicollector arrays provide precision that, with proper care, can be better than 100 ppm [44]. One price paid for this advantage is the necessity of calibrating the detectors with respect to each other. Constant signal sources are provided in commercial instruments to effect cross-calibration of detectors. The more subtle problem of loss of linearity of individual pockets with use has been addressed by Fiedler and Donohue [45]. The concern of these authors was that, as sample elements accumulate in the Faraday pockets with time, the amplification characteristics might change; this effect is a small one and

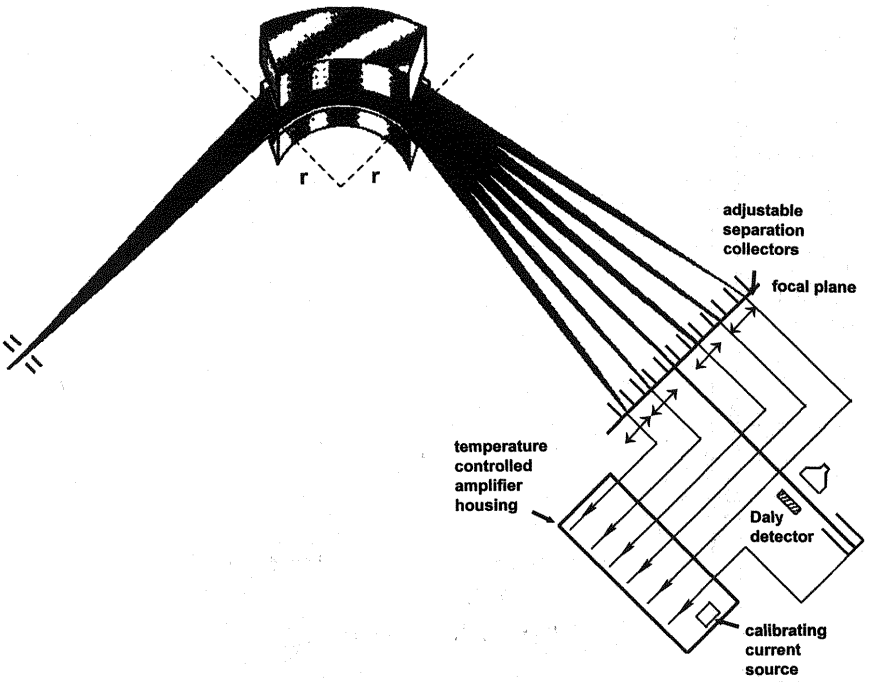

Figure 8 Schematic drawing of a multicollector mass spectrometer.

would be predicted to be element-dependent. At the time of writing detector arrays are available only as Faraday cups; it has thus far not been possible to reduce the size of electron multipliers sufficiently to use them in arrays, and position-sensitive detectors lack the necessary dynamic range ($>10^6$) and tend to be too noisy. The trade-offs between detector systems thus involve balancing precision requirements against those of sample size.

1.4.3 Scanning the Mass Spectrum

Either the ion source high voltage or the magnetic field can be swept to scan the mass spectrum—unless, of course, a multidetector array is used, in which case the spectrum need not be swept. Magnetic sweeping is in general to be preferred to high-voltage sweeping because, when the voltage is swept, each isotope experiences a slightly different extraction field; this introduces mass-dependent bias for which correction must be made. There are circumstances, however, when the advantages of voltage scanning outweigh the drawbacks. One occurs when the mass spectrometer has two magnetic sector fields in tandem; it is difficult to make

the two magnetic fields track together with enough precision to preserve the flat-topped peaks required for isotope ratio measurements. The only other time high-voltage scanning is desirable is when the smallest possible samples must be analyzed; because the voltage can be scanned many times faster than the magnetic field, more information can be obtained from a rapidly diminishing signal when it is near its maximum intensity.

In all cases, one goal of sweeping the mass spectrum is to combine it with slit settings to achieve flat-topped peaks. The sharp, triangular peaks commonly seen in organic applications are undesirable when the primary goal is to determine the areas of the peaks (which are more reliable measures of peak intensity than peak heights) rather than their locations on the mass scale. Resolution in isotope ratio mass spectrometers is usually about 500; therefore, it is not possible to separate molecular isobars from the isotopes of interest. This places stringent demands on sample preparation, a topic addressed in Sec. 1.6.

1.4.4 Mass Spectrometers

The goal of any sector mass spectrometer is to transfer an ion beam from the image point of the ion source to the detector without significant degradation of beam shape. One of the earliest extensive treatments of ion optics in mass spectrometry was presented by Hintenberger and König in 1959 [46]. As computers have become more powerful, programs to assist in designing mass spectrometers have become more common. There are now programs of great sophistication available to help design instruments of whatever characteristics of almost any configuration.

A critical measure of performance in isotope ratio measurements is *abundance sensitivity*, which is defined as the intensity of a large peak divided by the intensity of the background 1 mass unit lower; it is sometimes defined as the reciprocal of this ratio. This means that, for uranium, for example, if 10^6 counts are collected for ^{238}U and there is one count at $m/z = 237$, the abundance sensitivity is 10^6 (or 10^{-6}). The reason the low-mass side of the intense peak is specified is that gas-phase collisions cause scatter in the ion beam that reduces abundance sensitivity; these collisions result in loss of energy far more often than gain, which means scatter is greater on the low-mass side of the peak. Most mass spectrometers used with thermal ionization sources are designed to have high abundance sensitivity. These most commonly feature a single magnetic sector. A drawing of one of these instruments is given in Fig. 1.9. First developed at what was then the National Bureau of Standards by Shields [47], it is in use in several laboratories around the world. Its magnet has a 30.5-cm radius of curvature with a 90-degree angle of deflection. An extended flight path combined with nonnormal exit from the magnetic field (82°) are used to correct for fringe fields [48].

Very high abundance sensitivity ($>5 \times 10^5$) can be achieved by adding a second magnet after the first, as first suggested by White and Collins [49]. The

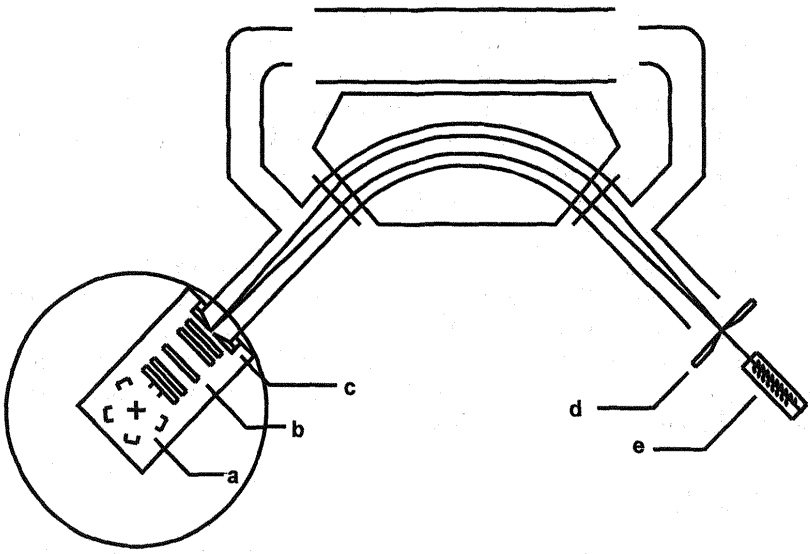

Figure 9 Magnetic sector pulse-counting mass spectrometer: (a) ion source, (b) ion lens, (c) source defining slit, (d) collector slit, (e) electron multiplier. (From Ref. 47.) (Courtesy of P. H. Hemberger, Los Alamos National Laboratory.)

function of this magnet is not to effect mass separation, which is accomplished in the first magnetic field, but to clean up the tails of the peaks and thus improve abundance sensitivity. Because it is energy spread that is being addressed, the same result can be accomplished through use of an electrostatic analyzer [50] or a quadrupole filter [51].

Most analytical problems do not require an abundance sensitivity of more than 500,000, which is about the maximum available with a single magnetic sector of reasonable size. Instruments with additional stages, either magnets or electrostatic analyzers or both, have been constructed to provide abundance sensitivity greater than 10^8; Fig. 1.10 is a photograph of one such instrument at Oak Ridge National Laboratory [50].

1.5 CALIBRATION

Accuracy of isotope ratio measurement is critically dependent on having the instrument properly calibrated and following correct analytical protocol. Mass bias is present to some degree in all thermal ionization analyses, and a lot of ingenuity has been invested in mitigating its effect. Mass bias arises from a

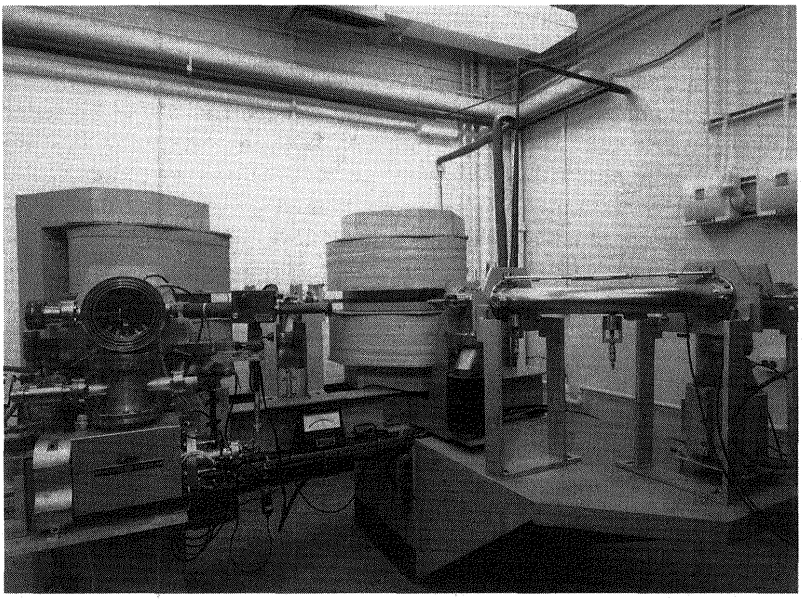

Figure 10 Three-stage sector mass spectrometer with high-abundance sensitivity.

number of different causes. Evaporation of the sample is to some degree mass-dependent; light isotopes evaporate more readily than heavy, presumably as the inverse square root of their masses. Extraction of the ions into the source-focusing lens has similar mass dependence. Transmission through some types of mass analyzers (quadrupoles) is a function of mass. Conversion of the ion to a pulse of electrons at the collector is also mass-dependent. It is experimentally extremely difficult to isolate these effects individually. The usual way of dealing with them is to lump them into one bias correction factor and not worry about the values of the individual contributions.

Certified isotopic standards are available for some elements but by no means all. Such standards are available from the National Institute of Standards and Technology [52] and New Brunswick Laboratory [53] in the United States, and from the Institute for Reference Materials and Measurements [54] in Belgium. De Bievre et al. have published a review of reference materials available for isotope ratio measurements [55]. It is clearly desirable to use certified materials for instrument calibration if at all possible. If no standard is available for the element in question, the analyst has little choice but to obtain a pure sample of it and assume it has the composition listed by IUPAC [1]. A few elements, with lead being the outstanding example, have isotopic compositions that vary widely in

nature; care must be exercised in these cases (although there is a NIST certified isotopic standard for lead).

Certified standards or no, the same procedure is followed. The value of an isotopic calibration ratio is measured for the reference material and compared to the certified (or accepted) value. The correction factor necessary to adjust the measured value to the certified is calculated; it is then the bias correction for that ratio. Most often, a bias correction per mass is used. Even though the actual variation of bias is not strictly linear, the limited mass range swept for a single element makes it a good approximation; any deviation from linear is insignificant in comparison to measurement uncertainties. Typical biases are a few tenths of a percent per mass when a single-filament configuration is used and somewhat less for multifilament. Multifilament analyses are in general less susceptible to variations in bias correction than single-filament, but they are by no means immune.

Bias corrections determined from analysis of standards are applied to the samples under test. Use of such an average bias correction can be viewed only as an approximation to the truth; so many factors contribute to bias that it is impossible to control them all. For example, as previously stated, the work function of a rhenium filament is determined by which crystal face is involved. One way of loading samples on filaments is through use of single resin beads [56,57]. The beads are 100–200 μm in diameter, which is about the size of rhenium crystallites in a polycrystalline filament [17]. Clearly the work function applicable to the analysis in question may or may not be that operative when instrument calibration was carried out. Another parameter difficult to control in real-world conditions is sample purity, which also affects bias. It is impossible to purify all samples to the same degree, and contaminants adversely affect ionization efficiency; low efficiency means higher filament temperatures, which in turn mean a different bias correction. These are only two of sundry variables that can affect ionization efficiency.

In practice, the analyst monitors the bias correction through analysis of a reference standard on a routine, often daily, basis. This value comes to be known very well and makes insignificant contributions to overall precision. Even though it may not be truly applicable to the sample being analyzed, using it is far better than applying no correction; it is the best that can be done in an imperfect world. A model of thermal fractionation on mass spectrometer filaments has been developed by Habfast [58].

Fractionation is such a vexing problem that other means of addressing it have been devised. One is *total exhaustion*, in which the entire sample is consumed; it has been successfully applied to uranium [59] and the rare earths [60]. The idea here is that, if all ions emitted from the sample are collected, they will be representative of the sample itself, and no bias correction will be required. Because signal intensity varies rapidly, running to exhaustion can only be accomplished using a multicollector mass spectrometer. It also requires a reasonable

estimate of the amount of the target element in the sample, information not always available.

Another way of addressing variations in bias is through the use of an internal calibration ratio. In this technique, there are two isotopes of the analyte element whose ratio is well known that can be used to calculate the specific bias applicable to the analysis in question. It has long been used in geological applications; in strontium analysis, for example, the $^{86}Sr/^{88}Sr$ ratio is invariant in nature and can be used to calculate the bias necessary to apply to correct the $^{87}Sr/^{88}Sr$ ratio [2]. Dietz et al. were the first to suggest use of internal calibration through addition of a two-isotope spike to the sample [61]; they tested it with uranium. If the ratio of the two reference isotopes is well known, it can serve as the comparison necessary to effect internal calibration. This ratio is measured for each run and its value compared to the known. The bias factor required to bring the measured ratio into agreement with the known is calculated and applied to all other ratios. The theory underlying internal calibration has been described by Dodson [62,63]. It has been applied to uranium [64,65] and to molybdenum [66], plutonium [67], and lead [68]. In principle it should be applicable to concentration measurements of any element with three isotopes, two for the spike and one for the sample; it can also be used to refine the value of a ratio of two isotopes, both of which are either absent or present only in low abundance in the spike. One of the most attractive features of the double spike is that it should produce results independent of individual laboratory calibration methods. Instrumental bias is one of the major causes of disagreement between laboratories, but use of the same double spike requires that all laboratories make corrections based on the same isotopic ratio independently of differences in their methods. This matter was addressed in a recent study [69].

1.6 ION EMISSION

A long-standing and still-current challenge in thermal ionization mass spectrometry is to improve ionization efficiency. This is usually defined experimentally as the ratio of ions collected to the number of atoms loaded; it thus includes all aspects of the ionization, extraction, transmission, and collection processes.

One obvious way to improve ionization efficiency is to make sure the sample is as clean as possible. A heated filament provides a constant amount of energy, and any devoted to evaporating or forming ions of contaminant species is lost to the desired process. Sodium, potassium, calcium, and other readily ionized elements are bad actors; the fact they are also ubiquitous makes the problem just that much more difficult. Every element presents its own challenges, and much effort has been invested in purifying target elements of interest. Loading a chemically pure sample on the filament is one way to improve ion emission.

There are many instances in which it is highly desirable to analyze the smallest possible sample. This is of obvious importance when radioactive species are involved, but it is also advantageous when analyzing smaller samples means processing smaller amounts of material for an analysis, as is often the case in geological applications, among others. Measurement of isotopic ratios from picogram or smaller quantities of analyte has been reported for technetium [70,71], actinide elements [72], and rare earth elements [73].

Since analysis of small samples requires pulse-counting detection systems, most of the effort directed toward improving ionization efficiency has involved the single-filament configuration. Most ion-optical systems are designed on the assumption that there will be a point source of ions. Many ion source lenses are very strongly focusing, and even slight deviations in sample location from the object point of the source cause marked reduction in ion extraction efficiency. A loading technique that serves to concentrate the sample in a very small area of the filament, and thus to approximate a point source, is highly desirable. Two such techniques have been developed in which this is just one of several attractive features. One is electroplating the sample from a very small (ca. 1 μL) volume onto the rhenium filament [18]. The other is to load samples on the filament using single resin beads [74]. Because each of these methods provides advantages in addition to providing point sources (discussed later), it is difficult to quantify the benefits of this particular aspect. Overall improvement in performance with regard to reduction in sample size is in the range of 5 to 10 for each technique.

A different issue is the challenge of improving ionization efficiency. Two situations have been addressed. One is to combat the combination of high volatility and high first ionization potential, which prevents effective production of singly charged positive ions. The classical example here is lead, an element important in geological age dating [2]. Its combination of first ionization potential (7.4 eV) and melting point (328°C) militates against efficient ionization. Loading lead onto a single filament as a solution produces ionization characteristics almost impossible to reproduce, but using silica gel slurried in phosphoric acid produces a glass that serves as an emitter and reproducibly yields intense, long-lasting, stable ion signals and allows analysis of nanogram-sized samples [16].

The second situation to be addressed involves improving ionization yields from elements refractory enough that loss of sample due to volatility is not a major problem but whose ionization potential is high enough to cause difficulty. Since the first ionization potential of an element cannot readily be altered, it is the work function of the surface that has drawn investigators' attention. The work function of polycrystalline rhenium is about 5.4 eV [36], but there are other materials with higher values. One is platinum, whose work function is about 5.7 eV [75], but whose melting point is too low for use with many elements. Perrin and coworkers developed a method in which a plutonium sample is electroplated directly onto a rhenium mass spectrometer filament [18]. This was followed by electroplating a

layer of platinum over the sample. The sample atoms are thus forced to migrate through the platinum layer before leaving the filament. In this manner, the advantages of using rhenium as a filament material (high melting point, ductility) were retained while the higher work function of platinum was exploited to enhance ionization efficiency. A mean ionization efficiency of 0.34% for plutonium was reported; that efficiency is a substantial improvement when compared to analyzing samples loaded as solutions, which is generally an order of magnitude lower.

Similar reasoning led Smith and Carter to develop a method using an overlayer of pure rhenium powder slurried with a source of carbon, such as starch solution [19]. Rhenium and carbon do not form a stoichiometric compound, but carbon dissolves in the metal to form a composite surface that has higher work function than pure polycrystalline rhenium; this has been measured as 5.8 eV, about the same as the work function of platinum [26]. Rhenium powder, when heated to the operating temperatures required for many elements (>1500°C), sinters to form a barrier to evaporation that forces analyte atoms to migrate through it before leaving the filament. Thus, in a manner similar to the platinum overcoat electrolytically deposited, the advantages of rhenium as a filament material and an emitting surface of high work function are both exploited. The higher work function explains in part the benefits derived from loading samples on resin beads; the carbon skeleton of the bead that remains after its thermal decomposition dissolves in the rhenium substrate, forming a local surface with a higher work function than that of the surrounding metal [17].

It is not clear which of the two overcoating methods provides greater enhancement in ionization efficiency. Smith et al. report ion collection efficiencies of 4%–9% for plutonium [76], but this was for an experiment specifically designed to evaluate this ability; Perrin et al. [18] were more concerned with improving the stability of their ion beam (and hence precision) than they were with determining ionization efficiency. Substantially improved ion beam stability and reduced isotopic fractionation were noted by both sets of authors as a significant benefit of both methods of overcoating.

1.7 APPLICATIONS

Thermal ionization has widespread application in areas where measurement of isotope ratios is the goal of the analysis. Each area has its unique problems and challenges, and there is considerable cross-fertilization among disciplines. Exhaustive treatment would require a book of its own; no attempt has been made here to cover all areas addressed by thermal ionization. Rather, a few areas of current and historical interest have been selected; these should give the reader a good idea of the versatility of the technique.

1.7.1 Geological Applications

One area of major importance is in geological applications. There are about 25 radionuclides whose half-lives are long enough that they are still present in the Earth's crust, having been there at the Earth's formation; these range from ^{235}U with a half-life of 7.1×10^8 years to ^{209}Bi with a half-life in excess of 10^{19} years [77]. There are in addition about 30 radionuclides whose half-lives are too short for them to have survived from the primordial Earth that are present because they are decay products of uranium and thorium; the most abundant is ^{234}U, whose half-life is 2.45×10^5 years and which comprises 55 ppm of naturally occurring uranium [72]. Radioactive decay is a statistical process whose rate is measured by the nuclide's half-life. A radionuclide and one of its stable daughters constitute a geological clock from which the age of the formation in question can be determined. Some of the common methods involve performing mass analysis using thermal ionization. Among these are Rb-Sr, U-Pb, and Nd-Sm. The interested reader is referred to the excellent book by Faure, which covers application of isotope ratio measurements to all aspects of geology [2].

Deviation of an isotopic ratio in a mineral from its normal value can give insight into climatic conditions of past ages during which the mineral deposits formed. Because isotopic fractionation is a function of the mass of the isotopes, lighter elements are more sensitive probes than heavier elements in this area. Boron is an example; even though its two isotopes differ by only 1 mass unit (m/z 10 vs. 11), the 10% difference is quite high. This is in a sense a two-edged sword, for the very reason it is a sensitive geological probe makes isotopic fractionation of the elemental ions at m/z 10 and 11 under thermal ionization conditions unacceptably high and difficult to control. For this reason, a molecular metaborate ion is usually monitored; $Cs_2BO_2^+$ (m/z 308, 309) is a common choice [78]. For example, the $^{10}B/^{11}B$ ratio was used to study the origins of zoned deposits that crystallized from ancient lakes [79]. The investigators were able to identify borate deposits originating via several different mechanisms in a commercially important source of boron.

1.7.2 Cosmological Applications

Among the questions of importance to cosmology are the elemental composition of stars and other galactic matter and the isotopic compositions of those elements. Investigations of this type have covered several decades and represent a nice collaboration between theoretical astrophysicists and mass spectrometrists [80]. Thermal ionization has played a role in analysis, both isotopic and, through isotope dilution, of concentration, of many of the elements and helped resolve some of the anomalies that were present in the results of early work. Isotope dilution is inherently a precise method of quantification and was able to reduce

uncertainties in the concentrations of many elements [see, for example, Nakamura (81)].

Elements are formed by three different mechanisms in stars, as elucidated by Burbidge et al. [82]. In brief, these are the *s* process, involving the capture of slow neutrons by nuclei; the *r* process, involving the capture of rapid neutrons; and the *p* process, which leads to neutron-deficient nuclides that are generally less abundant than those generated by the *s* and *r* processes. The relative abundances of the various isotopes of a given element reveal which processes, or combinations thereof, are involved in their creation in the nuclear reactions that power stars. Measurements of isotopic and elemental abundances in stars thus serve to test theories of stellar processes.

Mass spectrometry in general and thermal ionization in particular have helped identify type 1 carbonaceous chondrites (C1) as the extraterrestrial bodies that best represent the composition of stars, gaseous nebulae, and other galactic entities [80]. This is because, of all the meteorites that fall to Earth (known as the poor man's space probes), carbonaceous chondrites have undergone the least metamorphism and thus retain more of their original volatile element content. There is excellent agreement between the composition of these chondrites and measurements of the elemental composition of the solar photosphere and of many other stars [83]. The distribution of even and odd mass nuclides in carbonaceous chondrites forms a smooth curve, whereas such distributions in other meteorites do not; a plot of this elemental distribution is given in Fig. 1.11. The fact that even-proton elements are more abundant than odd-proton elements and have more isotopes has long been known and is confirmed in this plot [84]. The most recent of numerous tables of cosmic elemental abundances was published by Anders and Grevasse in 1989 [85]. Cosmological application of mass spectrometry was recently reviewed by De Laeter [80].

1.7.3 Nuclear Applications

The nuclear area is one that has been heavily dependent upon isotope ratio mass spectrometry performed by thermal ionization. Applications in this area are among the major reasons for the continued push to analyze smaller and smaller samples. There are two primary reasons for this: (1) maximum practicable reduction of the hazards associated with radioactivity and (2) presence of often only a very small amount of the target element available. Areas addressed include evaluation of uranium enrichment processes [86], isotopic analysis of transuranium elements (all elements through einsteinium have been analyzed) [87], and environmental monitoring for release of uranium and other actinides [88,89]. This last area has received renewed emphasis in the wake of the Gulf War [90].

Isotopic analysis has been used extensively in addressing questions of fundamental physics. Walker et al. used the Dounreay reactor to refine values of

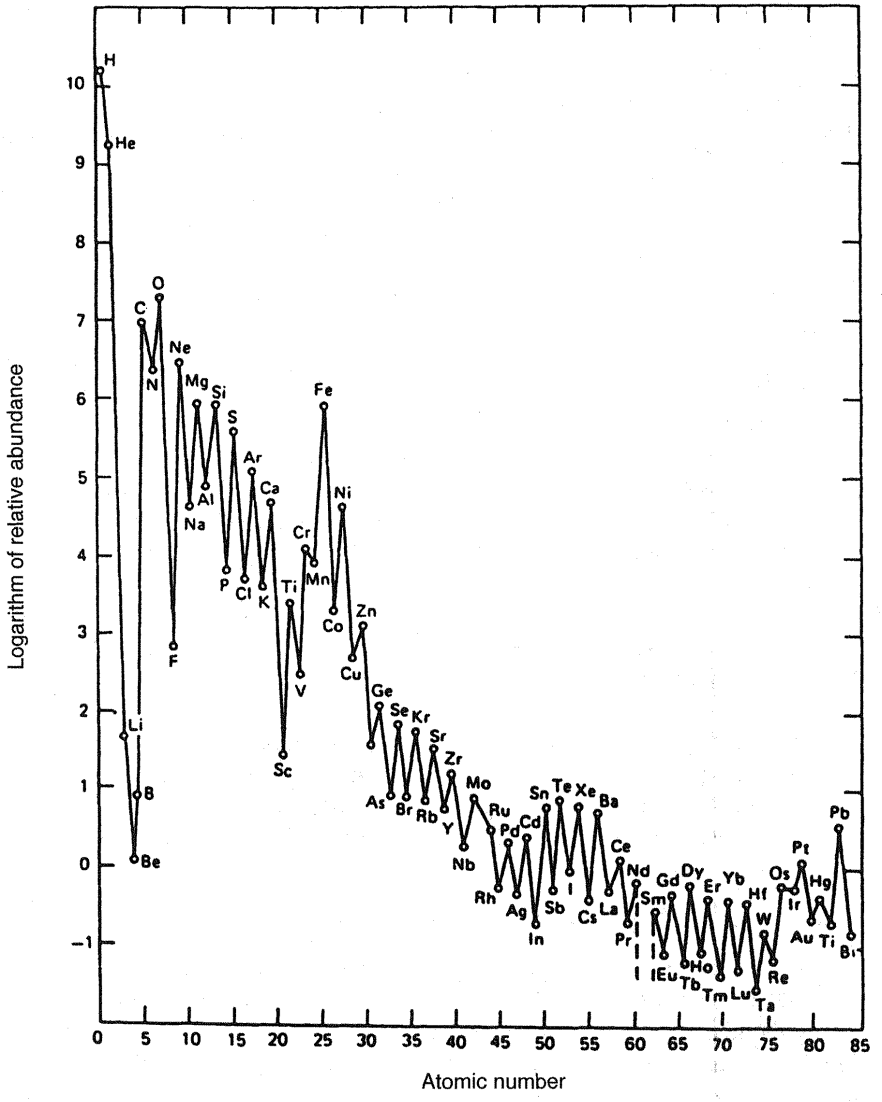

Figure 11 Relative galactic abundances of the elements normalized to Si = 10^6 atoms. (From Refs. 80 and 111.)

cross sections and other nuclear parameters [91–93]. The half-life of ^{241}Pu (14.35 years), about which there was much uncertainty, was measured by DeBievre et al. to unprecedented accuracy [94]. Kelly described procedures to eliminate systematic bias due to isotopic fractionation and interference from ^{241}Am in this measurement [95]. Economical operation of power reactors is dependent upon changing of fuel rods at optimum intervals. To do this, the amount of fuel consumed (called burn-up) with time must be determined; an ASTM procedure prescribes how this is achieved [96]. The information required is the isotopic compositions and concentrations of uranium, plutonium, and neodymium, all of which are determined using thermal ionization mass spectrometry. Green et al. described determination of this important parameter [97]. De Laeter has published a review of the role of mass spectrometry, including thermal ionization, in studies of nuclear fission [3].

One of the most fascinating events in the Earth's history was the naturally occurring reactor at Oklo in Gabon. It was discovered in 1972 through the insistence of a French mass spectrometrist that the measured ^{235}U abundance of 0.7171% (0.5% low) was significantly different from the natural value and warranted investigation. Subsequent measurement of the isotopic composition of the rare earth elements (particularly neodymium) revealed the existence of a natural reactor about 2 billion years ago when the abundance of ^{235}U was much higher than it is today [98,99]. Subsequent studies were performed to characterize various reactor parameters; mobility and retentivity, properties of importance in the isolation of nuclear waste, of many elements have also been studied. These investigations revealed that criticality was reached in several zones in the ore body; new ones are still being discovered. The uranium itself has been preserved virtually intact in its original distribution, a remarkable fact after the passage of so much time. Loss et al. were able to show that the fission process at Oklo lasted for hundreds of thousands of years [100]; criticality in Zone 9, for example, lasted approximately 2.2×10^5 years. Investigations of the Oklo phenomenon have been summarized by De Laeter [3] and extensively described in two publications from the International Atomic Energy Agency [101,102]. Aside from the inherent scientific interest in such an apparently unlikely phenomenon, Oklo studies have direct bearing on various issues involving isolating nuclear waste, as has been pointed out by Ruffenach et al. [103].

1.7.4 Atomic Weights

Thermal emission has played a role in determination of atomic weights. Such work is of great importance and requires scrupulous attention to detail. For the many elements for which no certified isotopic standard is available, it is the abundance measurements made during such experiments that serve as the reference values for calibration of mass spectrometers in other laboratories. Sample

preparation, elimination of contamination, and calibration of the mass spectrometer all need to be meticulously addressed. All sources of bias must be identified and corrected. This often requires making synthetic mixtures of chemically pure and isotopically pure (as nearly as possible) enriched isotopes. Very few laboratories have the interest, the ability, and the support to perform such measurements. DeBievre and Peiser have described the history of, and some of the issues involved in, atomic weight measurements [104]. Recent determinations of atomic weights using positive thermal ionization include those for tin [105], europium [106], iron [107], antimony [108], and titanium [109]. This subject and others associated with metrology have been extensively treated in a review by De Laeter et al. [110].

1.8 SUMMARY

Thermal ionization mass spectrometry is an exceptionally valuable analytical tool. Its combination of high precision and high sensitivity makes it applicable in a wide variety of situations in which isotopic ratios are sought. In conjunction with isotope dilution, it provides quantitative analyses that are usually of higher quality than those yielded by any other method.

Isotope ratios provide insight into the physical and chemical processes that cause alteration of their values. Their application is expanding as analytical procedures become more sophisticated and sensitive, and as the extent of scientific knowledge increases. As in many fields, much work done today would have been impossible a few years ago. With the advent of multicollector inductively coupled plasma (ICP) mass spectrometers, it is probable that routine use of thermal ionization will diminish, but it seems that it will always play a role in applications in which utmost sensitivity is required.

REFERENCES

1. IUPAC Commission on Atomic Weights and Isotopic Abundances. *Pure Appl. Chem.* **1994**, *66*, 2423.
2. Faure, G. *Principles of Isotope Geology*, 2nd Edition, John Wiley & Sons, New York, 1986.
3. De Laeter, J. R. *Mass. Spectrom. Rev.* **1996**, *15*, 261.
4. Nusko, R.; Heumann, K. G. *Fresenius J. Anal. Chem.* **1997**, *357*, 1050.
5. Eisenhut, S.; Heumann, K. G. *Fresenius J. Anal. Chem.* **1996**, *354*, 903.
6. Eagles, J.; Fairweathertait, S. J.; Portwood, D. E.; Self, R.; Gotz, A.; Heumann, K. G. *Anal. Chem.* **1989**, *61*, 1023.
7. Gotz, A.; Heumann, K. G. *Fresenius J. Anal. Chem.* **1987**, *326*, 118.
8. Heumann, K. G. *Int. J. Mass Spectrom. Ion Processes* **1992**, *118, 119*, 575.

9. Heumann, K. G. *Mass Spectrom. Rev.* **1992**, *11*, 41.
10. Heumann, K. G.; Eisenhut, S.; Gallus, S.; Hebeda, E. H.; Nusko, R.; Vengosh, A.; Walczyk, T. *Analyst* **1995**, *120*, 1291.
11. Gehrcke, E.; Reichenheim, O. *Berichte der Deutschen Physikalischen Gesellschaft* **1906**, *8*, 559.
12. Dempster, A. J. *Phys. Rev.* **1918**, *11*, 316.
13. Kunsman, C. H. *Science* **1925**, *62*, 269.
14. Kunsman, C. H. *Proc. Natl. Acad. Sci.* **1926**, *12*, 659.
15. Langmuir, I.; Kingdon, K. H. *Proc. R. Soc. (London)* **1925**, *A107*, 61.
16. Cameron, A. E.; Smith, D. H.; Walker, R. L. *Anal. Chem.* **1969**, *41*, 525.
17. Smith, D. H.; Christie, W. H.; Eby, R. E. *Int. J. Mass Spectrom. Ion Processes* **1980**, *36*, 301.
18. Perrin, R. E.; Knobeloch, V. M.; Armijo, V. M.,; Efurd, D. W. *Int. J. Mass Spectrom. Ion Processes* **1985**, *64*, 17.
19. Smith, D. H.; Carter, J. A. *Int. J. Mass Spectrom. Ion Processes* **1981**, *40*, 211.
20. Kaminsky, M. *Atomic and Ionic Impact Phenomena on Metal Surfaces*, Academic Press, New York, 1965, Chapter 8.
21. Saha, M. N. *Phil. Mag.* **1923**, *46*, 534.
22. Tracy, J. C.; Blakely, J. M. *Surf. Sci.* **1969**, *15*, 157.
23. Kawano, H.; Itasaka, S.; Ohnishi, S. *Int. J. Mass Spectrom. Ion Processes* **1986**, *73*, 145.
24. Kaminsky, M. *Ann. Phys.* (Leipzig) **1966**, *18*, 53.
25. Hertel, G. R. *J. Chem. Phys.* **1967**, *47*, 335.
26. Smith, D. H. *J. Chem. Phys.* **1971**, *55*, 4152.
27. Hertel, G. R. *J. Chem. Phys.* **1968**, *48*, 2053.
28. Hughes, F. L. *Phys. Rev.* **1959**, *113*, 1036.
29. Smith, D. H. *J. Chem. Phys.* **1970**, *53*, 299.
30. Smith, D. H. *J. Chem. Phys.* **1971**, *55*, 1482.
31. de Boer, J. H. *Advances in Catalysis and Related Subjects*, Academic Press, New York, 1956, Vol. 8, p. 41.
32. Dobretsov, L. N. *Electron and Ion Emission*, National Aeronautics and Space Administration Technical Translation F-73, Washington, DC, 1952, pp. 280–287.
33. Frenkel, J. *Ann. Phys.* (Leipzig) **1937**, *28*, 319.
34. Smith, D. H. *J. Chem. Phys.* **1971**, *54*, 170.
35. Götz, A.; Heumann, K. G. *Int. J. Mass Spectrom. Ion Processes* **1988**, *83*, 319.
36. Zandberg, E. Y.; Tontegode, A. Y. *Zh. Tekh. Fiz.* **1965**, *35*, 325 (*Sov. Phys. Tech. Phys.* **1967**, *10*, 260).
37. Dian, Y.; Chamberlin, E. P.; Olivares, J. A. *Int. J. Mass Spectrom. Ion Processes* **1997**, *161*, 27.
38. Peast, B.; Harrison, M. F. A. *J. Phys. E* **1981**, *14*, 1374.
39. Dietz, L. A. *Rev. Sci. Instrum.* **1965**, *36*, 1763.
40. Cooper, G.; Zheng, Y.; Burton, G. R.; Brion, C. E. *Rev. Sci. Instrum.* **1993**, *64*, 1993.
41. Hayes, J. M.; Schoeller, D. A. *Anal. Chem.* **1977**, *49*, 306.
42. Micromass UK, Limited, Floats Road, Wythenshawe, Manchester, UK M23 9LZ.
43. Finnigan Corporation, 355 River Oaks Drive, San Jose, CA 95134 USA.
44. McBay, E. H.; Smith, D. H., unpublished results.

45. Fiedler, R.; Donohue, D. L. *Fresenius Z. Anal. Chem.* **1988**, *331*, 209.
46. Hintenberger, H.; König, L. A. *Advances in Mass Spectrometry*, J. D. Waldron, ed., Pergamon Press, New York, 1959.
47. Shields, W. R. *NBS Technical Note No. 426* **1967**.
48. Rokop, D. J.; Perrin, R. E.; Knobeloch, G. W.; Armijo, V. M.; Shields, W. R. *Anal. Chem.* **1982**, *54*, 957.
49. White, F. A.; Collins, T. L. *Appl. Spectrosc.* **1954**, *8*, 169.
50. Smith, D. H.; Christie, W. H.; McKown, H. S.; Walker, R. L.; Hertel, G. R. *Int. J. Mass Spectrom. Ion Phys.* **1972/73**, *10*, 343.
51. Schwieters, J. B.; Bach, P. *Proceedings of the 2nd Alfred O. Nier Symposium on Inorganic Mass Spectrometry*, Durango, CO, May 1–12, 1994, D. J. Rokop, J. E. Delmore, and L. W. Green, eds., AECL-11342, Chalk River Laboratory, Chalk River, Ontario, Canada, pp. 49–56.
52. National Institute of Standards, Gaithersburg, MD 20899.
53. New Brunswick Laboratory, 9800 South Cass Avenue, Argonne, IL 60439-4899.
54. Institute for Reference Materials and Measurements, Joint Research Centre, B-2440, Geel, Belgium.
55. De Bievre, P.; De Laeter, J. R.; Peiser, H. S.; Reed, W. P. *Mass. Spectrom. Rev.* **1993**, *12*, 143.
56. Freeman, D. H.; Currie, L. A.; Kuehner, E. C.; Dixon, H. D.; Paulson, R. A. *Anal. Chem.* **1970**, *42*, 203.
57. Walker, R. L.; Eby, R. E.; Pritchard, C. A.; Carter, J. A. *Anal. Lett.* **1974**, *7*, 563.
58. Habfast, K. *Int. J. Mass Spectrom. Ion Phys.* **1983**, *51*, 165.
59. Callis, E. L.; Abernathy, R. M. *Int. J. Mass Spectrom. Ion Processes* **1991**, *103*, 93.
60. Dubois, J. C.; Retali, G.; Cesario, J. *Int. J. Mass Spectrom. Ion Processes* **1992**, *120*, 163.
61. Dietz, L. A.; Pachucki, C. F.; Land, G. A. *Anal. Chem.* **1962**, *34*, 709.
62. Dodson, M. H. *J. Sci. Instrum.* **1963**, *40*, 289.
63. Dodson, M. H. *J. Sci. Instrum.* **1969**, *2*, 490.
64. Ridley, R. G.; Daly, N. R.; Dean, M. H. *Nucl Instrum Methods* **1965**, *34*, 163.
65. Callis, E. L. *Analytical Chemistry in Nuclear Technology*, W. S. Lyon, ed., Ann Arbor Science, Ann Arbor, MI, 1982, pp. 115–123.
66. Moore, L. J.; Machlan, L. A.; Shields, W. R.; Garner, E. L. *Anal. Chem.* **1974**, *46*, 1082.
67. Smith, D. H.; Walker, R. L.; Carter, J. A. USDOE Report ORNL/TM-9774, 1985.
68. Hamelin, B.; Manhes, G.; Albarede, F.; Allegre, C. J. *Geochim. Cosmochim. Acta* **1985**, *49*, 173.
69. Smith, D. H.; Hemberger, P. H., in preparation.
70. Anderson, T. J.; Walker, R. L. *Anal. Chem.* **1980**, *52*, 709.
71. Rokop, D. J.; Schroeder, N. C.; Wolfsberg, K. *Anal. Chem.* **1990**, *62*, 1271.
72. Rokop, D. J.; Efurd, D. W.; Perrin, R. E. Report IAEA-SM-333/99, undated but about 1994.
73. Nakamura, N.; Yamamoto, K.; Noda, S.; Nishikawa, Y.; Komi, H.; Nagamoto, H.; Nakayama, T. *Anal. Chem.* **1989**, *61*, 755.
74. Smith, D. H.; Walker, R. L.; Carter, J. A. *Anal. Chem.* **1982**, *54*, 827A.
75. Weast, R. C., ed., *CRC Handbook of Chemistry and Physics*, 64th Edition, CRC Press, Boca Raton, FL, 1983–1984, p. E76.

76. Smith, D. H.; McKown, H. S.; Bostick, D. T.; Coleman, R. M.; Duckworth, D. C.; McPherson, R. L. USDOE Report ORNL/TM-12632, January, 1994.
77. Walker, F. W.; Miller, D. G.; Feiner, F. *Chart of the Nuclides*, 13th Edition, General Electric, San Jose, CA, 1984.
78. Xiao, Y.; Beary, E. S.; Fassett, J. D. *Int. J. Mass Spectrom. Ion Processes* **1988**, *85*, 20.
79. Swihart, G. H.; McBay, E. H.; Smith, D. H.; Siefke, J. W. *Chem. Geol.* **1996**, *127*, 241.
80. De Laeter, J. R. *Mass. Spectrom. Rev.* **1994**, *13*, 3.
81. Nakamura, N. *Geochim. Cosmochim. Acta* **1974**, *38*, 757.
82. Burbidge, E. M.; Burbidge, G. R.; Fowler, W. A.; Hoyle, F. *Rev. Mod. Phys.* **1957**, *29*, 547.
83. Trimble, V. *Rev. Mod. Phys.* **1975**, *47*, 877.
84. Harkins, W. D. *J. Am. Chem. Soc.* **1917**, *39*, 856.
85. Anders, E.; Grevasse, N. *Geochim. Cosmochim. Acta* **1989**, *53*, 197.
86. Smith, D. H.; Walker, R. L., unpublished results.
87. Cameron, A. E. *Actinides Rev.* **1969**, *1*, 299.
88. Hembree, D. M.; Carter, J. A.; Ross, H. H. USDOE Report K/NSP-275, Oak Ridge, TN, March, 1995.
89. Rokop, D. J.; Efurd, D. W.; Perrin, R. E. IAEA Report IAEA-SM-333/99, undated but about 1994.
90. Zeisler, R.; Donohue, D. L. *J. Radioanal. Nucl. Chem.* **1995**, *194*, 229.
91. Gilai, D.; Williams, M. L.; Cooper, J. H.; Laing, W. R.; Walker, R. L.; Raman, S.; Stelson, P. H. USDOE Report ORNL-5791, Oak Ridge, TN, October, 1982.
92. Walker, R. L.; Botts, J. L.; Cooper, J. H.; Adair, H. L.; Bigelow, J. E.; Raman, S. USDOE Report ORNL-5986, Oak Ridge, TN, October, 1983.
93. Walker, R. L.; Botts, J. L.; Hydzik, R. J.; Keller, J. M.; Dickens, J. K.; Raman, S. USDOE Report ORNL-6837, Oak Ridge, TN, December, 1994.
94. DeBievre, P.; Gallet, M.; Werz, R. *Int. J. Mass Spectrom. Ion Phys.* **1983**, *51*, 111.
95. Kelly, W. R. *Int. J. Mass Spectrom. Ion Processes* **1985**, *64*, 85.
96. *Annual Book of ASTM Standards*. Part 45 Nuclear Standards, American Society for Testing and Materials, Philadelphia, PA, 1981, Procedure E321, pp. 978–989.
97. Green, L. W.; Elliot, N. L.; Miller, F. C.; Leppinen, J. J. *J. Radioanal. Nucl. Chem.* **1989**, *131*, 299.
98. Neuilly, M.; Bussac, J.; Frejacques, C.; Nief, G.; Vendryes, G.; Yvon, J. *Comptes Rendus Acad. Sci.* **1972**, *275*, 1847.
99. Baudin, G.; Blain, C.; Hagemann, R.; Kremer, M.; Lucas, M.; Merlivat, L.; Molina, R.; Nief, G.; Prost-Marechal, F.; Regnault, F.; Roth, E. *Comptes Rendus Acad. Sci.* **1972**, *275*, 2291.
100. Loss, R. D.; De Laeter, J. R.; Rosman, K. J. R.; Benjamin, T. M.; Curtis, D. B.; Gancarz, A. J.; Delmore, J. D.; Maeck, W. J. *Earth Planet Sci. Lett.* **1988**, *89*, 193.
101. *International Atomic Energy Agency*. IAEA Symposium, Libreville, Gabon, **1975**.
102. *International Atomic Energy Agency*. IAEA Technical Committee Meeting, Paris, **1978**.
103. Ruffenach, J. C.; Hagemann, R.; Roth, E. *Zeit. Naturforsch.* **1980**, *35a*, 171.
104. DeBievre, P.; Peiser, H. S. *Pure. Appl. Chem.* **1992**, *64*, 1535.

105. Rosman, K. J. R.; Loss, R. D.; De Laeter, J. R. *Int. J. Mass Spectrom. Ion Processes* **1984**, *56*, 281.
106. Chang, T-L; Qian, Q-Y. *Int. J. Mass Spectrom. Ion Processes* **1991**, *103*, 193.
107. Taylor, P. D. P.; Maeck, R.; DeBievre, P. *Int. J. Mass Spectrom. Ion Processes* **1992**, *121*, 111.
108. Chang, T-L; Qian, Q-Y; Zhao, T-T; Wang, J. *Int. J. Mass Spectrom. Ion Processes* **1993**, *123*, 77.
109. Shima, M.; Torigoye, N. *Int. J. Mass Spectrom. Ion Processes* **1993**, *123*, 29.
110. De Laeter, J. R.; De Bievre, P.; Peiser, H. S. *Mass. Spectrom. Rev* **1992**, *11*, 193.
111. Goldschmidt, V. M. *Nor. Vidensk. Akad. Oslo Mat. Nat. Kl.* **1937**, 4.

2
Glow Discharge Mass Spectrometry*

Christopher M. Barshick
Oak Ridge National Laboratory
Oak Ridge, Tennessee

2.1 INTRODUCTION

Although the strengths of the glow discharge (GD) were recognized by inorganic mass spectrometrists over 70 years ago, it was only during the last 20 years that the technique gained acceptance by the mainstream analytical community. Success can be attributed to several factors, including the tireless efforts of investigators in this field and the willingness of several instrument vendors to produce commercial products. No matter what the reason for its recent popularity, its appeal today is the same as it was more than 70 years ago: the GD is a rugged device that is simple to construct, operates at relatively low power and moderate pressure, and can be used to analyze nearly all elements [1]. The classical application for glow discharge mass spectrometry is trace elemental analysis of solid, conducting materials, such as refractory metals and alloys. Indeed, this remains its strength. However, this has not prevented researchers from pushing the technique in many different directions, including the analysis of nonconducting materials (e.g., ceramics, glasses, and polymers), the analysis of powders (e.g., soils and cements), and even the analysis of liquids as dried solution residues and finely aspirated

aerosols. The purpose of this chapter is to provide some historical background for today's research and development in this field. The fundamental operation of the discharge will be described, as well as various instrumental configurations and analytical applications. This discussion serves as an introduction to two other chapters in the book, where glow discharge mass spectrometry (GDMS) of nonconductors and elemental analysis using glow discharge ion trap instrumentation are covered.

2.2 HISTORY

Unlike most of the ionization sources found on modern mass spectrometers, discharge devices actually preceded the mass spectrometer itself. Pioneers like Thomson, Aston, and Bainbridge used electrical discharges as ionization sources on some of the earliest mass spectrometers constructed [2]. Many of these investigations centered on elucidating information about the "positive rays" or *canalstrahlen* reported several years earlier by Goldstein [2]. What Thomson and others found was that the spectra generated from these sources provided information not only about discharge phenomena, but about the atomic masses and isotopic abundances of the elements in the support electrodes as well. Thomson's work with positive rays emerging from gas discharges led to Aston's development of ion sources for elements available only as solids of low volatility (i.e., refractory metals, metallic oxides, etc.) [3]. These types of ion sources dominated the mass spectrometry landscape in the 1920s and 1930s. During World War II (and for about 20 years after), discharges were largely ignored because a new ion source appeared, the vacuum spark [4]. This source, still in use today on many emission spectrometers, has been shown to provide almost full elemental coverage with only a few exceptions. Detection limits are on the order of 0.1 ppm [5]. The technique does, however, suffer from several drawbacks, including the need for a double-focusing mass spectrometer to overcome the wide energy spread and a plethora of polyatomic interferences. In addition, long integration times are required to average out the inherent instability of the ion signal. These instruments were designed so that all ions could be detected simultaneously with photographic plates, although some instruments have been fitted with electronic detectors. Most recently, spark source mass spectrometry has largely been replaced by inductively coupled plasma mass spectrometers (see Chapter 3) or glow discharge mass spectrometers.

During the 20-plus years that mass spectrometrists lost interest in glow discharges, optical spectroscopists were pursuing these devices both as line sources for atomic absorption spectroscopy and as direct analytical emission sources [6–10]. Traditionally, inorganic elemental analysis has been dominated by atomic spectroscopy. Since an optical spectrum is composed of lines corre-

sponding to the accessible transitions of each element, identification and quantification of a sample's elemental composition are straightforward. For a sample composed of a single pure element, spectral interpretation is easy. However, when it is applied to the analysis of multicomponent materials, the spectral complexity often makes interpretation problematic. Mass spectrometry has an advantage in this area since there exist far fewer isotopes of a given element than potentially populated energy levels. Coburn and coworkers recognized the power of mass spectrometry when they brought the glow discharge source back to the attention of mass spectrometrists in the analysis of solids using both direct current (dc) and radio frequency (rf) discharges [11–13]. Other milestones occurred when Harrison and Magee [14] and later Colby and Evans [15] demonstrated that a hollow cathode glow discharge coupled to a magnetic sector instrument could be used to provide elemental analysis of the cathode. In 1978, Bruhn et al. [16] reported the use of a quadrupole-based glow discharge mass spectrometer. This work indicated that a relatively low-cost mass spectrometer could be dedicated to trace elemental analysis of solids. Since this time there have been many advances made in instrumentation, sample preparation, and techniques for data analysis. Several good review articles give further insight into the historical developments of the glow discharge as an ion source for mass spectrometry [17–19]. Two achievements worth noting are the introduction of commercial instrumentation [20] and the development of a radio frequency glow discharge as an analytical tool for the direct analysis of nonconducting samples [21]. As more individuals "rediscover" the power of the glow discharge for trace elemental analysis of solids, the future of GDMS is promising.

2.3 THEORY

The purpose of this section is to provide a basic understanding of glow discharge (GD) processes; it is in no way intended to be a complete treatment of GD theory. For a complete treatise on fundamental glow discharge plasma processes, the reader is referred to an excellent chapter by Fang and Marcus in *Glow Discharge Spectroscopies* [22].

Before glow discharge atomization and ionization processes can be explained, it is necessary to establish a vocabulary of the terms used. The glow discharge is a specific example of a gaseous discharge, which is one type of plasma. A *plasma* is a partially ionized gas consisting of equal numbers of positive and negative charges and a larger number of neutral molecules [23]. The term *gas discharge* refers to the flow of electric current through a gaseous medium [24]. For this to occur, a fraction of the gas particles must be ionized. In addition, an electric field must exist to accelerate the charged particles, thereby allowing current to flow. In the classical version of the glow discharge, a voltage source develops a

potential between the negatively biased cathode and the anode. Free electrons in the gas are accelerated toward the positively biased anode by the resulting potential gradient. These free electrons collide with gaseous species, producing gas-phase ions. Positive ions are accelerated toward and impinge on the negatively biased electrode. On impact, a variety of secondary species are liberated, including electrons and species formed from the cathode material. The ions and atoms from the cathode have analytical utility since they represent the sample. The entire process is considered self-sustaining on the basis that electrons are created at the cathode to replace those lost at the anode. Hence, no external ionization is required [25].

The relationship between current and operating voltage is a characteristic by which gas discharges can be identified. Figure 2.1 illustrates this relationship; several types of discharges are identified along with their associated electrical behavior [26]. In the 10^{-10}- to 10^{-15}-A region (regions *B* and *C*) are the electrical discharges requiring an external source of ionizing radiation to maintain current flow [24]. A feature of these discharges is the lack of luminosity resulting from the small number of collisional excitation processes. At 10^{-10} A the discharges possess the ability to sustain current flow independently of external assistance,

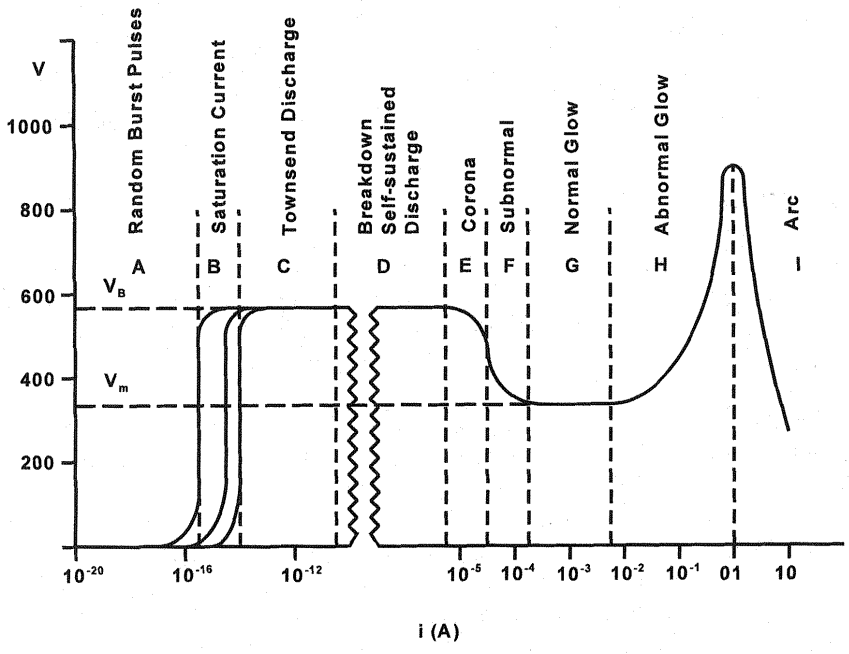

Figure 1 Voltage versus current characteristics of gas discharges. (From Ref. 26.)

with 10^{-7} A (region *D*) marking the beginning of those discharges that typically show luminosity [27]. At the point where the discharge is carrying approximately 10^{-6} A of current, the realm of the glow discharge is reached. As current continues to increase, a transition occurs from the corona discharge (region *E*) to the subnormal discharge (region *F*) to the normal discharge (region *G*). While operating in the normal discharge mode, an increase in current will produce no change in voltage (i.e., current density is constant) [24,25]. Physically, the luminous region is observed to increase its coverage over the cathode. When the entire cathode is covered, the abnormal region is reached (ca. 10^{-2} A) (region *H*), and any increase in current produces an increase in the discharge potential [25]. Beyond the abnormal region is the transition to high current arc discharges (region *I*).

The most common gas discharge is the low-pressure (typically 0.10–10 torr) glow discharge. Typified by the familiar neon light, the appearance of glow discharges varies with the gas (type, pressure, purity, etc.), the dimensions of the vessel, and the geometry of the electrodes. Figure 2.2 is a common depiction of the luminous and nonluminous regions of a glow discharge; this figure is often termed the "architecture of the glow" [25]. Below the diagram are plots that show the status of luminosity, potential, field, charge density, and current density with respect to the specific discharge regions.

Moving left to right away from the cathode, the first region encountered is the Aston dark space. This region has a net negative space charge resulting from secondary electrons released during the sputtering event [24]. Beyond the Aston dark space and up to the negative glow, positive ions are acting as the primary charge carriers. Interaction of these positive ions with slow electrons creates energetic neutrals that radiatively relax to produce luminosity and the cathode layer (see Fig. 2.2) [24]. Electrons that pass through the cathode layer without undergoing collisions acquire energies up to that of the cathode fall potential. This increase in energy results in a lower probability for collision between electrons and gas atoms, and the creation of a low-emission intensity region called the *cathode dark space* (also termed the *cathode fall region*). Throughout the cathode dark space, a net positive space charge exists. This positive space charge produces a large enough potential gradient that the majority of the discharge voltage is dropped across this region. Because of this potential gradient, electrons are accelerated to a sufficient energy to ionize the discharge gas on collision. Consequences of these ionizing collisions are the multiplication in the number of electrons [23] and the reduction in their energy. As the energy of the electrons is reduced, the cross section for excitation of atoms increases. Radiative relaxation of excited atoms leads to visible radiation and the formation of the negative glow region. As more collisions occur, electrons are slowed further, decreasing the collisional cross section until excitation of atoms is no longer favorable. This results in the formation of the Faraday dark space. Continuing toward the anode, the potential gradient accelerates the electrons to the point where excitation and

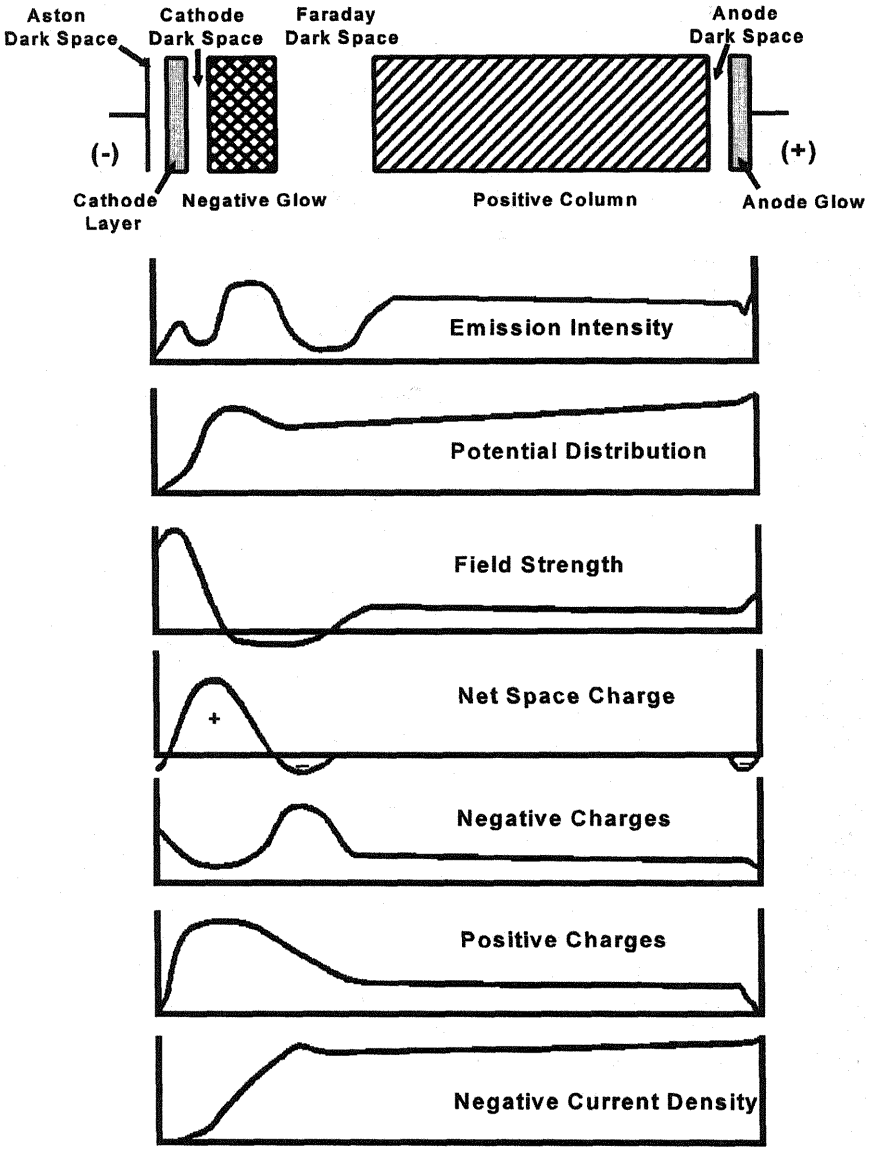

Figure 2 Architecture of the glow discharge. (From Ref. 25.)

ionization begin again. Here, a faintly luminous region called the *positive column* can form, and positive charge carriers are balanced by negative charge carriers [23,24]. Electrons are accelerated out of the positive column, attaining a velocity that favors only ionization and not excitation in the anode dark space region [24]. Here, the field strength, negative space charge, and negative current density all increase. Adjacent to the anode, the cross section for electron impact excitation is large, and the negative current density is the greatest; a luminous region, the anode glow, is created.

In most glow discharges only a few of these regions are observable, many of them disappearing as the cathode-to-anode distance is decreased. Generally, in glow discharges used for analytical applications, only the cathode dark space, the negative glow, and the Faraday dark space are distinguishable. The only region absolutely necessary for the existence of the discharge is the cathode dark space; all other regions serve to maintain the current flow [28]. If the anode is moved into the cathode dark space region, the discharge is extinguished, a feature often employed in shielding certain parts of the discharge hardware from the glow.

2.3.1 Sputter Atomization

One oft-touted strength of the glow discharge is that the sampling step is separate from the excitation and ionization steps [29]. This aspect of the glow discharge is unique, providing atoms that retain little "memory" of the chemical environment from which they came, thus reducing matrix effects. The process of cathodic sputtering for creating a representative gas-phase sample population is central to the analytical utility of the glow discharge. Once sample atoms are liberated, excitation and ionization occur, the latter process placing the species of interest in a form suitable for mass spectrometric detection.

The cathodic sputtering process liberates atoms directly from the solid cathode into the gas phase [30]. Unlike thermal processes (see Chapter 1), cathodic sputtering results in the release of atoms on impingement of gaseous species. In the steady state, positive gas ions are accelerated across the cathode fall region toward the cathode surface. Before impact, these ions recombine with Auger electrons released from the surface [31]. These newly created gas neutrals strike the cathode and implant themselves into the atomic lattice, transferring their momentum and kinetic energy to the lattice through a collisional cascade. A fraction of the energy transferred to the lattice is reflected to the surface. If an atom absorbs energy greater than its binding energy, the atom may be released into the gas phase above the surface. Figure 2.3 is an illustration useful in visualizing the sputtering process [32]. As a result of the sputtering event, not only are individual atoms released, but clusters of atoms, secondary ions, and electrons are liberated from the surface. Electrons are accelerated across the cathode fall region into the negative glow, where they are available to participate in excitation and ionization.

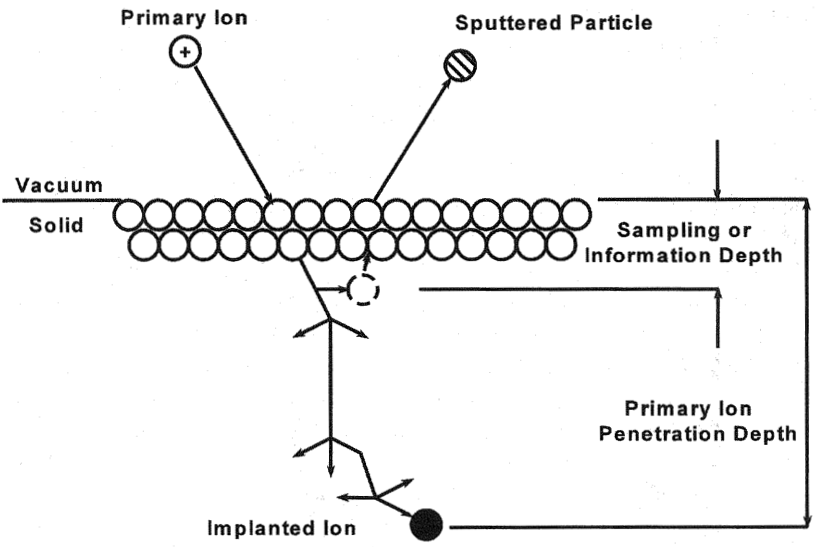

Figure 3 The process of cathodic sputtering.

Secondary ions return to the sample surface through the influence of the electric field at the cathode. Individual atoms and clusters of atoms undergo collisions that may dissociate the clusters and redeposit material at the surface. A percentage of these sputtered atoms, however, diffuse into the negative glow for subsequent excitation and ionization.

The effect of an ion's impact on a sample lattice is measured by the sputter yield, Y [7]. This value is a measure of the number of atoms removed from the surface as a result of an impact by one primary ion. Several physical parameters affect sputtering [33], including the angle of incidence of the incoming ion, the masses of the incident ion and the sputtered atom, the incident ion energy, and the surface binding energy [34]. The sputter yield is often expressed by the following equation:

$$Y = 10^{-6}(q \cdot N \cdot e/M \cdot i^{+}) \tag{2.1}$$

where q is the sputtering rate of the sample measured in micrograms per second, N is Avogadro's number (mole^{-1}), e is the electronic charge (coulombs), M is the atomic weight, and i^{+} is the ion current in amperes. The ion current is related to the total current, i, by the expression

$$i^{+} = i/(1 + \gamma) \tag{2.2}$$

where γ is the number of secondary electrons released, on the average, by one incident ion. For argon, γ is approximately 0.1 [35].

Most sputter yield data involve tightly focused, highly energetic primary ion beams; this is the basis for secondary ion mass spectrometry (SIMS) (see Chapter 4). Because the physical processes are identical in the two techniques, sputter yield data reported in the SIMS literature are often used to explain the parameters influencing glow discharge sputtering. One should recognize, however, that incident ion energies are much lower in the glow discharge than in SIMS, and that there is a significant amount of sample redeposition in the GD due to the ambient fill pressure. For a detailed discussion of the influence of these parameters the reader is referred elsewhere [22,36,37]. In general, the sputter yield increases as the ratio of the mass of the incident ion to the mass of the target atom (M_1/M_2) approaches unity, as the angle of incidence moves away from normal (up to 70°), and as the incident ion energy increases. The dependence of sputtering on the target material is a slightly more complicated relationship. The yield is seen to increase going from left to right in any one row of the periodic table. Carter and Colligon [38] and Wehner [36] have shown that, with minor exceptions, the sputter yield closely follows the state of the electron concentrations in the atoms' "d" shells (i.e., the greater d-shell filling, the great the sputter yield). This phenomenon is believed to be related to the penetration depth of primary ions. In targets with more open electronic structures, ions penetrate to such depths that the transmission of energy back to the surface where sputtering occurs is less efficient. In filled d-shell atoms, the penetration of ions is relatively small and energy is more readily projected back toward the target surface, resulting in larger sputter yields.

Besides the general sputtering theory that was developed to accompany experimental ion beam data [39], several mathematical models have been developed [40–42]. The success of these models to the physicist is measured by how accurately they predict sputter yields; to the rest of the scientific community, the success of these models is measured by how well they convey the sputtering theory to their audiences. Sophisticated computer programs, often employing Monte Carlo calculations and requiring large amounts of computer memory, have generated data about primary ion penetration depth, sampling depth, and collisional transfer of energy, as well as information about the nature of the ejected species. To this author's knowledge, however, no satisfactory model has been developed to explain glow discharge sputter/atomization.

2.3.2 Ionization

Once cathodic species are atomized, sufficient energy must be imparted to ionize them. Collisions occurring throughout the discharge volume are central to maintaining the stability of the discharge. However, only those collisions that occur in the negative glow region (less than one mean free path from the ion exit orifice) produce a significant enough population of ions to permit trace elemental analysis. Figure 2.4 illustrates the three principal types of collisions in the negative glow

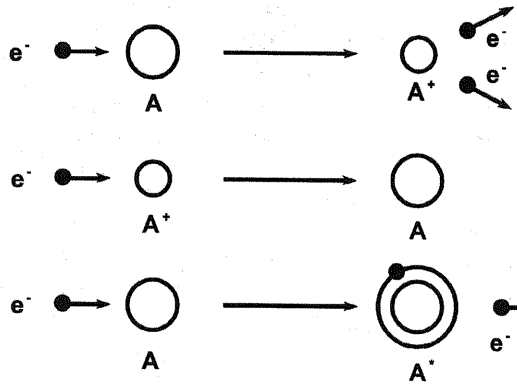

Collisions Involving Discharge Electrons

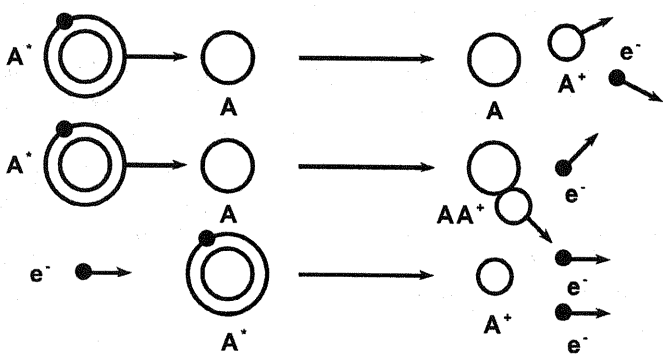

Collisions Involving Excited State Discharge Species

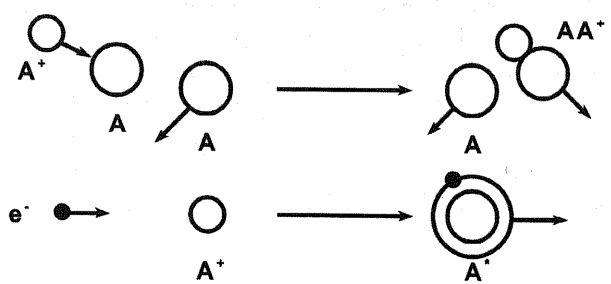

Collisions Involving Discharge Ions

Figure 4 Principal types of collisions occurring in the glow. (From Ref. 43.)

Electron impact (EI) ionization

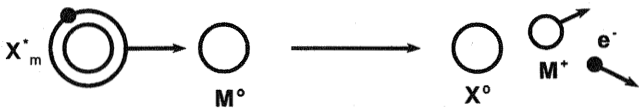

Penning (metastable) ionization

Figure 5 Electron impact and Penning (metastable) ionization processes.

[43]: those involving electrons (e^-), excited state species (A^*), and ions (A^+). Within the framework of these collisional processes are two principal mechanisms that serve to remove completely an electron and cause ionization: electron impact (*EI*) ionization and Penning (metastable) ionization. These ionization mechanisms are illustrated in Fig. 2.5, where M^0 is a sputtered atom and X_m^* is a metastable atom created from the inert discharge gas X.

Electron impact ionization occurs when an electron of sufficient kinetic energy comes in close contact with an atom. The incident electron undergoes an elastic collision with an electron in an atomic orbital of the atom with which it collides. This can result in kinetic energy transfer from the first electron to the second and subsequent ejection of the second electron from the target atom [44, 45]. However, there is only a small probability that a collision with an electron will result in ionization. The probability is zero below some threshold value and increases as the electron energy increases [at a rate of $C^{1.127}$, where C is the cross section (46)]; eventually the probability reaches a maximum and then decreases. At the threshold value only collisions that result in complete transfer of all kinetic energy of the impinging electron produce ionization. Above this value, glancing collisions of higher energy transfer enough energy to cause ionization. At very high energies, however, the duration of the overlap of the wave functions, through which energy is transferred, becomes too short and the cross section begins to fall [46].

Although the average energy of glow discharge electrons (reported to be on the order of 2–4 eV) is not high enough to ionize many elements or the discharge gas [23,47,48], the Boltzmann distribution of energies provides a fraction of electrons with enough energy to ionize all elements. Chapman [23] has performed calculations using the Maxwell-Boltzmann distribution to determine the fraction of electrons with enough energy to cause ionization of the noble gases. For a thorough account of these calculations, the reader is referred to the book *Glow Discharge Processes* [23].

The second major ionization mechanism in an abnormal glow discharge is named for F. M. Penning, who discovered the effect in 1925 [49]. Penning ionization involves the transfer of energy from a metastable state of the discharge gas to an atom or molecule. If the ionization potential of the atom or molecule is lower than the energy of the metastable state, ionization can occur. This process may be thought of as nonselective since different elements generally exhibit similar ionization cross sections for Penning ionization. Metastable states are created through the excitation of discharge gas atoms into an electronic level from which radiative decay is forbidden by transition selection rules. For argon these are the $^3P_0$ and $^3P_2$ states at 11.5 eV and 11.7 eV, respectively. Metastable species are long lived, existing for several milliseconds under typical discharge conditions [50]. In addition, metastable species have a reported cross section for ionization an order of magnitude or more higher than electrons. For these reasons, metastable atoms play a disproportionate role in ionization in some discharges [12,51–53]. Table 2.1 lists the metastable states for the rare gases most often used in GDMS.

Other mechanisms besides electron and Penning ionization have been shown to contribute to the ionization of sputtered neutral species, but their roles are believed to be less significant. Table 2.2 is a partial list of these mechanisms. These are reviewed in detail elsewhere [54–57]. Since factors such as discharge pressure, type of discharge gas, electron energy and number density, and cathode geometry all influence the ionization process, no one mechanism has surfaced as dominant in all glow discharge devices.

Table 1 Low-Lying Metastable Levels of Rare Gas Atoms

Gas	Metastable energy (eV)	Ionization potential (eV)	Spectroscopic notation
He	19.8, 20.7	24.58	2^3S, 2^1S
Ne	16.6, 16.7	21.56	$^3P_2$, $^3P_0$
Ar	11.5, 11.7	15.76	$^3P_2$, $^3P_0$
Kr	9.9, 10.5	14.00	$^3P_2$, $^3P_0$
Xe	8.3, 9.4	12.13	$^3P_2$, $^3P_0$

Source: Ref. 25.

Table 2 Seconary Ionization Mechanisms in the Glow Discharge

Nonsymmetric charge transfer	$X^+ + M^0 \rightarrow M^+ + X^0$
Symmetric (resonance) charge transfer	$A^+_{fast} + A^0_{slow} \rightarrow A^+_{slow} + A^0_{fast}$
Dissociative charge transfer	$X^+ + MA \rightarrow M^+ A + X^0$
Associative ionization	$X^*_m + M \rightarrow XM^+ + e^-$
Photoionization	$M^0 + h\nu \rightarrow M^+ + e^-$
Cumulative ionization	$M^0 + e^- \rightarrow M^* + e^- \rightarrow M^+ + 2e^-$

Source: Ref. 19.

2.3.3 Glow Discharge Modeling

During the last few years, several groups (primarily led by Professor R. Gijbels at the University of Antwerp) have been trying to model the interactions of atoms, electrons, ions, and excited state species in the glow discharge. Using sophisticated mathematical relationships in concert with an abundance of previously obtained experimental information, these investigators have, among other things, attempted to predict the role of metastable argon atoms [58], simulated the motion of species in the cathode dark space [59], and described the thermalization process of sputtered atoms [60]. In most instances these calculations have agreed well with experimental data. The real success of these efforts, however, will be the extension of the work to predict some as yet undiscovered glow discharge phenomenon, or to explain data for which no answer has been previously hypothesized (e.g., relative sensitivity factors for exotic matrices). In the next several years, the benefits of this approach may be realized in improved analytical performance in GDMS.

2.4 INSTRUMENTATION

The instrumental components of a glow discharge mass spectrometer are a hodgepodge of ionization sources in combination with virtually every type of mass spectrometer that exists today. Several commonalities, however, can be found among the wide number of possible combinations. First, all of the sources considered here operate at reduced pressures (0.01–10 torr for the examples given). Typically, this pressure is for an ambient rare gas; however, examples can be found in which other fill gases have been employed [61,62]. Because most mass analyzers operate optimally at a lower pressure than the ion source, differential pumping is required to obtain pressures $<10^{-5}$ torr. These pressures facilitate a collision-free ion flight path but cause problems in interfacing GD sources to certain analyzers (e.g., Fourier transform mass spectrometers). Often the operating pressure, cathode/anode arrangement, and power supply output dictate what

type of operating mode is being employed; however, the primary consideration is the formation of ions for subsequent mass analysis. The variations employed often result from personal preference combined with the desire to perform a certain type of experiment or analysis or from availability of equipment.

2.4.1 Sample Preparation Schemes

Unlike solution based methods in which the sample is dissolved in an aqueous medium that usually includes some small percentage of mineral acid, in GDMS the sample is not a homogeneous liquid, but a solid, and can therefore take a number of forms (e.g., machined hollow cathodes, compacted disks, and dried solution residue). In the next section, cathode/anode geometry is discussed; in the section presented here, an equally important but often overlooked issue, the physical form of the sample, is discussed.

The simplest sample preparation involves machining the material into the desired shape immediately prior to analysis. Even with this approach, however, the sample is usually etched in a dilute mineral acid or electropolished to remove surface impurities, rinsed with an organic solvent to remove oil residue, and dried in an oven. Often, however, the sample is not large enough to be machined into a cathode, or it is in the form of a powder. In this latter case, the sample is usually pressed into the desired shape in a die. The mechanics of this process varies widely, but there are usually a grinding step, a homogenization step, and a pressing step. In our laboratory we press pin-shaped cathodes by drilling a 2-mm hole in a polyethylene slug 2.54 cm in diameter by 5.08 cm in length. The powder is poured into the void made by the drill bit, and 11 metric tons of pressure is applied to the slug. This compresses the slug enough to compact the powder into a rod ~1.5 mm in diameter. When the pressure is released, the sample falls out of the slug. The pin is then trimmed to the desired length prior to analysis. This technique works equally well for conducting and nonconducting samples. We have found that powders of 325 mesh hold together better than those that are more coarse. A slight variation of this approach is to mix a nonconducting sample with a conducting binder prior to pressing the mixture. This allows the material to be run with a conventional direct current (dc) discharge. We have found empirically that samples with greater than 10 weight percent nonconducting material perform poorly in the discharge. A similar approach to compacting samples has been applied to dried solution residues [63]. In a series of articles, Barshick et al. [63–65] demonstrated how as little as 100 μL of a 1-ppm solution can be analyzed as a dried residue homogenized with silver powder. Unique to this approach was the homogenization of the residue with a binder. This provided a stable ion signal for more than 1 hour, compared with a transient signal lasting less than 15 minutes when the solution is dried on the surface of a target cathode [66,67]. If an additional step

(low-temperature ashing) is applied to the solution prior to homogenization, metals can be analyzed in organic solutions (e.g., oil) [65].

Several disadvantages to using compacted samples have been cited [68], including surface contamination of the sample from the die, adsorption of water vapor on the individual powder grains, need to homogenize the material carefully to ensure a representative sample, and need for a high-purity binder. These problems, although often easily overcome, have prompted individuals to search for alternative methods of sample preparation. One method is to mix the sample with gallium [69]. At slightly elevated temperatures (~30°C) gallium is a liquid. Once homogenized with the powder, it can be poured into an appropriately shaped mold and cooled. The cooled metal is removed from the mold and analyzed in a cryogenically cooled discharge cell as if it were a machined solid.

A second approach that has been used extensively in our laboratory is to roll a high-purity indium pin (99.999%) in the powder we wish to analyze [70]. Because indium is soft, a fraction of the powder is impregnated into the metal. The indium serves solely as a host, supporting the discharge processes (i.e., the sample is atomized along with the indium). This approach has proved especially useful when we have small amounts of powder to analyze (<1 mg) or when the material is difficult to get into solution. Using this approach, we have observed ion signals lasting up to 1 hour from discharge initiation and precision comparable to that in other sample preparation methods. Battagliarin et al. have reported a variation of this approach [68] that uses a special pressurized vessel of their own design. The powdered sample is placed in this vessel. An indium rod is inserted into the vessel so that it is brought into contact with the powder. The die is heated for 2 hours at 190°C at atmospheric pressure until the chamber has reached a uniform temperature; the oven is then pressurized to 70 bar with N_2. The high pressure forces the now-liquid indium into a mold. On cooling, the solid sample can be removed from the die and trimmed to the appropriate length for analysis.

Hess et al. have developed a novel sample preparation scheme based on electrochemical deposition [71]. Although this approach was not designed for routine sample analysis, it has been advocated for preparing standard materials to aid in quantitative analysis. The procedure is as follows: silver pins (1.5 mm in diameter × 20.0 mm in length) are first pressed from pure silver powder. These pins are then polished to a high luster and inserted into an electrochemical cell consisting of a working electrode, an auxiliary electrode, and a salt bridge. The necessary potentials are supplied by an IBM EC/225 voltammetric analyzer with a variable potential of −5 to +5 V. The metal ions used for deposition are obtained by pipetting the appropriate amount of a 1000-μg/mL standard solution into a reaction vessel. After removal from the electrochemical cell, the samples are washed with deionized water (while the voltage is still applied) and dried overnight at 110°C. Once they are dried, the cathodes are weighed, crushed, and

homogenized; the resulting powder is then mixed with an equivalent weight of silver to assure sufficient material for preparing compacted pin cathodes of the type described. Linear calibration curves (analyte signal intensity versus cathode concentration) have been demonstrated, although relative sensitivity factors agree only marginally well with those obtained for solid samples [71].

2.4.2 Ionization Sources

There are several ways of categorizing glow discharge ion sources. The one most often employed considers the arrangement of the cathode with respect to the anode. Another is to consider the operating characteristics (pressure and power) of the various sources, and another is to separate them on the basis of whether they operate with a direct current (dc) or radiofrequency (rf) supply, or with a supply that operates in a constant or pulsed voltage mode. Because all of the discharges under consideration can be operated in either the dc or rf mode, a brief review of each type of operation is presented next; then cathode and anode arrangements are considered, with operating characteristics such as pressure and power highlighted. Finally, there exist several unique sources that do not fit conveniently into any one category but deserve mention.

Direct Current and Radio Frequency Glow Discharge Operation

Analytical glow discharges have conventionally operated with a constant negative dc potential applied to the cathode. There is no reason, however, that they can't be operated through the application of a pulsed potential, an applied rf potential, or a positive potential applied to the cathode. Many variations have been tried alone and in combination with one another. Perhaps the most interesting among these (because of the unique capabilities that it provides) is the radio-frequency-powered discharge. The analysis of nonconductors is covered extensively in a later chapter, but a brief overview is in order here.

Because current cannot flow through an insulating substrate, the application of a potential to a ceramic, glass, soil, or other insulating sample produces an effect analogous to a charging capacitor. On the application of a negative dc potential to the surface of the material, negative charge exists. Unlike the charge on a conducting surface, however, this charge decays rapidly to a more positive potential as a result of charge neutralization reactions with ions at the surface [72]. The result is a short-lived discharge that exists until a minimum threshold voltage is reached; at that point the plasma is extinguished [73]. If one applies an alternating current (ac) potential to the cathode, the surface is bombarded by an alternating source of electrons and positive ions. The greater mobility of the electrons results in the accumulation of more electrons than ions during the respective half-cycles, resulting in a time-averaged negative dc bias. This phe-

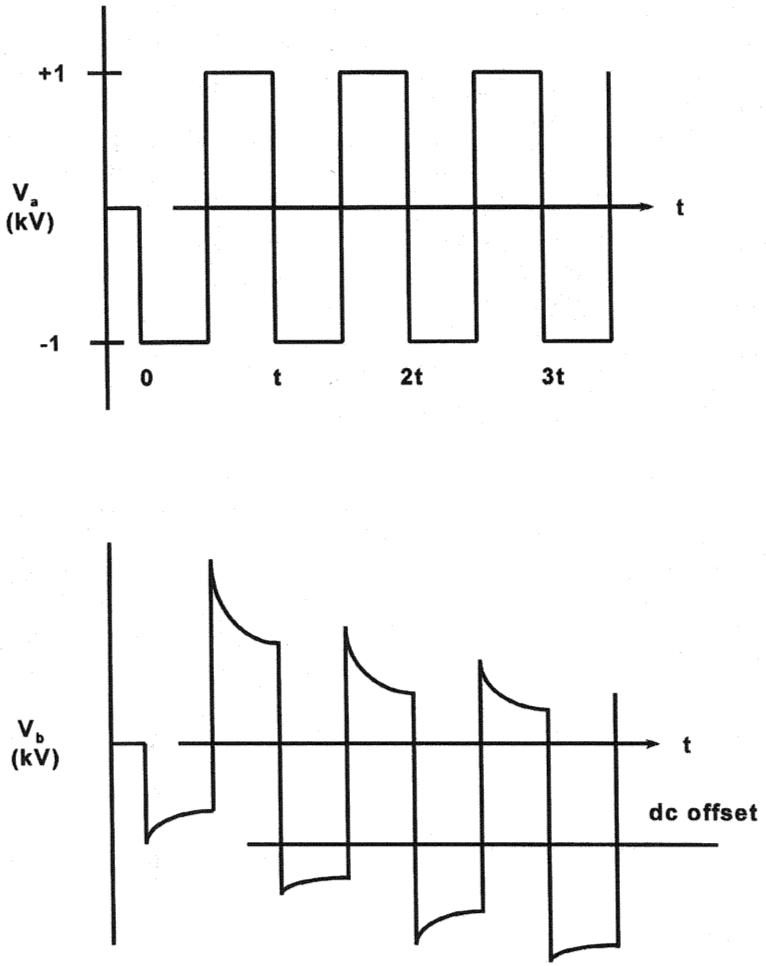

Figure 6 Voltage characteristics versus time for pulsed direct current and radio frequency discharges. (From Ref. 73.)

nomenon is illustrated in Fig. 2.6. For illustrative purposes, consider a 2-kV peak-to-peak radio frequency potential (V_a) and the resulting potential on the cathode surface (V_b). As the potential is applied during the first half-cycle, the surface charges to -1 kV and then decays to ~ -0.7 kV as the surface is bombarded by positive ions. As the second half-cycle begins, the applied positive potential results in a 1.3-kV potential on the surface. It is during this cycle that electrons are accelerated to the insulator surface, neutralizing the positive charge. Because of

the greater mobility of the electrons (compared to that of positive ions), the surface potential decays toward zero faster than in the previous half-cycle; the resulting potential on the surface is 0.5 kV. As the second full cycle is initiated and the polarity of the electrode is switched, the resulting potential is −1.5 kV. After several cycles, the waveform of V_b reaches a constant negative dc offset; this is the *self-bias potential.* The dc offset is approximately one half the applied peak-to-peak voltage. The exact value depends on the discharge pressure and source geometry. The sample surface is alternatively bombarded by high-energy ions and low-energy electrons but for most purposes can be considered a continuous dc discharge with a superimposed ac potential.

Pin and Planar Cathode Discharge Geometries

Pin cathodes (such as that shown in Fig. 2.7) and planar cathodes (such as that shown in Fig. 2.8) are the two discharge geometries used most extensively in GDMS. This pattern is due primarily to the simplicity of their construction and operation, and the relative ease of sample interchange. Typical operating conditions for the pin cathode include pressures that range from 0.5 to 5 torr of a rare gas, voltages of between 500 and 3000 V, and currents of between 0.5 and 5 mA. The sample is usually a cylindrical rod, 1–3 mm in diameter, with 5–15 mm of length exposed to the discharge. Because of their convenient sample geometry, pin cathodes have found widespread use in trace elemental analysis of bulk solids.

A planar cathode operates under similar pressure and voltage conditions to a coaxial cathode. To maintain comparable current densities, however, these

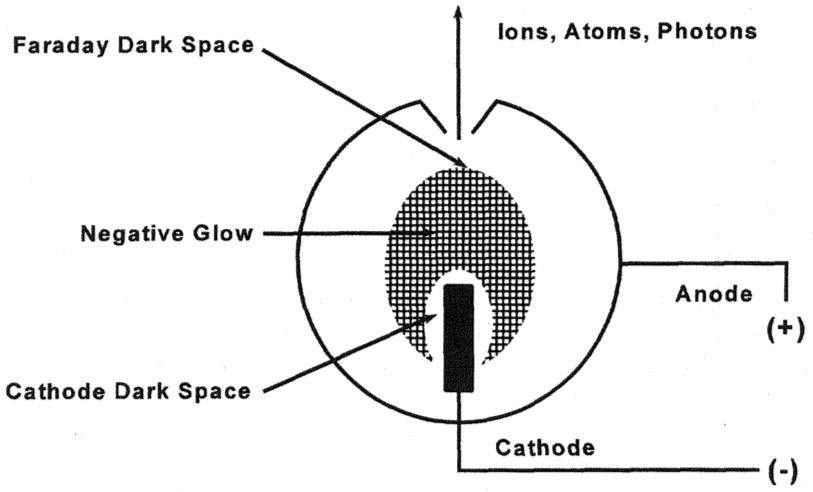

Figure 7 Schematic diagram of a coaxial cathode glow discharge source.

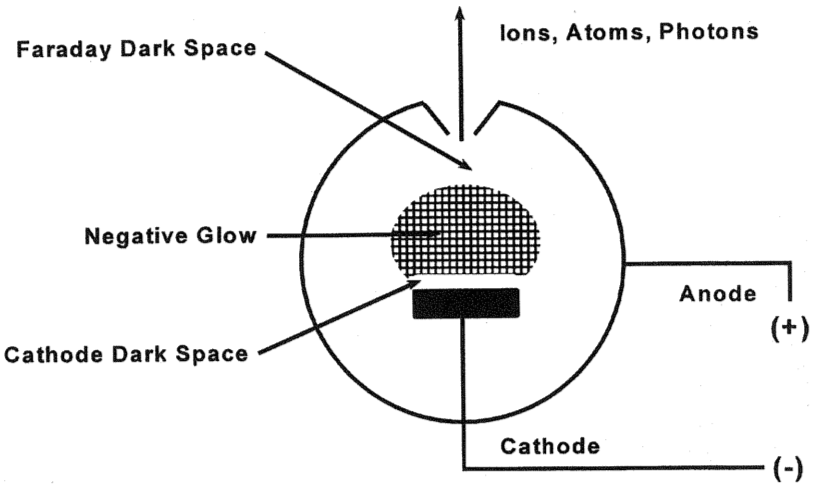

Figure 8 Schematic diagram of a planar cathode glow discharge source.

sources need to be operated at currents up to 15 mA. Planar cathodes are typically 5 mm to 5 cm in diameter and are between 1 and 5 mm in thickness. Cathodes are formed in the same manner as the coaxial geometry, by machining or pressing. Because these sources can accommodate larger samples, however, machining the sample is often not necessary. Instead, a portion of the sample is simply masked with a nonconducting sleeve to localize sputtering. Planar cathodes have also found wide application in trace elemental analysis; one area in which they are especially useful is in the depth profiling analysis of thin films.

A variation of the planar cathode is shown in Fig. 2.9, the Grimm source. Named for W. Grimm [74], this source is an obstructed discharge in which the anode extends into the cathode dark space, defining the area of the sample sputtered. Because the sample is located outside the cell, easy sample interchange is facilitated. Like other planar cathode sources, the Grimm source is particularly useful for the analysis of large metal sheets and thick disks. These discharges typically operate at between 500 and 1000 V, with 25 to 100 mA applied current and a pressure of between 1 and 5 torr. These sources are used extensively in atomic emission spectrometry, and several have been interfaced with mass spectrometric detection [75].

Hollow Cathode Discharges

Hollow cathode discharges are perhaps the most common glow discharges used in analytical chemistry. Most spectroscopists are familiar with these devices as hollow cathode lamps used for atomic absorption spectroscopy. Figure 2.10 contains

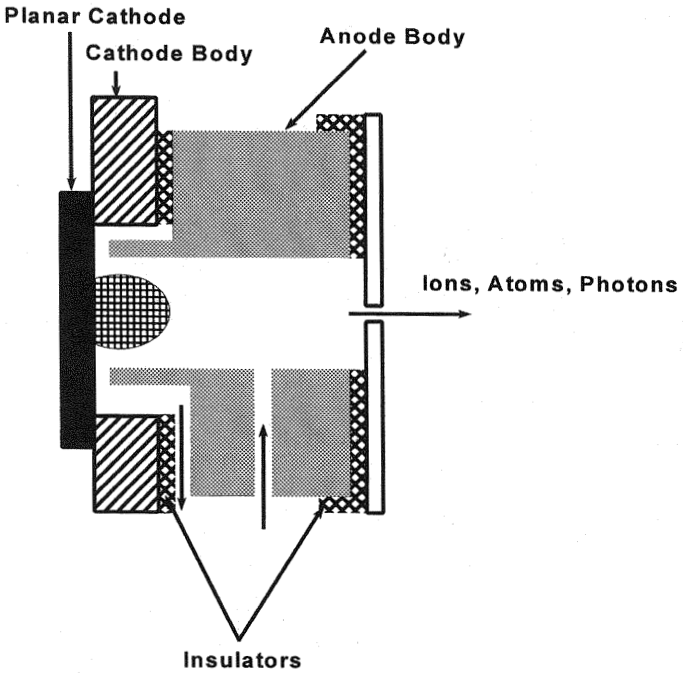

Figure 9 Schematic diagram of a Grimm-type glow discharge source. (From Ref. 29.)

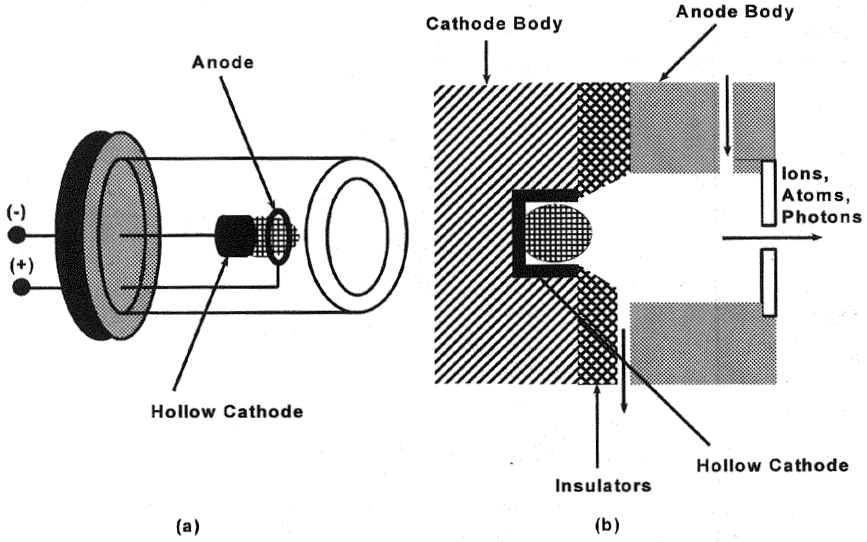

Figure 10 Schematic diagram of two hollow cathode discharge sources. (From Ref. 29.)

illustrations of two hollow cathode sources: (a) a conventional hollow cathode lamp and (b) a slightly different version of the source that can be used for atomic absorption, atomic emission, or mass spectrometry. These devices operate by means of the hollow cathode effect [76,77]. As a result of the coalescing of two discharges from parallel plates, the current density in a hollow cathode can be several orders of magnitude larger than that obtained by using a single planar cathode at the same cathode fall potential [78]. This results in atom densities that far exceed those found with planar cathodes. As with other GD sources, ionization occurs in the hollow cathode lamp's negative glow. Ionization, too, is greater than that produced by conventional discharges, and many investigations that take advantage of it have been conducted; the reader is referred to several excellent articles [76,79–81]. The hollow cathode operates at somewhat lower voltages than other discharges (200–500 V) but at similar pressures (1–5 torr). Discharge currents may range up to 200 mA. Hollow cathode lamps may be sampled in several different ways, including near the anode or alternatively on the reverse side of the cathode [82,83].

A variation of the hollow cathode discharge that holds potential for glow discharge mass spectrometry is the hollow cathode plume. Developed primarily as an atomic emission source by Marcus and Harrison [83], a hollow cathode plume is formed when the discharge is restricted to a small orifice in the base of a conventional hollow cathode [83–85]. Samples take the shape of disks, 4.5 mm in diameter and 2 mm in height with a 1.5-mm diameter orifice. Like more conventional discharges, cathodes can either be machined directly or pressed into the desired shape. Operating conditions are comparable to those of other discharges (pressures range from 1 to 10 torr with currents of between 50 and 200 mA and voltages of up to 1000 V). Physically, the hollow cathode plume plasma resembles a torch protruding from a narrow opening. The plume is believed to arise from pressure and field gradients caused by its construction [83–85]. Preliminary mass spectrometric data showed several advantageous characteristics [86] that as yet have not been exploited fully.

Novel Glow Discharges

A number of variations of the conventional glow discharge have been developed for specialized applications. Some of these are of particular interest to optical spectrometrists and have not been used for mass spectrometry beyond proof-of-principle experiments. An excellent article by Harrison et al. [87] reviews many of these sources, highlighting applications in atomic emission, atomic absorption, and atomic fluorescence spectroscopies. Two of these sources deserve mention here. The jet-enhanced glow discharge is similar to the Grimm source but with six strategically located gas jets that improve the analytical performance. Argon from these jets helps direct the atoms sputtered from the surface away from the sample at a much faster rate than ordinary discharges. These devices have been marketed

under the name Atomsource by Analyte Corporation [88]. Piepmeier et al. have used these sources extensively for atomic spectroscopy as well as mass spectrometry and have demonstrated performance better than that of conventional Grimm-type sources [89,90]. Typical operating conditions approximate those of a Grimm source: 30 mA current, 900 V, and 2.5 torr argon in the cell. Widespread use of these sources for mass spectrometry has not been observed, perhaps because the vendor has primarily marketed these sources for atomic absorption spectrometry, or perhaps because there is little flexibility in the size and shape of the sample that can be analyzed (i.e., as in the Grimm source, samples are disks a few centimeters in diameter by a few millimeters thick).

Another novel source is the atmospheric sampling glow discharge [91]. This device is based on establishing a glow discharge in ambient air that is drawn into a region of reduced pressure between two parallel plates. Unlike in conventional glow discharges, ionization occurs as a result of chemical ionization (CI), presumably from ion-molecule reactions. The sample is often entrained in the airstream flowing through a 0.2-mm orifice in the first plate. The discharge is maintained in the central region at a pressure of ~0.5 torr; 300–400 V is applied between the electrodes. Under these conditions, the discharge current is 3–10 mA. Air is pulled through the orifice at a rate of ~5 mL/sec; because of this relatively high flow rate, analyte response is almost instantaneous. Although this device holds the potential for analyzing inorganic analytes entrained in air, to date it has been used almost exclusively for detecting highly volatile organic analytes [91,92]. Ease of operation, part-per-trillion (ppt) detection limits, and a wide linear dynamic range have made it an ideal source for explosive detection. A portable version is being developed for use in airport security [93].

Secondary Cathodes

Clearly, nonconducting samples pose a special challenge for the analyst, and yet a sizable fraction of the materials desirable to analyze by GDMS are nonconducting. Two alternatives that aid in the analysis of these materials have already been discussed: the use of a radio frequency glow discharge and mixing of the nonconducting sample with a conducting binder. A third, a secondary or surrogate cathode in combination with a conventional dc discharge, has also been used. Such an approach consists simply of "masking" the insulating cathode with a thin (~0.25 mm) high-purity metal (e.g., gold or tantalum). A number of configurations have been tried, and each has met with a degree of success. The most widely used approach is to use a solid disk with an orifice in the center (~3–6 mm in diameter) as the secondary cathode [94–96]. In most discharges a large fraction of the sputtered atoms are deposited back on the conducting cathode and subsequently sputtered again. Because the conducting mask has a hole in it, a fraction of the atoms from the mask are redeposited on the insulator beneath it. The sample

surface soon becomes conducting and begins to attract argon ions. Because the energy of the impinging ions is sufficient to penetrate the thin metallic film, atoms from the underlying insulator are sputtered. An equilibrium is soon established between the redeposition of metal atoms and the sputtering of insulator atoms, resulting in a steady-state discharge with ions representative of the insulating material and the cathode metal. Several investigations have focused on the surrogate cathode material and geometry [94–96]. The results obtained have been on par with radio frequency analysis for similar samples, with one group demonstrating precision of 6% relative standard deviation (RSD) at the part-per-million (ppm) level and detection limits in the part-per-billion range [94]. Interferences from the mask are a concern, however, because of the relative sputtered atom densities (i.e., the atom density of the mask material is orders of magnitude greater than that of the sample).

2.4.3 Mass Analyzers

Unlike in optical methods, in GDMS it is necessary to transfer species out of the plasma and into the detection system. Although the pressure differential alone is sufficient to transfer a mixture of atoms and ions from the plasma, an extraction voltage applied just beyond the exit orifice of the cell enhances the fraction of ions in the final beam. Depending on the type of mass analyzer used, an additional degree of energy filtering may be necessary to reduce the energy spread of the ions. Two commonly employed energy filters are Bessel boxes and electrostatic analyzers (see Fig. 2.11). Five types of mass analyzers are used extensively with glow discharge plasmas. Two of these, magnetic sectors and quadrupole, are illustrated schematically in Fig. 2.12; ion traps and time-of-flight analyzers are discussed in later chapters. For a magnetic sector, fields generated by spinning charged particles (ions) interact with a magnetic field imposed on their flight. The particles follow a curved path with a radius proportional to their mass-to-charge ratios, separating ions of different mass in space. A series of mechanical slits define the beam shape and hence the resolution. Electrostatic energy analyzers (ESAs) are often employed in combination with magnetic sector devices. In the case of the commercially available VG9000 [20,97] glow discharge mass spectrometer, the ESA is positioned after the magnetic sector (in the so-called reverse Nier-Johnson geometry). The ESA deflects the ion beam 90° to select and transmit a nominal ion energy, and the unwanted ions deviate from this path and are absorbed by the walls (Fig. 2.11).

A second commonly used mass analyzer is the quadrupole. A quadrupole acts as a mass filter, allowing a certain mass-to-charge ratio of ions to be transmitted while filtering out all others. The quadrupole consists of a set of four electrodes positioned in an array. Superimposed radio frequency and direct current electric fields can be mutually tuned to allow transmission of ions of the selected mass-to-

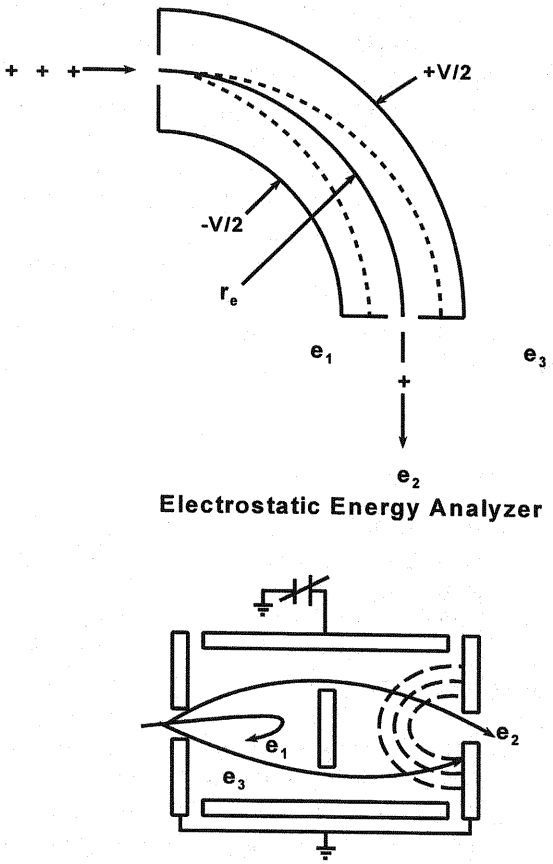

Figure 11 Schematic diagram of (a) an electrostatic energy analyzer and (b) a Bessel box energy analyzer. (From Ref. 19.)

charge. A Bessel box is often positioned in front of the quadrupole rods to define a narrow energy window of ions that may enter. An ion entering the Bessel box may take one of several trajectories (see Fig. 2.11). If the ion does not possess a minimum energy, as determined by the potentials on the Bessel box lenses, it is repelled back toward the entrance aperture (e_1). If the energy of the ion is too great, the field does not deflect the ion sufficiently to move it around the center stop and it collides with the exit plate (e_3). If the ion has the right energy, it is deflected around the center stop and out the other side (e_2).

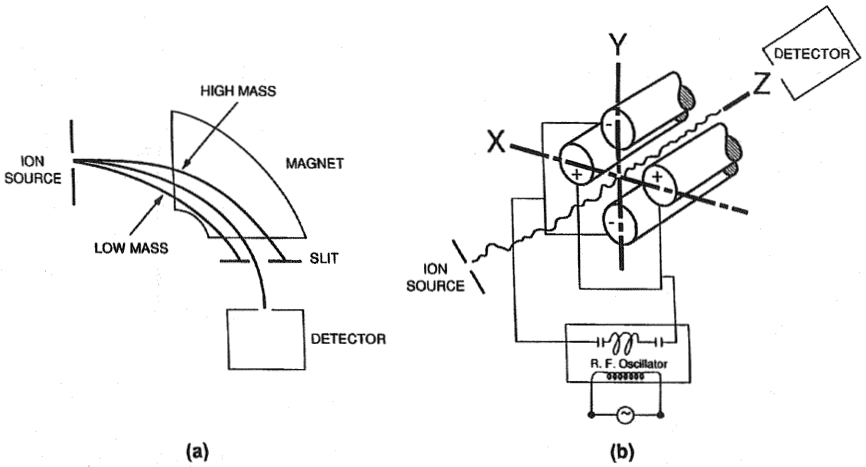

Figure 12 Schematic diagram of (a) a magnetic sector mass spectrometer and (b) a quadrupole mass spectrometer.

Once the ions exit the mass spectrometer, they must be detected. Several different detection systems are used with glow discharge mass spectrometers, including Faraday cups, electron multipliers, and microchannel plates. Choice of detector is often independent of the kind of mass spectrometer, although some combinations of mass analyzer and detector are more common than others (e.g., microchannel plates are used extensively with time-of-flight mass spectrometers). Faraday plates are the simplest type of detectors. These devices usually consist of a thin metal plate, electrically isolated from the housing and positioned to intercept the charge flux emerging from the mass separating device (i.e., quadrupole rods, magnetic sector, etc.). Collisions of ions with the plate induce a current that can be amplified and, by dropping it across a resistor, converted to an output voltage. This detector requires a relatively large current flux (typically greater than 10 pA) and is used primarily for monitoring major species in a spectrum. To detect the trace constituents, an electron multiplier is often employed. The multiplier is usually positioned off the ion axis to reduce high-energy ion and stray photon noise. The aperture of the multiplier is held at a large negative potential to accelerate the ions emerging from the mass spectrometer toward the surface of the device. At the surface, ions impact and release free electrons that are multiplied through a cascade process, generating gains of up to 10^6. Some multipliers can be operated in both the analogue and pulse-counting modes. In the analogue mode, the current generated by the multiplier is output in a similar fashion to that generated by a Faraday plate. In ion counting mode, each incident ion on the

surface of the multiplier generates a pulse of electrons. This pulse is fed to an amplifier and then to a discriminator that conditions the pulse, filters out the background, and directs it into a counter/processor whose output consists of a digital count rate.

One specific type of pulse-counting detector is called a Daly detector after its developer [98]. In this system, the ion beam is accelerated to 20 kV and directed to a highly polished surface of a material with a large cross section for secondary electron emission. Ejected electrons impinge on a plastic scintillator, whose flashes of light are registered by a photomultiplier outside the vacuum system. Data processing then proceeds as with the other pulse-counting detectors.

2.5 APPLICATIONS

GDMS has found widespread analytical application in trace element analysis, and its greatest use in the routine analysis of metals, alloys, and semiconductors. In the last 10 years, GDMS has become a routine technique, providing reliable data in commercial laboratories. Semiconductor materials compose the majority of sample types analyzed by GDMS, but as new methods are developed to analyze such things as solution residues and nonconductors (e.g., glasses, ceramics, and soils), analysis of other types of samples may become more common among GDMS practitioners. This section highlights some of the novel applications of GDMS; most of the examples are from the past 10 years. The discussion is not intended to be all-inclusive but to provide an overview of the direction in which the field is moving.

2.5.1 Isotope Ratio Measurements

The precise measurement of isotope ratios of solids has always been an important area in inorganic mass spectrometry. These measurements are usually performed by using thermal ionization [see Chapter 1, as well as excellent reviews by Heumann (99) and DeLaeter (100)]. However, recent interest in environmental chemistry and the expanding role of mass spectrometry in nuclear technology have generated a need for rapid, relatively precise measurement of isotope ratios in bulk solids. Most of the work in this field has proceeded in two laboratories: the Institute for Transuranium Elements in Karlsruhe, Germany [101], and the Oak Ridge National Laboratory in Oak Ridge, Tennessee. The instrument used in both cases was the VG-9000 double-focusing magnetic sector with reverse Nier-Johnson geometry. A direct current discharge was used for all of the studies reported; the Karlsruhe group used a secondary cathode for nonconducting samples and the Oak Ridge group mixed their nonconducting samples with copper or silver powder prior to analysis.

Zirconium, aluminum, lithium, and boron are all important elements in nuclear chemistry [101]; zirconium alloys, for example, are used as cladding for nuclear fuel. Because nuclear processes distort the isotopic composition of these elements, measuring them before and after a process provides important information with regard to reactor operation. Glow discharge mass spectrometry is well suited to this type of measurement, as exemplified by the isotopic analysis of zirconium samples containing plutonium [101]. It had been proposed that the analysis of zirconium alloys could be hindered by the presence of multiply charged isobaric interferences formed through the combination of plutonium with argon [101]. No evidence of the formation of the plutonium argide bivalent and trivalent species was found, however, and the isotopic composition of zirconium in an unknown sample compared well with the composition of natural zirconium [101].

In many applications, discerning the importance the abundance of a particular isotope is difficult without a precise measurement. Experiments at the Oak Ridge National Laboratory were directed at establishing how well isotope ratios could be measured with GDMS. External precision was better than 0.03% for ratios measured for the matrix element [102]. When the element was present in concentrations of ~0.5 weight percent, external precision was better than 0.1%; this value worsened to 1% for elements with concentrations in the 10- to 20-ppm range [102]. Although these ratios are of sufficient quality for many applications, some results suggest that better values would have been obtained by better controlling discharge conditions. One specific observation, a linear drift in the values of the ratios that correlated with the argon gas pressure (see Fig. 2.13), gave

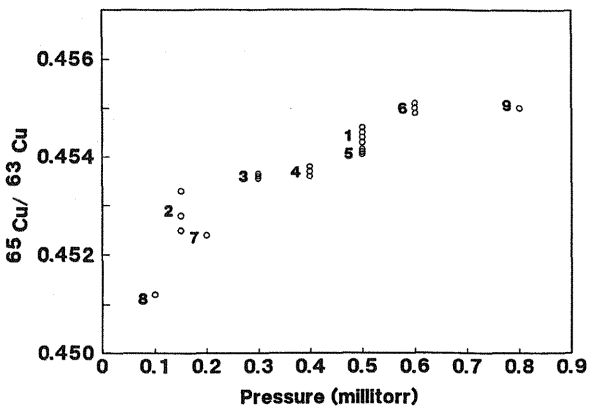

Figure 13 Measured copper isotope ratio as a function of argon discharge gas pressure in torr. Numbers indicate the order in which measurements at a particular pressure were taken. (From Ref. 102.)

reason to believe that more accurately controlling the source pressure would lead to improved external precision. It is not clear why the discharge pressure influences the measured isotope ratio; one possible explanation is related to the changing discharge geometry that accompanies the pressure change. Because extraction efficiency varies as a function of mass and distance from the ion exit orifice, isotope bias may be introduced with the changing spatial relationship between the sample and the extraction optics. This explanation has not been verified, however; the whole phenomenon of isotopic bias is difficult to access experimentally in nearly all fields of mass spectrometry.

2.5.2 Detection of Radionuclides in Soils, Sediment, and Vegetation

The rapid development of commercial instrumentation has meant that analyses that were previously carried out only by thermal ionization (often with isotope dilution) can now be done with inductively coupled plasma mass spectrometry (ICP-MS) or GDMS. The advantages and disadvantages of each of these techniques are described in various chapters in this book. One limitation of thermal ionization mass spectrometry (TIMS) and ICP-MS is the need for digestion prior to analysis. Certain elements in difficult matrices (e.g., soils, sediments, and vegetation) often pose problems because of their low solubilities and element-specific chemistries. In addition, the time-consuming nature of dissolution with its inherent risks of contamination make the choice of performing the analysis directly on the solid attractive. Several investigations have focused on the analysis of uranium in soil [103,104]. To demonstrate the power of the technique for analyzing other radionuclides, Betti et al. [104] have measured cesium, strontium, plutonium, uranium, and thorium in soils, sediments, and vegetation. Because all of these materials are nonconducting, they had to be analyzed with the surrogate cathode approach. Table 2.3 compares GDMS results with certified values for several elements in several different standard samples. Errors ranged

Table 3 Comparison of Glow Discharge Mass Spectrometry (GDMS) Results with Certified Values

Radioisotope	GDMS value (pg/g)	Reference value (pg/g) (reference sample)	Errors %
^{137}Cs	5	3.86 (IAEA 373)	29.5
^{239}Pu	100	92[a] (IAEA 135)	8.7
^{234}U	1.0	1.1 (IAEA 375)	9.0
^{234}U	1.0	1.2 (IAEA 135)	17.0
^{235}U	25	22 (IAEA 4350)	13.6

[a]Value given as $^{239}Pu + ^{240}Pu$.
Source: Ref. 104.

from 8.7% to 29.5%, which are quite good percentages given the low concentrations in the samples. Detection limits in the picogram per gram (pg/g) (part per trillion) range were reported. Integration times necessary to obtain these values, however, ranged up to 1 hour. The authors noted the need for mass resolving power in excess of 2×10^6 to analyze ^{137}Cs, ^{90}Sr, ^{241}Pu, and ^{238}Pu when interferences from barium, zirconium, americium, and uranium complicate the spectrum [104]. The use of Fourier transform ion cyclotron resonance mass spectrometry in combination with a glow discharge was suggested.

2.5.3 Isotope Dilution Glow Discharge Mass Spectrometry

Isotope dilution mass spectrometry (IDMS) is a powerful technique for establishing the concentration of a target species in a sample of unknown elemental composition. It has received widespread application with gaseous and liquid samples, yet it has seen little use with solids because of the need to establish isotopic equilibrium between the sample and the isotopic spike. The technique has largely been confined to gas [105] or thermal ionization mass spectrometry [106], although some work has also been carried out using spark source [107] and inductively coupled plasma mass spectrometries [108]. Recently, isotope dilution has been used in combination with glow discharge mass spectrometry for analysis of solution residues. The problem of equilibrating the sample and the isotopic spike was overcome by mixing the sample and spike as solutions and then analyzing them as dried residues by GDMS [64]. Cathodes were prepared by pipetting ~200 μL of a spiked aqueous oil leachate that had been digested according to EPA SW-846 Method 3050 into 1.0 g of 99.99$^+$% silver powder. The resulting slurry was then dried at 100°C for 6 hours, mixed to obtain homogeneity, and pressed in to a pin 1.5 mm in diameter by 20 mm in length. Isotope ratio measurements were made for the isotopically enriched spike, the unspiked samples, and the mixtures. Figure 2.14 shows representative spectra obtained from the three sample types [(a) is the isotopically enriched spike, (b) is the unspiked sample, and (c) is the mixture]. Table 2.4 lists the ratio for the sample (R_s), the spike (also called the tracer, R_T), and the mixture (R_M), along with the concentrations for each sample calculated from the isotope dilution equation. These results were in good agreement with those obtained by inductively coupled plasma atomic emission spectroscopy. Internal precisions of better than 5% were obtained, even when the concentration was just above the detection limit; external precision was about 2%. These values were 3–10 times better than those normally obtained by using GDMS sensitivity factors [64].

2.5.4 Development of a High-Purity Support Gas System for C, N, and O Analysis

Perhaps one of the most severe limitations of glow discharge mass spectrometry is that any contaminants entering the discharge cell along with the support gas have a

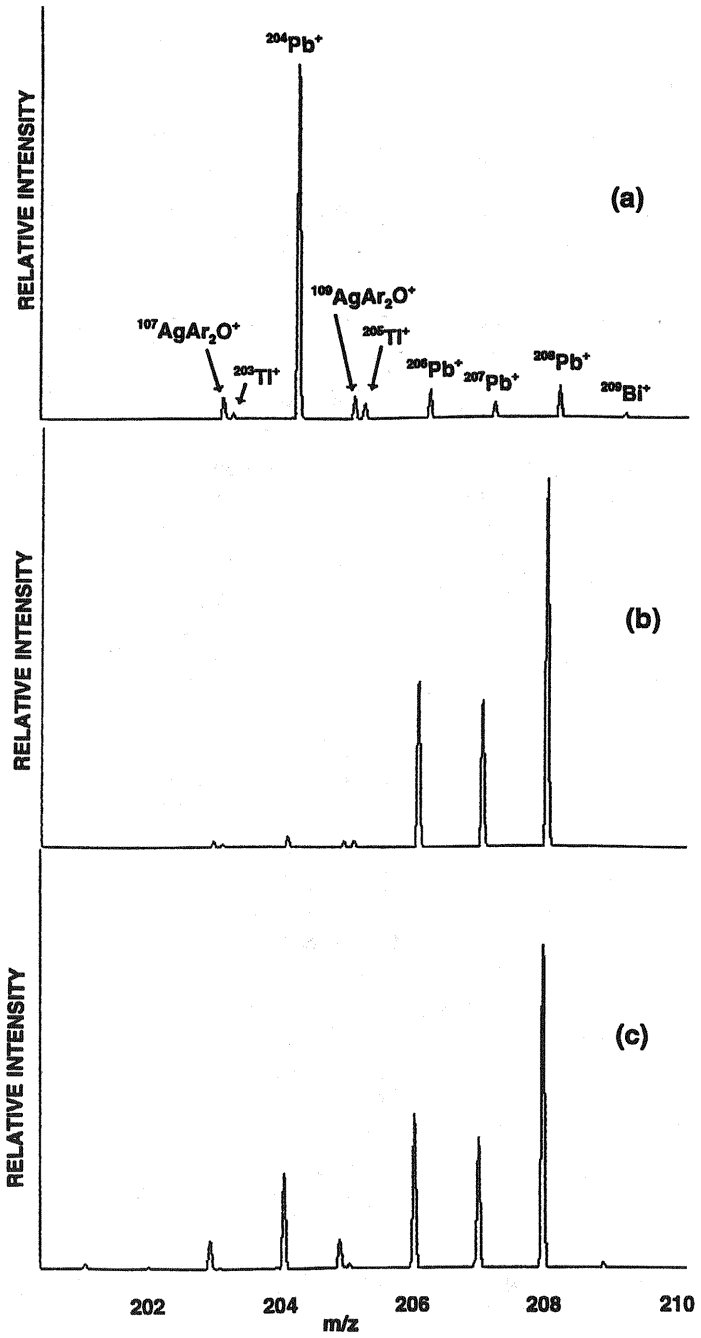
RELATIVE INTENSITY
$^{204}Pb^+$
(a)
$^{107}AgAr_2O^+$
$^{203}Tl^+$
$^{109}AgAr_2O^+$
$^{205}Tl^+$
$^{206}Pb^+$
$^{207}Pb^+$
$^{208}Pb^+$
$^{209}Bi^+$
RELATIVE INTENSITY
(b)
RELATIVE INTENSITY
(c)
202
204
206
208
210
m/z

Table 4 Bias Corrected Isotope Ratio Measurements in the Unspiked Sample, Isotopically Enriched Spike, and Spiked Sample for Three Oil Leachate Samples as Determined by Glow Discharge Mass Spectroscopy Solution Residue Method

Sample	R_S $^{207}Pb^+/^{204}Pb^+$ (sample)	R_T $^{207}Pb^+/^{204}Pb^+$ (spike)	R_M $^{207}Pb^+/^{204}Pb^+$ (mixture)	Concentration (ppm)
A	14.9 ± 0.5	0.029 ± 0.001	0.192 ± 0.004	2.69 ± 0.05
B	7.5 ± 0.2	0.029 ± 0.001	0.130 ± 0.001	3.5 ± 0.1
C1	15.2 ± 0.2	0.029 ± 0.001	1.44 ± 0.01	82.5 ± 0.7
C2	15.9 ± 0.3	0.029 ± 0.001	1.46 ± 0.02	83.2 ± 0.8
C3	15.1 ± 0.2	0.029 ± 0.001	1.41 ± 0.02	80.2 ± 0.8

Source: Ref. 64.

deleterious effect on the resulting mass spectrum. This effect is multiplied by several orders of magnitude because the support gas is far and away the most abundant constituent of the discharge. Complicating this effect further is the production of polyatomic species such as CO^+, ArC^+, ArN^+, and ArO^+. Several methods have been used to reduce interferences in the glow discharge to acceptable levels. One is to dissociate the molecular ions into their component elements through the use of gas-phase collisions [109–111], a second is to resolve the interferences with a high-resolution mass spectrometer [112], and a third is to used gated detection with a pulsed discharge [113,114]. None of these methods, however, reduces the contributions of residual gases (C, N, or O). Among the methods specifically designed to remove contaminants, heating the gas to drive them out, cryocooling to condense them from the gas phase [115], using getters as a conductive binder [116], and using a high-purity support gas [117] hold the most promise. Mykytiuk et al. [69] and Valiga et al. [118] have used a combination of approaches to analyze C, N, and O at the tens of part per million level and lower in samples. In particular, Valiga's work was impressive because he used a low-resolution quadrupole mass spectrometer, an inherently less expensive instrument than a sector. Table 2.5 shows these results for the analysis of a National Institute

Figure 14 Three glow discharge mass spectra taken over the mass range *m/z* 200–210 for three different cathodes doped with (a) 500 μL of a 40.9-ppm ^{204}Pb spike, (b) 500 μL of an unknown waste oil sample, and (c) 500 μL of a mixture consisting of 1.0 mL of the unknown and 100 μL of the 40.9-ppm ^{204}Pb spike. The discharge conditions of all three cathodes were −1000 V dc, 2.0 mA, and 133.3 Pa argon.

Table 5 Analysis of National Institute of Standards and Technology (NIST) 685/W High Purity Gold

Element	Certified value (ppm)	GloQuad value (ppm)	Element	Certified value (ppm)	GloQuad value (ppm)
Cu	0.1	0.02	Mg	<0.2	<0.02
In	0.007	<0.006	Mn	<0.01	<0.03
Fe	0.3	0.3	N	<0.03	<2
O	2	<0.4	Na	<0.2	<0.08
Ag	0.1	0.03	Nb	<0.1	<0.001
Al	<0.03	<0.002	Ni	<0.05	<0.02
Ba	<0.03	<0.002	S	<0.07	<0.07
C	<0.01	<2	Sc	<0.01	<0.001
Ca	<1	<0.6	Si	<0.03	0.3
Cl	<0.1	<0.01	Sn	<0.07	<0.05
Cr	<0.05	<0.02	Sr	<0.03	<0.001
F	<0.02	<40	V	<0.05	<0.09
K	<0.2	<0.1	Zn	<0.04	<0.01

Source: Ref. 118.

of Standards and Technology high-purity gold sample (Standard Reference Material 658/W). The general observation is that most of the measured values, including those of transition elements, are present, or have background equivalent concentrations (BECs), at the low part-per-billion levels. Elements that pose particular problems when analyzed by a quadrupole instrument (primarily as a result of interfering polyatomic species), such as Fe, Ca, Cl, Cr, K, Ni, S, and Si, are present at or have BECs of less than 1 ppm (0.6 to 0.02 ppm). Meticulous attention to gas purity resulted in obtaining much higher performance from a quadrupole-based system than had previously been achieved.

2.6 SUMMARY

Although gaseous discharges have been used in one form or another for more than 80 years, it has been the developments of the last 30 years that have been the major benefit to analytical spectroscopists. The glow discharge's strengths are well established now, and new applications, like those highlighted in this chapter and in other chapters in this book, keep pushing the technique into new areas as a tool for solving problems in the chemical sciences. Novel instrumentation, like the ion trap and the time-of-flight, promise new and exciting opportunities for GDMS, and developments with new and existing sources offer the hope that the technique

will ultimately hold universal appeal. A core of innovative investigators continue to do fine work in the field, and new individuals are beginning to discover the numerous benefits of the technique. This author believes that there are many good experiments, both fundamental and applied, yet to be done and looks forward to seeing how GDMS unfolds in the next 30 years.

REFERENCES

1. Bainbridge, K. T.; Jordan, E. B. *Phys. Rev.* **1936**, *50*, 282.
2. Aston, F. W. *Isotopes*, 2nd ed.; Longmans, Green: New York, 1924.
3. Aston, F. W. *Proc. Roy. Soc. A* **1937**, *163*, 391.
4. Dempster, A. J. MDDC 3770, United States Department of Commerce, Washington, DC, 1946.
5. Ramendik, G.; Verlinden, J.; Gijbels, R. in *Inorganic Mass Spectrometry*; Adams, F.; Gijbels, R.; Van Grieken, R., Eds.; John Wiley & Sons: New York, 1988; Chapter 2.
6. Green, J. E.; Sequeda-Osorio, F.; Natarajan, B. R. *J. Vac. Sci. Technol.* **1975**, *12*, 336.
7. Boumans, P. W. J. M. *Anal. Chem.* **1972**, *44*, 1219.
8. Harrison, W. W.; Prakash, N. J. *Anal. Chim. Acta* **1970**, *49*, 151.
9. Grimm, W. *Spectrochim. Acta* **1968**, *23B*, 443.
10. Pevtsov, G. A.; Krasilshchik, V. Z.; Yabovlera, A. F. *J. Anal. Chem. USSR* **1968**, *23*, 1569.
11. Coburn, J. W.; Kay, E. *J. Appl. Phys.* **1972**, *43*, 4965.
12. Coburn, J. W.; Kay, E. *Appl. Phys. Lett.* **1971**, *18*, 435.
13. Coburn, J. W. *Rev. Sci. Instrum.* **1970**, *41*, 1219.
14. Harrison, W. W.; Magee, C. W. *Anal. Chem.* **1974**, *46*, 461.
15. Colby, B. N.; Evans, Jr., C. A. *Anal. Chem.* **1974**, *46*, 1236.
16. Bruhn, C. G.; Bentz, B. L.; Harrison, W. W. *Anal. Chem.* **1979**, *51*, 673.
17. King, F. L.; Harrison, W. W. *Mass Spectrometry Reviews* **1990**, *9*, 285.
18. Harrison, W. W. in *Inorganic Mass Spectrometry*; Adams, F.; Gijbels, R.; Van Grieken, R., Eds.; John Wiley & Sons: New York, 1988; Chapter 3.
19. Harrison, W. W.; Bentz, B. L. *Prog. Analyt. Spectrosc.* **1988**, *11*, 53.
20. Hall, D. J.; Robinson, P. K. *Am. Lab.* **1987**, 74.
21. Duckworth, D. C.; Marcus, R. K. *Anal. Chem.* **1989**, *61*, 1879.
22. Fang, D.; Marcus, R. K. in *Glow Discharge Spectroscopies*; Marcus, R. K., Ed.; Modern Analytical Chemistry; Plenum: New York, 1993; Chapter 2.
23. Chapman, B. *Glow Discharge Processes: Sputtering and Plasma Etching*; John Wiley & Sons: New York, 1980; Chapter 3.
24. Howatson, A. M. *An Introduction to Gas Discharges*; 2nd ed.; Pergamon: New York, 1976; Chapter 1.
25. Von Engel, A. *Electrical Plasmas: Their Nature and Uses*; International Publications Service Taylor and Francis: New York, 1983; Chapter 7.
26. Swift, D. A. *Contemp. Phys.* **1981**, *22*, 37.
27. Brown, S. C. *Introduction to Electrical Discharges in Gases*; John Wiley & Sons: New York, 1966; Chapter 13.

28. Cobine, J. D. *Gaseous Conductors: Theory and Engineering Applications*; Dover: New York, 1958; Chapter 8.
29. Harrison, W. W.; Barshick, C. M.; Klingler, J. A.; Ratliff, P. H.; Mei, Y. *Anal. Chem.* **1990**, *62*, 943A.
30. Westwood, E. D. *Prog. Surf. Sci.* **1976**, *7*, 71.
31. Wehner, G. K.; Anderson, G. S. in *Handbook of Thin Film Technology*; Maissel, L. I.; Glang, R., Eds.; McGraw-Hill Book: New York, 1970; Chapter 2.
32. McHugh, J. A. in *Methods of Surface Analysis*; Czanderna, Ed.; Elsevier: New York, 1975.
33. Sigmund, P. *Phys. Rev.* **1969**, *184*, 383.
34. Winters, H. F. in *Topics in Current Chemistry No. 94, Plasma Chemistry III*; Veprek, S.; Vervgopalen, M., Eds.; Springer-Verlag: Berlin, 1980.
35. Fetz, H.; Oechsner, H. *Proc. VI Conf. Int. Phen. D'Ionisation dans le Gaz, Vol. II*, 1963.
36. Wehner, G. K. *Methods and Phenomena: Their Applications in Science and Technology, Vol. 1*; Wolsky, S. P.; Czandera, A. W., Eds.; Elsevier Scientific: New York, 1975.
37. Anderson, H. H.; Bay, H. L. in *Sputtering by Particle Bombardment I, Physical Sputtering by Single-Element Solids*; Behrish, R., Ed.; Springer-Verlag: Berlin, 1981; Chapter 4.
38. Carter, G.; Colligon, J. S. *Ion Bombardment of Solids*; American Elsevier: New York, 1968.
39. Sigmund, P. in *Sputtering by Particle Bombardment I, Physical Sputtering by Single-Element Solids*; Behrish, R., Ed.; Springer-Verlag: Berlin, 1981; Chapter 2.
40. Harrison, D. E.; Delaplain, C. B. *J. Appl. Phys.* **1976**, *47*, 2252.
41. Harrison, D. E.; Levy, N. S.; Johnson, J. P.; Effron, H. M. *J. Appl. Phys.* **1968**, *39*, 3742.
42. Gibson, J. B.; Goland, A. N.; Milgram, M.; Vineyard, G. H. *Phys. Rev.* **1960**, *120*, 1229.
43. Nasser, E. *Fundamentals of Gaseous Ionization and Plasma Electronics*; Wiley-Interscience: New York, 1971.
44. *Electron Impact Ionization*; Mark, T. D.; Dunn, G. H., Eds.; Springer-Verlag Wien: New York, 1985.
45. Valyi, L. *Atom and Ion Sources*; John Wiley & Sons: New York, 1977.
46. Field, F. H.; Franklin, J. L. *Electron Impact Phenomena*; Academic: New York, 1970.
47. Delcroix, J.; Ferreira, C.; Richard, A. in *Principles of Laser Plasmas*; G. Bekefi, Ed.; John Wiley & Sons: New York, 1976; Chapter 5.
48. Bordin, V. S.; Kagan, Y. M. *Opt. Spec.* **1967**, *23*, 108.
49. Penning, F. M. *Z. Physik* **1925**, *46*, 225.
50. Stedman, D. H.; Stetser, D. W. *Prog. React. Kinet.* **1971**, *6*, 193.
51. Eckstein, E. W.; Coburn, J. W.; Kay, E. *Int. J. Mass Spec. Ion Phys.* **1975**, *17*, 129.
52. Strauss, J. A.; Ferreira, N. P.; Human, H. G. C. *Spectrochim. Acta* **1982**, *37B*, 947.
53. Smith, R. L.; Serxner, D.; Hess, K. R. *Anal. Chem.* **1989**, *61*, 1103.
54. Hecq, M.; Hecq, A.; Fontignies, M. *Thin Solid Films* **1984**, *115*, L45.

55. Smyth, K. C.; Bentz, B. L.; Bruhn, C. G.; Harrison, W. W. *J. Am. Chem. Soc.* **1979**, *101*, 797.
56. Hotop, H.; Niehaus, A. *Z. Physik* **1969**, *228*, 68.
57. Knewstubb, P. F.; Tickner, A. W. *J. Chem. Phys.* **1963**, *38*, 464.
58. Bogaerts, A.; Gijbels, R. *Phys. Rev. A.* **1995**, *52*, 3743.
59. Bogaerts, A.; van Straaten, M.; Gijbels, R. *Spectrochim. Acta* **1995**, *50B*, 179.
60. Bogaerts, A.; van Straaten, M.; Gijbels, R. *J. Appl. Phys.* **1995**, *77*, 1868.
61. Jakubowski, N.; Stuewer, D. *Fresenius Zeitschrift fur Analytische Chemie* **1989**, *335*, 680.
62. Barshick, C. M., Ph.D. Dissertation, University of Virginia, 1990.
63. Barshick, C. M.; Duckworth, D. C., Smith, D. H. *J. Am. Soc. Mass Spectrom.* **1993**, *4*, 47.
64. Barshick, C. M.; Smith, D. H.; Wade, J. W.; Bayne, C. K. *J. Anal. Atom. Spectrom.* **1994**, *9*, 83.
65. Barshick, C. M.; Smith, D. H.; Hackney, J. H.; Cole, B. A.; Wade, J. W. *Anal. Chem.* **1994**, *66*, 730.
66. Daughtrey, E. H.; Harrison, W. W. *Anal. Chem.* **1975**, *47*, 1024.
67. Donohue, D. L.; Harrison, W. W. *Anal. Chem.* **1975**, *47*, 1528.
68. Battagliarin, M.; Sentimenti, E.; Scattolin, R. *Spectrochim. Acta* **1995**, *50B*, 13.
69. Mykytiuk, A. P.; Semeniuk, P.; Berman, S. *Spectrochim. Acta Rev.* **1990**, *13*, 1.
70. Barshick, C. M.; Duckworth, D. C. unpublished results.
71. Hess, K. R.; Day, D. A.; Zook, A. L.; Barshick, C. M. *Microchem. J.* **1997**, *55*, 208.
72. Nasser, E. *Fundamentals of Gaseous Ionization and Plasma Electronics*; Wiley-Interscience: New York, 1971.
73. Duckworth, D. C., Ph.D. Dissertation, Clemson University, 1991.
74. Grimm, W. *Spectrochim. Acta* **1968**, *23B*, 433.
75. Jakubowski, N.; Stuewer, D.; Vieth, W. *Anal. Chem.* **1987**, *59*, 1825.
76. Weston, G. F. *Cold Cathode Glow Discharge Tubes*; ILIFFE Books: London, 1968.
77. Pillow, M. E. *Spectrochim. Acta* **1981**, *36B*, 821.
78. Little, P. F.; von Engel, A. *Proc. R. Soc. London* **1954**, *224A*, 209.
79. Slevin, P. J.; Harrison, W. W. *Appl. Spectros. Rev.* **1975**, *10*, 201.
80. Caroli, S. *Prog. Anal. At. Spectrosc.* **1983**, *6*, 253.
81. Bentz, B. L.; Bruhn, C. G.; Harrison, W. W. *Int. J. Mass Spectrom. Ion Phys.* **1978**, *28*, 409.
82. Daughtrey, E. H.; Harrison, W. W. *Anal. Chem.* **1975**, *47*, 1024.
83. Marcus, R. K.; Harrison, W. W. *Spectrochim. Acta B* **1985**, *40*, 933.
84. Marcus, R. K.; Harrison, W. W. *Anal. Chem.* **1986**, *58*, 797.
85. Marcus, R. K.; Harrison, W. W. *Anal. Chem.* **1987**, *59*, 2369.
86. Marcus, R. K.; King, F. L.; Harrison, W. W. *Anal. Chem.* **1986**, *58*, 972.
87. Harrison, W. W.; Barshick, C. M.; Klingler, J. A.; Ratliff, P. H.; Mei, Y. *Anal. Chem.* **1990**, *62*, 943A.
88. Analyte Corporation, Medford, OR.
89. Shields, J. P.; Lee, G. H.; Piepmeier, E. H. *Appl. Spectrosc.* **1988**, *42*, 684.
90. Kim, H. J.; Piepmeier, E. H.; Beck, G. L.; Brumbaugh, G. G.; Farmer, O. T. *Anal. Chem.* **1990**, *62*, 1368.

91. McLuckey, S. A.; Glish, G. L.; Asano, K. G.; Grant, B. C. *Anal. Chem.* **1988**, *60*, 2220.
92. McLuckey, S. A.; Glish, G. L.; Asano, K. G. *Anal. Chim. Acta* **1989**, *225*, 25.
93. McLuckey, S. A., Oak Ridge National Laboratory, personal communication, 1997.
94. Milton, D. M. P.; Hutton, R. C. *Spectrochim. Acta* **1993**, *48B*, 39.
95. Schelles, W.; DeGendt, S.; Muller, V.; van Grieken, R. *Appl. Spectrosc.* **1995**, *49*, 939.
96. Schelles, W.; DeGendt, S.; Maes, K.; van Grieken, R. *Fresenius J. Anal. Chem.* **1996**, *355*, 858.
97. VG Elemental, Ion Path Road Three, Winsford, Cheshire, CW7 3BX, England.
98. Daly, N. R. *Rev. Sci. Instrum.* **1960**, *31*, 264.
99. Heumann, K. G. in *Inorganic Mass Spectrometry*; Adams, F.; Gijbels, R.; van Grieken, R., Eds.; John Wiley & Sons: New York, 1988; Chapter 7.
100. DeLaeter, J. R. *Mass Spectrom. Rev.* **1994**, *13*, 3.
101. Betti, M.; Rasmussen, G.; Koch, L. *Fresenius J. Anal. Chem.* **1996**, *355*, 808.
102. Riciputi, L. R.; Duckworth, D. C.; Barshick, C. M.; Smith, D. H. *Int. J. Mass Spectrom. Ion Proc.* **1995**, *146/147*, 55.
103. Duckworth, D. C.; Barshick, C. M.; Bostick, D. A.; Smith, D. H. *J. Anal. At. Spectrom.* **1993**, *47*, 243.
104. Betti, M.; Giannarelli, S.; Hiernaut, T.; Rasmussen, G.; Koch, L. *Fresenius J. Anal. Chem.* **1996**, *355*, 642.
105. Mook, W. G.; Grootes, P. M. *Int. J. Mass Spectrom. Ion Phys.* **1973**, *12*, 273.
106. Heumann, K. G. *Fresenius's Z. Anal. Chem.* **1986**, *324*, 601.
107. Farrar, H. in *Trace Analysis by Mass Spectrometry*; Ahern, A. J., Ed.; Academic Press: New York, 1972; p. 239.
108. Garbarino, J. R.; Taylor, H. E. *Anal. Chem.* **1987**, *59*, 1568.
109. McLuckey, S. A.; Glish, G. L.; Duckworth, D. C.; Marcus, R. K. *Anal. Chem.* **1992**, *64*, 1606.
110. Duckworth, D. C.; Marcus, R. K. *Appl. Spectrosc.* **1990**, *44*, 649.
111. King, F. L.; Harrison, W. W. *Int. J. Mass Spectrom. Ion Proc.* **1989**, *89*, 171.
112. Watson, C. H.; Wronka, J.; Laukien, F. H.; Barshick, C. M.; Eyler, J. R. *Anal. Chem.* **1993**, *65*, 2801.
113. Klingler, J. A.; Barshick, C. M.; Harrison, W. W. *Anal. Chem.* **1991**, *63*, 2571.
114. Pan, C.; King, F. L. *Anal. Chem.* **1993**, *65*, 3187.
115. Ohorodnik, S. K.; DeGendt, S.; Tong, S. L.; Harrison, W. W. *J. Anal. Atom. Spectrom.* **1993**, *8*, 859.
116. Mei, Y.; Harrison, W. W. *Spectrochim. Acta* **1991**, *46B*, 175.
117. King, F. L.; McCormack, A. L.; Harrison, W. W. *J. Anal. Atom. Spectrom.* **1988**, *3*, 883.
118. Valiga, R. E.; Duckworth, D. C.; Smith, D. H. *Rapid Communications in Mass Spectrometry* **1996**, *10*, 305.

3

Inductively Coupled Plasma Mass Spectrometry

John W. Olesik
The Ohio State University
Columbus, Ohio

Since the introduction of the first commercial instrument in 1983, inductively coupled plasma mass spectrometry (ICP-MS) has become widely accepted as a powerful technique for elemental analysis. Two excellent books on ICP-MS have been published [1,2]. ICP-MS provides rapid, multielement analysis with detection limits at single parts part trillion or below for about 40 to 60 elements in solution and a dynamic range of 10^4 to 10^8. These are the main reasons most ICP-MS instruments have been purchased. Two additional, unique capabilities of ICP-MS have also contributed to its commercial success: elemental isotope ratio measurements and convenient semiquantitative analysis. The relative sensitivities from element to element are predictable enough that semiquantitative analysis (with accuracy within a factor of 2 to 5) for up to 80 elements can be obtained using a single calibration solution containing a few elements and a blank solution.

The analytical performance and ease of use of commercial ICP-MS instruments have grown rapidly since the introduction of the first instruments from Sciex (now sold by PE-Sciex) and VG (now VG Elemental, a subsidiary of Thermo Optek). Detection limits, stability, and instrument computer-controlled automation have all improved dramatically. At the same time the instruments have become smaller and less expensive. Although most of the ICP-MS instruments are based on quadrupole mass spectrometers, time-of-flight- and magnetic sector–based instruments are now also commercially available. Several additional companies now sell ICP-MS instruments, including Finnigan, HP, Micromass, Sieko, Shimadzu, Spectro, Thermo Jarrell Ash, and Varian. Leco and GBC sell time-of-flight ICP-MS instruments. The use of an ICP ion source with ion trap and Fourier

transform ion cyclotron resonance mass spectrometers has also been reported. Although most samples are introduced into the instrument as solutions, laser ablation and other solid sampling approaches are also available commercially.

Although ICP-MS is a highly successful and powerful technique, several problems remain. When attempting to measure low concentrations (sub–part per billion) spectral overlaps due to polyatomic ions can be difficult to identify and overcome, particularly with quadrupole or time-of-flight mass spectrometers. Iron, calcium, and potassium typically suffer from rather severe spectral overlaps unless special steps are taken. Arsenic, selenium, chromium, vanadium, and titanium often suffer from polyatomic ion spectral overlaps that degrade detection limits. Molecular ion spectral overlaps are most common below mass 82 [3]. Matrix effects due to high concentrations of concomitant species, particularly heavy elements, can be severe when conditions are optimized for maximum analyte sensitivity. Because the sample must be physically transported into the mass spectrometer, deposition and contamination of the instrument can be problems (unlike ICP optical emission spectroscopy, in which photons are clean). For some applications short- and long-term precision is inadequate. In some applications, even better detection limits or sensitivities are required. The initial equipment and operating costs are high.

3.1 INSTRUMENTATION

The typical ICP-MS instrument (Fig. 3.1) consists of a sample introduction system (a nebulizer and spray chamber), an inductively coupled plasma source, a differ-

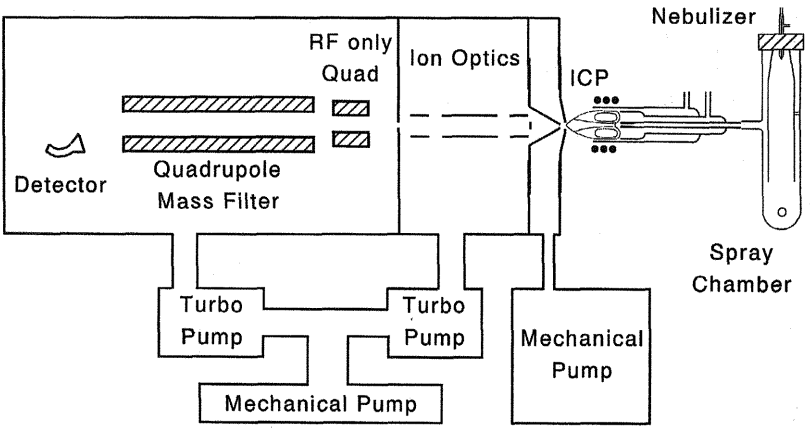

Figure 1 Components of a typical ICP-MS instrument.

entially pumped interface, ion optics, a mass spectrometer, and a detector. Ionization efficiencies in the plasma are nearly 100% for elements with ionization potentials less than about 9 eV. However, only about 1 in 10^4 to 1 in 10^6 atoms in the original sample are detected, so extensive loss of ions occurs during their transport from the plasma to the MS detector.

The sample is typically pumped at a rate of 0.4 to 1.0 mL/min to a nebulizer that produces an aerosol with a range of drop sizes from submicrometer to 40 μ in diameter [4,5]. Recently, nebulizers with small dead volumes that can be used with sample uptake rates as low as 10 μL/min have been introduced. The aerosol is modified as it passes through a spray chamber. Most aerosol drops that are too large to be vaporized effectively in the plasma (>20 μm diameter) are eliminated in the spray chamber. The spray chamber also limits the total amount of solvent liquid aerosol and vapor that enters the plasma. The aerosol exiting the spray chamber enters the hot, atmospheric pressure plasma gas (typically argon).

Each aerosol drop undergoes a series of processes (Fig. 3.2) in the hot plasma. The solvent evaporates from each drop, leaving a particle. The particle vaporizes and is converted into atoms and ions in the plasma. The atoms and ions

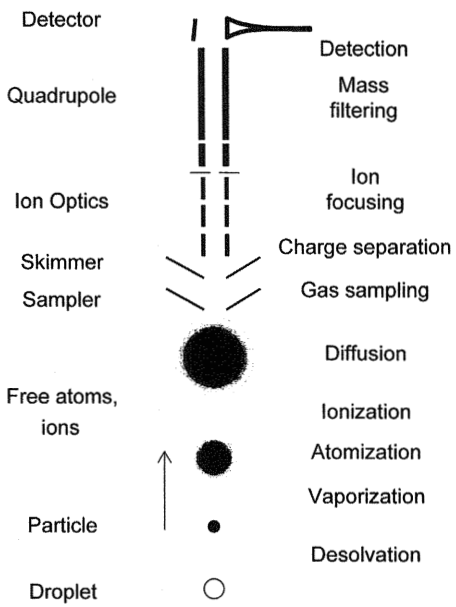

Figure 2 Series of processes a drop of sample undergoes in the ICP to produce ions, some of which are transported through the sampler and skimmer, focused into the mass spectrometer, filtered on the basis of their mass-to-charge ratio, and detected.

diffuse outward as they travel though the plasma toward the sampling orifice of the mass spectrometer.

Analyte ions generated in the plasma pass through the sampling orifice (Fig. 3.2) and then the gas expands. A fraction of the gas is sampled through the skimmer. A positive ion beam is formed as the electrons diffuse and charge separation occurs. A series of ion optics and typically a radio frequency– (rf-) only quadrupole lens focus positive ions into the mass spectrometer. Ions of a particular mass-to-charge ratio exit the mass spectrometer and are detected. Many of the commercial instruments use dual-mode (pulse counting and analogue) detection in order to provide an extremely wide dynamic range.

3.1.1 Inductively Coupled Plasma Characteristics and Generation

The inductively coupled plasma (ICP) is a flowing, partially ionized gas (typically Ar). The ICP is sustained in a quartz torch that consists of three tubes (Fig. 3.3).

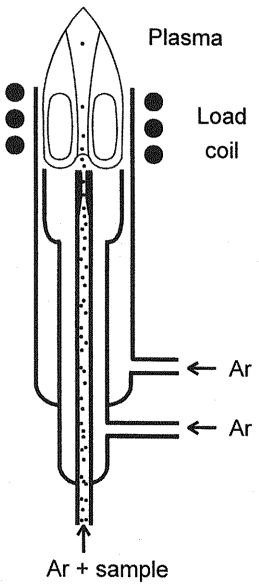

Figure 3 Typical quartz plasma torch positioned within a (induction) load coil. The center (injector) tube can be made of quartz or inert materials (alumina, platinum, or sapphire) to allow corrosive samples (including those containing hydrofluoric acid) to be introduced into the plasma. One-piece quartz torches, torches with demountable injector tubes, or completely demountable tubes are used.

A 1- to 2-kW radio frequency power supply, either free-running or crystal-controlled, drives current through a water- or air-cooled copper tube that acts as the induction coil (often called a *load coil*). The oscillating current through the load coil produces an oscillating electromagnetic field.

A tesla coil or high-voltage spark is used to seed the argon gas with electrons in order to start the discharge. Once the plasma discharge has been initiated, electrons in the plasma are accelerated by the oscillating magnetic field. Collisions between electrons and argon atoms lead to heating of the argon gas. Collisions between electrons and analyte atoms are thought to be the main mechanism for analyte ionization although charge exchange may also be important. Typically, less than 1% of the Ar (15.8-eV ionization potential) is ionized. The Ar plasma is about 14 mm wide (in a torch with an 18-mm-inner-diameter outer tube) and 30 to 40 mm long. Gas temperatures of 3000 to 7000 K and electron temperatures of 4000 to 8000 K are produced [6].

Argon is the most commonly used plasma gas because it is generally inexpensive (except in some parts of the world), inert (although Ar^+ ions are reactive), and monoatomic and produces a relatively simple background spectrum. Mixed gas plasmas (Ar/N_2) have been used to reduce signals from some molecular ions. Helium plasmas may more effectively ionize elements with high ionization energies, such as As, Se, and halogens [7]. Elements that suffer from interferences with polyatomic argide ions are better detected in He plasmas [7]. However, practical problems with helium plasmas have limited their use [7]. Helium plasmas have lower gas temperatures and are more severely affected by solvent loading as sample aerosol is introduced into the plasma. The potential necessary to sustain a He plasma is higher than for an argon plasma so problems with discharges between the plasma and the mass spectrometer tend to be more severe and difficult to control than for argon plasmas.

Gas flows into the plasma through the three tubes of the torch. The sample aerosol is carried into the cooler, center channel of plasma through the center tube by the Ar gas used for the nebulizer (0.5 to 1.0 L/min). The Ar gas flowing between the outer tube and the intermediate tube (10 to 20 L/min), often called the *plasma* or *outer gas*, cools the outer tube between the plasma and the load coil as well as providing plasma gas. A third Ar gas flow (0 to 1.0 L/min) between the intermediate tube and the center tube, often called the *auxiliary gas*, is used mainly to push the plasma up above the top of the inner tube of the torch to prevent it from overheating. In some cases, small amounts of nitrogen, oxygen, or other gases are added to the argon (this is discussed in more detail later).

The plasma has an annular (or doughnut) shape because most of the radio frequency current is carried in a thin skin on the outside of the plasma. The plasma structure is important for two reasons: First, the sample is more easily carried into the center of the discharge and confined from flowing around the outside of the plasma by the hot, rapidly expanding gas in the outer ring of the plasma doughnut.

Second, the sample is isolated, to a large degree, from the doughnut region of the plasma where most of the energy is coupled. As a result, the energy coupling is not strongly dependent on the composition of the sample (in contrast to a discharge between two electrodes, for example). Gas velocities in the center of the plasma are typically 15 to 20 m/sec [8]. The plasma may be about 20 to 30 mm long before ions are sampled into the mass spectrometer, so the sample spends 1 to 2 msec in the plasma.

The radio frequency plasma power supply must be designed specifically for ICP-MS. Radio frequencies between 27 and 40 MHz are typically used for ICP generation. During ignition, the impedance of the plasma varies dramatically from nearly infinite to nearly zero. The plasma impedance is also a function of the applied power, gas flow rates, solvent loading (the amount of solvent aerosol and vapor entering the plasma per second), and plasma gas composition. ICP-MS signals are very sensitive to small changes (more than about 1%) in power so power fluctuations and drift must be minimal. Finally, the plasma potential, dependent on the power supply and load coil configuration, must be properly controlled. If the plasma potential is too high relative to the sampling plate of the mass spectrometer, a secondary rf discharge or arc forms. The electric field can also propagate along the ion beam into the interface region between the sampling orifice and skimmer, so that a discharge forms in this region.

The presence of a strong secondary discharge has several deleterious effects. The sampling orifice can be slowly vaporized by the arc. This leads to a higher background for the elements that make up the sampling cone and a reduced lifetime of the sampling cone. Formation of doubly charged ions (Ba^{2+}, for example, because barium has a relatively low second ionization energy, 10 eV, compared to other elements) is more likely, although molecular oxides might be more effectively atomized. The ion kinetic energy and spread of ion kinetic energies are larger, thus reducing the resolution and abundant sensitivity (ratio of signal at the mass of an ion to that one mass unit away, produced by ions of the same mass) provided by quadrupole mass spectrometers.

Several different approaches have been used to minimize formation of a secondary discharge, which results from parasitic capacitance between the plasma and the load coil. A balanced load coil can be used where the two ends of a single load coil are driven by rf signals of opposite phase but nearly equal amplitude [9] (as is done on Perkin Elmer/Sciex instruments, called PlasmaLok). Then the center of the load coil is at 0 V. In some cases the center of the load coil can be directly connected to ground or to the sampling plate of the mass spectrometer. Alternatively, two separate load coils can be interlaced to form a balanced rf drive system (as is done on Varian instruments).

A grounded, electrical shield can be placed between the load coil and torch to reduce the capacitive coupling between the load coil and the plasma in order to reduce the plasma potential [10]. A thin metal cylinder, split along its length (to

prevent circular current flow), is often used (as is done on the HP 4500 ICP-MS, called PlasmaShield). The extent of capacitive coupling is also a function of the rf power, distance between the load coil and sampling plate, center gas flow rate, and diameter of the load coil (the capacitive coupling decreases the farther the load coil is from the plasma, i.e., the larger the inner diameter of the load coil).

3.1.2 Sample Introduction

The role of the sample introduction system is to convert a sample into a form that can be effectively vaporized into free atoms and ions in the ICP. A peristaltic pump is typically used to deliver a constant flow or sample solution (independent of variations in solution viscosity) to the nebulizer. Several different kinds of nebulizers are available to generate the sample aerosol, and several different spray chamber designs have been used to modify the aerosol before it enters the ICP. Gases can be directly introduced into the plasma, for example, after hydride generation. Solids can be introduced by using electrothermal vaporization or laser ablation.

Pneumatic Nebulizer/Spray Chamber Combinations

Pneumatic Nebulizers. Pneumatic nebulizers, either concentric or cross-flow designs, are the most commonly used to generate aerosols for ICP-MS. In the concentric nebulizer (Fig. 3.4a), the liquid carrying tube is surrounded by a ring through which gas passes at a sonic velocity. The average drop size of the aerosol depends on the gas flow rate, ring orifice area, inner diameter of the sample carrying capillary, and thickness of the wall of the center capillary [4]. In the cross-flow nebulizer (Fig. 3.4b), the gas is introduced through an orifice at a right angle to the solution carrying tube. Shear produced by differences in the gas and liquid velocities breaks the liquid up into filaments that relax to form droplets [11]. Typically, the nebulizer gas flow rate is 0.5 to 1.0 L/min at a pressure of 50 psi or less. Most concentric, pneumatic nebulizers are made of glass, so they cannot be

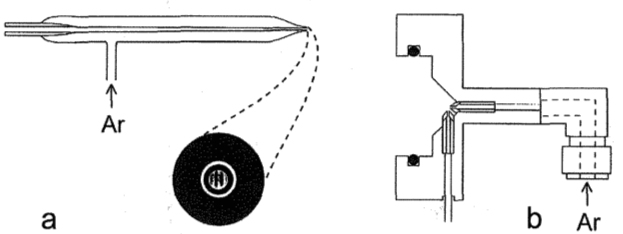

Figure 4 Concentric (a) and cross-flow (b) pneumatic nebulizers.

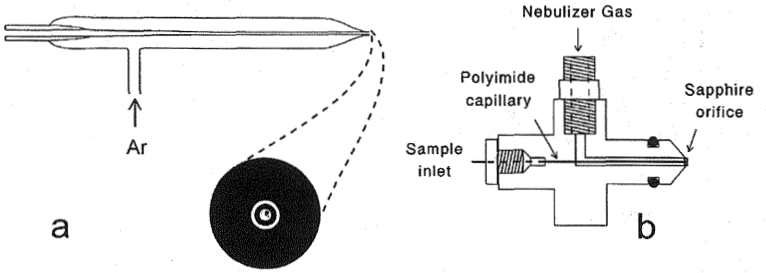

Figure 5 Micronebulizers: (a) Meinhard high-efficiency nebulizer (HEN). (b) Cetac microconcentric nebulizer (MCN).

used for solutions containing hydrofluoric acid. Cross-flow nebulizers are typically made from materials that are resistive to corrosive acids and bases, and some concentric nebulizers from inert materials have also been recently introduced.

Pneumatic, concentric micronebulizers have become available in recent years (Fig. 3.5) with very small internal dead volume. The Meinhard high-efficiency nebulizer (HEN) is a glass nebulizer with a very small gas ring area and thin-walled, small-inner-diameter (90-μm) sample carrying capillary. Although the HEN requires a higher-pressure Ar gas supply (approximately 170 psi at an argon gas flow rate of 1.0 L/min) than the conventional concentric pneumatic nebulizers, it produces a somewhat smaller aerosol than other, "conventional" concentric nebulizers [12]. Also, because of the small gas ring area, the HEN produces sonic gas velocities and fine aerosols even at nebulizer gas flow rates as low as 0.2 L/min. The Cetac MCN-100 microconcentric nebulizer (MCN) has a gas ring orifice that is slightly smaller than that of a conventional nebulizer. The most unique property of the MCN is that it is made of HF-resistant materials, including a narrow polyimide nebulizer capillary [13]. Therefore, the MCN is particularly attractive for the analysis of small volumes of HF solutions such as those used for analysis of semiconductor wafers and small volumes of biological samples including metalloproteins (which may be more likely to adsorb to glass surfaces). The main advantage of the micronebulizers is their low internal volume (9 and 0.5 μL for the HEN and MCN, respectively, compared to 90 μL typical of a conventional pneumatic concentric nebulizer). This makes analysis of sample volumes as low as a few microliters possible by ICP-MS.

Spray Chambers. Spray chambers [14] were designed mostly empirically for use with conventional pneumatic nebulizers during the development of ICP optical emission spectrometry. The main purpose of the spray chamber was thought to be to remove large droplets that would not have sufficient time to be completely vaporized during their 1- to 2-msec travel in the plasma, although what

size was too large was not directly known until recently. At the most commonly used rate of sample delivery to the nebulizer (1 mL/min), only 1% to 3% of the analyte enters the plasma. The rest (97% to 99%) goes down the drain. However, as discussed later, the analyte transport efficiency increases as the sample uptake rate delivered to the nebulizer decreases so that similar detection limits can be obtained at 50 μL/min as at 1 mL/min [12].

A spray chamber also is necessary to limit the amount of solvent that enters the ICP (less than about 20 μL/min of aqueous aerosol and 30 mg/min of water vapor). When water aerosol and vapor loading are higher, the plasma is cooled and molecular oxide formation increases.

Three different spray chamber designs (Fig. 3.6) are most often used for ICP-MS: the Scott [15] (double-barrel) chamber, a conical chamber with an impact bead, and a cyclonic chamber [14,16,17]. The cyclonic spray chamber typically provides a slightly (up to about a factor of 2 or 3) higher analyte transport efficiency as well as somewhat shorter washout times. In some cases the spray chamber is cooled (such as on the HP 4500 ICP-MS double-pass spray chamber, which is cooled to 4°C) to reduce the amount of water vapor that enters the ICP further so that signals from polyatomic ions containing oxygen are reduced. The cooled spray chamber also helps maintain a stable spray chamber temperature.

Fundamental Processes That Control Aerosol Generation and Transport. The size of the aerosol drops in the initial (primary) aerosol depends on the design of the nebulizer, the nebulizer gas flow rate, and, to a lesser extent, the sample

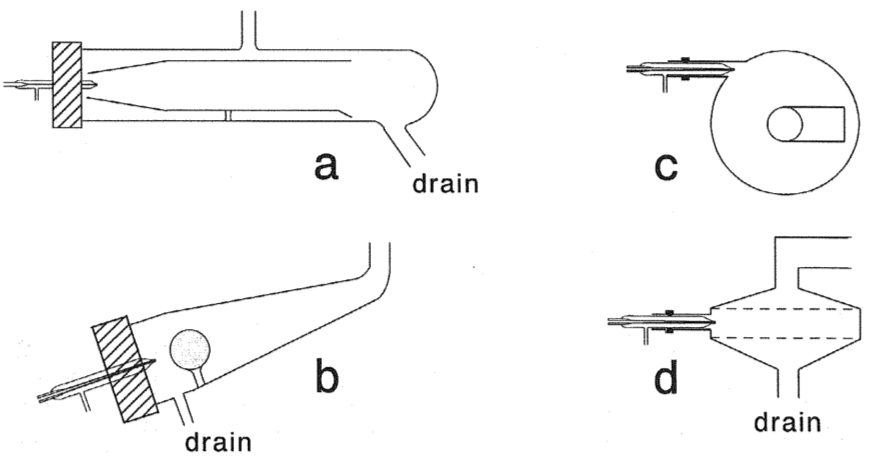

Figure 6 Spray chambers: (a) Scott, double-pass design. (b) Conical chamber with impact bead. (c) Cyclone spray chamber (top view). (d) Cyclone spray chamber (side view).

uptake rate [11]. The key nebulizer design parameters are the area through which the nebulizer gas flows at the nebulizer tip, the inner diameter of the capillary that the liquid sample flows through, and (for concentric nebulizers) the thickness of the wall of the center capillary [11]. There are a variety of designs of concentric, cross-flow, and high-solids nebulizers. Most of the concentric nebulizers are made of glass and their dimensions can vary significantly from one nebulizer to the next, even of the same type [18]. As a general rule, the gas must reach sonic velocity (approximately 320 m/sec) in order to produce a fine aerosol effectively. Cross-flow nebulizers are typically made of corrosion-resistant materials so that even solutions containing hydrofluoric acid can be nebulized and introduced into the ICP.

The primary aerosol droplets become smaller as the nebulizer gas flow rate is increased (Fig. 3.7). Often, the average aerosol size is described by the Sauter

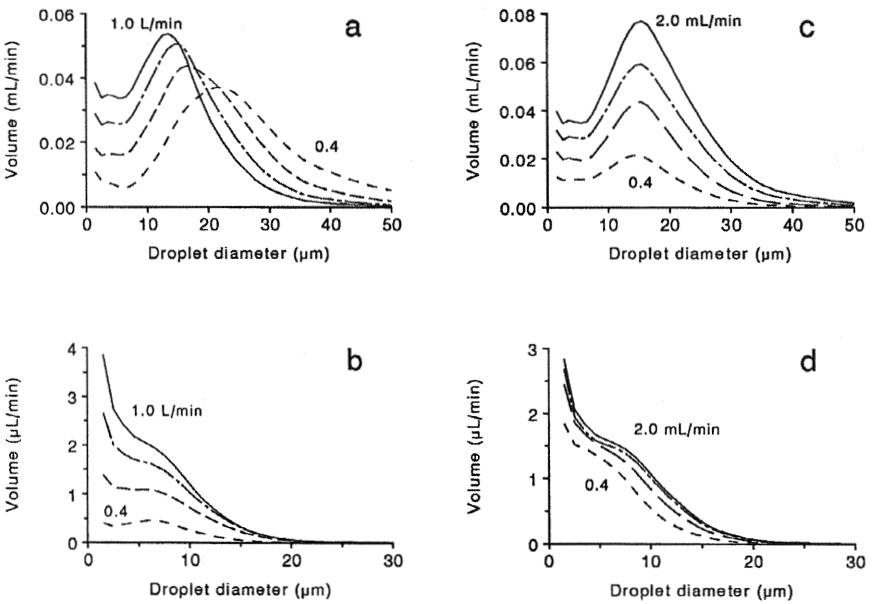

Figure 7 Effect of nebulizer gas flow rate and sample uptake rate on primary and tertiary aerosol drop size distributions. A Meinhard TR-30 nebulizer was used with a double-pass spray chamber. (a) Primary aerosol produced by nebulizer as a function of nebulizer gas flow rate for a 1-mL/min sample uptake rate. (b) Tertiary aerosol exiting spray chamber as a function of nebulizer gas flow rate. (c) Primary aerosol as a function of sample uptake rate at a nebulizer gas flow rate of 0.8 L/min. (d) Tertiary aerosol exiting spray chamber as a function of sample uptake rate. (From Ref. 18.)

mean diameter, $D_{3,2}$ (a ratio of the total volume of aerosol to the total surface area). When the nebulizer gas flow rate for a Meinhard TR-30 nebulizer was increased from 0.6 to 1.0 L/min, the $D_{3,2}$ decreased by approximately a factor of 2, from 18 to 8.7 μm [5].

The primary aerosol droplets also become slightly smaller as the sample uptake rate is decreased. However, the Sauter mean diameter is not as sensitive to changes in sample uptake rate as it is to the nebulizer gas flow rate. For example, when the uptake rate was decreased from 1.0 to 0.6 mL/min, the $D_{3,2}$ value decreased by only 4% (10.9 to 10.5 at a nebulizer gas flow rate of 0.8 L/min) [5].

As the sample uptake rate is increased, the amount of analyte transported into the ICP increases [19], but not proportionately (Fig. 3.8). The efficiency of analyte transport improves as the sample uptake rate is decreased. The analyte transport efficiencies were 60%, 14%, and 3% at sample uptake rates of 10, 100, and 1000 μL/min, respectively. As a result, detection limits obtained using a sample uptake rate of 50 to 85 μL/min are similar to those for a 1-mL/min uptake rate [12].

Three main processes appear to control the modification and loss (or transport) of analyte aerosol in the spray chamber: droplet-droplet collisions resulting in coagulation, evaporation, and impact of larger droplets into the walls of the spray chamber. Aerosol droplets can be "lost" (impact the walls and flow down the drain) as a result of several processes in the spray chamber [11,20]. Because turbulent gas flows are key to generating aerosols with pneumatic nebulizers, the gas in the spray chamber is also turbulent. Droplets with a variety of diameters

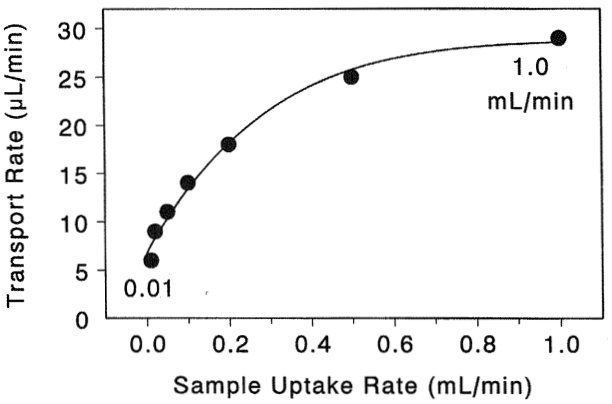

Figure 8 Analyte transport rate (expressed as equivalent volume of sample solution) as a function of sample uptake rate. A Cetac microcentric nebulizer (MCN) was used in a double-pass spray chamber. (From Ref. 422.)

have a wide distribution of velocities. As a result, droplet-droplet collisions are likely, depending on the number of droplets per unit volume. Larger aerosol drops may collide with the walls of the spray chamber as a result of turbulence induced losses. Drops with sufficient momentum may not be able to follow the gas flow through the spray chamber, so these drops impact on the walls of the spray chamber (this is called *inertial deposition*). Gravitational settling is another potential means to lose large droplets as they pass through the spray chamber. Evaporation results in a decrease in aerosol drop size, thereby improving the chances for the analyte to follow the gas flow through the spray chamber and into the ICP.

The spray chamber is often erroneously thought to act as a simple cut-off filter that removes only droplets with diameters greater than some maximum diameter. However, even very small (<3-μm diameter) droplets have a low probability of passing through the spray chamber and reaching the plasma [5] when the sample uptake rate is 1 mL/min (Fig. 3.9). This is most likely due to droplet-droplet collisions, coagulation, and subsequent loss of the larger, coagulated droplets by turbulence losses, inertial impact, or gravitational settling. As is also seen in Fig. 3.9, droplets with initial diameters greater than about 15 μm are not transported through the spray chamber with good efficiency, even at low sample uptake rates.

If the sample uptake rate is decreased, the number of droplets per cubic centimeter in the spray chamber decreases, droplet-droplet collisions resulting in coagulation are less likely, and the analyte transport efficiency increases, as shown

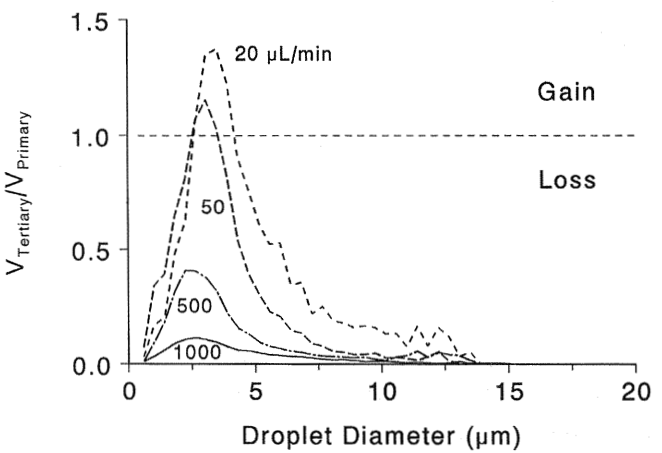

Figure 9 Ratio of tertiary to primary aerosol volume as a function of drop size for different sample uptake rates. A Cetac microconcentric nebulizer (MCN) was used in a double-pass spray chamber. Other concentric nebulizers behave similarly. (From Ref. 422.)

Table 1 Analyte Transport Efficiency as a Function of Sample Uptake Rate for Three Different Nebulizers Used with a Scott Double-Pass Spray Chamber[a]

	Analyte transport efficiency (%)		
Liquid uptake rate (mL/min)	Meinhard TR-30-A3	Meinhard HEN	Cetac MCN
0.010	50%	60%	60%
0.020	40%	55%	45%
0.050	20%	30%	22%
0.100	13%	16%	14%
0.200	8%	9.5%	9%
0.500	4%	5.2%	5%
1.000	2.5%	3%	2.9%

[a]Nebulizer gas flow rare was 1.0 L/min in all cases.
Source: Ref. 422.

in Fig. 3.8 and Table 3.1. Argon at room temperature becomes saturated when it contains about 25 mg/L of water vapor. At an uptake rate of 1 mL/min, less than 2% of the aerosol can evaporate in the spray chamber when a gas flow rate of 1 L/min is used. Then the argon is saturated with water vapor and no further evaporation of the aerosol takes place. However, as the sample uptake rate is decreased, the percentage of the sample aerosol that can evaporate increases. At sample uptake rates below 25 μL/min, all of the water aerosol can evaporate in the spray chamber, thereby increasing the transport efficiency of analyte into the ICP. The largest drops may not have sufficient time to evaporate before impacting the walls of the spray chamber.

As can be seen from the results in Table 3.1, the analyte transport efficiency is similar for both "conventional" and "micro-" or "high-efficiency" nebulizers when compared under identical flow rates. The increase in analyte transport efficiency with decrease in the sample uptake rate (sometimes called "starving" the nebulizer because uptake rates less than the natural aspiration rate are used) was reported long ago [21,22]. So the main advantage of the newer "micronebulizers" is that their internal volume is small, a feature that becomes more important as the uptake rate is reduced. A capillary can also be inserted into a "conventional" concentric, pneumatic nebulizer to decrease its internal dead volume [23,24].

Ultrasonic Nebulizers

Ultrasonic nebulizers are unique in that a piezoelectric transducer, powered at frequencies of 200 kHz to 10 MHz, is used to generate aerosol from sample that

flows across the transducer surface. This has three important implications: No turbulent gas is needed to produce the aerosol, so turbulence induced aerosol losses and droplet-droplet coagulation in the spray chamber should be reduced compared to those of pneumatic nebulizers. The flow rate of the gas used to carry the aerosol to the ICP can be optimized independently of the aerosol generation process. Finally, there are no small orifices to become clogged.

Most ultrasonic nebulizers use a somewhat larger sample uptake rate (2–3 mL/min) than pneumatic nebulizers. Typically the spray chamber and/or a tube following the spray chamber is heated to evaporate water partially from the aerosol. Because the aerosol transport efficiency is higher when an ultrasonic nebulizer is used, particularly with a heated spray chamber, a system to remove solvent (typically a condenser and/or membrane separator) is essential to prevent deleterious cooling of the ICP by excess water.

The combination of the ultrasonic nebulizer, heated spray chamber and condenser/desolvator leads to improvements in detection limits by a factor of about 10 compared to that of a pneumatic nebulizer without a desolvation system. This is the main reason ultrasonic nebulizers are used despite their higher cost (approximately U.S. $15,000 in 1998).

There are several drawbacks to ultrasonic nebulizer/desolvation systems. Precision is typically somewhat poorer (1% to 3% relative standard deviation) than for pneumatic nebulizers (0.5% to 1.0% relative standard deviation) and washout times are often longer (60 to 90 sec compared to 20 to 30 sec for a pneumatic nebulizer/spray chamber without desolvation). Furthermore, chemical matrix effects are dependent on the amount of concomitant species that enter the ICP per second. Therefore, use of any sample introduction device that increases the amount of sample entering the plasma per second also naturally leads to more severe matrix effects when the sample contains high concentrations of concomitant species.

Desolvation Systems

Desolvation systems can provide three potential advantages for ICP-MS: higher analyte transport efficiencies, reduced molecular oxide ion signals, and reduced solvent loading of the plasma. Two different approaches have been used for desolvation in ICP-MS. The heated spray chamber/condenser combination has been discussed; it is the most commonly used system. The extent of evaporation of the solvent from the aerosol and cooling to reduce vapor loading varies from system to system. The second approach is the use of a membrane separator to remove solvent vapor before it enters the ICP.

Heated Spray Chambers. The use of a heated spray chamber to evaporate the aerosol partially leads to reduction in drop size and therefore higher analyte transport efficiencies. Often the drying of the aerosol droplets is incomplete.

Typically, either the walls of the spray chamber have been heated or, in the case of the Mistral system from VG Elemental, infrared radiation heating is used [25]. Microwave heating of the aerosol seems to be inefficient. It is unlikely that the aerosol is completely dried in these systems.

Using a microcentric nebulizer at low flow rates (typically about 50 μL/min), a heated spray chamber, and a heated microporous membrane desolvator, the Cetac MCN-6000 system can provide analyte transport efficiencies of 50% to 90%. This system is made completely of HF resistance materials.

Recently, Legere [26] presented some very interesting results using a specially designed spray chamber to heat a secondary gas before it enters the spray chamber and then efficiently mix that gas with the aerosol produced by the nebulizer. Because the aerosol "jet" typically entrains large volumes of gas, the additional, heated gas can be very efficiently mixed with the gas from the nebulizer in order to promote rapid heating and evaporation of the sample aerosol. The goals of this design include virtually complete vaporization of liquid aerosol, prevention of aerosol from striking the walls of the spray chamber, and 100% analyte transport efficiency. It appears that the liquid water is almost completely removed from the aerosol for sample uptake rates up to 300 μL/min (then the heated Ar becomes saturated with water vapor and the dew point is reached). A Nafion membrane desolvator is used to remove most of the water vapor before it enters the ICP. As the sample uptake rate is increased from 25 to 250 μL/min, the ICP-MS signal increases by a factor of 10 (in stark contrast to the data shown in Fig. 3.8). This is strong evidence that the analyte transport efficiency is constant and virtually 100%, even at a sample uptake rate of 250 μL/min. As a result, sensitivities are enhanced by about a factor of 10 compared to those of a conventional pneumatic nebulizer/Scott spray chamber used with an uptake rate of 1 mL/min. Washout times are also very fast.

Condensers to Remove Solvent Vapor. The use of a condenser to cool the vapor and remove it by condensation on the walls of the condenser is one means to reduce solvent vapor loading of the ICP. However, this approach entails a problem: the solvent recondenses on the desolvated particles as well. In an attempt to get around this problem and to remove as much solvent vapor as possible, Houk et al. [27] have used a three-stage cryogenic desolvation system. The sample aerosol passes through a heated spray chamber, a condenser at 0°C to −10°C, and a cryogenically cooled condenser, and then goes through three cycles of heating and cryogenic cooling before entering the plasma. Although this is an elaborate and inconvenient system, signals from polyatomic ions including ArO^+, ClO^+, and $ArCl^+$ are reduced by a few orders of magnitude. This reduction significantly enhances detection limits for Fe, V, and As [27].

Membrane Separators. Solvent vapor can be removed from the sample carrying gas by establishing a concentration gradient across a membrane. The

sample vapor travels inside the membrane tube and a dry, sweep gas is passed in a tube surrounding the membrane. The removal of the solvent is driven by a concentration gradient between the inside of the membrane tube, where the sample and solvent vapor are, and the outside of the tube, where the sweep gas flows. The advantage of this approach is that solvent vapor can be removed without the deleterious effects of cooling with a condenser. The use of membrane separators for solvent removal in ICP-MS was first described in 1990 [28,29].

Two membrane types that operate on different principles have been used in commercially available membrane separators: microporous membranes and selectively permeable, nonporous polyimide or Nafion membranes. The microporous Teflon PTFE membrane can be used to remove water vapor or organic solvent vapor. Any gaseous component, *including volatile analytes* such as Hg, is partially or extensively removed. The sweep gas flow rate is typically similar to the sample carrier gas flow rate.

In contrast, Nafion removes water vapor by a process called *perevaporation.* Water is absorbed onto the walls of the Nafion, moves through the walls, and evaporates into the sweep gas [30]. As a result, volatile analytes should not be lost through the membrane. The efficiency of removal depends on diffusion of water vapor to the walls of the membrane. When the water vapor load is significantly less than the dew point, the efficiency also improves as the temperature of the dryer is reduced [31]. This membrane separator does not remove organic solvent vapor from the Ar gas stream, but it also does not suffer from loss of volatile analytes.

A nonporous aromatic polyimide membrane that is selectively permeable to H_2, H, and H_2O has also been used for water vapor removal before the sample enters the ICP-MS [32]. Molecular analyte oxide ion signals were reduced approximately two orders of magnitude and O-containing polyatomic ions, such as ArO^+ and ClO^+, were reduced by one to two orders of magnitude.

Although the membrane separators are useful for solvent vapor, care must be taken to prevent fouling the membranes with liquid solvent, as occurs when incompletely desolvated aerosol enters the membrane separator.

Direct Injection Nebulizers

Direct injection nebulizers are operated without a spray chamber. Instead, the concentric, pneumatic nebulizer is positioned just below the plasma and 100% of the sample is sprayed into the ICP. The nebulizer replaces the center tube of the ICP torch. The direct injection nebulizers are particularly attractive for the analysis of small sample volumes and for elements, such as Hg, I, and B, that stick to surfaces in the spray chamber and therefore have long washout times when a spray chamber is used. The dead volume of the direct injection nebulizers is small, so they have often been used to couple capillary separations with ICP-MS detec-

tion [33] and to increase sample throughput rates [34]. One of the disadvantages of the direct injection nebulizers is that molecular oxide ion/elemental ion signal ratios are higher by about a factor of 3 [35]. The sample liquid uptake rate to the nebulizer is limited to 120 μL/min or less to prevent solvent overloading of the ICP.

Two different kinds of direct injection nebulizers are available commercially. The total consumption nebulizer was developed by Greenfield et al. [36] for ICP optical emission spectrometry. The concept for the Cetac direct injection nebulizer (DIN) was developed by Fassel, Houk, and coworkers [35,37]. It has a narrow sample-carrying capillary [30–50 μm inner diameter (i.d.), 0.5 to 1 m long] that extends slightly past the nebulizer gas tube. A second, auxiliary or makeup, nebulizer gas is introduced through another concentric tube outside the nebulizer gas tube. A gas displacement pump (up to 1500 psi) or HPLC pump is used to deliver the sample to the nebulizer through the long, narrow capillary.

The second type of direct injection nebulizer, called the *direct injection high-efficiency nebulizer* (DIHEN), is a specific type of the Meinhard HEN [38] that is inserted into the ICP torch in place of the center, injector tube. The main advantage of the DIHEN compared to the Cetac DIN is that a high-pressure pump is not needed to deliver sample to the nebulizer. An unusually low nebulizer gas flow rate (0.25 L/min) and high ICP power (1.5 kW) were found to provide optimal ICP-MS sensitivity when DIHEN is used [38].

Hydride Generation Sample Introduction

Several elements (including As, Bi, Ge, Pb, Sb, Se, Sn, and Te) form volatile hydrides when reacted with sodium borohydride at room temperature. By introducing the analyte as a volatile hydride, high-transport efficiencies, and therefore improved detection limits, can be achieved. Often as importantly, much of the sample matrix is not introduced into the ICP because those species do not form volatile compounds. Commercial hydride generation sample introduction systems are available.

Continuous, batch, and flow injection modes of hydride generation have been used successfully [39–41]. In the commonly used continuous mode the sample and sodium borohydride solutions are pumped by using a dual-channel peristaltic pump into a mixing chamber. The volatile hydride gas and hydrogen are carried into the plasma with a flowing argon gas and the excess liquid is directed to the drain.

Key experimental and chemical considerations are necessary for successful use of hydride generation [39,40]. The reaction to form the volatile hydride may be highly species- as well as element-dependent. Therefore, the analyst must be aware of the chemistry and realize that the response may be species-dependent. The signal may not be directly related to the total elemental concentration in the

sample. For example, As(III) more readily forms a hydride than As(VI). So, it may be necessary to pretreat the sample to reduce the analyte to the proper oxidation state. Arsenobetaine and arsenochlorine do not react to form volatile arsenic hydride [42]. The species-dependent hydride generation can be used to advantage for elemental speciation. For example, As(III) can be measured by hydride generation, and then As(VI) can be determined by determining the difference from a total As concentration measurement [43].

The acid content of the sample, the reactant concentration, the liquid flow rates of the sample and reactant, the argon carrier gas flow rate, and the reaction cell design can all affect the hydride generation and transport. If too much H_2, CO_2, and H_2O is generated, the plasma may be overloaded. This effect can be minimized by proper control of flow rates, pumping the drain to remove the liquid after reaction and adding NaOH to the solution waste. The transfer of analyte hydrides into the ICP [44] and the pH dependence of hydride forming elements [45] have been investigated theoretically and experimentally. Some sample components can interfere with the hydride generation process. Transition metals can interfere with the hydride generation process by being preferentially reduced.

Separation of the hydride gas from the liquid is key to stable signals. Pulses of hydride can be produced if the reaction solution is not well mixed, gas bubbles form in the tubing as the reaction occurs, and the generated gas is not well mixed with the carrier gas. A variety of gas-liquid separation devices have been used, including gas-permeable, microporous membranes. If an appropriate membrane is chosen, the hydride gas passes through it efficiently, but aerosol and liquid do not [42,46]. Effective separation of the gas from the liquid also minimizes introduction of sample matrix species into the ICP. For example, the $ArCl^+$ spectral overlap at mass 75 with the only isotope of As can be prevented by using hydride generation sample introduction rather than introducing an aqueous solution containing a high concentration of chlorides into the ICP as an aerosol [42,46,47].

Flow Injection Sample Introduction

Flow injection analysis involves a flowing stream of solvent into which a discrete volume of sample is injected. Many different chemical sample treatments, including on-line dilution, extraction, preconcentration, matrix removal, separations, dissolution, precipitation reactions, and generation of volatile species, can be effectively used in a flow injection mode [48]. Exponential dilution can be used for calibration. Internal standards can be added on-line to the sample [49]. One of the main advantages of flow injection is that these processes can be easily automated. Another potential advantage of ICP-MS is that samples containing high concentrations of dissolved solids can be analyzed during short pulses in order to prevent excessive deposition of salt on the sampler or skimmer.

Selected elements can be preconcentrated by using a short column onto

which the analytes are absorbed. The preconcentration factor can be controlled because it depends on the amount of time sample is flowed through the column [49]. After a fixed time the analytes can be eluted from the column in a "plug" by an acidic solution, for example, and carried to the nebulizer in a flowing stream. Alternatively, a column can be used to remove particular components of the sample from the stream while allowing analytes of interest to pass through the column [50].

Solid Sample Introduction

Dissolution of solid samples for ICP-MS analysis has several disadvantages, including time consuming procedures, difficulty in gaining complete dissolution, potential loss of elements that form volatile species, potential contamination by reagents and vessels, and loss of information on the spatial distribution of elemental composition. Furthermore, the introduction of solvent aerosol and vapor into the ICP leads to the production of molecular ions that can cause spectral overlaps with analyte elemental ions of interest. Several solid-sampling techniques have been developed to overcome some or all of the disadvantages of sample dissolution and solution sample introduction for ICP-MS. These include laser ablation, electrothermal vaporization, spark and arc ablation, and powder injection devices. The major problem with solid sample introduction is calibration for quantitative analysis, often requiring standards that are well matched to the sample.

Many of the solid sample introduction techniques produce transient signals or at least signals that fluctuate on short time scales. The combination of time-of-flight ICP-MS and solid sampling approaches that generate a transient signal may be particularly attractive because all elements can be monitored simultaneously. Multielement analysis from transient electrothermal vaporization or direct insertion sample introduction will become more viable. It is even possible to monitor signals for all elements from material produced from a single laser pulse.

Laser Ablation. When a laser is focused on or just above a solid sample, the surface can be ablated to produce particulates and vapor by sputtering and thermal vaporization processes. The sample vapor and dry aerosol can be carried in a flowing gas stream into the ICP [51,52]. Laser ablation (LA) sampling is amenable to a wide variety of materials, conducting and nonconducting, inorganic and organic. The ablated spot size can be as small as a few micrometers, so spatially resolved measurements can be made. Recently introduced lasers with flat beam profiles also allow depth-resolved measurements. Laser ablation–ICP-MS has been widely used for geological samples.

The ICP-MS signal depends on the amount of analyte entering the plasma per second. The amount of material ablated per laser pulse is strongly dependent on the sample properties and the surface morphological features. In addition, the amount of material is dependent on the laser properties, including wavelength,

pulse length, spot size, repetition rate, energy per square centimeter, and laser mode [53–55]. The spot size and amount of material ablated also depend on the focal length of the optic used to focus the laser, where the beam is focused relative to the surface of the sample and the laser beam profile.

Signals from laser ablation ICP-MS are transient and can vary widely over time. Therefore, a simultaneous detection system, using time-of-flight mass spectrometry [56] or a multiple detector sector–based mass spectrometer [57–59] is preferable. Quadrupole mass spectrometers can be used, with some limitations, if signals are properly acquired and processed [60].

The laser ablation system consists of a high-power pulsed laser, optics to focus the laser at or near the surface of the sample, and an ablation cell. Small ablated particles are swept out of the ablation cell and carried into the ICP in a flowing gas. Often a microscope lens and video camera are positioned to allow the operator to view the sample surface before and after ablation. A high-quality microscope and precise positioning of the sample relative to the laser beam are essential for good spatially resolved sampling.

To obtain accurate, quantitative results, either the amount of material ablated per laser pulse must be similar for the standards and samples or the relative ablation rates must be experimentally measurable (through use of an internal standard, for example). The size distribution of the ablated particles must be similar enough for the standards and samples so that that transport efficiency of ablated material is similar or again can be accounted for accurately. Ideally, the ablation process should produce particles and sample vapor that have the same chemical composition as the sample. However, elemental fractionation can occur, particularly if the ablation process is predominantly thermal [61].

Excimer and frequency tripled or quadrupled Nd:YAG lasers are most commonly used for LA-ICP-MS. Early laser ablation systems for ICP-MS were infrared lasers. These were chosen because many materials absorb infrared (IR) radiation strongly. However, the ablation process tends to be more thermal for IR wavelengths compared to ultraviolet (UV) wavelengths. As a result, there is less elemental fractionation when UV lasers are used rather than IR lasers [62]. Furthermore, smaller spot sizes can typically be obtained with UV lasers, so spatial resolution is improved and swelling of polymeric materials is reduced [63]. Therefore, most laser ablation systems for ICP-MS now use UV radiation. The output of the Nd:YAG laser (1064 nm) is typically quadrupled (to 266 nm) by using nonlinear crystals, although the conversion of energy is relatively inefficient (1/100, for example), leading to much lower pulse energies. Excimer lasers based on XeCl (308 nm) or ArF (193 nm) have been used. The effect of laser pulse width on the ablation process has also been investigated [54].

Detection limits for most reported LA-ICP-MS studies have been near 1 μg/g, although these limits are very dependent on the element, sample type, laser system, laser parameters, pit size, and ICP-MS used. Detection limits in the 1- to

10-ng/g range in geological materials have been reported recently [62]. Precision of 5% to 10% is typical, although this is also strongly dependent on experimental parameters as well as sample homogeneity [64]. If a simultaneous detection system is used, such as a dual-quadrupole [65] or multicollector sector MS [57,58, 66], isotope ratio precision of 0.24% to 0.004% can be obtained, respectively.

The major limitation of LA-ICP-MS is the need for standards that closely match the properties of the samples. In some cases it is possible to use NIST glass standard reference materials for calibration in the analysis of geological materials [67,68]. Internal standardization employing MS signals from elements at known concentrations has been used to improve precision and accuracy. Other techniques, such as acoustic [69] and light scattering [70] measurements, have been used in an attempt to monitor the relative amount of material ablated. These approaches seem to work well for variations in the amount of material sampled for similar sample matrices but not for very different types of solids. Dual-sample introduction systems with either wet [71] or dry [72] aerosol introduction in addition to laser ablation have also been reported.

By positioning the sample just below the ICP, sample transport losses can be dramatically reduced [73]. This "in situ" sampling approach suggests some interesting possibilities for laser ablation sampling. A narrow-signal (0.7-msec) pulse was produced after each laser pulse. The peak signals were approximately 1000 times the steady-state signal observed when a conventional ablation cell and transfer tubing were used. However, fast, simultaneous detection (such as is provided by time-of-flight mass spectrometers) is required to take full advantage of this approach in ICP-MS.

Electrothermal Vaporization. Samples may be introduced into the ICP as vapor, including atoms, molecules, small clusters, and small particles [74] by electrothermal heating [75]. A small liquid (~10 μL) or solid (~10 mg) sample is placed on a graphite furnace or tantalum filament, which is heated by passing a high dc current through it. The electrothermal source, unlike in electrothermal vaporization (ETV)-atomic absorption spectrometry, does not have to atomize the sample, only to transfer it into a form that can be efficiently carried into the ICP. The vaporizer is part of a closed system through which a carrier gas flows to take the vaporized sample through a length of tubing into the ICP. The advantages of this approach are direct sampling without requiring dissolution and ability to vaporize the water before vaporizing the sample so that molecular ions that involve O, such as ArO^+, are much less common.

The ETV parameters, including vaporizer temperature, carrier gas flow rate, drying temperature and duration, pyrolysis temperature, and duration and vaporization temperature, all affect the transient signal produced. Different elements are carried into the plasma at different times, depending on their volatility.

The transport of sample into the ICP appears to be more efficient when the

sample is carried as small particles. These particles can be formed by self-nucleation or by addition of physical carriers, such as high concentrations of NaCl. Several groups have investigated the use of chemical modifiers and their effect on analyte transport [76–78].

Detection limits are typically less than picograms per milliliter (pg/mL) [79,80] with absolute detection limits as low as 2 attograms [81]. Often standard addition calibration and a good knowledge of the chemistry of the sample in the vaporizer are required for successful use of ETV-ICP-MS.

Direct Sample Insertion. In direct sample insertion (DSI) [82], the sample is placed on a rod, metal loop, or cup on a rod. After desolvation (by inductive heating of the rod or use of a heat gun), the sample is inserted into the plasma. The advantages of the DSI system include nearly 100% sample transport efficiency into the ICP and use of a single power source. The most exciting capability of DSI is preconcentration using aerosol deposition that can provide two orders of magnitude of improvement in ICP-MS detection limits [83]. Detection limits as low as 0.06 parts per trillion were obtained.

Other Solid Sample Introduction Systems. Arc discharges (continuous discharges between two electrodes, one of which is the sample) have been used to generate dry aerosols from conducting samples [84] and powders mixed with a conducting matrix. Spark discharges (short, pulsed discharges) have also been used for solid sampling into ICP-MS [85,86]. A unique system to introduce powders quantitatively directly into the ICP at a controlled rate has also been described [87,88].

3.1.3 Ion Sampling from an Inductively Coupled Plasma: The Inductively Coupled Plasma Interface

The interface used today between the atmospheric-pressure plasma and the low-pressure mass spectrometer is based on a differentially pumped two-stage interface similar to those used for molecular beam techniques [89–91]. The key to successful development of ICP-MS instruments was the use of a relatively large (~1-mm-diameter) sampling orifice so that continuum flow was attained with an unrestricted expansion of the plasma to form a free jet. When small orifices were used, a cold boundary layer formed in front of the orifice, resulting in substantial cooling of the plasma, including extensive ion-electron recombination and molecular oxide formation. The smaller orifices were also susceptible to clogging.

Plasma gas (overall neutral) flows through the sampling orifice and expands in the first stage of the mass spectrometer (at a pressure of a few torr). Assuming ideal, neutral gas flow, approximately 2 atm L/min [at standard temperature and pressure (STP)] of gas flows through the sampling orifice [92]. Therefore, most of the analyte ions from the center channel of the ICP pass through the sampling orifice.

The free jet forms downstream of the sampling orifice with a barrel shock and Mach disk [93]. A skimmer (also with a diameter of ~1 mm) is placed approximately two thirds of the distance between the sampling orifice and the Mach disk for optimal sampling. Flow along the center line travels through the skimmer to form a directed beam into the second stage of the ICP-MS (0.1 to 1 mtorr). Although most analyte ions likely pass through the sampling orifice, only ions from a narrow spatial region of the plasma (approximately 0.2- to 0.3-mm wide) appear to reach the detector of the mass spectrometer [94,95].

It appears that the sampling process is mainly determined by neutral atoms. This is reasonable because only a small percentage of the plasma is ionized (Ar is about 0.1% to 0.2% ionized). Therefore, there are orders of magnitude more Ar atoms than any atoms of other species, including sample ions, in the plasma. Moreover, it has been concluded that ion-molecule reactions are not a major source of molecular ions observed in ICP-MS [92]. This conclusion is consistent with theoretical calculations of collision rates [95]. Recently, Houk has reported that theoretical calculations of the relative abundance of molecular ions in the ICP itself are consistent with ICP-MS experimental observations [96].

If the flow of gas through the sampling and skimmer orifices is predominantly determined by neutral gas, then the analyte ions should be traveling at the same velocity, regardless of mass. As a result, the ion kinetic energy increases with the mass of the ion [97,98]. Ion kinetic energies vary with ICP power, nebulizer gas flow rate, and MS interface pressure [99,100]. Ion kinetic energies typically range from about 3 to 10 eV for ions of mass 7 to 250. The spread of ion kinetic energies for midmass ions is typically about 3.8 eV (full width half maximum).

3.1.4 Ion Transfer from the Skimmer to the Mass Spectrometer

Because of the higher mobility of electrons compared to much heavier elemental ions and the electrostatic field produced by the ion optics designed to focus positive ions, charge separation occurs so the overall neutral plasma gas beam becomes a positive ion beam. This most likely occurs in the region near or just after the skimmer [99,101–103]. If the number of ions in the positive ion beam is large enough, space charge defocusing occurs. The ion current passing through the skimmer has been estimated to be as high as 1.5 mA [104]; therefore, space charge defocusing is significant.

Ion Optic Designs

The function of the ion optics is to maximize transmission of ions from the skimmer into the mass spectrometer while minimizing background due to photons or fast neutrals. The ion optics need to focus ions with a relatively wide spread of

ion kinetic energies 1–4 eV) for a single mass as well as over a wider range of mass-dependent ion kinetic energies. Calculation of ion trajectories in order to design optimal ion optics is complicated by two processes: space charge effects and scattering of ions by collisions with the background gas. Furthermore, the location and distance over which charge separation occurs are critical and not well known. Tanner has described the development of the ion optics for ICP-MS as a combination of "modeling, intuition and blind luck" [105].

High-energy photons and fast neutrals can produce a signal if they strike the detector. Two main approaches have been used to minimize this potential background signal. A stop can be placed on-axis and ions focused in a path around or in back of the stop. Alternatively, an offset ion lens can be used or the ions can be directed through a 90° angle into the mass spectrometer to prevent a straight line of sight between the sampler-skimmer and the mass spectrometer.

A variety of ion optic designs have been used (Fig. 3.10). Most consist of several lenses in combination to deal with the wide range of mass-dependent ion kinetic energies. One arrangement (Fig. 3.10a) used a combination of a Bessel box and an Einzel lens. Both experimental studies of ion signals as a function of lens voltages and theoretical calculations using Simion or MacSimion [106,107] have been reported for this set of ion optics. Another set of ion optics using a stop on-axis is shown in Fig. 3.10b. Hu and Houk [108,109] described offset ion optics

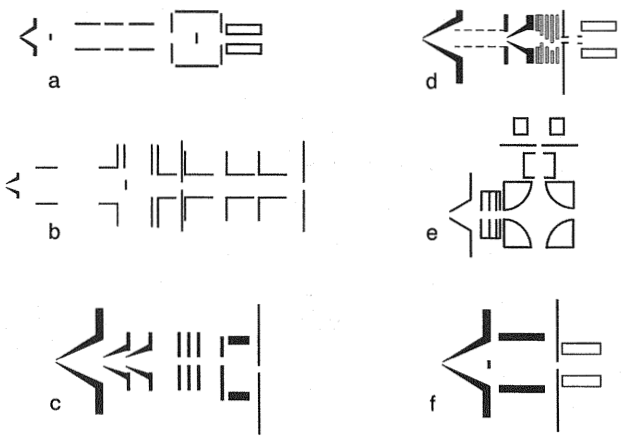

Figure 10 Ion optics: (a) Einzel lens/Bessel box similar to optics used in Sciex ELAN 250, 500, and 5000 ICP-MS instruments. (b) Multiple lens stack similar to those used in VG instruments. (c) Optics similar to those used in HP 4500. (d) Offset ion lens system developed by Hu and Houk [108,109] and used in Thermo ICP-MS. (e) Ion optics used in Seiko instrument with the quadrupole mounted perpendicular to the sampler-skimmer axis. (f) Single-lens-based ion optics similar to the Perkin-Elmer ELAN 6000 system.

(Fig. 3.10c) that deflected ions off center and then back on center, thus preventing a straight line of sight for photons for fast neutrals to travel from the skimmer into the quadrupole mass spectrometer without the need for a stop. In some instruments (Fig. 3.10d, e) the mass spectrometer is placed off axis from the sampler-skimmer axis in order to minimize background without the use of a stop. The effective focal length of an ion lens depends on the ion kinetic energy (analogous to the focal length dependence of an optical lens on the wavelength of light). Ion optic systems for ICP-MS are therefore normally designed from multiple lenses in order to focus ions with a range of ion kinetic energies with fixed lens voltages. An alternative approach is shown in Fig. 3.10f. A stop and a single cylindrical lens are used to focus ions into the mass spectrometer, but the lens voltage is scanned synchronously with the quadrupole mass spectrometer for best focusing of ions of each mass/charge ratio.

Space Charge Effects

The transmission of ions from the skimmer to the quadrupole mass spectrometer is generally poor (0.1% to 0.01%) [92,105,110], mainly as a result of space charge induced loss of ions from the beam. Space charge effects can be thought of in two ways. Positive ions, in the absence of electrons, in close proximity repel each other. This tends to force positive ions away from the beam axis, thus reducing the number of ions that pass through the next aperture or into the mass spectrometer. Alternatively, the large number of ions in the beam can be considered to shield ions from the applied electrostatic field produced by the ion optics, resulting in a defocusing of the positive ion beam. The radial electric field due to the positive ion beam can become as large as the electric field produced by the ion lens. As a result, there are severe losses of ion transmission to the mass spectrometer due to space charge effects.

The space charge field is due mainly to the predominant positive ion, Ar^+, when only trace amounts of analyte are present in the plasma. Initially, almost all of the ions are moving at the same velocity through the skimmer, independently of their mass. Because heavy ions have a higher kinetic energy than light ions, light ions are more severely defocused by the space charge field. As a result, a mass bias toward heavier ions is induced. If sufficiently high concentrations of heavy elements are present in the sample, they can contribute significantly to the total positive ion beam current and produce increasingly severe losses of lighter ions from the positive ion beam, as will be discussed further.

The effect of the ion beam current on model predicted ion trajectories [105] is shown in Fig. 3.11. Important inputs for the model are the location and distance over which charge separation occurs to produce a positive ion beam. A charge separation function was assumed (Fig. 3.11a) for the simulation. When space charge effects are not included, a large fraction of the ions pass from the skimmer

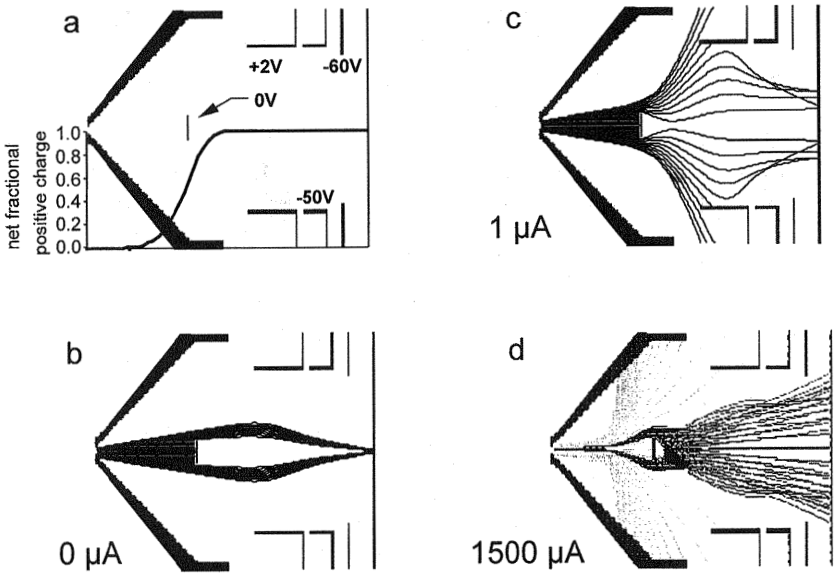

Figure 11 Simulated Sc^+ ion trajectories: (a) Ion optic geometry and voltages. Plot shows assumed charge separation function. (b) No space-charge effect included. (c) Total beam current through skimmer of 1 μA (d) Total beam current through skimmer of 1500 μA. (Note that darker trajectories correspond to 1% of the ion beam; 99% of the ion beam is lost as indicated by the lighter trajectories.) (From Ref. 105.)

through the ion optics (Fig. 3.11b). For a total positive ion beam current of only 1 μA, defocusing of the beam can be clearly seen from the model predictions (Fig. 3.11c). When the total ion current is increased to 1500 μA, a value close to experimentally measured currents, about 98% of the Sc^+ ions are deflected, impact on the inside of the skimmer cone, and are lost (Fig. 3.11d).

3.1.5 Collision-Reaction Cells

A multipole cell at pressures around 1 to 15 mtorr, placed between the sampler-skimmer interface and the mass spectrometer, can serve two functions: reduce the kinetic energy of the ions to nearly thermal energies (<0.5 eV) and carry out reactions with analyte or background ions. Of particular interest for ICP-MS are reactions that would dramatically reduce spectral overlaps due to elemental or polyatomic ions. Two potentially undesirable processes must be considered for successful use of a collision-reaction cell. Scattering losses can be severe if the mass of the collision or reaction gas is high compared to that of the analyte ion

mass. Reaction product ions could produce new spectral overlaps. They could also react further through a series of reactions to produce other potentially interfering background ions.

Collisional fragmentation cells have been used in triple quadrupole MS-MS instruments for organic mass spectrometer for some time. However, scattering losses of Ce^+ analyte ions in ICP-MS were found to be greater than the reduction in the CeO^+ signal. It is unlikely that collisional fragmentation will be effective for reduction of spectral overlaps in ICP-MS.

Ion-molecule reactions can be very efficient. Douglas [111] showed, using ICP-MS-MS, that CeO_2^+ could be formed in a reaction cell with the addition of oxygen. Rowan and Houk [112], using a double-quadrupole instrument, demonstrated that ArO^+, ArN^+, and Ar_2^+ signals were reduced more rapidly than some of the elemental ions when Xe or CH_4 was used as a reaction gas. Eiden et al. [113] were able to reduce the Ar^+ signal by six orders of magnitude by adding H_2 to an ICP-ion trap mass spectrometer.

Turner et al. [114] described an ICP-MS with a hexapole transfer lens (Fig. 3.12a) in a tube that allows the pressure to be maintained. The cell was initially reported to contain He, although it is likely that H_2 or H_2O vapor was also in the cell and is now purposely added to the cell [115]. Ar_2^+, $ArCl^+$, ArO^+, and Ar^+ signals were reduced relative to Se^+, As^+, Fe^+, and Ca^+, respectively. Detection limits for Fe, Ca, K, Se, and As near 10 parts per trillion (ppt) have been reported [115]. Recently, Beaty and Liezers [116] also described a collision-reaction cell at a pressure of 30 mtorr that reduced the ion kinetic energy spread as well as "continuum" ICP-MS background to less than 1 count/sec. Previously, Douglas and French had described the use of an rf-only quadrupole for collisional focusing and reduction of the ion kinetic energy spread [117].

Recently, Tanner et al. [118–120] described a quadrupole reaction cell they have termed a *dynamic reaction cell* (DRC) used with a quadrupole mass spectrometer (Fig. 3.12b). Reactive gases, such as NH_3, H_2, O_2, and H_2O, were investigated. Charge transfer or proton transfer reactions could be used to advan-

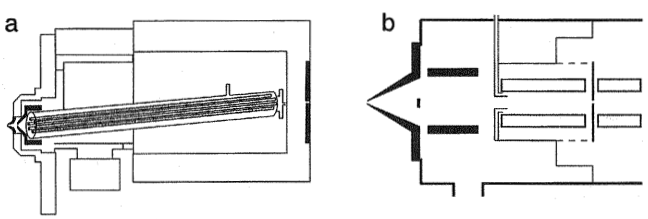

Figure 12 (a) ICP-MS with hexapole collision-reaction cell similar to that used by Micromass. (b) ICP-MS with dynamic reaction cell as described by Perkin-Elmer Sciex.

tage. Dramatic [119] reduction, up to nine orders of magnitude, of Ar^+ and molecular ion signals was observed. Analyte ion sensitivities could be maintained or increased while "continuum" background count levels were decreased to less than 1 count/sec. Iron detection limits of 0.3 ppt were reported. The background preventing lower detection limits appeared to be iron in the blank water supply as the background spectrum showed an isotope pattern matching that of Fe. Other reported detection limits included 1 ppt As, 1 ppt Ca, 1 ppt K, and 10 ppt Se.

Several important concepts for successful operation of the dynamic reaction cell were described [118]. The contribution of the rf field of the quadrupole to ion energy must be considered together with the thermodynamics of the desired (and undesired) ion-molecule reactions. This is because the rf field can impart kinetic energy to the ions in the cell. Endothermic reactions could proceed at significant rates if sufficient ion energy were available for the ion-molecule reaction. The cell pressure and rf field must be properly controlled in order to obtain an appropriate number of reactive collisions in the cell. A balance between promotion of desirable reactions at sufficient rates and unwanted scattering losses of analyte ions or loss of ion transmission due to nearly complete thermalization (so that ions no longer have a significant velocity along the beam axis) must be struck. The production of ions from single-step reactions and sequences of reactions must be considered.

Discrimination against undesirable reaction product ions is important. The quadrupole cell can be used in a bandpass mode to remove the product ions of intermediate reactions and thus intercept the series of sequential reactions that might otherwise introduce new spectral interferences. The selection of the appropriate reaction gas and cell operating conditions must be assessed, depending on the analyte ion of interest and the spectral overlap ions to be removed.

3.1.6 Mass Spectrometers

Quadrupole mass spectrometers were used in both the early ICP-MS instrument development research and the first commercial instruments. To date, quadrupole-based ICP-MS instruments continue to be predominant. During the last several years, ICP ion sources have been coupled with mass spectrometers of several different designs, including double-sector, single-sector, time-of-flight, ion trap, and Fourier transform ion cyclotron resonance.

The operation of the quadrupole mass spectrometer is only briefly described here. Excellent descriptions are available in the literature including an introduction to quadrupole mass spectrometers [121,122], analysis of the mathematics associated with quadrupole [123], and extensive treatises [124,125].

The quadrupole mass filter (Fig. 3.13a) passes ions with a particular range of mass-to-charge ratios. Four precisely made rods are mounted with stringent (10-μm) tolerances. Opposing pairs of rods are connected to a radio frequency

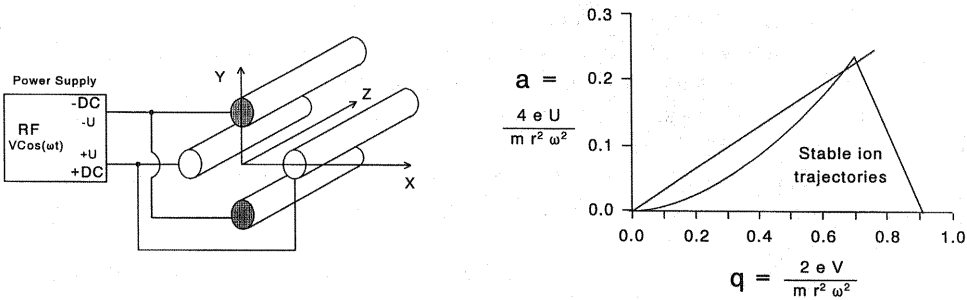

Figure 13 Quadrupole mass filter: (a) Diagram of quadrupole and connections to rf/dc power supply. (b) Side view of ion trajectories in two planes.

power supply with a direct current (dc) offset. The voltage on one pair is opposite to the polarity of the other pair. The rf voltage on one pair is 180° out of phase with the rf voltage on the other pair.

Although the ideal cross section of the rods is hyperbolic, the best approximation using circular rods is obtained when the radius of each rod, r, is equal to 1.148 times the radius from the center of the four rods to the inside edge of the rods, r_0 [126].

The operation of the quadrupole can be understood by considering the movement of the ions in the two planes perpendicular to their flight through the quadrupole. When the potential on two opposite rods is negative, positive ions are attracted radially outward from the center of the quadrupole toward the negatively biased rods. Conversely, when the potential on two opposite rods is positive, positive ions are repelled from the rods, effectively focused toward the center of the quadrupole. The alternating current (ac) portion of the voltage waveform oscillates with time. The distance ions travel outward from the center during the portion of the waveform when the ac potential of two opposite rods is negative depends on the mass-to-charge ratio of the ion, the time the potential remains negative (inversely proportional to the ac frequency), the magnitude of the applied ac potential, the location of the ion relative to the center of the quadrupole, and the velocity of the ion. If the mass/charge ratio of the ion is large and the ac frequency is high, the ion does not move far during each half-cycle of the ac waveform. Therefore, the heavy ions are most affected by the average (dc) voltage applied to the rods. In contrast, lighter ions are more significantly affected by the oscillating, ac voltage.

If the average (dc) voltage on the rods is positive (as is true for the rods in the x-z plane, as defined in Fig. 3.13a), ions tend to be repelled from the rods toward the center of the quadrupole on average. Ions that have a mass/charge ratio less

than a critical value are accelerated far enough away from the center of the quadrupole during a half-cycle of the ac voltage to hit the rods and be lost. Ions that have a mass/charge ratio greater than a critical value have a stable path through the quadrupole. As a result, the rods in the *x*-*z* plane, as defined in Fig. 3.13a, act as a high-pass filter.

Remember that ions with a large mass/charge ratio are affected more by the average (dc) voltage than by the rapidly changing ac voltage. If the average (dc) voltage on the rods is negative (*y*-*z* plane, as defined in Fig. 3.13a), ions with a mass/charge ratio greater than a critical value are attracted to the rods until they collide with the rods and are lost. Light ions follow the rapidly changing ac potential so they are refocused toward the center of the quadrupole during the portion of the waveform when the ac potential is more positive than the dc potential. As a result, the rods in the *y*-*z* plane, as defined in Fig. 3.13a, act as a low-pass filter.

Only ions that have a stable path in both the *x*-*z* and *y*-*z* planes pass through the quadrupole. The result is a bandpass filter that allows only ions with mass/charge ratios within a narrow range to pass through the quadrupole and be detected. The range of mass/charge ratio ions that pass through the quadrupole (the resolution of the quadrupole) depends on the ratio of the dc to ac amplitude, the ac frequency, and the quadrupole radius.

The mass/charge ratio ions that are stable in both the *x*-*z* and *y*-*z* planes can be described in terms of a stability diagram (Fig. 3.13b) with variables *a* and *q*. As shown in Fig. 3.13b, *a* depends on the magnitude of the dc voltage and *q* depends on the amplitude of the ac voltage. Both *a* and *q* also depend on the mass/charge ratio of the ion, the radius of the quadrupole, and the frequency of the ac voltage applied to the rods. The mass/charge ratio for ions that pass through the quadrupole is varied by changing the dc voltage magnitude and the ac amplitude while maintaining a constant ratio (as shown by the mass scan line in Fig. 3.13b).

Sector instruments for ICP-MS are commercially available. These instruments can provide either high resolution, to overcome spectral overlaps requiring a resolution of about 9000 or less, or high sensitivity when used in a low-resolution mode [127,128]. Because the main source of signal fluctuations are the sample introduction system and plasma ion source themselves, simultaneous, multicollector sector mass spectrometers can provide high precision ratios, approaching the precision of thermal ionization mass spectrometry. Typically, multicollector instruments cannot provide resolution as high as single-detector sector based instruments can. Multicollector sector mass spectrometers are discussed in detail in Chapter 8. Recently, an instrument that consists of a hexapole collision-reaction cell and a single-sector mass spectrometer has been introduced. The collision-reaction cell is used to reduce the spread of ion kinetic energies so that an electric sector for energy filtering is unnecessary.

Time-of-flight (TOF) ICP-MS instruments are also now commercially

available. The main advantages of TOF-ICP-MS are due to the simultaneous sampling of ions of all masses. As a result, transient signals for all elements and isotopes can be monitored with high temporal resolution. Because ions are extracted and injected into the TOF-MS simultaneously, high-precision isotope ratios and analyte/internal standard ratios should be attainable. Ion trap mass spectrometers have been used in combination with a quadrupole mass filter and alone with an ICP ion source [129–133]. Initially the large ratio of Ar^+ to analyte ions in the ICP was thought to make ion trap mass spectrometers impractical because of the limited total number of ions that can be stored in the trap. However, the number of Ar^+ ions observed in the ion trap is orders of magnitude less, on a relative basis, than in the ICP itself.

High-resolution Fourier transform ion cyclotron resonance mass spectrometers have also been used for ICP-MS [134,135]. Quadrupole mass spectrometers used in alternate stability regions to obtain higher resolution than typical have also been used for ICP-MS [136,137].

3.1.7 Detectors

Several different detectors have been used in ICP-MS instruments (Fig. 3.14). A range of ion signals from less than 1 to 10^8 ions/sec can be produced. Counting-based detection is typically used for signals of about 10^6 ions/sec or less. For larger

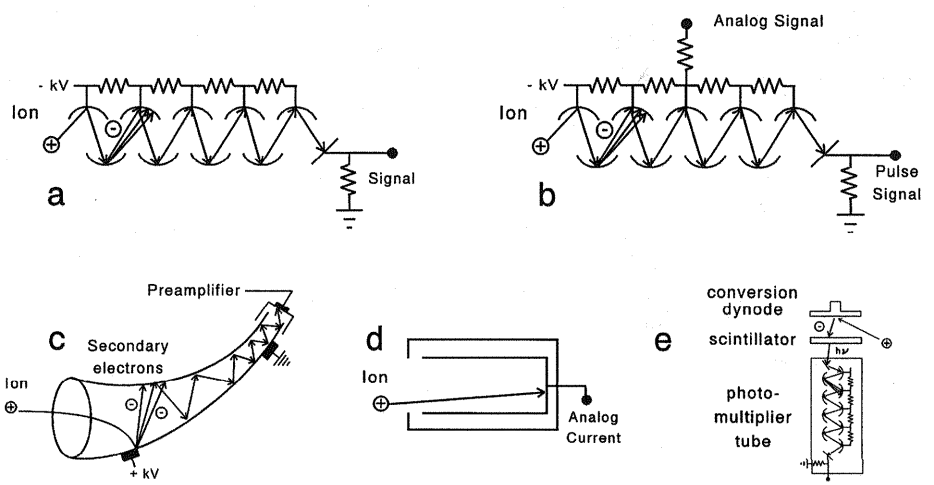

Figure 14 Detectors: (a) Discrete dynode electron multiplier. (b) Dual-mode discrete dynode electron multiplier detector. (c) Channeltron electron multiplier. (d) Faraday collector. (f) Daly detector.

signals either an analogue detection system must be used or the ion transmission to the detector can be reduced by defocusing or other means. Channeltron electron multipliers, discrete dynode electron multipliers, Daly detectors, and Faraday collector detectors have been used.

Continuous dynode electron multipliers (such as the Channeltron) are horn-shaped detectors (Fig. 3.14b). A high voltage is applied between the input and output ends of the detector. When an ion strikes the detector, secondary electrons are produced. These electrons in turn strike the wall of the detector, generating more electrons. Up to 10^8 electrons are produced and collected at a collector electrode at the output end of the detector for each incident ion, depending on the applied voltage.

Discrete dynode detectors (Fig. 3.14a) are similar in concept except that there are separate dynodes rather than a continuous dynode surface. The voltage applied to each dynode stage can be controlled. A dual-mode variation of the discrete dynode detector (Fig. 3.14c) allows signals to be measured partway down the dynode chain (with analogue detection for large signals) or at the end of the dynode (with pulse-counting detection for signals of less than about 10^6 counts/sec). The two signals can be monitored simultaneously. Furthermore, the voltage applied to the dynodes past the point of analogue detection can be turned off to prevent damage when signals are large. The analogue gain of the detector is a function of mass and can change over time. Therefore, the analogue signal must occasionally be calibrated relative to the pulse-counting mode.

Current from a Faraday cup detector (Fig. 3.14d) is measured with an analogue amplifier. The resulting analog output voltage can be converted to pulses by using a voltage-to-frequency converter. The pulses can then be counted with the same electronics used for ion counting. Ion signals corresponding to a minimum of about 10^4 ions/sec can be detected.

A Daly detector [138,139] (Fig. 3.14e) is also being used in some instruments. Ions strike a negatively charged target (an aluminum surface, for example) to produce secondary electrons. The electrons are accelerated to a thin metal film held at ground on top of a scintillator. Light is produced when the secondary electrons strike a scintillator. The light is detected by a photomultiplier tube. Advantages of the Daly detector include long lifetime, a wide linear dynamic range, and lack of gain loss after monitoring a very strong signal.

3.2 ANALYTICAL CHARACTERISTICS AND EFFECT OF EXPERIMENTAL PARAMETERS

3.2.1 Spectra

Mass spectra produced by ICP-MS consist of elemental ions, polyatomic ions produced from plasma and solvent species, and polyatomic ions produced from

sample and solvent or plasma species. The vast majority of ions observed in ICP-MS are singly charged. A few elements, such as Ba, that have a relatively low second ionization potential, are observed as +2 ions, but their signal is small (typically less than 2%) compared to that of the singly charged ion. Several elements (including Na, P, Al, Sc, Mn, Co, As, Y, Nb, Rh, Ag, and Au) have only one isotope. Most elements have a few to several isotopes. Sn has 10 isotopes.

Spectral Overlaps Due to Elemental Ions

If the spectra consisted only of elemental ions, every element except In would have at least one isotope that was free of spectral overlaps from other elemental ions (Table 3.2). In most cases, the isobaric overlaps are easily predictable. The contribution of the interferent ion to the signal measured at the mass of the analyte elemental ion can be subtracted by measuring the interferent ion signal at a second mass. The known isotopic distribution of the interferent element can be used to determine the contribution of the interferent ion at the analyte ion mass. Alternatively, a solution containing only the interferent element can be measured in order to determine the interferent signal at the analyte mass and at another isotope of the interferent element.

Spectral Overlaps Due to Molecular Ions from Plasma and Solvent Species

Molecular ions present a more complex problem in ICP-MS. With a combination of molecular ion interferences and isobaric interferences, all of the isotopes of the analyte ion of interest may suffer from a spectral overlap. The molecular ion signals can also be strongly dependent on the sample composition and experimental parameters. It is often more difficult to identify and correct for molecular ion spectral overlaps than for isobaric overlaps. Because the resolution of the commercial quadrupole mass spectrometers is 0.5 dalton or less, isotopic patterns, rather than exact mass, must be used in an attempt to identify the interfering molecular ion.

The molecular ion overlaps due to plasma and solvent species are most severe below mass/charge 82. A high-resolution, double-focusing mass spectrometer was used to identify molecular ions observed in ICP-MS (Table 3.3) [3]. Common molecular ions that produce intense signals from plasma and solvent species include ArO^+, $ArOH^+$, ArH^+, ArN^+, Ar_2^+, Ar_2H^+, O^+, N_2^+, NO^+, and O_2^+. Other molecular ions become a problem at lower analyte concentrations. These include CO_2^+, CO_2H^+, NO_2^+, ArO^+ ions with minor isotopes of Ar or O, ArC^+, ArN_2^+, and minor isotopes of Ar as Ar_2^+.

Ca, Fe, S, Si, P, and Se are most severely affected by spectral overlaps in ICP-MS. The main isotope of calcium, $^{40}Ca^+$ (96.9%), occurs at the same mass as the main isotope of argon, $^{40}Ar^+$. The second most abundant isotope of calcium,

Table 2 Elemental Ion Isotope Abundances

u	Element (abundance, %)	u	Element (abundance, %)
1	H (99.985)	41	K (6.73)
2	H (0.015)	42	Ca (0.647)
3		43	Ca (0.135)
4	He (100)	44	Ca (2.086)
5		45	Sc (100)
6	Li (7.5)	46	Ti (8.01), Ca (0.004)
7	Li (92.5)	47	Ti (7.33)
8		48	Ti (73.81), Ca (0.187)
9	Be (100)	49	Ti (5.5)
10	B (19.9)	50	Ti (5.4), Cr (4.34), V (0.25)
11	B (80.1)	51	V (99.75)
12	C (98.9)	52	Cr (83.79)
13	C (1.1)	53	Cr (9.50)
14	N (99.6)	54	Cr (2.36), Fe (5.9)
15	N (0.4)	55	Mn (100)
16	O (99.8)	56	Fe (91.72)
17	O (0.04)	57	Fe (2.11)
18	O (0.2)	58	Fe (0.28), Ni (68.08)
19	F (100)	59	Co (100)
20	Ne (90.5)	60	Ni (26.22)
21	Ne (0.27)	61	Ni (1.14)
22	Ne (9.25)	62	Ni (3.63)
23	Na (100)	63	Cu (69.17), Ni (0.93)
24	Mg (78.99)	64	Zn (48.63)
25	Mg (10)	65	Cu (30.83)
26	Mg (11)	66	Zn (27.9)
27	Al (100)	67	Zn (4.1)
28	Si (92.23)	68	Zn (18.8)
29	Si (4.67)	69	Ga (60.1)
30	Si (3.10)	70	Ge (21.24), Zn (0.62)
31	P (100)	71	Ga (39.89)
32	S (95.02)	72	Ge (27.66)
33	S (0.75)	73	Ge (7.72)
34	S (4.21)	74	Ge (35.94), Se (0.89)
35	Cl (75)	75	As (100)
36	S (0.02), Ar (0.34)	76	Se (9.36), Ge (7.44)
37	Cl (24.23)	77	Se (7.63)
38	Ar (0.063)	78	Se (23.77), Kr (0.35)
39	K (93.26)	79	Br (50.69)
40	Ar (99.6), Ca (96.94), K (0.01)	80	Kr (2.25), Se (49.61)

Table 2 Continued

u	Element (abundance, %)	u	Element (abundance, %)
81	Br (43.9)	121	Sb (57.4)
82	Se (8.7), Kr (11.6)	122	Sn (4.6), Te (2.6)
83	Kr (11.5)	123	Sb (42.6), Te (0.91)
84	Kr (57), Sr (0.56)	124	Sn (5.8), Te (4.8), Xe (0.1)
85	Rb (72.2)	125	Te (7.1)
86	Kr (17.3), Sr (9.9)	126	Te (18.9), Xe (0.09)
87	Rb (27.8), Sr (7)	127	I (100)
88	Sr (82.6)	128	Te (31.7), Xe (1.9)
89	Y (100)	129	Xe (26.4)
90	Zr (51.5)	130	Te (33.8), Xe (4.1), Ba (0.11)
91	Zr (11.2)	131	Xe (21.2)
92	Zr (17.2), Mo (14.8)	132	Xe (26.9), Ba (0.1)
93	Nb (100)	133	Cs (100)
94	Zr (17.4), Mo (9.3)	134	Xe (10.4), Ba (2.4)
95	Mo (15.9)	135	Ba (6.6)
96	Zr (2.8), Mo (16.7), Ru (5.5)	136	Xe (8.9), Ba (7.9), Ce (0.19)
97	Mo (9.6)	137	Ba (11.2)
98	Mo (24.1), Ru (1.9)	138	Ba (71.7), La (0.09), Ce (0.25)
99	Ru (12.7)	139	La (99.9)
100	Mo (9.6), Ru (12.6)	140	Ce (88.5)
101	Ru (17)	141	Pr (100)
102	Ru (31.6), Pd (1)	142	Ce (11.1), Nd (27.1)
103	Rh (100)	143	Nd (12.2)
104	Ru (18.7), Pd (11.1)	144	Nd (23.8), Sm (3.1)
105	Pd (22.3)	145	Nd (8.3)
106	Pd (27.3), Cd (1.3)	146	Nd (17.2)
107	Ag (51.7)	147	Sm (15)
108	Pd (26.5), Cd (0.89)	148	Nd (5.8), Sm (11.3)
109	Ag (48.2)	149	Sm (13.8)
110	Pd (11.7), Cd (12.5)	150	Nd (5.6), Sm (7.4)
111	Cd (12.8)	151	Eu (47.8)
112	Cd (24.1), Sn (0.97)	152	Sm (26.7), Yb (0.13)
113	Cd (12.2), In (4.3)	153	Eu (52.2)
114	Cd (28.7), Sn (0.65)	154	Sm (22.7), Gd (2.2)
115	In (95.7), Sn (0.36)	155	Gd (14.8)
116	Cd (7.5), Sn (14.5)	156	Gd (20.5), Dy (0.06)
117	Sn (7.7)	157	Gd (15.7)
118	Sn (24.2)	158	Gd (24.8), Dy (0.1)
119	Sn (8.6)	159	Tb (100)
120	Sn (32.6), Te (0.095)	160	Gd (21.9), Dy (2.3)

Table 2 Continued

u	Element (abundance, %)	u	Element (abundance, %)
161	Dy (18.9)	201	Hg (13.2)
162	Dy (25.5), Er (0.14)	202	Hg (29.9)
163	Dy (24.9)	203	Tl (29.5)
164	Dy (28.2), Er (1.6)	204	Hg (6.9), Pb (1.4)
165	Ho (100)	205	Tl (70.5)
166	Er (33.6)	206	Pb (24.1)
167	Er (23)	207	Pb (22.1)
168	Er (26.8), Yb (0.13)	208	Pb (52.4)
169	Tm (100)	209	Bi (100)
170	Er (14.9), Yb (3.1)	210	
171	Yb (14.3)	211	
172	Yb (21.9)	212	
173	Yb (16.1)	213	
174	Yb (31.8), Hf (0.16)	214	
175	Lu (97.4)	215	
176	Yb (12.7), Lu (2.6), Hf (5.2)	216	
177	Hf (18.6)	217	
178	Hf (27.3)	218	
179	Hf (13.6)	219	
180	Hf (35.1), Ta (0.01), W (0.13)	220	
181	Ta (99.99)	221	
182	W (26.3)	222	
183	W (14.3)	223	
184	W (30.7), Os (0.02)	224	
185	Re (37.4)	225	
186	W (28.6), Os (1.6)	226	
187	Re (62.6), Os (1.6)	227	
188	Os (13.3)	228	
189	Os (16.1)	229	
190	Os (26.4)	230	
191	Ir (37.3), Pt (0.01)	239	
192	Os (41), Pt (0.79)	232	Th (100)
193	Ir (62.7)	233	
194	Pt (32.9)	234	U (0.006)
195	Pt (33.8)	235	U (0.72)
196	Pt (25.3), Hg (0.15)	236	
197	Au (100)	237	
198	Pt (7.2), Hg (10)	238	U (99.3)
199	Hg (16.9)	239	
200	Hg (23.1)	240	

$^{44}Ca^+$ (2.1%), suffers from a spectral overlap with CO_2^+. The third most abundant isotope of calcium, $^{42}Ca^+$ (0.65%), suffers from a spectral overlap with ArH_2^+. The main isotope of iron, $^{56}Fe^+$ (91.7%), is at the same mass as the intense ArO^+ signal. The next most abundant isotope of iron, $^{54}Fe^+$ (5.8%), suffers from a spectral overlap with ArN^+. The third most abundant isotope of iron, $^{57}Fe^+$ (2.2%), is at the same nominal mass as $ArOH^+$. Molecular ions consisting of Ar, O, and sometimes H cause some degree of overlap with all of the isotopes of Cr, Fe, Mn, and Co as well as the most abundant isotope of Ni, as can be seen in Table 3.3. The main isotope of sulfur, $^{32}S^+$ (95.0%), occurs at the same nominal mass as O_2^+. Both minor isotopes of S suffer from spectral overlaps with N or O containing polyatomic ions. The main isotope of silicon, $^{28}Si^+$, is at the same nominal mass as N_2^+ and both minor isotopes also suffer from overlaps with molecular ions. Phosphorus is monoisotopic at the same nominal mass as NOH^+ and $^{15}NO^+$. The two most abundant isotopes of selenium suffer from overlaps with Ar_2^+ ions ($^{38}Ar^{40}Ar^+$ and $^{40}Ar_2^+$).

The choice of acids to use in sample preparation for ICP-MS can also be affected by potential spectral overlaps. High concentrations of chloride ions in solution, from HCl, for example, result in Cl-containing molecular ions that produce intense signals. Arsenic, which is monoisotopic (75 daltons), suffers from a spectral overlap with $ArCl^+$. Analysis of V is also severely affected. The main isotope of vanadium, $^{51}V^+$ (99.8%), has the same nominal mass as $^{35}Cl^{16}O^+$. The only other isotope of vanadium, $^{50}V^+$ (0.2%), suffers from a spectral overlap with $^{36}Ar^{14}N^+$ or $^{35}Cl^{15}N^+$. Manganese, which is monoisotopic, suffers from an interference with $^{37}Cl^{18}O^+$. The main isotope of chromium, $^{52}Cr^+$, is at the same mass as $ClOH^+$. Both Ga isotopes overlap with a Cl containing molecular ions. All of the germanium isotopes except the minor isotope $^{76}Ge^+$ overlap with a Cl containing molecular ion.

Use of sulfuric acid also leads to many spectral overlaps with the most intense molecular ion signals, including SO^+, SOH^+, S_2^+, SO_2H^+, and SO_2^+. Elements including Ti, V, Ni, Zn, and Ge suffer from molecular overlaps as a result. Phosphoric acid also leads to molecular ions, including POH^+, P_2^+, and PO_2^+.

Spectral Overlaps Due to Oxide and Hydroxide Species

Monoxide (MO^+) and hydroxide (MOH^+) ions, where M can be any one of many elements, are observed in ICP-MS [140]. Typically the molecular oxide or molecular hydroxide signals are small (<3%) relative to the elemental ion signal. However, if one is trying to measure a small concentration of one element in the presence of a high concentration of a second element that forms a molecular oxide or hydroxide ion at the same mass as an analyte, the problem can be severe. Furthermore, the molecular ions may overlap with an elemental ion isotope that is

Table 3 Polyatomic Ions with Mass/Charge Ratios of 80 or Less

u	Polyatomic ions
1	
2	H_2
3	H_3
4	
5	
6	
7	
8	
9	
10	
11	
12	
13	CH
14	^{13}CH, CH_2
15	NH
16	
17	OH, NH_3
18	O^2H, NH_4
19	^{18}OH, $H_2{}^{18}O$
20	$H_2{}^{18}O$, $^2HH_2O$
21	^2H_2HO, $^{18}OH_3$
22	
23	
24	C_2
25	C_2H, ^{13}CC
26	CN, $^{13}C_2$, BO, C_2H_2, ^{13}CCH
27	$C^{15}N$, ^{11}BO, HCN
28	N_2, CO
29	CHO, N_2H, ^{13}CO, ^{15}NN
30	NO, $^{15}N_2$, $N_2{}^2H$, $C^{18}O$
31	NOH, ^{15}NO, $C^{18}OH$, $^{13}C^{18}O$, $^{15}N_2H$
32	O_2, $N^{18}O$, ^{15}NOH, NOH_2
33	O_2H, $^{15}N^{18}O$, $O^{17}O$, $^{15}N^{18}O$, $^{14}N^{18}OH$, SH
34	H_2O_2, $^{17}O_2$, ^{18}OO, $^{15}N^{18}OH$, ^{33}SH
35	$H^{17}O_2$, ^{34}SH
36	ClH
37	^{36}ArH
38	^{37}ClH
39	^{38}ArH
40	MgO
41	ArH, $Na(H_2O)$, $Mg^{17}O$
42	ArH_2, $Mg^{18}O$
43	AlO

Table 3 Continued

u	Polyatomic ions
44	CO_2, N_2O, CS, SiO
45	CO_2H, N_2OH, PN, ^{29}SiO, SiOH, Zr^{2+}
46	NO_2, $^{13}CO_2$, $^{5}LiAr$, Na_2, $^{92}Zr^{2+}$
47	CCl, PO, LiAr, NO_2H, $^{15}NO_2$, $S^{15}N$, $^{30}SiOH$
48	$NO(H_2O)$, $NO^{18}O$, $N^{17}O_2$, SO, C_4, ^{36}ArC, Mg_2, POH
49	ClN, $C^{37}Cl$, $Mg^{25}Mg$, $N^{17}O_2H$, NCl, SOH, $^{36}Ar^{13}C$, $^{36}ArCH$
50	^{38}ArC, $^{24}Mg^{26}Mg$, ^{36}ArN, HNCl, $S^{18}O$, $S^{17}OH$, $^{34}S^{15}OH$
51	^{37}ClN, ClO, $^{38}Ar^{13}C$, $^{25}Mg^{26}Mg$, $^{36}ArNH$, $S^{18}OH$
52	ClOH, $Ar^{13}C$, ^{38}ArN, ^{36}ArO, $^{26}Mg_2$
53	$^{36}ArOH$, ^{37}ClO, $^{38}ArNH$, $^{37}Cl^{17}OH$, $Ar^{13}C$
54	ArN, $^{37}ClOH$, ^{38}ArO, $^{36}Ar^{18}O$, $^{37}Cl^{17}O$, $^{36}S^{18}O$
55	ArNH, $^{27}Cl^{18}O$, NaS, $^{38}ArOH$, $Ar^{15}N$, $^{110}Cd^{2+}$
56	ArO, $^{38}Ar^{18}O$, $Ar^{15}NH$, $^{37}Cl^{18}OH$, CaO, $^{112}Cd^{2+}$
57	ArOH, $^{38}Ar^{18}OH$, $Ar^{17}O$, CaOH, Cd^{2+}
58	$Ar^{18}O$, $Ar^{17}OH$, NaCl, $^{29}Si_2^+$, $Ca^{18}O$, $^{116}Cd^{2+}$
59	MgCl, $^{42}Ca^{17}O$, $^{42}CaOH$
60	$Na^{37}Cl$, $^{25}NaCl$, ^{44}CaO
61	MgCl, ScO, $^{44}CaOH$
62	P_2, $^{25}Mg^{37}Cl$, Na_2O, ^{46}TiO, $^{44}Ca^{18}O$
63	ClN_2, PO_2, NaAr, $^{26}Mg^{37}Cl$, OCCl, $NC^{37}Cl$, $^{36}ArCNH$, TiO, $^{36}Ar^{37}Cl$
64	HPO_2, TiO, $^{46}Ca^{18}O$, $Na_2{}^{18}O$, $^{38}ArCN$, SiClH, $^{29}SiCl$, $^{37}Cl^{15}NC$, S_2^+, SO_2, O_4, ArC_2, $^{36}ArCO$, $^{36}ArN_2$
65	$^{37}ClN_2$, ^{49}TiO, Ba^{2+}, $^{36}ArN_2H$, SO_2H
66	ClNOH, ClCOH, $^{33}S_2$, ^{34}SS, $^{36}ArON$, $^{38}ArN_2$, ArCN, Cs^{2+}, $^{132}Ba^{2+}$
67	ClO_2, $^{36}ArNOH$, $^{37}ClNO$, SCl, $^{33}S^{34}S$, $^{34}SO_2H$, $^{36}ArNOH$, $Ti^{18}O$, VO, $^{50}C^{17}O$, $^{134}Ba^{2+}$, Cs^2
68	ClO_2H, ^{36}ArS, $^{34}S_2$, $^{38}ArNO$, $^{36}ArO_2$, ArCO, CrO, ArN_2, $^{136}Ba^{2+}$, $^{136}Ce^{2+}$
69	$^{37}ClO_2$, $^{36}Ar^{32}SH$, ^{53}CrO, Ba^{2+}, La^{2+}, $^{138}Ce^+$, $^{34}H^{18}OO$, ^{36}ArS, $^{36}ArO_2H$
70	ArNO, Cl_2, $^{37}ClO_2H$, $^{38}ArO_2$, $^{38}ArN^{18}O$, $Cl^{33}S$, $Na^{33}SN$, $Cr^{18}O$, ^{54}FeO, La^{2+}, Ce^{2+}, Pr^{2+}
71	$Ar^{15}NO$, HCl_2, $^{36}ArCl$, ArP, $^{54}FeOH$, MnO, Pr^{2+}, $^{142}Ce^{2+}$, Nd^{2+}
72	$^{35}ClCl$, $Cl^{18}O_2H$, $^{36}Ar_2$, $^{36}ArO_2$, ArS, $^{38}Ar^{34}S$, $^{36}Ar^{36}S$, $^{36}S_2$, FeO, MnOH, $^{144}Nd^{2+}$, $^{144}Sm^{2+}$
73	$^{38}ArCl$, $^{35}Cl^{37}ClH$, ArSH, $Ar^{33}S$, ArO_2H, $Fe^{17}O$, FeOH, $^{146}Nd^{2+}$, $^{147}Sm^{2+}$
74	$^{36}Ar^{38}Ar$, $^{37}Cl_2$, $^{38}Ar^{36}S$, $Ar^{34}S$, NiO, ^{58}FeO, $^{57}FeOH$, $^{148}Nd^+$, $^{148}Sm^{2+}$
75	ArCl, $^{37}Cl_2H$, $^{36}Ar^{38}ArH$, $Ar^{34}SH$, CoO, $^{58}FeOH$, $^{150}Sm^{2+}$, $^{150}Nd^{2+}$, Eu^{2+}
76	$Ar^{36}Ar$, AsH, ^{60}NiO, Eu^{2+}, Sm^{2+}
77	$Ar^{37}Cl$, $^{38}Ar_2H$, ^{61}NiO, $^{153}Eu^{2+}$, $^{154}Sm^{2+}$
78	$^{38}ArAr$, ^{62}NiO, $^{46}TiOO$, Gd^{2+}
79	$^{38}ArArH$, KAr, $^{47}TiO_2$, Tb^{2+}, Gd^{2+}
80	Ar_2, TiO_2, $^{62}Ni^{18}O$, Tb^{2+}, $^{160}Gd^{2+}$, $^{160}Dy^{2+}$

Source: Refs. 3 and 423.

being used for an isobaric interference correction. The molecular ion overlap in this case would result in an overcorrection for an isobaric overlap.

Among the commonly observed spectral overlap problems due to molecular oxide and molecular hydroxide ions are those due to TiO^+ (with 5 isotopes of Ti from mass 46 to 50) that result in overlaps with a minor isotope of nickel, $^{62}Ni^+$; both isotopes of copper, $^{63}Cu^+$ and $^{65}Cu^+$; and the two major isotopes of zinc, $^{64}Zn^+$ and $^{66}Zn^+$. Calcium oxide and hydroxide ions overlap with all five isotopes of nickel, both isotopes of zinc, and three of the four isotopes of iron. The analysis of rare earth elements is particularly complicated by molecular oxide and hydroxide ion spectral overlaps [141,142].

There are several sources of information that can aid in identifying potential spectral overlaps. Instrument manufacturers typically include spectral overlap information in the instrument software. An atlas of elemental ion spectra as well as many of the molecular ions is available in a very convenient software package, MS InterView, that was published in *Spectrochimica Acta Electronica* and is available in the Program Library at http://www.elsevier.nl:80/inca/homepage/saa/sab (download file 47/1621/92 for the Apple MacIntosh version, file 48/1063/93 for the PC version). This program also allows users to add additional ions to the spectral database.

Unfortunately, the severity of the molecular ion overlaps can be more difficult to predict because the molecular ion signal magnitude can be very dependent on the sample composition (including solvent and acid), the extent of solvent loading, and instrument parameters. Drift in the polyatomic ion signals is often more severe than for elemental ions.

Reducing the Severity of Molecular Ion Spectral Overlaps

There are several ways to reduce the signals due to molecular ions in ICP-MS. Oxide and hydroxide molecular ion signals can be reduced by greatly decreasing the amount of water that enters the ICP or by using mixed gas plasmas. "Cold" or "cool" plasma conditions can be used but with some potentially severe trade-offs including chemical matrix effects and loss of sensitivity for analyte ions with high ionization energies. Recently, reaction cells to remove the polyatomic ions that cause spectral overlaps by reaction with a reagent gas in a several-torr cell between the skimmer and mass spectrometer have been described. Alternatively, high-resolution instruments can be used to separate many of the molecular ion signals from elemental ion signals.

Mixed Gas Plasmas. Water loading can be reduced by a desolvation system (condenser or membrane separator) only if the vast majority of the water can be removed. One way to eliminate the introduction of water into the plasma during measurement of the analyte signals is with electrothermal vaporization, laser ablation, or other direct solid sampling techniques. Mixed gas plasmas,

particularly the addition of 5% or less N_2 to the plasma, can also reduce the molecular ion signals. A combination of reduced water loading and use of a mixed gas plasma can be particularly effective [143]. The addition of CH_4, CHF_3, and C_2H_2 has also been reported to reduce the $ArCl^+$, Ar_2^+, ArO^+, ClO^+, and MO^+ ion signals dramatically [144,145].

Cool or Cold Plasma. "Cool" or "cold" plasma conditions can be used to reduce the magnitude of the Ar containing molecular ions whereas the sensitivities for many elements with ionization potentials less than 6 eV are not significantly affected [10,146]. By using low powers (600 W) and high nebulizer gas flow rates (1.0 L/min or greater) signals due to several ions that are dominant under normal plasma conditions (Fig. 3.15a) can be reduced. The Ar^+ signal can be reduced by six orders of magnitude or more, ArH^+ can be reduced by four orders of magnitude, and ArO^+ can be reduced by three orders of magnitude or more [147]. As a result, detection limits for K, Ca, and Fe can be dramatically improved. The signals from other ions, including H_3O^+, NO^+, and O_2^+, increase dramatically, to become the dominant ions in the mass spectrum, as shown in Fig. 3.15b. To attain "cold" plasma conditions that are analytically useful, the plasma potential must be low enough to prevent discharge formation. This can be done either by using an instrument with a balanced or interlaced load coil or by using a grounded electrical shield between the load coil and the torch to reduce capacitive rf coupling.

Use of "cold" plasma conditions is not recommended for elements with high ionization potentials, elements that form refractive oxides, or samples with total dissolved solid concentrations greater than about 50 ppm. Sensitivities for elements with ionization potentials between 6 and 8 eV are up to 100 times lower under "cold" plasma conditions than under normal plasma conditions, and elements with ionization energies greater than 8 eV exhibit sensitivities that are several orders of magnitude lower under "cold" plasma conditions. Analyte oxides are much more readily formed under "cold" plasma conditions. For example, the formation of scandium oxide results in a Sc^+ ion signal that is several orders of magnitude lower under "cold" plasma conditions than under normal conditions [147]. In some cases it is possible to attain better detection limits for the analyte oxide ion, MO^+, than by measuring the elemental analyte ion, M^+. Finally, chemical matrix effects that originate in the ICP, and are therefore similar for light and heavy mass analytes, are severe under "cold" plasma conditions. Changes in the extent of ionization due to the addition of efficiently ionized elements occur because the plasma temperature and electron number density are much lower than under normal plasma conditions. Under "cold" conditions the addition of large concentrations of efficiently ionized elements affects the electron number density in the plasma and results in significant decreases in the number of analyte ions produced. As a result, "cold" plasma conditions are useful mainly for very clean samples, such as acids used in the semiconductor industry.

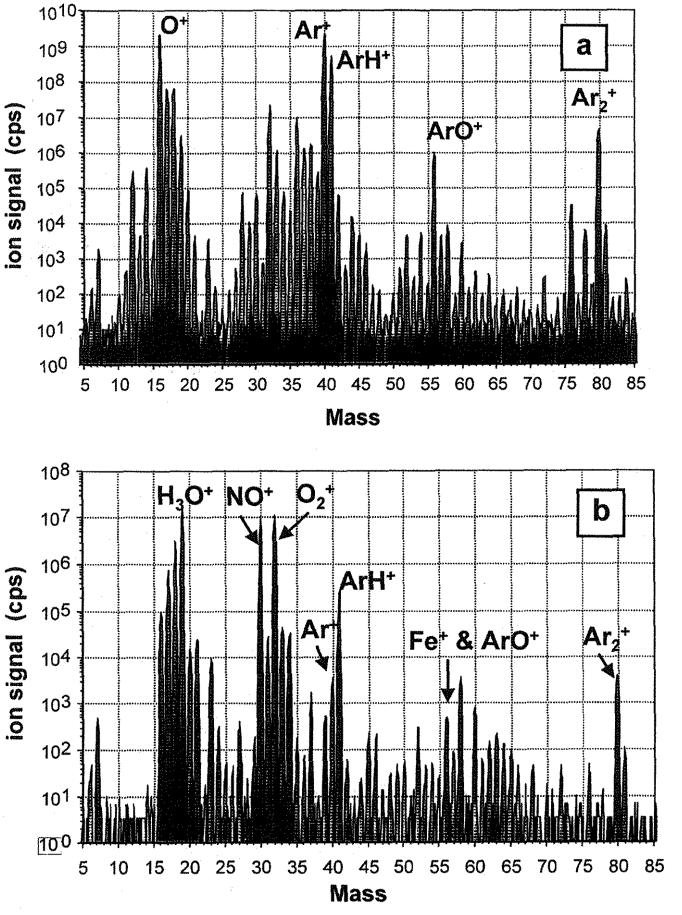

Figure 15 ICP-MS background spectra (plotted on a logarithmic scale) for a sample containing 0.1% nitric acid: (a) Conventional plasma conditions (1000 W, 0.77 L/min nebulizer gas flow rate). The Ar^+ and O^+ signals are saturating the detector, so their signals are greater than 2×10^9 counts/sec. (b) "Cold" plasma conditions (600 W, 1.08 L/min nebulizer gas flow rate). Note that full scale in (a) is 10^{10} whereas in (b) it is 10^8. (From Ref. 147.)

Collision-Reaction Cells. Perhaps the most exciting development regarding molecular ion removal in ICP-MS is the use of collision or reaction cells, introduced in Sec. 3.1.5. These rf-only quadrupole, hexapole, or octapole cells, typically operated at pressures around 10 mtorr, can provide two benefits: The collision cell can be used to reduce the ion kinetic energy and to focus ions toward

the center axis through collisions with a low-molecular-weight neutral gas [117]. Second, efficient chemical reactions that reduce or nearly eliminate reactive polyatomic ions can be attained. Attempts to use collisions, without reaction, to fragment polyatomic ions in ICP-MS are of limited value because the scattering cross section is typically larger than the fragmentation cross section [111]. Therefore, losses of analyte ions due to scattering are large compared to the additional fragmentation of polyatomic ions.

Results from initial ion trap ICP-MS experiments indicated that signals due to argon ions and many polyatomic ions were much smaller than expected [133]. Reactions between Ar^+ and H_2 result in formation of low-mass ions such as H^+ and H_3^+ and Ar atoms [148,149]. Ar-containing polyatomic ions, such as ArO^+, $ArOH^+$, $ArCl^+$, Ar_2^+, and ArC^+, can also be removed by reaction with H_2 or water vapor in a reaction cell [115,148,149]. Other gases, such as oxygen, may be useful reagents to remove other molecular ions.

Reaction cells appear to be a much better way to reduce signals due to Ar-containing molecular ions and Ar^+ itself than the use of "cold" plasma conditions. Because normal plasma conditions are used, elements with high ionization energies, such as Se and As, do not suffer from sensitivity losses, unlike "cold" plasma conditions. The severe chemical matrix effects that are typical of "cold" plasma conditions are prevented. The first commercial ICP-MS instrument to use this concept was introduced by Micromass UK Ltd. However, as noted, reaction product ions must be controlled or removed to prevent other (new) spectral overlaps.

Mathematical Correction for Spectral Overlaps

Mathematical correction procedures can be used to remove the contribution of a spectral overlap from a measured signal. However, if the signal due to the spectral overlap is much larger than the analyte signal, the signal-to-noise ratio of the corrected signal may be poor. Furthermore, it may not be easy to predict and account for quantitatively all of the potential sources of spectral overlap, particularly those due to polyatomic ions. For isobaric overlaps (Table 3.2), for which the relative isotopic abundances are predictable, mathematical corrections are straightforward. Instrument software often has built-in correction equations for this case.

Contributions from molecular ions are typically more difficult to correct quantitatively because there may be many molecular ions important over a short mass range; the molecular ion intensity varies, depending on the sample matrix; and the intensities may vary over time more dramatically than elemental ion signals. Multivariant methods including multiple linear regression [150,151], principal component analysis [152], and multicomponent analysis [153] have been used. Improvements in detection limits by up to two orders of magnitude

have been obtained for elements that suffer from extensive molecular ion spectral overlaps [153].

The multicomponent spectral fitting approach has been the most successful for a broad range of sample types [153,154]. A linear combination of spectra of all of the individual components (elemental ions and polyatomic ions) is optimized for best fit of the experimental spectrum. "Model" spectra are determined from the natural abundances of the elements and polyatomic "model" spectra are calculated from the isotopic abundances of the individual element isotopes. Therefore, experimental "model" spectra are not required.

Several problems can be encountered with multicomponent spectral fitting. If the signal is too large to be measured directly at some masses, those masses must not be included. An initial mass scan can be used to identify regions of the spectrum that should be skipped [153]. The initial mass scan might also be used to determine whether certain molecular ions can be excluded from the model because they are at insignificantly low levels. If there are more individual components in a segment of the spectrum than masses, there are more variables than unknowns and a unique solution to multicomponent fitting is not found. This can be dealt with by establishing relationships between components and constraining the signals due to certain ions in order to have at least as many equations as unknowns (independent variables). Ions such as oxides and hydroxides containing a common element (e.g., CaO^+ and $CaOH^+$) should maintain a relatively constant relationship [154]. Blank spectra can be used to establish limits for ArN^+ compared to the signal at mass 54, ArO^+ compared to the signal at mass 56, and $ArOH^+$ compared to the signal at mass 57. A lower limit for Kr in relation to the signal at mass 84 and a value for the "continuum" background (measured at mass 220) can also be set from the blank spectrum. Mass bias must be determined and included. Experimental spectra form Ca and sulfate standard solutions can be used to establish limits for the CaO^+-to-$CaOH^+$ ratio and the ratios for S species [S_2^+/SO_2^+, $SO_2H^+/(S_2^+ + SO_2^+)$, and $SO_3^+/(S_2^+ + SO_2^+)$] [154]. An Excel based spreadsheet template is available for download from a *Spectrochimica Acta Electronica* article by DeBoer [154] at http://www.elsevier.nl:80/inca/homepage/saa/sab/ (download file 52/0389/97).

3.2.2 Influence of Instrumental Parameters on Signals

Many experimental parameters and components affect sensitivity, including the analyte transport efficiency of the sample introduction system and the mean size and size distribution of the aerosol entering the ICP. The plasma torch design, rf generator, load coil, interface between the atmospheric pressure ICP and mass spectrometer, ion optics, mass spectrometer itself, and detector also affect sensitivity.

Center (Nebulizer) Gas Flow Rate, Applied Power, and Sampling Depth

For a particular instrument the most influential experimental parameters are the applied ICP power, the nebulizer (center) gas flow rate, and the sampling depth (typically described as the distance from the sampling orifice to the end of the load coil) [155,156]. For a particular sampling depth and power, the signal magnitude is highly dependent on the nebulizer gas flow rate, as shown in Fig. 3.16. Therefore, the nebulizer gas must be very precisely controlled, typically using a mass flow controller. If the applied power is increased, a higher nebulizer gas flow rate is required to obtain the maximum signal, as seen in Fig. 3.16.

To a first approximation, this behavior can be understood by considering the processes that a drop of sample undergoes in the ICP (Fig. 3.2) and the main effects of a change in nebulizer gas flow rate on the plasma. After the sample aerosol exits the center tube of the torch, it travels a short distance (2 to 10 mm) before it enters the plasma's center channel. As the nebulizer gas flow rate is increased, the location where the plasma begins (and the temperature increases rapidly) in the center of the plasma moves downstream (Fig. 3.17). Therefore, for

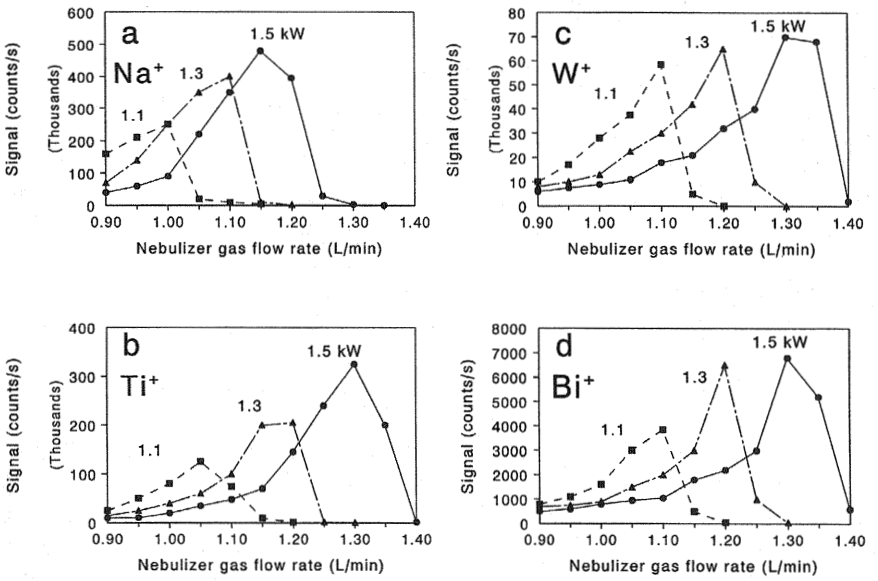

Figure 16 Effect of nebulizer gas flow rate and power on Na^+, Ti^+, W^+, and Bi^+ ICP-MS signals. (From Ref. 156.)

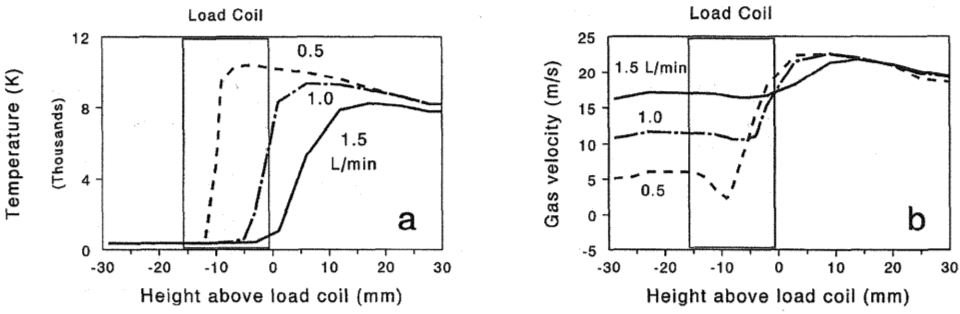

Figure 17 The effect of center (nebulizer) gas flow rate plasma temperature and gas velocity profiles. Calculations were performed by using a simulation program, HiFI 2.0. (From Ref. 424.)

a fixed sampling depth, an increase in nebulizer gas flow rate decreases the distance in the plasma that the sample travels before reaching the sampling orifice. Furthermore, for pneumatic nebulizers and conventional spray chambers without desolvation, the aerosol and water vapor transport into the plasma increases with increasing nebulizer gas flow rate. This tends to cool the plasma and delay completion of vaporization and ionization.

A certain amount of time is required to desolvate, vaporize, atomize, and ionize a drop of sample. If the ions are sampled too early, vaporization and ionization of the sample may not be complete. Furthermore, a significant number of incompletely desolvated droplets may survive to the sampling orifice [157]. Even a small number of incompletely desolvated droplets can affect signals significantly because each droplet can cool a 1- to 2-mm-wide region of the plasma [158]. After the sample is completely vaporized and converted into ions, the ions diffuse outward in the plasma, reducing the number of ions that enter the mass spectrometer [159,160]. The optimal sampling location depends on a trade off between a distance far enough so that most of the sample aerosol has been converted into ions and a distance not so far that diffusion reduces the number of ions sampled by the mass spectrometer.

If the plasma power is increased, the location where the plasma begins along the center axis moves upstream (closer to the injector tube of the torch) and the plasma temperature increases. Therefore, if the nebulizer gas flow rate were optimized at a power of 1.0 kW and the power were increased to 1.2 kW, ions would be produced farther from the sampling orifice. There would be more extensive diffusion of the ions before they reached the sampling orifice. This could be overcome by either moving the sampling orifice closer to the load coil or increasing the nebulizer gas flow rate.

The optimal nebulizer gas flow rate for a particular power also depends on the sampling depth. At a power of 1.1 kW and a sampling depth of 15 mm, a nebulizer gas flow rate of 1.05 L/min produces the peak Li^+ signal. At a sampling depth of 10 mm, the optimal nebulizer gas flow rate is 0.90 L/min. At a sampling depth of 5 mm, the optimal nebulizer gas flow rate is 0.85 L/min. Again, this can be understood from the processes described in Fig. 3.2 and the effect of changes in nebulizer gas flow rate on the plasma temperature profile shown in Fig. 3.17. As the sampling depth is increased, the optimal nebulizer gas flow rate increases. The optimal signal should occur when the majority of the sample has been converted into ions but the ions have not diffused significantly out of the center of the plasma. When ions are sampled farther from the load coil, a higher nebulizer gas flow rate is needed so that the initial hot region of the plasma in the ICP center is moved farther away from the load coil as well, as shown in Fig. 3.18. The "mountain" behavior of the signals as a function of nebulizer gas flow rate and sampling depth is also likely affected by variations in ion energy and ion transmission efficiency.

Under normal plasma and sampling conditions, the elemental ion is dominant compared to doubly charged ions or the molecular oxide or molecular hydroxide ions. Barium has an unusually low second ionization potential (10 eV). Under conditions in which the plasma temperature near the sampling orifice is hot (well after the sample aerosol has been completely vaporized and ionized), Ba^{2+} signals are significant. Therefore, the Ba^{2+} signals are maximum at a lower nebulizer gas flow rate than that of Ba^+ (Fig. 3.19). Doubly charged ions may also be created if there is a discharge between the plasma and the mass spectrometer, or in the interface region. Molecular oxide signals are high when plasma conditions are colder. Near incompletely desolvated droplets molecular oxide ion signals are high and elemental ion signals are low [160]. As a result, BaO^+ and

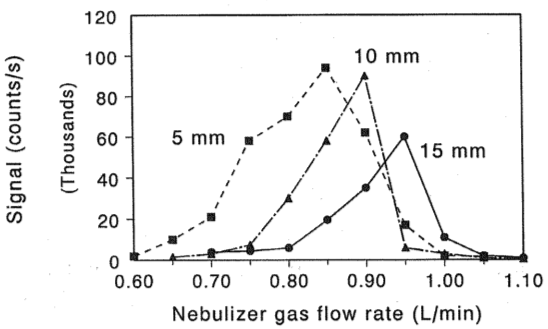

Figure 18 Effect of sampling depth on Cs^+ ICP-MS signals versus nebulizer gas flow rate. Power was 1.1 kW. (From Ref. 156.)

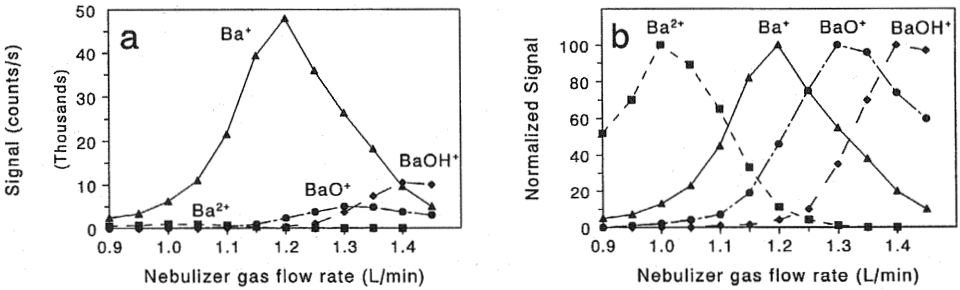

Figure 19 Effect of power and nebulizer gas flow rate on Ba^{2+}, Ba^{+}, BaO^{+}, and $BaOH^{+}$. Power was 1.3 kW. (From Ref. 140.)

$BaOH^{+}$ signals reach a maximum at higher nebulizer gas flow rates than does the Ba^{+} signal (Fig. 3.19).

Most sample introduction systems produce a wide range of aerosol drop sizes, so although small droplets vaporize early in the plasma, larger droplets survive much farther toward the sampling orifice. Two different approaches have been reported to separate the elemental ion "mountain" from the molecular oxide ion "mountain" further: French et al. used a monodisperse dried microparticulate injector (MDMI) to introduce monodisperse droplets into the ICP [161]. All of the aerosol droplets complete vaporization at a similar point in the plasma and are then quickly atomized and ionized. Atoms survive only a very short time and only 50 μsec is required from the first appearance of atoms until ionization is complete [160]. Clemons et al. used a hot graphite torch injector [162]. They observed a larger than typical difference in nebulizer gas flow rate between the peak in elemental ion signal and molecular oxide signal. Furthermore, the rise in the molecular oxide signal was much steeper. They visually observed a smaller region over which atom emission was observed, similar to that indicated in reports using the MDMI. It also appeared that the ions did not expand as much as with a ceramic or quartz injector so that signals sampled farther downstream of the point of initial emission did not fall off as rapidly.

Ion Lens Voltages

Analyte ions of different mass travel through the skimmer at about the same velocity because the gas is neutral overall so gas flow is determined predominantly by the neutral Ar atoms. As a result, the ion kinetic energy increases with increasing mass over a range from about 3.3 to 7.3 eV [97,98]. The focusing of ion lenses is dependent on ion kinetic energy. Therefore, the optimal lens voltages are mass-dependent.

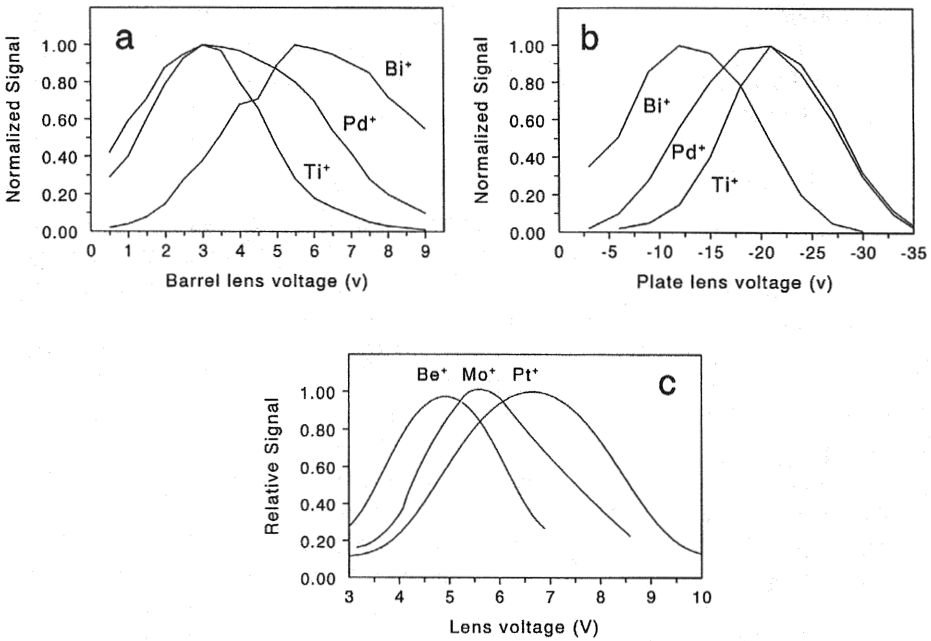

Figure 20 Effect of ion optic lens voltages on ICP-MS signals: (a) Effect of barrel lens (Fig. 10a) voltage. (From Ref. 106.) (b) Effect of plate (Fig. 10a) voltage. (From Ref. 106.) Effect of single-lens (Fig. 10f) voltage.

A variety of ion lens configurations continue to be developed and used, so the exact dependence of ion lens voltages is a function on the particular configuration used. However, the optimal lens voltages are a function of mass, as shown for a Bessel box/Einzel lens combination in Fig. 3.20a,b [106] and for a single lens behind a grounded stop [163] in Fig. 3.20c. Therefore, relative analyte ion signals depend on the lens voltages.

3.2.3 Quantitative Analysis

Detection limits at or below 1 ppt (1 pg/mL) are routinely attainable for many elements by ICP-MS as long as sources of contamination and reagent purity are carefully controlled. Detection limits as low as 10 ppq (10 fg/mL) are attainable in some cases. A linear dynamic range of up to 10^8 can be provided by ICP-MS. Short-term precision (relative standard deviation) of 1% to 3% is typical for clean samples. Long-term precision (relative standard deviation) of 5% or better over 8 hours is common for clean samples. Spectral overlaps, discussed previously, can

be a problem. For analyte elements with masses less than about 40 u, chemical matrix effects are noticeable for concentrations of concomitant species as low as 50 ppm. The signal suppression can be severe (more than an order of magnitude) if the sample contains high (1000 ppm) concentrations of heavy elements.

Detection Limits

When using a pneumatic nebulizer, an unheated spray chamber, and a quadrupole mass spectrometer, ICP-MS detection limits are 1 part per trillion or less for 40 to 60 elements (Table 3.4) in "clean" solutions. Detection limits in the parts per quadrillion range can be obtained for many elements with higher-efficiency sample introduction systems and/or a magnetic sector mass spectrometer used in low-resolution mode. Blank levels, spectral overlaps, and control of sample contamination during preparation, storage, and analysis often prohibit attainment of the ultimate detection limits.

Attainable detection limits depend on the amount of analyte that enters the ICP per second, the efficiency of aerosol conversion into analyte ions in the ICP, and the transmission efficiency of ions from the plasma to the MS detector. The detection limits also depend on the variation of the background and the integration time. Typical pneumatic nebulizer/spray chamber systems operated at sample uptake rates from 0.1 to 2.0 mL/min introduce an amount of analyte equivalent to that in 10 to 30 μL/min of sample solution into the ICP. At a sample uptake rate of 1 mL/min, only 1% to 2% of the analyte enters the plasma; most of the sample is lost in the spray chamber and exits through the drain. Concentration based detection limits can be improved by approximately a factor of 10 by using a high-

Table 4 Typical Detection Limits Using a Quadrupole Inductively Coupled Plasma Mass Spectrometer (ICP-MS)[a]

Less than 1 ppt					Less than 5 ppt		Less than 50 ppt
Ag	Eu	Mg	Re	Th	Be	Mn	Ca
Al	Gd	Mo	Rh	Tl	Cd	Ni	K
Au	Hf	Nb	Sb	Tm	Co	Rb	Se
Ba	Ho	Nd	Sm	U	Cu	Sn	
Bi	In	Pb	Sr	Y	Ga	Te	
Ce	Ir	Pr	Ta	Yb	Ge	V	
Cs	La	Pt	Tb	W	Hg	Zn	
Dy	Lu	Os	Tc	Zr	Li		
Er							

[a]Parts per trillion (ppt), picograms per milliliter (pg/mL).

efficiency sample introduction system such as an ultrasonic nebulizer with a desolvation system [164,165]. The ICP is an efficient ionization source. Elements with ionization potentials less than about 8 eV are over 90% ionized in the ICP under normal operating conditions. Elements with higher ionization energies, such as As and Se, are typically 20% to 50% ionized in the ICP. Elements such as C, Cl, Br, F, S exist mainly as atoms rather than ions in the ICP so their ICP-MS sensitivities are much lower than those of more efficiently ionized elements. For quadrupole ICP mass spectrometers typically only 1 in about 10^5 ions produced in the ICP reaches the MS detector. For sector-based instruments, used in a low-resolution mode, 1 in 10^3 ions produced in the ICP may reach the MS detector.

The transport of ions from the ICP to the MS detector depends on travel through three different regions: from the ICP through the sampler and skimmer, from the skimmer to the mass spectrometer, and through the mass spectrometer itself to the detector. As discussed, to a first approximation, the flow through the sampler and skimmer orifice is dominated by neutral gas flow. The gas flow through the skimmer depends linearly on the area of sampling orifice and the area of the skimmer orifice, and inversely on the square of the distance from the sampler orifice to the skimmer orifice [92]. As long as the skimmer is upstream of the Mach disk, the gas flow through the skimmer should not be dependent on the interface pumping speed because the expanding gas and shock structures prevent background gas from entering.

When sector-based mass spectrometers are used in a low-resolution mode the sensitivity can be higher than attainable with current quadrupole mass spectrometers. Random background count rates are also typically lower for sector-based mass spectrometers. As a result, detection limits are one to two orders of magnitude better than for typical quadrupole ICP-MS instruments.

Particularly for low-mass analytes, sector-based mass spectrometers used in a high-resolution mode can reduce spectral overlaps due to polyatomic ions, thereby improving detection limits compared to those of quadrupole mass spectrometers. However, ion transmission efficiency decreases significantly as the resolution is increased. For example, increasing the resolution provided by the sector mass spectrometer from 300 to 3000 reduces the ion transmission efficiency by about a factor of 14 [127]. Further increasing the resolution to 7500 results in another order of magnitude loss in ion transmission efficiency [127]. The use of reaction cells may provide an alternative or complementary means to reduce background due to polyatomic ions.

Generally, dissolved solid concentrations should be kept below 0.2% for ICP-MS. Higher dissolved solid concentrations can lead to deposition of sample on the sampling and skimmer orifices, partial orifice plugging, or deposition of material on ion lenses that degrade sensitivity and medium-term to long-term precision. Furthermore, relatively small concentrations of a heavy element (100 ppm or greater) in a sample can cause a decrease in analyte sensitivity, particularly

for light analyte ions. As a result, detection limits for light elements in a sample containing high concentrations of heavy elements are degraded significantly.

Nonspectral Chemical Matrix Effects

Changes in sensitivity (signal/concentration) can occur in ICP-MS, depending on the identity and concentration of elements in the sample solution and the solvent. Chemical matrix effects can be due to changes in the analyte transport efficiency from the nebulizer into the plasma or modification of ion generation in the plasma. The severity of this matrix effect depends on the concentration of matrix ions generated in the ICP, not the matrix-to-analyte ratio. Whenever the matrix ion current becomes significant compared to other ion currents, matrix effects are observed [166]. Therefore, sample introduction systems that increase the sample transport rate into the ICP suffer from chemical matrix effects at lower dissolved solid concentrations in the sample.

Matrix Effects Originating in the Sample Introduction System. Solid samples are often dissolved by using acids. Variations in the concentration and type of acids used can result in both transient (over several minutes) [167] and steady-state changes [168,169] in analyte sensitivity due mainly to processes that occur in the spray chamber. Fortunately, the acid-dependent changes in analyte transport efficiency are typically less than 20% unless the variations in acid concentration are large. However, significant changes in sensitivity can occur as small initial amounts of acid are added [170]. Furthermore, the severity of the acid effects can be dependent on the nebulizer gas flow rate. Large variations in dissolved solid concentrations can also cause changes in the analyte transport efficiency.

Matrix Effects Originating in the Plasma. The number of ions generated in the ICP per part per billion in the sample can also vary, depending on the concentration of efficiently ionized elements in the sample. Most elements are efficiently ionized in the ICP, so high concentrations of most elements in the sample cause a decrease in the number of analyte ions produced in the ICP [160,171,172]. The total dissolved solid concentration for solutions to be analyzed by ICP-MS is generally kept below 0.2%. Typically the matrix-dependent change in the number of ions generated in the ICP is less severe than about a 30% decrease. However, the severity of the matrix-dependent change in signal depends critically on several experimental variables including plasma power, nebulizer gas flow rate, and sampling depth. For matrix effects that originate in the plasma itself, there is little if any dependence on the analyte or concomitant element mass [173], in contrast to changes in the transmission efficiency of ions from the plasma to the MS detector.

Matrix-Induced Changes in the Transmission of Ions from the Inductively Coupled Plasma to the Mass Spectrometer Detector. The most severe chemical matrix effects in ICP-MS are due to changes in the transmission efficiency of ions

from the ICP to the MS detector. Decreases in sensitivity up to a factor of 10 have been reported for 0.04 M matrix element [174].

If the concentration of dissolved solids is sufficiently high, sample material is deposited on the sampler and/or skimmer cones. In an extreme case this can cause partial blocking of the orifice(s). Although there has been little investigation reported [175,176], the severity of deposition and blocking appears to be dependent on the sample chemistry. High concentrations of Al seem to cause more severe deposition and blocking than those of most other elements. Calcium deposition and blocking also tend to cause more problems than those of many other elements, although less severe than Al problems. Deposition of sample on ion lenses can affect the fields produced by the lenses. This can result in a change in ion focusing and therefore ion transmission. Changes in sensitivity due to deposition or partial blocking occur slowly and normally irreversibly. The orifices and/or ion optics typically need to be cleaned in order to eliminate the loss of sensitivity.

Models [105,177] and experimental measurements [178–180] suggest that the most severe chemical matrix effects are due to space charge induced decreases in the ion transmission efficiency from the plasma to the detector of the mass spectrometer. Unlike the deposition effects, these depend only on the composition of the sample being introduced into the plasma, not on previously run samples.

Sample matrix–induced changes in analyte transmission efficiency are most severe for light analyte ions when high concentrations of heavy ions are present in the sample (Fig. 3.21) [74]. For example, 0.0042 M U^+ caused more than an 80% decrease in the $^7Li^+$ signal, about a 50% decease in the $^{138}Ba^+$ signal, and only a 30% decrease in the $^{232}Th^+$ signal. Matrix elements with ionization energies greater than 8 eV (see B, Zn, Cd, and Au effects in Fig. 3.21) have a less severe effect on analyte sensitivity than elements with lower ionization energies. These elements are less extensively ionized so their influence on the beam current is smaller than that of elements that are nearly 100% ionized.

Significant changes in sensitivity can occur, even for matrix element concentrations of 100 ppm [174], as can be seen in Fig. 3.22. The severity of the matrix effect depends on the concentration of the matrix element(s), not on the ratio of matrix to analyte element concentrations.

Reducing Chemical Matrix Effects. The easiest way to reduce sample matrix-induced changes in ICP-MS sensitivity is to dilute the sample, if detection limits are sufficient. Alternatively, the severity of matrix effects can be reduced by decreasing the nebulizer gas flow rate below that which produces the highest sensitivity. Similar improvements could be made by increasing the sampling depth beyond the depth of highest sensitivity or by increasing the applied power while maintaining the sampling depth and nebulizer gas flow rate. Decreasing the nebulizer gas flow rate reduces the total amount of sample entering the plasma per

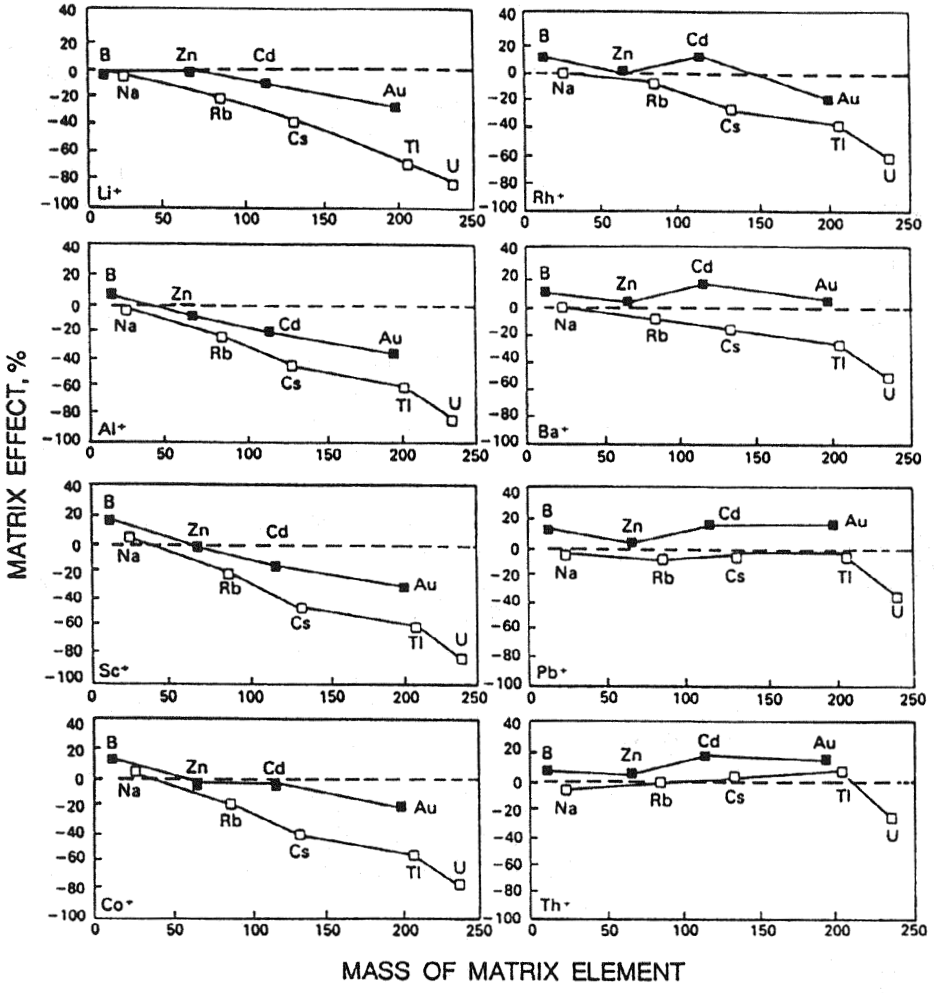

Figure 21 Effect of 0.0042 M Matrix ions with a range of masses on ICP-MS signals for analyte ions ($^{7}Li^{+}$, $^{27}Al^{+}$, $^{45}Sc^{+}$, $^{59}Co^{+}$, $^{103}Rh^{+}$, $^{138}Ba^{+}$, $^{208}Pb^{+}$, and $^{232}Th^{+}$). (From Ref. 174.)

second, reduces the number of large droplets that remain incompletely desolvated in the ICP, and allows more time for diffusion of ions radially outward from the center channel of the ICP. As the concentration of matrix ions in the plasma gas sampled by the mass spectrometer is reduced, the extent of space-charge-induced analyte ion transmission loss is decreased.

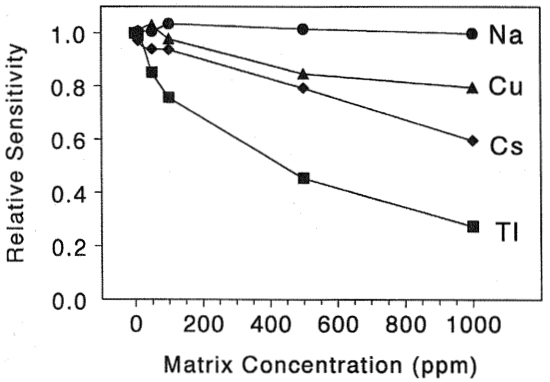

Figure 22 Matrix effects on $^{138}Ba^{+}$ ICP-MS signal as a function of matrix element concentration. Lens voltage was fixed.

Matrix-matched standards or standard additions can be used to prevent analysis errors when chemical matrix effects due to space-charge-induced ion transmission changes are significant. However, these approaches do not prevent analysis errors if there is significant drift due to orifice plugging or lens coating. Flow injection approaches may be useful to reduce the rate of orifice plugging or lens coating as a function of time. If dilution is impractical because of sensitivity loss, it may be necessary to separate the analytes of interest from the sample matrix.

Some researchers have reported instrumental modifications to reduce chemical matrix effects, including a three-aperture interface [103,181] and removal of the ion optics [182]. These modifications appear to reduce the total ion current, and therefore, space-charge effects, before ions enter the quadrupole mass spectrometer. Modification of ion optic lens voltages and configurations may also reduce space-charge-induced chemical matrix effects [183–186].

There have also been reports of reduced matrix-induced suppression of analyte sensitivity when nitrogen is added to the plasma [187,188]. However, only high matrix concentrations of K and Na, both relatively light elements, were investigated.

Compensating for Chemical Matrix Effects Using Internal Standards or Isotope Dilution. If the analyte and internal standard signals are affected similarly by the sample matrix, internal standardization can effectively compensate for changes in sensitivity. For analytes that are efficiently ionized in the ICP the matrix-induced change in sensitivity depends on analyte mass [174]. Therefore, the internal standard must have a similar mass to the analyte ion [189,190].

Because the severity of the matrix effect varies smoothly with analyte mass, it is possible to use a limited number of internal standards (three, for example) across the mass range and then to interpolate to correct analyte sensitivities of analyte ions with masses between those of the internal standards [191].

The ideal internal standard is the same element as the analyte because it has similar mass, ionization energy, and chemical properties. Therefore, isotope dilution based calibration provides high accuracy as long as isotope equilibration is attained and the measured isotopes are free of spectral overlaps [192,193]. Standards do not need to be matrix-matched. Quadrupole-based ICP-MS instruments can typically provide isotope ratio precision of 0.1% to 0.5%. Much better isotope ratio precision can be obtained by using simultaneous MS detection, such as a multicollector-based instrument or perhaps time-of-flight MS. In comparison to thermal ionization mass spectrometry, ICP-MS provides much higher sample throughput and simpler, faster sample preparation.

Because interference-free isotopes are most effective for isotope dilution analysis, potential sources of interference may need to be removed before analysis. Separation procedures based on anion exchange [194–197], cation exchange [198], solvent extraction [199], and anodic stripping [200] prior to isotope dilution analysis have been described.

Propagation of errors using isotope dilution ICP-MS has been considered to determine how to optimize the measurements [201]. Comparison of analysis results from external calibration versus isotope dilution can be used to assess the quality of external calibration results and the effectiveness of internal standards with external calibration [202,203]. Because isotope ratio precision depends on the total ion count rate, the use of high-efficiency sample introduction to generate larger signals can improve isotope ratio precision and, therefore, analysis precision [204].

3.2.4 Semiquantitative Analysis

ICP-MS can provide semiquantitative analysis for about 70 elements by using element response functions built into the instrument software and calibration of only a few elements [205,206]. Most elements are more than 90% ionized in the ICP (with the exception of elements with ionization potentials greater than about 8 eV). Ion transmission efficiency is a smooth function of mass. The natural isotopic abundances of the elements are well known. Therefore, it is possible to predict the relative sensitivities of the elements and any isobaric overlaps.

Semiquantitative analysis is carried out by comparing or fitting spectra for elemental ions (based on their natural abundances or response factors determined previously) and molecular ions to the experimental mass spectrum acquired over a wide mass range. Day to day changes in sensitivity and mass bias are corrected by measuring signals for a few elements in a standard solution. The keys to

successful semiquantitative analysis include properly choosing the elements to use in the model or fitting process, choosing the molecular ions to include, and accounting for changes in mass bias, day to day instrument sensitivity, and sample matrix–induced changes in analyte sensitivity. Properly identifying and modeling the molecular ion signals are probably the most challenging problems. Accuracy obtained is sample matrix–dependent and is typically good to within a factor of 2 to 5 for most elements. Higher accuracy (sometimes within ±30%) can be obtained for many elements that are in "clean" solutions or when a few (typically three) internal standards are used across the mass range. However, care is necessary to assess accuracy for different sample types.

Different approaches have been used to assign the signals in the measured mass spectrum to particular elements and polyatomic ions. The TotalQuant approach by PE-Sciex uses a combination of equations and heuristics ("rules of thumb") [207]. For example, constraints are included on the relative detected oxide ion (such as LaO^+) to elemental ion (such as La^+) signals. The LaO^+ signal is assumed to be no more than 2% of the La^+ signal. Instrument response values for each isotope of each elemental ion are stored in the computer, as are spectra of potential interferents. The steps for the semiquantitative determination are shown in Table 3.5. The approach takes advantage of the isotopic pattern of masses for elemental, polyatomic, and doubly charged ions. Monoisotopic element

Table 5 Steps in Semiquantitative Analysis by PE-Sciex TotalQuant

1. Measure spectrum for a blank.
2. Measure spectrum for a standard containing a few elements. This is used to update elemental response values to account for day to day changes in sensitivity and mass bias.
3. Measure the full mass spectrum for the sample.
4. Make a preliminary estimate of the intensity for each element, based on isotopic natural abundances.
5. Initial estimates of signals polyatomic ions are made and are constrained to be less than a given percentage of a constituent element.
6. Assignments of intensity are made for elements with multiple isotopes in a prioritized order that depends on the relative signal intensities observed. The assignments are evaluated and adjusted if necessary for elements with overlapping isotopes.
7. The data are evaluated for apparent inexact isotopic abundances caused by nonideal measurement precision.
8. Assignments are made for polyatomic and doubly charged ions associated with the multi-isotope elements. These assignments are constrained to given percentages of the elemental ion signals.
9. Assignments are made for monoisotopic elements and associated polyatomic and doubly charged ions.

Source: Ref. 207.

concentrations are assigned last because they do not have a unique isotopic pattern to aid in their identification. This approach was used to reduce the computation time that would be necessary to solve a complete set of simultaneous equations and to deal with species in the spectrum that might not be anticipated in the model.

Recently, a full multicomponent analysis approach for automated semiquantitative survey analysis by ICP-MS has been described [153,208,209]. The computing power of personal computers (PCs) has increased sufficiently that modeling a matrix of 250 masses by 105 species can be done quickly (about 10 sec on a 100-MHz Pentium PC). A database of the isotopic patterns of all elemental ions and interferent ions is used. The database can be expanded beyond the current 400 interferent ions. Elemental and polyatomic ions with signals below the estimated standard deviations in the total measured intensities are excluded from the model. To assess which elemental and polyatomic ions are in the experimental spectrum a relative standard deviation (RSD) function that has been modeled in terms of source and shot noise is used [208]. Diagnostics for goodness of fit of the model include graphical comparison of mass spectra with elemental ion or interferent ion spectra and precision for each element or interferent ion. The measured intensity at each isotope for a given elemental or polyatomic ion is divided by the corresponding natural abundance to calculate a set of *element intensities*. The RSD of the element intensities is a measure of the quality of the model fit. The precision information can also be used to determine true detection limits in the sample.

There are three potential limitations of the MCA approach. If the signals at some masses (such as $m/z = 56$) are over range because of large signals (ArO^+, Fe^+, and/or CaO^+), it is more difficult to assign their element intensities at other masses. Monoisotopic elements have more uncertainty because there is no isotopic pattern to assess the model fit. If there are more species than masses over a region of the spectrum, there is not a unique solution. For example, Cr^+ may require correction for Ti^+, V^+, Fe^+, and ArO^+.

Semiquantitative analysis procedures have also been used with laser ablation ICP-MS [71,210–213]. The effect of experimental parameters and potential improvements in accuracy of semiquantitiative analysis using ICP-MS have also been discussed recently [208,214–216], along with the use of semiquantitative analysis with a double-focusing ICP-MS in both low- and high-resolution modes [217].

3.3 APPLICATIONS OF INDUCTIVELY COUPLED PLASMA MASS SPECTROMETRY

ICP-MS is used for elemental analysis of every type of sample imaginable, including gases, liquids, and solids. Element concentrations in natural, process, and waste waters; biological tissues, hair, and fluids; metalloproteins; and drugs

can be determined by using ICP-MS. Plants, animal feeds, fertilizers, food, rocks, ores, alloys, semiconductors, superconductors, high-purity acids, high-purity bases, reagents, plastics, and polymers have also been analyzed by ICP-MS. For each of these sample types one or more of the attributes of ICP-MS (rapid, multielement analysis; part-per-trillion to part-per-billion detection limits; large dynamic range; high selectivity and specificity; isotope measurement; and small required sample size) make it the method of choice. More than 2000 articles describing applications of ICP-MS have been published. A small sample of these applications is described later.

For many of samples, sample preparation is the most time-consuming step, the step in which error is most readily introduced, and the process that is most difficult to assess. Procedures for sample dissolution, filtering, extraction, etc., must be considered and chosen specifically for ICP-MS [218,219]. Spectral overlaps due to molecular ions can be directly dependent on sample preparation procedures. Contamination from reagents, glassware (or plastic ware), vessels, sampling, handling, and sample exposure to the surrounding environment must be very carefully controlled and assessed in order to make quantitative measurements at concentrations as low as those measurable by ICP-MS. The use of closed vessel microwave digestion has grown increasingly more popular for ICP-MS sample preparation because it often allows use of nitric acid for digestion, avoiding the spectral overlaps caused by sulfuric, hydrochloric, and perchloric acids, and minimizes sample contamination [219–226].

There are still a good deal of art and experience as well as science required for development of successful ICP-MS methods. A huge database of specific sample preparation and ICP-MS analysis procedures is available in the literature and should be consulted before beginning the analysis of samples. Many of the instrument manufacturers maintain databases of downloadable methods and technical reports on their web sites. Despite the low detection limits and high selectivity of ICP-MS, preconcentration or separation of sample components before analysis may be required. Numerous articles describing new analysis approaches using ICP-MS continue to be published.

3.3.1 Biological Applications

The role of metals and other elements in the health of humans, animals, and plants continues to be of great interest both on a routine basis and in research. Two recent reviews described the important impact of ICP-MS in biomedical research [227, 228]. ICP-MS provides the ability to measure multiple elements at ultratrace levels rapidly and to measure isotope ratios at low enough concentrations so that stable isotope tracers can be used for biomedical research [229]. Much remains unknown about the role of metals and their speciation on biological activity, in large part as a result of inadequate measurement techniques.

Elemental Analysis of Biological Fluids

ICP-MS has been used to measure a variety of elements in urine, serum, and blood [230]. The main problems are sample-dependent changes in sensitivity and spectral overlaps due to polyatomic ions. Elements with masses below about 85 are particularly prone to spectral overlaps.

Nuttall et al. [231] reported the use of ICP-MS for routine determination of As, Bi, Cd, Pb, Sb, Te, and Tl in a clinical laboratory. Blood was deproteinized, centrifuged, and passed through a 2-μm filter before analysis. Other specimens were diluted or digested with dilute mineral acids. Se, Zn, and As suffered from interferences that could be overcome by proper isotope selection or mathematical correction. The authors [231] concluded that Cr and Fe were too prone to interferences (due to spectral overlaps) to be practically measured by ICP-MS in clinical samples.

Nixon and Moyer [232] described the use of ICP-MS for routine screening measurement of Pb, As, Cd, and Tl in urine and blood. As, Cd, and Tl are cleared rapidly from the blood, so that if significant concentrations are found in the blood, acute exposure is indicated and immediate action is necessary. Pb is more slowly cleared from the blood. Significant concentrations found in urine indicate chronic exposure or a delay in treatment since exposure. Compared to graphite furnace atomic absorption analysis, ICP-MS provides better sensitivities and more rapid sample throughput. However, two problems must be overcome for the ICP-MS analysis to be successful: The spectral overlap of $^{40}Ar^{35}Cl^+$ at mass 75, the mass of the only As isotope, must be corrected. Sample-induced changes in sensitivity, due to the high concentration of dissolved solids in urine and blood, must be corrected. An empirically determined relationship between $^{16}O^{35}Cl^+$ and $^{40}Ar^{35}Cl^+$ was used to subtract the contribution of $^{40}Ar^{35}Cl^+$ at mass 75. Several internal standard elements were tested to compensate for the changes in sensitivity. Ga was the best internal standard for As, Rh was best for Cd, and Bi was best for Tl and Pb. Table 3.6 shows the certified and measured concentrations using the different internal standards.

The analysis of Cr and V in biological fluids is difficult because of $^{40}Ar^{12}C^+$ overlapping with $^{52}Cr^+$, the most abundant isotope of Cr, and $^{35}Cl^{16}O^+$ overlapping with the $^{51}V^+$, the predominant isotope of vanadium. Recently, a procedure using high-pressure thermal and moderate-pressure microwave digestion with vapor-phase acid digestion was reported to reduce the carbon- and chloride containing molecular overlaps [233]. The vapor phase acid digestion with microsample quartz vessels reduced the blank signals. However, blank levels still limited the method to Cr concentrations greater than 2.8 ng/g in biofluids. Moens et al. [234] measured Fe, Cu, V, and Zn using high-resolution ICP-MS to prevent many of the common molecular ion spectral overlaps. Drying and ashing of the sample before dissolution and analysis can also help to reduce spectral overlaps [235].

Table 6 Comparisons of Certified and Measured Concentrations in National Institute of Standards and Technology (NIST-SRM) 2670 Urine Using Different Internal Standards

Element/internal standard	Concentration (ppb/ng/mL)
As (target value)	480 ± 21
As/none	626
As/Ga	491
As/Y	491
Cd (target value)	88 ± 3.4
Cd/Rh	80
Cd/Ag	85
Cd/In	78
Cd/Sb	67
Pb (target value)	109 ± 3.7
Pb/Re	86
Pb/Bi	110

Source: Ref. 232.

There are many examples of relatively straightforward use of ICP-MS for the analysis of biological fluids. Antimony has been measured in blood after a 14:1 dilution [236]. Cesium serum levels were found to be elevated in patients with alcohol dementia but not in Alzheimer's disease patients [237]. Cobalt levels in rat serum depended on the form of cobalt [238] ingested. Bismuth levels were measured in human blood and urine by using a direct injection nebulizer [239]. Lead was measured in the blood and blood plasma of smelter workers and the general population [240]. The measurement of trace elements in serum by ICP-MS has been compared to results from neutron activation analysis and proton-induced x-ray emission [241]. Semiquantitative analysis can also be used to obtain a rapid screening of samples [242].

In some cases ICP-MS now allows measurement of elements that previously were difficult or impossible to measure at low enough levels to set reliable reference ranges for humans. Reference ranges for Li, B, Mo, Sn, Sb, Cs, Ba, Hg, Pb, and Bi were reported [243]. Measurement of uranium levels in an unexposed population has also been reported [244].

Biological Tissue

ICP-MS analysis of human tissue [245] has been described in several reports. Microwave digestion was commonly used for sample preparation. Analysis of tissues can provide information on essential elements as well as toxic elements.

Pb isotope ratios depend on the source of lead. Therefore, ICP-MS isotopic

analysis can be used to identify sources of lead. In one study [246], people with low lead concentrations in the United Kingdom had $^{206}Pb/^{207}Pb$ isotope ratios of 1.13 ± 0.01. Lead uptake from drinking water (source isotope ratio 1.18) in parts of Scotland was found to contribute 60% to body lead. Lead from gasoline in inner London (source isotope ratio approximately 1.07) contributed 30% to 40% of lead in inner London children.

The accuracy of autopsy tissue elemental analysis has been assessed [247]. Results indicated that differences in elemental concentrations depend on age. Tissue of patients in chronic renal failure and treated by hemodialysis can accumulate higher concentrations of Cr and Al. Black particles observed in a spleen fragment from a patient who had previously had a hip replacement were found by ICP-MS to contain high titanium concentrations [248].

Trace metals have been measured in various tissues by ICP-MS to investigate Alzheimer's disease [249–252]. Various sample preparation and processing approaches have been used, including flow injection analysis and extraction. Al, Si, and Sn levels were reported to be higher than in healthy tissue, whereas zinc and selenium concentrations were lower. In the temporal cortex there were also reductions of cesium and cerium concentrations. The mechanisms responsible and the key elements remain incompletely understood.

Laser ablation ICP-MS can be used to obtain spatial maps of elemental composition in tissues. In one study [253], LA-ICP-MS was used for "elemental tagging" of fish scales, rat kidney cross sections, and examination of the blood/bone interface in a pig femur. Ca and Mg were used as "natural" internal standards.

A variety of elements have been measured in fish tissue to determine the cause of fish kills and to assess water quality. Slurry samples were introduced into the ICP by using electrothermal vaporization in one report [254] with isotope dilution based determination of Cu, Zn, Cd, and Pb. Sample preparation was simplified by using slurries rather than complete dissolution. Electrothermal vaporization can be used to reduce spectral overlaps due to molecular ions that contain oxygen. The sample can be dried in the furnace before vaporization of the analytes. The time-dependent vaporization can also be used to reduce some matrix effects. Isotope dilution improves precision and accuracy of the analysis. The uptake and organ-dependent accumulation of cadmium in carp have also been investigated by ICP-MS analysis [255].

Platinum-based compounds are commonly used as cancer treatment agents. Pharmacokinetic studies of these antitumor drugs require ultratrace analysis. Electrothermal vaporization ICP-MS provides low detection limits for small samples [256]. High-performance liquid chromatography with ICP-MS detection allows speciation of platinum compounds in tissues [256]. LA-ICP-MS can be used to study the distribution of platinum in tissues and tumors [256]. Natural levels of Pt are below typical quadrupole ICP-MS detection limits [257].

Selenium has also been investigated extensively with ICP-MS. It can be efficiently introduced into the plasma by hydride generation in order to improve detection limits. The analyte is efficiently transported into the plasma as a gas and the sample matrix is left behind. The hydride generator design can influence interferences and sensitivity [258]. Sample cross-contamination was eliminated when the air bubble normally entrained between samples was removed [258]. Isotope dilution can be used to obtain high accuracy.

Isotope Tracers

Stable isotope tracers can be conveniently measured by using ICP-MS [259,260]. The low ICP-MS detection limits allow small amounts of stable isotope tracers to be given to subjects, including infants [261].

The first complete study of nickel metabolism in humans involved ingestion of 10 μg of ^{62}Ni/kg body weight [262]. Isotope dilution (with $^{61}Ni^+$) was used to measure $^{62}Ni^+$ tracer concentrations in blood, urine, and feces. Potential complications due to contamination and dietary intake of nickel were eliminated by using the isotope tracer approach.

ICP-MS allows multiple element isotopic tracers to be monitored simultaneously. For example, zinc metabolism in heathly women was investigated by oral ingestion of a ^{67}Zn trace and an intravenous (i.v.) tracer highly enriched in ^{70}Zn. Ratios of ^{67}Zn to ^{66}Zn and ^{70}Zn to ^{66}Zn in plasma, urine, and feces were determined to trace the Zn from the oral and i.v. sources independently.

Plant Analysis

Uptake of elements by plants is important in understanding essential nutrients for plants, potential health concerns for humans and animals that eat the plants, and use of plants as a remediation agent to remove toxic elements from soils. The uptake of heavy metals by wheat from fertilizers and sewage sludge applied to agricultural lands was investigated by using ICP-MS [263].

Wet and dry ashing sample preparation procedures for plant materials and subsequent analysis by ICP-MS have been assessed [264]. Closed vessel microwave digestion nitric acid and added hydrogen peroxide can often be employed for dissolution of plant materials [265]. H_2O_2 helps to allow a higher temperature to be maintained without excessive pressure buildup as well as to reduce the carbon content in the sample. However, impurities in the hydrogen peroxide can degrade detection limits for some elements [265]. Ultrasonic slurry sampling ETV-ICP-MS was used to measure Ge, As, Se, Cd, and Pb in plant tissues [266].

Plants such as mung bean seedlings can be used as bioindicators for toxic elements such as As [267]. Analysis of tree rings can provide information on short-term variations in pollution sources [268]. Elemental "fingerprints" have also been used to identify sources of plants, including cannabis [269].

Foods

The use of ICP-MS for the analysis of foods has been reviewed recently [270]. Food analysis can provide information on potentially toxic elements, nutrient elements, or geographical origin of the food. The application of ICP-MS to experimental nutrition has recently been reviewed [271]. The importance of quality control for multielement analysis of complex sample matrices like foods by ICP-MS was shown [272].

Tin levels in fruits, vegetables, and juices were found to be higher when unlaquered cans were used [273]. Ethanol affects ICP-MS sensitivity for many elements. Sample preparation can affect the extent of the change in sensitivity. Internal standardization can be used to improve Pb concentration measurement accuracy in wine [274]. Isotope dilution analysis can be used for accurate concentration measurements in wine [275].

The iodine content of a variety of foods in East Africa was measured by ICP-MS [276]. Samples were dried and homogenized prior to dissolution. Tellurium was used as an internal standard. Only saltwater fish were found to be a sufficient dietary source of iodine.

Plants have trace element concentrations that are characteristic of the soil they are grown in. For example, the pattern of rare earth element concentrations in wines produced from vineyards in different geographical regions was unique, and grapes grown in the same area even in different years had similar patterns [277]. In another study trace element concentration patterns could be used to differentiate among Spanish wines from three different regions and between Spanish and English wines [278]. Changes in soil acidity and oxidation were found also to affect the uptake of particular elements and therefore the concentration of elements in wine [279]. The geographic origin of orange juices has also been identified by ICP-MS. Variance analysis using the measurements of up to 64 elements was used to identify elements that could best be used as geographic indicators [280].

3.3.2 Geological Applications

Geologists have been involved in the development of ICP-MS since its beginning [281]. The key capabilities of ICP-MS for geological samples include low detection limits and isotopic measurement [282–285]. The most prevalent use of laser ablation ICP-MS is probably in the analysis of geological materials [286,287]. Geological applications have also driven the development of laser sampling from small (<10 μm) spots with sufficiently high sensitivity. Sector, multicollector ICP-MS instruments are used mainly for isotope ratio measurements of geological samples [58]. More than 400 articles have been published on the use of ICP-MS

for the analysis of geological samples. A few selected areas of geology in which ICP-MS has been used are described here.

Lanthanide and Actinide Elements

Insight into melting and fractionation during the formation of rocks can be gained by measuring the relative concentrations of rare earth elements. Therefore, ICP-MS has been used since its introduction for the measurement of rare earth elements in geological materials [282]. Recently, basalt from Mauna Kea was investigated by ICP-MS using this approach [288].

A wide variety of sample types, sample preparations, and processes have been used. Powdered rock samples were fused with K_2BO_7 or K_2CO_3, followed by precipitation of the potassium using perchloric acid, separation with methanol-perchloric acid, evaporation to a residue, and dissolution of the residue in dilute nitric acid. Detection limits in the solid were in the microgram per gram (μg/g) to nanogram per gram (ng/g) levels in the solid without preconcentration.

Rare earth elements have been measured in fluid inclusions using flow injection [289]. Rare earth oxides cause spectral overlaps, so ion chromatography or other separation techniques are often used. High-resolution mass spectrometers have also been used. By reducing the amount of water entering the ICP using a desolvation and membrane, molecular oxide ion signals can be reduced by a factor of 100 [290]. Enhanced isotopes for a light rare earth element and a heavy rare earth element were used for mass bias correction, internal standardization, and isotope dilution so that all of the rare earth elements could be determined in one measurement [290].

Naturally occurring zircon crystals are very stable and include structures from a succession of geological events. Therefore, rare earth measurements in zircons have also been of great interest [291]. Zircons are often difficult to put into solution completely so laser ablation is often used. Laser ablation is also particularly advantageous in probing small zircons embedded in other materials and in measuring different structures within a zircon crystal.

Precious Metals and Exploration

Trace element measurements by ICP-MS have been used for geological exploration [292]. The use of ICP-MS for measurement of precious metals in rocks has been recently reviewed [293]. Typically sample preparation includes extraction and concentration of precious metals and separations from potentially interfering elements [293]. For example, HfO^+ of masses 194, 195, and 196 overlaps with Pt^+ isotopes. Limits on dissolved solid concentrations to about 0.2% also limit the detection of small quantities of precious metals in the solid.

Sample preparation is especially key to the measurement of precious metals.

Fire assay techniques with large (15–30 g) samples of crushed, ground rocks; soils; and sediments are often used to concentrate precious metals such as Au, Pt, and Pd while providing a more homogeneous sample. Appropriate assays using Pb or NiS, for example, and their subsequent dissolution depend on the elements of interest [293]. Reagent blank levels often limit detectable levels of platinum group elements and gold. Chlorination methods have been used [294] in large part because of the very low reagent blank levels attained. Acid dissolution and extraction procedures have also been described, although acid extractions often do not yield quantitative extraction of the precious metals. Because acid extractions are often more rapid and inexpensive, they are sometimes used to screen large numbers of samples. Sodium peroxide fusions have also been used to form salts that are water-soluble. Purification and preconcentration using precipitation, ion exchange separation, and solvent extraction are then often used [294]. By using a lead fire assay followed by cupellation and AgCl separation, detection limits for Pt, Pd, and Au of 0.1 ng/g in soil and sediment have been attained [295].

Isotope Ratio and Isotope Dilution Measurements

Isotope ratio precision provided by quadrupole ICP-MS instruments is much poorer (typically 0.2% to 0.8% RSD) than can be obtained by thermal ionization mass spectrometry (TIMS). Plasma fluctuations and short-term variations in the aerosol introduced into the plasma are the main sources of noise in ICP-MS. Multicollector sector-based ICP-MS instruments can provide isotope ratio precision of 0.003% to 0.05% RSD, in some cases rivaling that of TIMS [58]. Sector-based instruments can also provide very high sensitivity compared to that of TIMS, particularly for elements with higher ionization energies or those that form refractory compounds. In these cases isotope ratio precision can be superior to TIMS precision. Sample preparation for TIMS is generally much more time-consuming and restrictive than for ICP-MS. Measurement times for ICP-MS are generally shorter because of higher ion signals so that counting statistics are better on a relative basis. Elements that form refractory compounds or have high ionization energies are not amenable to TIMS. Multicollector sector-based ICP-MS instruments can provide isotope ratio precision that rivals that of TIMS [58]. However, there are several applications in which the isotope ratio precision provided by quadrupole or single-collector sector instruments is sufficient.

Os isotope ratios vary as a function of age as a result of radioactive decay of ^{187}Re to ^{187}Os. Os is much more extensively ionized in the ICP than by TIMS. Precision provided by quadrupole ICP-MS (0.3% relative standard deviation) is sufficient to gain useful dating by Os isotope ratio measurement [296,297]. Pb isotope ratios vary, depending on the geological history of the sample, because of decay of ^{238}U, ^{235}U, and ^{232}Th to ^{206}Pb and ^{207}Pb.

Often high accuracy is required for geological interpretation of trace ele-

ment patterns. Therefore, isotope dilution–based concentration measurements have often been used [298–302].

3.3.3 Environmental Applications

The low detection limits and rapid, multielement analysis provided by ICP-MS make it particularly attractive for environmental applications, in which high sample throughput is often essential. For several elements, including Pb, the maximum acceptable levels have decreased as the ability to measure lower and lower concentrations has improved. ICP-MS measurements are used to assess environmental quality, including meeting legislated requirements; to investigate the natural sources and transport of elements; and to identify sources of pollutants.

Nonsaline Water Analysis

River, stream, and lake water; groundwater; as well as atmospheric precipitation are commonly analyzed by using ICP-MS [303]. Often the samples can be run directly or after simple filtration or centrifugation to remove suspended particulates [304]. Typically samples can be preserved by the addition of 1% to 2% concentrated nitric acid by volume [305]. Nitric acid is preferable to hydrochloric or sulfuric acid because of the lack of molecular ion spectral overlaps from nitric acid or its reaction products in the ICP, as discussed earlier. In most cases preconcentration or separation is unnecessary. In some cases preconcentration and removal of chlorides from the sample are advantageous and can be done by using a simple flow injection approach [306].

ICP-MS is widely used to assess drinking water quality. Environmental Protection Agency (EPA) methods 200.8 and 1638 for the analysis of drinking and waste waters use ICP-MS [307–309]. Sources of Pb in drinking water can be assessed from Pb isotope ratios. In one study, $^{206}Pb/^{207}Pb$, $^{206}Pb/^{208}Pb$, $^{207}Pb/^{208}Pb$ isotope ratios in tap water were compared to those of plumbing materials [310]. The authors were able to conclude that the copper pipe and solder were the main sources of Pb.

In some cases, ultrasonic nebulization or preconcentration is used to enhance detection limits. As, Se, and Sb were measured in cloud water; detection limits were 20, 100, and 20 pg/mL, respectively, using pneumatic nebulization and four to five times lower using ultrasonic nebulization [311]. In another study [312], activated charcoal from a 1-L sample volume was used to preconcentrate Pd and Pt in fresh waters. Detection limits were 0.3–0.8 ng/L. An automated online preconcentration system based on a cationic resin (AG50W-X8) was used to measure Cd, Pb, Ni, Cu, and Zn. A preconcentration factor of 30 was obtained even with a sample throughput of 20 samples per hour [313].

Seawater

Analysis of seawater by ICP-MS is complicated by low concentrations of many elements of interest, sensitivity reductions due to the high salt concentrations, and Cl containing molecular ion spectral overlaps [314]. Standard reference seawaters are available from the National Research Council (Canada).

Several different approaches to preconcentration and matrix elimination have been reported. A commercially available chelation system based on silica-immobilized 8-hydroxyquinoline has been used for on-line preconcentration and matrix separation [315,316]. Detection limits using a 90-fold concentration were 0.04 ng/dm^3 for U to 6.3 ng/dm^3 for Zn.

Off-line dicarbamate solvent extraction and ICP-MS analysis [317] provided part-per-trillion detection limits: Cd (0.2 ppt), Co (0.3 ppt), Cu (3 ppt), Fe (21 ppt), Ni (2 ppt), Pb (0.5 ppt), and Zn (2 ppt). Off-line matrix removal and preconcentration using cellulose-immobilized ethylenediaminetetraacetic acid (EDTA) have also been reported [318]. Transition metals and rare earth elements were preconcentrated and separated from the matrix using on-line ion chromatography with a NTA chelating resin [319]. Isotope-dilution-based concentration measurement has also been used after matrix separation with a Chelex ion-exchange resin [320]. The pH, flow rate, resin volume, elution volume, and time required for isotope equilibration were optimized. A controlled-pore glass immobilized iminodiacetate based automated on-line matrix separation system has also been described [321]. Recoveries for most metals were between 62% and 113%.

Electrothermal vaporization has also been used for seawater sample introduction into an ICP-MS. Trace metals were complexed and then vaporized as dithiocarbamate complexes in one study [322]. Addition of a matrix modifier [$Pd(NO_3)_2$-$Mg(NO_3)_2$] enhanced analyte sensitivity. Addition of a matrix modifier to act as a physical carrier in ETV-ICP-MS has become common. Seawater was used as a matrix modifier for ETV-ICP-MS in one report [323].

Sector-based ICP-MS instruments have recently been used for seawater analysis. These instruments can provide high resolution to minimize spectral overlaps or high sensitivity when used in a low-resolution mode. The sample can be diluted to reduce sample-dependent variations in sensitivity while maintaining sufficient detection limits. Diluted seawater was introduced into the ICP without further sample preparation in one recent report [324]. Nonspectral matrix effects due to seawater for quadrupole and sector-based ICP-MS instruments have been compared [325].

Soils and Sediments

The use of ICP-MS for trace analysis in sediments has recently been reviewed [326]. The advantages and disadvantages of acid digestion versus fusion-based sample dissolution were discussed. The problems involved in ICP-MS analysis of

soils have been considered [327]. Analysis of marine sediments by ICP-MS was assessed by using external calibration, standard addition, and isotope dilution [328,329] with comparison of experimental results for standard reference materials. The influence of sample preparation on spectral overlaps was demonstrated. Spectral overlaps due to molecular oxides can also present problems [327].

Total mercury in soils can be measured by ICP-MS [330]. Mercury was extracted by using a microwave assisted flow injection system. A complexing agent and surfactant were added to eliminate the long memory effects typically observed with mercury.

A mobile ICP-MS has been used for on-site measurements of polluted soils [331]. A rapid digestion procedure was developed in order to reduce sample analysis time for the rapid identification of heavy metal anomalies near a mine dump where no vegetation was growing.

Slurries have been used to introduce soil samples into an ETV with ICP-MS detection [332] as well as directly into an ICP-MS using a Babington-type nebulizer [333]. Although slurry sample introduction eliminates the problems associated with sample dissolution, care is required to ensure that the slurry particles are small enough to be completely vaporized in the ICP. Agglomeration of particles in the slurry before introduction to the nebulizer must be prevented in order to maintain constant transport efficiency into the ICP.

Coal, Fly Ash, and Dust

Combustion of coal produces ash that can be transported through the air. Slagging and fouling problems can also be predicted from elemental analysis. Therefore, elemental analysis of both the coal as well as the ash are important. Procedures for dissolution and analysis of coal and combustion products of coal have been reported [334–336]. Laser ablation sampling has been successfully used for coal and combusted materials [337,338]. The direct introduction of slurries has also been used [339]. Comparison of ICP-MS and PIXE analysis of coal combustion aerosols showed that analysis errors can occur in ICP-MS if particle vaporization is incomplete in the ICP [340].

Flow injection hydride generation has been used to measure As, Hg, and Se in coals with detection limits in the 2- to 5-ng/g range [341]. Comparison of ICP-MS and neutron activation analysis results showed good agreement.

ICP-MS isotope ratio measurements of house dust samples were used to assess potential sources of Pb [342]. Street dust and soil outside the house showed similar Pb isotope ratios, but lead paint in the house had a different isotopic pattern. Sources of lead outside the home were found to contribute as much to lead in most of the house dusts as did lead from lead-based paints inside the house.

Dissolution of dust and other atmospheric aerosol samples by microwave

digestion is faster than hot plate methods. However, Teflon vessels can become contaminated. It is useful to keep a history of the Teflon vessels and to assess method blank levels by processing a blank through the entire dissolution process.

3.3.4 Industrial Materials Analysis

ICP-MS has been used for the analysis of many materials, including alloys, steels, nuclear materials, ceramics, superconductors, plastics, polymers, and catalysts. Semiquantitative analysis by ICP-MS is often a convenient method to screen samples for trace elements and impurities. Measurement of impurities can be complicated by sample matrix–dependent degradation of sensitivity, particularly if the samples contain high concentrations of heavy elements that create extensive space-charge-induced ion transmission losses. Matrix matching is complicated by the need for ultrapure materials.

Metals and Alloys

Even sub-ppm levels of some elements can affect properties and processing of steel and other alloys. The analysis of low- and high-alloy steels for environmentally important elements (Cd, Hg) as well as elements that affect the steel (Sb and Bi, for example) has been discussed [343]. ICP-MS has been used for semiquantitative and quantitative measurement of Gd, Sm, and Th in zirconium alloys [344].

ICP-MS has also been used to measure trace elements in archaeological native silver artifacts [345] in order to identify their geographical origins. The low detection limits provided by ICP-MS allowed analysis of trace elements on 3 to 15 mg of sample. The passivation of alloy steels using acid solutions has been studied by XPS measurements of the solid in combination of ICP-MS analysis of the passivation solutions [346,347]. When bullets are crushed on impact, striations cannot be used for identification. The percentage of antimony, trace element composition, and lead isotope ratios in bullets was measured for forensic evidence [348]. The lead isotope ratios were found to be the most useful evidence.

To analyze metals and alloys directly without dissolution, both spark ablation [349] and laser ablation [61,211] dry aerosol generation systems have been used to introduce samples into an ICP-MS. These approaches often require matrix-matched standards, although several active research groups are focusing on techniques to reduce that requirement. The amount of material ablated depends on the sample type. Fractionation of elements can also be a problem, depending on the sample, the laser fluence, the laser wavelength, and the number of laser pulses used to sample from a fixed location. Volatile elements that are segregated in the samples appear to be most prone to fractionation problems [61].

Materials Used in the Nuclear Industry

Although ICP-MS has been used for analysis of nuclear materials, often the entire instrument must be in an enclosed "hot" enclosure [350]. Sample preparation equipment, inlets to sample introduction systems, vacuum pump exhaust, and instrument ventilation must be properly isolated. Many of the materials used in the nuclear industry must be of very high purity, so the low detection limits provided by ICP-MS are essential. The fission products and actinide elements have been measured by using isotope dilution ICP-MS [351]. Because isotope ratios are not predictable, isobaric and molecular oxide ion spectral overlaps cannot be corrected mathematically, so chemical separation is required.

Plastics

Metal doped polymers or plastics that might come in contact with food or drinks have been analyzed by ICP-MS. Plastics may be contaminated with elements used in the production process including catalysts. Plastic food wraps have been analyzed after microwave acid digestion [352,353]. Results were in good agreement with those of neutron activation analysis. Laser ablation of plastics and polymers [51,352,354] is particularly convenient for semiquantitative analysis to eliminate the need for dissolution or to examine the homogeneity of inorganic elements within the materials [352]. The effect of the polymer composition and laser wavelength on laser ablation sampling efficiency has been investigated [63], again illustrating the potential difficulties in obtaining quantitative analysis without matrix-matched standards.

Catalysts

ICP-MS is useful for analysis of catalysts from two perspectives: The composition of the catalysts must be carefully controlled, particularly because the active elements are often expensive. The catalysts are often finely distributed in a substrate material so their concentration in the bulk material may be quite low. Second, catalysts, particularly those used in automotive catalytic converters, can be a significant source of platinum group elements in the environment. Re and Pt have been measured in catalysts by ICP-MS [193]. Procedures for the analysis of used catalytic converter materials by ICP-MS have been reported [355]. Accurate measurements are essential for many of these applications so isotope dilution–based concentration calibration is commonly used.

3.3.5 Applications in the Semiconductor Industry

High-purity acids, silicon, and other materials are essential for acceptable yields in the production of semiconductor devices. Contamination becomes a more and

more important problem as the size of the structures in the semiconductor devices is reduced. Metal contamination levels in processing solutions as low as 50 parts per quadrillion have been identified as potentially deleterious. The operating properties, dark current, and oxide breakdown voltage are dependent on contaminant and dopant element levels in semiconductors [356]. Particulates collected in traps used to maintain clean conditions must be identified in order to reduce their occurrence. The use of ICP-MS for the analysis of samples related to semiconductor device production has recently been reviewed [357–359].

The needs of the semiconductor industry have been one of the main driving forces to attain detection limits in the low parts-per-quadrillion level. Sector-based ICP-MS instruments are often used in a low-resolution mode to provide the very high sensitivities that are needed. Many of the elements of interest are below mass 80. Therefore, the use of reaction cells in ICP-MS instruments in order to reduce molecular ion signals and other background is likely to have a major impact on the analysis of materials used in the semiconductor industry. The importance of procedures for analysis of these materials with very low detection limits is so key to the commercial success of the semiconductor manufacturers that details of the ICP-MS-based methods may not be published. Those that are published may be modified somewhat from what is done in practice.

High-purity acids are used for cleaning and etching of semiconductor materials. The analysis challenges include attaining sufficiently low detection limits, avoiding contamination (including from the extraction of elements on tubing and sample introduction systems), and dealing with molecular ion spectral overlaps from plasma species, water decomposition products, and the acids themselves. Among examples of ICP-MS analysis of acids used in semiconductor processing are hydrofluoric acid [360,361], sulfuric acid [362], hydrochloric acid [363], and phosphoric acid [364].

Several approaches have been used to reduce spectral overlaps due to molecular ions. The use of "cold plasma" conditions, described earlier, is well suited to the analysis of high-purity acids. Fe, Ca, and K, which suffer from severe spectral overlaps with ArO^+, Ar^+, and $^{38}ArH^+$, under normal plasma conditions, can be measured in the low-ppt level. The argon ion number density in the ICP is greatly reduced by operating at lower temperatures. Analyte ion signals for elements with low ionization energies are not significantly degraded. Sector-based ICP-MS instruments have been used for acid analysis in low-resolution mode to provide high sensitivity and in high-resolution mode to overcome spectral overlaps [365]. ETV-ICP-MS has also been used for high-purity acid analysis [366–368] to avoid ArO^+ and other O- or H-containing molecular ions.

The sample introduction system, sampler, skimmer, and ion optics can be sources of contamination that produces high ICP-MS blank signals so proper cleaning and maintenance are essential [369]. Some have argued that no dilution or evaporation (for preconcentration) of high-purity acid samples should be used

because any sample preparation or handling enhances chances of contamination [368]. However, many of the acids can cause sample introduction problems if run directly. Often, large sample volumes of high-purity acids are evaporated in order to improve detection limits. Great care must be taken to prevent contamination.

The purity of silicon and gallium arsenide starting materials has been measured by using ICP-MS [370–372]. Impurities in materials used as dopants for semiconductors have also been measured by using ICP-MS [373].

Vapor phase dissolution (VPD) is commonly used for surface and contamination analysis of semiconductor wafers [374–379]. HF vapor is used to remove a silicon oxide or native silicon layer. A drop of hydrofluoric acid or deionized water (with a volume of 50 to 200 μL) is placed on the surface and rolled around the surface to dissolve the metals. The small drop is then analyzed by ICP-MS by using either a direct injection nebulizer, a micronebulizer, or ETV. The ability of ICP-MS to measure several elements rapidly in a small volume of solution is essential.

Trace impurities in some gases used for semiconductor processing have also been monitored using ICP-MS [380–382]. It may be necessary to use specialized materials for the sampler and skimmer to prevent degradation. In one study, the level of iron from a hydrogen chloride cylinder was found to increase as the cylinder was used and to depend on the cylinder-valve package [382].

Impurities in photoresists have also been measured by ICP-MS [383,384]. Ultrasonic nebulization and electrothermal vaporization sample introduction approaches have been used.

The current analytical capabilities of ICP-MS provide a means to assess new low levels of contamination in the semiconductor industry [385]. Contamination in clean room air can be detected at very low levels. Dopant and trace metal contamination on semiconductor wafer surfaces can be monitored. Ultratrace metals in deionized water, high-purity acids, and other process chemicals can often be measured at concentrations less than 1 part per trillion.

3.3.6 Speciation Analysis

In many chemical systems, the form of an element controls its biological or chemical effect and its transport or remediation. Elemental ions in different oxidation states, as different metal-ligand complexes and various organometallic molecules, often have very different toxicity. Certain species are essential nutrients [Cr(III), for example], whereas others are toxic or carcinogenic [such as Cr(VI)]. Organometallic mercury compounds, such as methylmercury, are far more toxic than inorganic mercury. Trialkyltin compounds are highly toxic and tin is present in some food cans. The transport of metals through soils and water systems is highly species-dependent. Industrial processes may also be highly dependent on elemental speciation. Therefore, elemental analysis alone often provides insuffi-

cient information. For example, a high concentration of arsenic in blood could be due to a lethal ingestion of inorganic arsenic or of shellfish that contain seemingly unharmful arsenobetaene.

The evolution and trends in elemental speciation have recently been assessed [386–388]. Speciation is essential in many developing areas, including biomedical, food, environmental, industrial processes, and industrial hygiene. Among the elements for which species determination can be necessary are Al, As, Br, Cd, Cr, Cu, Fe, Hg, I, P, Pb, Pt, Se, Sb, Sn, and the actinides [386].

Elemental speciation presents many analysis challenges. Often species are important at very low concentrations. Stable storage is a problem as often the speciation changes over time after the sample is collected. The elemental speciation could be changed by processing of the sample. ICP-MS has become popular as a detector for separation techniques in order to identify and quantify different species, as described in a recent review [389]. Different species are separated and introduced into the ICP-MS as a function of time. Time-resolved ICP-MS signals then provide information on the species containing each detected element (from the time the signal appears) as well as specifically identifying the elements present and quantitatively measuring their concentration. Among the separation techniques that have been used with ICP-MS detection are gas chromatography [390, 391], liquid extractions [392], high-performance liquid chromatography [393, 394], size exclusion chromatography [395,396], and capillary electrophoresis [24,397].

The choice of ICP-MS is mainly due to the low detection limits and high elemental specificity. Because the sample must be physically transported from the separation column or capillary into the plasma, the interface is important. High analyte transport efficiency is desirable to obtain low detection limits, but care must also be taken in designing the interface so that the separation is not degraded. Dead volume and induced laminar flow due to the interface [398] must be considered.

Although there is clear agreement on the importance of elemental speciation, routine applications have not grown as quickly as predicted [386]. The market for commercial instruments for elemental speciation has not risen significantly. There are several reasons for this. The initial groups interested in speciation are researchers who have put together their own instruments. Sample preservation and measurement without changes in speciation can be problems; therefore, court cases based on evidence from elemental speciation measurements have not been successful. Recently, an approach using isotope dilution has been described to assess quantitatively and correct for changes in speciation during sample storage and analysis [399,400]. Standards are lacking, in part because it may be difficult to ensure their stability. Elemental speciation typically requires much more knowledge about the sample chemistry than does total elemental analysis. Separation systems for specific sample and analyte types must often be developed. Therefore, there is not a method that is as "universal" as for total elemental analysis.

For some specific cases such as Cr(VI) versus CR(III) measurement in waters, commercial products, based on short columns that can be used in a flow injection mode with ICP-MS, have become available. Separation times of less than 3 minutes, low cost, and convenience make this approach viable for routine use in some applications.

The importance of elemental speciation in environmental systems, biomedicine, and other areas is becoming more widely realized. Initial regulations for elemental speciation [such as regulations specifying Cr(VI) measurement rather than total Cr measurement—EPA 7196A and 3060A, for example] are being proposed and adopted.

One of the main problems with speciation measurement is that the speciation may change during sampling, sample preparation, or analysis. Furthermore, spikes added to samples for standard addition calibration or spike recovery measurements may not remain as the same species once in the sample. For example, oxidation or reduction can take place, depending on the sample chemistry. Recently, speciated isotope dilution mass spectrometry (SIDMS) using an ICP ion source has been developed to account for these changes in speciation [399]. The SIDMS method was used to show that Cr(III) could be oxidized during alkaline extraction using EPA method 3060A and Cr(VI) could be reduced by using EPA method 7196A, leading to errors [400].

Speciation of As has been of great interest because of the wide range of species-dependent toxicity. HPLC coupled with ICP-MS has been used to measure arsenite and arsenate, monomethylarsonic acid, dimethylarsinic acid, arsenobetaine, and arsenocholine in mussels and fish [401]. A Dionex AS7 column with an on-guard AG7 column was used. A gradient mode separation was carried out by using a bicarbonate buffer mobile phase. Detection limits were in the 0.001- to 0.003-μM range. Cation- and anion-exchange HPLC-ICP-MS were used to measure arsenic speciation in shrimp, crab, fish, fish liver, shellfish, and lobster [402] as well as human urine [403]. Ion exchange HPLC-ICP-MS was used to monitor the bioavailability and speciation of As in carrots grown in As contaminated soil [404]. HPLC-ICP-MS was also used to study arsenic speciation in soils as a function of pH [405]. Capillary electrophoresis-ICP-MS has also been used for As speciation in drinking water [406].

Several potential problems with As speciation have been described [407]. $ArCl^+$ causes a spectral overlap in ICP-MS detection. Speciation can change between the time the sample is obtained and when it is measured. Field separations or preservations can be developed to prevent that problem. Particulates in drinking water can contain a significant portion of the As, so filtering the sample without also analyzing the composition of the particulates can lead to measurements that are too low [407].

Selenium speciation has also been measured by a variety of approaches for several different applications. Size exclusion chromatography was coupled with ICP-MS detection to measure selenium speciation (especially Se-containing pro-

teins) in human serum [408]. Selenite and selenate were measured by gas chromatography–(GC)-ICP-MS after derivatization [409] using isotope dilution calibration. HPLC-ICP-MS was used to measure selenium species in gastrointestinal extracts of cooked cod [410]. Retention times for selenomethionine, selenocystine, sodium selenite, and sodium selenate standards were determined. One of the peaks observed from the gastrointestinal extracts did not match any of the standard compounds but appeared to be consistent with an organic species. This points out one of the limitations of separation techniques coupled to ICP-MS. The retention or migration time is used to identify the species, but this may not be unequivocal (in contrast to the certainty of the identification of a particular element in a sample using ICP-MS). Capillary electrophoresis-ICP-MS was used to measure selenium species in human milk and serum with detection limits in the 10- to 50-μg/L range [411].

Chromium is used in a number of industrial processes and, as noted, has toxicity that is highly dependent on its speciation. The combination of ion chromatography and ICP-MS detection has been used to measure Cr(III) and Cr(VI) in waste water [412]. Ion-pairing HPLC-ICP-MS was used to measure chromium species in seawater [413]. Speciation of chromium dyes was also reported by HPLC-ICP-MS [414].

Transport of metals in the environment is critically dependent on speciation. Often metals are associated with colloidal materials, fulvic acid, or humic acid. Extensive research is ongoing to study the uptake capacity of these materials as well as minerals, the distribution of elements in natural water samples, and species-dependent means of remediation. Speciation of yttrium and lanthanides in natural water has been reported [415] using size exclusion chromatography and ICP-MS. Multistage filtration has also been used with ICP-MS measurement of the separated fractions [416]. Kinetic studies of metal uptake rate as a function of EDTA, NTA, and fulvic acid concentrations in the water have been described [417].

Speciation of tin and lead is important in identifying their source in the environment and pathway into humans and food. Organotin compounds were commonly used in paints for ocean ships but are toxic to humans. Dibutyltin (DBT), tributyltin (TBT), diphenyltin (DPhT), and triphenyltin (TPhT) were measured in harbor water [418] and fish [419]. Organolead compounds were commonly used in gasoline and still are in some countries. Ion-pairing reverse-phase liquid chromatography with ICP-MS detection was used to measure inorganic Pb^{2+}, triethyllead, triphenyllead, and tetraethyllead [420]. After derivatization, GC-ICP-MS has also been used [421].

3.4 CONCLUSIONS

Inductively coupled plasma mass spectrometry is becoming more and more popular because of the low detection limits, high selectivity, and rapid multiele-

ment analysis. Convenient, rapid semiquantitative analysis and isotope measurements are additional capabilities that make ICP-MS popular. As indicated by the wide range of applications, ICP-MS currently provides solutions to analysis problems in a wide range of disciplines.

Substantial improvements have been made in ICP-MS instruments just over the last few years and further advances are on the horizon. The quadrupole ICP-MS instruments have become smaller, more sensitive, easier to use, and less expensive. Sector-based ICP-MS instruments are growing in popularity and performance, although they are still expensive compared to quadrupole instruments. Second- and third-generation sector-based instruments hold promise for further performance improvements. Multicollector sector-based instruments that were previously useful only for isotope ratio measurements may now provide excellent elemental analysis performance as well, because of new instrument designs. Detection limits and precision provided by time-of-flight instruments have improved, and commercial instruments have recently become available. Further improvements in sensitivity may be possible. The speed of complete spectral acquisition provided by time-of-flight ICP-MS could be particularly valuable with sample introduction systems that produce transient signals, such as laser ablation, electrothermal vaporization, and capillary chromatography. Laser ablation solid sampling continues to improve with the use of ultraviolet (UV) lasers and flat beam profiles. Sample introduction systems for solution samples also continue to improve. Systems with high analyte transport efficiencies and membrane desolvation are particularly promising.

ICP-MS currently has several limitations. Research continues to develop new ways to overcome these limitations and improve ICP-MS performance further. At the same time steps to lower the instrument cost continue to progress.

Spectral overlaps, particularly those due to polyatomic ions, remain a problem in many applications. High-resolution mass spectrometers can overcome many, but not all, of these overlaps. The use of reaction cells to remove particular molecular ions chemically is an exciting development that could have a major impact on ICP-MS performance.

Chemical matrix effects due to space-charge ion transmission loss remain a problem. Concentrations of heavy ions as low as 100 ppm can affect sensitivity and therefore produce an analysis error. Perhaps alternative designs will reduce space-charge effects, but can the space-charge effects be significantly reduced while maintaining or continuing to improve sensitivity?

Deposition of sample on the sampler, skimmer, ion optics, and other parts of the interface can lead to elevated blank levels as well as drift. This, in combination with the space-charge-induced chemical matrix effects, often requires further dilution of samples than is desirable. This can also limit the range of concentrations that can be measured for a set of samples even though the dynamic range may in theory be sufficient. An improved understanding of the chemical and physical characteristics of the deposition process and means to minimize them is needed.

Sample introduction systems still require further improvement in terms of efficiency, noise, solvent removal, and ease of use. Analysis of small volumes is becoming more common with micronebulizers and efficient desolvation systems. However, these systems are often more difficult to use than conventional nebulizer/spray chamber systems. Nebulizer clogging and fouling of membrane desolvators by aerosol remain problems. Sample introduction systems that may provide nearly 100% analyte transport efficiency at sample uptake rates of more than 0.5 mL/min may be within reach. As the amount of sample entering the plasma increases, chemical matrix effects tend to become more severe. Calibration for laser ablation sampling is still a problem because of sample-dependent changes in the amount of material ablated and elemental fractionation, although progress has been made. Electrothermal vaporization still requires the art of modifiers; again progress is being made.

Instrument and maintenance costs are high. Prices range from about $180,000 (U.S. dollars, 1998) for quadrupole instruments to almost $1,000,000 (U.S. dollars, 1998) for a fully capable multicollector sector–based instrument and laser ablation sampling. About 10 to 20 L/min of Ar is used by the ICP. Sampling and skimmer cones cost $800 to $3000 (U.S. dollars, 1998), depending on material. Detector lifetime may be less than 1 year. Vacuum pumps have limited lifetimes. Of course, the rapid multielement analysis capabilities, low detection limits, and isotope measurements often provide information that makes ICP-MS successful financially as well as scientifically.

Intelligent instruments could broaden the use of ICP-MS while enhancing analysis reliability. The effect of spectral overlaps, chemical matrix effects, and drift due to sample deposition or orifice clogging may not be obvious to the operator unless knowledge of the sample chemistry is sufficient or procedures are specifically designed to check for these potential problems. Because the instruments can rapidly scan the entire mass spectrum, information on components in the sample at high concentration, changes in background ion signals, and isotope ratios might be used as part of a diagnostic system built into the instrument.

REFERENCES

1. Jarvis, K. E.; Gray, A. L.; Houk, R. S. *Handbook of inductively coupled plasma mass spectrometry*; Blackie; Chapman and Hall: Glasgow; New York, 1992.
2. Montaser, A. *Inductively Coupled Plasma Mass Spectrometry*; Wiley-VCH: New York, 1997.
3. Reed, N. M.; Carins, R. O.; Hutton, R. C. *J. Anal. Atom. Spectrom.* **1994**, *9*, 881–896.
4. Canals, A.; Wagner, J.; Browner, R. F.; Hernandis, V. *Spectrochim. Acta, Part B* **1988**, *43B*, 1321–1335.
5. Olesik, J. W.; Bates, L. C. *Spectrochimica Acta* **1995**, *50B*, 285–303.

6. Huang, M.; Lehn, S. A.; Andrews, E. J.; Hieftje, G. M. *Spectrochim. Acta, Part B* **1997**, *52B*, 1173–1193.
7. Nam, S.-H.; Zhang, H.; Cai, M.; Lim, J.-S.; Montaser, A. *Fresenius J. Anal. Chem.* **1996**, *355*, 510–520.
8. Cicerone, M. T.; Farnsworth, P. B. *Spectrochim. Acta, Part B* **1989**, *44B*, 897–907.
9. Douglas, D. J.; French, J. B. *Spectrochim. Acta, Part B* **1986**, *41B*, 197–204.
10. Sakata, K.; Kawabata, K. *Spectrochim. Acta, Part B* **1994**, *49B*, 1027–1038.
11. Sharp, B. L. *J. Anal. Atom. Spectrom.* **1988**, *3*, 613–652.
12. Nam, S.-H.; Lim, J.-S.; Montaser, A. *J. Anal. Atom. Spectrom.* **1994**, *9*, 1357–1362.
13. Vanhaecke, F.; Van Holderbeke, M.; Moens, L.; Dams, R. *J. Anal. Atom. Spectrom.* **1996**, *11*, 543–548.
14. Sharp, B. L. *J. Anal. Atom. Spectrom.* **1988**, *3*, 939–963.
15. Scott, R. H.; Fassel, V. A.; Kniseley, R. N.; Nixon, D. E. *Anal. Chem.* **1974**, *46*, 75–80.
16. Hettipathirana, T. D.; Davey, D. E. *Appl. Spectrosc.* **1996**, *50*, 1015–1022.
17. Wu, M.; Hieftje, G. M. *Appl. Spectrosc.* **1992**, *46*, 1912–1918.
18. Bates, L. C.; Olesik, J. W. *J. Anal. Atom. Spectrom.* **1990**, *5*, 239–247.
19. Farino, J.; Miller, J. R.; Smith, D. D.; Browner, R. F. *Anal. Chem.* **1987**, *59*, 2303–2309.
20. Fuchs, N. A. *The Mechanics of Aerosols*; Dover Publications: New York, 1989.
21. Longerich, H. P.; Strong, D. F.; Kantipuly, C. J. *Can. J. Spec.* **1985**, *31*, 111–121.
22. Routh, M. W.; Goulter, J. E.; Tasker, D. B.; Arellano, S. D. *Am. Lab.* **1987**, 98–104.
23. Ramsey, M. H.; Thompson, M.; Coles, B. J. *Anal. Chem.* **1983**, *55*, 1626–1629.
24. Olesik, J. W.; Kinzer, J. A.; Olesik, S. V. *Anal. Chem.* **1995**, *34*, 1–12.
25. Schroen, W.; Mueller, U. *Fresenius J. Anal. Chem.* **1997**, *357*, 22–26.
26. Legere, G. PittCon '98, New Orleans, 1998.
27. Houk, R. S.; Alves, L. C.; Wiederin, D. R. *Anal. Chem.* **1992**, *64*, 1164–1169.
28. McLaren, J. W.; Lam, J. W.; Gustavsson, A. *J. Anal. Atom. Spectrom.* **1990**, *5*, 419–424.
29. Gustavsson, A.; Hietala, P. *Spectrochimica Acta* **1990**, *45B*, 1103–1108.
30. Xie, G.; Okada, T. *J. Chem. Soc., Faraday Trans.* **1996**, *92*, 663–669.
31. Lecrone, K. J.; Hayes, J. M. *Anal. Chem.* **1997**, *69*, 911–918.
32. Tao, H.; Miyazaki, A. *J. Anal. Atom. Spectrom.* **1995**, *10*, 1–5.
33. Shum, S. C. K.; Pang, H. M.; Houk, R. S. *Anal. Chem.* **1992**, *64*, 2444–2450.
34. Vaughan, B.; Claassen, L. *Commun. Soil Sci. Plant Anal.* **1996**, *27*, 819–827.
35. Houk, R. S.; Wiederin, D. R.; Smith, F. G. *Anal. Chem.* **1991**, *63*, 219–225.
36. Greenfield, S.; Jones, I. L.; Berry, C. T.; Spash, D. I. In *Improvements Relating to Spectroscopic Methods and Apparatus*; UK Patent #1,109,602 (1968).
37. Fassel, V. A.; Lawrence, K. E.; Rice, G. W. *Anal. Chem.* **1984**, *56*, 289–292.
38. McLean, J. A.; Zhang, H.; Dubow, S. R.; Minnich, M. G.; Huff, R. A.; Haydar, D. A.; Montaser, A. *Anal. Chem.* **1998**, *70*, 1012–1020.
39. Montaser, A.; Minnich, M. G.; McLean, J. A.; Liu, H.; Caruso, J. A.; McLeod, C. W. In *Inductively Coupled Plasma Mass Spectrometry*; Montaser, A., Ed.; Wiley-VCH, New York, 1997.
40. Nakahara, T. In *Sample Introduction in Atomic Spectrometry*; Sneddon, J., Ed.; Elsevier: Amsterdam, 1990.

41. Nakahara, T. *Adv. At. Spectrosc.* **1995**, *2*, 139–178.
42. Magnuson, M. L.; Creed, J. T.; Brockhoff, C. A. *J. Anal. Atom. Spectrom.* **1996**, *11*, 893–898.
43. Van Den Broeck, K.; Vandecasteele, C. *Anal. Lett.* **1998**, *31*, 1891–1903.
44. Wang, X.; Barnes, R. M. *Spectrochim. Acta, Part B* **1986**, *41B*, 967–977.
45. Wang, X.; Barnes, R. M. *Spectrochim. Acta, Part B* **1987**, *42B*, 139–156.
46. McCurdy, E. J.; Lange, J. D.; Haygarth, P. M. *Sci. Total Environ.* **1993**, *135*, 131–136.
47. Story, W. C.; Caruso, J. A.; Heitkemper, D. T.; Perkins, L. *J. Chromatogr. Sci.* **1992**, *30*, 427–432.
48. Burguera, J. L.; Burguera, M. *J. Anal. Atom. Spectrom.* **1997**, *12*, 643–651.
49. Beauchemin, D. *Anal. Chem.* **1995**, *67*, 1553–1557.
50. Fukuda, M.; Hayashibe, Y.; Sayama, Y. *Anal. Sci.* **1995**, *11*, 13–16.
51. Arrowsmith, P. *Anal. Chem.* **1987**, *59*, 1437–1444.
52. Gray, A. L. *Analyst (London)* **1985**, *110*, 551–556.
53. Chan, W. T.; Leung, A. P. K.; Mao, X. L.; Russo, R. E. *Appl. Surf. Sci.* **1998**, *127–129*, 269–273.
54. Russo, R. E.; Mao, X. L.; Caetano, M.; Shannon, M. A. *Appl. Surf. Sci.* **1996**, *96–98*, 144–148.
55. Borisov, O. V.; Mao, X. L.; Ciocan, A. C.; Russo, R. E. *Appl. Surf. Sci.* **1998**, *127–129*, 315–320.
56. Mahoney, P. P.; Li, G.; Hieftje, G. M. *J. Anal. Atom. Spectrom.* **1996**, *11*, 401–405.
57. Halliday, A. N.; Der-Chuen, L.; Christensen, J. N.; Walder, A. J.; Freedman, P. A.; Jones, C. E.; Hall, C. M.; Wen, Y.; Teagle, D. *Int. J. Mass Spectrom. Ion Proc.* **1995**, *146–147*, 21–33.
58. Halliday, A. N.; Lee, D.-C.; Christensen, J. N.; Rehkamper, M.; Yi, W.; Luo, X.; Hall, C. M.; Ballentine, C. J.; Pettke, T.; Stirling, C. *Geochim. Cosmochim. Acta* **1998**, *62*, 919–940.
59. Burgoyne, T. W.; Hieftje, G. M.; Hites, R. A. *J. Am. Soc. Mass Spectrom.* **1997**, *8*, 307–318.
60. Longerich, H. P.; Jackson, S. E.; Günther, D. *J. Anal. Atom. Spectrom.* **1996**, *11*, 899–904.
61. Cromwell, E. F.; Arrowsmith, P. *Appl. Spectrosc.* **1995**, *49*, 1652–1660.
62. Günther, D.; Frischknecht, R.; Heinrich, C. A.; Kahlert, H.-J. *J. Anal. Atom. Spectrom.* **1997**, *12*, 939–944.
63. Hemmerlin, M.; Mermet, J. M. *Spectrochim. Acta Part B* **1996**, *51*, 579–589.
64. Scholze, H.; Stephanowitz, H.; Hoffmann, E.; Skole, J. *Fresenius J. Anal. Chem.* **1994**, *350*, 247–252.
65. Allen, L. A.; Leach, J. J.; Pang, H.-M.; Houk, R. S. *J. Anal. Atom. Spectrom.* **1997**, *12*, 171–176.
66. Christensen, J. N.; Halliday, A. N.; Lee, D.-C.; Hall, C. M. *Earth Planet. Sci. Lett.* **1995**, *136*, 79–85.
67. Norman, M. D.; Pearson, N. J.; Sharma, A.; Griffin, W. L. *Geostand. Newsl.* **1996**, *20*, 247–261.
68. Norman, M. D.; Griffin, W. L.; Pearson, N. J.; Garcia, M. O.; O'Reilly, S. Y. *J. Anal. Atom. Spectrom.* **1998**, *13*, 477–482.

69. Pang, H. M.; Wiederin, D. R.; Houk, R. S.; Yeung, E. S. *Anal Chem.* **1991**, *63*, 390–394.
70. Baker, S. A.; Smith, B. W.; Winefordner, J. D. *Appl. Spectrosc.* **1998**, *52*, 154–160.
71. Cromwell, E. F.; Arrowsmith, P. *Anal. Chem.* **1995**, *67*, 131–138.
72. Guenther, D.; Cousin, H.; Magyar, B.; Leopold, I. *J. Anal. Atom. Spectrom.* **1997**, *12*, 165–170.
73. Liu, X. R.; Horlick, G. *Spectrochim. Acta, Part B* **1995**, *50B*, 537–548.
74. Spark, C. M.; Holcolme, J.; Pinkston, T. L. *Spectrochim. Acta Part B* **1993**, *48B*, 357–363.
75. Gregoire, D. C. *Can. J. Anal. Sci. Spectrosc.* **1997**, *42*, 1–9.
76. Ediger, R. D.; Beres, S. A. *Spectrochim. Acta Part B* **1992**, *47B*, 907–922.
77. Gregoire, D. C.; Almaawali, S.; Chakarbarti, C. L. *Spectrochim. Acta Part B* **1992**, *47B*, 1123–1132.
78. Sparks, C. M.; Holcolme, J. A.; Pinkston, T. L. *Appl. Spectrosc.* **1996**, *50*, 86–90.
79. Sturgeon, R. E.; Willie, S. N.; Zheng, J.; Kudo, A.; Gregoire, D. C. *J. Anal. Atom. Spectrom.* **1993**, *8*, 1053–1058.
80. Kubota, R. T. a. M. *Spectrochim. Acta Part B* **1990**, *45B*, 779–787.
81. Goltz, D. M.; Gregoire, D. C.; Byrne, J. P.; Chakrabarti, C. L. *Spectrochim. Acta Part B* **1995**, *50B*, 1365–1382.
82. Salin, E. D.; Horlick, G. *Anal Chem.* **1979**, *51*, 2284–2286.
83. Rattray, R.; Salin, E. *J. Anal. Atom. Spectrom.* **1995**, *10*, 829–836.
84. Jiang, S.-J.; Houk, R. S. *Anal. Chem.* **1986**, *58*, 1739–1743.
85. Ivanovic, K. A.; Coleman, D. M.; Kunz, F. W.; Schuetzle, D. *Appl. Spectrosc.* **1992**, *46*, 894–899.
86. Hirata, T.; Akagi, T.; Masuda, A. *Analyst* **1990**, *115*, 1329–1333.
87. DeSilva, K. N.; Guevremont, R. *Spectrochim. Acta Part B* **1990**, *45B*, 997–1011.
88. DeSilva, K. N.; Guevremont, R. *Spectrochim. Acta Part B* **1990**, *45B*, 933–939.
89. Campargue, R. *Rev. Sci. Instrum.* **1964**, *35*, 111–112.
90. Campargue, R. *J. Chem. Phys.* **1970**, *52*, 1795–1802.
91. Beijerinck, H. C. W.; Gerwin, R. J. F.; Kerstel, E. R. J.; Martens, J. F. M.; Vliembergen, E. J. W. V.; Smuts, M. R. T.; Kaashoek, G. H. *Chem. Phys.* **1985**, *96*, 153–173.
92. Douglas, D. J.; Tanner, S. D. In *Inductively Coupled Plasma Mass Spectrometry*; Montaser, A., Ed.; Wiley-VCH: New York, 1998, 615–679.
93. Gray, A. L. *J. Anal. Atom. Spectrom.* **1989**, *4*, 371–373.
94. Niu, H.; Houk, R. S. *Spectrochim. Acta, Part B* **1996**, *51B*, 779–815.
95. Douglas, D. J.; French, B. J. *J. Anal. Atom. Spectrom.* **1988**, *3*, 743–747.
96. Houk, R. S. Federation of Analytical Chemistry and Spectroscopy Societies Meeting, 1997, Providence, RI, paper 253.
97. Fulford, J. E.; Douglas, D. J. *Appl. Spectrosc.* **1986**, *40*, 971–974.
98. Olivares, J. A.; Houk, R. S. *Spectrochim. Acta B* **1985**, *40B*, 1301–1311.
99. Tanner, S. D. In *Applications of Plasma Source Mass Spectrometry*; Holland, G., Eaton, E. A., Eds.; Royal Society of Chemistry: Cambridge, 1993; Vol. II, 222–234.
100. Tanner, S. D. *J. Anal. Atom. Spectrom.* **1993**, *8*, 891–897.
101. Niu, H.; Houk, R. S. *Spectrochim. Acta Part B* **1995**, *49B*, 1247–1261.
102. Niu, H.; Houk, R. S. *Spectrochim. Acta Part B* **1994**, *49B*, 1283–1303.

103. Tanner, S. D.; Cousins, L. M.; Douglas, D. J. *Appl. Spectrosc.* **1994**, *48*, 1367–1372.
104. Gillson, G. R.; Douglas, D. J.; Fulford, J. E.; Halligan, K. W.; Tanner, S. D. *Anal. Chem.* **1988**, *60*, 1472–1474.
105. Tanner, S. D. In *Plasma Source Mass Spectrometry: Developments and Applications*; Holland, G. P., Tanner, S. D., Eds.; Royal Society of Chemistry: Cambridge, 1997, 13–27.
106. Vaughan, M. A.; Horlick, G. *Spectrochim. Acta Part B* **1990**, *45B*, 1301–1311.
107. Horlick, G.; Shao, Y. In *Inductively Coupled Plasmas in Analytical Atomic Spectrometry*; Montaser, A., Golightly, D. W., Eds.; VCH: New York, 1992, 551–662.
108. Hu, K.; Clemons, P. S.; Houk, R. S. *J. Am. Soc. Mass Spectrom.* **1993**, *4*, 16–27.
109. Hu, K.; Houk, R. S. *J. Am. Soc. Mass Spectrom.* **1993**, *4*, 28–37.
110. Hieftje, G. M. *J. Anal. Atom. Spectrom.* **1992**, *7*, 783–790.
111. Douglas, D. J. *Can. J. Spec.* **1989**, *34*, 38–49.
112. Rowan, J. T.; Houk, R. S. *Appl. Spectrosc.* **1989**, *43*, 976–980.
113. Eiden, G. C.; Barinaga, C. J.; Koppenaal, D. W. *J. Anal. Atom. Spectrom.* **1996**, *11*, 317–322.
114. Turner, P.; Merren, T.; Speakman, J.; Haines, C. In *Plasma Source Mass Spectrometry Developments and Applications*; Holland, G., Tanner, S., Eds.; Royal Society of Chemistry: Cambridge, 1997.
115. Turner, P. J.; Mills, D. J.; Schroder, E.; Lapitajs, G.; Jung, G.; Iacone, L. A.; Haydar, D. A.; Montaser, A. In *Inductively Coupled Plasma Mass Spectrometry*; Montaser, A., Ed.; Wiley-VCH: New York, 1998, 421–501.
116. Beaty, J. H.; Liezers, M. Durham Conference on Plasma Source Mass Spectrometry, Durham, United Kingdom, 1998.
117. Douglas, D. J.; French, J. B. *J. Am. Soc. Mass Spectrom.* **1992**, *3*, 398–408.
118. Tanner, S. D.; Baranov, V. I. In *Plasma Source Mass Spectroscopy: New Developments and Applications*; Holland, G., Tanner, S. D., Eds.; Royal Society of Chemistry: Cambridge, 1999, 46–62.
119. Baranov, V. I.; Tanner, S. D. In *Plasma Source Mass Spectroscopy: New Developments and Applications*; Holland, G., Tanner, S. D., Eds.; Royal Society of Chemistry: Cambridge, 1999, 34–45.
120. Vollkopf, U.; Baranov, V.; I. Tanner, S. D. In *Plasma Source Mass Spectroscopy: New Developments and Applications*; Holland, G., Tanner, S. D., Eds.; Royal Society of Chemistry: Cambridge, 1999, 63–79.
121. Miller, P. E.; Denton, M. B. *J. Chem. Educ.* **1986**, *63*, 617–622.
122. Watson, J. T. *Introduction to Mass Spectrometry*; Lippincott-Raven: Philadelphia, 1997.
123. Leary, J. J.; Schmidt, R. L. *J. Chem. Educ.* **1996**, *73*, 1142–1145.
124. Dawson, P. H. *Quadrupole Mass Spectrometry and Its Applications*; Elsevier Scientific: New York, 1976.
125. Dawson, P. H. *Adv. Electron. Electron Phys., Suppl.* **1980**, *13B*, 173–256.
126. Denison, D. R. *J. Vacuum Tech.* **1971**, *8*, 266.
127. Moens, L.; Vanhaecke, F.; Riondato, J.; Dams, R. *J. Anal. Atom. Spectrom.* **1995**, *10*, 569–574.
128. Stuewer, D.; Jakubowski, N. *J. Mass Spectrom.* **1998**, *33*, 579–590.
129. Duckworth, D. C.; Barshick, C. M. *Anal. Chem.* **1998**, *70*, 709A–717A.

130. Eiden, G. C.; Barinaga, C. J.; Koppenaal, D. W. *Rapid Commun. Mass Spectrom.* **1997**, *11*, 37–42.
131. Barinaga, C. J.; Eiden, G. C.; Alexander, M. L.; Koppenaal, D. W. *Fresenius J. Anal. Chem.* **1996**, *355*, 487–493.
132. Barinaga, C. J.; Koppenaal, D. W. *Rapid Commun. Mass Spectrom.* **1994**, *8*, 71–76.
133. Koppenaal, D. W.; Barinaga, C. J.; Smith, M. R. *J. Anal. Atom. Spectrom.* **1994**, *9*, 1053–1058.
134. Milgram, K. E. Abatement of spectral interferences in elemental mass spectrometry: design and construction of inductively coupled plasma ion sources for Fourier Transform ion cyclotron resonance instrumentation, Ph. D. Thesis, University of Florida, 1997, Diss. Abstr. Int., B **1998**, *59(2)*, 639.
135. Milgram, K. E.; White, F. M.; Goodner, K. L.; Watson, C. H.; Koppenaal, D. W.; Barinaga, C. J.; Smith, B. H.; Winefordner, J. D.; Marshall, A. G.; Houk, R. S.; Eyler, J. R. *Anal. Chem.* **1997**, *69*, 3714–3721.
136. Du, Z.; Olney, T. N.; Douglas, D. J. *J. Am. Soc. Mass Spectrom.* **1997**, *8*, 1230–1236.
137. Douglas, D. J.; Konenkov, N. V. *J. Am. Soc. Mass Spectrom.* **1998**, *9*, 1074–1080.
138. Daly, N. R. *Rev. Sci. Instrum.* **1960**, *37*, 1385–1390.
139. Huang, L. Q.; Jiang, S.-J.; Houk, R. S. *Anal. Chem.* **1987**, *59*, 2316–2320.
140. Vaughan, M. A.; Horlick, G. *Appl. Spectrosc.* **1986**, *40*, 434–445.
141. Dulski, P. *Geostand. Newsl.* **1992**, *16*, 325–332.
142. Longerich, H. P.; Fryer, B. J.; Strong, D. F.; Kantipuly, C. J. *Spectrochim. Acta, Part B* **1987**, *42B*, 75–92.
143. Lam, J. W.; McLaren, J. W. *J. Anal. Atom. Spectrom.* **1990**, *5*, 419–424.
144. Ebdon, L.; Ford, M. J.; Hutton, R. C.; Hill, S. J. *Appl. Spectrosc.* **1994**, *48*, 507–516.
145. Hill, S. J.; Ford, M. J.; Ebdon, L. *J. Anal. Atom. Spectrom.* **1992**, *7*, 1157–1165.
146. Jiang, S.-J.; Houk, R. S.; Stevens, M. A. *Anal. Chem.* **1988**, *60*, 1217–1221.
147. Tanner, S. D. *J. Anal. Atom. Spectrom.* **1995**, *10*, 905–921.
148. Eiden, G. C.; Barinaga, C. J.; Koppenaal, D. W. *Rapid Commun. Mass Spectrom.* **1997**, *11*, 37–42.
149. Gregory, C. E.; Barinaga, C. J.; Koppenaal, D. W. *J. Am. Soc. Mass Spectrom.* **1996**, *7*, 1161–1171.
150. Ketterer, M. E.; Reschl, J.J.; Peters, M. J. *Anal. Chem.* **1989**, *61*, 2031–2040.
151. Ketterer, M. E.; Biddle, D. A. *Anal. Chem.* **1992**, *64*, 1819–1823.
152. Vaughan, M. A.; Templeton, D. M. *Appl. Spectrosc.* **1990**, *44*, 1685–1689.
153. van Veen, E. H.; Bosch, S.; de Loos-Vollebregt, M. T. C. *Spectrochim. Acta, Part B* **1994**, *49B*, 1347–1361.
154. de Boer, J. L. M. *Spectrochim. Acta Part B* **1997**, *52B*, 389–403.
155. Horlick, G.; Tan, S. H.; Vaughn, M. A.; Rose, C. A. *Spectrochim. Acta Part B* **1985**, *40B*, 1555–1572.
156. Vaughan, M. A.; Horlick, G.; Tan, S. H. *Journal of Analytical Atomic Spectroscopy* **1987**, *2*, 765–772.
157. Hobbs, S. E.; Olesik, J. W. *Anal. Chem.* **1992**, *64*, 274–283.
158. Olesik, J. W.; Fister, J. C., III. *Spectrochim. Acta Part B* **1991**, *46B*, 851–868.
159. Dziewatkoski, M. P.; Daniels, L. B.; Olesik, J. W. *Anal. Chem.* **1996**, *68*, 1101–1109.
160. Olesik, J. W. *Appl. Spectrosc.* **1997**, *51*, 158A–175A.
161. French, J. B.; Etkin, B.; Jong, R. *Anal. Chem.* **1994**, *66*, 685–691.

162. Clemons, P. S.; Minnich, M. G.; Houk, R. S. *Anal. Chem.* **1995**, *67*, 1929–1934.
163. Denoyer, E. R.; Jacques, M. D.; Debrah, E.; Tanner, S. D. *At. Spectrosc.* **1995**, *16*, 1–6.
164. Montaser, A.; Tan, H.; Ishii, I.; Nam, S. H.; Cai, M. *Anal. Chem.* **1991**, *63*, 2660–2665.
165. Hutton, R. C.; Grote, B. *Analusis* **1996**, *24*, M29–M31.
166. Olivares, J. A.; Houk, R. S. *Anal. Chem.* **1986**, *58*, 20–25, 13, 843–854.
167. Stewart, I. I.; Olesik, J. W. *J. Anal. Atom. Spectrom.* **1998**.
168. Mermet, J.-M. *J. Anal. Atom. Spectrom.* **1998**, *13*, 419–422.
169. Canals, A.; Hernandis, V.; Todoli, J. L.; Browner, R. F. *Spectrochim. Acta Part B* **1995**, *50B*, 305–321.
170. Marichy, M.; Mermet, M.; Mermet, J. M. *Spectrochim. Acta, Part B* **1990**, *45B*, 1195–1201.
171. Gillson, G.; Horlick, G. *Spectrochim. Acta, Part B* **1986**, *41B*, 619–624.
172. Olesik, J. W.; Williamsen, E. J. *Appl. Spectrosc.* **1989**, *43*, 1223–1232.
173. Hobbs, S. E.; Olesik, J. W. *Appl. Spectrosc.* **1991**, *45*, 1395–1407.
174. Tan, S. H.; Horlick, G. *J. Anal. Atom. Spectrom.* **1987**, *2*, 745–763.
175. Douglas, D. J.; Kerr, L. A. *J. Anal. Atom. Spectrom.* **1988**, *3*, 749–752.
176. Hutton, R. C.; Eaton, A. N. *J. Anal. Atom. Spectrom.* **1988**, *3*, 547–550.
177. Tanner, S. D. *Spectrochim. Acta, Part B* **1992**, *47B*, 809–823.
178. Olesik, J. W.; Dziewatkoski, M. P. *J. Am. Soc. Mass Spectrom.* **1996**, *7*, 362–367.
179. Allen, L. A.; Leach, J. J.; Houk, R. S. *Anal. Chem.* **1997**, *69*, 2384–2391.
180. Stewart, I. I.; Olesik, J. W. *J. Am. Soc. Mass Spectrom.* **1999**, *10*, 159–174.
181. Tanner, S. D.; Douglas, D. J.; French, J. B. *Appl. Spectrosc.* **1994**, *48*, 1373–1378.
182. Ross, B. S.; Hieftje, G. M. *Spectrochim. Acta, Part B* **1991**, *46B*, 1263–1273.
183. Crain, J. S.; Houk, R. S.; Smith, F. G. *Spectrochim. Acta, Part B* **1988**, *43B*, 1355–1364.
184. Evans, E. H.; Caruso, J. A. *Spectrochim. Acta, Part B* **1992**, *47B*, 1001–1012.
185. Wang, J.; Shen, W.-L.; Shepard, B. S.; Evans, E. H.; Caruso, J. A. *J. Anal. Atom. Spectrom.* **1990**, *6*, 39–44.
186. Denoyer, E. R.; Jacques, D.; Deborah, E.; Tanner, S. D. *Atomic Spectrometry* **1995**, *16*, 1–6.
187. Xiao, G.; Beauchemin, D. *J. Anal. Atom. Spectrom.* **1994**, *9*, 509–518.
188. Craig, J. M.; Beauchemin, D. *J. Anal. Atom. Spectrom.* **1992**, *7*, 937–942.
189. Thompson, J. J.; Houk, R. S. *Appl. Spectrosc.* **1987**, *41*, 801–806.
190. Vanhaecke, F.; Vanhoe, H.; Dams, R.; Vandecasteele, C. *Talanta* **1992**, *39*, 737–742.
191. Doherty, W. *Spectrochim. Acta, Part B* **1989**, *44B*, 263–280.
192. McLaren, J. W.; Beauchemin, D.; Berman, S. S. *Anal. Chem.* **1987**, *59*, 610–613.
193. Van Heuzen, A. A.; Hoekstra, T.; Van Wingerden, B. *J. Anal. Atom. Spectrom.* **1989**, *4*, 483–489.
194. Yi, Y. V.; Masuda, A. *Anal. Chem.* **1996**, *68*, 1444–1450.
195. Rehkamper, M.; Halliday, A. N. *Talanta* **1997**, *44*, 663–672.
196. Luong, E. T.; Houk, R. S.; Serfass, R. E. *J. Anal. Atom. Spectrom.* **1997**, *12*, 703–708.
197. Colodner, D. C.; Boyle, E. A.; Edmond, J. M. *Anal. Chem.* **1993**, *65*, 1419–1425.
198. Croudace, I. W.; Marshall, S. *Geostand. Newsl.* **1991**, *15*, 139–144.
199. Katoh, T.; Akiyama, M.; Ohtsuka, H.; Nakamura, S.; Haraguchi, K.; Akatsuka, K. *J. Anal. Atom. Spectrom.* **1996**, *11*, 69–71.

200. Hwang, T.-J.; Jiang, S.-J. *J. Anal. Atom. Spectrom.* **1996**, *11*, 353–357.
201. Patterson, K. Y.; Veillon, C.; O'Haver, T. C. *Anal. Chem.* **1994**, *66*, 2829–2834.
202. Freydier, R.; Dupre, B.; Polve, M. *Eur. Mass Spectrom.* **1995**, *1*, 283–291.
203. Zhang, L.-S.; Combs, S. M. *J. AOAC Int.* **1998**, *81*, 1060–1064.
204. Wildner, H.; Wuensch, G. *Fresenius J. Anal. Chem.* **1996**, *354*, 807–810.
205. Ekimoff, D.; Van Norstrand, A. M.; Mowers, D. A. *Appl. Spectrosc.* **1989**, *43*, 1252–1257.
206. Amarasiriwardena, C. J.; Gercken, B.; Argentine, M. D.; Barnes, R. M. *J. Anal. Atom. Spectrom.* **1990**, *5*, 457–462.
207. Ediger, R. D.; Polk, D. *Perkin Elmer Technical Summary TSMS-10.*
208. van Veen, E. H.; Bosch, S.; de Loos-Vollebregt, M. T. C. *Spectrochim. Acta, Part B* **1996**, *51B*, 591–608.
209. van Veen, E. H.; de Loos-Vollebregt, M. T. C. In *Plasma Source Mass Spectrometry Developments and Applications*; Holland, G., Tanner, S. D., Eds.; The Royal Society of Chemistry: Cambridge, 1997, 77–84.
210. Broadhead, M.; Broadhead, R.; Hager, J. W. *At. Spectrosc.* **1990**, *11*, 205–209.
211. Van de Weijer, P.; Baeten, W. I. M.; Bekkers, M. H. J.; Vullings, P. J. M. G. *J. Anal. Atom. Spectrom.* **1992**, *7*, 599–603.
212. Denoyer, E. R. *J. Anal. Atom. Spectrom.* **1992**, *7*, 1187–1193.
213. Pearce, N. J. G.; Perkins, W. T.; Fuge, R. *J. Anal. Atom. Spectrom.* **1992**, *7*, 595–598.
214. Krushevska, A.; Lasztity, A.; Kotrebai, M.; Barnes, R. M. *J. Anal. Atom. Spectrom.* **1996**, *11*, 343–352.
215. Amarasiriwardena, D.; Durrant, S. F.; Lasztity, A.; Krushevska, A.; Argentine, M. D.; Barnes, R. M. *Microchem. J.* **1997**, *546*, 352–372.
216. Soldevila, J; El Himri, M.; Pastor, A.; de la Guardia, M. *J. Anal. Atom. Spectrom.* **1998**, *13*, 803–807.
217. Montes Bayon, M.; Garcia Alonso, J. I.; Sanz Medel, A. *J. Anal. Atom. Spectrom.* **1998**, *13*, 277–282.
218. Jarvis, I. In *Handbook of Inductively Coupled Plasma-Mass Spectrometry*; Blackie; Chapman and Hall: Glasgow; New York, 1992, 172–224.
219. Kingston, H. M.; Walter, P. J. In *Inductively Coupled Plasma Mass Spectrometry*; Montaser, A., Ed.; Wiley-VCH: New York, 1997.
220. Kingston, H. M.; Haswell, S. J.; Eds. *Microwave-Enhanced Chemistry: Fundamentals, Sample Preparation, and Applications.*; ACS, Washington, DC, 1997.
221. Matusiewicz, H. Microwave-Enhanced Chemistry; American Chemical Society: Washington, DC, 1997, 353–369.
222. Knapp, G.; Panholzer, F.; Schalk, A.; Kettisch, P. Microwave-Enhanced Chemistry; American Chemical Society: Washington, DC, 1997, 423–451.
223. Kingston, H. M.; Walter, P. J.; Chalk, S.; Lorentzen, E.; Link, D., Microwave-Enhanced Chemistry; American Chemical Society: Washington, DC, 1997, 223–349.
224. Kingston, H. M.; Jassie, L. B.; Eds. *Introduction to Microwave Sample Preparation: Theory and Practice*; ACS: Washington, DC, 1988.
225. Kingston, H. M.; Jassie, L. B. *J. Resp Natl. Bur. Stand. (U. S.)* **1988**, *93*, 269–274.
226. Kingston, H. M.; Walter, P. J. *Spectroscopy (Eugene, Oreg.)* **1992**, *7*, 20, 22, 24–27.
227. Barnes, R. M. *Fresenius J. Anal. Chem.* **1996**, *355*, 433–441.

228. Patriarca, M. *Microchemical Journal* **1996**, *54*, 262–271.
229. Moens, L. *Fresenius J. Anal. Chem.* **1997**, *359*, 309–316.
230. Pruszkowski, E.; Neubauer, K.; Thomas, R. *At. Spectrosc.* **1998**, *19*, 111–115.
231. Nuttall, K. L.; Gordon, W. H.; Ash, K. O. *Ann. Clin. Lib. Sci.* **1995**, *25*, 264–871.
232. Nixon, D. E.; Moyer, T. P. *Spectrochim. Acta, Part B* **1996**, *51B*, 13–25.
233. Krushevska, A.; Waheed, S.; Nobrega, J.; Amarisiriwardena, D.; Barnes, R. M. *Appl. Spectrosc.* **1998**, *52*, 205–211.
234. Moens, L.; Verrept, P.; Dams, R.; Greb, U.; Jung, G.; Laser, B. *J. Anal. Atom. Spectrom.* **1994**, *9*, 1075–1078.
235. Vanhoe, H.; Vandecasteele, C.; Versieck, J.; Dams, R. In *Plasma Source Mass Spectrometry*; Holland, G., Ed.; Royal Society of Chemistry: Cambridge, 1990; Vol. 85, 66–78.
236. Delves, H. T.; Sieniawska, C. E.; Fell, G. S.; Lyon, T. D. B.; Dezateux, C.; Cullen, A.; Variend, S.; Bonham, J. R.; Chantler, S. M. *Analyst (Cambridge)* **1997**, *122*, 1323–1329.
237. Gibb, R. C.; Corrigan, F. M.; Welsh, S.; Smith, I.; Ward, M. I. *Trace Elem. Electrolytes* **1996**, *13*, 205–208.
238. Godlewska, B.; Hulanicki, A.; Abou-Shakra, F. R.; Ward, N. I. *Anal. Lett.* **1994**, *27*, 2647–2662.
239. Li, H.; Keohane, B. M.; Sun, H.; Sadler, P. J. *J. Anal. Atom. Spectrom.* **1997**, *12*, 1111–1114.
240. Schutz, A.; Bergdahl, I. A.; Ekholm, A.; Skerfving, S. *Occup. Environ. Med.* **1996**, *53*, 736–740.
241. Vandecasteele, C.; Vanhoe, H.; Dams, R.; Versieck, J. *Biol. Trace Elem. Res.* **1990**, *26–27*, 553–560.
242. Vaughan, M. A.; Baines, A. D.; Templeton, D. M. *Clin. Chem. (Winston-Salem, N. C.)* **1991**, *37*, 210–215.
243. Vanhoe, H.; Dams, R.; Versieck, J. *J. Anal. Atom. Spectrom.* **1994**, *9*, 23–31.
244. Lorber, A.; Halicz, L.; Karpas, Z.; Elish, E.; Roiz, J.; Marko, R. *Spec. Publ. R. Soc. Chem.* **1997**, *202*, 202–210.
245. Shiraishi, K.; McInroy, J. F. *J. Trace Elem. Exp. Med.* **1991**, *4*, 191–202.
246. Delves, H. T.; Campbell, M. J. *Environ. Geochem. Health* **1993**, *15*, 75–84.
247. Lyon, T. D. B.; Fell, G. S.; McKay, K.; Scott, R. D. *J. Anal. Atom. Spectrom.* **1991**, *6*, 559–564.
248. Ducros, V.; Peoc'h, M.; Moulin, C.; Ruffieux, D.; Amosse, J.; Favier, A.; Pasquier, B. *Clin. Chem. (Washington, D. C.)* **1996**, *42*, 1875–1877.
249. Beauchemin, D.; Kisilevsky, R. *Anal. Chem.* **1998**, *70*, 1026–1029.
250. Corrigan, F. M.; Reynolds, G. P.; Ward, N. I. *BioMetals* **1993**, *6*, 149–154.
251. Corrigan, F. M.; Reynolds, G. P.; Ward, N. I. *Trace Elem. Med.* **1991**, *8*, 1–5.
252. Emmett, S. E. *Prog. Clin. Biol. Res.* **1989**, *317*, 1077–1086.
253. Wang, S.; Brown, R.; Gray, D. J. *Appl. Spectrosc.* **1994**, *48*, 1321–1325.
254. Li, Y.-C.; Jiang, S.-J. *Anal. Chim. Acta* **1998**, *359*, 205–212.
255. de Conto Cinier, C.; Petit-Ramel, M.; Faure, R.; Garin, D. *Ecotoxicol. Environ. Saf.* **1997**, *38*, 137–143.
256. McKay, K. *Cancer Surv.* **1993**, *17*, 407–414.
257. Webster, P. J.; Ng, K.; Snitch, P.; Jones, S. L.; Amos, N.; Harnett, P. R. *J. Oncol. Pharm. Pract.* **1995**, *1*, 41–48.

258. Buckley, W. T.; Budac, J. J.; Godfrey, D. V.; Koenig, K. M. *Anal. Chem.* **1992**, *64*, 724–729.
259. Janghorbani, M.; Ting, B. T. G.; Zeisel, S. H. *Curr. Top. Nutr. Dis.* **1988**, *18*, 545–556.
260. Janghorbani, M.; Ting, B. T. G.; Lynch, N. E. *Mikrochim. Acta* **1989**, *3*, 315–328.
261. Schuette, S. A.; Ziegler, E. E.; Nelson, S. E.; Janghorbani, M. *Pediatr. Res.* **1990**, *27*, 36–40.
262. Patriarca, M.; Lyon, T. D. B.; Fell, G. S. *Am. J. Clin. Nutr.* **1997**, *66*, 616–621.
263. Frost, H. L.; Ketchum, L. H., Jr.; Jain, J. C.; Neal, C. R. *Proc. Ind. Waste Conf.* **1998**, *52*, 395–400.
264. Curdova, E.; Szakova, J.; Koplik, R.; Suchanek, M. In *Plasma Source Mass Spectrometry*; Royal Society of Chemistry: Cambridge, 1997; Vol. 202, 223–230.
265. Wu, S.; Feng, X.; Wittmeier, A. *J. Anal. Atom. Spectrom.* **1997**, *12*, 797–806.
266. Li, Y.-C.; Jiang, S.-J.; Chen, S.-F. *Anal. Chim. Acta* **1998**, *372*, 365–372.
267. van den Broeck, K.; Vandecasteele, C.; Geuns, J. M. C. *J. Anal. Atom. Spectrom.* **1997**, *12*, 987–991.
268. Watmough, S. A.; Hutchinson, T. C. *Environ. Pollut.* **1996**, *93*, 93–102.
269. Watling, R. J. *J. Anal. Atom. Spectrom.* **1998**, *13*, 917–926.
270. Crews, H. M. Prog. Food Contam. Anal.; Blackie: London, 1996; 147–186.
271. Barnes, R. M. *Adv. Exp. Med. Biol.* **1998**, *445*, 379–396.
272. Baxter, M. J.; Crews, H. M.; Robb, P.; Strutt, P. R. In *Plasma Source Mass Spectrometry*; Holland, G., Tanner, S. D., Eds.; Royal Society of Chemistry Cambridge, 1997; Vol. 202, 95–108.
273. Biego, G. H.; Biaudet, H.; Joyeux, M.; Debry, G. *Sci. Aliments* **1997**, *16*, 623–630.
274. Goossens, J.; De Smaele, T.; Moens, L.; Dams, R. *Fresenius J. Anal. Chem.* **1993**, *347*, 119–125.
275. Augagneur, S.; Medina, B.; Grousset, F. *Fresenius J. Anal. Chem.* **1997**, *357*, 1149–1152.
276. Eckhoff, K. M.; Maage, A. *J. Food Compos. Anal.* **1997**, *10*, 270–282.
277. Augagneur, S.; Medina, B.; Szpunar, J.; Lobinski, R. *J. Anal. Atom. Spectrom.* **1996**, *11*, 713–721.
278. Baxter, M. J.; Crews, H. M.; Dennis, M. J.; Goodall, I.; Anderson, D. *Food Chem.* **1997**, *60*, 443–450.
279. Greenough, J. D.; Longerich, H. P.; Jackson, S. E. *Can. J. Appl. Spectrosc.* **1996**, *41*, 76–80.
280. Martin, G. J.; Fournier, J. B.; Allain, P.; Mauras, Y. *Analusis* **1997**, *25*, 7.
281. Date, A. R.; Gray, A. L. *Analyst* **1981**, *106*, 1255–1267.
282. Doherty, W.; Vander Voet, A. *Can. J. Spectrosc.* **1985**, *30*, 135–141.
283. Date, A. R.; Hutchison, D. *Spectrochim. Acta, Part B* **1986**, *41B*, 175–181.
284. Date, A. R.; Gray, A. L. *Spectrochim. Acta, Part B* **1985**, *40B*, 115–122.
285. Jarvis, K. E. *Chem. Geol.* **1988**, *68*, 31–39.
286. Nesbitt, R. W.; Hirata, T.; Butler, I. B.; Milton, J. A. *Geostand. Newsl.* **1997**, *21*, 231–243.
287. Perkins, W. T.; Pearce, N. J. G.; Westgate, J. A. *Geostand. Newsl.* **1997**, *21*, 175–190.
288. Feigenson, M. D.; Patino, L. C.; Carr, M. J. *J. Geophys. Res., [Solid Earth]* **1996**, *101*, 11815–11829.

289. Eaton, A. N.; Hutton, R. C.; Holland, J. G. *Chem. Geol.* **1992**, *95*, 63–71.
290. Field, M. P.; Sherrell, R. M. *Anal. Chem.* **1998**, *70*, 4480–4486.
291. Hoskin, P. W. O. *J. Trace Microprobe Tech.* **1998**, *16*, 301–326.
292. Hall, G. E. M. *J. Geochem. Explor.* **1998**, *61*, 1–19.
293. Barefoot, R. R. *J. Anal. Atom. Spectrom.* **1998**, *13*, 1077–1084.
294. Perry, B. J.; Barefoot, R. R.; Van Loon, J. C. *Trends Anal. Chem.* **1995**, *14*, 388–397.
295. Hall, G. E. M.; Pelchat, J. C. *Chem. Geol.* **1994**, *115*, 61–72.
296. Dickin, A. P.; McNutt, R. H.; McAndrew, J. I. *J. Anal. Atom. Spectrom.* **1988**, *3*, 337–342.
297. Hulbert, L. J.; Gregoire, D. C. *Can. Mineral.* **1993**, *31*, 861–876.
298. Heumann, K. G. *Fresenius Z. Anal. Chem.* **1986**, *324*, 601–611.
299. Enzweiler, J.; Potts, P. J.; Jarvis, K. F. *Analyst (Cambridge)* **1995**, *120*, 1391–1396.
300. Lasztity, A.; Viczian, M.; Wang, X.; Barnes, R. M. *J. Anal. Atom. Spectrom.* **1989**, *4*, 761–766.
301. Moraes, N. M. P.; Iyer, S. S. *Anal. Chim. Acta* **1990**, *236*, 487–493.
302. Xie, Q.; Kerrich, R. *Chem. Geol.* **1995**, *123*, 17–27.
303. Hall, G. E. M. *J. Geochem. Explor.* **1993**, *49*, 89–121.
304. Pearce, F. M. *Environ. Geochem. Health* **1991**, *13*, 50–55.
305. Creed, J. T.; Martin, T. D.; Sivaganesan, M. *J. Am. Water Works Assoc.* **1995**, *87*, 104–114.
306. Beauchemin, D.; Specht, A. A. *Can. J. Anal. Sci. Spectrosc.* **1998**, *43*, 43–48.
307. Garman, D. E. J.; MacKenzie, D. *At. Spectrosc.* **1991**, *12*, 233–234.
308. Long, S. E.; Martin, T. D. In *Methods for the Determination of Inorganic Compounds in Drinking Water. Methods 300.0, 200.8*; 1989.
309. In *EPA Method 1638: Determination of Trace Elements in Ambient Waters by Inductively Coupled Plasma-Mass Spectrometry, B95-219937GAR. Avail. HTIS. From: Gov. Rep. Announce. Index (U. S.) 1995, 95(16), Abstr. No. 16-01,260*; 1995.
310. Hall, E. S.; Murphy, E. *J. Radioanal. Nucl. Chem.* **1993**, *175*, 129–138.
311. Richter, R. C.; Swami, K.; Chace, S.; Husain, L. *Fresenius J. Anal. Chem.* **1998**, *361*, 168–173.
312. Hall, G. E. M.; Pelchat, J. C. *J. Anal. Atom. Spectrom.* **1993**, *8*, 1059–1065.
313. Packer, A. P.; Gine, M. F.; Miranda, C. E. S.; Dos Reis, B. F. *J. Anal. Atom. Spectrom.* **1997**, *12*, 563–566.
314. Beauchemin, D. *Mikrochim. Acta* **1989**, *3*, 273–281.
315. McLaren, J. W.; Lam, J. W. H.; Berman, S. S.; Akatsuka, K.; Azeredo, M. A. *J. Anal. Atom. Spectrom.* **1993**, *8*, 279–286.
316. Akatsuka, K.; McLaren, J. W.; Lam, J. W.; Berman, S. S. *J. Anal. Atom. Spectrom.* **1992**, *7*, 889–894.
317. Batterham, G. J.; Munksgaard, N. C.; Parry, D. L. *J. Anal. Atom. Spectrom.* **1997**, *12*, 1277–1280.
318. Jarvis, K. E.; Williams, J. G.; Alcantara, E.; Wills, J. D. *J. Anal. Atom. Spectrom.* **1996**, *11*, 917–922.
319. Kumagai, H.; Yamanaka, M.; Sakai, T.; Yokoyama, T.; Suzuki, T. M.; Suzuki, T. *J. Anal. Atom. Spectrom.* **1998**, *13*, 579–582.
320. McKelvey, B. A.; Orians, K. J. *Mar. Chem.* **1998**, *60*, 245–255.
321. Nelms, S. M.; Greenway, G. M.; Koller, D. *J. Anal. Atom. Spectrom.* **1996**, *11*, 907–912.

322. Santosa, S. J.; Tanaka, S.; Yamanaka, K. *Fresenius J. Anal. Chem.* **1997**, *357*, 1122–1127.
323. Hughes, D. M.; Chakrabarti, C. L.; Goltz, D. M.; Gregoire, D. C.; Sturgeon, R. E.; Byrne, J. P. *Spectrochim. Acta, Part B* **1995**, *50B*, 425–440.
324. Rodushkin, I.; Ruth, T. *J. Anal. Atom. Spectrom.* **1997**, *12*, 1181–1185.
325. Rodushkin, I.; Ruth, T.; Klockare, D. *J. Anal. Atom. Spectrom.* **1998**, *13*, 159–166.
326. Hall, G. E. M., Man. Phys.-Chem. Anal. Aquat. Sediments; Lewis: Boca Raton, FL, 1997, 85–145.
327. Dolan, R.; Van Loon, J.; Templeton, D.; Paudyn, A. *Fresenius J. Anal. Chem.* **1990**, *336*, 99–105.
328. McLaren, J. W.; Beauchemin, D.; Berman, S. S. *J. Anal. Atom. Spectrom.* **1987**, *2*, 277–281.
329. McLaren, J. W.; Beauchemin, D.; Berman, S. S. *Spectrochim. Acta, Part B* **1988**, *43B*, 413–420.
330. Woller, A.; Garraud, H.; Martin, F.; Donard, O. F. X.; Fodor, P. *J. Anal. Atom. Spectrom.* **1997**, *12*, 53–56.
331. Duane, M. J.; Facchetti, S.; Pigozzi, G. *Sci. Total Environ.* **1996**, *177*, 195–214.
332. Liaw, M.-J.; Jiang, S.-J. *J. Anal. Atom. Spectrom.* **1996**, *1*, 555–560.
333. Williams, J. G.; Gray, A. L.; Norman, P.; Ebdon, L. *J. Anal. Atom. Spectrom.* **1987**, *2*, 469–472.
334. Beckwith, P. M. *Proc. Am. Power Conf.* **1995**, *57*, 266–269.
335. Dale, L. S.; Riley, K. W. *Prepr. Pap. Am. Chem. Soc., Div. Fuel Chem.* **1996**, *41*, 756–760.
336. Bettinelli, M.; Spezia, S.; Baroni, U.; Bizzarri, G. *Microchem. J.* **1998**, *59*, 203–218.
337. Chenery, S.; Querol, X.; Fernandez-Turiel, J. L. *Coal Sci. Technol.* **1995**, *24*, 327–330.
338. Lichte, F. E. Elem. Anal. Coal Its By-Prod., Int. Conf. Proc., 2nd, 1992; World Sci; 80–96.
339. Parry, H. G. M.; Ebdon, L. *Anal. Proc. (London)* **1988**, *25*, 69–71.
340. Maenhaut, W.; Roeyset, O.; Vadset, M.; Kauppinen, E. I.; Lind, T. M. *Nucl. Instrum. Methods Phys. Res., Sect. B* **1993**, *B75*, 266–272.
341. Bettinelli, M.; Spezia, S.; Baroni, U.; Bizzari, G. In *Plasma Source Mass Spectrometry*; Holland, G., Tanner, S. D., Eds.; Royal Society of Chemistry: Cambridge, 1997; Vol. 202, 152–158.
342. Adgate, J. L.; Rhoads, G. G.; Lioy, P. J. *Sci. Total Environ.* **1998**, *221*, 171–180.
343. Pettersson, J.; Gustavsson, I. In *Plasma Source Mass Spectrometry*; Royal Society of Chemistry: Cambridge, 1997; Vol. 202, 284–290.
344. Beck, G. L.; Farmer, O. T., III. *J. Anal. Atom. Spectrom.* **1988**, *3*, 771–773.
345. Longerich, H. P.; Fryer, B. J.; Strong, D. Y. *Spectrochim. Acta, Part B* **1987**, *42B*, 101–109.
346. Castle, J. E.; Qiu, J. H. *Corros. Sci.* **1989**, *29*, 605–616.
347. Castle, J. E.; Qiu, J. H. *J. Electrochem. Soc.* **1990**, *137*, 2031–2038.
348. Dufosse, T.; Touron, P. *Forensic Sci. Int.* **1998**, *91*, 197–206.
349. Coedo, A. G.; Dorado, M. T.; Fernandez, B. *J. Anal. Atom. Spectrom.* **1995**, *10*, 859–863.

350. Zopajtic, K.; Rollin, S.; Wernli, B.; Hochstrasser, C.; Ledergerber, G.; Jurcek, P. *J. Anal. Atom. Spectrom.* **1995**, *10*.
351. Ignacio G. A. *J. Anal. Chim. Acta* **1995**, *312*, 57–78.
352. Fordham, P. J.; Gramshaw, J. W.; Castle, L.; Crews, H. M.; Thompson, D.; Parry, S. J.; McCurdy, E. *J. Anal. Atom. Spectrom.* **1995**, *10*, 303–309.
353. Fordham, P. J.; Gramshaw, J. W.; Crews, H. M.; Castle, L. *Food Addit. Contam.* **1995**, *12*, 651–669.
354. Wolf, R. E.; Thomas, C.; Bohlke, A. *Appl. Surf. Sci.* **1998**, *127–129*, 299–303.
355. Berry, E. S.; Paulsen, P. J. *J. Anal. Atom. Spectrom.* **1995**, *67*, 3193–3201.
356. Burkman, D.; Peterson, C.; Zaxxwra, L.; Kopp, R. *Microcontamination* **November 1988**, 57–62.
357. Fabry, L.; Pahlke, S.; Kotz, L.; Toelg, G. *Fresenius J. Anal. Chem.* **1994**, *349*, 260–271.
358. Sushida, K. *J. Mass Spectrom. Soc. Jpn.* **1997**, *45*, 159–174.
359. Tsoupras, G. *Analusis* **1996**, *24*, M23–M28.
360. Denoyer, E. R.; Brueckner, P.; Debrah, E. *At. Spectrosc.* **1995**, *16*, 12–15.
361. Horn, M.; Heumann, K. G. *Fresenius J. Anal. Chem.* **1994**, *350*, 286–292.
362. Heo, Y. W.; Gil, J. I.; Lim, H. B. *Anal. Sci. Technol.* **1998**, *11*, 311–315.
363. Jacksier, T.; T. J. Gluodenis, J.; Thomas, R. J. *Micro (Anal. Technologies)* **1996**.
364. Aleksejczyk, R. A. *MICRO* **1997**, 39.
365. Dahmen, J.; Pfluger, M.; Martin, M.; Rottmann, L.; Weichbrodt, G. *Fresenius J. Anal. Chem.* **1997**, *359*, 410–413.
366. Samuel, L.; Nakagawa, K.; Kimijima, T. *Fresenius J. Anal. Chem.* **1996**, *356*, 31–36.
367. Laly, S.; Nakagawa, K.; Arimura, T.; Kimijima, T. *Spectrochim. Acta, Part B* **1996**, *51B*, 1393–1401.
368. Kawanabe, I.; Murase, G.; Yonezawa, T.; Maeno, M.; Miki, N.; Ohmi, T. *Semicond. Pure Water Chem. Conf.* **1993**, *12*, 27–44.
369. Wildner, H.; Hearn, R. *Fresenius J. Anal. Chem.* **1998**, *360*, 800–803.
370. Streusand, B. J.; Yost, V. E.; Govorchin, S. W.; Fry, R. C.; Padula, F. J.; Hughes, S. K. Tungsten Other Adv. Met. VLSI/ULSI Appl. 5, Proc. Workshop, 6th, 12990; Mater; 251–255.
371. Becker, J. S.; Soman, R. S.; Becker, T.; Panday, V. K.; Dietze, H.-J. *J. Anal. Atom. Spectrom.* **1998**, *13*, 983–987.
372. Matsunaga, H.; Hirate, N.; Nishikida, K. *Bunseki Kagaku* **1989**, *38*, T21–T25.
373. Graf, H. J.; Reynolds, W. L. *Solid State Technol.* **1985**, *28*, 141–147.
374. Rath, H. J.; Neunteufel, R. *Proc. Electrochem. Soc.* **1990**, *90–11*, 335–352.
375. Fucsko, J.; Tan, S. S.; Balazs, M. K. *J. Electrochem. Soc.* **1993**, *140*, 1105–1109.
376. Tan, S. S.; Balazs, M. K.; Fucsko, J. *Semicond. Pure Water Chem. Conf.* **1993**, *12*, 82–92.
377. Fujimoto, K.; Okano, T. *Bunseki Kagaku* **1993**, *42*, T135–T142.
378. Takenaka, M.; Yamada, Y.; Hayashi, M.; Omori, H.; Ito, S.; Okada, A. *Bunseki Kagaku* **1997**, *46*, 743–747.
379. Frost, M. R.; Harrington, W. L.; Downey, D. F.; Walther, S. R. *J. Vac. Sci. Technol., B* **1996**, *14*, 329–335.
380. Lee, J. W.; Pearton, S. J.; Abernathy, C. R.; Vawter, G. A.; Shul, R. J.; Bridges, M. M.; Willison, C. G. *Mater. Res. Soc. Symp. Proc.* **1998**, *483*, 191–196.

381. Hutton, R. C.; Bridenne, M.; Coffre, E.; Marot, Y.; Simondet, F. *J. Anal. Atom. Spectrom.* **1990**, *5*, 463–466.
382. Stanescu, M. S.; Conroy, M. Proc. Inst. Environ. Sci., Contamination Control, 1995; 509–516.
383. Pinkston, T. L., Future Pract. Contam. Control, Proc. Int. Symp. Contam. Control, 11th, 1992; Mech; 535–540.
384. Ulieru, D. G., Proc. SPIE-Int. Soc. Opt. Eng. Metrology, Inspection, and Process Control for Microlithography XII, 1998; SPIE; 721–726.
385. Fucsko, J.; Mikulsky, J.; Balazs, M. K. Semiconductor, Pure Water and Chemical Conference, Santa Clara, CA 1996; SPWCC Show Management, Balazs Analytical Laboratory, Sunnyvale, CA.
386. Donard, O. F. X.; Caruso, J. A. *Spectrochim. Acta Part B* **1998**, *53B*, 157–163.
387. Lobinski, R. *Spectrochim. Acta Part B* **1998**, *53B*.
388. Welz, B. *Spectrochim. Acta Part B* **1998**, *53B*, 169–175.
389. Zoorob, G. K.; McKiernan, J. W.; Caruso, J. A. *Mikrochim. Acta* **1998**, *128*, 145–168.
390. Heitkemper, D. T.; Caruso, J. A. *J. Chromatogr. Libr.* **1991**, *47*, 49–73.
391. Lobifiskia, R.; Adams, F. C. *Spectrochim. Acta, Part B* **1997**, *52B*, 1865–1903.
392. Marin, B.; Valladon, M.; Polve, M.; Monaco, A. *Anal. Chim. Acta* **1997**, *342*, 91–112.
393. Houk, R. S.; Jiang, S. J. *J. Chromatogr. Libr.* **1991**, *47*, 101–122.
394. Larsen, E. H. *Spectrochim. Acta, Part B* **1998**, *53B*, 253–265.
395. Szpunar, J.; Pellerin, P.; Makarov, A.; Doco, T.; Williams, P.; Medina, B.; Lobinski, R. *J. Anal. Atom. Spectrom.* **1998**, *13*, 749–754.
396. Shum, S. C. K.; Houk, R. S. *Anal. Chem.* **1993**, *65*, 2972–2976.
397. Barnes, R. M. *Fresenius J. Anal. Chem.* **1998**, *361*, 246–251.
398. Kinzer, J. A.; Olesik, J. W.; Olesik, S. V. *Anal. Chem.* **1996**, *68*, 3250–3257.
399. Kingston, H. M.; Huo, D.; Lu, Y.; Chalk, S. *Spectrochim. Acta, Part B* **1998**, *53B*, 299–309.
400. Huo, D.; Lu, Y.; Kingston, H. M. *Environ. Sci. Technol.* **1998**, *32*, 3418–3423.
401. Caroli, S.; Torre, F. L.; Petrucci, F.; Violante, N. *Environ. Sci. Pollut. Res. Int.* **1994**, *1*, 205–208.
402. Larsen, E. H.; Pritzl, G.; Hansen, S. H. *J. Anal. Atom. Spectrom.* **1993**, *8*, 1075–1084.
403. Larsen, E. H.; Pritzl, G.; Hansen, S. H. *J. Anal. Atom. Spectrom.* **1993**, *8*, 557–563.
404. Helgesen, H.; Larsen, E. H. *Analyst (Cambridge)* **1998**, *123*, 791–796.
405. Pantsar-Kallio, M.; Manninen, P. K. G. *Sci. Total Environ.* **1997**, *204*, 193–200.
406. Magnuson, M. L.; Creed, J. T.; Brockhoff, C. A. *J. Anal. Atom. Spectrom.* **1997**, *12*, 689–695.
407. Edwards, M.; Patel, S.; McNeill, L.; Chen, H.-W.; Frey, M.; Eaton, A. D.; Antweiler, R. C.; Taylor, H. E. *J. Am. Water Works Assoc.* **1998**, *90*, 103–113.
408. Bricker, T. M.; Houk, R. S. *Spec. Publ. R. Soc. Chem.* **1995**, *163*, 109–116.
409. Gallus, S. M.; Heumann, K. G. *J. Anal. Atom. Spectrom.* **1996**, *11*, 887–892.
410. Crews, H. M.; Clarke, P. A.; Lewis, D. J.; Owen, L. M.; Strutt, P. R.; Izquierdo, A. *J. Anal. Atom. Spectrom.* **1996**, *11*, 1177–1182.
411. Michalke, B.; Schramel, P. *J. Chromatogr., A* **1998**, *807*, 71–80.
412. Pantsar-Kallio, M.; Manninen, P. K. G. *J. Chromatogr., A* **1996**, *750*, 89–95.

413. Posta, J.; Alimonti, A.; Petrucci, F.; Caroli, S. *Anal. Chim. Acta* **1996**, *325*, 185–193.
414. Zoorob, G. K.; Caruso, J. A. *J. Chromatogr., A* **1997**, *773*, 157–162.
415. Haraguchi, H.; Itoh, A.; Kimata, C.; Miwa, H. *Analyst (Cambridge)* **1998**, *123*, 773–778.
416. Shkinev, V. M.; M. Fedorova, O.; Spivakov, B. Y.; Mattusch, J.; Wennrich, R.; Lohse, M. *Anal. Chim. Acta* **1995**, *327*, 167–174.
417. Chakrabarti, C. L.; Lu, Y.; Gregoire, D. C..; Back, M. H.; Schroeder, W. H. *Environ, Sci. Technol.* **1994**, *28*, 1957–1967.
418. Yang, H.-J.; Jiang, S.-J.; Yang, Y.-J.; Hwang, C.-J. *Anal. Chim. Acta* **1995**, *312*, 141–148.
419. Kumar, U. T.; Dorsey, J. G.; Caruso, J. A.; Evans, E. H. *J. Chromatogr.* **1993**, *654*, 261–268.
420. Al-Rashdan, A.; Vela, N. P.; Caruso, J. A.; Heitkemper, D. T. *J. Anal. Atom. Spectrom.* **1992**, *7*, 551–555.
421. Heisterkamp, M.; De Smaele, T.; Candelone, J.-P.; Moens, L.; Dams, R.; Adams, F. C. *J. Anal. Atom. Spectrom.* **1997**, *12*, 1077–1081.
422. Hartshorne, J. A. Speciation by Carbon Phase Liquid Chromatography-Inductively Coupled Plasma Emission Spectrometry and Studies of Aerosol Formation and Characteristics, M. S. Thesis, The Ohio State University, Columbus, 1996.
423. Tan, S. H.; Horlick, G. *Appl. Spectrosc.* **1986**, *40*, 445–460.
424. Boulos, M. I.; Mostaghimi, J.; Proulx, P. In *High Frequency Induction Plasma*; Sherbrooke, 1989.

4
Secondary Ion Mass Spectrometry

Stephen S. Cristy
Lockheed Martin Energy Systems
Oak Ridge, Tennessee

4.1 INTRODUCTION

Secondary ion mass spectrometry (SIMS) is a highly sensitive surface technique for characterizing materials. The procedure is based on the mass analysis of ions created when an impinging beam strikes the surface of a solid (or liquid, in a few special applications). The impinging ion beam, usually referred to as the *primary ion beam*, is generally accelerated to energies between 0.2 and 40 keV. Figure 4.1 shows the essential elements of SIMS.

Because SIMS is a mass analysis technique, it is possible to analyze for all elements and to measure isotopic abundances of those elements having more than one isotope. The removal of surface layers, a few atoms at a time, allows high-resolution depth profiling into the nanometer range. Mass imaging with x-y resolution of 4–8 nm is theoretically possible [1,2] and 20-nm resolution has been achieved [3]. With the application of computerized data collection and analysis, three-dimensional imaging is available. In general the technique is highly sensitive, with detection limits extending to parts per billion in favorable cases. These strengths have led to its application in fields as diverse as genetics, semiconductors, polymers, metallurgy, geology, and catalysts. The following discussion of SIMS is limited to inorganic applications.

4.2 HISTORY

The history of SIMS began with the father of mass spectrometry, J. J. Thomson [4], who reported the emission of "secondary Canalstrahlen" when "primary Canalstrahlen strike against a metal plate." Further studies on secondary ion phe-

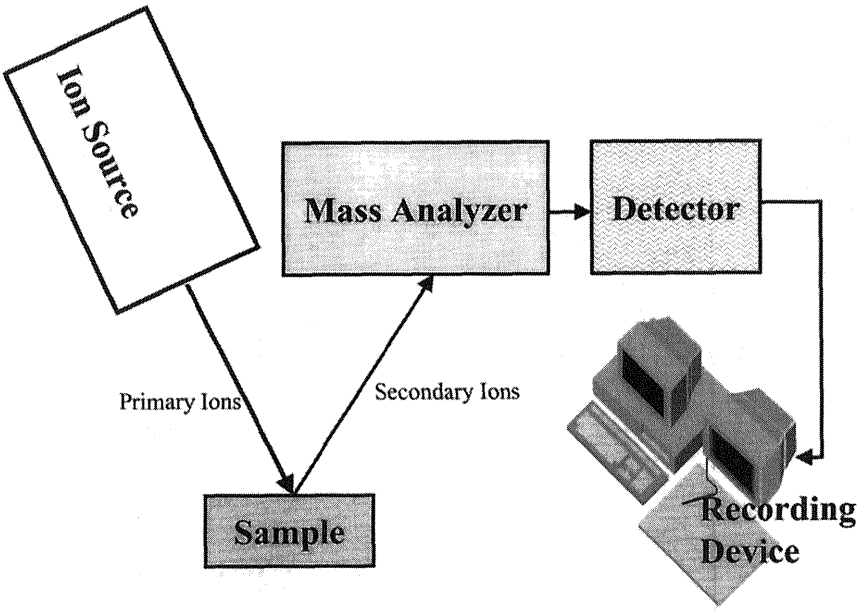

Figure 1 Essential elements of secondary ion mass spectrometry.

nomena were slow in coming. In 1931 Woodcock published the first spectra of negative secondary ions produced by bombarding NaF and CaF_2 with 500 eV Li^+ ions [5]. Sloane and Press [6,7] and Arnot and Beckett [8] in the late 1930s studied negative ion formation resulting from ion bombardment of metal surfaces. Sloane and Press designed a mass spectrograph that accelerated positive ions through a magnetic field onto a target. Negative ions from the target were accelerated back through the same magnetic field to a Faraday cage detector.

In 1949 Herzog and Viehböck reported a novel "ion source for mass spectrography" (Fig. 4.2) [9]. This source provided separate accelerating fields for the primary and secondary ions and thus became the first modern instrument designed specifically for SIMS. The design included acceleration of the positive secondary ions from an equipotential surface through an electric field acting as an electron-optic lens.

Increasing interest in SIMS was evident in the late 1950s with publications by Veksler and Ben'iaminovich [10], Honig [11], Bradley [12], and Stanton [13]. In the early 1960s the technique was further boosted by new developments in instrumentation leading to the first commercial instrument (Geophysics Corporation of America), based on designs by Liebl and Herzog [14]. This instrument [15] used a high brightness source, the duoplasmatron—based on a design by V. Ardenne [16]—and produced a small primary beam spot, ~300 μm diameter. The developers demonstrated the high sensitivity of SIMS by determining limits of detection for a number of elements. This was also the first observation that ion yields vary greatly from element to element [15,17].

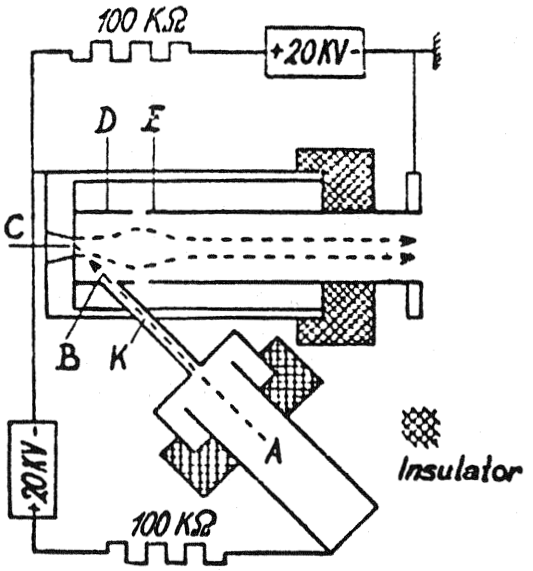

Figure 2 Ion source of Herzog and Viehböck: A, ion source (canal ray tube) at independent potential; B, primary beam; C, sample; D and E, immersion lens, independent potentials. (From Ref. 9.)

In 1962 Castaing and Slodzian [18,19] reported the development of the secondary ion microscope (Fig. 4.3). This was the first microscope to have mass analysis capabilities and the first imaging SIMS instrument. In this instrument, the sputtered ions are collected by an immersion lens, passed through a stigmatic magnetic field, and projected onto an ion-to-electron converter that accelerates the electrons to a fluorescent screen, where a mass analyzed image of the sample surface is formed. Rouberol et al., at Cameca Instruments, developed an improved version of this instrument in 1968 [20,21], the IMS-300 (Fig. 4.4). Unique features of this instrument were the Castaing-Henry magnetic prism [22,23] and an electrostatic mirror for mass and energy filtration that maintained the optical axis of the microscope. The IMS-300 imaged a field of view 165–330 μm with a lateral resolution to about 1 μm Mass resolution of ~1000 could be achieved.

In 1967 Liebl reported the development of the first imaging SIMS instrument based on the principle of focused ion beam scanning [24]. This instrument, the ion microprobe mass analyzer, was produced by Applied Research Laboratories (Fig. 4.5). It used an improved hollow cathode duoplasmatron [25] ion source that eliminated filaments used in earlier sources and allowed stable operation with reactive gases. The primary ion beam was mass analyzed for beam purity and focused in a two-lens column to a spot as small as 2 μm. The secondary ions were accelerated from the sample surface into a double focusing mass spectrometer of Mattauch-Herzog geometry. Both positive and negative secondary ions were de-

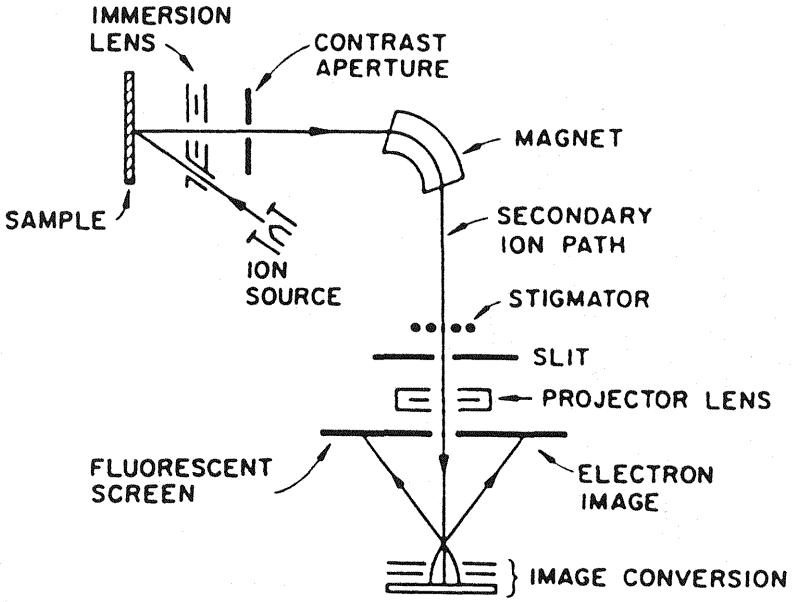

Figure 3 First ion microscope of Castaing and Slodzian. (From Ref. 18.)

tected in a manner similar to that described by Bernhard et al. [26]. Isotope deflector plates (Fig. 4.6) between the secondary magnet and the detector slit allowed rapid sweeping of the secondary ions across the detector slit. Mass resolution was on the order of 600.

In 1965 Long published a proposed ion microprobe analyzer [27]. Long's student, Drummond, began construction and in 1967 published secondary electron micrographs showing 0.5-μm resolution [28] using a primary beam column. This became the basis for the Associated Electrical Industries (AEI) Ltd. SIMS instrument [29]. This instrument utilized AEI's MS702R spark source mass spectrometer for secondary ion analysis and had a mass resolution of ~5000.

Hitachi announced the development of the third commercial microprobe instrument, the ion microprobe analyzer IMA-2 in 1969 [30]. This instrument placed a scintillator close to the sample for secondary electron imaging. A Wien filter, for primary beam mass selection [31], and an electron spray, for charge compensation on insulating samples [32], were added later.

In 1969 Benninghoven introduced the concept of static SIMS for the determination of the chemical composition of the uppermost monolayer of a material [33]. This technique required ultrahigh vacuum conditions and very low primary beam currents, ~10^{-9} A/cm^2, so that less than 1% of the surface was removed dur-

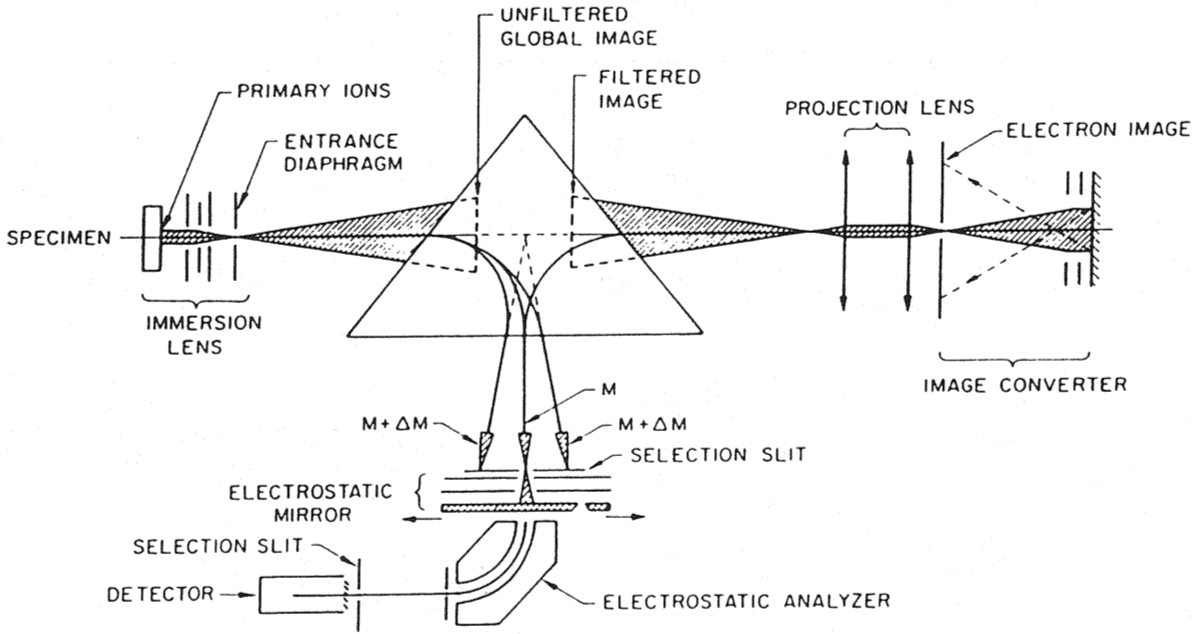

Figure 4 IMS-300, first commercial stigmatic ion microscope. (From Ref. 20.)

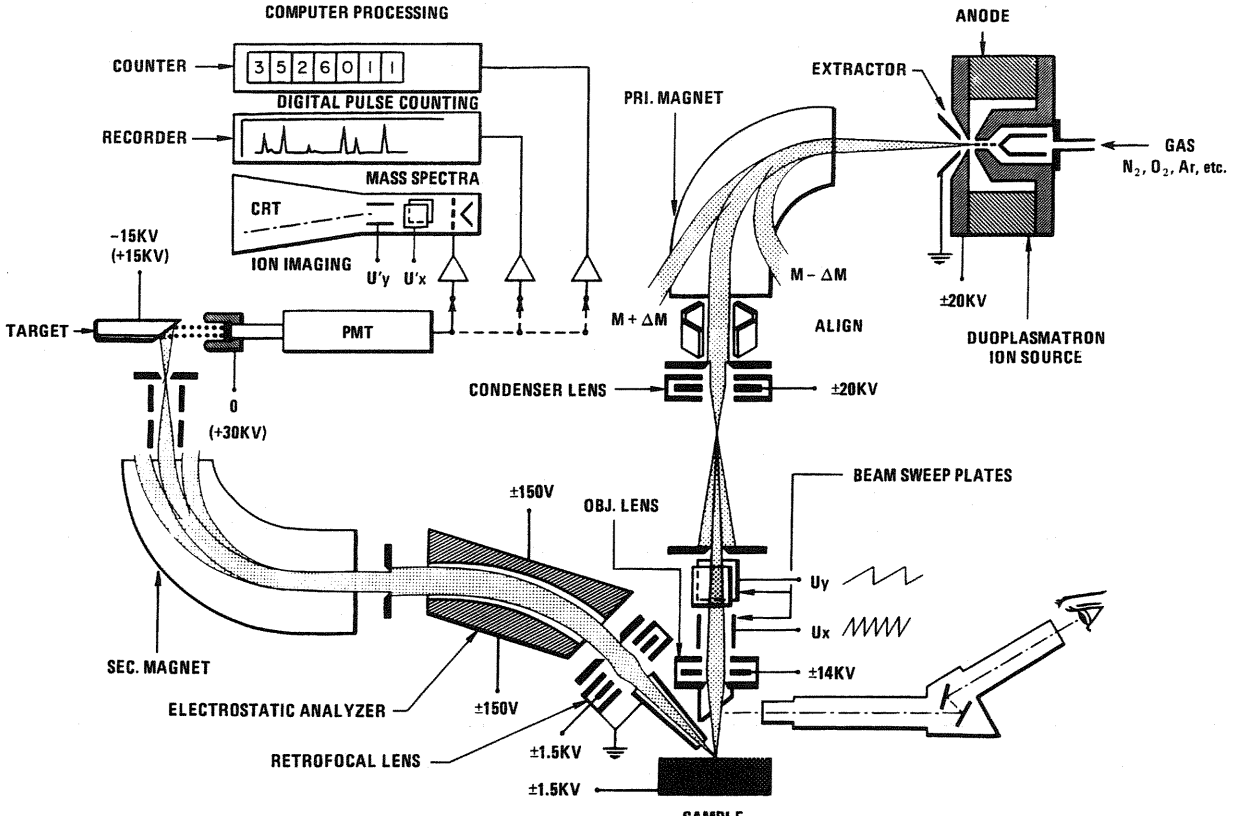

Figure 5 Ion microprobe mass analyzer, first scanning-probe imaging secondary ion mass spectrometer (SIMS). (From Ref. 24.)

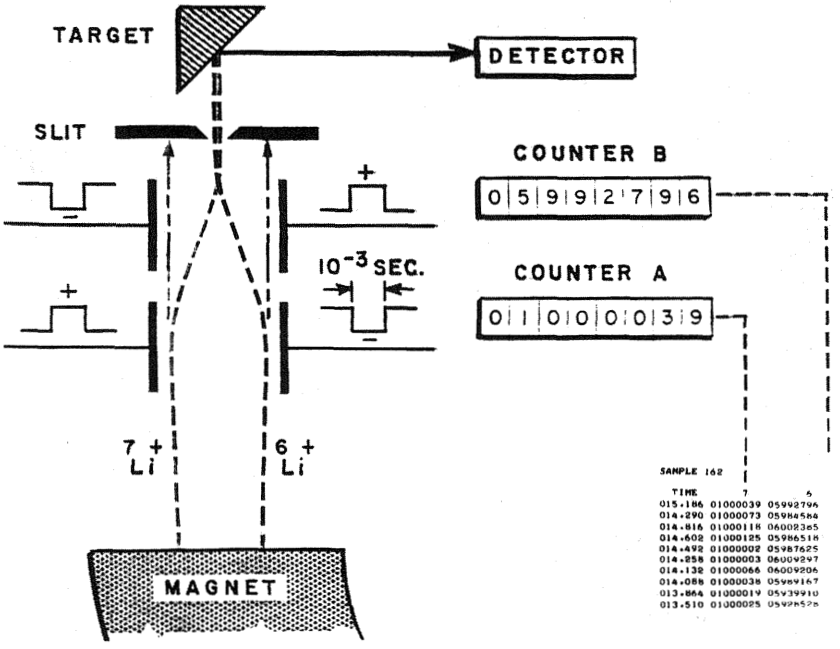

Figure 6 Isotope deflector plates in ion microprobe mass analyzer.

ing the analysis. In 1971 Benninghoven and Loebach described an instrument specially constructed for static SIMS [34] (Fig. 4.7). This instrument utilized turbomolecular pumping of the mass analyzed primary beam column, and ion and titanium sublimation pumping of the target chamber to achieve ultimate vacuum (10^{-11} torr). A quadrupole was used for secondary ion analysis.

In the late 1960s and early 1970s, much effort was focused on development of secondary ion emission models in the hope of placing quantitative SIMS analysis on a good theoretical footing. A brief outline of these models has been given by Schroeer [35]. One extensive model was developed by Andersen and Hinthorn [36–38]; it was based on the concept of a local thermal equilibrium among the atoms, molecules, electrons, and ions formed in the sputtering process. The Saha-Eggert ionization equation [39–41] was used to calculate the equilibrium constant for the secondary ions. Andersen and Hinthorn developed a computer program, Corrections to Applied Research Laboratories Ion Sputtering Mass Analyzers (CARISMA), for quantification based on this model.

Wittmaack developed the first quadrupole-based imaging SIMS instrument in 1975 [42]. This instrument was commercialized in 1976 by Atomika Technis-

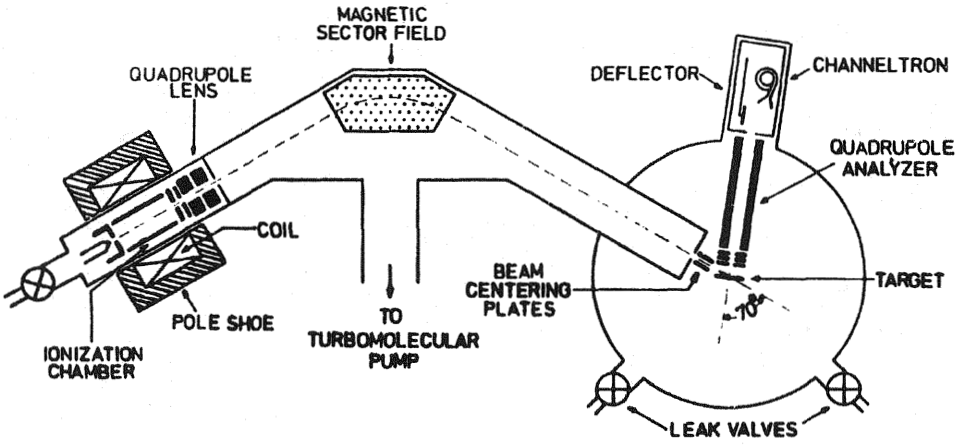

Figure 7 Static secondary ion mass spectrometry (SIMS) instrument of Benninghoven and Loebach. (From Ref. 34.)

che Physik as the Atomika Dynamic In Depth Analyzer (ADIDA) [43] (Fig. 4.8). The primary beam was purified by using a Wien filter. Ion energy was adjustable between 1 and 15 keV.

In 1977 Cameca introduced an improved stigmatic ion microscope, the IMS-3f [44] (Fig. 4.9). This instrument used a double-focusing Nier-Johnson geometry mass spectrometer for secondary ion analysis with mass resolution of ~5000. Transfer optics were designed that tied sensitivity of the instrument to the imaged area. The primary beam could be focused to 1–2 μm. Depth profiling with a dynamic range of seven decades was demonstrated for boron in silicon using beam rastering and field aperturing (to eliminate crater edge effects). This instrument was the first of the f series of Cameca instruments that use the same basic design. The 4f introduced in 1985 provided scanning probe imaging as well as stigmatic microscopic imaging.

An important development for the field was the institution of an international conference dedicated to secondary ion mass spectrometry. Benninghoven hosted the first conference in Muenster, Germany, in September 1977. The proceedings were not published, but led to the formation of an International Organizing Committee and the establishment of the Second International Conference on Secondary Ion Mass Spectrometry (SIMS II) at Stanford University, Stanford, California, on August 27–31, 1979. The proceedings of this conference were published through the efforts of the local organizers [45]. An international conference has been held every 2 years since. The history of the field since 1979 may be followed through these proceedings.

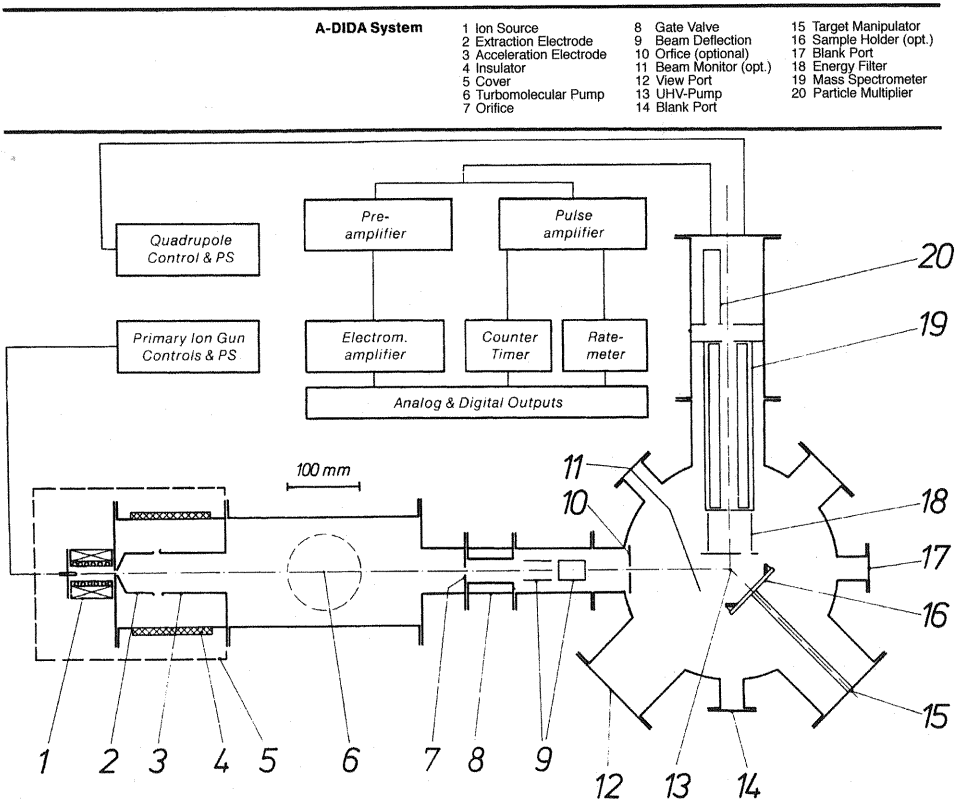

Figure 8 Atomika Dynamic In Depth Analyzer (ADIDA), quadrupole-based-imaging secondary ion mass spectrometry (SIMS) instrument.

The development of high-brightness field desorption liquid metal ion sources allowed submicrometer images to be obtained. In 1975 Krohn and Ringo suggested that a finely focused liquid metal ion source could be used for scanning probe SIMS imaging [46]. In 1979 Seliger et al. demonstrated a liquid gallium ion source with a 100-nm-diameter beam with a current density of 1.5 A/cm^2 [47]. In 1980 Prewitt and Jeffries obtained the first secondary ion images, using a liquid gallium source [48]. A notable application of the liquid metal ion source was the development of a high-image-resolution SIMS instrument by Levi-Setti and coworkers at the University of Chicago [49] (Fig. 4.10). This instrument operated in the 40- to 60-keV range and demonstrated image resolution of 20 nm with a 40-keV In^+ probe [3].

The application of time-of-flight (TOF) mass spectrometers to SIMS was first reported by Chait and Standing in 1981 [50]. Their instrument used a pulsed alkali metal ion source and a linear flight tube. Steffens et al. developed an im-

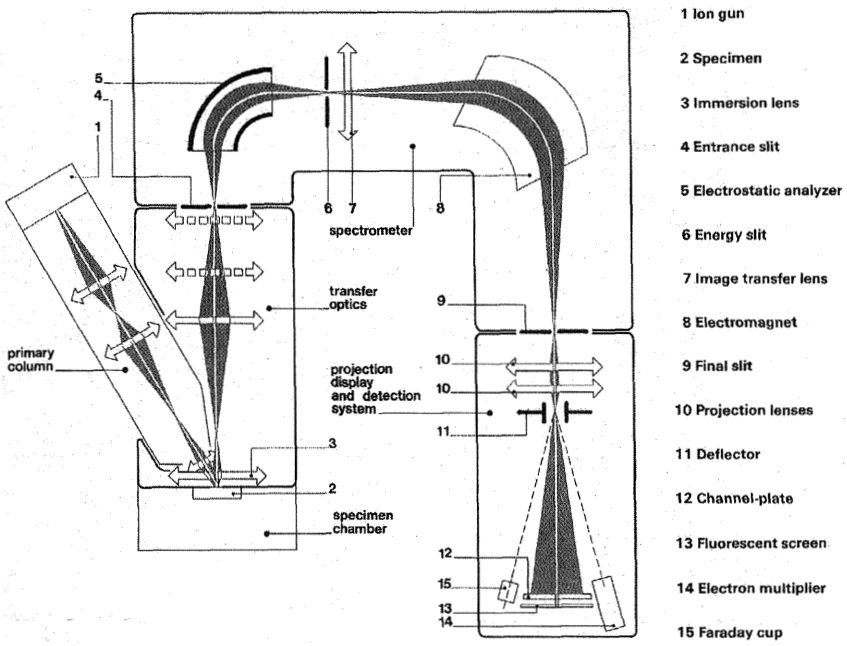

Figure 9 IMS-3f, improved stigmatic ion microscope, Nier-Johnson geometry.

proved TOF for SIMS that had a mass analyzed, pulsed primary beam [51]. This instrument had two linear drift spaces, with a 163° electrostatic sector between, and provided energy focusing, stigmatic imaging of the secondary ions, and a mass resolution of about 750. Niehuis et al. improved the mass resolution of the TOF SIMS to about 7000 (10% valley) by using an ion reflector (reflectron-type analyzer) that reflects the secondary ions at an angle of 177° and provides second-order energy focusing [52] (Fig. 4.11). Waugh et al. [53] and Eccles and Vickerman [54] reported combining a liquid metal ion source with a TOF SIMS for high-spatial-resolution imaging. Schueler et al. developed a stigmatic imaging TOF secondary ion microscope that employed three electrostatic analyzers in the secondary column [55] (Fig. 4.12). A dual-microchannel plate detector was followed by a resistive anode encoder for position information. This instrument achieved a lateral resolution of 1 μm in a 60-μm image field. Mass resolution was ~3000.

In 1982 Compsten et al. [56] reported the design and performance of the Sensitive High-Resolution Ion Micro Probe (SHRIMP I), a large double-focusing SIMS instrument designed specifically for determining the Pb isotopic ratios required for dating zircons using the U-Pb decay systems. To maximize transmittance of the secondary analyzer at high mass resolution (10,000), the designers used a large (1.3-m-radius) cylindrical electrostatic analyzer (an electrostatic

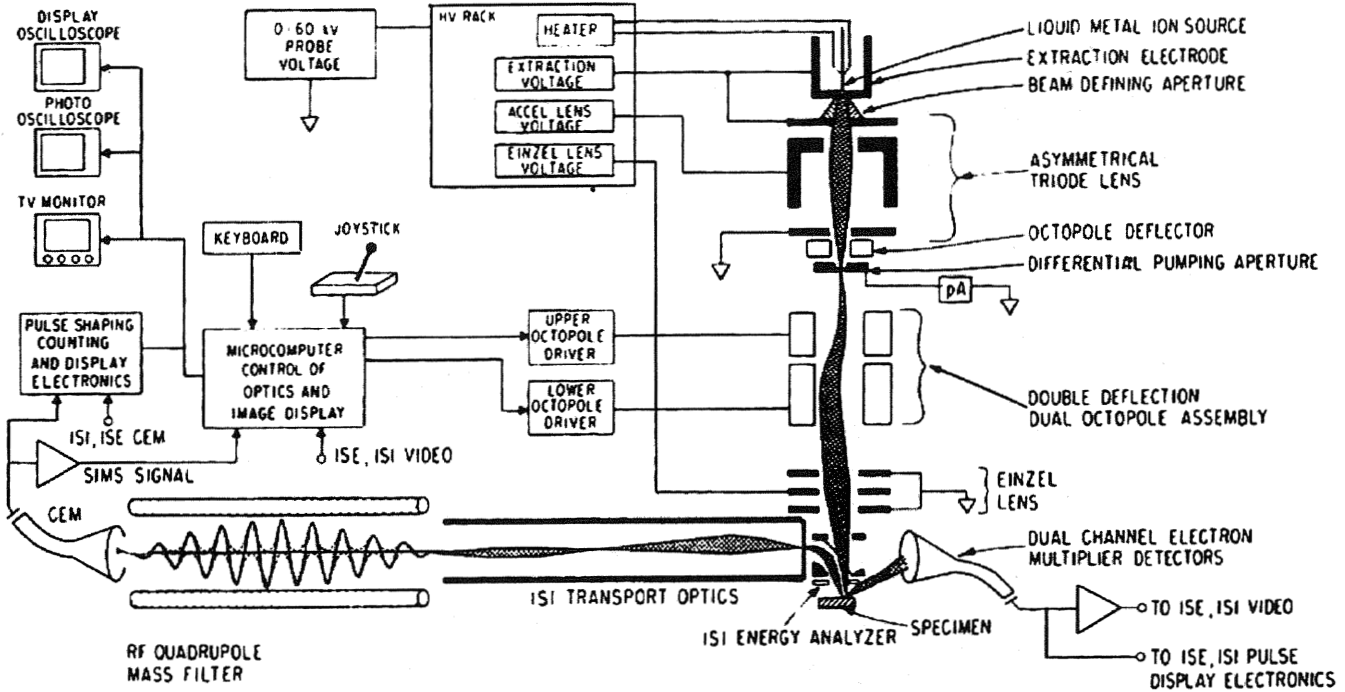

Figure 10 University of Chicago high-spatial-resolution instrument with liquid metal ion source. (From Ref. 49.)

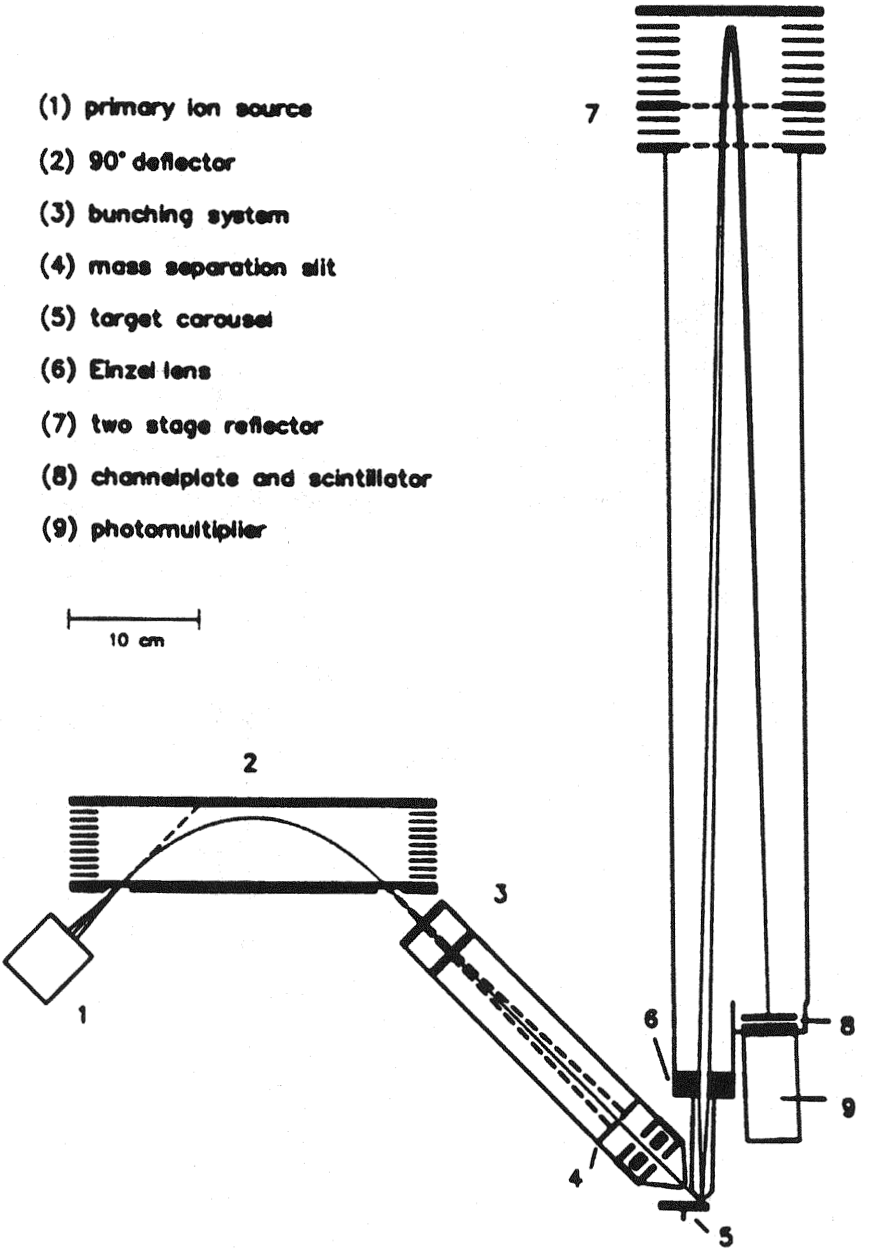

Figure 11 High-mass-resolution time-of-flight instrument with reflectron analyzer. (From Ref. 52.)

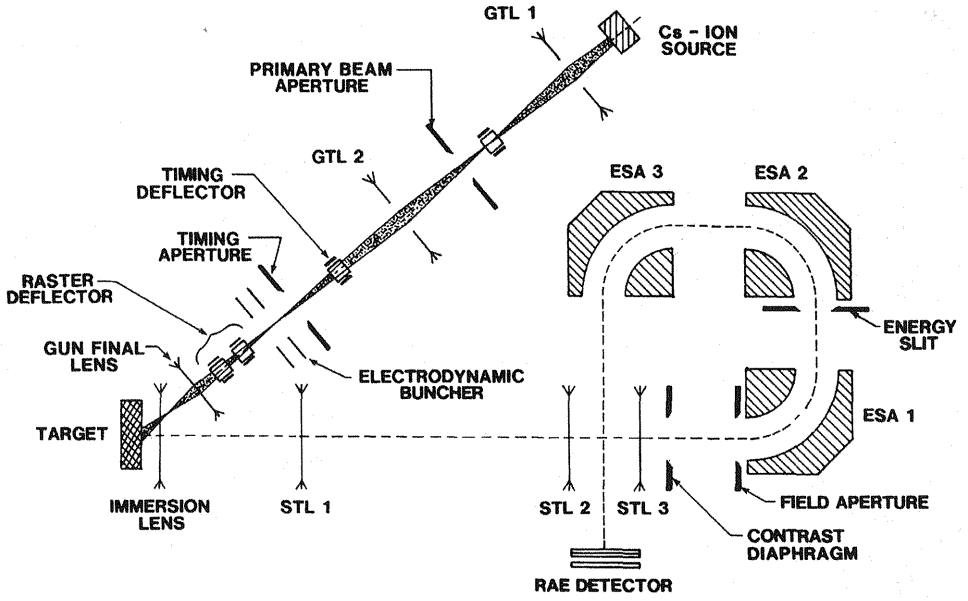

Figure 12 Stigmatic imaging time-of-flight instrument of Schueler et al. (From Ref. 55.)

quadrupole lens) followed by a large 1.0-m-radius magnetic sector (Matsuda geometry [57]). Clement and Compsten [58] added a "Kohler" aperture in the primary column after the first lens in an updated SHRIMP II (Fig. 4.13). The first lens illuminates the Kohler aperture, and the source aperture is imaged on the focal plane of the second lens. The resulting "Kohler" focusing provides a very uniform, flat-bottomed sputter crater without rastering. The size of the Kohler aperture determines the primary beam diameter. A reverse geometry (RG) (magnetic sector before electrostatic) version, SHRIMP RG, was completed in 1998 [59]. The reverse geometry gives four times the mass dispersion and thus better mass resolution. Abundance sensitivity is improved with the mass separation first, but the possibility of simultaneous collection of isotopes is relinquished.

Another large instrument with emphasis on high transmission at high resolution for isotopic measurements in geological applications is the IMS 1270 [60]. This instrument is similar in design to the IMS-3f and other Cameca f-series instruments but is much larger. It operates in either microprobe or microscope mode. Four auxiliary detector assemblies, containing an electron multiplier or Faraday cup plus the central beam primary detector, provide simultaneous detection of five isotopes.

Hillion et al. [61] reported the development of the Cameca NanoSIMS 50, a commercial instrument for the analysis of submicrometer features. This instru-

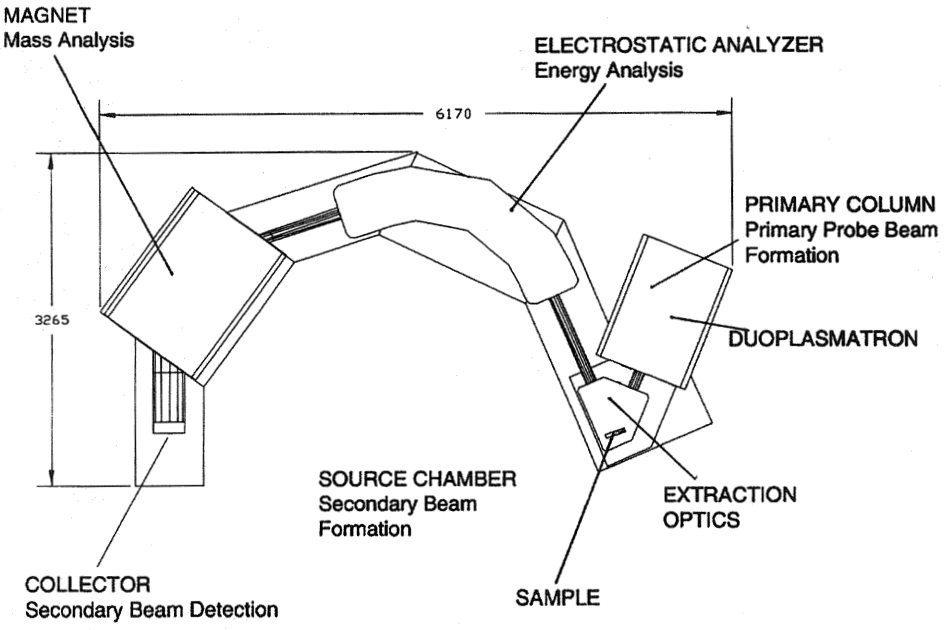

Figure 13 Sensitive high-resolution ion micro probe (SHRIMP II) high-mass-resolution, high-sensitivity instrument designed for isotopic geochronology, dimensions in millimeters.

ment, based on an original design by G. Slodzian, features 50-nm resolution with a Cs source (Fig. 4.14). The design incorporates normal incident primary ions and normal extraction of secondary ions (coaxial) to optimize objective lens performance and ion collection. This requires that primary and secondary ions be of opposite polarity. Thus, Cs^+ primary is used to produce negative secondary ions, and O^- primary is used to produce positive secondary ions. The analyzer is based on the Mattauch-Herzog geometry and includes five movable detectors for parallel ion detection and simultaneous secondary electron imaging.

In response to the necessity for SIMS to provide profiling with resolutions approaching or exceeding 1 nm, Dowsett et al. developed an ultralow-energy floating ion gun (FLIG) [62] for semiconductor processing. This gun was designed to maintain high profiling currents with energies between 200 eV and 5 keV (Fig. 4.15). Depth resolution of 1 nm and currents >1 μA at 1 keV and >200 nA at 250 eV on spot sizes of 100 μm were reported; a 30-μm probe size was achieved.

Some good books, reviews, and historical perspectives of the field of secondary ion mass spectrometry have been published, including *Secondary Ion Mass Spectrometry*, proceedings of a workshop held at the National Bureau of Standards in Gaithersburg, Maryland, September 16–18, 1974 [63]. The proceedings include

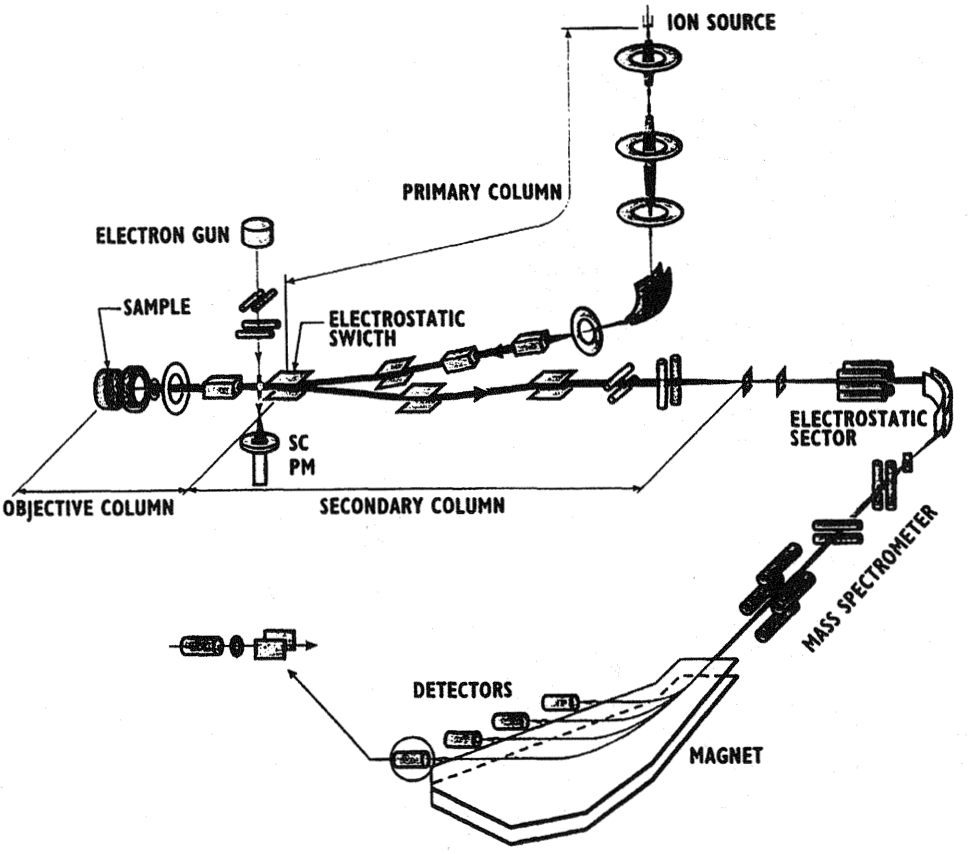

Figure 14 Ion optical system of the NanoSIMS 50 high-spatial-resolution, high-mass-resolution scanning-probe instrument. (From Ref. 61.)

reviews of instrumentation by H. Liebl and of optics by G. Slodzian and discussions of quantification and applications. A good introduction to SIMS was written by J. A. McHugh in *Methods of Surface Analysis*, edited by A. W. Czanderna [64]. R. E. Honig gives a personal view of the development of SIMS in the SIMS V proceedings [65]. An excellent review, *Mass Analyzed Secondary Ion Microscopy* by Bernius and Morrison, appeared in *Review of Scienti c Instruments* in 1987 [66]. A comprehensive text, *Secondary Ion Mass Spectrometry: Basic Concepts, Instrumental Aspects, Applications and Trends*, by Benninghoven et al. also appeared in 1987 [67]. In 1989, two additional textbooks on SIMS were published: *Secondary Ion Mass Spectrometry: Principles and Applications*, edited by Vickerman et al., which is especially strong in the area of static SIMS [68], and *Secondary Ion*

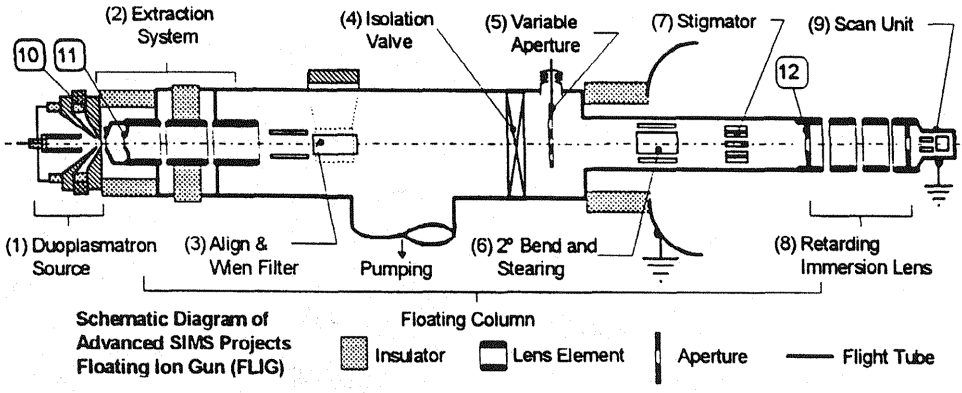

Figure 15 Floating ion gun for low-energy depth profiling [62]: (10), extraction aperture; (11), extraction collimating aperture; (12), objective aperture.

Mass Spectrometry: A Practical Handbook for Depth Pro ling and Bulk Impurity Analysis, by Wilson et al. [69]. This book is focused on profiling and quantitative analysis primarily in semiconductors and contains many tables of relative sensitivity factor (RSF) data, profile illustrations, and SIMS spectra.

4.3 THEORY

4.3.1 Ion Sputtering/Depth Profiling

When an ion beam in the energy range of 0.2–40 keV strikes a solid surface, it may collide with a surface atom and rebound, but this is a low-probability event. Most ions penetrate the surface, lose their energy through a series of collisions with lattice atoms, and come to rest in the solid. The atoms in the solid, energized by the primary collisions, in turn collide with other atoms, creating a zone of damage and atomic mixing in the solid. A portion of the collisional energy is directed to the surface and causes atoms and molecules to be ejected from the surface. This process is known as *sputtering*. In the sputtering process, a fraction of the surface atoms are ionized. The ions that are created and accelerated from the surface successfully are used as the basis of the SIMS analysis. Figure 4.16 illustrates the basic sputtering process. Sigmund has described many features of the sputtering process with a collisional cascade model [70]. This model, however, does not predict ion yields.

The atomic sputtering yields determine the rate at which material is removed and thus determines the depth profiling rates. These yields are a function of the sample, the bombarding ion, and the energy and angle of the bombarding ion with respect to the sample. A simple model developed by Rol et al. [71] illustrates the general sputtering parameters:

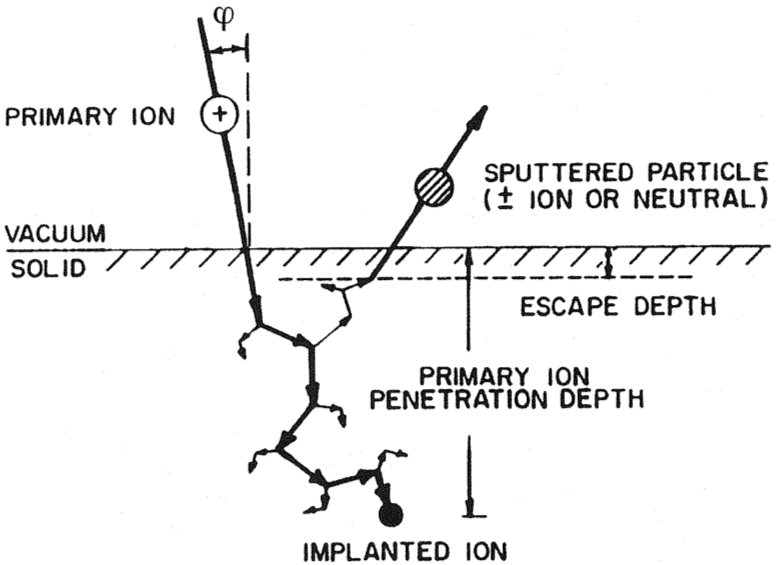

Figure 16 Representation of ion-solid interaction and sputtering process. (From Ref. 64.)

$$S_{(\text{atoms/ion})} = ck(\pi R^2 n_0 / \cos \varphi)[M_1 M_2/(M_1 + M_2)^2]E_0 \tag{4.1}$$

where S is the atom yield, c is a proportionality constant, k is a negative exponential function of the binding energy of the surface atoms [72], R is the collision radius calculated by using a rigid sphere model, n_0 is the number of lattice atoms per unit volume, φ is the angle between the sample normal and the direction of incidence, M_1 and M_2 are the masses of the bombarding and target atoms, respectively, and E_0 is the energy of the bombarding ion. The term $(\pi R^2 n_0)$ is the reciprocal of the mean free path of the ion in the solid. This equation illustrates the effects of incidence angle, mass and size of the target and bombarding ions, surface binding energy, and energy of the incident ions. It also explains the finding that sputtering rates are minimized for bombarding directions in which the crystal is transparent (the mean free path for the ion is the greatest), and maximized in the directions in which crystal density is greatest (mean free path for the ion is least). The equation was developed for the energy range 5–25 keV. At higher energies the bombarding ions begin to go so deep into the solid that the fraction of energy available at the surface for sputtering is reduced. The applicability of this equation is demonstrated by comparison of theoretical sputtering yields and experimental sputtering yields measured by using noble gas ions to sputter gold [73] (Fig. 4.17). In general, sputtering yields for a given bombarding ion vary by factors up to about 100 and in a periodic fashion, as shown by the data of Almén and Bruce [72] and Wilson and Brewer [74] in Fig. 4.18 for 45 keV Kr^+ sputtering.

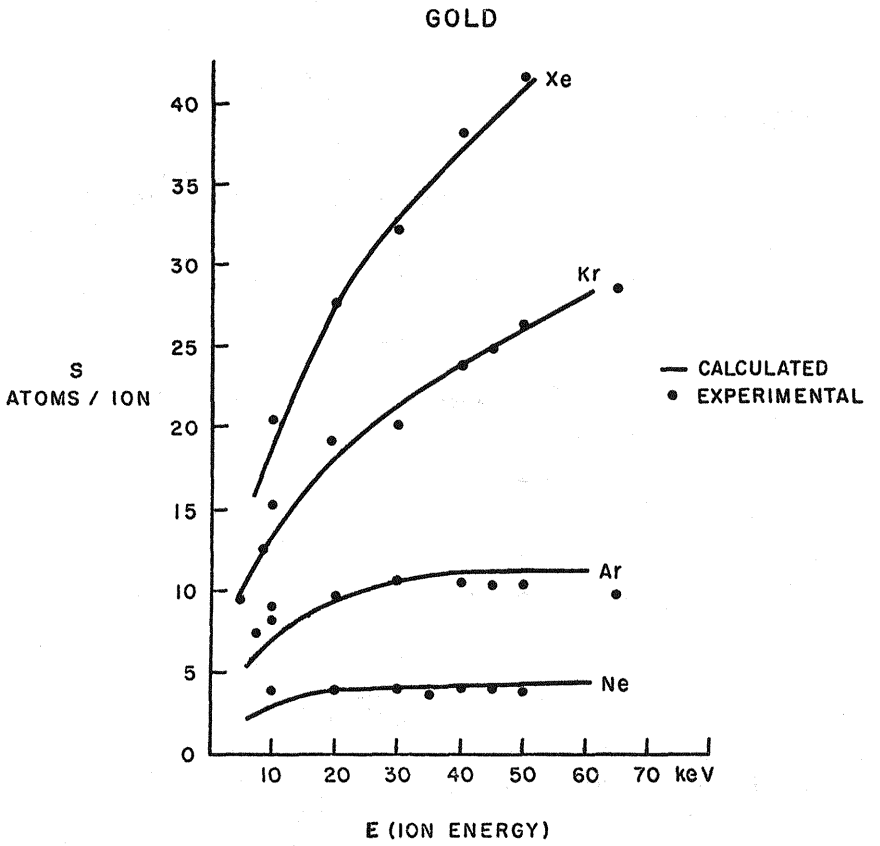

Figure 17 Comparisons of gold sputter yields as a function of mass of bombarding ion with calculations of Rol's collision model. (From Ref. 73.)

The depth of penetration of the primary ion and the width of the damage zone in the solid increase with the energy of the primary ion. Thus, in profiling, in which depth resolution is important, lower-energy ion beams are used to keep the damage zone as narrow as practicable. Figure 4.19 shows the effect of primary ion energy on profile resolution [75]. Depth resolution also depends on the angle of impact. Impact angles are normally quoted as degrees off normal incidence. Ion beams striking at larger angles penetrate to shallower depths and, thus, provide greater depth resolution.

A number of effects lead to loss of profile depth resolution. The effect of crystallite orientation on sputtering rate is shown in Fig. 4.20, in which 10 keV Kr^+ ions at 50° incidence were used to sputter polycrystalline iron [76]. This ion etching may be useful to bring out grain structure but leads to loss of depth resolution

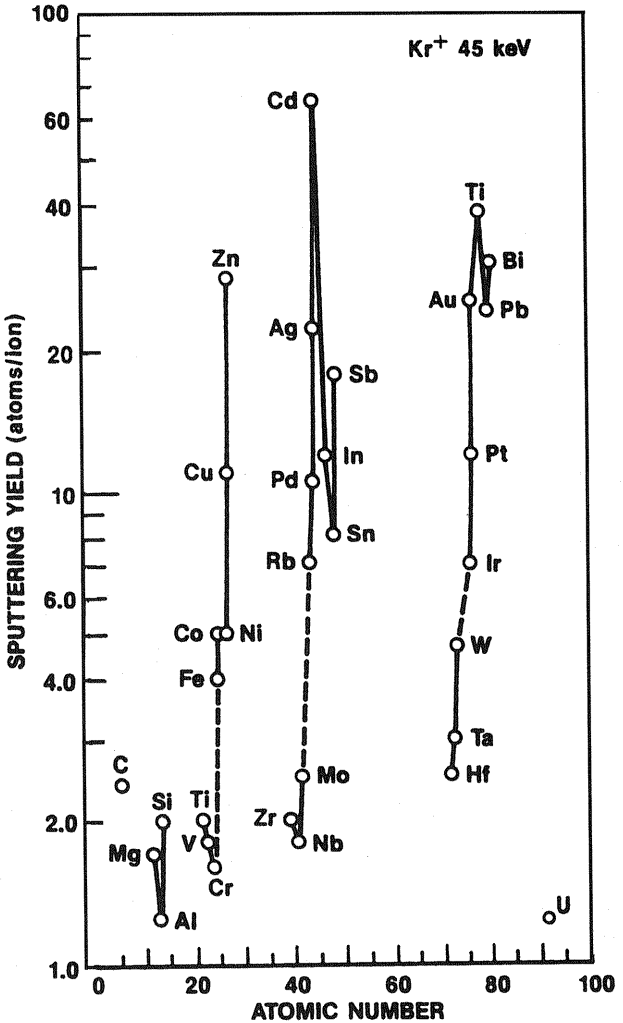

Figure 18 Periodic relationship observed for sputtering yields. (From Ref. 71 and 74.)

when profiling a field containing more than one grain. With extensive sputtering on crystalline surfaces, ripples, cones, and other features that can have deleterious effects on depth resolution are often created. Figure 4.21 shows SEM micrographs of ripples formed in (100) Si after sputtering with 6 keV O_2^+ to depths of 2.1, 2.8, and 4.3 μm [77]. Tsunoyama et al. [78] found that the development of surface structure when sputtering with O_2^+ was related to the binding energy, B_{MO}, of the monoxide MO for the target atom M. Where B_{MO} was high, for example, Si and

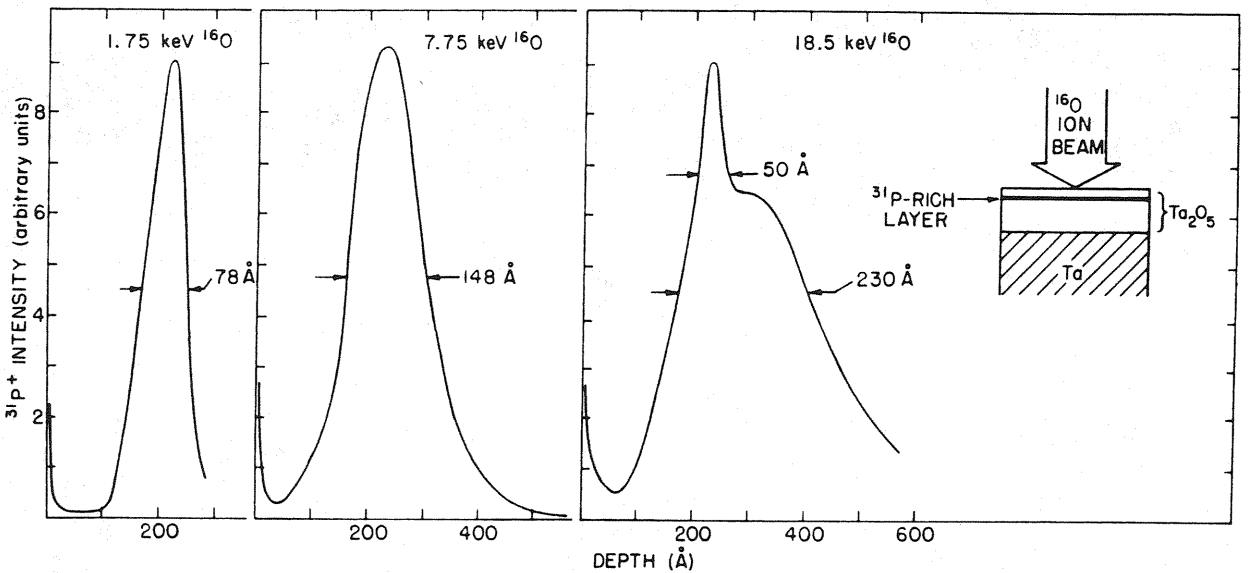

Figure 19 The effect of sputtering ion energy on depth profile shape. A subsurface phosphorus-rich layer in Ta_2O_5 was sputtered by using ^{16}O at normal incidence with energies of 1.75 keV, 7.75 keV, and 18.5 keV. (From Ref. 75.)

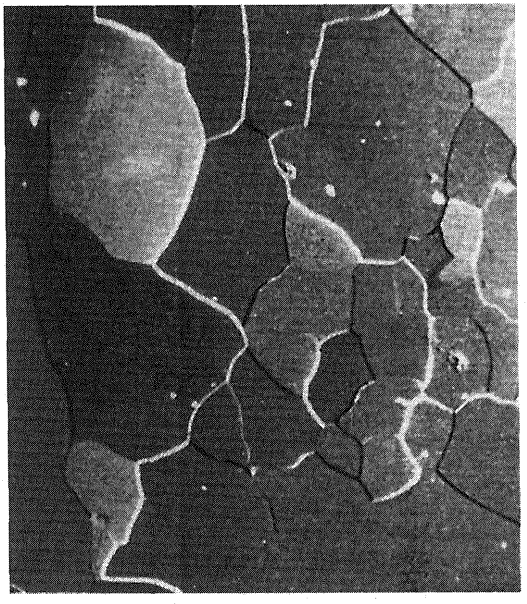

Figure 20 Surface topography effects on polycrystalline iron surface after sputtering with 10 keV Kr^+ ions at 50° incidence. (From Ref. 76.)

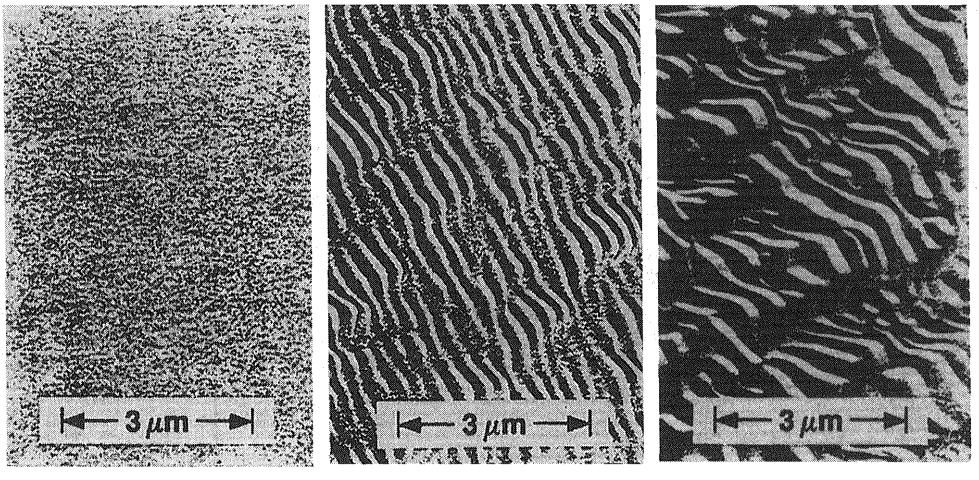

Figure 21 Sputter crater bottoms in (100) Si after 6 keV O_2^+ sputtering to different depths: (left) 2.1 μm; (center) 2.8 μm; (right) 4.3 μm. (From Ref. 77.)

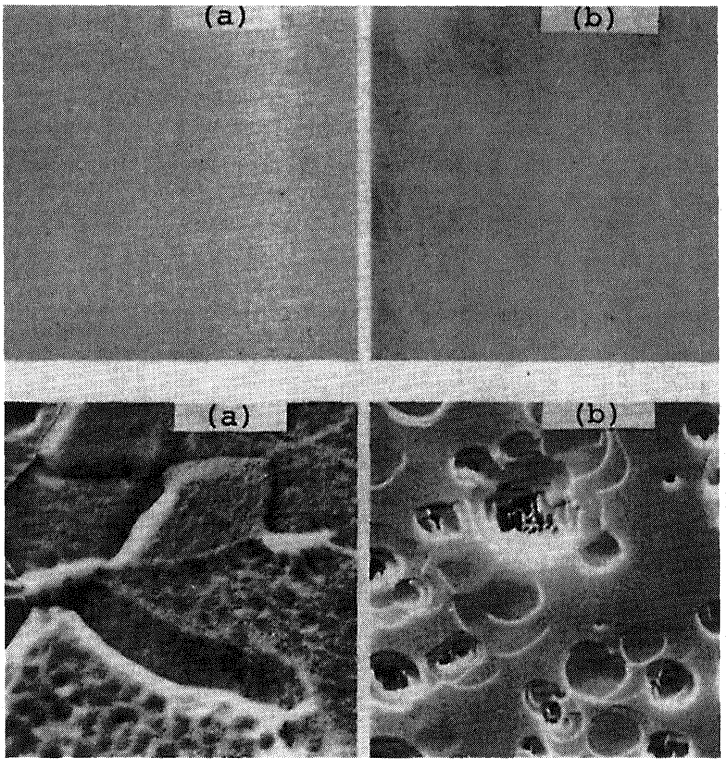

Figure 22 Surface topography on 20 keV O_2^+ bombarded surfaces: a (above), silicon (high B_{MO}); b (above), germanium (high B_{MO}); a (below), tin (low B_{MO}); b (below), aluminum (low B_{MO}). Doses ~1 × 10^{19} ions/cm^2. (From Ref. 78.)

Ge at 8.3 and 6.8 eV, respectively, the ion-bombarded area was quite uniform, but as B_{MO} decreased, more surface topography developed. Their SEM images of Si, Ge, Sn, and Al after sputtering with 20 keV O_2^+ are shown in Fig. 4.22. Rotation of the sample (sometimes called *Zalar rotation*) [79] is commonly used with off normal incidence sputtering to minimize the formation of sputter-induced topography.

Surface roughness, primary beam current density uniformity, and primary current stability are extrinsic factors that affect the flatness of the advancing crater bottom and thus depth resolution. Usually electronic or mechanical aperturing is used to limit collection of secondary ions to the central, flattest portion of the sputter crater, thereby reducing edge effects and maximizing depth resolution. Electronic aperturing is used with microprobe instruments in which the primary beam is deflected in a raster pattern. The electronic aperture allows counting to take place

only when the beam is located within a preselected portion of the raster. Mechanical aperturing is used with microscope imaging instruments.

A neutral component of the primary beam is formed when the primary ions collide with residual gas in the primary beam column. This component is minimized by designing the primary column for rapid pumping to maintain ultrahigh-vacuum conditions. The neutral component is not focused and thus sputters surfaces around the crater formed by the ion beam. If elements at the surface are being profiled, the continued presence of these elements, due to the neutral beam sputtering, leads to errors in the profile and limits the dynamic range of the profile. Coating the surface with a thin layer of a nonprofiled element reduces the effect.

Gross discrepancies from actual in-depth distribution can result from electrical or chemical potential gradients produced as a result of the ion bombardment. Electrical gradients that are created by charge buildup of imperfectly compensated insulators can have dramatic effects, as shown in Fig. 4.23, where sodium is profiled in silicon dioxide on silicon [80]. With positive ion bombardment the insulator is charged positively, driving the electropositive sodium into the matrix. When the conducting silicon substrate was reached, the charging field collapsed and a large spike of sodium was encountered as the sodium lost its mobility. Gibbsian, or chemical potential, segregation effects have been demonstrated by profiling a number of oxides with widely varying heats of formation in a silicon matrix (with and without an oxygen leak, Fig. 4.24) [81]. For elements with heats of formation less than that of silicon, the decay length with the oxygen leak increased as silicon segregated to the surface to form the oxide. For elements with heats of formation greater than that of silicon, the decay length shortened as they preferentially segregated to the surface.

4.3.2 Secondary Ion Formation and Quantitative Analysis

The formation of secondary ions in the sputtering process depends strongly on the electronic structure of the target matrix and the ionization potential of the atoms (positive ions) or the electron affinity (negative ions). In the sputtering process, collisions between the bombarding ions and the target atoms cause excitation of the atoms, which may de-excite through photon or electron emission. The probability of electron emission depends upon the ionization potential; thus, alkali and alkaline earth metals with low ionization potentials form positive ions with much higher probability than elements with higher ionization potentials. In the sputtering process, electrons are also liberated and negative ions are formed by electron capture. Thus, the halogens and group VI A elements preferentially form negative ions. These periodic trends may be noted in the positive and negative secondary ion yields of a large number of elements [82] (Figs. 4.25 and 4.26). The observed intensity is dependent not only on the number of ions generated but also on the survivability of the ion as it leaves the surface. For positive ions, survivability de-

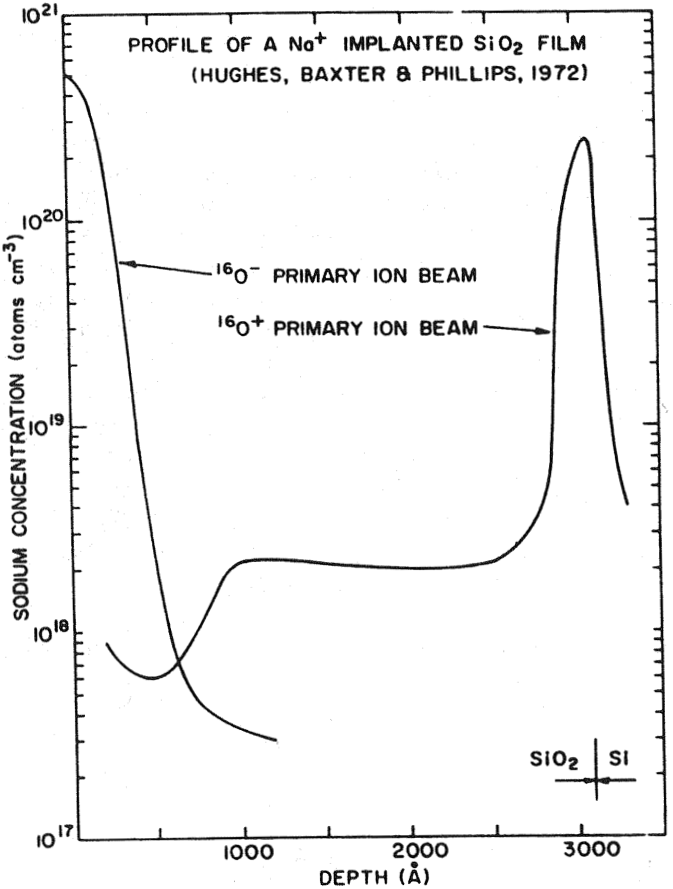

Figure 23 Profile of sodium in SiO_2 acquired with $^{16}O^+$ primary beam shows effect of charge-driven diffusion. Profile acquired with $^{16}O^-$ primary beam shows normal profile. (From Ref. 80.)

creases with increasing availability of free electrons. Therefore, targets with low work function surfaces, such as gold, have very low positive secondary ion yields. The work function of metal surfaces can be increased and, thus, the positive secondary ion yields improved by the chemisorption of reactive electronegative gases or by the use of a reactive gas ion beam to form strongly bonded compounds in the target. Conversely, negative secondary ion yields are enhanced by increasing the availability of free electrons, by using a very electropositive bombarding ion such as Cs^+. As can be observed in Figs. 4.25 and 4.26, high-sensitivity analyses for a

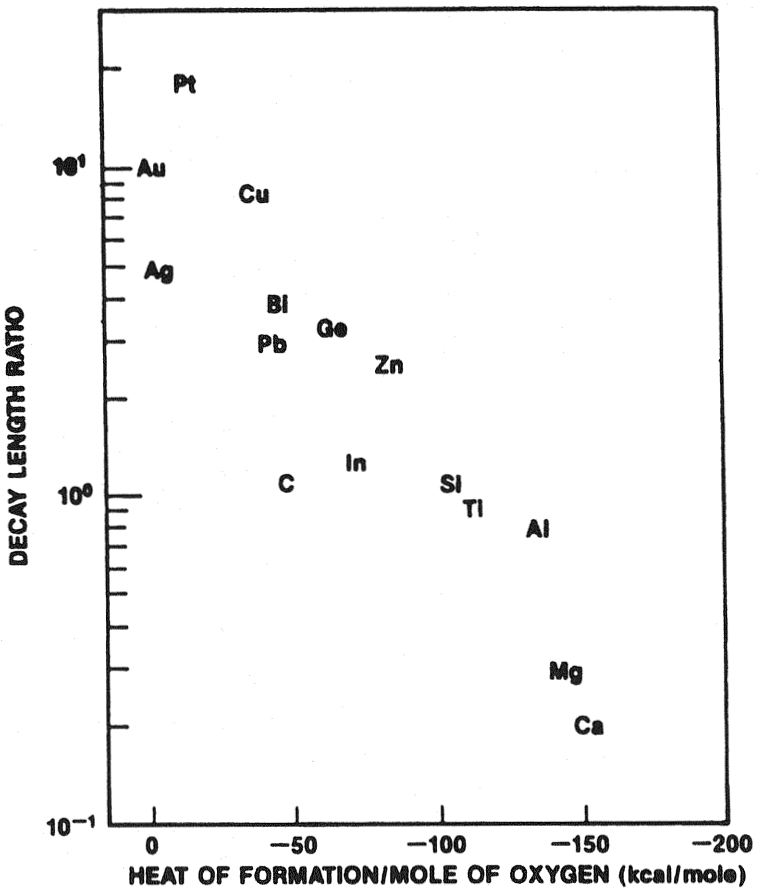

Figure 24 Gibbsean segregation effects illustrated by ratio of profile decay length with an oxygen leak to that without an oxygen leak plotted versus oxide heat of formation. The substrate was silicon, and the primary ion was Ar^+. (From Ref. 81.)

large number of elements may be made by proper choice of bombarding ion and polarity of the secondary ion.

Velocity of the secondary positive ion also has an effect on its survivability. A high-velocity ion is more likely to escape the surface without being neutralized than is a slower one. This effect is illustrated by the fact that in isotopic measurements higher-mass ions have a lower probability of detection. This isotopic mass effect, usually called *mass discrimination*, can be compounded by instrument design effects.

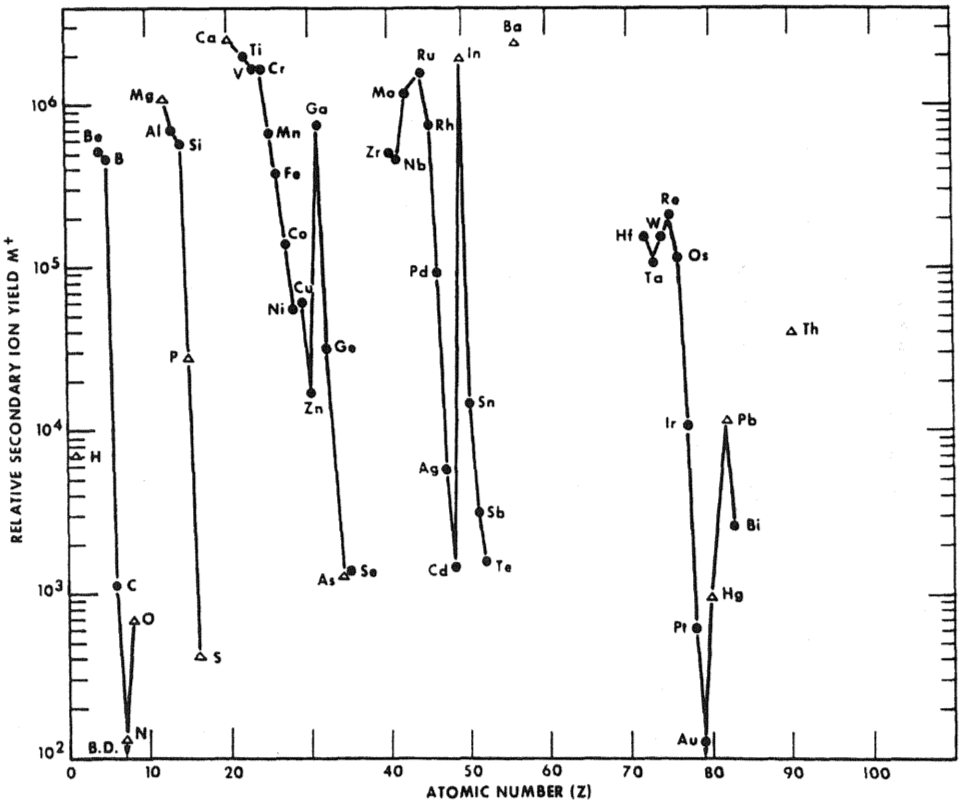

Figure 25 Relative secondary positive ion yield (M^+) vs. atomic number of secondary ion. O^- primary beam. •, pure element; △, compound. (From Ref. 82.)

The use of reactive gases for sputtering was a great advance for SIMS. When sputtering with an inert gas beam, such as Ar^+, an exponential fall in the signal is observed as the oxide layer is removed. Figure 4.27 compares the profiles experienced by sputtering aluminum with Ar^+ and with O_2^+ [83]. With oxygen bombardment, a small drop in the signal is observed between the surface oxide and the depth where the implanted oxygen reaches its equilibrium concentration. The high and stable secondary ion signal obtained at this depth makes reactive gases, and in particular oxygen, the bombardment gas of choice for most dynamic secondary ion mass analyses. With static SIMS analysis, the primary ion current is kept low enough to prevent significant change in the surface composition; thus, noble gas ions such as Ar^+ are still used.

The typical SIMS mass spectrum is dominated by singly charged atomic and molecular ions. Doubly charged ions are typically two or more orders of magni-

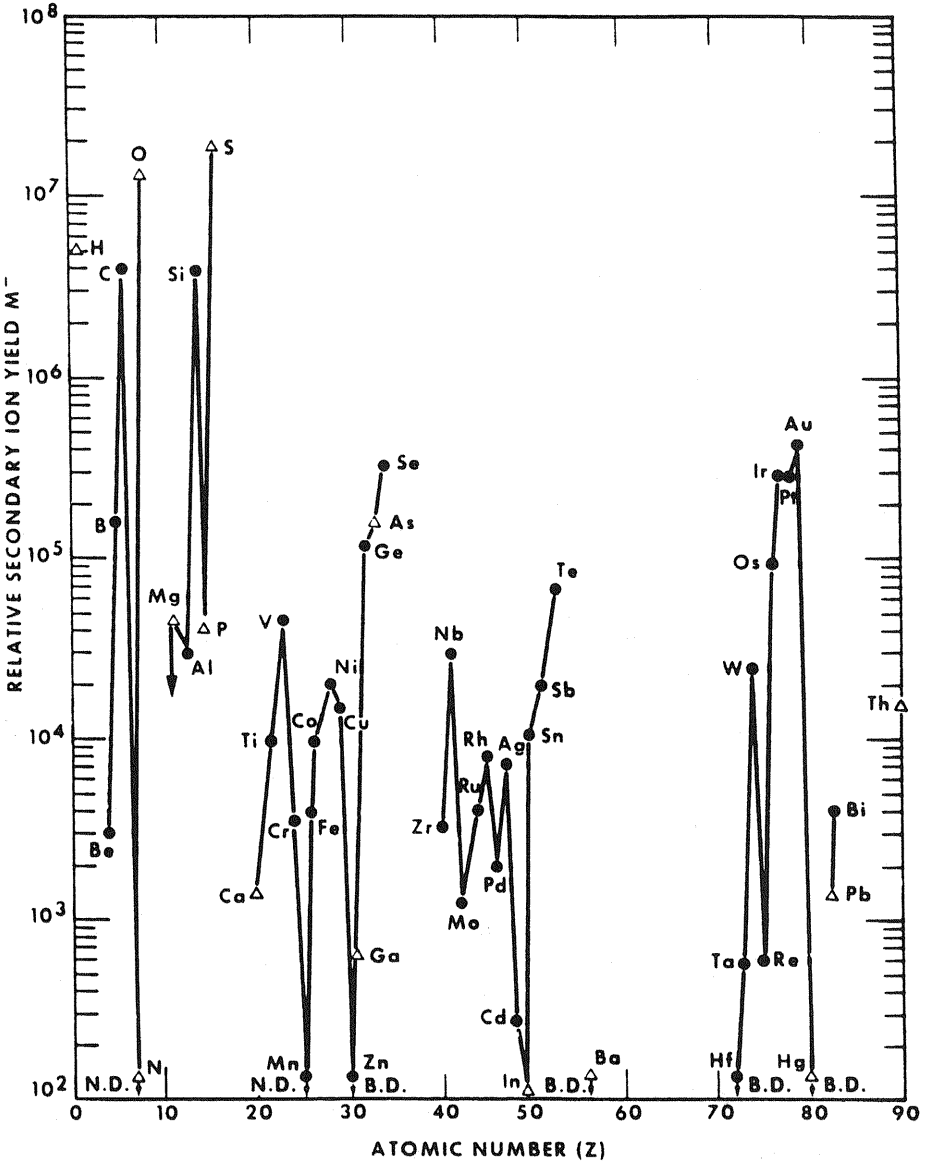

Figure 26 Relative secondary negative ion yield (M^-) vs. atomic number of secondary ion. Cs^+ primary beam. •, pure element; △, compound; B.D., barely detectable; N.D., not detected. (From Ref. 82.)

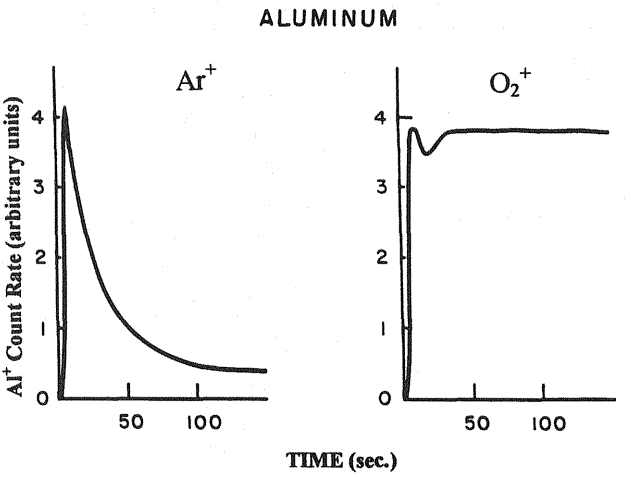

Figure 27 Comparison of Al^+ profiles on aluminum using Ar^+ or O_2^+ primary beam. Beam current 4 nA, beam energy 11 keV. (From Ref. 83.)

tude less abundant. Doubly charged ions of the group II elements, however, may exceed this abundance rule by an order of magnitude. Dimers, trimers, and higher-order molecular ions diminish as the order increases. Figure 4.28 illustrates a typical positive SIMS mass spectrum of 347 stainless steel and a negative SIMS mass spectrum of 304 stainless steel. Both spectra were generated by using an $^{16}O^-$ ion beam [84]. The energy bandpass of the SIMS instrument has an effect on the abundance of molecular ions in the mass spectrum because molecular ions have narrower energy distributions than monatomic ions (Fig. 4.29) [85]. Al^+ is seen to have a measurable number of ions with energies beyond 500 eV, whereas Al_2^+ and Al_3^+ have diminished six orders of magnitude at 300 eV and 100 eV, respectively. By rejecting ions with energies of less than 400 eV, this effect was used to discriminate against cluster ions and successfully profile $^{31}P^-$ in silicon without interference from $^{30}SiH^-$ [86]. This method is called *energy ltering*. Alternatively, and perhaps more commonly, high-mass resolution is used to separate isobaric atomic ions and cluster ions.

The raw SIMS mass spectrum provides a means for qualitatively identifying the chemical composition of the atomic layers near the surface of the sample. Molecular structure and atomic bonding information from the spectra are obtained when the primary ion dose is kept low (static SIMS) [33]. However, quantitative analysis is an important goal of any analytical technique. In SIMS, quantitative analysis is complicated by the fact that elemental ion yields range over several orders of magnitude and are sensitive to matrix, crystallographic orientation, surface adsorbed species, and bombarding ion and angle of incidence. As a result, many

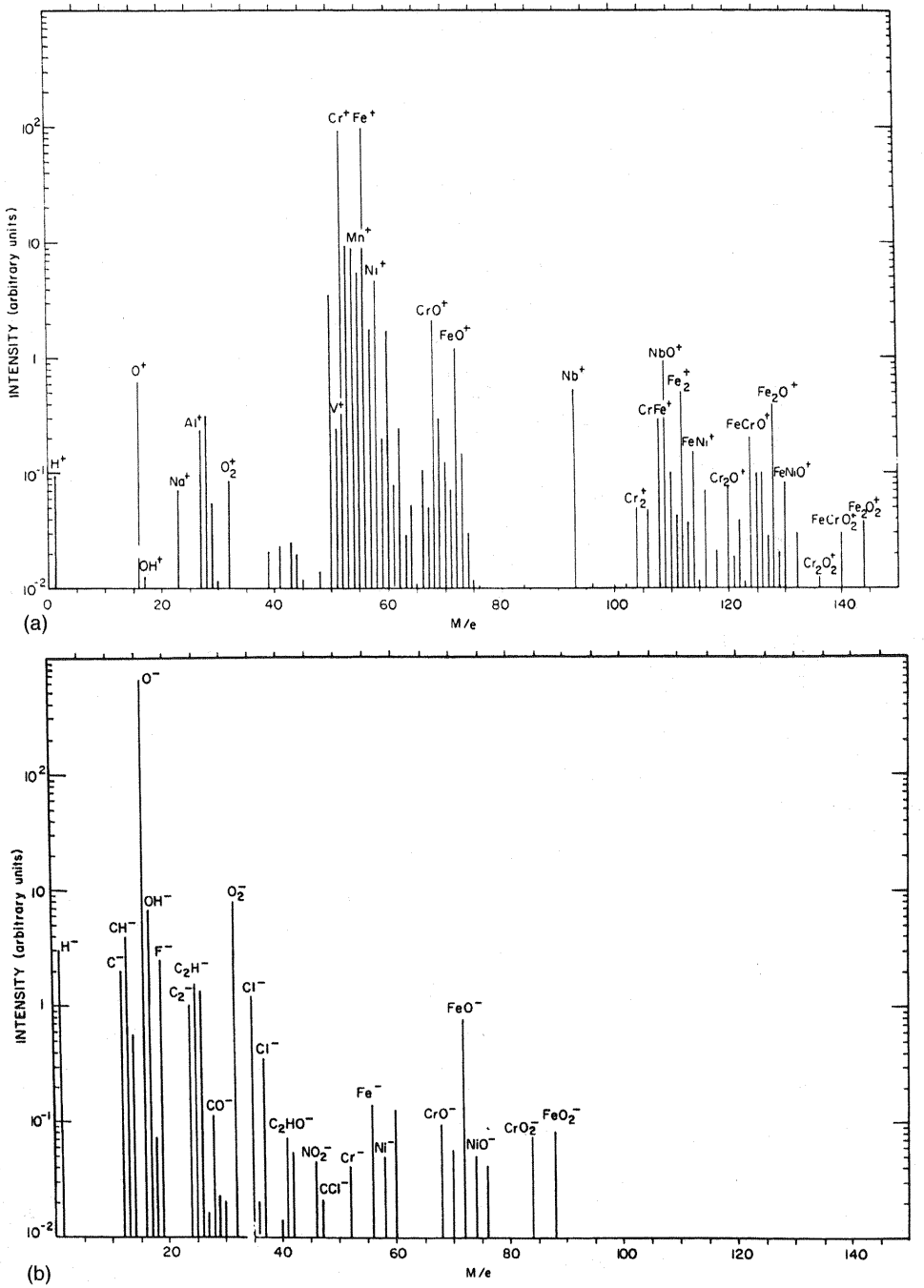

Figure 28 Example of positive and negative secondary ion mass spectrometer (SIMS) mass spectra. An $^{16}O^-$ primary beam of 1 nA at 15 keV was used for these spectra of 347 and 304 stainless steels. (a) Positive ion spectrum 347 stainless steel; and (b) negative ion spectrum 304 stainless steel. (From Ref. 84.)

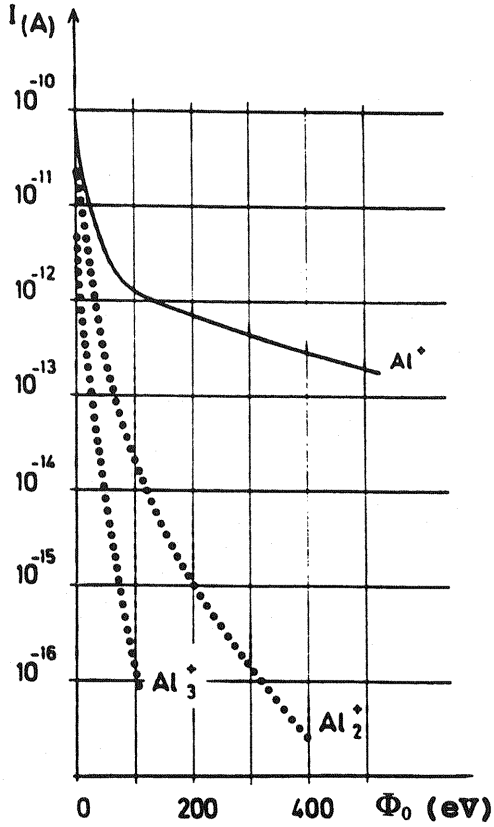

Figure 29 Energy distribution of Al^+, Al_2^+, and Al_3^+ ions sputtered from aluminum target. An energy window of 4 eV was used. (From Ref. 85.)

attempts at quantification based on various theories of sputtering and ion formation have met with limited success. The use of standards and relative sensitivity factors for calibration of instruments and procedures has proved more successful. Each of these is discussed briefly.

The ion yield S_i (ions per incident ion) of element i in a sample matrix M under ion bombardment may be expressed as

$$S_i = \alpha_i C_i Y_M \tag{4.2}$$

where α is the ratio of the secondary ions of element i to the total number of i atoms sputtered. C_i is the atomic concentration of i in the sample. Y_M is the total sputter yield of the sample. The secondary ion current, I, of isotope j of element i is given by

$$I_{ij} = Ip\ \gamma_{ij}\ \eta_{ij}\ S_i \tag{4.3}$$

where Ip is the total primary ion current, γ_{ij} is the isotopic abundance of isotope j, and η_{ij} is the acceptance, transmission, and detection efficiency of the instrument for this isotope. I_{ij} may be for any selected positive or negative secondary ion and S_i is the corresponding positive or negative ion yield.

The object of any quantitative scheme is to convert the measured I_{ij} to elemental concentration. The unknowns are the α_i ion yield fraction and η_{ij} instrument transmission parameters.

Many attempts have been made to quantify SIMS data by using theoretical models of the ionization process. One of the early ones was the local thermal equilibrium model of Andersen and Hinthorne [36–38] mentioned in the Introduction. The hypothesis for this model states that the majority of sputtered ions, atoms, molecules, and electrons are in thermal equilibrium with each other and that these equilibrium concentrations can be calculated by using the proper Saha equations. Andersen and Hinthorne developed a computer model, CARISMA, to quantify SIMS data, using these assumptions and the Saha-Eggert ionization equation [39–41]. They reported results within 10% error for most elements with the use of oxygen bombardment on mineralogical samples. Some elements such as zirconium, niobium, and molybdenum, however, were underestimated by factors of 2 to 6. With two internal standards, CARISMA calculated a plasma temperature and electron density to be used in the ionization equation. For similar matrices, temperature and pressure could be entered and the ion intensities quantified without standards. Subsequent research has shown that the temperature and electron densities derived by this method were not realistic and the establishment of a true thermal equilibrium is unlikely under SIMS ion bombardment. With too many failures in other matrices, the method has fallen into disuse.

Other early attempts at quantification from first principles included use of the Dobretsov equation for surface ionization through nonequilibrium thermodynamics [87], use of quantum mechanical models [88,89], and others, including surface bond breaking and dissociative [90] or chemical ionization [91]. None of these led to successful quantification schemes. An evaluation of several of these methods was made by Rudat and Morrison [92].

A recent proposal for quantification of SIMS data from first principles is the infinite velocity (IV) method of van der Heide et al. [93]. The basis for this method is the quantum mechanical argument derived by Norskov and Lundquist [94]; the SIMS matrix effect is removed if secondary ions are emitted from the sample surface with "infinite velocity" (i.e., the secondary ion yield for all elements is the same at infinite emission velocity). Under this condition, the relative concentration of an element, i, can be calculated from

$$C_i = \frac{I_i}{\sum I_{xyz}} \tag{4.4}$$

where I are the corrected intensity values at infinite velocity for the element of interest, i, and for all the matrix elements x, y, and z. The infinite velocity intensity for each element is obtained by altering the extraction voltage and measuring the secondary ion intensities over four or more increments, plotting the intensity of each element versus the reciprocal velocity (obtained from the kinetic energy expression, $E = \frac{1}{2} mv^2$), and extrapolating to $1/v = 0$. This method was tested independently by Lösing et al. [95] on three homogeneous metal alloys with trace, major, and minor elements. Negative secondary ions were generated by using a Cs^+ beam, and positive secondary ions were generated by using an O_2^+ beam. Extraction offsets were 80, 120, 160, and 200 V. The results on these samples were generally within a factor of 3. A major drawback found was that application of the high offsets reduced sensitivity by a factor of about 100, thereby requiring higher primary beam currents and energies to get adequate counting rates for the minor elements. The method also requires a SIMS instrument that allows changing of the extraction field in the necessary increments. This technique appears promising for quantification of samples for which no standards are available, but more research and application to a wider variety of samples are needed to validate the theory.

Although a Cs^+ primary beam was used originally to enhance the formation of negative secondary ions, its use has been further popularized by the discovery that MCs^+ ions (where M is any element in the specimen) are formed with greatly reduced matrix effects [96]. It is believed that the MCs^+ ions are formed by combining an independently sputtered neutral M atom and a Cs^+ ion in the near-surface region. With greatly reduced, and in some cases negligible, matrix effects, the difficulty of quantification in SIMS is reduced. Without a matrix effect, the individual MCs^+ ion yields could be determined by using a reference standard, and the corrections applied from one type of sample to another or throughout the depth profile. Schroeer et al. [97] measured relative yields of secondary ions from five different metals and found the relative yields from matrix to matrix varied no more than a factor of 2, with the exception of Cr from Si, which varied by a factor of 4. They also reported that the yields of the MCs^+ ions were independent of the ambient oxygen pressure up to about 10^{-5} torr. Their primary beam was set at an angle of 42° to the target normal. Wittmaack [98] found that MCs^+ yields were strongly dependent on the primary impact angle for materials with low sputtering yields such as Si and Al. Homma et al. [99] studied MCs^+ ion yields in Si and SiO_2 and found group II, III, and IV MCs^+ yields in SiO_2 lower or comparable to that in Si whereas group V, VI, and VII elements had higher yields in SiO_2. The use of MCs^+ ions lowers the ion yields for most elements but greatly improves the sensitivity for the group II B elements (Zn, Cd, and Hg). These elements tend to have lower signals when analyzed with conventional primary ions as a result of their high first ionization potentials (i.e., low positive ion yields) and negative electron affinities (i.e., no negative ion yield). Overall, the use of the MCs^+ cesium attachment ions leads to easier quantification of SIMS data.

The most satisfactory results for SIMS quantification have been achieved through the use of relative sensitivity factors (RSFs). In its simplest form, RSFs are determined by measuring ion collection efficiencies from known matrices and recording them as a ratio to a reference element that is usually the most abundant metallic atom in the matrix. A matrix that matches the unknown is necessary. If a good matrix match is available, excellent results can be achieved—especially in the dilute concentration range. A *relative sensitivity factor* (RSF) may be defined as

$$S_{i,m} = \frac{I_{ij}/(C_i\gamma_{ij})}{I_{mn}/(C_m\gamma_{mn})} \tag{4.5}$$

where $S_{i,m}$ is the RSF for element i with respect to the matrix element m; C_i and C_m are the atomic concentrations of impurity element i and matrix element m, respectively; and the isotopes measured are j for element i and n for element m. If relative sensitivity factors for all the elements in an unknown of similar matrix have been determined, then the concentration of each element x in the unknown may be calculated from

$$C_x = \frac{I_{xy}/(\gamma_{xy}S_{x,m})}{\sum_{i=1}^{n} \frac{I_{ij}}{\gamma_{ij}S_{i,m}}} \tag{4.6}$$

If only some of the elements are of concern and the concentration of the matrix element is known or can be reasonably estimated, then Eq. (4.5) can be used to solve for each unknown.

The method of defining RSFs described is traditional in analytical chemistry, generates RSFs without units, results in larger numbers for elements for which the SIMS instrument is more sensitive, and is essentially the same as Wittmaack's proposed use of "scaled sensitivity ratios" [100]. However, an alternative definition of sensitivity factors that has gained much popularity with semiconductor specialists is that of Wilson [69,101]:

$$\rho_i = (I_i/I_m)\, RSF \tag{4.7}$$

where ρ_i is the impurity atom density in atoms per cubic centimeter (atoms/cm^3) and the other symbols are as described. For practical use with nonmonoisotopic elements, the ion intensities need to be corrected for isotopic abundance, and the equation becomes

$$\rho_i = \left(\frac{I_i/\gamma_{ij}}{I_m/\gamma_{mn}}\right) RSF \tag{4.8}$$

With this definition, RSF has units of atoms per cubic centimeter, and an element that is detected with more sensitivity in the SIMS instrument has a smaller RSF.

Thus the SIMS analyst must be aware of the definition of RSF being used when reading the literature.

An excellent way to create standards is ion implantation of the elements of interest into the matrix. This works exceptionally well for semiconductors since one can usually start with high-purity single-crystal materials that represent the matrix of interest. Also the use of Eq. (4.8) is well suited for this purpose since ion implanters usually quote doses in atoms per square centimeter. However, Eq. (4.5) serves just as well by converting the matrix concentration to atoms per cubic centimeter. In this procedure, the implant profile is sputtered through, the implant element secondary ions and the matrix element secondary ions are each summed, and the depth of the sputter profile is determined, usually by using a stylus profilometer. The sensitivity factor is then calculated from

$$S_{i,m} = \frac{(\sum I_i) d \rho_m}{\phi (\sum I_{mn}) / \gamma_{mn}} \tag{4.9}$$

where ΣI_i and ΣI_{mn} are the sum of the counts of the implanted impurity ion and matrix ion, respectively; d is the depth of the sputtered profile in centimeters; ρ_m is the atom density of the matrix element in atoms per cubic centimeter; and ϕ is the implant fluence in atoms per square centimeter. Usually the implant ion is isotopically pure, so no correction for its isotopic abundance is shown in this equation. Again the RSF, $S_{i,m}$, is unitless. Note that one needs to know the atom density of the matrix element in this application.

If one uses the RSF as defined in Eq. (4.8) for the ion implant calibration, the expression becomes

$$\text{RSF} = \frac{(\phi \sum I_{mn}) / \gamma_{mn}}{d \sum I_i} \tag{4.10}$$

where all symbols are defined as earlier and RSF has units of atoms per cubic centimeter.

In SIMS, small changes in concentration have nonlinear effects on the relative sensitivities of the components; changes in vacuum environment or current density of the primary ion beam also affect the relative sensitivities. Because it is unreasonable to have precisely matching standards for every matrix and because precise matching of instrument and vacuum parameters, although desirable, is often difficult to achieve in practice, empirical methods to extend and adjust the sensitivity factors (determined from a reasonable number of standards) are important. McHugh suggested [64] that sensitivity factors would show a dependence on ε_s, a parameter reflecting the electronic properties of the secondary ion-emitting surface. Then, by plotting RSFs versus ε_s, derived from a few standard matrices,

as shown in Fig. 4.30, unknowns could be quantified by determining their ε_s and selecting the modified RSFs from the chart. He also suggested that ε_s could be established by measuring ratios such as M^{2+}/M^+, MO^+/M^+, MN^+/M^+, or others that might be sensitive to ε_s and independent of element concentration. Ganjei et al. [102] applied this idea and made it practical by using changes in ambient oxygen pressure to induce a range of sampling environment changes over which sensitivity factors could be measured from one standard. Sensitivity factors were plotted versus a matrix ion species ratio such as $^{56}Fe_2{}^+/^{54}Fe^+$ in a steel standard. They called this technique the *matrix ion species ratio* (MISR) method. Accuracies achieved on a number of steels, aluminum alloys, and copper alloys were on the order of 10% relative. The best accuracy and precision were achieved with the introduction of small additions of oxygen to the surface of the unknowns.

For successful quantification in SIMS, great care must be taken to reproduce instrument conditions as closely as possible. These conditions include energy and current density of the primary beam, type and purity of the primary, vacuum conditions, angle of incidence of the beam with the sample, energy bandpass of the mass spectrometer, and detector efficiency. In addition, correct identification of the secondary ions (i.e., without interference) is crucial to good quantification. As discussed in other chapters, this can be achieved with high mass resolution to separate ions of interest from interfering species, through energy filtering, or by manual or computer spectral stripping (i.e., subtraction). The sample and standards are also important. A good standard is homogeneous on a micrometer scale and characterized. These may be reference materials generated by organizations such as the National Institute of Standards and Technology, standards from independent material specialists, or ion implantation standards in which care is taken to measure dose accurately and maintain purity of the implanted ion. Samples that have second-phase inclusions are very difficult to quantify completely. Each phase must be treated separately as ion formation conditions are quite different. Where multiple crystal orientations exist on the sample surface, each crystallite needs to be quantified separately as ion emission varies greatly, depending on the orientation with respect to the primary beam and the secondary ion extraction field.

4.4 INSTRUMENTATION

4.4.1 General

At its simplest the secondary ion mass spectrometer needs only five elements. These are an ion source to create the bombarding primary ions, a target or sample holder, a mass analyzer for analysis of the secondary ions, a detector to transform the ions to recordable form, and a recording device. Usually, the practical SIMS

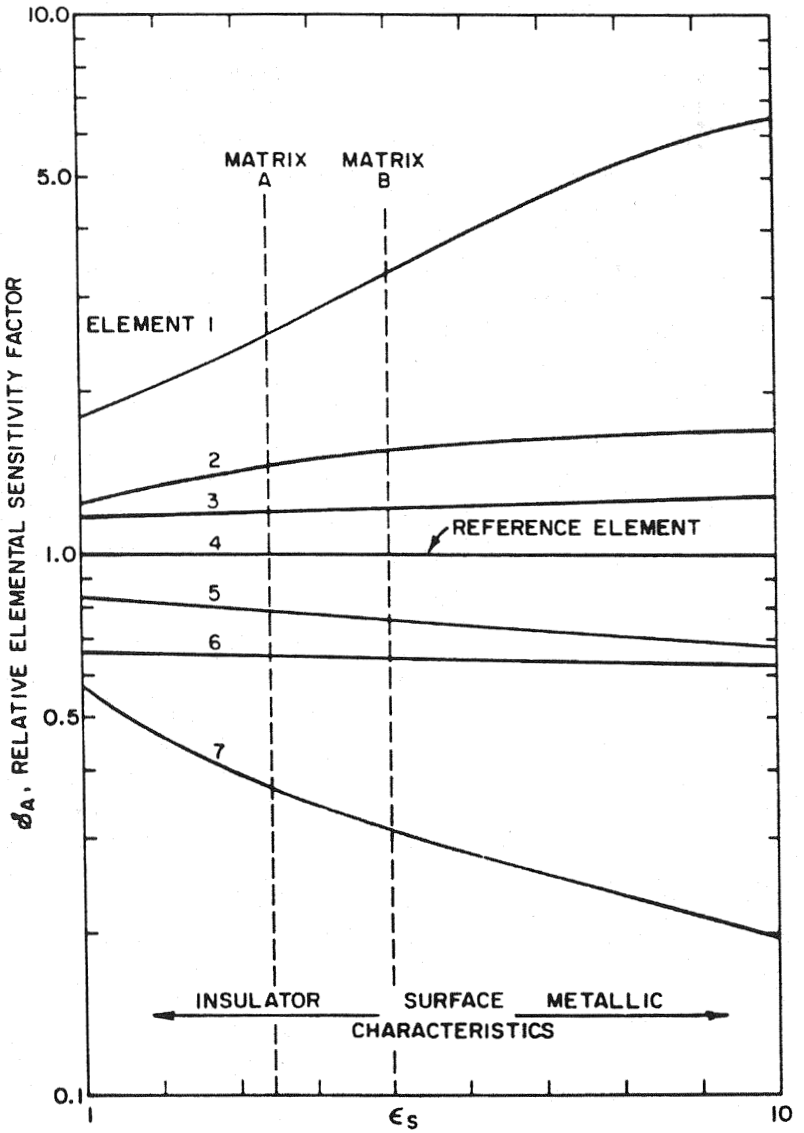

Figure 30 Method for broadening application of standards by determining relative sensitivity factors as a function of a property, ϵ_s, sensitive to changing electronic properties of the matrix. (From Ref. 64.)

instrument has additional features such as primary beam filtering and focusing, energy filtering of the secondary ions, counting systems for highest detection sensitivity, and sometimes an electron flood gun for charge neutralization on insulators.

SIMS instruments may be conveniently divided into three general types: (1) nonimaging, (2) scanning probe imaging, and (3) microscope imaging. Nonimaging instruments are concerned only with surface or profile analysis within the area covered by the primary beam, irrespective of the precise location of the emitted secondary ion. Scanning probe imaging instruments such as the ion microprobe mass analyzer (IMMA), Fig. 4.5, and the NanoSIMS 50, Fig. 4.14, form secondary ion images of the surface by scanning a focused ion beam over the sample surface and displaying the detector signal on a synchronously scanning oscilloscope or as a function of scan position with a computer. The image resolution in these instruments depends on how finely the ion beam can be focused on the sample surface. Microscope imaging instruments such as the IMS-3f, Fig. 4.9, and the triple-electrostatic-sector TOF, Fig. 4.12, form secondary ion images by stigmatically transferring each secondary ion from the sample surface through the mass analyzer to the detector. The detector may be a video camera that records the image formed on a fluorescent screen when the secondary ions are converted to electrons by a channel plate, or, in an alternative arrangement, a dual-microchannel plate electron multiplier used with a resistive anode encoder [103] to record counts as a function of position. Some modern commercial instruments have capability for both probe and microscope imaging, which allows the analyst to select the type of measurement needed for optimal analysis.

Imaging instruments offer the advantage of analysis of much finer details on nonhomogeneous samples. Scanning probe imaging instruments have the advantage of being able to achieve the highest spatial resolution; 20 nm has been achieved [3]. Microscope imaging instruments have the advantage of simultaneous transfer of all ions of the analyzed mass from the total image area. Thus, images are formed in much shorter times. In the microscope imaging instruments, large-diameter ion beams with larger currents mean that profiling and formation of images as a function of depth are much faster. The best image resolution achieved with microscope imaging instruments is about 200 nm.

4.4.2 Primary Ion Sources

Current density and the type of primary ion have a critical effect on SIMS analyses. High current densities are desirable for rapid profiling and high-sensitivity analysis, whereas low current densities are chosen when the analyte layer is thin or when using static SIMS. Exotic polyatomic ion sources are an area of active research today; ReO_4^- [104], SF_5^+ [105], SF_6^-, $NO_2^{\pm}$, CF_3^+, C_{60}^+, and many others [106,107], have been reported to provide exceptional enhancement of secondary ion yields and ultrashallow depth profiling. However, the most heavily used ion sources today are the hollow cathode duoplasmatron (Fig. 4.31) [108], the thermal

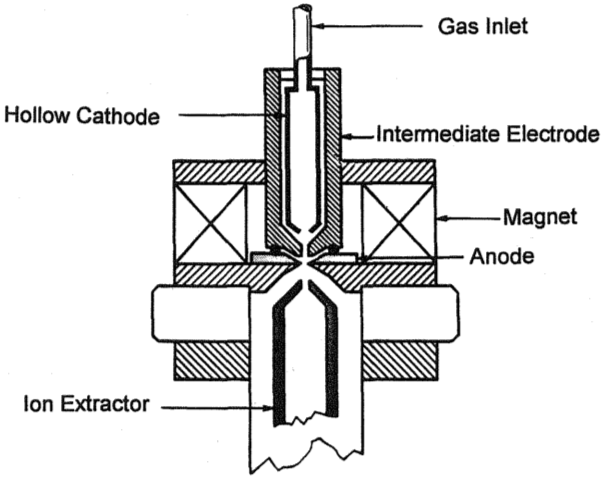

Figure 31 Duoplasmatron ion source schematic. (From Ref. 108.)

ionization cesium ion source (Fig. 4.32), and the liquid metal ion gun (Fig. 4.33). Desirable features of any ion source are high brightness, high current density, low energy spread, long-term stability, and long life.

The most common species used with SIMS sources are Ar^+, O_2^+, O^-, and N_2^+. These ions and other permanent gas ions are formed easily with high brightness and stability with the hollow cathode duoplasmatron. Ar^+ does not enhance the formation of secondary ions but is popular in static SIMS, in which analysis of the undisturbed surface is the goal and no enhancement is necessary. O_2^+ and O^- both enhance positive secondary ion count rates by formation of surface oxides that serve to increase and control the work function of the surface. O_2^+ forms a more intense beam than O^- and thus is used preferentially, except in the case of analyzing insulators (see Chapter 11). In some cases the sample surface is flooded with O_2 gas for surface control and secondary ion enhancement. An N_2^+ beam enhances secondary ion formation, but not as well as O_2^+. It is very useful for profiling and analysis of oxide films on metals, however. It also is less damaging to duoplasmatron hollow cathodes and extends their life by a factor of 5 or more compared to oxygen.

The detection sensitivity for carbon; hydrogen; the electronegative elements—F, Cl, O, S, etc.—and certain metals with low work functions (such as Au and Pt) is greatly enhanced by analyzing their negative secondary ions, sputtered by a Cs^+ ion beam. Most cesium ion sources use heated metal to provide vapor to

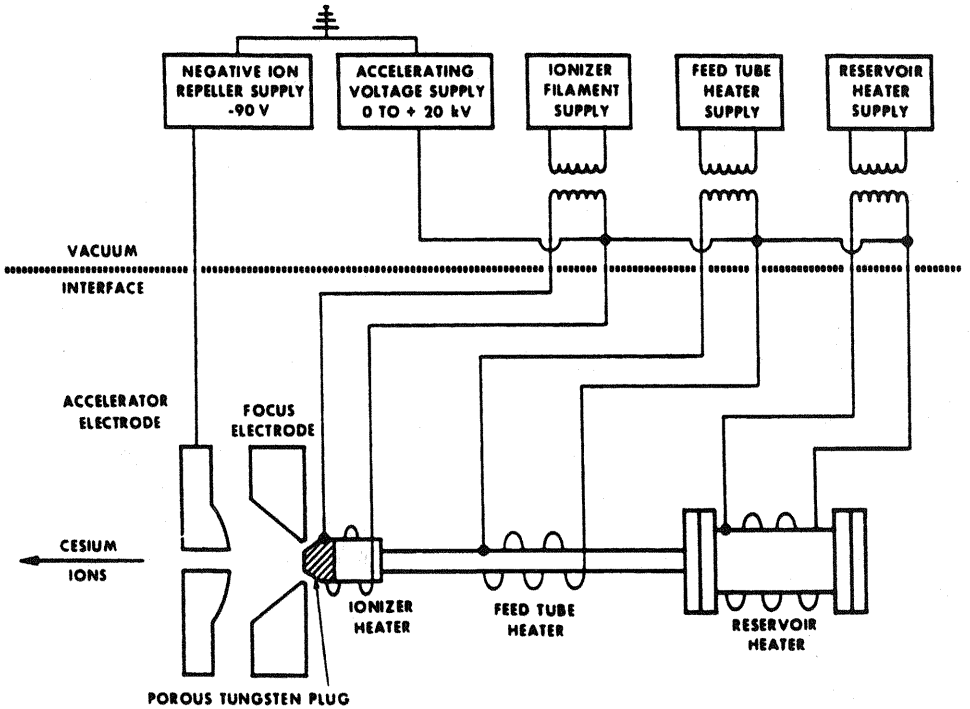

Figure 32 Cesium ion source schematic. (From Ref. 82.)

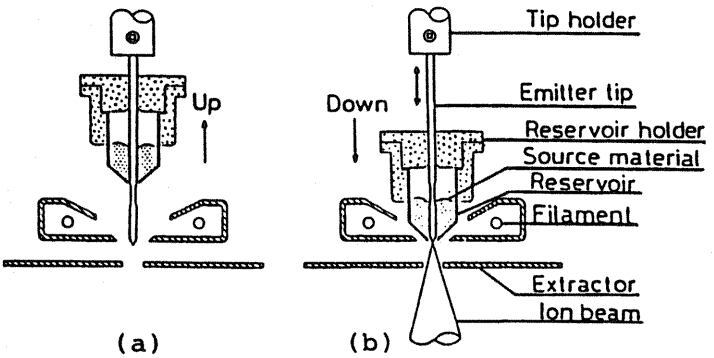

Figure 33 Liquid-metal ion source of Okutani et al. With movable tip and reservoir. (From Ref. 109.)

the back of a tungsten frit. The cesium diffuses through the frit, where it is thermally ionized. In the presence of an electrostatic field, Cs^+ is accelerated into the instrument (Fig. 4.32). A drawback of cesium is the necessity of handling the metal in inert gas glove boxes. Some have overcome this problem by using cesium compounds that decompose or react to release cesium in situ. Okutani et al. [109] heated cesium chromate with silicon, which reacted to release Cs and form residues of SiO_2 and Cr_2O_3. As with oxygen, cesium is sometimes evaporated onto the surface directly. This ensures saturation of the work function effect for Cs^+ sputtering, or alternatively it enhances the negative ion yield for noble gas sputtering.

The liquid metal ion source (LMIS) provides the highest current density and the smallest probe size. In the LMIS (Fig. 4.33), a tungsten emitter tip is coated with a liquid metal such as Cs, Hg, Ga, In, Sn, Bi, or Au; a high potential field is then applied. Under these conditions, the liquid metal forms a "Taylor" cone with a small tip from which ions are emitted. This small, very-high-brightness, very-high-current-density ($\sim 10^6$ A/cm^2) source allows focusing to spots as small as 20 nm with current densities up to 5 A/cm^2. High-resolution secondary ion imaging, most commonly with Ga^+ and In^+ ions, is the forte of LMIS. The very fine intense LMIS beam has also been used for micromilling and cutting in semiconductor analysis and repair.

4.4.3 Primary Ion Column

The primary ion column may be nothing more than a vacuum between the ion source and the sample target, but generally it contains some beam shaping and controlling elements. The IMMA diagram in Fig. 4.5 illustrates common features. The ion extractor may be considered to be part of the ion source or the first element of the primary column. A potential difference between the extractor and the ion source accelerates the primary ions to the desired energy, generally between 0.2 and 40 keV. It is desirable to filter the primary ion beam so that only the selected species strike the sample. The IMMA does that with a primary magnetic sector; other instruments use a Wien filter. Beam shaping and directing are done with electrostatic alignment plates, apertures, and one or more electrostatic lenses. With scanning probe-imaging instruments, electrostatic deflection plates are required to control the position of the beam on the target. Time-of-flight instruments require pulsed acceleration of the primary ions and often have electric or magnetic field "bunching" elements to sharpen the pulse of primary ions.

4.4.4 Sample Mount

The sample mount requires an electrical connection to maintain a constant potential on the sample surface. In quadrupoles this is generally ground, and extraction lenses are biased to collect the secondary ions. Magnetic sector instruments usu-

ally bias the sample to accelerate the secondary ions. A Faraday cup designed to trap the beam and any sputtered particles is often provided to measure the primary beam current at the target. Sample current is not an accurate measure of the beam current, as significant numbers of charged particles are emitted in the sputtering process and add to or subtract from the primary current (depending on their charge polarity). The beam diameter on the sample in scanning probe instruments can be measured by scanning the beam across the Faraday cup and measuring the distance required for the beam current to drop from the level with the beam outside the cup to that inside the cup.

The sample mount also positions the sample properly for analysis. This includes x and y lateral motion, z height, and angle with respect to primary beam and secondary extraction. It may vary from a simple mechanical mount to a sophisticated stage with stepping motors under computer control.

4.4.5 Secondary Mass Analyzers

SIMS instruments are generally grouped by type of secondary analyzer as well as by imaging type. Three general types enjoy wide popularity, and each has its distinct advantages. They are the magnetic sector, the quadrupole, and the time-of-flight (TOF).

Magnetic sector instruments are popular because of their high mass resolution and high transmission of the secondary ions. Transmission figures of 10% to 40% at low mass resolution are common. Most SIMS magnetic sector instruments are designed to be double-focusing, combining the direction focusing of the magnetic sector with the velocity focusing of an electrostatic sector. Useful mass resolution in current magnetic sector SIMS instruments ranges from about 5000 to 10,000. Examples of magnetic sector instruments include nonimaging (the SHRIMP II in Fig. 4.13), microscope imaging (IMS 300—Fig. 4.4 and IMS-3f—Fig. 4.9), and scanning probe imaging (IMMA—Fig. 4.5, and NanoSIMS 50—Fig. 4.14). Secondary ion extraction elements, apertures, and lens elements vary widely, depending on the requirements.

A novel way of providing electron charge compensation for insulators was developed for the f-series Cameca instruments, Fig. 4.34 [110]. Electrons from a gun are turned 90° to pass coaxially through the objective lens of the secondary ion extractor, which works as an electron mirror to provide a self-regulated potential on the sample surface.

Simultaneous secondary ion detection is limited to the number of detectors placed in the transmission plane of the magnetic sector. Quasi-simultaneous detection of two or more ions may be achieved by programming electrostatic deflection plates to switch ions rapidly within a fairly narrow mass range (see Fig. 4.6). Simultaneous or quasisimultaneous collection of ions is especially helpful for measurement of isotopic ratios.

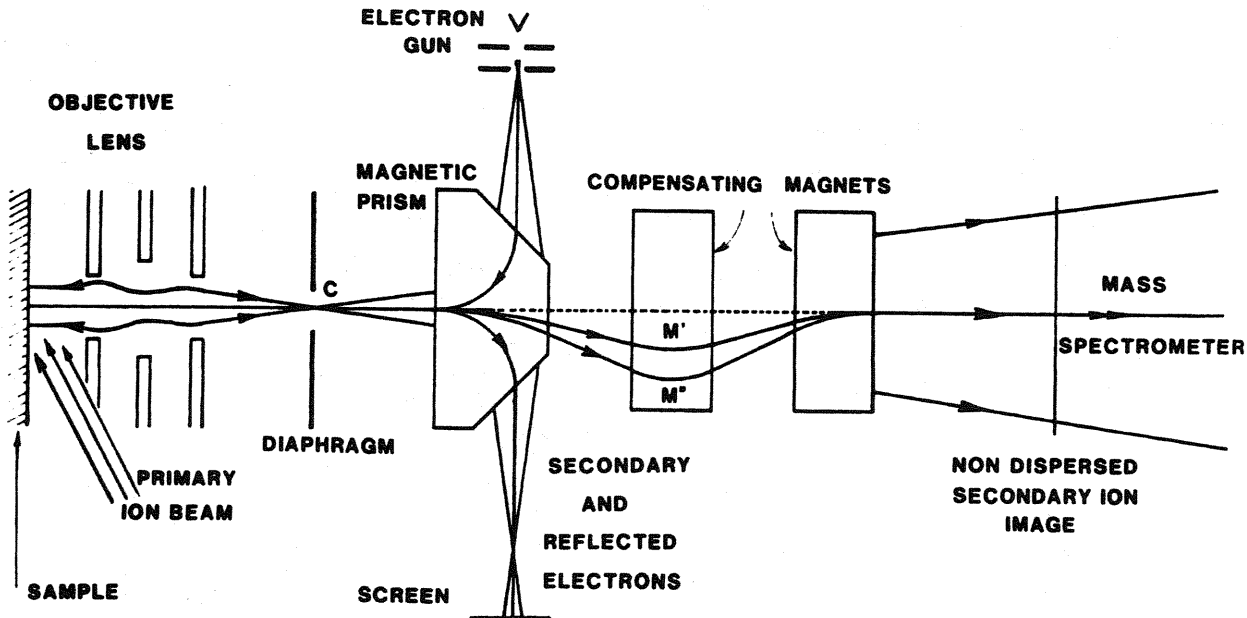

Figure 34 Coaxial, self-regulating electron compensation for charging on electrically insulating samples. (From Ref. 110.)

Quadrupole SIMS instruments have the advantage of low extraction fields and ground-potential samples; this makes them readily applicable to low-energy ion beams and high-resolution depth profiling. Also, the sample orientation may be adjusted without serious effect on the primary beam so that beam incidence angles may be adjusted freely to maximize sputtering or ion yield. Quadrupoles are less complex and thus somewhat less expensive than other instruments. The mass spectra may be rapidly acquired, an advantage if the sample composition is changing rapidly. Quadrupoles have the disadvantage of lower mass resolution, generally less than 1000; lower transmission of secondary ions than sector or TOF instruments; and mass discrimination against higher masses. Examples of quadrupoles are the static SIMS of Benninghoven and Loebach (Fig. 4.7), the Atomika ADIDA (Fig. 4.8), and the University of Chicago instrument (Fig. 4.10).

In the time-of-flight (TOF) instrument, the primary beam is pulsed and a packet of secondary ions is extracted into the drift region. Every secondary ion in the packet is detected rapidly in mass sequence. Thus, every ion that passes through the mass spectrometer is detected (with the exception of deadtime counting losses). This essentially simultaneous detection of all masses with transmission of 10% or greater gives the TOF very high useful yields (number of ions detected/atoms sputtered). Thus, the TOF is very popular for static SIMS and surface analysis when the analyte is very limited in quantity. The mass range is unlimited and transmission is constant over the mass range. Current commercial TOFs have mass resolutions of 3000–10,000, which give them the capability of resolving many isobaric atomic and molecular ions. A disadvantage of the TOF is a low duty cycle, perhaps 0.2% at best and often much less. Sputtering and ion formation are only taking place in the very small time fraction when the primary is pulsed on. The low duty cycle means longer times are required to collect counts on low-abundance ions. Also depth profiling becomes very slow. An auxiliary sputtering beam could be used intermittently with analysis when rapid depth profiling is required. Examples of TOFs are Niehuis's reflectron type [52] (Fig. 4.11) and Scheuler's triple-electrostatic-sector instrument [55] (Fig. 4.12).

4.4.6 Detectors and Recording Systems

Both positive and negative secondary ions are important in SIMS, and the dynamic range is very large, sometimes covering seven orders of magnitude. Electron multipliers are commonly used in SIMS because they have high gain, low intrinsic background, and large dynamic range. A polarity-switchable accelerating potential between the exit slit of the spectrometer and the first dynode of the electron multiplier gives them dual-polarity capability. Some instruments, especially those with large current primary ion beams, use a Faraday cup detector for the major ion species and the electron multiplier for the rest. The detector on the IMMA (Fig. 4.5) was a modified Daly [111] type in which the secondary ions are accelerated

onto an aluminized surface from which electrons are liberated and accelerated to a scintillating phosphor that emits light. The light pulses are piped outside the vacuum system to a photomultiplier. Analogue currents from either electron multipliers or photomultipliers may be amplified and displayed on *X-Y* plotters, strip chart recorders, or oscilloscopes. For greatest sensitivity, pulse counting of the individual ion-produced cascades is done. In this mode signals ranging from a few ions per second to over 10^7 per second may be detected. To cover the high counting rates that are not uncommon in SIMS, 200-MHz or faster counters should be used. At the higher counting rates ($>10^5$ sec^{-1}), deadtime corrections need to be made for accurate counting.

In microscope imaging instruments the detection/recording system requires the amplification and collection of the ion signal from all portions of the detector plane while maintaining the position information. One technique is to focus the secondary ion image onto a microchannel plate that converts the ions to electrons; these electrons are then projected onto a fluorescent screen. The image on the fluorescent screen may be viewed, recorded on photographic film, or recorded by a sensitive CCD video camera. These images on film may be digitized with an optical scanner. The video camera images may be digitized by using an analog-to-digital converter. The digitized image frames are sent to a computer for frame image integration, quantification, storage, and display. An alternate method is to focus the secondary ion image on a dual-microchannel plate electron multiplier that provides pulse counting and, in conjunction with a resistive anode encoder, position information [103]. These count-quantified images may be displayed on an oscilloscope and/or stored and displayed by computer.

The detector for time-of-flight SIMS must be capable of counting pulses very rapidly and accurately recording the time of arrival of each pulse. The time function is usually handled by a time-to-digital converter that must have ~0.1-nsec time resolution. In Schueler's microscope imaging TOF [55], ions are detected by using a dual-microchannel plate (DMCP). The arrival time of the ion is extracted from the second plate of the DMCP. The pulse is amplified and routed to a time-to-digital converter. A resistive anode encoder that determines position information for the pulse follows the DMCP. Arrival time (mass) and position for each secondary ion detected are stored in a computerized data system. Integration of data over a sufficient number of primary pulses results in count-quantified secondary ion images for every ion mass collected.

4.5 APPLICATIONS AND TRENDS

4.5.1 Static Secondary Ion Mass Spectrometry

The idea in static SIMS (SSIMS) is to analyze only surface areas that have not been affected by prior ion bombardment. Thus, the SSIMS experimenter is limited to

$<10^{13}$ primary ions/cm^2 (the static SIMS limit) striking the surface. This requirement for limited bombardment of the surface puts a premium on efficient use of the available ions. The availability of high mass resolution, high transmission, and high useful yields (with the advent of a new generation of time-of-flight SIMS mass spectrometers in the late 1980s) provided a strong boost for SSIMS applications. Since the late 1980s there has been a blossoming of SSIMS, primarily in the area of organic and polymer applications. Of prime importance in SSIMS is determining the relationship between the sputtered species and the molecules on the surface. Two libraries of SSIMS spectra are available to help the analyst, the *Munster High Mass Resolution Static SIMS Library* [112] and *The Static SIMS Library* [113]. Also critically important to SSIMS is ultrahigh vacuum in the 10^{-10}-torr range or lower in the sample chamber to prevent contamination of the surface.

A classic example of SSIMS is a study of the initial stages of oxidation of chromium [114]. Figure 4.35 shows the changes in the CrO_2^-, CrO_3^-, and CrO^+ ions as oxygen exposure was increased from 0 to 1000 langmuir (L). After ~50 L of exposure the CrO_2^- and CrO_3^- species begin to increase. At about 300 L, CrO^+

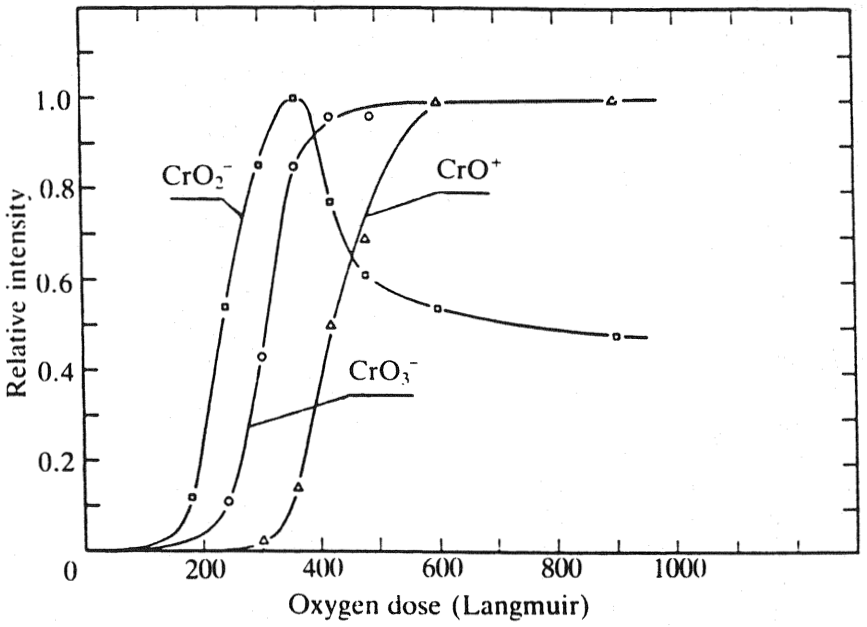

Figure 35 Static secondary ion mass spectrometry (SIMS) study of the initial stages of oxidation on chromium surface. (From Ref. 114.)

begins to increase on the surface and $CrO2^-$ decreases. When the oxide was profiled, the CrO^+ species dropped rapidly; the CrO_2^- species remained at a constant level for a period before decreasing. This simple experiment showed that one oxide species was forming initially and progressed into the bulk. A later forming oxide characterized by CrO^+ formed on the surface but apparently remained in a monolayer on the surface even though additional oxygen exposure occurred.

In a more recent application of SSIMS, the ratios MO_2^-/MO^- and MO_3^-/MO^- for transition metal oxides of the type M_xO_y were measured to demonstrate a fingerprint spectrum characteristic of the oxidation state of the metal. The data for iron oxide were then compared to oxide found on a steel sample with an oxide film 4 nm thick. The best match was to Fe_2O_3 [115].

SSIMS has been applied to the study of molecular adsorption on metal surfaces [116], catalytic surfaces [117], surfaces of HF- and NH_4F-treated silicon [118], and many others in which surface chemistry is important.

4.5.2 Profiling

Profiling or other applications of SIMS that are not static are sometimes referred to as dynamic, although that connotation seems superfluous. The limits of SIMS profiling resolution are being driven by the requirements of the semiconductor industry, in which device size is getting smaller and doping implants are getting shallower. As a result, primary beam energies are being reduced. Quadrupole instruments with low extraction potentials can easily accommodate lower primary beam energies (e.g., 200 eV) [119]. However, modifications to magnetic sector instruments so they can work with lower secondary ion extraction energies have resulted in impact energies as low as 1 keV.

In profiling, there is a transition region at the surface due to initial sputtering where the implantation of the bombarding beam has not reached its full equilibrium value. By sputtering with 250 to 500 eV O_2^+ at normal incidence for most rapid incorporation of the oxygen, transition depths of less than 1 nm have been observed in silicon [120,121]. Subkiloelectron-volt sputtering can also be achieved by higher primary ion energy at glancing incidence, but transition depths become greater as incorporation of the primary beam is reduced. Oxygen flooding was used to overcome this effect in profiling a boron implant in silicon, as shown in Fig. 4.36. A comparison is made by using 1 keV O_2^+ at 60° incidence to profiles made by using 250 and 500 eV O_2^+ at normal incidence [122]. Another method of overcoming the transition region is capping the sample with a thin layer of the substrate element so that implant equilibrium has been reached when the capped material is sputtered through [123].

In addition to the transient sputtering region, a thin layer of native oxide on the surface complicates profile interpretation. Iltgen et al. [124] described a method

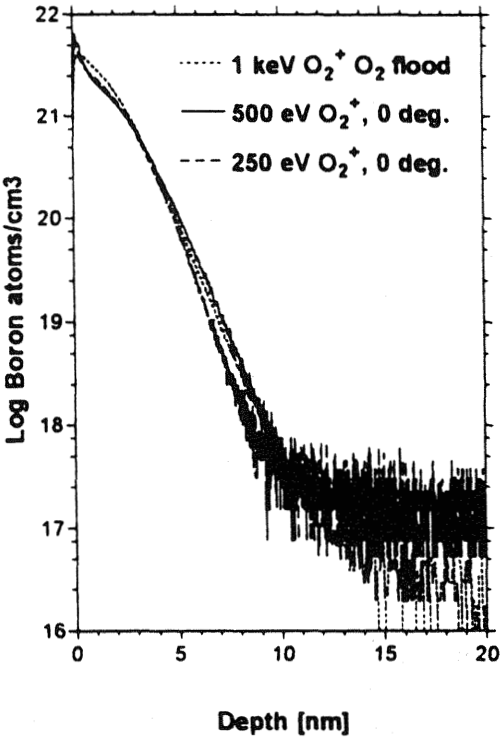

Figure 36 Comparison of normal incidence profiling in vacuum to 60° incident profiling with oxygen flooding. Profiles of boron implanted in silicon. (From Ref. 122.)

for continuous correction of the depth and concentration scale based on knowledge of the matrix sputter yield and the relative sensitivity factor [RSF (^{11}B, ^{30}Si)]. These authors also used SF_5^+ sputtering to provide the smallest transient depth. The large six-atom ion implantation is very shallow as a result of fragmentation that reduces the effective energy of the beam.

Magee et al. [125] used O_2^+ with a quadrupole SIMS to profile an epitaxial silicon grown with five boron delta-doped layers, each 5.4 nm thick. Bombardment energies from 400 eV to 1.5 keV were used with angles of incidence from 0° to 70°. Analyses were performed with and without oxygen flooding. With a sputtering energy of 500 eV (at 50° incidence, and oxygen flooding), no measurable change in sputtering rate was found in the transient region or between any of the layers. A similar sample was profiled in a magnetic sector instrument, using O_2^+ with 1 keV, at 56° incidence, and oxygen flooding [126]. There was a small 0.6-

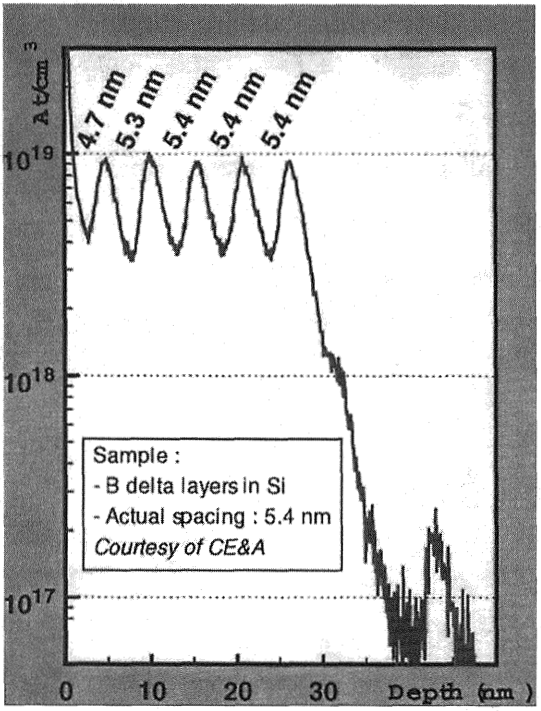

Figure 37 High-depth-resolution profiling with a magnetic sector instrument using a 1-keV O_2^+ primary beam at 56° incidence with oxygen flooding. (From Ref. 126.)

nm shift in the first layer, as shown in Fig. 4.37, but the results were similar to the quadrupole results with 400 eV O_2^+ at 0° and no flooding.

A profile of a 500-eV arsenic implant by Hitzman and Mount [127] shows the effect of Cs^+ primary ion energy and incidence angle on depth resolution (Fig. 4.38). These As^- profiles also demonstrate the high sensitivity of the SIMS technique.

The use of MCs^+ to make quantitative profiling easier is illustrated in Fig. 4.39 [128]. Each element in the structure GaAs/AlGaAs/InGaAs/quantum-well (20 × AlGaAs/GaAs)/GaAs is profiled as MCs^+.

4.5.3 Imaging

Imaging of elemental and isotopic distributions on surfaces has proved useful for diffusion measurements, corrosion and reactivity studies, contamination identification, and many other applications. SIMS imaging is particularly useful because of its high sensitivity. An example was the application to a problem in which a U-

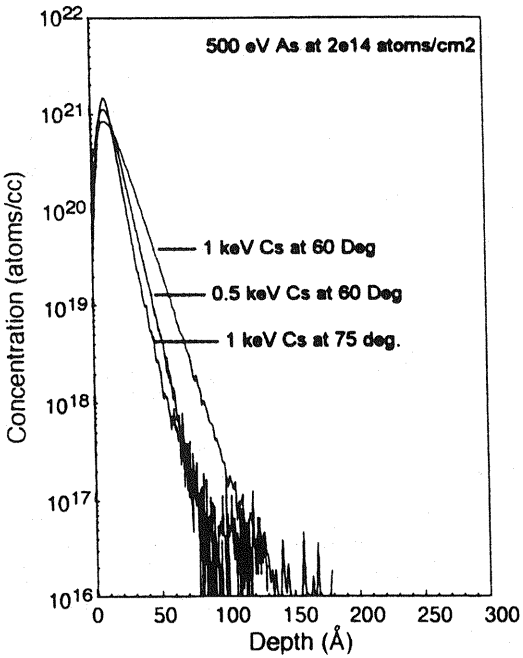

Figure 38 Effect of beam energy and angle of incidence on depth resolution. Profiles of arsenic in silicon using Cs^+ primary beam. (From Ref. 127.)

Zr-Nb alloy was being attacked and seriously weakened by an unknown agent. SIMS spectra showed the presence of a fluoride. Imaging of cross sections of the metal showed that fluorine was attacking and reacting along the grain boundaries (Fig. 4.40) [129]. The fact that the grain boundary fluoride always ended abruptly showed that a reaction in the grain boundary, not just simple diffusion, was occurring. By using SIMS images to measure the extent of the attack at a series of times and temperatures, the complete kinetics of the process were solved.

The isotopic imaging capability of SIMS provides a way of rapidly screening particles when isotopic information is important. An example is the location of rare, isotopically distinct material in interplanetary dust particles that are collected by high-flying aircraft [130]. Another example is the monitoring of nuclear enrichment facilities by environmental sampling that requires quick scanning of particles to detect enriched uranium [131]. Simons et al. reported an automated SIMS for rapidly determining isotopic distributions in particles [132].

A study of engineered silver halide crystals used the high resolving power of a liquid metal ion gun to image 0.1- to 0.5-μm-thick layers of AgBr and $AgBr_{0.9}I_{0.1}$ that were grown on AgBr platelets (Fig. 4.41) [133]. The flat platelets

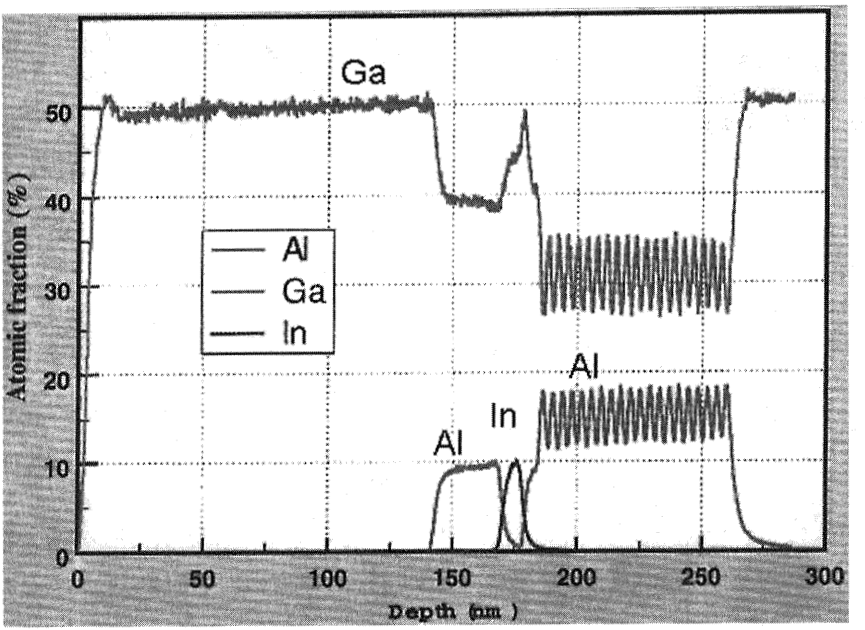

Figure 39 Quantitative depth profile on III–V compound structure using MCs^+ molecular ions. (From Ref. 128.)

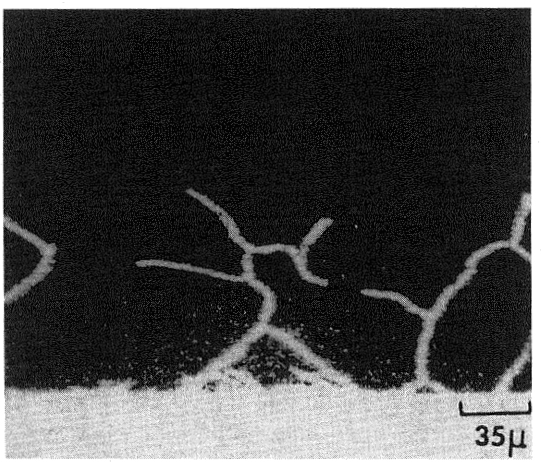

Figure 40 F^- secondary ion image on cross section of uranium-niobium-zirconium alloy. (From Ref. 129.)

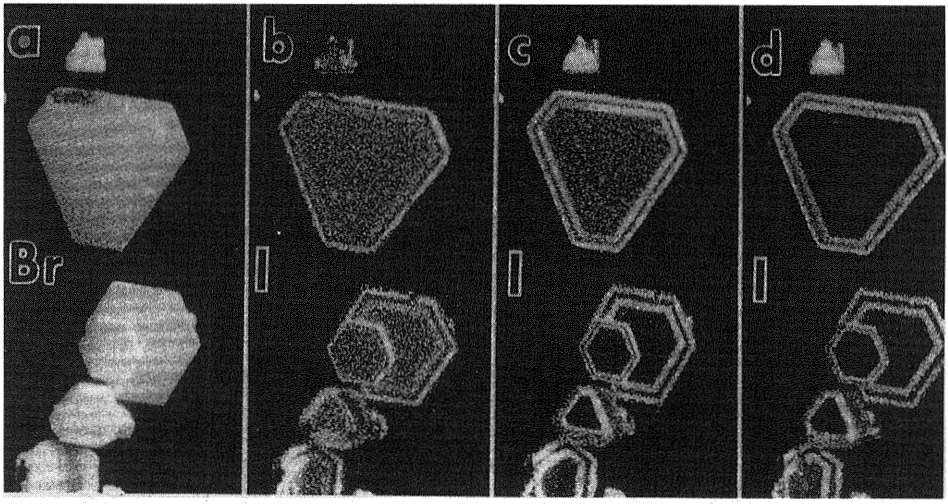

Figure 41 High-resolution secondary ion mass spectrometry (SIMS) images on silver halide microcrystals. Large crystal at top is 6.5 μm across. Crystals have four alternating layers of AgBr and $AgBr_{0.9}I_{0.1}$ on a AgBr core. A, Br^- image; b, I^- after ~3 nm removed; c, I^- after ~24 nm removed; d, I^- after ~46 nm removed. (From Ref. 133.)

are 3 to 7 μm across and <0.3 μm thick. The high resolving power of SIMS allowed the photographic materials engineers to study directly the effects of controlled physical and chemical conditions on composition and morphological characteristics.

The capability of SIMS to record all elements and isotopes with high spatial resolution in three dimensions is making it popular in solid-state science. Three-dimensional (3-D) imaging is done retrospectively, using a computer to stack a series of 2-D images. A good example of the visualization that may be done using 3-D data is shown in Fig. 4.42 [134]. The $^{16}O^-$ image of a separation by implanted oxygen (SIMOX) structure is 150 μm in diameter and 2.5 μm deep. The upper left shows a "pie slice" to reveal some inner structure that includes an oxide defect extending from the surface to a depth of about 2 μm. The bottom left is a horizontal slice showing the oxygen defect to be ~4 μm in diameter. At the right are O^- depth profiles from the defect at position A (top) and a typical region at position B (bottom). To show internal structure better, a "volume rendering," as illustrated in Fig. 4.43 [134], may be done. In this technique a gray and a partial transparency value for each voxel (3-D volume element) are calculated. Regions of low intensity are made transparent to maximize the visibility of internal structure. Since sputtering rates may not be uniform over the area viewed, topographical corrections of the 3-D images may be made by making maps of the surface before and after sputtering using atomic force microscopy [134,135].

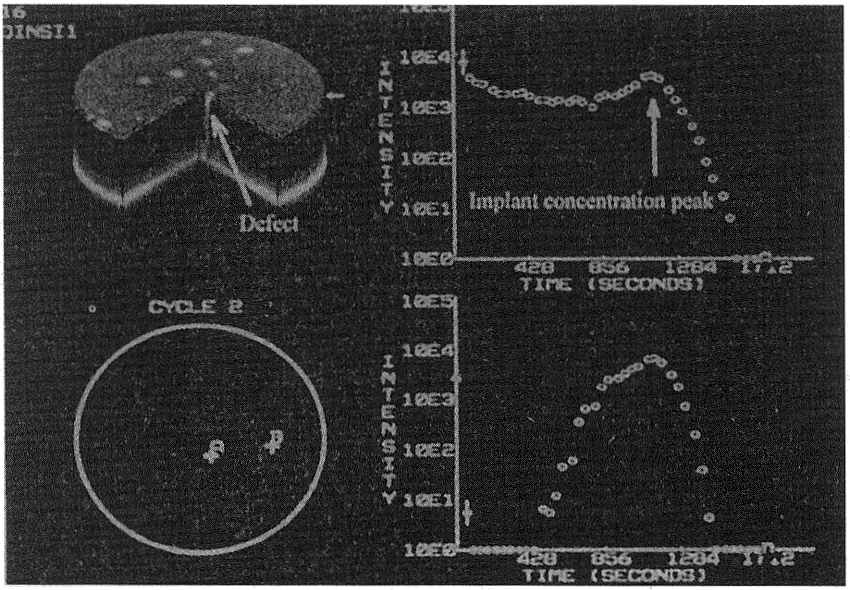

Figure 42 $^{16}O^-$ 3-D images and profiles from separation by implanted oxygen (SIMOX) structure illustrating computerized retrospective imaging capabilities. Field of view is 150 μm; depth is 2.5 μm. Cs^- primary beam. See text for details. (From Ref. 134.)

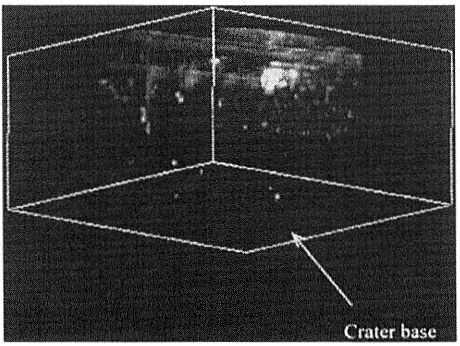

Figure 43 Volume rendering of D^- secondary ion distribution from a ZrO_2/Zr-2.5 Nb sample. Field of view is 150 μm; depth is 10 μm. (From Ref. 134.)

4.5.4 Isotopic

The ability of SIMS to measure isotopic ratios is one of its great strengths in surface analysis. This capability may be utilized in two ways: first, to determine isotopic ratios in dating (geological chronology), cosmology, nuclear physics, chemistry, monitoring of nuclear enrichment activities, etc., and second, to study or monitor diffusion, corrosion, or reaction mechanisms in solid materials through stable isotope substitution.

Measurement of isotopic composition in a mass spectrometer is natural, but not as simple a process as might be perceived at first glance. In SIMS, the measurements are complicated by isotopic fractionation, which is generally systematic and characterized by enrichment of the lighter ions with respect to the heavier ions. Shimizu and Hart [136] found that secondary ions were always enriched in the lighter ions and the fractionation per atomic mass unit (amu) followed a dependence proportional to high mass/low mass (M_H/M_L). Enrichment factors ranged from 6.5%/amu for boron to 0.6%/amu for lead. They also found that fractionation was dependent on the spatial location and kinetic energy of the extracted ions relative to the sputtered site. Thus, reproducing instrument parameters is important. Schwarz [137], however, found negative fractionation coefficients for MO^+, M^-, and M_2^- ions in certain energy ranges. Gnaser and Hutcheon [138] found that isotope fractionation depended linearly on the inverse velocity of the ejected ions. They showed that this correlation followed from an exponential dependence of the ionization probability, P, on the inverse velocity, v^{-1}, such that

$$P \propto \exp\left(\frac{-v_0}{v}\right) \tag{4.11}$$

In experiments on B, Si, and Ca, they found a value of $\sim 2 \times 10^6$ cm/sec for v_0. Lyon and Saxton [139] found fractionation due to sample chemical characteristics and crystallographic orientation in some cases but stated that with extensive calibration and careful control of parameters, reproducible isotopic ratios could be determined to one to two parts per thousand.

An illustration of the power of using isotopic substitution with SIMS to study reactions on the surface, and in the solid near the surface, involves isotopic substitution on the solid surface. The differences in the oxidation and fluorination of nickel were illustrated by depositing a thin layer (~10 nm) of ^{62}Ni-enriched nickel on the surface of a nickel substrate, exposing the surface to the reactant, and depth profiling the ^{62}Ni/^{58}Ni isotopic ratio [140,141]. In the oxidation case, the profile showed a low ratio of ^{62}Ni/^{58}Ni at the surface, then a higher ratio of ^{62}Ni/^{58}Ni as the oxide was sputtered through, and finally the normal substrate ratio. This showed that Ni atoms diffuse through the oxide to react at the surface with the oxygen. In the fluorination case, however, the ^{62}Ni layer was not displaced as fluorine diffused through the fluoride layer to react at the metal-fluoride interface.

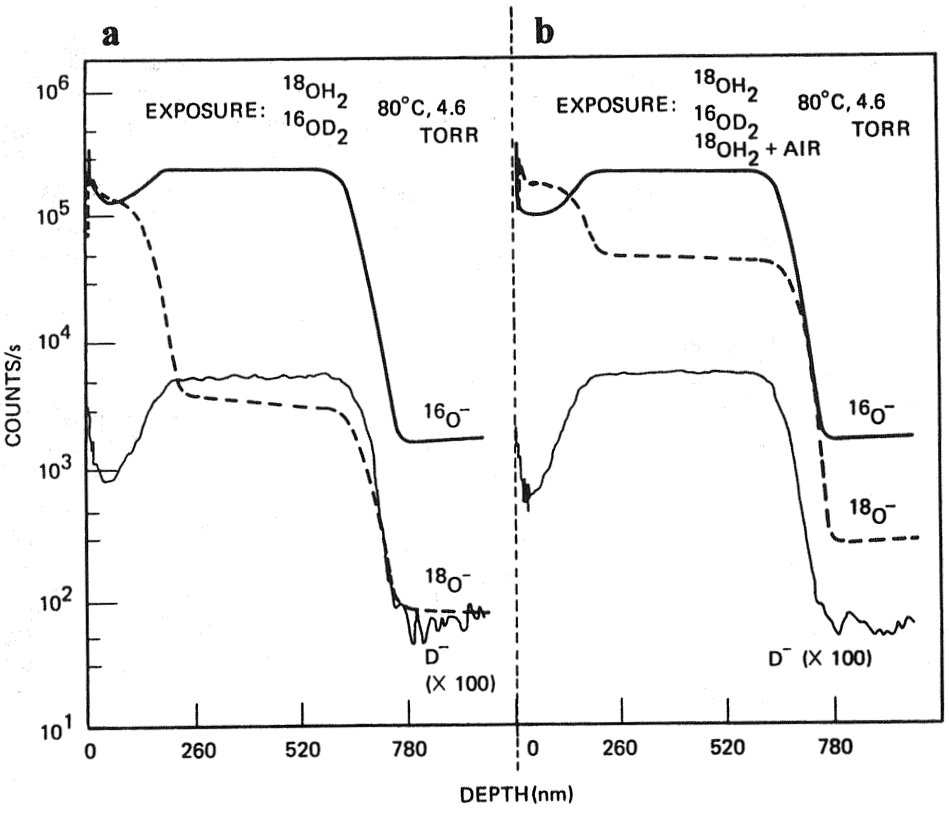

Figure 44 Depth profiles using stable isotopic substitution of reactants to reveal oxidation mechanism of water reaction with uranium and its inhibition in the presence of oxygen. N_2^+ primary beam used. See text. (From Refs. 142 and 143.)

Isotopically altered reactants were used to characterize many aspects of the reaction between uranium and vapor-phase water and to show the effect of oxygen on this reaction [142,143]. This study began with simple exposure of a polished uranium surface to $^{18}OH_2$ and $^{16}OH_2$. A profile of the oxide layers showed that the water adsorbed last produced the oxide nearest the metal. Thus, oxygen in some form diffused through the oxide to react at the oxide-metal interface. This is illustrated in Fig. 4.44a, where uranium was exposed to $^{18}OH_2$ for 6 hr, followed by exposure to $^{16}OD_2$ for 18 hr. Multiple exposures of equal length showed that the reaction rate was linear, except for a short delay in initiation (Fig. 4.45). These experiments also showed that the oxygen migration was strictly interstitial, as op-

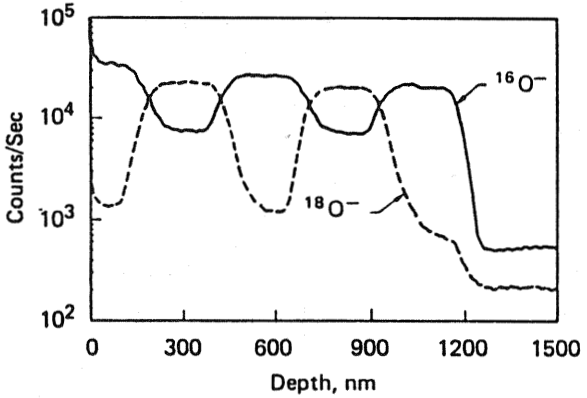

Figure 45 Depth profile on uranium sample exposed sequentially to $^{16}OH_2$, $^{18}OH_2$, $^{16}OH_2$, $^{18}OH_2$, $^{16}OH_2$, for 6 hr each at 80°C and 0.6 kPa. See text. (From Ref. 143.)

posed to vacancy migration (i.e., the slope of the $^{16}O^-$ signal between the first and second layers is the same as that between the third and fourth layers). Vacancy migration would involve the permanent oxide positions and broaden the interfaces with time. The deuterium isotope in the water of the second exposure shows that the oxygen is traveling with deuterium (or hydrogen) through the lattice probably as OD (or OH). The deuterium is a trapped species that exchanges very little [i.e., little change is seen after a third exposure to $^{18}OH_2$ (Fig. 4.44b)]. The profiles in Fig. 4.44 and 4.45 also show that the oxygen isotope from the last exposure is higher throughout the oxide. The change in ^{18}O in the ^{16}O oxide layer is very rapid. Using a series of short exposures, the half-life for exchange between the migrating species and the gas phase was measured as 6 min at 80°C. At 21°C the half-life was ~125 min. These experiments also showed that the rate-limiting step for the oxidation process is the reaction at the metal interface and is not due to the diffusion rate of migrating species. Although the migration is rapid, the migrating species could not be removed in vacuum or by exposure to a strong desiccant at 80°C. Thus the migrating species is not likely OH_2.

Before this study was done, it was known that the presence of oxygen inhibited the reaction between water and uranium. However, it was incorrectly assumed (and mathematically inferred) from weight gain studies that the mechanism for the inhibition was the formation of a monolayer of adsorbed or chemisorbed oxygen atoms on the oxide surface that served to block the adsorption of water molecules [144]. The SIMS profiles in Fig. 4.44b made after the final exposure to $^{18}OH_2$ clearly show that the ^{18}O migrating species has traveled to the metal surface without inhibition, and additional reaction with the metal has not occurred to

a measurable degree. Thus, the inhibition by oxygen occurs in the reaction process at the oxide-metal interface, not by blocking reaction at the oxide surface.

4.5.5 Surface Diffusion

Surface diffusion is an area in which SIMS is unmatched because of its good resolution and high sensitivity. An illustration of this was an experiment to determine the diffusion of molecular oxides over the surface of salt to ascertain whether surface diffusion would be a serious pathway for migration of plutonium oxides or daughter products from storage locations in salt formations [145]. In the experiment, La_2O_3 was substituted for plutonium oxides and SrO for daughter products. La_2O_3 and SrO (600 and 1400 nm thick, respectively) were deposited on a polished NaCl substrate by using an electron beam. Each sample was heated to 693°K for 473–920 hr. The samples were carbon coated to provide conductivity. An O^- beam was used to sputter areas 30×38 μm starting at a point distant from the edge of the deposit and moving toward the deposit. The resultant concentration data were superposed on plots generated from the usual one-dimensional diffusion equation for a semi-infinite source. The fit of the data for SrO annealed for 473 hr is shown in Fig. 4.46. At the low end of the plot, SIMS is detecting $\sim 10^{-15}$ g of SrO. The diffusion rate of 2.0×10^{-10} cm^2/sec indicated that surface diffusion would not be a serious loss mode for salt formation storage.

4.6 CONCLUSIONS

The closely allied topics of secondary neutral mass spectrometry (SNMS), fast atom bombardment (FAB), and laser ablation SIMS are important, but are beyond the scope of this chapter. SNMS is a technique in which neutral atoms or molecules, sputtered by an ion beam, are ionized in an effort to improve sensitivity and to decouple ion formation from matrix chemical properties, making quantification easier. This ionization is commonly effected by electron beams or lasers. FAB uses a neutral atom beam to create ions on the surface. It is often useful for insulator analysis. Laser ablation creates ions in either resonant or nonresonant modes and can be quite sensitive and complex.

Computer software and hardware are also important to the modern SIMS laboratory for automated instrument control, data acquisition, data display, interpretation, and quantitation.

Although SIMS has reached the status of a mature technique, instrumentation hardware and software improvements continue at a rapid pace as range and applications continue to grow. High detection sensitivity, high spatial resolution in three dimensions, detection of all elements, and isotopic capability give SIMS a strong and unique position among surface analysis techniques.

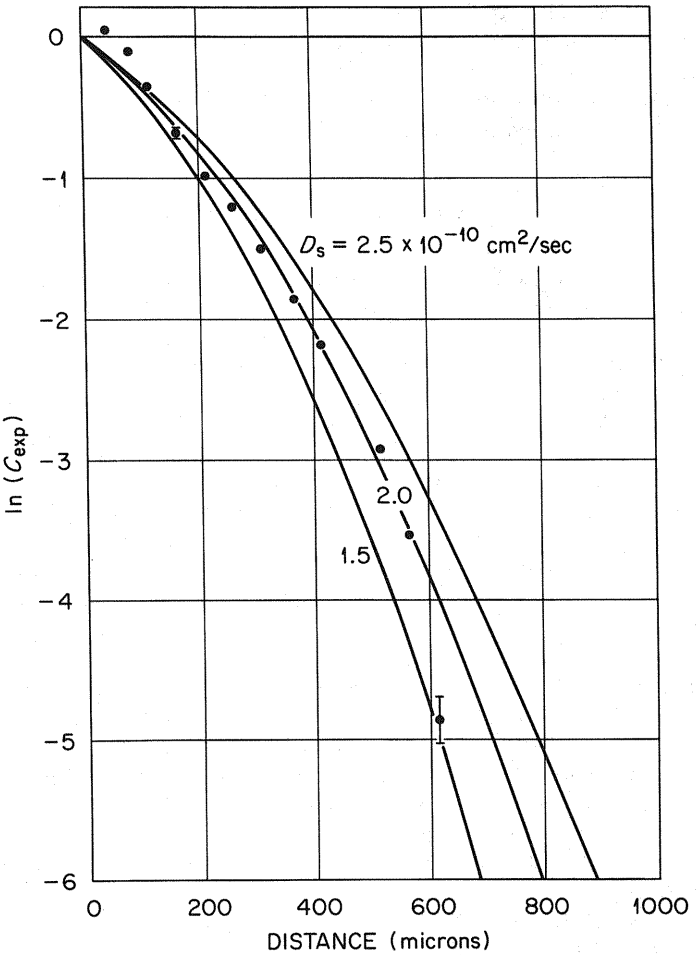

Figure 46 Superposition of secondary ion mass spectrometry (SIMS) concentration data for SrO on theoretical surface diffusion curves. SrO had diffused for 473 hr at 693K. (From Ref. 145.)

REFERENCES

1. Wei, C. Y., Current, M. I., and Seidman, D. N., *Philos. Mag. A*, *14*, 459 (1981).
2. Heinisch, H. L., *Philos. Mag A*, *45*, 1085 (1982).
3. Levi-Setti, R., Crow, G., and Wang, Y. L., in *Secondary Ion Mass Spectrometry, SIMS V*, Benninghoven, A., Colton, R. J., Simons, D. S., and Werner, H. W., eds., Springer-Verlag, Berlin, 132 (1986).
4. Thomson, J. J., *Philos. Mag.*, *20*, 252 (1910).
5. Woodcock, K. S., *Phys. Rev.*, *35*, 1090 (1930).

6. Sloane, R. H. and Press, R., *Nature, London, 141*, 872 (1938).
7. Sloane, R. H. and Press, R., *Proc. R. Soc. Ser. A, 168*, 284 (1938).
8. Arnot, F. L. and Beckett, C., *Proc. R. Soc. Ser. A, 168*, 103 (1938).
9. Herzog, R. F. K. and Viehböck, F. P., *Phys. Rev., 76*, 855L (1949).
10. Veksler, V. I. And Ben'iaminovich, M. B., *Sov. Phys. Tech. Phys., 1*, 1626 (1957).
11. Honig, R. E., *J. Appl. Phys., 29*, 549 (1958).
12. Bradley, R. C., *J. Appl. Phys., 30*, 1 (1959).
13. Stanton, H. E., *J. Appl. Phys., 31*, 678 (1960).
14. Liebl, H. J. and Herzog, R. F. K., *J. Appl. Phys., 34*, 2893 (1963).
15. Barrington, A. E., Herzog, R. F. K., and Poschenrieder, W. P., *Progress in Nuclear Energy, Series IX, Analytical Chemistry*, Elion, H. A. and Stewart, D. C., eds., 243 (1966).
16. v. Ardenne, M., *Tabellen der Elektronenphysik, Ionenphysik und Ubermikroskopie*, VEB Deutscher Verlag der Wissenschaften, Berlin, *I*, 554 (1956).
17. Barrington, A. E., Herzog, R. F. K., and Poschenrieder, W. P., *J. Vac. Sci. Techn., 3*, 239 (1966).
18. Castaing, R. and Slodzian, G., *J. Microsc., 1*, 395 (1962).
19. Castaing, R. and Slodzian, G., *C. R. Acad. Sci. (Paris) 255*,1893 (1962).
20. Rouberol, J. M., Guernet, J., Deschamps, P., Dagnot, J. P. and Guyon de la Berge, J. M., in *Proceedings of the 5th International Conference on X-Ray Optics and Microanalysis*, Tubingen, 1968, Mollenstedt, G. M. and Gaukler, K. M., eds., Springer, Berlin, 311 (1969).
21. Rouberol, J. M., Basseville, P., and Lenoir, J. P., in *Proceedings of the 6th International Conference on X-Ray Optics and Microanalysis*, Osaka, 1971, Shinoda, G., Kohra, K., and Ichinokawa, T., eds., University of Tokyo, Tokyo, 409 (1972).
22. Castaing, R., and Henry, L., *C. R. Acad. Sci. (Paris) 255*, 76 (1962).
23. Castaing, R., Hennequin, J. F., Henry, L., and Slodzian, G., in *Focusing of Charged Particles*, Vol. II, Septier, A., ed., Academic, New York, 265, (1967).
24. Liebl, H., *J. Appl. Phys., 38*, No. 13, 5277 (1967).
25. Robinson, C. F., Liebl, H. J., and Andersen, C. A., *Third National Conference on Electron Microprobe Analysis*, Chicago, 1968.
26. Bernhard, F., Krebs, K. H., and Rotter, I. *Z. Phys., 16*, 103 (1961).
27. Long, J. V. P., *J. Appl. Phys., 16*, 1277 (1965).
28. Drummond, I. W. and Long, J. V. P., *Nature, 215*, 950 (1967).
29. Banner, A. E., Bateman, R. H., Halliday, J. S., and Wildig, E., *AEI New Product Information*, (1972).
30. Tamura, H., Kondo, T., Doi, H., Omura, I., and Taya, S., in *Recent Developments in Mass Spectrometry, 205*, Univ. Tokyo Press (1970).
31. Tamura, H., Kondo, T., Hirano, T., *Proceedings of the 6th International Conference on X-Ray Optics and Microanalysis*, University Tokyo Press 423 (1970).
32. Nakamura, K., Aoki, S., Tamura, H., and Doi, H. *Proceedings of the 6th International Conference on X-Ray Optics and Microanalysis*, 447, University Tokyo Press (1970).
33. Benninghoven, A., *Phys. Status Solidi, 34*, K169 (1969).
34. Benninghoven, A., and Loebach, E., *Rev. Sci. Instr., 42*, No. 1, 49 (1971).

35. Schroeer, J. M., in *Secondary Ion Mass Spectrometry*, Heinrich, K. F. J. and Newbury, D. E., eds., National Bureau of Standards Special Publication 427, Washington, DC, 121 (1975).
36. Andersen, C. A., *Fifth, Sixth, and Seventh National Electron Microprobe Conference*, New York, 1970; Pittsburgh, 1971; and San Francisco, 1972.
37. Andersen, C. A. and Hinthorne, J. R., *Anal. Chem.*, *45*, 1421 (1973).
38. Andersen, C. A., in *Secondary Ion Mass Spectrometry*, Heinrich, K. F. J. and Newbury, D. E., eds., National Bureau of Standards Special Publication 427, Washington, DC, 79 (1975).
39. Saha, M. N., *Philos. Mag.*, *40*, 472 (1920).
40. Saha, M. N., *Z. Phys.*, *6*, 40 (1921).
41. Eggert, J., *Z. Phys.*, *20*, 570 (1919).
42. Wittmaack, K., *Rev. Sci. Instr.*, *47*, 157 (1976).
43. Wittmaack, K., in *Advances in Mass Spectrometry 7A*, Daly, N. R., ed., Heyden & Sons, London, 758 (1978).
44. Slodzian, G. and Figueras, A., in *Proceedings of the 8th International Conference on X-Ray Optics and Microanalysis*, Boston, 1977, Beamon, D. R., Olgivie, R. E., and Wittry, D. B., eds., Pendell, Midland, MI, 659 (1980).
45. *Secondary Ion Mass Spectrometry, SIMS II*, Benninghoven, A., Evans, C. A. Jr., Powell, R. A., Shimizu, R., and Storms, H. A., eds., Springer Verlag, Berlin-Heidelberg, New York, 1979.
46. Krohn, V. E. and Ringo, G. R., *Int. J. Mass Spectrom. Ion Phys.*, *22*, 307 (1975).
47. Seliger, R. L., Ward, J. W., Wang, V., and Kubena, R. L., *Appl. Phys. Lett.*, *34*, 310 (1979).
48. Prewett, P. D. and Jeffries, D. K., *Inst. Phys. Conf. Ser. No. 54*, 316 (1980).
49. Levi-Setti, R., Wang, Y. L., and Crow, G., *J. de Physique*, *45*, *C9*, 197 (1984).
50. Chait, B. T. and Standing, K. G., *Int. J. Mass Spectrom. Ion Phys.*, *40*, 185 (1981).
51. Steffens, P., Niehuis, E., Friese, T., Greifendorf, D., and Benninghoven, A., in *Secondary Ion Mass Spectrometry, SIMS IV*, Benninghoven, A., Okano, J., Shimizu, R., and Werner, H. W., eds., Springer Verlag, Berlin, Heidelberg, New York, 404 (1984).
52. Niehuis, E., Heller, T., Feld, H., and Benninghoven, A. in *Secondary Ion Mass Spectrometry, SIMS V*, Benninghoven, A., Colton, R. J., Simons, D. S., and Werner, H. W., eds., Springer-Verlag, Berlin, 188 (1986).
53. Waugh, A. R., Kingham, D. R., Hearn, M. J., and Briggs, D. A., in *Secondary Ion Mass Spectrometry, SIMS VI*, Benninghoven, A., Huber, A. M., and Werner, H. W., eds., John Wiley & Sons, Chichester, 231 (1988).
54. Eccles, A. and Vickerman, J. C., in *Secondary Ion Mass Spectrometry, SIMS VI*, Benninghoven, A., Huber, A. M., and Werner, H. W., eds., John Wiley & Sons, Chichester, 239 (1988).
55. Schueler, B., Sander, P., and Reed, D. A., in *Secondary Ion Mass Spectrometry, SIMS VII*, Benninghoven, A., Evans, C. A., McKeegan, K. D., Storms, H. A., and Werner, H. W., eds., John Wiley & Sons, Chichester, 851 (1990).
56. Compston, W., Williams, I. S., and Clement, S. W. J., *Am. Soc. Mass Spectrom. Conf., 30th*, Honolulu, 593 (1982).
57. Matsuda, H., *Int. J. Mass Spect. Ion Phys.*, *14*, 219 (1974).

58. Clement, S. W. J. and Compston, W., in *Secondary Ion Mass Spectrometry, SIMS VII*, Benninghoven, A., Evans, C. A., McKeegan, K. D., Storms, H. A., and Werner, H. W., eds., John Wiley & Sons, Chichester, 815 (1990).
59. Stanford University Web Site: *http://shrimprg.stanford.edu/MainMenu.html*
60. Conty, C., Rasser, B., and Migeon, H. N., in *Secondary Ion Mass Spectrometry, SIMS VII*, Benninghoven, A., Evans, C. A., McKeegan, K. D., Storms, H. A., and Werner, H. W., eds., John Wiley & Sons, Chichester, 831 (1990).
61. Hillion, F., Daigne, B., Girard, F., Slodzian, G., and Schuhmacher, M., in *Secondary Ion Mass Spectrometry, SIMS IX*, Benninghoven, A., Nihei, Y., Shimizu, R., and Werner, H. W., eds., John Wiley & Sons, Chichester, 254 (1994).
62. Dowsett, M. G., Smith, N. S., Bridgeland, R., Richards, D., Lovejoy, A. C., and Pedrick, P., in *Secondary Ion Mass Spectrometry, SIMS X*, Benninghoven, A., Hagenhoff, B., and Werner, H. W., eds., John Wiley & Sons, Chichester, 367 (1997).
63. *Secondary Ion Mass Spectrometry: Proceedings of a Workshop on Secondary Ion Mass Spectrometry and Ion Microprobe Mass Analysis*, Heinrich, K. F. J. and Newbury, D. E., eds., National Bureau of Standards Special Publication, Washington, DC, 427 (1975).
64. McHugh, J. A., in *Methods of Surface Analysis*, Czanderna, A. W., ed., Elsevier Scientific, New York, 223 (1975).
65. Honig, R. E., in *Secondary Ion Mass Spectrometry, SIMS V*, Benninghoven, A., Colton, R. J., Simons, D. S., and Werner, H. W., eds., Springer-Verlag, Berlin, 2 (1986).
66. Bernius, M. T. and Morrison, G. H. *Rev. Sci. Instrum.*, *58*(10), 1789 (1987).
67. *Secondary Ion Mass Spectrometry: Basic Concepts, Instrumental Aspects, Applications and Trends*, Benninghoven, A., Rüdenauer, F. G., and Werner, H. W., John Wiley & Sons, New York (1987).
68. *Secondary Ion Mass Spectrometry: Principles and Applications*, Vickerman, J. C., Brown, A., and Reed, N. M., eds., Clarendon Press, Oxford, (1989).
69. Wilson, R. G., Stevie, F. A., and Magee, C. W., *Secondary Ion Mass Spectrometry: A Practical Handbook for Depth Pro ling and Bulk Impurity Analysis*, John Wiley & Sons, New York (1989).
70. Sigmund, P., in *Topics in Applied Physics*, Vol. 47, *Sputtering by Particle Bombardment*, Behrisch, R., ed., Springer-Verlag, Berlin, 9 (1981).
71. Rol, P. K., Fluit, J. M., and Kistemaker, J. *Physica*, *26*, 1009 (1960).
72. Almen, O. and Bruce, G., *Nucl. Instr. Meth.*, *11*, 257 (1961).
73. Rol, P. K., Onderdelinden, D., and Kistemaker, J. *Trans. Third Internatl. Vacuum Congr.*, Pergamon Press, 75 (1966).
74. Wilson, R. G. and Brewer, G. R., *Ion Beams*, John Wiley & Sons, New York, p. 325 (1973).
75. McHugh, J. A. *Radiat. Eff.*, *21*, 209 (1974).
76. Hauffe, W., in *Secondary Ion Mass Spectrometry, SIMS III*, Benninghoven, A., Giber, J., Laszlo, J., Riedel, M., and Werner, H. W., eds., Springer Verlag, Berlin, Heidelberg, New York, 206 (1982).
77. Wilson, R. G., Stevie, F. A., and Magee, C. W., *Secondary Ion Mass Spectrometry: A Practical Handbook for Depth Pro ling and Bulk Impurity Analysis*, John Wiley & Sons, New York, 2.7-4, (1989).

78. Tsunoyama, K., Suzuki, T., Ohashi, Y., and Konishi, M., in *Secondary Ion Mass Spectrometry, SIMS III*, Benninghoven, A., Giber, J., Laszlo, J., Riedel, M., and Werner, H. W., eds., Springer Verlag, Berlin, Heidelberg, New York, 211 (1982).
79. Zalar, A., *Thin Solid Films*, *124*, 223 (1985).
80. Hughes, H., Baxter, R. D., and Phillips, B. *IEEE, Trans. Nucl. Sci.*, *NS-19*, 256 (1972).
81. Hues, S. M., Arizona State University, Ph.D. Dissertation (1986).
82. Storms, H. A., Brown, K. F., and Stein, J. D., *Anal. Chem.*, *49*(13), 2023 (1977).
83. Andersen, C. A., *Int. J. Mass Spectrom. Ion Physics*, *2*, 61 (1969).
84. McHugh, J. A., in *Methods of Surface Analysis*, Czanderna, A. W., ed., Elsevier Scientific, New York, 235 (1975).
85. Slodzian, G., *Surf. Sci.*, *48*, 161 (1975).
86. Schauer, S. N. and Williams, P., in *Secondary Ion Mass Spectrometry, SIMS VII*, Benninghoven, A., Evans, C. A., McKeegan, K. D., Storms, H. A., and Werner, H. W., eds., John Wiley & Sons, Chichester, 827 (1990).
87. Jurela, Z., *Int. J. Mass Spect. Ion Phys.*, *12*, 33 (1973).
88. Shroeer, J., Rhodin, T., and Bradley, R., *Surface Sci.*, *34*, 571 (1973).
89. Sroubek, Z., *Surface Sci.*, *44*,47 (1974).
90. Benninghoven, A., *Z. Phyzik*, *220*, 419 (1969).
91. Castaing, R. and Hennequin, J. F., *Adv. Mass Spectrom.*, *5*, 419 (1971).
92. Rudat, M. A. and Morrison, G. H., *Anal. Chem.*, *51*(8), 1179 (1979).
93. van der Heide, P. A. W., McIntyre, N. S., Sodervall, U., Odelius, H., and Lodding, A., in *Secondary Ion Mass Spectrometry, SIMS X*, Benninghoven, A., Hagenhoff, B., and Werner, H. W., eds., John Wiley & Sons, Chichester, 677 (1997).
94. Norskov, J. K. and Lundquist, B. I. *Phys. Rev. B.*, *19*, 5661 (1979).
95. Lösing, R., Reger, N., Stadermann, F. J., and Ortner, H. M., in *Secondary Ion Mass Spectrometry, SIMS XI*, Gillen, G., Lareau, R., Bennett, J., Stevie, F., eds., John Wiley & Sons, Chichester, 1019 (1998).
96. Gao, Y., *J. Appl. Phys.*, *64*, 3760 (1988).
97. Shroeer, J. M., Gnaser, H., and Oechsner, H., in *Secondary Ion Mass Spectrometry, SIMS IX*, Benninghoven, A., Nihei, Y., Shimizu, R., and Werner, H. W., eds., John Wiley & Sons, Chichester, 386 (1994).
98. Wittmaack, K., *Nucl. Instr. Methods B64*, 621 (1992).
99. Homma, Y., Higashi, Y., Maruo, T., Maekawa, C., and Ochiai, S., in *Secondary Ion Mass Spectrometry, SIMS IX*, Benninghoven, A., Nihei, Y., Shimizu, R., and Werner, H. W., eds., John Wiley & Sons, Chichester, 398 (1994).
100. Wittmaack, K., in *Secondary Ion Mass Spectrometry, SIMS X*, Benninghoven, A., Hagenhoff, B., and Werner, H. W., eds., John Wiley & Sons, Chichester, 657 (1997).
101. Wilson, R. G., *J. Appl. Phys.*, *63*, 5121 (1988).
102. Ganjei, J. D., Leta, D. P., Morrison, G. H. *Anal. Chem.*, *50*, 285 (1978).
103. Odom, R. W., Furman, B. K., Evans, C. A., Jr., Bryson, C. E., Petersen, W. A., Kelley, M. A., and Wayne, D. H., *Anal. Chem.*, *55*, 574 (1983).
104. Delmore, J. E., Appelhans, A. D., and Peterson, E. S., *Int. J. Mass Spec. Ion Proc.*, *146/147*, 15, (1995).
105. Appelhans, A. D. and Delmore, J., *Anal. Chem.*, *61*, 1087 (1989).
106. Gillen, G., *11th Annual SIMS Workshop*, Abstracts, 27 (1998).

107. *Secondary Ion Mass Spectrometry, SIMS XI*, Gillen, G., Lareau, R., Bennett, J., Stevie, F., eds., John Wiley & Sons, Chichester, 581 (1998).
108. Robinson, C. F., Andersen, C. A., and Roden, H. J., The Pittsburgh Conference, Cleveland, Ohio, Paper #122 (1969).
109. Okutani, T., Shinoyama, T., Ohshima, M., and Noda, T., in *Secondary Ion Mass Spectrometry, SIMS V*, Benninghoven, A., Colton, R. J., Simons, D. S., and Werner, H. W., eds., Springer-Verlag, Berlin, 139 (1986).
110. Slodzian, G., Chaintreau, M., and Dennebouy, R., in *Secondary Ion Mass Spectrometry, SIMS V*, Benninghoven, A., Colton, R. J., Simons, D. S., and Werner, H. W., eds., Springer-Verlag, Berlin, 158 (1986).
111. Daly, N. R., *Rev. Sci. Instr.*, *31*, 264 (1960).
112. Schwede, B. C., Heller, T., Rading, D., Niehuis, E., Hagenhoff, B., Wiedmann, L., and Benninghoven, A., in *Secondary Ion Mass Spectrometry, SIMS XI*, Gillen, G., Lareau, R., Bennett, J., Stevie, F., eds., John Wiley & Sons, Chichester, 509 (1998).
113. Vickerman, J. C., Briggs, D., and Henderson, A., *The Static SIMS Library*, Surface Spectra (1997).
114. Benninghoven, A., *Surf. Sci.*, *35*, 427 (1973).
115. Chartogne, A. and Saldi, F., in *Secondary Ion Mass Spectrometry, SIMS XI*, Gillen, G., Lareau, R., Bennett, J., Stevie, F., eds., John Wiley & Sons, Chichester, 943 (1998).
116. Barber, M., Vickerman, J. C., and Wolstenholme, J., *Surf. Sci.*, *68*, 130 (1977).
117. Gillet, E., Channakhone, S., Matolin, V., and Gillet, M., *Surf. Sci.*, *152/153*, 603 (1985).
118. Karen, A., Man, N., Okumura, H., Okuno, K., Soeda, F., and Ishitani, A., in *Secondary Ion Mass Spectrometry, SIMS X*, Benninghoven, A., Hagenhoff, B., and Werner, H. W., eds., John Wiley & Sons, Chichester, 481 (1997).
119. Dowsett, M. G., in *Secondary Ion Mass Spectrometry, SIMS XI*, Gillen, G., Lareau, R., Bennett, J., Stevie, F., eds., John Wiley & Sons, Chichester, 259 (1998).
120. Wittmaack, K., *Surf. Interf. Anal.*, *24*, 389 (1996).
121. Smith, N. S., Dowsett, M. G., McGregor, B., and Phillips, P., in *Secondary Ion Mass Spectrometry, SIMS X*, Benninghoven, A., Hagenhoff, B., and Werner, H. W., eds., John Wiley & Sons, Chichester, 363 (1997).
122. Ronsheim, P. A., Lee, K. L., Patel, S. B., and Schuhmacher, M., in *Secondary Ion Mass Spectrometry, SIMS XI*, Gillen, G., Lareau, R., Bennett, J., Stevie, F., eds., John Wiley & Sons, Chichester, 301 (1998).
123. Vanberkum, J. G. M., Collart, E. J. H., Weemers, K., Gravesteijn, D. J., Iltgen, K., Benninghoven, A., and Niehuis, E., *J. Vac. Sci. Technol. B.*, *16*, 298 (1998).
124. Iltgen, K., Brox, O., and Benninghoven, A., in *Secondary Ion Mass Spectrometry, SIMS XI*, Gillen, G., Lareau, R., Bennett, J., Stevie, F., eds., John Wiley & Sons, Chichester, 305 (1998).
125. Magee, C. W., Mount, G. R., Smith, S. P., Herner, B., and Gossmann, H. J., *J. Vac. Sci. Technol. B.*, *16*, 3099 (1998).
126. CAMECA Technical Note, *Shallow Depth Pro ling with the CAMECA IMS 6f*, 11 (1998).

127. Hitzman, C. J. and Mount, G., in *Secondary Ion Mass Spectrometry, SIMS XI*, Gillen, G., Lareau, R., Bennett, J., Stevie, F., eds., John Wiley & Sons, Chichester, 273 (1998).
128. CAMECA Technical Note, *Shallow Depth Pro ling with the CAMECA IMS 6f*, 15 (1998).
129. Cristy, S. S., unpublished.
130. Messenger, S., *11th Annual SIMS Workshop*, Abstracts, 26 (1986).
131. *IAEA Bull.*, *38*(4) (1996).
132. Simons, D. S., Gillen, G., Zeissler, C. J., Fleming, R. H., and McNitt, P. J., in *Secondary Ion Mass Spectrometry, SIMS XI*, Gillen, G., Lareau, R., Bennett, J., Stevie, F., eds., John Wiley & Sons, Chichester, 59 (1998).
133. Chabala, J. M., Bohonek, J., Levi-Setti, R., Maternaghan, T. J., and Kriebel, A. N., in *Secondary Ion Mass Spectrometry, SIMS XI*, Gillen, G., Lareau, R., Bennett, J., Stevie, F., eds., John Wiley & Sons, Chichester, 651 (1998).
134. van der Heide, P. A. W., in *Secondary Ion Mass Spectrometry, SIMS XI*, Gillen, G., Lareau, R., Bennett, J., Stevie, F., eds., John Wiley & Sons, Chichester, 821 (1998).
135. Gnaser, H., in *Secondary Ion Mass Spectrometry, SIMS XI*, Gillen, G., Lareau, R., Bennett, J., Stevie, F., eds., John Wiley & Sons, Chichester, 827 (1998).
136. Shimizu, N. and Hart, S. R., *J. Appl. Phys.*, *53*, 1303 (1982).
137. Schwarz, S. A., in *Secondary Ion Mass Spectrometry, SIMS V*, Benninghoven, A., Colton, R. J., Simons, D. S., and Werner, H. W., eds., Springer-Verlag, Berlin, 38 (1986).
138. Gnaser, H. and Hutcheon, I. D., *Phys. Rev. B*, *35*, 877 (1987).
139. Lyon, I. C. and Saxton, J. M., in *Secondary Ion Mass Spectrometry, SIMS XI*, Gillen, G., Lareau, R., Bennett, J., Stevie, F., eds., John Wiley & Sons, Chichester, 55 (1998).
140. Cristy, S. S., Ferree, D. V., Nolan, T. A., and McCulla, W. H., *Studies of Oxide and Fluoride Films on Metals Using an Ion Microprobe Mass Analyzer*, Y-DA 4815, Union Carbide Corporation—Nuclear Division, Oak Ridge Y-12 Plant, Oak Ridge, TN (1972).
141. Cristy, S. S. and Condon, J. B., in *Secondary Ion Mass Spectrometry, SIMS II*, Benninghoven, A., Evans, C. A. Jr., Powell, R. A., Shimizu, R., and Storms, H. A., eds., Springer Verlag, Berlin, Heidelberg, New York, 151 (1979).
142. Condon, J. B., Cristy, S. S., and Kirkpatrick, J. R., Final Progress Report—Uranium Reactions with Water Vapor, Y/DU-274, Union Carbide Corporation—Nuclear Division, Oak Ridge Y-12 Plant, Oak Ridge, TN (1983).
143. Cristy, S. S. and Condon, J. B., in *Secondary Ion Mass Spectrometry, SIMS V*, Benninghoven, A., Colton, R. J., Simons, D. S., and Werner, H. W., eds., Springer-Verlag, Berlin, 405 (1986).
144. Totemeier, T. C., ANL/ED/95-2, Argonne National Laboratory-West, Idaho Falls, ID, 10 (1995).
145. Cristy, S. S. and Annis, B. K., *Scripta Metallurgica*, *8*, 695 (1974).

5
Isotope Dilution Mass Spectrometry

David H. Smith
Oak Ridge National Laboratory
Oak Ridge, Tennessee

5.1 INTRODUCTION

Isotope dilution mass spectrometry is a powerful method for determining the quantity of an element or an associated compound in a sample. It requires that a spike of the same element but with an isotopic composition different from that of the sample be introduced to it in a controlled manner. The mass spectrum of the mixture of spike and sample is then used to determine the concentration of the target element in the original sample. In most cases, a single ratio is used, one that incorporates the major isotope in the spike and the major isotope in the sample; these must be different isotopes. The difference in the value of this ratio in the sample and in the mixture of sample and spike is proportional to the amount of the target element in the sample.

Isotope dilution has been in use for well over 40 years, having been developed by Inghram in 1954 for determination of minor and trace level elements [1]. It had its first major application in conjunction with thermal ionization mass spectrometry but is today used with virtually every kind of instrumentation and in virtually every analytical area in which elemental concentrations are of importance. It also has been applied to the determination of compound concentrations by using an appropriate molecular spike containing an enriched isotope of one of its elements. It has gone beyond its original application in elemental analysis of inorganic materials and is used routinely in fields far removed from its origins.

Isotope dilution is usually the most accurate and most sensitive quantification technique when sample size is limited. It has in recent years even been used in certifying the compositions of reference materials [2]. The use of isotope dilution mass spectrometry in the standard reference materials program of the National

Institute of Science and Technology has been described by Bowers et al [3]. A recent report describes using isotope dilution to calibrate analysis of solid samples using electrothermal vaporization with inductively coupled plasma mass spectrometry (ICP-MS) [4].

It is obvious that, no matter what kind of mass spectrometer or ionization method is used, correction for isotopic bias is mandatory for successful application of isotope dilution. The basis of the whole technique rests on trustworthy measurement of the isotope dilution ratio [R_m in Eq. (5.7)], which necessitates application of a bias correction. Accuracy of the final result is critically dependent upon accurate calibration of the instrumentation, and, as always, it is important to have analysis of reference materials mimic as closely as possible that of samples.

5.2 SAMPLE PREPARATION

An absolutely essential step in isotope dilution is to achieve equilibration of spike and sample. The spike is usually added as a solution whose concentration is accurately known; since many samples are not solutions, chemical processing is usually required to equilibrate the two. This invariably involves dissolving the sample, not always a simple task. The spike solution is added to the sample, and the two are thoroughly mixed. Equilibration for some elements requires nothing more than to have spike and sample in solution together. Some elements, like plutonium, have a multiplicity of oxidation states and require more effort; this very often includes drying the sample and redissolving it, and adding an oxidizing or reducing agent to ensure that the target element in both spike and sample assumes the same oxidation state. Once equilibration is attained, it is unnecessary to achieve full recovery of the analyte element in subsequent chemical processing, one of the big advantages of isotope dilution. Full recovery is not required because chemical processes do not cause isotopic fractionation, at least to the degree necessary to affect results significantly. This characteristic of isotope dilution is particularly advantageous when the sample is a complex matrix such as vegetation, soil, or animal tissue. To exploit this attribute, the spike should be added to the sample as early in the chemical preparation process as possible. For example, in the author's laboratory the ^{233}U spike is added to the platinum dish containing a vegetation sample whose uranium content is desired before it is inserted into the muffle furnace; the spike is thus introduced before any chemical processing has occurred.

Because extensive chemical processing is involved in using isotope dilution, it is important to determine the level of the process blank before analyzing samples. Although there are a few instances in which doing so is unnecessary, the vast majority of problems require it; it obviously becomes more important with decreasing concentration of the analyte element. Many elements are ubiquitous in nature and occur at some level in virtually all reagents, including purified water. In numerous applications the blank level rather than the instrumentation determines

the process detection limit. A *process blank* is one that tests the whole chemical procedure, including the instrument and all reagents. A known amount of calibrated spike is added to the solvent (usually acid) and the mixture subjected to all steps a real sample would undergo. The amount of the target element is measured in the same way a normal isotope dilution analysis is carried out. If the blank is unacceptably high, the source of contamination must be identified and eliminated. This can be a tedious, time-consuming operation. Once the blank level is established, samples must be corrected for its contribution unless it is deemed insignificant.

Isotope dilution involves isotopes of the same element, thus eliminating differences in chemical behavior that can plague techniques that use different elements for the spike than the one being analyzed. This, along with the fact that quantitative recovery is not necessary once spike and sample have been equilibrated, makes isotope dilution less subject to error arising in chemical processing than many elemental assay techniques, a fact of great importance at low concentration levels.

5.3 ISOTOPE DILUTION EQUATION

Isotope dilution was first developed by Inghram in 1954 [1]. Since that time its application has become very widespread, and has been used in numerous disciplines. The following derivation is based on that of Hintenberger [5]. The following notation is used:

C = concentration
W = weight
A = atomic weight
a = atomic abundance
R = ratio
N = number of atoms

The subscripts are defined as follows:

s = unspiked sample
t = tracer (spike)
m = mixture of spike and sample
i = major isotope in the sample
k = major isotope in the spike

The ratios (R_x)are defined as follows:

$$R_x = a_{xi}/a_{xk} \tag{5.1}$$

Note that isotope i is usually that of high abundance in the sample and k the isotope of high abundance in the spike, but using the reverse definition is algebraically equivalent. Note that the equation simplifies if the spike isotope is not present in the sample.

We start with the following equation:

$$R_m = \frac{N_i}{N_k} = \frac{N_{is} + N_{it}}{N_{ks} + N_{kt}} \tag{5.2}$$

This is simply the ratio of isotope i (sample) to isotope k (tracer or spike) in the mixture of the two as measured by the mass spectrometer. Each isotope has a contribution from each component of the mixture.

Because we want the concentration of the total element and not just that of a single isotope, we modify the equation to include the total number of atoms in the sample:

$$R_m = \frac{N_s a_{is} + N_t a_{it}}{N_s a_{ks} + N_t a_{kt}} \tag{5.3}$$

A few algebraic steps to solve for N_s yield

$$N_s = \frac{N_t (a_{it} - R_m a_{kt})}{(R_m a_{ks} - a_{is})} \tag{5.4}$$

Rearranging terms gives an expression in terms of isotope ratios:

$$N_s = \frac{N_t a_{kt}}{a_{ks}} \frac{(R_t - R_m)}{(R_m - R_s)} \tag{5.5}$$

Recall that N_s and N_t are the numbers of atoms in the mixture due to sample and tracer, respectively. To convert them to weight requires use of the familiar Avogadro relationship and involves multiplying both sides of the equation by 1.0 twice, thereby introducing the atomic weights of sample and tracer (i.e., multiply each side by A_s/A_s and A_t/A_t). Note that Avogadro's number appears on both sides of the equation and cancels out. A_s and A_t, on the other hand, are not equal and do not cancel. The resulting equation is one form of the isotope dilution equation.

$$W_s = W_t \frac{A_s}{A_t} \frac{a_{kt}}{a_{ks}} \frac{(R_t - R_m)}{(R_m - R_s)} \tag{5.6}$$

In terms of concentration:

$$C = \frac{W_t}{W_s} \frac{A_s}{A_t} \frac{a_{kt}}{a_{ks}} \frac{(R_t - R_m)}{(R_m - R_s)} \tag{5.7}$$

This formulation is only one of several that, although differing in notation and in formulation of the collection of R terms, are algebraically identical. The most common formulation seems to use Eq. (5.4) as the starting point for conversion from atomic units to weight; see, for example, Faure [6] and Jarvis et al. [7].

Others make use of concentrations in terms of atoms, as does, for example, Heumann [8,9]. Others use concentrations in terms of moles, as do Fassett and Paulsen [10] and Dean [11]. Clearly each investigator selects the form with which he or she feels most comfortable. Due caution is indicated to make sure of one's units of concentration before blindly using an equation from the literature.

There are several features to note about this equation. It is important to recognize that it calls for weights that include all isotopes of the spike and sample and not solely the weight of the isotopes used in R_m; the equation simplifies if these latter are used, but most chemists think in terms of weight of the element (as in parts per million) and not one of its isotopes. The right side of the equation is unitless except the W_t/W_s term; the units used in this numerator and denominator thus define the units of the concentration calculated. Even though the symbols assume weights, volumes can of course be substituted. Typical units are micrograms per gram (ppm) or micrograms per liter, but they can be whatever units the analysis requires. Another point to note is that the only isotopes that need be measured from the mixture of sample and spike are the two involved in the isotope dilution ratio; none of the other isotopes in the mixture plays a role. The same is not the case for the spike and the unspiked sample, however; the full isotopic composition of each of these components is required to calculate their atomic weights. The amount of laboratory work required is reduced when the isotopic composition of the sample is known, as would usually be the case if it were the naturally occurring element, for which the International Union of Pure and Applied Chemistry (IUPAC) tabulated values of isotopic composition [12] are invaluable; enriched isotopic spikes usually have a certificate listing their isotopic compositions. In these relatively common circumstances, the only analysis required is that of the mixture.

Isotope dilution is applicable to any element for which an enriched isotope is available. Figure 1.1 of Chapter 1 indicates which elements are amenable to isotope dilution; in most cases the natural element has at least two stable isotopes, but this is not necessarily the case. For example, ^{232}Th, though radioactive (half-life of 1.4×10^{10} years), is present in the earth's crust; ^{230}Th (half-life of 7.5×10^4 years), an isotope present in nature at such low levels as to be negligible for most applications, is used as a spike for isotope dilution purposes in the author's laboratory. Another common example is the use of ^{233}U (a synthetic isotope) as a spike for uranium analyses. The only elements not amenable to the technique are those, like cobalt and arsenic, that have only one stable isotope and all of whose radioactive isotopes have half-lives so short as to preclude their use.

In the laboratory, the isotope dilution procedure involves adding a known amount of spike of known isotopic composition to a known amount of sample of known isotopic composition; the mixture of spike and sample is equilibrated; the ratio of the sample isotope to the spike isotope is then measured; and the resulting R_m is inserted into the equation. For replicate analyses, this is the only parameter

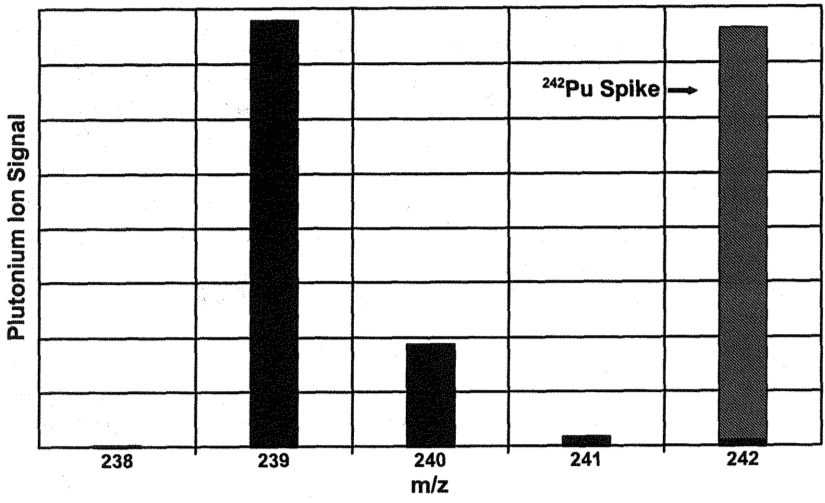

Figure 1 Schematic mass spectrum illustrating isotope dilution. ^{239}Pu is the sample isotope, and ^{242}Pu is the spike.

in the equation that varies; the rest are constant. Figure 5.1 is a schematic drawing of the mass spectrum produced by a mixture of sample and spike.

If the greatest accuracy is required for a given concentration, a double spike (a mixture of two enriched isotopes) may be used; this subject is described in detail in Chapter 1.

5.4 CHOICE OF SPIKE ISOTOPE

For the best analytical precision, a good rule of thumb is to make the spike isotope in the mixture approximately equal to that of the major sample isotope—i.e., $R_m \approx 1.0$. This is only a generality, however, and factors such as the relative abundances of the two isotopes in the spike and sample play a role. In addition, the concentration of the target element is not always known in advance (it is, after all, the goal of the analysis to establish what it is!), and there are many times when a less-than-optimum ratio of spike to sample must be dealt with. The issue is complicated by the fact that in most cases the spike isotope is present in the sample and the sample isotope in the spike. Clearly it is desirable to minimize the degradation of results caused by correcting for this situation. The ideal situation is one in which the spike isotope is not present in the sample, as is often the case for uranium, as the ^{233}U spike most commonly used is not present in nature. Failing that, the most highly enriched spike of the least abundant natural isotope is the best choice. Un-

fortunately, however, low abundance and high enrichment equate to high cost, frequently making the best solution impracticable; in cases where cost is prohibitive, another stable isotope of greater natural abundance than that of the smallest must be chosen. It is for this reason, for example, that enriched ^{42}Ca (0.65% natural abundance) and ^{44}Ca (2.09%) are more often used than ^{46}Ca (0.004%); the cost of enriched ^{46}Ca is many times higher than that of the other isotopes.

All of the considerations discussed lead naturally to the question of what price the analyst pays for this less-than-ideal spike/sample ratio. In most cases, error in the measurement of R_m makes the largest contribution to analytical uncertainty; the isotopic compositions of sample and spike are usually well known in comparison to R_m. The matter of error propagation in isotope dilution analyses has been extensively treated by Adriaens et al., [13], and Patterson et al. used Monte Carlo simulation to study the problem [14]. Using propagation of error laws, Heumann derived the following relationship with which to calculate R_{opt}, the optimum spike-to-sample ratio (neglecting cost and availability) [8]:

$$R_{opt} = [(a_{sk}/a_{si})(a_{tk}/a_{ti})]^{1/2} = (R_s R_t)^{1/2} \tag{5.8}$$

where the terms are as defined for Eq. (5.7). The factor by which error is multiplied for given isotopic enrichments is illustrated for thallium in Fig. 5.2. Inspection of Fig. 5.2 reveals that relatively large deviations from the optimum sample-to-spike ratio can be tolerated in most analyses; in addition, the greater the enrichment of the spike isotope, the less sensitive the analysis is to deviation from optimum. With spikes of 80% or more enrichment in ^{203}Tl, sample-to-spike ratios from 0.1 to 10.0 should give acceptable results. In critical applications where highly accurate concentration measurements are desired, it is advisable to obtain an estimate of the sample concentration to use in determining how much spike to add. This analysis, of course, need not be by isotope dilution mass spectrometry; a less time-consuming and less expensive method would be preferred in most cases.

Enriched stable isotopes for use as spikes are available from several sources; Oak Ridge National Laboratory sells them for most solid elements [15].

5.5 APPLICATIONS

The literature on isotope dilution is so voluminous that it is impossible to cover the subject thoroughly in a single chapter. It is in fact tantamount to impossible to locate all relevant papers, let alone read them. There are also questions arising from the definition of "inorganic." Elemental assay has traditionally been an inorganic discipline and analysis of, say, body fluids biological. The question is where, for example, to place analysis of lead in human serum. The area into which such analyses fall depends on whether it is the analyte or the sample that is used for the def-

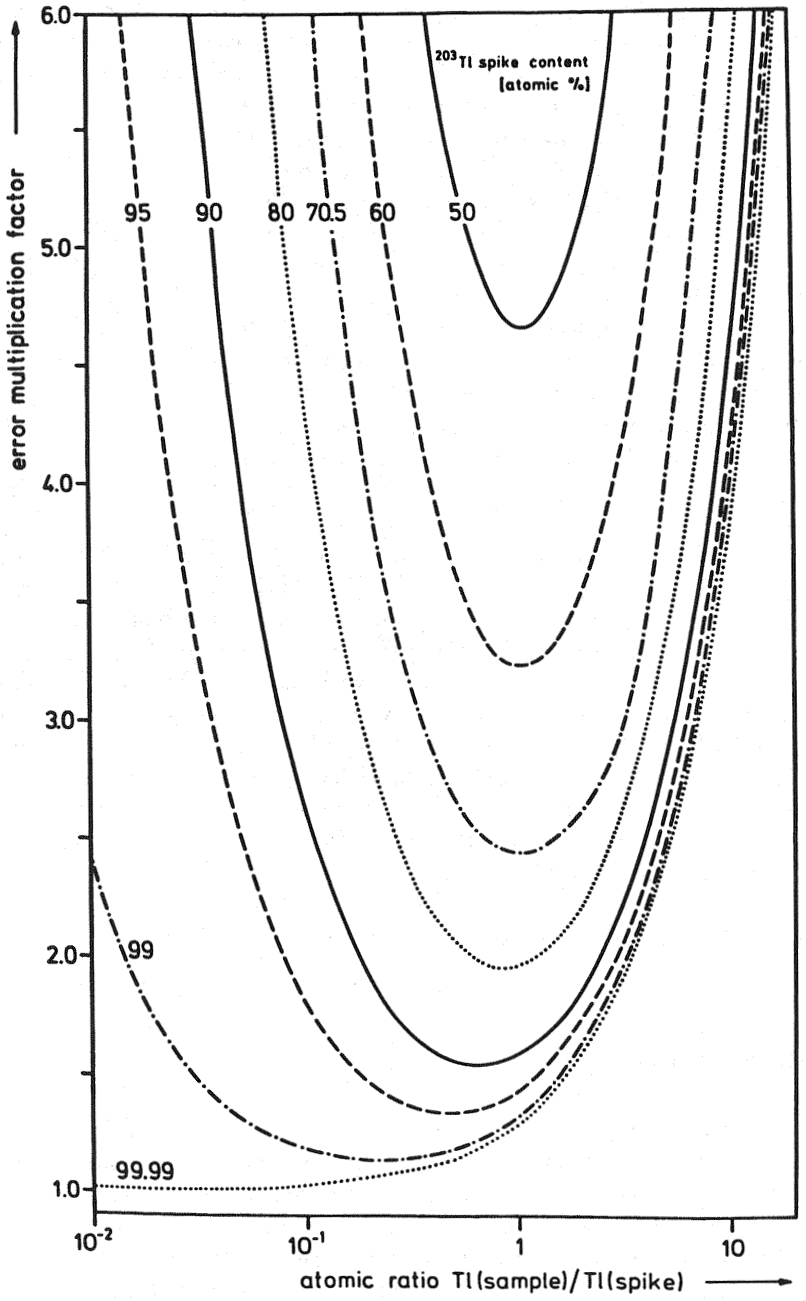

Figure 2 Variation of error multiplication factor with enrichment of ^{203}Tl. (From Ref. 8.)

inition. Elemental assay of biological systems is of such importance that a short section of this chapter is devoted to it.

The following material has been chosen as representative of current trends but makes no claim for completeness. It does not even pretend to consistency, the author consoling himself with Emerson's famous dictum "Consistency is the hobgoblin of little minds" [16]. Reviews are cited where known, and references should be considered as guides to further information rather than to definitive sources.

As mentioned, thermal ionization mass spectrometry is the area in which isotope dilution developed and in which it has received the widest range of applications. One of thermal ionization's major limitations is that it is essentially a single-element technique; in no way can it be considered multielement in the sense that numerous elements can be assayed in a single analysis. It is thus highly desirable to mate isotope dilution with multielement analysis capability. Spark source mass spectrometry for years dominated elemental analysis, but the nature of the samples (solids) made use of isotope dilution difficult. Use of a multielement spike was reported as long ago as 1970 by Paulsen et al. [17], however, and more recently by Carter et al. [18] and by Jochum et al. [19,20].

In the last decade or two, the advent of new instrumentation directed at elemental analysis has provided fertile new ground for expanded use of isotope dilution. Glow discharge mass spectrometry is in many ways the modern replacement for spark source and has similar impediments to ready application of isotope dilution. A recent report of Barshick et al. describes assaying lead in oil residues using the technique [21]. The obstacles spark source and glow discharge mass spectrometry both present to ready use of isotope dilution make it unlikely that widespread application of the technique will occur in conjunction with them.

The same cannot be said for ICP-MS, however. Samples are usually in solution form, ideal for mixing spike and sample. This instrument, described in detail in Chapter 3, has had huge impact on many areas of science in which trace elemental analysis is important. The use of isotope dilution in association with ICP-MS has been described by Jarvis et al. in their book devoted solely to ICP-MS [7]. It has become widely accepted as a reference method in fields not normally thought of as mass spectrometric such as in analysis of medical specimens [22], and a review describing isotope dilution's role in clinical, pharmacological, and toxicological applications has recently appeared [23]. Fassett has summarized its application, along with other traditionally inorganic techniques, to biological systems [24]. There has been a spate of papers in recent years describing results obtained by using isotope dilution in association with ICP-MS in inorganic applications, many of them dealing with environmental issues; two recent reviews by Heumann bring the subject into focus [8,9].

Because ICP-MS is multielemental and samples are normally in solution form, use of a multielement isotope dilution spike has many attractive features. Spikes for individual elements can be kept separate and mixed in appropriate concentrations for the problem at hand. Many samples are from the environment, so

for most elements natural isotopic composition as specified by International Union of Pure and Appliced Chemistry (IUPAC) can be assumed. The only instances in which this might not apply are those in which elements have isotopic compositions that are not constant in nature. Examples are fission products (such as neodymium), in which small deviations from primordial composition might be encountered, and the end products of naturally occurring decay chains. Lead, the end product of the decay of uranium and thorium, is the outstanding example of the latter. ^{235}U and ^{238}U decay to ^{207}Pb and ^{206}Pb, respectively; ^{232}Th decays to ^{208}Pb. ^{204}Pb is thus the only stable lead isotope that has no radioactive precursors. There are numerous steps in each decay chain, mostly through short-lived nuclides. There was considerable uranium, thorium, and lead present in the primordial earth, and the ratio of the three elements varies widely with location. This causes the isotopic composition of natural lead to display enormous variation; assuming any given composition is ill advised. Such variation in lead isotopes is only to be expected when one recognizes that the half-life of ^{238}U (4.5×10^9 years) is about the age of the earth; half the ^{238}U present at the earth's formation has thus decayed to ^{206}Pb. These and other naturally occurring radioactive isotopes distort the isotopic compositions of their decay products, thus providing the basis of isotope geochronology. Examples are cited in the next section.

5.5.1 Geological Applications

By determining the amounts of a naturally occurring radioactive isotope and its daughter in a given sample, geoscientists are able to calculate its age [6]. The fact that the isotopes are naturally occurring means that half-lives are very long. Several systems, including Rb-Sr, Sm-Nd, Lu-Hf, Re-Os, and Th-Pb, use isotopes with half-lives in excess of 10^{10} years. Many age-dating techniques use isotope dilution to establish how much of each element is present. Plots of one ratio versus another, called *isochrons*, allow determination of the specimen's age. As one example, ^{176}Lu emits a beta particle, decaying to ^{176}Hf with a half-life of 4.58×10^{10} years. Figure 5.3 is the isochron for samples from Greenland; it establishes the date at which Amitsoq gneisses separated from the mantle as $3.59 \pm 0.33 \times 10^9$ years ago [25]; this is very old, for the age of the earth is about 4.5×10^9 years.

Studies such as this one allow geoscientists to investigate the past and to get some idea of geological conditions then. Because a small error in the measurement of the ratio translates into a large uncertainty in the calculated age of the sample, isotope dilution mass spectrometry's superior sensitivity and accuracy are important in obtaining meaningful results.

5.5.2 Environmental Applications

Mounting concern worldwide about emission of toxic substances into the environment has driven elemental analysis to new levels of sensitivity and accuracy,

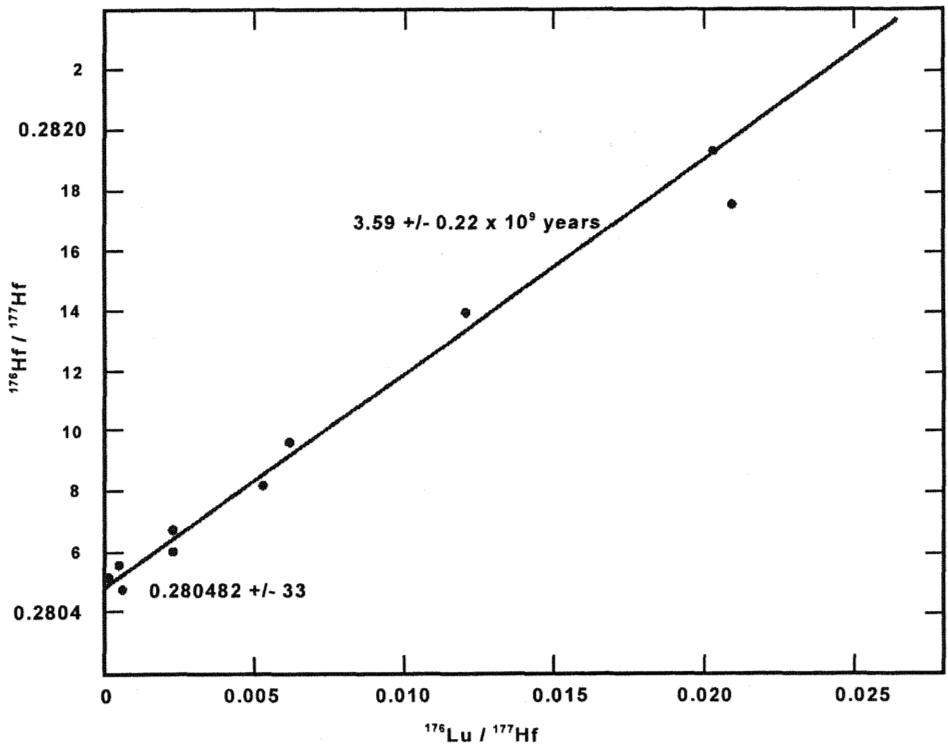

Figure 3 Lu-Hf isochron for samples from Greenland. (From Ref. 25.)

and one important recent trend in environmental applications is the analysis of elemental concentrations at extremely low levels. Detection limits in the picogram per gram (ppt) range for numerous elements have been achieved by several teams of investigators. Positive thermal ionization mass spectrometry was used to measure concentrations in these ranges for Pb, Rb, and Ba in the atmosphere over the Pacific Ocean [26], as were those for Pb, Ni, Cu, Cd, and Tl over the South Atlantic Ocean [27]. Concentrations of heavy metals in Antarctic ice normally fall below 10 pg/g and for some (Tl, Cd, Pb) are below 1 pg/g [28,29]. Concentrations in the picogram per gram range have been reported for Re, Pt, and Ir in sediments and for Re and Pt in natural waters using a flow injection introduction system for an ICP-MS [30].

In a radically different analytical situation, Kelly et al. used thermal ionization and isotope dilution to determine the amount of sulfur in fossil fuels [31]. These materials (oil and coal) were to be used as reference materials for analyses by other analytical techniques; the superior accuracy and precision of isotope di-

lution mass spectrometry were put to good use. Quoted precision for oil samples was 0.5% and for coals, which are more inhomogeneous than oil, 1% to 4%.

ICP-MS dominates the field of environmental assay; most metallic and amphoteric elements are susceptible of analysis, and it is often a great convenience (to say nothing of being relatively economical) to be able to assay for all elements of interest in a single analysis. Another feature of ICP-MS, however, has been exploited perhaps even more tellingly than multielement analysis. This is that the sample introduction system lends itself to a wide variety of enhancement schemes, in part because the sample is introduced to the instrument at atmospheric pressure and in part because samples are most often in a water-based (dilute acid) medium. These attributes combine to allow various separation and preconcentration schemes to be implemented on-line or nearly so.

Information of critical importance for many elements of environmental concern is the identification of their species. For example, chromium in the +3 oxidation state is relatively innocuous, whereas in the +6 state it is extremely toxic. Speciation is such an important issue that an entire chapter in this book is devoted to it. Only a few aspects related to isotope dilution are mentioned here.

One ineluctable aspect of isotope dilution is that enriched stable isotopes range in cost from moderately expensive to prohibitively so. It is thus highly desirable to minimize consumption of spike isotopes, and, since environmental samples are often large in volume, it is undesirable to spike the original sample directly. Heumann et al. addressed this issue by developing a dual delivery system for ICP-MS interfaced to a high-pressure liquid chromatography (HPLC) separation system [32,33]; a schematic drawing of this system is shown in Fig. 5.4. The system allows simultaneous introduction of two streams of solution to the ICP torch. One is the sample, which is the effluent from the HPLC column; the other contains the solution of the spike for the analyte element. For species-specific quantification, the spike is added to the sample in the usual way. For determining the total amount of the target element in the sample independent of species, the HPLC is not used, and spike is added through the second introduction line to the ICP torch. By this means, spike consumption can be minimized and, through HPLC, speciation achieved. The two different spikes are often in different oxidation states. One is used to quantify the species of concern (e.g., Cr^{VI}); the other is not specific and measures total element concentration. The system was first demonstrated for copper and molybdenum [32] and extended to analysis of natural waters with high humus concentrations, which is a challenging matrix [34]. A multielement spike of 10 ng/mL of each element was used to determine Cr, Ni, Cu, Mo, I, and Pb from several rivers and other natural waters.

Heumann's group also interfaced a gas chromatograph to an ICP-MS for analysis of volatile elements in environmental samples [35]. The big advantage of introducing gas-phase samples over the more conventional solutions is that elements can be transferred to the ICP without incurring the losses attendant on nebulization. Figure 5.5 is a drawing of the apparatus involved. Using isotope dilu-

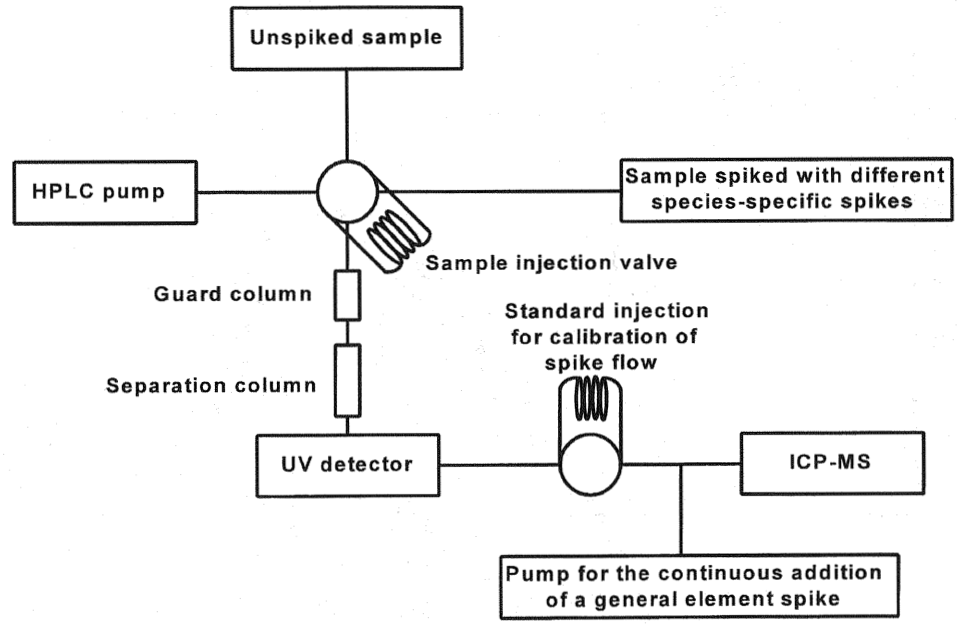

Figure 4 Schematic diagram of high-pressure liquid chromatography inductively coupled plasma mass spectrometry (HPLC-ICP-MS) system with dual-inlet system for isotope dilution analyses. (From Ref. 32.)

tion, the authors were able to obtain good agreement with standards for selenium at the 10-ng/mL level. The spike was ^{82}Se, and two isotope dilution ratios (^{77}Se/^{82}Se and ^{78}Se/^{82}Se) were used to improve the accuracy of the speciation analyses.

Barshick et al. adopted a different approach for the speciation of mercury [36]. These investigators used a commercial gas chromatograph-mass spectrometer (GC-MS) in their work; the mass spectrometer was a quadrupole ion trap. A solid phase microextraction fiber was employed to collect volatile organic species, which were then desorbed and subjected to GC-MS analysis. Subsequent to analysis of organic mercury compounds, inorganic species were converted to a volatile organic form and analyzed, thus providing total mercury in the sample. Quantification of mercury at the 400-ppb level using a calibration curve yielded precisions of about 15%, whereas use of a ^{204}Hg spike and isotope dilution yielded 1% [37]. This is a good example of the power of isotope dilution to deliver improved results even when a mass spectrometer not designed for isotope ratio measurements is involved.

Joining another type of ancillary device to ICP-MS, Beary et al. developed a continuous-flow microwave digestion apparatus for isotope dilution analysis of lead in environmental samples [38]. Although introduction to the ICP torch was

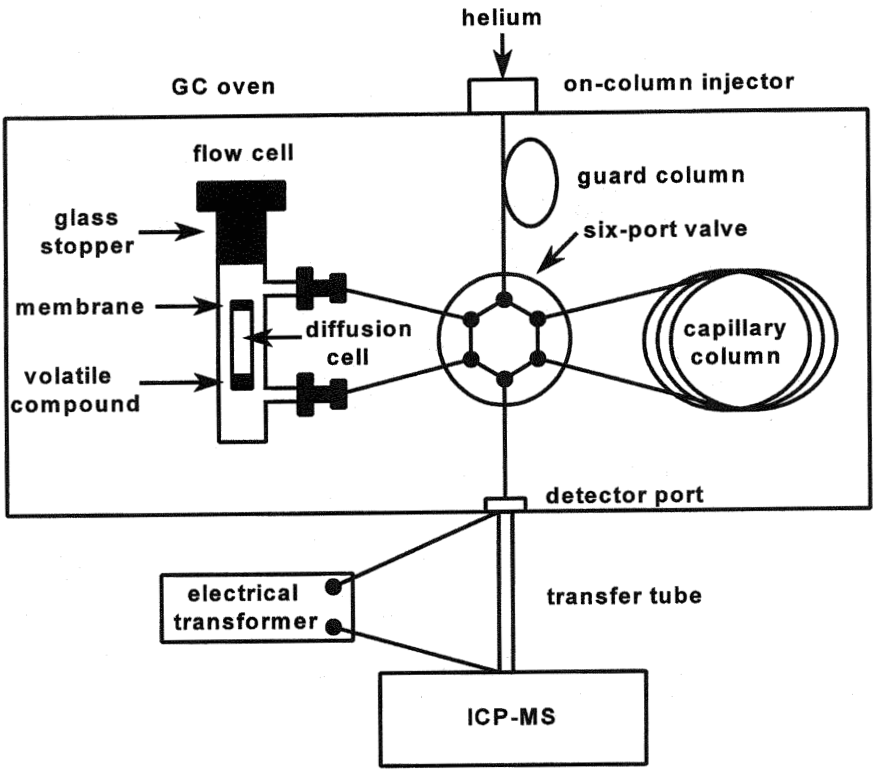

Figure 5 Schematic diagram of gas chromatograph inductively coupled plasma mass spectrometry (GC-ICP-MS) system. (From Ref. 35.)

not continuous, sample preparation time was reduced to about 10 min, and the authors were able to exploit the ability of microwave digestion to dissolve a large number of sample types and at the same time benefit from the accuracy and precision that isotope dilution provides. Good agreement between their results and other techniques was obtained for leaves, air filters, sludge, dust, paint, and urine.

5.5.3 Biological Applications

Use of stable isotope dilution to assay elemental concentrations in biological samples has increased markedly in the recent past. Part of the reason is that use of radioactive isotopes previously employed as tracers has declined, and part is that interest in the effect of various elements on biological systems and their fate once they enter the food chain has increased. This important field is far from the author's area of expertise, so what follows should be considered a rather haphazard survey

of some recent publications in which isotope dilution mass spectrometry was used to good advantage.

One excellent example was the determination of lead in human plasma at sub–nanogram per milliliter (sub-ppb) levels by Bowins and McNutt [39]. Detection limits of 16×10^{-15} g were reported. Use of a ^{204}Pb spike and electrothermal vaporization provided excellent sensitivity and accuracy, with precision better than 2% at the 1.3-ng/mL level.

Jiang et al. recently reported use of two different sample introduction approaches to analyze Cu, Cd, and Pb in biological samples through use of a multielement isotopic spike. The first was anodic stripping voltammetry, first adapted for ICP-MS application by Caruso, Pretty, and coworkers [40–42]; this step achieves both elemental preconcentration and elimination of the matrix. Jiang et al. describe optimizing the system for use with isotope dilution and report good agreement (ca. 2%) of their results with certified reference materials [43]. The second development of this group was using isotope dilution in a system in which an electrothermal vaporization device converted the sample to the gas phase [44]. A palladium-treated graphite crucible was used to overcome the excessive volatility of cadmium. Again good results were obtained from reference materials.

Yoshinaga and Morita used isotope dilution in conjunction with ICP-MS to measure mercury in biological and environmental samples [45]. The same group used microwave-induced plasma mass spectrometry for the isotope dilution analysis of selenium in biological materials [46]. Analysis of nickel via isotope dilution and ICP-MS has been reported by Patriarca et al [47].

5.5.4 Nuclear Applications

Isotope dilution mass spectrometry was used in the nuclear area almost from its inception. Most Department of Energy (DOE) laboratories monitored uranium in some form or other, whether for process purposes or for evaluation of releases to the environment. Since this is a relatively mature field, and since the United States has curtailed its development of nuclear power, research in this area is much less active than it used to be.

One of the most significant parameters in reactor operation is burn-up—i.e., the amount of usable fuel consumed. One of the most important uses of this information is comparison of actual burn-up with predictions of computer codes; accurate codes are vital to efficient and safe reactor operation. The most commonly used calculations require knowledge of the isotopic compositions and amounts of uranium, plutonium, and neodymium [48]. The necessary analyses make the procedure both time-consuming and very expensive, especially as spent fuel rods are radioactive enough to require that initial operations be performed in a hot cell. Isotope dilution has traditionally been used as the means of quantification of all three elements. Green et al. report a thorough analysis of spent fuel rods in which nanogram quantities of the three elements were analyzed; precision ranged from

0.1% to 0.5% [49]. The same laboratory measured part per million (ppm) levels of iron in zirconium using isotope dilution [50]; the study was aimed at elucidating the deformation effects of iron contamination in alloys used in reactors. In both these studies, mass spectrometers specifically designed for the measurement of isotope ratios were used, and thermal ionization was employed to generate the ion beams.

In a different application not directly related to nuclear matters but nonetheless addressing a similar problem, Beer and Heumann used isotope dilution to quantify trace levels of U, Th, Cu, Lb, Cd, Cr, Ni, and Fe in titanium, a metal extensively used in the microelectronics industry, in which purity is of critical importance [51]. Detection limits ranged from 0.07 ng/g for U and Th to 35 ng/g for Fe.

An example of what one might call "double" isotope dilution was reported by Smith et al. [52]. The specific problem addressed was the determination of the quantity of material (either by weight or volume) in holding tanks in the nuclear fuel cycle. Safeguards require establishing a material balance for these tanks, which contain solutions of spent reactor fuel and, being highly radioactive, constitute a hostile matrix. The method is a general one, however, and can be applied to any situation in which the amount of solution is desired. The method involves adding a known amount of natural lutetium to the tank; this was the first spike. Lutetium was chosen because it was not present in the sample solutions and is well behaved under thermal ionization; other elements could of course be used. After addition of the spike, the contents of the tank were thoroughly mixed. An aliquot was withdrawn and a lutetium spike of enriched ^{176}Lu (the second spike) added. Isotope dilution analysis via thermal ionization mass spectrometry was carried out; knowledge of the amount of natural lutetium added to the tank and its concentration made calculation of the amount of solution in the tank simple. Precision and accuracy of about 0.5%, superior to those of other methods of tank calibration [53], were obtained.

5.6 CONCLUSIONS

It is with considerable gratification to the author that preparation of this chapter brought home the realization that in his professional lifetime isotope dilution has moved from a recondite technique used only by a few initiates into the mainstream of analytical science, making valuable contributions in a multitude of fields as disparate as the nuclear fuel cycle and the workings of the human body.

REFERENCES

1. Inghram, M. G.; Hayden, R. J. *Handbook on Mass Spectroscopy*, Nuclear Series, Report No. 14, NRC-USA, 1954.

2. De Bievre, P.; De Laeter, J. R.; Peiser, H. S.; Reed, W. P. *Mass Spectrom Rev* ***1993***, *12*, 143.
3. Bowers, G. N.; Fassett, J. D.; White V. E. *Anal Chem* ***1993***, *65*, 475R.
4. Vanhaecke, F.; Boonen, S.; Moens, L.; Dams, R. *J Anal Atomic Spectrom* ***1997***, *12*, 125.
5. Hintenberger, H. in *Electromagnetically Enriched Isotopes and Mass Spectrometry*, M. L. Smith, ed., Academic Press, New York, NY, 1957, pp. 177–189.
6. Faure, G. *Principles of Isotope Geology*, Second Edition, John Wiley & Sons, New York, 1986.
7. Jarvis, K. E.; Gray, A. L.; Houk, R. S. *Handbook of Inductively Coupled Plasma Mass Spectrometry*, Blackie, London, 1992, Chapter 6.
8. Heumann, K. G. *Mass Spectrom Rev* ***1992***, *11*, 41.
9. Heumann, K. G. *Int J Mass Spectrom Ion Processes* ***1992***, *118/119*, 575
10. Fassett, J. D.; Paulsen, P. J. *Anal Chem* ***1989***, *61*, 643A.
11. Dean, J. A. *Analytical Chemistry Handbook*, McGraw-Hill, New York, 1995, Chapter 13.
12. IUPAC Commission on Atomic Weights and Isotopic Abundances, *Pure Appl Chem* ***1994***, *66*, 2423.
13. Adriaens, A. G.; Kelly, W. R.; Adams, F. C. *Anal Chem* ***1993***, *65*, 660.
14. Patterson, K. Y.; Veillon, C.; O'Haver, T. C. *Anal Chem* ***1994***, *66*, 2829.
15. Isotope Distribution Office, Oak Ridge National Laboratory, Oak Ridge, TN.
16. Emerson, R. W., "Self Reliance" in *Essays, First Series*, publisher unknown, 1841.
17. Paulsen, P. J.; Alvarez, R.; Mueller, C. W. *Anal Chem* ***1970***, *42*, 673.
18. Carter, J. A.; Franklin, J. C.; Donohue, D. L. in *High Performance Mass Spectrometry: Chemical Applications*, R. F. Gould, ed., ACS Symposium Series # 70, 1977.
19. Jochum, K. P.; Seufert, H. M.; Medinet-Best, S.; Rettmann, E.; Schönberger, K.; Zimmer, M. *Fresenius Z. Anal Chem* ***1988***, *331*, 104.
20. Jochum, K. P.; Seufert, H. M.; Thirwall, M. F. *Geostandards Newslett* ***1990***, *14*, 469.
21. Barshick, C. M.; Smith, D. H.; Wade, J. W.; Bayne, C. K. *J Anal Atomic Spectrom* ***1994***, *9*, 83.
22. Thienpoint, L. M.; Stöckl, D.; De Leenheer, A. P. *J Mass Spectrom* ***1995***, *30*, 772.
23. De Leenheer, A. P.; Thienpoint, L. M. *Mass Spectrom Rev* ***1992***, *11*, 249.
24. Fassett, J. D. *Pure Appl Chem* ***1995***, *67*, 1943.
25. Pettengill, H. S.; Patchett, P. J.; Tatsumoto, M.; Moorbath, S. *Earth Planet Sci Lett* ***1981***, *55*, 150.
26. Rosman, K. J. R.; Patterson, C. C.; Settle, D. M. *J Geophys Res* ***1990***, *95D*, 3687.
27. Völkening, J.; Heumann, K. G. *J Geophys Res* ***1990***, *95D*, 20263.
28. Völkening, J.; Heumann, K. G. *Fresenius J Anal Chem* ***1988***, *331*, 174.
29. Boutron, C. F.; Görlach, U. *Metal Speciation in the Environment*, J. A. C. Broekaert, F. Adams, eds., NATO ASI Series, Vol. 23, Springer-Verlag, Heidelberg, 1990, p. 137.
30. Colodner, D. C.; Boyle, E. A.; Edmond, J. M. *Anal Chem* ***1993***, *65*, 1419.
31. Kelly, W. R.; Paulsen, P. J.; Murphy, K. E.; Vocke, R. D.; Chen, L.-T. *Anal Chem* ***1994***, *66*, 2505.
32. Rottmann, L.; Heumann, K. G. *Fresenius J Anal Chem* ***1994***, *350*, 221.
33. Heumann, K. G.; Rottmann, L.; Vogl, J. *J Anal Atomic Spectrom* ***1994***, *9*, 1351.
34. Rottmann, L.; Heumann, K. G. *Anal Chem* ***1994***, *66*, 3709.

35. Gallus, S. M.; Heumann, K. G. *J Anal Atomic Spectrom* ***1996***, *11*, 887.
36. Barshick, C. M.; Barshick, S.-A.; Britt, P. F.; Lake, D. A.; Vance, M. A.; Walsh, E. B. *Int J Mass Spectrom Ion Processes* ***1998***, *178*, 31.
37. Barshick, C. M.; Walsh, E. B.; Barshick, S.-A.; Britt, P. F. 46th Annual Conference on Mass Spectrometry and Allied Topics, Orlando, FL, June 1–5, 1998.
38. Beary, E. S.; Paulsen, P. J.; Jassie, L. B.; Fassett, J. D. *Anal Chem* ***1997***, *69*, 758.
39. Bowins, R. J.; McNutt, R. H., *J Anal Atomic Spectrom* ***1994***, *9*, 1233.
40. Pretty, J. R.; Evans, E. H.; Blubaugh, E. A.; Shen, W. L.; Caruso, J. A.; Davidson, T. M. *J Anal Atomic Spectrom* ***1990***, *5*, 437.
41. Pretty, J. R.; Blubaugh, E. A.; Evans, E. H.; Caruso, J. A.; Davidson, T. M. *J Anal Atomic Spectrom* ***1992***, *7*, 1131.
42. Pretty, J. R.; Blubaugh, E. A.; Caruso, J. A. *Anal Chem* ***1993***, *65*, 3396.
43. Hwang, T-J.; Jiang, S.-J. *J Anal Atomic Spectrom* ***1996***, *11*, 353.
44. Chang, C.-C.; Jiang, S.-J. *J Anal Atomic Spectrom* ***1997***, *12*, 75.
45. Yoshinaga, J.; Morita, M. *J Anal Atomic Spectrom* ***1997***, *12*, 417.
46. Yoshinaga, J.; Shirasaki, T.; Oishi, K.; Morita, M. *Anal Chem* ***1995***, *67*, 1568.
47. Patriarca, M.; Lyon, T. D. B.; McGaw, B.; Fell, G. S. *J Anal Atomic Spectrom* ***1996***, *11*, 297.
48. *Annual Book of ASTM Standards, Part 45: Nuclear Standards,* American Society for Testing and Materials, Philadelphia, 1981, Procedure E 321, pp. 978–989.
49. Green, L. W.; Elliot, N. L.; Miller, F. C.; Leppinen, J. J. *J Radioanal Nucl Chem* ***1989***, *131*, 299.
50. Elliot, N. L.; Campbell, M. A.; Green, L. W. *Int J Mass Spectrom Ion Processes* ***1995***, *146 147*, 99.
51. Beer, B.; Heumann, K. G., *Anal Chem* ***1993***, *65*, 3199.
52. Smith, D. H.; Walker, R. L.; Pritchard, C. A.; Carter, J. A. *Anal Chem* ***1983***, *55*, 578.
53. Bokelund, H.; Deron, S.; Dratschmidt, H. H.; Foggi, C; Hamilton, W. I.; Jones, T. L; Kinney, J; Neuilly, M.; Reed, W. J.; Taylor, G. E.; Smith, D. H.; Weh, R. ESARDA Bulletin No. 26, March, 1996, p. 1.

6

The Emission of Ions from High-Temperature Condensed Phase Materials

James E. Delmore
Idaho National Engineering and Environmental Laboratory
Idaho Falls, Idaho

6.1. INTRODUCTION

Surface ionization constitutes a wide range of processes whereby ions are emitted from a hot surface. The physics of Saha-Langmuir (S-L) ionization [1], whereby a neutral vapor-phase atom strikes a high-temperature solid surface and is re-emitted as either a positively or a negatively charged atom, has been understood for many years. The derivation of these formulas is specific for the removal or addition of an electron to a neutral vapor-phase atom striking a hot surface and is not valid for molecules or molecular transformations. The S-L equation can be fit reasonably well to experimental data (to at least a first approximation) for situations in which an element in the zero oxidation state sublimes from a hot surface—for example, sublimation of positive and negative rhenium ions from a pure rhenium filament at 2100°C [2]. These situations are referred to here as *pseudo—S-L processes* (as distinct from a true S-L process) and specifically situations in which an element in the zero oxidation state is volatilizing from the surface as a mix of positive ions, negative ions, and neutrals. Saha-Langmuir ionization is explained in detail in Chapter 1.

In practice there are few systems in which the S-L model actually describes the ion formation process, since molecular transformations are usually involved in this process. A more typical thermal ion source has a multiple-filament arrangement wherein a neutral molecule volatilizes from a sample filament at a modest temperature, undergoes fragmentation on a much hotter ionizing filament, and

revolatilizes as an atomic ion. These processes are less well understood since they involve a chemical change from a molecule to an atom in addition to the change in charge state. Experimentally the temperature and work function (WF) of the ionization surface, and the ionization potential (IP) or electron affinity (EA) of the ion species, continue to be important parameters. This chapter deals with the types of thermal ionization processes in which an inorganic solid is heated to a high temperature and ions are emitted directly from this deposit. These are referred to as *ion emitters* and are conveniently divided into two categories: ion emitters with the ion of interest presynthesized and embedded into a suitable matrix from which this preformed ion sublimes, and emitters in which the ion of interest is produced via a chemical or physical process either within the matrix or during volatilization from the matrix. Understanding of the basic principles of both types of ion emitters is still in an early state of development, and some of the concepts presented in this chapter are preliminary and in some cases are just now being submitted for journal publication. Still other topics are presented here as research opportunities.

The vast majority of materials vaporize only neutral species at elevated temperatures, and only a few materials emit ions to an appreciable extent. As an introduction to the topic of ion emitters it is useful to ask the question, What causes a thermally hot condensed phase material to vaporize atoms and/or molecules as ions rather than as neutral species? This is a nontrivial question and only recently have some models that address this question begun to emerge for a few ion emitters. These models are still in the conceptual state, and although they are consistent with limited sets of experimental data, ideally they will achieve considerable refinement in the coming years.

The IP for cation emission and the EA for anion emission continue to be important experimental parameters for ion emitters, as would be expected since these parameters define the thermodynamic stability of the particular ion. The WFs of the surfaces of the mixtures that constitute emitters are largely unknown and are a gap in our understanding of these materials, although it would be expected that this parameter would also be important. The work functions of the pure material that is blended into the emitters as the major constituent are known, however. Anion emitters tend to have a major constituent with a low work function, such as a rare earth oxide or an alkaline earth oxide. The situation for cation emitters is less clear, although they tend to be mounted on filaments made of a metal with a high work function such as metallic rhenium or platinum. Experimental measurement of the work functions of some of these surfaces is a good research opportunity. Since ion emission is from the deposit itself, one would think that the filament material would not be important as long as it could tolerate the required temperatures. Experimental results suggest this is not always true. In two instances [3,4] solubility of the base metal in the ion emitter has the effect of poisoning emission. On the other hand, in the case of the alkali metal zeolite cation emitters it has been shown that various supporting materials work equally well [5], as there does not seem to be a solubility problem for the metals in the zeolite at the experimental temperatures.

In general, pure materials do not emit appreciable quantities of ions; the one exception is self-ionization from high-temperature refractory metals [2]. In the majority of useful ion emitters the material from which ions are to be produced is embedded in a matrix that is usually more refractory than the material itself and allows migration of the species of interest. For many ion emitters the more refractory matrix is thought to have the effect of increasing the temperature of volatilization of the species from which ions are to be produced, and the higher operating temperature increases ionization efficiency for most emitters. There are other matrix effects that have been identified or hypothesized for various ion emitters such as migration of the species of interest, and these are mentioned as the emitters are discussed.

The importance of the chemical composition of these inorganic deposits in regard to ion emission has been understood for many years and is illustrated by the work of Studier et al. [6]. A deposit of uranium on a hot filament emitted a variety of ions, depending on the oxidizing and reducing agents added to the material. They presented their data in the following format:

Oxidizing agents (e.g., oxygen)

UC_2^+, U^+, UO^+, UO_2^+, UO_3^+

$\longrightarrow$

Reducing agents (e.g., carbon)

$\longleftarrow$

These results illustrate the importance of the chemical species of the element present in the deposit with regard to ion emission (and gives insight into the effect of the oxidizing/reducing nature of the ion emitter) but tell little about the actual mechanisms active in the ion emitting process. As an example, the ions could be emitted either from the deposit itself or from an intermediate material that formed as a consequence of the chemical properties, or it could be entirely an interface phenomenon in which the deposit only served as a repository for the uranium species and the supporting filament served as the ionization surface.

The study of the mechanistics of ion formation from hot ion emitters has become a topic of research in the author's laboratory in recent years. As with all research, the deeper one probes the more there is to study. Whenever a new level of understanding was achieved, new questions arose that required new approaches and in some instances new instruments custom designed and built to accomplish measurements needed to achieve the next level of understanding. These instruments are described with examples of how they are applied.

6.2 INSTRUMENTATION FOR THE STUDY OF ION EMISSION MECHANISMS

This work was initiated with a standard National Bureau of Standards (NBS) style single magnetic sector mass spectrometer (see Chapter 1). This capability was sup-

plemented with three new types of instruments constructed or modified from more standard designs to accomplish specific types of measurements:

1. An ion imaging instrument [5] for imaging the regions on an emitter from which ions are originating
2. An ion/neutral mass spectrometer [7] that allows the ions and the neutrals (via electron bombardment ionization) volatilizing from the emitter to be measured in sequence
3. A secondary ion mass spectrometer (SIMS) able to analyze the chemical composition and speciation of the surface of ion emitters at full operating temperature

Several new types of source mounts have also been developed to allow optimal placement and operation of the ion emitters in these instruments. These instruments provide complementary information on the properties of ion emitters that are helping to elucidate the mechanisms by which ion emitters function. This knowledge has allowed the development of better ion emitters.

6.2.1 The Sample as an Element in the Focusing Lens

Before describing sample mounting techniques it is important to discuss the issue of voltage spread across an ion emitting surface and the way it interacts with the extraction and focusing of the emitted ions. This is a very important aspect of both the experimental apparatus and the implementation in useful ion sources. In thermal ionization (and in SIMS), the single most important element in the ion lens system is the sample itself. This is because the ions are at their lowest velocity just as they are emitted from the sample surface, and thus their flight paths are more readily altered by either electric or magnetic fields. Another aspect of this issue is that it is physically more difficult to design and build a useful ion emitter/ion lens with a high level of symmetry around the emitter than for the rest of the lens. Any minor irregularities in the electrostatic fields in the region near the emitter have a far greater effect than in regions after the initial acceleration of the ions. This is why the NBS style mass spectrometer is operated with a nearly field-free region surrounding the filaments when a triple-filament source is used, and it is operated with a substantial draw-out voltage when a single-filament source is used. The triple-filament assembly adds sufficient electrostatic asymmetry to the source region that only a weak draw-out voltage can be tolerated.

In general, it is important to maintain electrostatic symmetry around the axis of a lens that has cylindrical geometry, and to maintain electrostatic symmetry along the y and z axes of a lens with planar geometry. Deflection electrodes violate this rule, but they are generally downstream in the lens, where the ions have much greater velocity and hence they have less effect on the focusing. Also, the deflection offset is quite small when the source is properly aligned, minimizing de-

focusing. Improperly designed deflection electrodes that deflect the ions a substantial distance can severely defocus a beam, however. A voltage spread across the face of the emitter adds an element of asymmetry at the worst possible location in the entire lens, causing random defocusing of the ion trajectories. Conventional thermal ionization sources have up to a 2-V drop along the length of the filament facing the lens from resistance heating. An experiment conducted in the author's laboratory, but never published, showed significant defocusing of a planar beam from this effect. In a lens with cylindrical geometry there is considerable defocusing, as is discussed in the section on ion imaging. Thus consideration must be given to constructing an ion emitter with little or no voltage spread across the face.

6.2.2 Methods for Mounting Samples

Two types of miniaturized sample mounting procedures have been developed. In the first, the sample is mounted on a miniature version of a single-filament design of the type described in Chapter 1 and mentioned previously. This design is shown schematically in Fig. 6.1. The distinguishing features of this design are that the

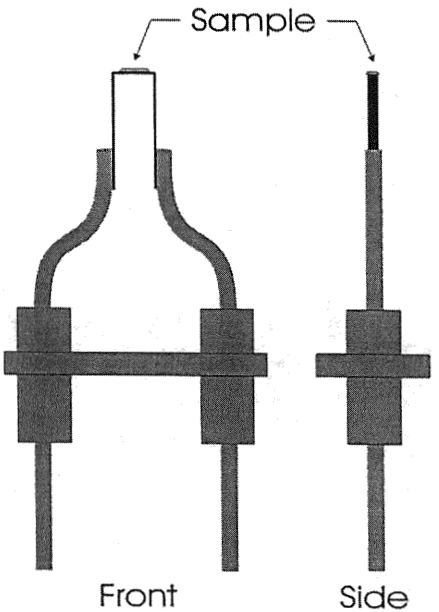

Figure 1 Illustration of the "minifilament" used to minimize voltage spread in the sample region of the ion source and to concentrate the sample closer to the central axis of the ion optics.

portion of the filament facing the lens is shortened by about a factor of 4, with a voltage drop of 0.5 V or less across the face, and the sample concentrated close to the lens on the face of the filament. This design has been useful for a variety of experiments in which the approximate 0.5-V spread across the ion emitter does not cause complications.

The other design, shown in Fig. 6.2, has the sample pressed into one end of a tube with the opposite end plugged. This tube is supported by filament material normally used in thermal ion sources, typically rhenium. The assembly is heated as a standard filament is, except the resistance across the tube is less than the resistance along the length of the filament. Essentially the entire voltage drop across the assembly occurs along the length of the filament, with the tube at a constant voltage that is close to one half of the voltage drop across the assembly. Since the resistance of the tube is so low, little heat is generated by the current flow, so the heat is supplied by thermal conduction from the filaments. This sample mounting also reduces the likelihood of the emitter's falling from the mount since it is contained in the tube. Most of the work described later in this chapter employed one of six variations of this design.

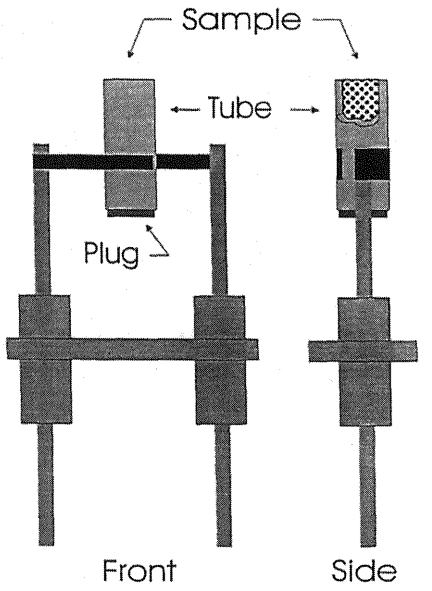

Figure 2 Illustration of a version of the "tube ion source." Voltage drop is primarily across the filament since the walls of the tube have much higher electrical conductivity than the filament as a result of wall thickness. The tube therefore has nearly constant voltage across the ion emitting face.

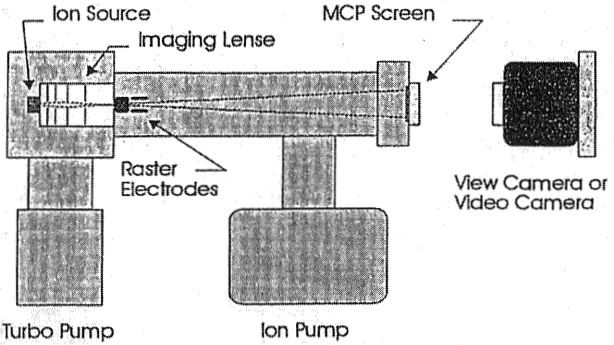

Figure 3 Diagram of the "ion source imaging instrument." The spatially resolved ion beam is projected onto the image intensifier to produce an image of the ion emitting regions of the emitter.

6.2.3 Ion Imaging Studies

In an attempt to gain an understanding of where ions originate on these materials, an instrument [5] was constructed for the purpose of imaging the ion emitting regions. Figure 6.3 is a diagrammatic view of the instrument. The heart of the instrument is the ion lens that projects a spatially resolved image of the ion emitting regions onto an image intensifier. The image intensifier consists of a chevron microchannel plate interfaced to a phosphor coating plated on the vacuum side of a fiber optic bundle sealed into a vacuum flange. The image of the beam striking the device can then be viewed from the other side of the fiber-optic bundle outside the vacuum. Details of the design and operation of the instrument are given elsewhere [5]. The instrument produces total ion images from the surface being studied, providing no mass resolution. The approach of not mass resolving the ion beam greatly enhances sensitivity and ease of operation and reduces the cost of the instrument by about an order of magnitude but limits usefulness to the study of emitters with relatively pure ions. This did not pose a problem for the types of studies of relatively pure ion beams for which this instrument was intended. When operating with high-intensity ion beams ($>10^{-10}$ A) the image on the image intensifier can be photographed with a camera, whereas at lower intensities the image is captured with a high-gain video camera. The photographic camera gives much higher resolution than the video camera but yields reduced sensitivity since the video camera can detect very low levels of light, allowing short exposure times with low-intensity beams.

Other than the issue of mass resolution, the major limitation of the instrument is the requirement that samples be at a constant voltage across the face of the emitter. The tube ion source gives about two orders of magnitude higher imaging resolution than the short filament source (3 μm vs. 200 μm) because of the issue

of voltage spread across the face of the emitter, as mentioned in the preceding section. Thus, even a 0.5-V spread across the emitter face causes considerable defocusing.

This ion imager has allowed answers to be obtained to the question, Where on the emitter do the ions originate? All of the systems studied to date emit ions from the surface of the main body of the emitter. This is illustrated in the images presented in Fig. 6.4a–d. The photographs of the first three of these emitters (Cs^+ in Fig. 6.4a, ReO_4^- in Fig. 6.4b, I^- in Fig. 6.4c) show the surface topographical features of the face of the solid emitter, with ion emission clearly emanating from the

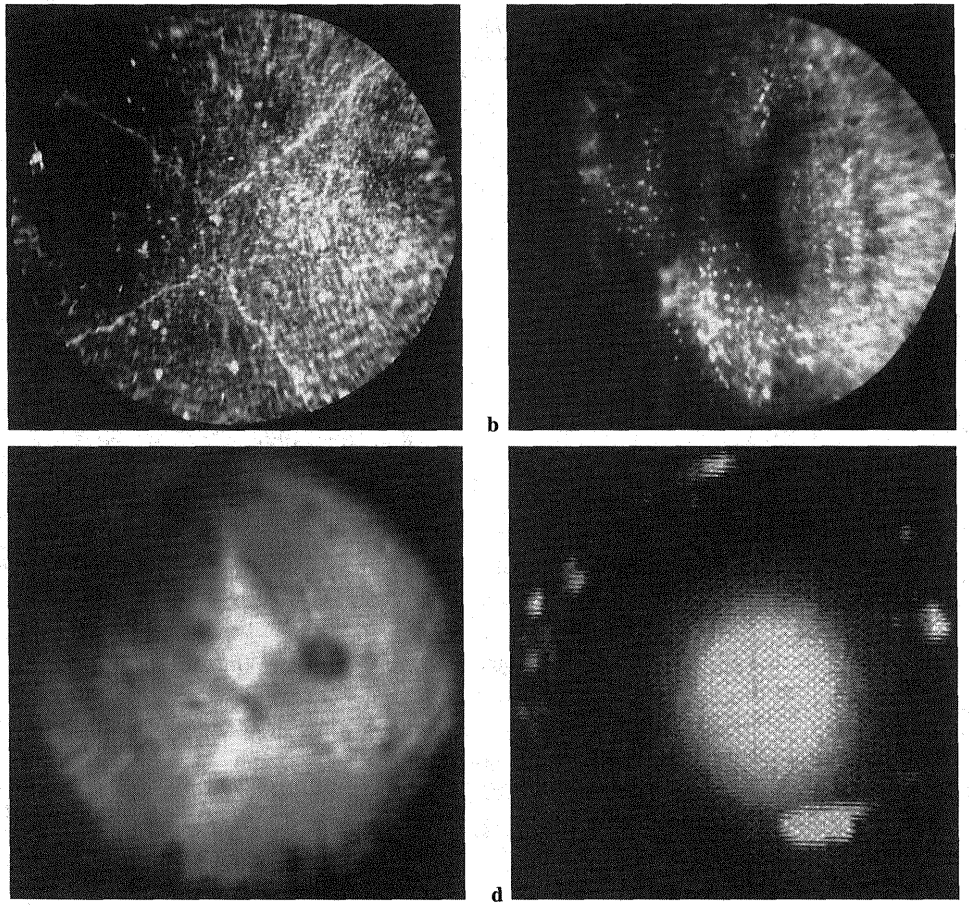

Figure 4 (a) Image of Cs^+ emission from cesium zeolite. Note enhanced emission from the cracks. (b) Image of ReO_4^- emission from a perrhenate emitter. (c) Image of I^- emission from an iodide emitter. (d) Image of Bi^+ emission from a molten glass ion emitter.

face of the emitter. An interesting feature is the enhanced ion emission from the cracks in the face of the emitter in Fig. 6.4a. These appear to be due to enhanced migration of ions along the surfaces within the cracks. This information by itself provides the insight that ions can migrate along surfaces prior to emission. Another possible interpretation of the enhanced ion emission from the cracks is that the edges may provide an enhancement effect, possibly due to electrostatic field gradients that are stronger at an edge. The fourth image is Bi^+ from a molten glass ion emitter. Although the image does not show any surface topographical features, the majority of the ions are originating from the face of the bulk of the deposit. The ions forming the ring around the main area of ion emission are thought to originate from sample residing on the outer rim of the tube source. The intensity was sufficiently low that an exposure of several minutes would have been required to obtain a good photograph. The features changed with time rapidly enough that this was not practical, hence the image in Fig. 6.4d is from the video camera. An interesting topographical feature of the molten ion emitter, which unfortunately cannot be demonstrated to the reader, was the fashion in which bubbles could be observed forming and bursting on the surface. If such a bubble were to occur in a sample for which an isotope ratio were being measured it would be impossible to get accurate results since the beam intensity would fluctuate excessively. This may be the reason why many analytical procedures that use silica gel require the use of very small loadings.

It is recognized that there may be other ion emitting condensed phase materials for which ions originate from a region other than from the bulk of the material, but since these have not been identified to date, the remainder of this chapter deals with those systems emitting ions from the bulk of the deposit.

6.2.4 Ion/Neutral Mass Spectrometry

Material volatilizing from the surface of most condensed phases at high temperatures consists predominantly of neutral species, with only a few materials emitting ions to an appreciable extent. Ion emitters are unique in this regard. In an effort to understand the mechanisms responsible for this phenomenon better an instrument was constructed to measure the ions and the neutrals volatilizing from a single specimen of an emitter sequentially. The purpose is to gain better understanding of the types and quantities of neutrals volatilizing from the materials along with the ions so as to gain new insights into the processes governing ion emission.

This instrument [7] measures three types of ions in a sequential mode: the positive and negative ions emitted from the surface of the ion emitter, and the neutral species volatilizing from the surface and ionized by electron impact (EI). A commercially available quadrupole mass spectrometer equipped with an EI source was modified to allot a specially designed thermal emitter to be just barely inserted into the ionization chamber. The chamber is much cooler than the emitter; there-

fore, condensable species must be ionized prior to striking the wall of the ionization chamber as they condense onto the walls. This is *Langmuir vaporization*, in contrast to *Knudsen vaporization,* in which the chamber walls are at the same temperature as the sample, which measures the vapors in thermodynamic equilibrium with the surface. Both the miniaturized filament source and the tube source have worked well in this instrument. On heating, neutral atoms and molecules are vaporized from the surface and ionized by electron ionization, allowing the determination of the chemical species in the neutral vapor. This requires a specific set of focusing voltages, which conveniently do not allow ions emitted from the surface of the emitter to pass into the mass spectrometer. Additional discrimination against any surface ions is obtained by biasing the emitter.

Both ions and neutrals volatilized into the chamber. Positive ions emitted from the surface of the emitter are focused into the mass spectrometer with a totally different set of focusing voltages. Negative surface ions are also focused into the mass spectrometer, again with a unique set of focusing voltages, and of course with the quadrupole voltages reversed and the detector configured for negative ions. Computer control of the voltages greatly simplifies rotating among the three modes. The filament producing electrons for EI is turned off when surface ions are being measured, further ensuring that ions of different origins are differentiated. Two to four minutes is allowed for spectral scanning and data storage prior to sequencing on to the next mode.

This instrument has allowed several studies that provide information not obtainable by other means to be conducted. Four examples are presented as follows: The first example concerns the question of the mechanism of emission of potassium ions from potassium zeolite [7]. Earlier studies had made the assumption that this was an S-L type of ion formation mechanism [8], implying that there was a neutral potassium atom flux accompanying the flux of atomic potassium cations. Experiments performed on this instrument clearly showed that this is not the case; there was no detectable neutral atomic potassium flux accompanying the cation flux. Thus this instrument was used to answer a long-standing question with an experiment conducted in one afternoon and allowed the conclusion to be reached that the mechanism is potassium ions in the solid state subliming into the gas phase.

The second example is the analysis of silver zeolite [7], in which it was shown that there is a substantial silver atom flux accompanying the relatively weak silver cation flux. There were no molecules or clusters containing silver in the gas phase. Pure silver metal heated to the sublimation point gives primarily neutral atoms and metallic clusters with no ions. Thus, sublimation of atomic silver ions from zeolite may be a pseudo–S-L type of process, although additional evidence concerning the species of silver in the solid state would be required prior to making this assertion.

The third example is the analysis of perrhenate emitters [3,9] discussed later in this chapter. Pure $Ba(ReO_4)_2$ volatilizes as neutral molecules, whereas the blend

of $Ba(ReO_4)_2$ into a rare earth oxide matrix gave a strong ReO_4^- flux and no evidence of Ba volatilizing as either a neutral or an ionic species. Here it can be concluded that $Ba(ReO_4)_2$ must be embedded in a matrix to allow ReO_4^- to migrate away from the Ba counter ion and to sublime as an anion.

The fourth example, an unpublished study [10], has demonstrated that silver molten glass ion emitters volatilize a considerable neutral silver atom flux accompanying the silver ion flux, again leaving open the possibility that this is a pseudo–S-L type of ion emission process.

Additional evidence, useful in supporting the concept that silver zeolite and silver molten glass ion emitters are S-L processes, would be that both ions and neutrals arise from the same species in the solid state; this issue is addressed in the following section, on high-temperature SIMS.

6.2.5 High-Temperature Secondary Ion Mass Spectrometry

High-temperature mass spectrometry (HT-SIMS) is a technique currently being developed that has not yet been described in the public literature, and hence is mentioned here only briefly. Our group has been developing SIMS as a technique for determining chemical speciation of inorganic solids at room temperature [11–13], and HT SIMS is an expansion of this effort. Most techniques for the determination of chemical species in solids (other than various crystallographic methods) rely on taking the solid material into solution, followed by some analytical technique such as liquid chromatography inductively coupled plasma mass spectrometry (LC-ICP-MS) or LC-electrospray-MS. This can be a definitive determination as long as the chemical species is unchanged by the process of dissolving the solid material. If the chemical species are altered by the dissolution process, then the altered species is determined rather than the original species.

Performing the chemical speciation analysis on the unaltered specimen with SIMS alleviates this uncertainty. However, the results are fundamentally more difficult to interpret, for certain species that are more ambiguous, and for other species with which the technique cannot be made to work. Each situation is obviously quite different and care must be exercised in choosing a method.

Because the goal is to determine the chemical species present on the surface of ion emitters at high temperatures, it is obviously impossible to dissolve the material; hence SIMS is used to determine the chemical species. One of our SIMS instruments has been modified so the ion emitting surface is at full operating temperature in the sample position, where it can be bombarded with a beam of perrhenate anions and the resulting sputtered secondary ions measured by mass spectrometry. This instrument is now operational and is being used to determine the practicality of this approach. The first study, which is presently being conducted, is an effort to determine the chemical species present on the surface of a silver molten glass ion emitter. The ion/neutral mass spectrometer results show that

both silver neutral atoms and silver atomic cations are emitted from the surface. If it can be determined that atomic silver in the condensed phase is the species that is responsible for the formation of both the neutral and the ionic silver species, then the conclusion can be drawn that the ion emission process is a pseudo–S-L-type process. Preliminary data are consistent with the conclusion that silver on the surface is in the zero oxidation state.

6.3 TYPES OF ION EMITTERS

There are dozens of analytical methods published in both the open literature and in government and other reports that describe the preparation of various ion emitters for the purpose of measuring isotope ratios. There are also many methods that various laboratories have developed that have never been published but are referred to in oral presentations. Thus there are probably many groups of ion emitters that have been developed and used but whose mechanistics properties are not understood. If the mechanism were understood, however, it is likely that the method could be improved. At the beginning of this chapter ion emitters were divided into two categories, presynthesized ion emitters and those with ongoing chemical and physical reactions that produce the ions in situ. Examples of each of these are presented here, and their mechanistic characteristics are described to the extent they are understood.

6.3.1 Emitters with Ions Presynthesized in the Solid State

In the class of ion emitters in which the ions are presynthesized in the solid state, the ion of interest is presynthesized and embedded in a suitable matrix. It is thought that ions are subliming directly from the solid state into the gas phase, as supported by the images in Fig. 6.4a–c. These images clearly demonstrate that ion emission is from the face of the bulk of the deposit. The enhanced ion emission from the cracks in Fig. 6.4a indicates that ions migrate from the bulk to a surface, and then migrate across the surface until reaching a location where they can sublime. The actual ion migration and sublimation mechanisms are not understood, and the role the electrostatic field may play in these processes has not been studied. Two broad classes of ion emitters of this type have been identified and studied:

1. Anion emitters: This category of emitters is based on the rare earth oxides [3,9], with the best characterized ones based on the Eu_2O_3 matrix, and have been shown to be efficient emitters of the perrhenate (ReO_4^-) and the halide (Cl^-, Br^-, and I^-) anions. It is probable that the analytical method for producing ions from technetium [14] also is in this category.

2. Cation emitters: The alkali metal zeolites, and other alkali metal aluminosilicates, are efficient emitters of alkali metal cations. The cation emitters have been known for a much longer time than the anion emitters, but the anion emitters are better understood from a chemical perspective; hence they are discussed here. Both types of emitters, however, can be scaled up in intensity readily to be used for the primary ion guns in static SIMS instruments. Ion beams of 50 pA to 1 nA focused to a 1-mm spot size are routinely produced by using these emitters. These emitters are primarily used in SIMS guns, as opposed to being used for isotope ratio analyses.

The importance of the work function and temperature of the surface, the ionization potential for positive ion emission, and the electron affinity for negative ion emission are well established for conditions in which the S-L equations are valid. Experimentally, the IP and EA are also important for thermal emitters. For example, the alkali metals all have low IPs and are emitted in good yields from the zeolites impregnated with the corresponding alkali metal. The halide and perrhenate anions all have high EAs and are emitted in good yield from certain of the rare earth oxides. The temperature is also quite important, but possibly not for the same reasons as for the S-L conditions. Under S-L conditions a higher temperature is more likely to strip an electron or to add an electron to an atom.

Sublimation of preformed ions from the surface is a process much different from S-L ionization since these ions already have their oxidation and charge states. It may be surmised that a higher temperature increases the migration rates of the preformed ions and increases the sublimation rate, until the temperature gets so high that some undesirable process occurs in the matrix. As an example, the oxidation state of the ion of interest could change with excessive temperature, destroying the ion emission properties, or the matrix could undergo an undesirable phase transformation. The importance of the IP and EA may be more related to the degree of polarization between the preformed ion and their counter ions. The WF of the surfaces of these emitters has never been measured, not even at low temperatures. The better anion emitters are in rare earth oxide matrices, and these materials are known to have relatively low WFs at low temperatures, but the effects of blending these components and elevating the temperature have the potential to alter these values. This area needs more study.

Experimentally, the compound consisting of the preformed ion and its counter ion (such as barium perrhenate for perrhenate emission) does not produce ions when heated—instead, only neutral species sublime. It must be embedded in a suitable matrix and then heated. The limited experimental evidence collected to date indicates that the ion to be emitted must have significantly greater mobility and/or vapor pressure in this matrix than its counter ion, allowing diffusion of the ion of interest. When the temperature gets sufficiently hot the ion migrates to the

surface and sublimes, leaving the counter ion behind. This process continues until something happens to limit further diffusion and/or sublimation. This limiting step is thought to be the buildup of charge (or color centers) within the matrix. The second major requirement seems to be some mechanism to compensate for the buildup of these charge centers.

The most successful of the anion emitters are based on rare earth oxide matrices, with the rare earth in the +3 oxidation state. Europium oxide, Eu_2O_3, is the most successful of these anion emitters and also has the most stable +2 oxidation state of all the rare earths. This feature of Eu_2O_3, the stability of the +2 oxidation state, is thought to be responsible for this compound's being the best matrix. Whereas the matrix in the +3 oxidation state allows the migration of the anions away from the counter ion, the stability of the +2 oxidation states allows reactions of the following type to take place:

$$Eu_2O_3 + Ba(ReO_4)_2 + 2e^- \Rightarrow 2ReO_4^- \text{ (gas phase)} + 2EuO + BaO \qquad (6.1)$$

This reaction involves the reduction of Eu in the +3 oxidation state to Eu in the +2 oxidation state, freeing an oxygen anion to combine with the Ba counter ion left after the perrhenate anion migrates. There are a variety of other chemical reactions of a similar type that can be written, such as the following:

$$Eu_2O_3 + 2Ba(ReO_4)_2 + 2e^- \Rightarrow 2ReO_4^- \text{ (gas phase)} + 2EuO + Ba_2O(ReO_4)_2 \qquad (6.2)$$

This equation has the advantage over the previous one that the barium containing molecule on the right of the equation retains a partial ionic character that permits it to serve as a "transfer station" for additional migration of perrhenate anions.

A model is proposed to account for the capability of these materials to be efficient emitters of ions:

1. The singly charged ion needs to be presynthesized, paired with a suitable counter ion (all successful systems studied to date have the ion of interest singly charged and the counter ion doubly charged), and embedded in a matrix that allows the singly charged ion to migrate away from the doubly charged counter ion when heated. Otherwise, the entire neutral molecule can sublime, bypassing the channel for ion emission.
2. The ion of interest needs to be stable in the matrix. This places various requirements on redox properties of the matrix for each type of ion.
3. There needs to be some mechanism available for maintaining charge neutrality in the lattice after ion migration. Electron migration between the filament and the power supply can maintain charge neutrality, but this alone cannot satisfy the bonding requirements of the counter ion.
4. For a cation emitter, an oxidation reaction within the matrix is required to generate a new cation to satisfy the bonding requirements of the anion

remaining after cation emission. For an anion emitter a reduction reaction within the matrix is required to generate a new cation to satisfy the bonding requirements of the remaining cation after anion emission.

5. It is probable that the oxidation or reduction occurs nearly simultaneously with ion migration, since any appreciable electrical charge buildup is thermodynamically improbable.

This model is based on studies of anion emitters in rare earth oxide matrices in the +3 oxidation state extending over several years. These studies can be summarized as follows:

1. It is an experimental observation that only the rare earths starting out in the +3 oxidation state are efficient ion emitters.
2. The rare earth must have a reasonably stable +2 oxidation state, although the majority of the material must be in the +3 state. The elements europium (Eu) and ytterbium (Yb) have by far the most stable +2 oxidation states of the rare earths, and the oxides of these elements make the most effective matrices for anion emission. Eu is approximately two orders of magnitude more effective as a matrix that Nd when perrhenate emission is not pushed to high levels.
3. The included anion to be emitted must have a high electron affinity. The species demonstrated to be emitted from these matrices are the halides (Cl^-, Br^-, I^-) and perrhenate (ReO_4^-). The electron affinities are 3.7 eV, 3.5 eV, 3.2 eV, and 4.5 eV, respectively. The borate anion (EA of 3.0 eV) can also be readily observed as an impurity in these emitters.
4. These anions appear to be quite stable in these matrices. Studies conducted with the ion/neutral mass spectrometer could not detect any gas-phase reduction products of perrhenate or any oxidized species of the halides, leading to the conclusion that the Eu_2O_3 matrix is neutral or nearly so in regard to oxidation/reduction potential.
5. Studies on the ion/neutral mass spectrometer have verified that the barium counter ion is nonvolatile in these matrices, and possibly nonmigratory.

6.3.2 Emitters with Ions Produced in Situ

Emitters that have ions produced in situ are by far the largest group of known ion emitters. They are much more difficult to scale in intensity than preformed ion emitters. In general, methods have been developed that give stable and reproducible ion beams with sufficient intensity to provide an isotope ratio analysis for the particular element to be analyzed. As stated earlier, it is not necessary to understand the mechanistics of ion emission to use these ion emitters for isotope ratio analysis as long as the ion beams are sufficiently stable with adequate intensity. There

is always the question, though, of whether the method could be improved significantly if the mechanism were understood. For this reason, it is useful to attempt to gain an understanding of these processes. Although the primary application of the preformed ion emitters tends to be as the primary ion guns in static SIMS instruments, the significant application of these emitters is the measurement of isotope ratios.

There are two main subdivisions of ion emitters in this group of which we have some understanding. The first of these subdivisions is an emitter in which an ongoing chemical reaction synthesizes an ion that is then sublimed. An example of this is the production of perrhenate anions [15] from the rare earth oxide catalyzed oxidation of rhenium by water vapor. The second subdivision is the production of neutral atoms within a matrix and the vaporization of fluxes of neutral and ionic species. This can be thought of as a type of pseudo-S-L process since there is an atom on the surface that has a finite probability of volatilizing as either an ion or the atom. The trick is to be able to produce these atoms in the zero charge state in the matrix. There are a number of ion emitters thought to be in this category, but none proven. There are many other "recipes" that have been used over the years; among these there are probably other types of ion emitters that have been used but whose mechanistics properties have never been identified. In truth, there is very little that is known with certainty about the mechanistics of ion emitters in these categories; hence the rest of this chapter primarily outlines areas that require research.

6.4 POSSIBLE PSEUDO–SAHA-LANGMUIR ION FORMATION PROCESSES

6.4.1 Ion Emission from Pure Metals

Several refractory metals emit the respective atomic cation and, in some cases, the atomic anion at temperatures approaching the burnout point of the material. The work of Scheer and Fine [2] demonstrates that tungsten and rhenium emit both atomic cations and anions of the respective metal, and that the ratio of cations to anions as a function of temperature is consistent with the S-L equations. Such behavior can be termed *pseudo—Saha-Langmuir* behavior, as the characterization *pseudo* indicates that this situation is not that of an atomic beam impinging on a hot metal surface. This does not conclusively prove that these are S-L processes, however, since no attempt was made to measure the neutral atom flux. This raises the question, If the S-L equation applies to the sublimation of atoms of the major (or only) element making up a high temperature metal, will it also be applicable to the emission of minor impurity metal ions? This has never been proved experimentally, but it seems a logical extension of the preceding conclusions. There are situations in which such processes may be occurring. First, there are analyses for

several elements that are limited by the levels of impurities in the filament materials such as Mo in Re filaments. Since Mo is more volatile than rhenium, it sublimes preferentially, causing spectral interferences with Zr and Ru. Also, there are a variety of isotope ratio analyses in which the chloride or nitrate salt is loaded directly onto a single filament, with the temperature slowly increased until ion emission is reached. The mechanisms have never been studied, but it is possible that the element alloys with the filament material before being re-emitted as the atomic cation. Thus these ion emitters may also fall into the category of being trace metals embedded into a refractory metal matrix. This provides a research opportunity.

6.4.2 Electrodeposited Emitters

Electrodeposition could be a pseudo-S-L type process, although definitive proof is lacking. The element to be ionized, uranium [16] or plutonium [17], is coelectrodeposited with a platinum metal layer, then covered with an additional layer of platinum. The U or Pu is believed to be electrodeposited as an oxide, and platinum is electrodeposited as the metal. Hence there is thought to be a U or Pu oxide buried in the metal matrix. When this deposit is heated, after a sufficient length of time atomic cations of U or Pu begin to sublime from the surface without measurable metal oxide ions. Metal oxide ions should be readily observable if they are present in the matrix. Thermodynamic calculations indicate that the hot platinum matrix will not reduce the U and Pu oxides to the metallic state, and yet the observed species are atomic ions and not oxide molecular ions.

6.4.3 Silica Gel (Molten Glass) Ion Emitters

The original work on silica gel ion emitters was first published in 1959 [18] and has typically been referred to as the "silica gel" method. This method has been widely adapted to the analysis of many elements. The basic method is to deposit silica gel in an aqueous suspension onto a filament, then to add a solution containing the element to be ionized, then to add either phosphoric acid or boric acid solutions. The mixture is dried and the filament mounted in the source. The source is evacuated and the temperature slowly increased to operating temperatures. In general, it is best to use solutions with the lowest practical strong acid (HCl, HNO_3) content to prevent dissolving filament material that poisons the emitter. The elements that can be analyzed by this technique can be classified into two main groups: those that are readily reduced to the metal and those that are not. It is unlikely that these two groups have the same ion formation mechanism. Elements in the first group include Pb, Bi, Ag, Au, Te, Sn, Ru, Pd, and Fe [19–25]. The alkaline earth elements [26] can also be analyzed by using variations of this method; they are clearly quite difficult to reduce to the metal and therefore constitute the second group. This analytical technique was originally developed for the isotope ratio analysis of lead for U/Pb age dating, and this is still the largest single application.

A recent study [4] conducted on large deposits of bismuth ion emitters prepared by a method of this type identified the material as a molten glass at operating temperatures. Figure 6.4d identifies the surface of the bulk of the material as the ion emitting surface. It has been known for many years that rhenium was a superior filament material to tantalum for these analyses, and this study identified the reason. Tantalum dissolves in the molten glass and poisons the emitter. Thus we have reason to believe that the molten glasses are highly corrosive, especially toward Ta, and are especially so if strong mineral acids are used.

A more recent study has been conducted on silver/silica gel ion emitters. Silver was chosen because it has only 0 and +1 oxidation states, greatly simplifying the determination of the oxidation state responsible for ion emission. The question is, Is it 0 or +1? If it is +1, it would be a preformed ion, whereas if it is 0 it would be a pseudo-S-L-type process with a mix of neutral and cationic species volatilizing from the surface. Silver oxides are known to decompose to the metal and gaseous oxygen at temperatures well below the operating temperatures of these ion emitters; hence there is a high probability that silver is reduced to the metal from the temperature alone. Indeed, oxygen is evolved from these emitters at approximately this temperature range. There is evidence that silver is in the 0 oxidation state at operating temperatures, in spite of the fact that it is in an oxide matrix. The reasons for this claim are as follows:

1. In the ion/neutral mass spectrometer the silver species identified were the atomic neutral and cationic species.
2. The HT SIMS data indicate that the only silver species on the surface of the emitter is metallic. Hence, if metallic silver on the surface is subliming to give a mix of atomic neutral and cationic species, this looks like a pseudo-S-L process. Again, the data are not quantitative enough to compare to the S-L equation.

If this model, where the metal is reduced to the zero oxidation state, applies to silver, it is conceivable that it applies to the other elements that can be readily reduced to the metal. The question that remains to be answered is, Does the model for silver apply to other elements that can be reduced to the metal in an aqueous solution?

Another concept that warrants mention is "desolvation." When silver metal in bulk is heated, it tends to sublime as neutral species. When both neutral and cationic silver species volatilize from these silica gel matrices they are exclusively monatomic. This indicates that silver atoms in the zero oxidation state are not "solvated" by each other or by a component in the matrix. This concept is admittedly speculative but does offer a concept as to how this ion emitter matrix may operate.

Thus, for those elements that are readily reduced to the zero oxidation state, a model that is consistent with experimental evidence can be offered. This model is the following:

1. The element to be ionized is reduced to the zero oxidation state.
2. The element is "desolvated" in the high-temperature molten glass matrix; therefore, the atoms of the element are not tightly bonded to each other or to other species.
3. The element volatilizes as a mix of neutral and singly charged positive atoms and perhaps is a pseudo-S-L process.

This model is offered somewhat tentatively, but the features are consistent with a body of experimental evidence. At a minimum, it offers a target against which to conduct additional experiments that will, it is hoped, shed light on this subject.

Ion formation mechanisms for silica gel matrices have never been studied for those elements that are not readily reducible to the metal. The solvation/desolvation mechanism hypothesized previously may have a role in enhancing ion emission from these materials, but it would not be expected that an alkaline earth element could exist in the zero oxidation state in these glass matrices, which are oxide based. The species in the molten glass would be expected to be in the standard +2 oxidation state, but the experimentally observed species is +1. Indeed, there has never been a +2 species reported from thermal ionization, so there is the question of how the +2 species in the molten glass is converted to and emitted as a +1 ion.

6.5 CONCLUSIONS

In concluding this chapter, we point out that there are far more research opportunities than hard answers in this field of ion emitters. This field is dominated by systems in which the element from which ions are emitted is embedded in a matrix that enhances ion emission. Indeed, with the exception of the small number of emitters in which ions are emitted from pure refractory metals at the temperature limits of the material, pure materials predominantly volatilize neutral atoms and/or molecules when heated to temperatures sufficiently high to force volatilization to the gas phase. Thus, the key to the development of superior ion emitters seems to be to develop better understanding of the processes that cause the matrices to force the element to volatilize as ions rather than neutrals. With this better understanding perhaps new and better ion emitters can be developed.

REFERENCES

1. I. Langmuir and K. H. Kingdom, Proc Royal Soc (London) 1925, A107, 61.
2. M. D. Scheer and J. Fine, J. Chem. Phys., vol. 46, No. 10, (1967) 3998–4003.
3. J. E. Delmore, A. D. Appelhans and E. S. Peterson, Int, J. Mass Spectro. Ion Processes, 146/147 (1995) 15–20.

4. T. Huett, J. C. Ingram and J. E. Delmore, Int. J. Mass Spectro. Ion Processes, 146/147 (1995) 5.
5. J. E. Delmore, A. D. Appelhans and J. E. Olson, Int. J. Mass Spectro. Ion Processes, 140 (1994) 111–122.
6. M. H. Studier, E. N. Sloth and L. P. Moore, J. Phys. Chem., 1962 pg. 133.
7. J. E. Delmore, T. Huett, J. E. Olson and A. D. Appelhans, Int. J. Mass Spectro. Ion Processes, 155 (1996) 149–162.
8. A. N. Parellis and M. Seidl, J. Applied Phys., 49 (1978) 4933.
9. J. E. Delmore, A. D. Appelhans and E. S. Peterson, Int. J. Mass Spectro. Ion Processes, 178 (1998) 9–17.
10. T. Huett and J. E. Delmore, unpublished results.
11. J. E. Delmore, A. D. Appelhans, J. E. Olson, T. Huett, G. S. Groenewold, J. C. Ingram and D. A. Dahl, J. Royal Soc. W. Australia, 79:iii (1996) pg. 103–108.
12. G. S. Groenewold, J. E. Delmore, J. E. Olson, A. D. Appelhans, J. C. Ingram and D. A. Dahl, Int. J. Mass Spectro. Ion Processes, 163 (1997) pg. 185–195.
13. G. S. Groenewold, A. D. Appelhans and J. C. Ingram, J. Am. Soc. Mass Spectrom., 9 (1998) pg. 35–41.
14. D. J. Rokop, N. C. Schroeder and K. Wolfsburg, Anal. Chem. 62 (1990) 1271.
15. J. E. Delmore, J. Phys. Chem., 91 (1987) 2883.
16. D. J. Rokop, R. E. Perrin, G. W. Knobeloch, V. M. Armijo and W. R. Shields, Anal. Chem. 54 (1982) 957–960.
17. R. E. Perrin, G. W. Knobeloch, V. M. Armijo and D. W. Efurd, Int. J. Mass Spectro. Ion Processes, 64 (1985) 17–24.
18. A. E. Cameron, D. H. Smith and R. L. Walker, Anal. Chem., 41 (1969) 525.
19. F. Tera and G. S. Wasserburg, Anal. Chem., 47 (1975) 2214.
20. W. R. Kelly, F. Tera and G. S. Wasserburg, Anal. Chem., 50 (1978) 1279.
21. K. J. R. Rosman, R. D. Loss, and J. R. De Laeter, Int. J. Mass Spectro. Ion Processes, 56 (1984) 281.
22. J. L. Birck and G. W. Lugmair, Earth Planet. Sci. Lett., 90 (1988) 131.
23. R. D. Loss, K. J. R. Rosman and J. R. De Laeter, Talanta, 30 (1983) 831.
24. K. J. R. Rosman and J. R. De Laeter, Int. J. Mass Spectro. Ion Processes, 16 (1975) 385.
25. A. Shukolyukov and G. L. Lugmair, Science, 259 (1993) 1138.
26. T. Lee, D. A. Papanastassiou, and G. J. Wasserburg, Geochim. Cosmochim. Acta 41 (1977) 1473.

7

Analysis of Nonconductive Sample Types by Glow Discharge Mass Spectrometry

R. Kenneth Marcus
Clemson University
Clemson, South Carolina

7.1. INTRODUCTION

One of the most challenging aspects of atomic spectrometry is the incredibly wide variety of sample types that require elemental analysis. Samples cover the gamut of solids, liquids, and gases. By the nature of most modern spectrochemical methods, the latter two states are much more readily presented to sources that operate at atmospheric pressure. The most widely used of these techniques are flame and graphite furnace atomic absorption spectrophotometry (FAAS and GF-AAS) [1,2] and inductively coupled plasma atomic emission and mass spectrometries (ICP-AES and MS) [3–5]. As described in other chapters of this volume, ICP-MS is the workhorse technique for the trace element analysis of samples in the solution phase—either those that are native liquids or solids that are subjected to some sort of dissolution procedure.

Although most analytical chemists would relate the field of direct solids elemental analysis to the characterization of metals and alloys, the fact is that a very large number of solid sample types require elemental analyses, with the range expanding on a continuous basis (e.g., glasses, ceramics, and even polymers). As such, the conventional techniques of arc [6] and spark atomic emission and mass spectrometries [7,8] must be evaluated with respect to whether or not they are applicable to the wide array of sample types.

Spark and arc spectrochemical sources rely on the ability of charged particles to heat the sample surface and ultimately desorb atoms from the solid matrix

into the gas phase for subsequent excitation and ionization [9]. In both cases, an electrical current must be maintained to sustain the respective plasma discharges. In this way, the sample serves as an electrode in a basic diode type of assembly. In the case of samples that are electrically insulating (nonconductive), this flow of current cannot be accommodated, so methods of remediation must be implemented. This is most typically achieved by mixing the sample with a powder of a conducting metal or graphite, and pressing this mixture into the form of a nominally conductive disk [10]. This process is usually referred to as *compaction*. If the sample is in *bulk* rather than powder form, it must first be ground or pulverized. In this instance, the primary benefit of using a solid sampling method, the elimination of a matrix modification step, is voided.

As described in previous chapters, glow discharge mass spectrometry (GD-MS) has established itself since the mid-1980s as one of the most sensitive and reliable methods for performing direct solids elemental analysis of conductive solid sample types [11–14]. The ability of the easily controlled low-pressure plasma to yield a reproducible ion beam affording sensitivities to the sub–parts per billion (ppb) level is its most outstanding feature. The successive removal of pseudoatomic layers provides additional information content because the technique is capable of performing very-high-sensitivity depth profiles for layers ranging from tens of nanometers to micrometers in thickness. It must be admitted, though, that the capability of performing quantitative depth profiles is still in an infant stage relative to its sister method, glow discharge atomic emission spectroscopy (GD-AES) [15–17].

In terms of the range of sample types amenable to glow discharge mass spectrometry (GD-MS) analysis, it must be realized that the glow discharge, like its spark and arc discharge cousins, is a diode-type electrical device. Electrical current must continuously flow [in the case of direct current (dc) powering] to and from the sample cathode. In the case of electrically insulating samples, the samples must be modified to become electrically conductive by the methods originally developed for spark and arc sources [18–20]. In doing so, however, one of the advantages of GD methods, the ability to create depth-resolved elemental profiles, is lost. Fortuitously, because glow discharges are low-pressure devices, alternative methods of applying the discharge power that allow sustaining of the plasma at the surface of nonconductors exist. These methods include the use of a secondary cathode [21–25] to provide a conductive coating on the sample and the use of radio frequency (rf) power [26–35] applied to the sample.

This chapter deals exclusively with the methods that have been developed for the direct solids analysis of nonconductive samples by glow discharge mass spectrometry. The basic approaches to operation and sample preparation for the three primary methodologies of compaction, secondary cathode, and radio frequency powering are described. Examples of source performance and practical applications of each are taken from the analytical literature. Whereas this chapter de-

scribes the analysis of insulating materials by GD-MS, a review by Winchester et al. provides additional background for such analyses for the complete family of GD spectroscopies [36]. It is hoped that the reader will see that there are indeed a number of options available for meeting the challenges presented by this ever-increasing and important set of sample types.

7.2 ANALYSIS BASED ON SAMPLE COMPACTION METHODS

The use of the sample compaction methodology is an effective means of analyzing powder-form samples such as geological materials and spent automotive catalysts. The mixing of powders with conductive host metals involves four basic steps: (1) drying of the sample to drive off residual water, (2) weighing appropriate amounts of sample and binder, (3) mixing mechanically to homogenize the components, and (4) pressing the sample into the appropriate size and shape as dictated by the sample holder. Each of these steps involves a finite period and requires judicious optimization and protocol development. The use of the sample compaction methodology was introduced early (1972) in the evolution of glow discharge atomic emission spectrometry by Dogan et al. [18]. Marcus and coworkers reviewed a great deal of the developmental aspects of the compaction methodology as it applies to GD-AES [36]. Loving and Harrison [37] published the first description of the use of the compaction procedure for mass spectrometry in 1983 as part of a study evaluating the role of water vapor on GD-MS performance with a dual-pin cathode geometry. Borrowing from the methodology developed for spark source mass spectrometry, pin electrodes composed of 90% graphite and 10% arsenic powder were formed by using a die and hydraulic press. Stable [~2% relative standard deviation (RSD)] As^+ signals were produced, though the published spectrum clearly displayed that residual water and atmospheric species were major spectral components. Harrison and coworkers [38] revisited the approach in an early investigation of a hollow cathode plume (HCP) ionization source, wherein an alumina-based automotive catalyst was mixed 50:50 in a silver matrix. Neither of these early studies delved into the determination of the most effective implementation of the compaction procedure, though they demonstrated characteristics that have launched a series of detailed studies.

7.2.1 Choice of Host Matrix Material

Throughout the literature describing the compacted sample methodology, the choice of the binder material has time and again been pointed to as the most important aspect in determining source performance. Papers by Tong and Harrison [39], Mei and Harrison [40,41], Smith and coworkers [42,43], and Wayne [44] have

all evaluated the role of metal matrix material on the performance of GD-MS ion sources. The choice of binder material is dictated by a combination of the sample disk's robustness, sample sputtering rate (affecting analyte signal intensity), ability to remove unwanted residual gases such as water vapor and air (i.e., gettering quality), binder purity, and possible isobaric interferences with target analytes.

A pair of papers from the Harrison laboratory form the most comprehensive body of work dealing with the use of the compaction methodologies in GD-MS. Tong and Harrison evaluated six different matrix materials: graphite, Ag, Al, Cu, Fe, and Ta. Going through the matrices, some generalities about each matrix can be provided [39]. Table 7.1 summarizes the metal binder materials investigated for GD-MS applications and the mass spectral features of the pure binder materials (i.e., without oxide samples added). First, graphite is available in high purity and fine composition but it sputters too slowly, tends to produce metal carbide (MC^+) species, and is susceptible to adsorbed water. The latter characteristic results in the presence of a large number of water- and atmosphere-related ions (e.g., H_3O^+, N_2^+) in the spectrum. Both copper and silver sputter very well and produce high ana-

Table 1 Major Ion Peaks in GDMS Spectra of Pure Compacted Discs[a]

		Faraday detector voltage, 1 V = 10^8 ions/s					
Ion species	m/z	C	Cu	Ag	Al	Fe	Ta
^{12}C	12	0.15	0.03	n.d.	n.d.	n.d.	n.d.
$^{16}OH_2$	18	0.20	0.58	0.35	n.d.	n.d.	n.d.
$^{16}OH_3$	19	0.05	0.45	0.20	n.d.	n.d.	n.d.
$^{40}Ar^{2+}$	20	0.54	0.27	0.25	0.50	0.45	0.68
^{27}Al	27	—	—	—	**1.17**	—	—
$^{14}N_2H$, $^{12}C^{16}OH$	29	0.43	0.20	0.08	n.d.	n.d.	n.d.
^{40}Ar	40	9.50	9.90	(13)	(12)	10.50	10.00
^{40}ArH	41	3.20	6.00	3.70	9.20	8.60	3.00
^{56}Fe	56	—	—	—	—	**4.68**	—
^{63}Cu	63	—	**2.79**	—	—	—	—
^{65}Cu	65	—	**1.38**	—	—	—	—
$^{40}Ar_2$	80	0.41	0.27	0.30	0.20	0.32	0.20
^{107}Ag	107	—	—	**7.12**	—	—	—
^{109}Ag	109	—	—	**6.86**	—	—	—
^{181}Ta	181	—	—	—	—	—	**4.22**
M^+/Ar		0.016	0.42	1.08	0.098	0.45	0.42

[a]Taken after obtaining steady state in discharge (1 hr). Bold values indicate peak intensities of matrix ions.

n.d., nondetectable (<0.01 V).

Source: Ref. 39.

lyte ion beam intensities. Unfortunately, the background spectra for both materials are quite complex, with many metal dimers present at high levels. Each of the first three matrices tends to yield mass spectra that have a large amount of metal oxide and hydroxide ions (MO^+ and MOH^+) because of the presence of residual gases.

To counter the negative effects of water vapor on the observed spectra, aluminum, iron, and tantalum (metals with high affinities for water and air species) were evaluated. These "getter" metals tend to act as water scavengers as the volatile molecules evolve into the gas phase during the early sputtering times as the sample temperature rises. The removal of residual vapor produces mass spectra that are more atomic in nature and also enhances the atomization/excitation processes for the desired analyte species. Iron, being multi-isotopic, produces a more complex mass spectrum than aluminum and tantalum and also yields greater amounts of dimer and argide ions. Other getter elements such as zirconium and titanium have too many isotopes in themselves; therefore they were not seen as viable candidates. Of the two remaining candidates, tantalum has a high mass and higher sputtering rates that make it the most effective matrix. Across the range of matrices and analytes studied by Tong and Harrison [39], data were tabulated to depict the direct relationship between the relative amount of the oxides of a given element (specifically the $MO^+/(M^+ + MO^+)$ ratio) and their respective metal-oxide bond energies. As would be expected, the rare earth elements are most affected by the presence of water vapor and air, and some of these elements show as much as a 10% oxide ion fraction [39]. Even so, as shown in Fig. 7.1, high-quality spectra were obtained with the use of tantalum as the host matrix for a mixture of rare earth oxides.

7.2.2 Fundamental Processes

Just as the previously cited work illustrated the role of matrix selection in the quality of the mass spectra, Mei and Harrison [40] studied the underlying equilibrium involved in the formation and removal of metal oxides from the spectra of compacted oxide samples. The analyte for these studies was La_2O_3, chosen because of the high affinity of lanthanum for atomic oxygen, a product of the dissociation of both residual air and water vapor in compacted samples. Because the La-O bond strength is very high (8.30 eV), this oxide represents a case in which the dissociation of the original "analyte" would be difficult as well. On the basis of previous studies [41], it was assumed that approximately 50% of the lanthanum species sputtered from the surface would be free La atoms, and the other half would exist as oxides of one form or another.

The GD plasma environment is an interesting vessel to study gas-phase chemical properties. The gettering qualities of carbon, silver, tantalum, titanium, and tungsten were compared by Mei and Harrison [40] on the basis of the atomic ion fraction of all of the observed lanthanum species; $R = La^+/(La^+ + LaO^+) \times$

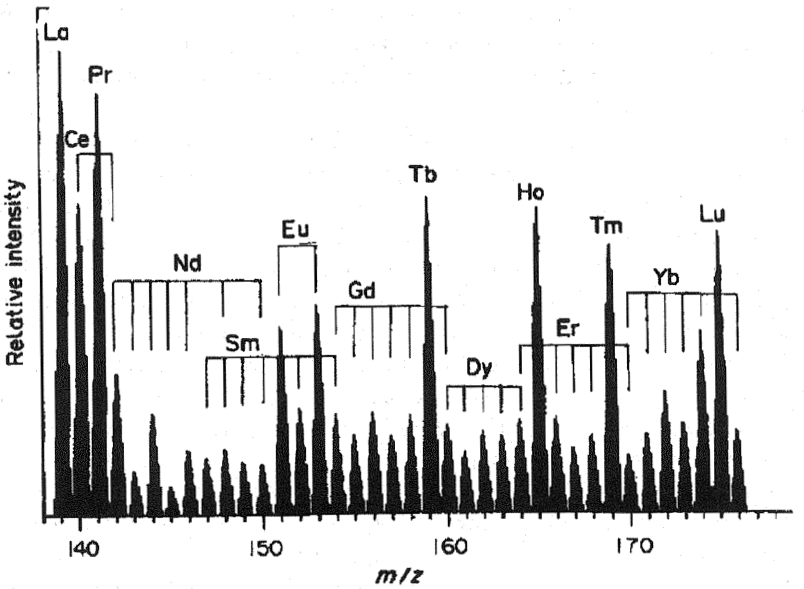

Figure 1 Glow discharge mass spectrometry (GD-MS) spectrum of a mixture of rare earth oxides compacted in a tantalum host matrix. Oxide composition 5% by weight in disk, each element present at 110 ppm. (From Ref. 39.)

100%. As such, a high R value represents the ability to produce analyte ions in favor of metal oxides. Temporal profiles of R values vs. time illustrated that the Ti, Ta and W (known getter) plasmas reached steady-state condition in approximately 1 hr, with plateau R values of Ti = ~100%, Ta = ~9%, and W = ~80%. High R values could be obtained for carbon (~90%), though a steady state was not achieved within the first 4 hr of operation. Silver had the lowest R value of the group (as might be expected), reaching a value of 20% after 3 hr of sputtering.

7.2.3 Analytical Applications

Three papers set out nicely the range of applicability of the compaction methodology in GD-MS. The analysis of soils was evaluated by Smith and coworkers [43] on a high-resolution VG9000 instrument. Sample pins (1.5-mm diameter, 18-mm length) were formed with a silver host and a 10:1 (Ag:soil) mixing ratio. Two National Institute of Standards and Technology (NIST) reference materials were used to demonstrate the analytical figures of merit. Fifty-one elements were analyzed in NIST 4355 Peruvian Soil. As in the case of most GD-MS analyses, an internal reference (^{107}Ag) was used to generate ion beam ratios for quantification and all analytical characterization. After a 20-min presputtering period, the variation in

ion beam ratios ranged from 1.2% to 3.6% RSD over an additional 20-min analysis period. The sample-to-sample precision, which is affected by the reproducibility of the sample drying, mixing, weighing, and pressing procedures, as well as the plasma/instrument operation, was found to range from 8.9% to 40% RSD for the 51 analytes. By looking at the variations across the range of elements, it was suggested that inhomogeneities in the sample pins were the dominant factor in the irreproducibility. The most important aspect of this work was the realization that the level of quantification for compacted soils was very similar to that of bulk solid GD-MS on the VG 9000. Raw ion signals produced qualitative analysis with accuracies within four times the certified values, and the use of "book-value" relative sensitivity factors (RSFs) produced values to within a factor of 2. Finally, the use of the NIST Peruvian Soil to produce RSFs to analyze NIST 2704 Buffalo River Sediment produced better accuracy, with only As (having a mass interference) producing an error of greater than 75%.

Stuewer and coworkers [45] described the use of a GD ion source that was similar in design to the Grimm-type lamps used in GD-AES for the analysis of aluminum oxide powders on a quadrupole analyzer. Copper was chosen as the host matrix and sample-to-host ratios of 1:1–1:10 were investigated to determine the role of composition in plasma stability. A 1:5 mixture was chosen for the analytical characterization on the basis of its high temporal stability and minimal analyte dilution. Both neon and argon were used as discharge gases, as the former generally provides a background mass spectrum that poses fewer interferences for elements commonly found in oxide samples [i.e., low-mass (<40 amu) elements]. Temporal profiles of both matrix and analyte species, as well as total ion current, give strong indication of two phases of plasma stabilization, as shown in Fig. 7.2. Early in the plasma lifetime (<10 min), a high-current situation exists, in which the ion beam is dominated by molecular species as the sample is suggested to be more "oxide" in nature. A definitive second phase occurs abruptly as the total ion current drops but is now composed mainly of atomic (analyte) ions. Spectral comparisons between compacted oxide and pure metal powder samples indicated that the plasma and ion beam characteristics were not appreciably different once the plasmas had reached the stable second phase. For example, limits of detection for the oxide samples (as determined through calibration curves) were generally in the single-microgram-per-gram range, in the absence of isobaric interferences. As a result of the nature of the compacted samples, of course, greater amounts of molecular species are present in the mass spectra obtained.

Another example of the analytical utility of the sample compaction methodology for GD-MS is work by Wayne [44] that used a Kratos double-focusing analyzer for the analysis of precious metals deposited on cordierite supports (i.e., automotive catalysts). Spectral interferences from TaO species on the target palladium, rhodium, and platinum analytes made aluminum a better choice as the matrix element. Because the Kratos instrument does not have cryogenic cooling

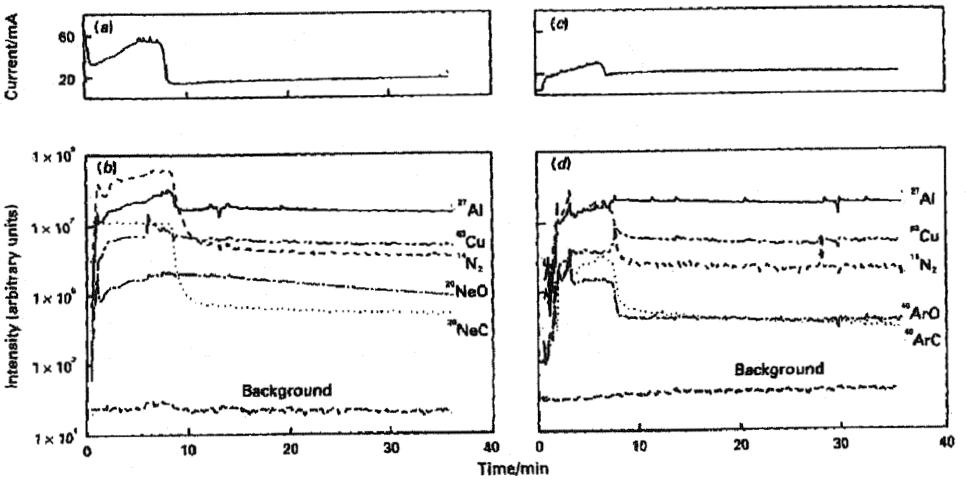

Figure 2 Total-ion (a, c) and single-ion monitoring (b, d) temporal profiles of Al_2O_3 samples compacted (1:5) in a copper matrix using Ne (a, b) and Ar (c, d) discharge gases. (From Ref. 45.)

capabilities, a 1-hour 200°C in vacuo bakeout was employed to drive off adsorbed water vapor. GD-MS is a very attractive alternative to ICP-MS in this application because of the great difficulty and cost of dissolving the cordierite sample matrix. The precision and accuracy of the methods (using Bi as an internal standard) were both found to be better than 10% RSD, quite acceptable values for the automotive industry. The increasing usage of zirconium in these catalysts poses a challenge because isotopes of zirconium oxides interfere with palladium isotopes. A mathematical model allows stripping of the oxide contributions and improvement in accuracy of palladium determinations by GD-MS.

Two related methods of nonconductive sample preparation should be mentioned here. The first, described by Battagliarin and coworkers [46], involves the use of a heated die assembly in which molten indium is added to the oxide powder sample. Continued heating and applied pressure cause the indium to flow through the interstices of the powder such that the sample (GeO_2) becomes dispersed in the metal. On cooling, the metal pin is easily removed from the die. The method produces very stable plasmas (~3% RSD) after 50-min presputtering times, and a favorable sample-to-sample reproducibility (<5% RSD). The authors state that the use of molten indium has promise as a general analytical strategy. The second method does not actually involve the sputtering of a nonconductive sample. Barshick and Harrison [47] have described the use of a 1-mJ pulse excimer laser to ablate compacted UO_2 samples into a pulsed glow discharge sustained at a copper pin electrode. In this way, the oxide material is introduced into the GD plasma,

where subsequent ionization occurs. Although there are many volatilization-related matrix effects in the laser ablation of nonconductors, this too would appear to be a general method for at least the qualitative analysis of nonconductive materials.

7.3 ANALYSIS BASED ON THE USE OF A SECONDARY CATHODE

One of the common methods of performing secondary ion mass spectrometry (SIMS) analysis of insulating samples involves the placement of a metallic electrode (grid) in contact with the sample such that the built-up charge can be removed [48,49]. Milton and Hutton extended this approach to GD-MS in an arrangement they termed a *secondary cathode* [21]. In short, a thin (0.25-mm) metal foil with a circular aperture is placed across the face of the flat sample such that when the discharge potential is applied, the secondary cathode is sputtered and the released atoms redeposit onto the exposed portion of the insulating sample surface. Westwood [50] showed many years ago that as much 50% of sputtered atoms are redeposited in low-pressure (150-mtorr) glow discharges, with higher pressures producing larger percentages. Figure 7.3 is a simple diagram of the discharge cell with

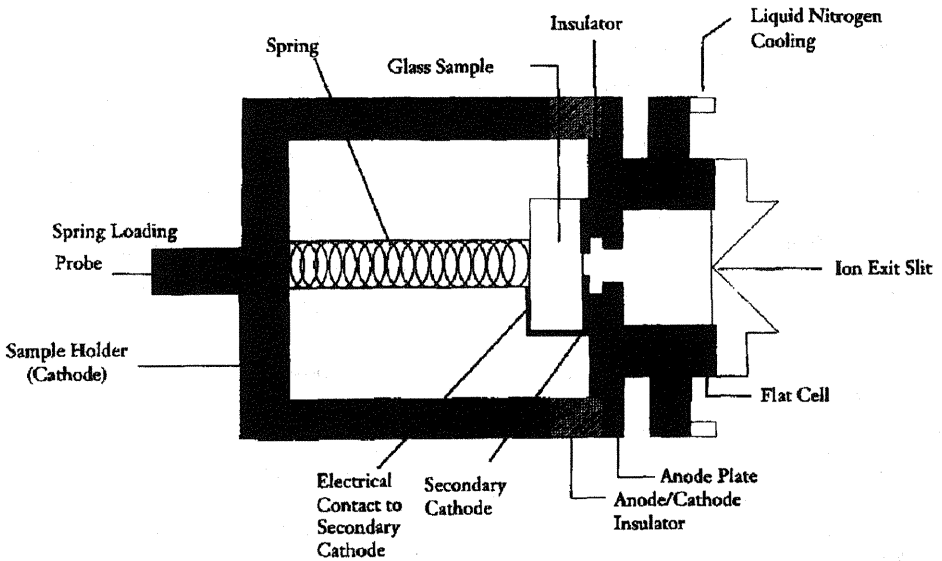

Figure 3 Schematic representation (not to scale) of the source assembly used in the *secondary cathode* approach to glow discharge mass spectrometry (GD-MS) analysis of nonconductive samples. (From Ref. 21.)

a flat sample holder and a secondary cathode. The formation of this new conductive layer on the insulating sample permits the formation of a cathode fall potential and the acceleration of discharge gas ions to the surface. On the basis of the assumption that sputtering ions will have hundreds of electron-volts of kinetic energy, incoming ions can penetrate distances of 2–10 Å [51]. So long as the metallic layer is not too thick, an incoming ion transfers momentum to the sublayer sample such that analyte atoms are sputtered into the gas phase. If the deposited layer is too thick, the incident ions do not penetrate the metallic coating, and so only the overlayer is sputtered. In this case, the resultant mass spectrum solely comprises elements making up the secondary cathode material. If the layer is too thin, a potential difference does not develop and sputtering does not occur. The plasma also tends to be unstable without complete coverage.

On the basis of the preceding discussion, it is not too difficult to imagine the parameters that are important in optimizing the secondary cathode approach to nonconductor analysis. Two groups have performed the majority of the evaluations of this method: Milton and Hutton at VG Elemental [21] and Van Grieken's group at the University of Antwerp [22–24]. It is difficult to treat the works of these groups separately as they mesh to form a very comprehensive picture of the relevant experimental factors affecting the use of this approach.

7.3.1 Role of Secondary Cathode Identity

The choice of the material from which the secondary cathode (also called the *mask* or *diaphragm*) is formed must address a few basic issues. First, the material must be available in high purity. It must be kept in mind that the cathode is continuously sputtered, and so the constituents of that material become ionized and contribute to the resultant mass spectrum. Thus, there is a definite concern about the ability to generate a clean analytical blank. Second, the matrix element should have as few isotopes as possible, preferably in mass ranges removed from target analytes. Finally, the sputter rate of the secondary cathode must be sufficiently high to form the conductive layer under typical discharge conditions, without being so high as to form too thick an overlayer.

Milton and Hutton [21] evaluated aluminum, copper, silver, indium, lead, and tantalum as possible secondary cathode materials. The first three candidates (Al, Cu, and Ag) sputtered at rates too high to allow production of ions characteristic of the glass sample (i.e., tended to produce too thick a metallic layer). Indium and lead are soft materials that lead to the overcompression of the insulator-cathode-sample sandwich, consistently resulting in electrical short-circuiting between the anode and cathode. Finally, tantalum does indeed exhibit the desirable characteristics for application as secondary cathode materials. Although not explicitly required, the fact that Ta is a getter element is likely to provide some added benefits as well.

7.3.2 Relative Sizes of the Anode Orifice and Cathode Aperture

In addition to the need to obtain a proper overlayer thickness for optimal sample sputtering, there is another consideration involving the relative amounts of ion signal derived from the sample and cathode species. In short, it is desirable to have the highest possible analyte signal intensity, while minimizing the contributions from possible contaminants in the secondary cathode. Therefore, the ratio of the analyte-to-cathode matrix ion signals is an important quantity. Both groups have evaluated the respective roles of the limiting anode diameter (which determines the total sputtering area) and the inner diameter of the secondary cathode (which determines the relative sputtering areas of the cathode and the sample). In addition to establishing stable discharges and minimizing the relative contribution of cathode species, the exposed area of the sample adds a temporal component, as large exposed areas require longer times for coverage. Conversely, very small regions tend to cover quickly to the point of forming too thick a metallic overlayer.

The "analytical" and temporal aspects of the choice of the secondary cathode geometry are summarized in Table 7.2. As seen in the table, Van Grieken and coworkers [22] found that the optimal situation is found in the case in which the anode diameter is just larger than the inner diameter of the mask (5 and 4 mm, respectively). In this instance, the "sample" signal intensity is only one fourth that obtained when the largest amount of sample is exposed, but the sample/mask ion beam ratio is eight times higher. Thus, although absolute signal intensity is sacrificed, it is more than compensated for by the reduced probability of interferences from contaminants in the mask material. This conclusion is consistent with the findings of the analogous study performed by Milton and Hutton [21]. Although there is no difference in the stability and reproducibility of the ion signals in the data tabulated here, the studies of Milton and Hutton involved a wider range of anode sizes that produced situations in which stable plasmas were not achieved.

Table 2 Glass Analysis Obtained with a Tantalum Mask

Cathode diameter	4 mm	4 mm	4 mm
Anode diameter	5 mm	7.5 mm	10 mm
Optimal discharge conditions	3 mA	3 mA	3 mA
	0.3 kV	0.4 kV	0.6 kV
Signal intensity (sample)	1E-12 A	3E-12 A	4E-12 A
Signal intensity (sample/mask)	0.16	0.08	0.02
Avg. intern. precision (%STD)	2–10%	2–10%	2–10%
Avg. extern. precision (%STD)	5–25%	5–25%	5–25%

Source: Ref. 22.

7.3.3 Role of Discharge Conditions and Sample Type

In any glow discharge device, there are complex interrelationships among the discharge voltage, current, and pressure. In the case of using a secondary cathode, these dependencies take on different meanings as the redeposition process is integral to the success of the methodology, whereas it is generally thought of as a negative attribute in other GD implementations. Simply put, these parameters must be balanced to achieve the formation of a metallic overlayer of proper thickness. Secondary issues come about from the desire to achieve rapid plasma stabilization, low amounts of signal drift, and uniform sputter-erosion in the case of depth profiling of insulators. Figure 7.4. illustrates the importance of choosing the proper discharge pressure (presented here as the pressure in the intermediate chamber between the ion source and mass analyzer) through temporal profiles of the ion signals for the case of using a tantalum mask for a glass sample [21]. At the highest pressure (curve a), extensive redeposition is evidenced by the steady decrease in Si^+ intensity over time. The lowest pressure (curve b) effects far less redeposition and so the opposite trend is seen. Finally, at a moderate pressure (curve c) the plasma is seen to reach a steady state in approximately 12 min. Source stability evaluated at this set of conditions using a NIST reference material was on the order of 6% RSD using ion beam ratios over a 150-min analysis period. Van Grieken et al. [22] also showed that variations in discharge power (voltage and current) at a single source pressure influence the extent of redeposition (via sample/mask ion beam ratios).

The group at the University of Antwerp has done extensive evaluations of the possible scope of the secondary cathode methodology [23]. The evaluations identified a number of other "electrical" dependencies. For example, the conductivity of the analytical sample influences the required voltage and current to sustain a stable discharge, and thus the interplay with source pressure to achieve a proper level of redeposition. This disparity was first evidenced in a comparison between the analysis of bulk nonconductors (glass) and compacted oxides. Although both sample forms can be grossly classified as "nonconductors", differences in absolute resistivity do affect performance. As is well known throughout the GD literature [52], the applied potential also plays a key role in the evolution of the sputtered crater. As such, there may exist trade-offs between the discharge conditions that produce the desired analyte signal qualities and those for obtaining adequate depth resolution for a given application. Finally, the surface roughness of the insulating sample has an effect on the optimal discharge conditions and equilibration times [22]. In the case of very rough samples, greater amounts of redeposition are required to fill crevices in the surface with the conductive overcoating.

7.3.4 Analytical Applications

The major advantage of using the secondary cathode method for nonconductor analysis is that the sample is analyzed directly in its native form. Because grind-

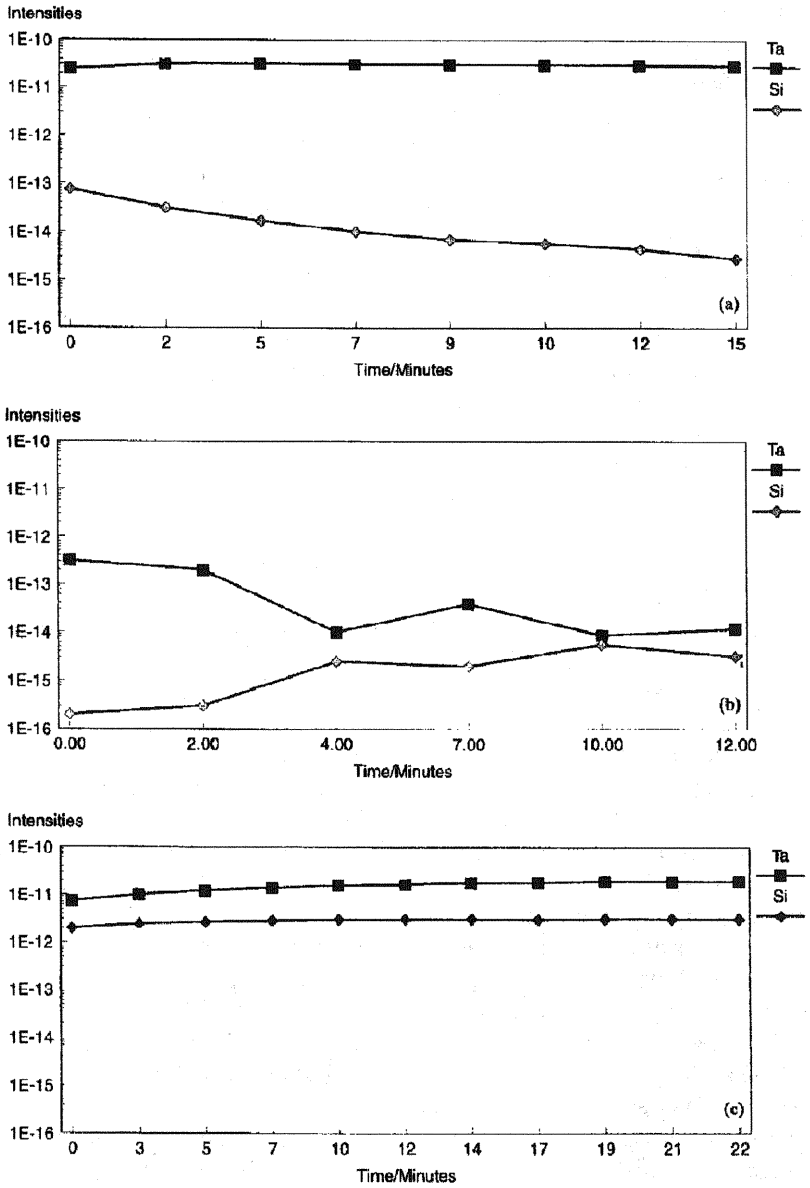

Figure 4 Temporal profiles of Ta (mask) and Si (sample) ion signals of plasmas operated under different discharge conditions: a, voltage = 1 kV, Ar pressure = 5.9×10^{-5} mbar; b, voltage = 1 kV, Ar pressure = 4.3×10^{-5} mbar; c, voltage = 1 kV, Ar pressure = $5.2 \times 10_{-5}$ mbar. Note: pressure measured in intermediate region of VG 9000 instrument. (From Ref. 21.)

ing and mixing are not part of the protocol, analysis speed, greater temporal stability, and retention of spatial information are key advantages. The applications highlighted here demonstrate these attributes and also provide a glimpse of a much higher level of analytical versatility than the sample compaction method. In addition to the glass and metal oxide samples described in the previous discussions, certain oxide and carbide materials have physical properties that simply prohibit mechanical grinding procedures. This of course makes solution-based analysis a less than attractive choice.

Glow discharge mass spectrometry is generally considered to be underutilized with regard to its inherent capabilities for isotope ratio analysis of solid materials. In fact, studies have shown that the technique can be applied to produce meaningful analytical precision and accuracy. The group of Betti and coworkers [25] has been a leader in GD-MS analysis of nuclear materials. In those instances in which nonconductive powders require analysis, direct compaction (i.e., without binder) with analysis through the use of a secondary cathode has shown to be an effective alternative to standard thermal ionization mass spectrometry (TIMS). Comparisons between the two techniques were made for the elements Li, B, Si, Zr, U, and Pu. Only in the case of Pu were the TIMS data appreciably better than the GD-MS, whereas mathematical corrections for interference from U and Am were required to produce comparable statistics to TIMS. The authors concluded that GD-MS was very competitive with thermal ionization; the former was considered to be virtually nondestructive since only very small amount (nanograms) of material are actually lost to the analysis, though the sample preparation required to isolate those materials is very time consuming and complex.

The most creative application of the secondary cathode approach was described by Schelles and Van Grieken [24], who investigated its ability to determine the elemental constituents of polymeric materials. Mass spectrometric analysis has almost exclusively been directed at the determination of molecular weights and disparity characteristics; secondary ion mass spectrometry (SIMS) [53,54] and matrix assisted laser desorption ionization (MALDI) [55,56] have carried the major share of the workload. Growing concerns over the fate of polymeric materials in the environment and the leaching of heavy metals into ground waters have necessitated the development of methods that permit the elemental analysis of bulk polymers. In addition, the use of polymers as immobilization media for waste remediation is also pressing these developments.

Schelles and Van Grieken [24] used a Ta secondary cathode for the sputtering of polytetrafluoroethylene (PTFE), polycarbonate (PC), and polyvinylchloride (PVC) sheets of 0.5- to 1.0-mm thickness. Very different from in the case of sputtering metals or oxides, the thermal energy deposited during the course of sputtering can be catastrophic for polymers that are subject to melting or even pyrolysis. This in fact was the case for PC, which melted under conditions in which the other two polymers operated stably. In general, the authors felt that practical analysis was only possible for polymers with melting points >100°C. In the case of PTFE

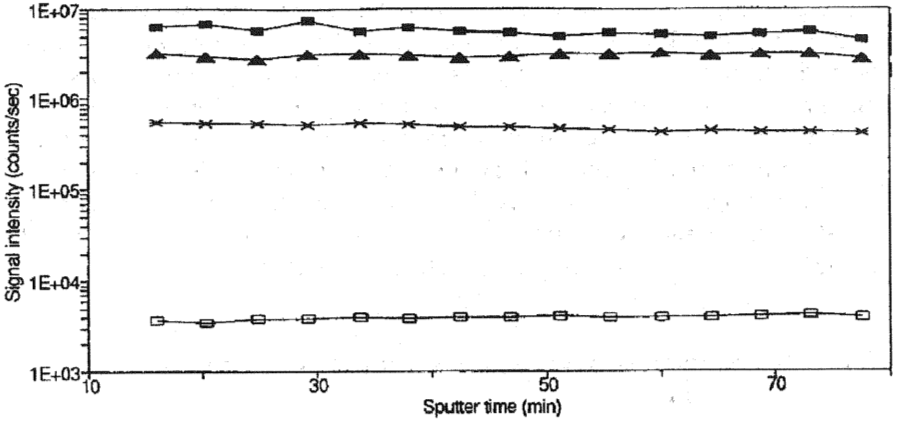

Figure 5 Temporal profile of ions produced from a polytetrafluoroethylene (PTFE) sample using a Ta secondary cathode. ■, C^+; ▲, F^+; X, CF^+; □, Fe^+. (From Ref. 24.)

and PVC, stable plasmas could be maintained for extended periods, with the spectra dominated by atomic ions rather than molecular fragments. Figure 7.5 depicts the ion signal stability achieved for a PTFE sample. The raw signal intensities were observed to vary by 3% to 20% RSD after the 15-min sputtering time. The $^{12}C^+$ signal was the base peak for each of the three polymers investigated in the study, with an average current value of 1–6 x 10^{-12} A. In general, small molecular clusters were present at levels of much less than 1% of the $^{12}C^+$ ntensity; the vast majority of the expected species appeared at far lower levels. Therefore, polyatomic ions do not provide substantive molecular information, but rather pose problems as isobaric interferences for trace elemental species. In the absence of interferents, the carbon matrix ion signal level would suggest that high part per billion limits of detection may be possible. As with the previous discussion, though, blank levels due to the mask material are a limiting factor. In any case, trace element analysis by direct current (dc) GD-MS with a secondary cathode appears to offer capabilities for polymer analyses that are not available from traditional atomic spectroscopic methods.

7.4 ANALYSIS BASED ON THE USE OF RADIO FREQUENCY POWERED SOURCES

The use of the sample compaction and secondary cathode sampling methodologies has certain positive attributes based on the initial sample form, analysis time constraints, and analytical performance criteria of a given application. A common shortcoming of both approaches is that a material other than the analytical specimen is subjected to the GD atomization/ionization processes, inflicting additional

costs, potential contamination, and a realm of additional considerations, as described in the previous sections. The use of radio frequency (rf) powering of the glow discharge plasma circumvents many of these challenges, providing a single methodology and apparatus for the analysis of both conductive and nonconductive sample types. As will be described, rf GD-MS has as its genesis the use of mass spectrometry to monitor and study plasma etching/deposition. It is interesting to note that although "analytical" rf GD-MS has been an active area of work over the last 10 years, the number of publications in this area easily outnumber all those of the other GD-MS methods for nonconductor analysis combined.

7.4.1 Fundamentals of Radio Frequency Glow Discharge Operation

The use of rf potentials (typically 13.56 MHz) to sustain low-pressure plasmas (particularly at nonconducting electrodes) is not new, as they have been used for over 30 years as sputter etching/deposition devices in the electronics industry [57]. A large number of detailed reports describe the underlying principles of analytical rf GD source operation as they are of high interest for applications in both the atomic emission and mass spectrometric sampling modes. The operation of the plasmas is easily understood when one considers a scenario of applying a high voltage to an insulating surface as depicted in Fig. 7.6 for the case of a ±1-kV square wave potential. At time zero, a large negative potential applied to the cathode surface causes breakdown of the discharge gas such that positive ions are accelerated to the electrode surface. This of course causes the negative potential to be neutral-

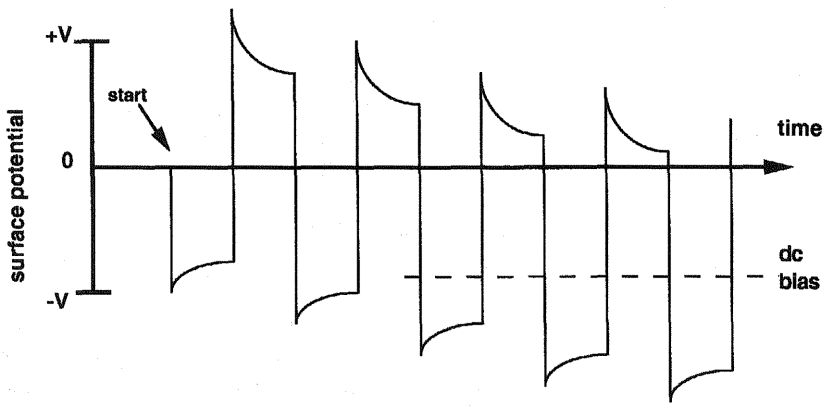

Figure 6 Response of an insulating electrode immersed in a low-pressure atmosphere to the application of a high-frequency square wave potential.

ized to some extent, until the potential swings to the positive portion of the waveform. At this point, negatively charged species (i.e., electrons) are accelerated to the cathode, effecting an opposing charge reduction. Because of their much lower mass, electrons cause the applied potential to approach 0 volt at a much higher rate than do ions in the negative potential half-cycles. This difference in charge mobility acts to displace the applied potential toward an average negative value over a number of voltage cycles. Thus the potential on the cathode surface alternates about a dc bias potential wherein there is a negative potential on the sample for >90% of the rf cycle and a positive potential for a relatively short period. The sample is therefore bombarded (sputtered) by positive ions for a majority of the time, and charge compensation by electrons occurs for the remainder of the cycle. In this way, all of the desired functions of an analytical GD source can be achieved for insulating samples and conductors.

Although rf GD-MS in spectrochemical analysis may have been underutilized to date, there is a substantial body of work regarding the fundamental traits of these plasmas that supports their use in analytical spectroscopy [58–60]. Many of these studies have dealt more generally with the use of rf sputter deposition plasmas but are important to our understanding for better source designs and applications in direct solids analysis. Because these plasmas operate on a different basic principle than the traditional dc sources, a few of the design and plasma characteristics are presented here. The establishment of the negative dc-bias potential is key to the ability to sputter the sample cathode and establish an effectively field-free region about the ion sampling orifice. Coburn and coworkers [58] have studied the role of the respective electrode sizes within the plasma in isolating sputtering to the target (i.e., the analytical sample). Very simply, the maximum dc bias is obtained when the area anode-to-cathode ratio is maximized. Therefore, it is advantageous to power a small sample housed in a relatively large-volume, grounded anode. Unlike in the case of dc GD-MS sources, the ionization processes in rf plasmas actually maximize at very different pressures than the atomization rates. In general, optimal analyte ion signals are obtained at pressures of an order of magnitude less than in the dc case (hundreds of milliTorrs vs. Torrs) [11,28–32]. The lower pressure leads to far greater spatial segregation of the plasma processes and resultant analyte ions. Therefore, ion sampling position is a key aspect in system optimization as discussed in the following sections. To a first approximation, operation of GD plasmas at lower pressures results in much higher cathode potentials, but this is not the case of the dc bias in the rf discharges. These values tend to be less than for the dc, implying that a greater fraction of the applied power is directed into the gas-phase excitation and ionization processes. Detailed Langmuir probe measurements in both process and analytical GD plasmas confirm that this is indeed the case as electron energies and temperatures are much higher in the rf discharges [59,61]. This is also true for the all-important metastable gas species that Coburn identified early on as crucial to analyte ionization in deposition plasmas [60].

7.4.2 Analytical Radio Frequency Glow Discharge Mass Spectrometry

The first real indication of the possible utility of the rf powering mode for "analytical" chemical applications was presented in a review article by Coburn and Harrison in 1981 [11]. In a way, the authors provided a bridge between two sides of a river: Coburn viewed mass spectrometry as a tool to understand fundamental processes occurring in plasma deposition sources, whereas Harrison, whose background was in spark and plasma source mass spectrometry, viewed it as a tool for spectrochemical analysis. At that time, rf GD-MS was simply a tool of physicists and engineers, but the ability to derive composition- and depth-resolved information about an insulating target was clearly presented. Soon after that publication, a single report describing the use of rf powering for a hollow cathode GD-MS source [termed an *rf cavity ion source* (CIS)] was presented by Donohue and Harrison in 1975 [62]; in it mass spectra derived from metallic, glass, and solution residue samples illustrated the possible utility of the approach. The analytical performance (i.e., spectral characteristics, sensitivity, and stability) of the source was found to be equivalent to or better than that of the much more fully developed dc powered hollow cathode sources, suggesting a great deal of promise.

Despite the possible utility demonstrated through the previously cited works, the field of rf GD-MS lay dormant for almost 15 years until a paper by Duckworth and Marcus reintroduced the concept in 1989 [26]. In that paper, the operating principles and basic design criteria for "analytical" rf GD-MS sources were presented for a simple diode source used for the analysis of 0.5-inch-diameter sample disks, including metals, solid glass, and compacted (without binder) metal oxide powders. In addition to illustrating the flexibility of the rf GD ion source, data were presented that indicated a more complex interrelationship between discharge conditions and ion extraction (sampling) position than had been seen for dc powered sources. The requirement to optimize ion sampling position and discharge conditions, along with a need for efficient sample interchange, has led to the implementation of more user-friendly designs based on ~0.5-inch-diameter direct insertion probes (DIPs) [27]. Figure 7.7 illustrates the general approaches used in rf GD-MS source design as implemented by the Clemson University laboratory. Use of DIPs provides a means of mounting the sample, providing electrical contact, position optimization, and introduction through a vacuum interlock. All subsequent rf GD-MS sources have employed some sort of DIP approach. On the basis of the diameter of the probe, implementing sample holders for pin-shape and small disk samples is relatively straightforward (Fig. 7.7a). A number of groups have described such designs. All of these designs are somewhat different in respect to the ion volume and spectrometer geometries (as well as investigators' preferences); however, the optimization of discharge and sampling positions are remarkably similar.

Given the wide diversity of solid sample forms and the particular difficulty of machining oxide (e.g., glass and ceramic) samples to a fixed form, rf GD ion

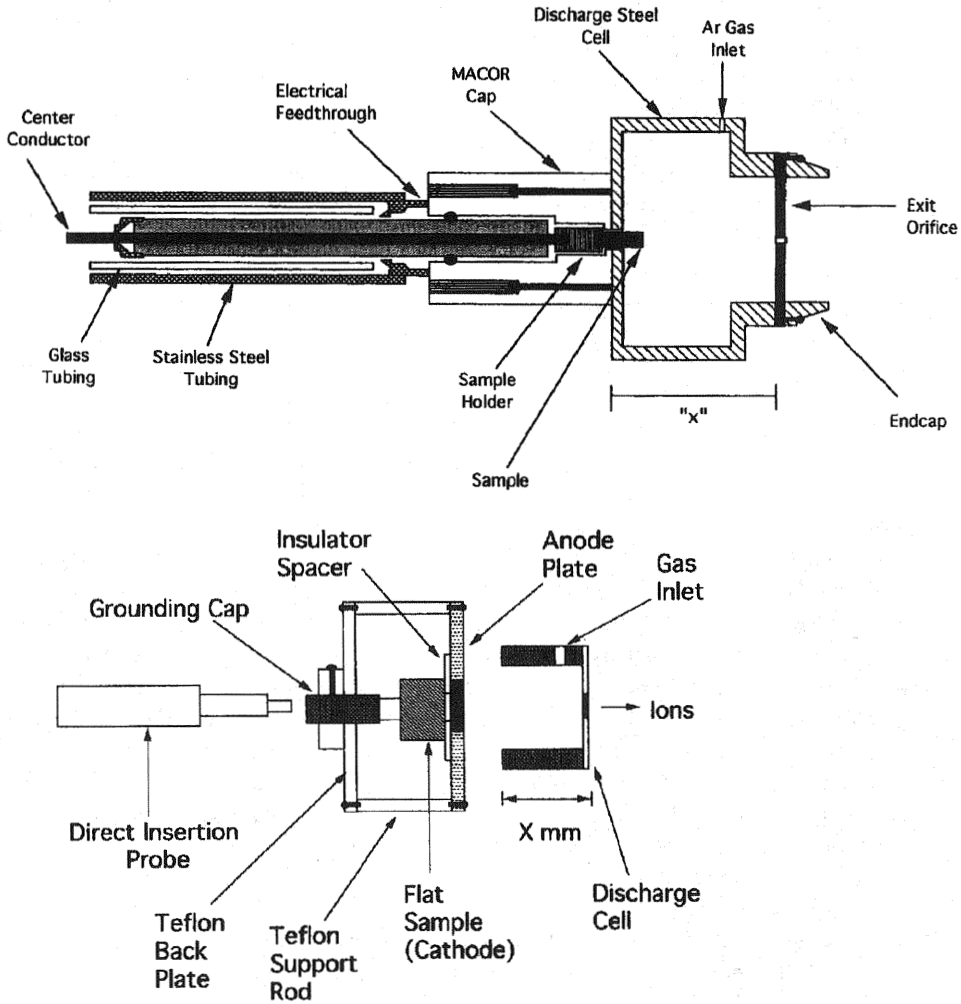

Figure 7 Radio frequency glow discharge mass spectrometry (rf GD-MS) source designs employed on a VG GloQuad instrument for the analysis of: a, Pin-type samples. (From Ref. 28.) b, Flat samples. (From Ref. 29.)

sources that allow for the analysis of flat, disk-type samples have been developed for mounting on the end of DIP devices (Fig. 7.7b). As in the case of the pin-type sources, detailed consideration of the interplay between discharge conditions and ion extraction geometries is key to these developments. The analysis of disk samples is accomplished with either suitable mounts on the end of a DIP or a probe that engages the sample against an ion volume anode to create an obstructed discharge geometry (in much the same manner as in the commercial GD-MS flat-cell

sources). In a number of implementations of this geometry, authors use the phrase *Grimm-type* geometry by analogy to the common GD-AES source. Although the Grimm-type discharge does indeed employ an obstructed electrode arrangement, most GD-MS sources are not truly of this geometry as auxiliary pumping between the cathode and anode is not employed as in the AES case.

In concluding the discussion of rf GD-MS source geometries, the number of works involving the use of magnetic plasma enhancement methods cannot be ignored [63–66]. These "magnetron" arrangements have their roots firmly grounded in the plasma deposition science and engineering literature [57]. Magnetron GD sources generally employ concentric permanent magnets (>100-G field strength) located behind the cathode/target and thus not exposed to the plasma. Magnetic fields permeate the cathode and trap plasma electrons in helical orbits close to the surface, decreasing the atom-electron mean free paths and thus increasing the overall plasma ionization efficiencies. As a result, magnetron enhanced GD sources can operate at two to three orders of magnitude lower pressures than standard rf GD ion sources (single vs. hundreds of millitorrs). This greatly reduces the entire system vacuum pumping requirements. Lower operating pressures would seem to hold the promise of lower amounts of molecular ion species in the spectra and perhaps higher ion signal fluxes as larger differential pumping apertures could be employed.

Interestingly, the groups describing the use of magnetron rf GD-MS sources each used different mass analyzer systems: Hecq and coworkers [63,64], a quadrupole mass filter; Saprykin et al. [65], a double-focusing instrument; and Hieftje and coworkers [66], a time-of-flight (TOF) spectrometer. Each group indeed found that lower source pressures could be utilized than in "normal" rf powering, though only Saprykin [65] reported obviously lower levels of polyatomic ion contributions. Hieftje [66] compared molecular and discharge gas ion ratios to those of analyte elements, with and without magnetic coupling. Lower amounts of molecular species were eventually attributed to differences in ion sampling position, with the magnetron producing Ar/Cu ratios that were 15–20 times higher than in the "normal" rf source operation. Although magnetron use was proposed as a means to reduce the deleterious effects of nonconductive sample thickness by virtue of enhanced plasma density, differences in magnetic field strength permeating through to the sample surface (even for conductive samples) add yet another sample-dependent variable to complicate quantification.

In addition to the differences in magnetic coupling described, two other limitations hinder the use of magnetron geometries: (1) the sample must be in a disk form and (2) the sputtered crater is a circular "track" rather than a flat surface. Saprykin [65] presents profilometer tracings of "normal" and magnetron craters that illustrate that although the sputtering rate is higher with magnetic coupling, the ability to perform depth profiling is greatly compromised. Another aspect of the circular sputtering track was indirectly addressed by Hecq and coworkers [64], who sampled ions in the normal axial (end-on) and radial (side-on) directions. Very

simply, the inhomogeneous magnetron plasma requires greater spatial selectivity than the more diffuse plasma produced in the "normal" powering mode.

7.4.3 Analytical Applications

The major driving force for the development of rf-powered GD-MS sources is of course the broad diversity of possible analytical samples to which the devices may be applied. It should be noted at the outset that a number of the cited works have shown that the performance characteristics of the sources are equal to or better than that of dc GD-MS for metallic, conductive samples. In the discussion that follows, the use of rf GD-MS is highlighted for the analysis of bulk insulators, oxide powders, and polymeric materials.

The analysis of bulk nonconductive materials by rf GD-MS has been undertaken with greater emphasis on source development and characterization than on pure quantitative analysis within specific analytical systems. For the most part, studies by Marcus and coworkers have demonstrated general analytical figures of merit that could be attained for given source geometries on commercial GD-MS systems [28–30,33]. As such, the results are something of benchmarks relative to dc source operation, but for the case of nonconductive samples in rf powering. Throughout these studies, a few general observations can be made; they are for the most part consistent throughout the rf GD-MS literature cited in this section. These traits include (1) lower operating pressures relative to those of dc powered systems (hundreds of milliTorrs vs. Torrs), (2) high degree of signal and spectral responsivity to changes in discharge conditions and ion sampling position, (3) faster plasma stabilization times for metals relative to dc discharges (single minutes versus tens of minutes), and (4) an inverse relationship between nonconductive sample thickness and ion signal intensities. The latter factor would be expected to provide severe limitations to quantification. Although these limitations have been successfully addressed in this laboratory [29], it is still true that absolute sensitivity is sacrificed as thicker samples are analyzed.

Many of the primary analytical characteristics of rf GD-MS analyses of flat glass samples are demonstrated in the data presented in Table 7.3 [29]. These data were obtained for NIST 610 Trace Elements in Glass samples that are in the form of 1-mm-thick, 10-mm-diameter disks analyzed on a VG GloQuad (Winsford, Cheshire, UK) spectrometer system equipped with a flat sample holder cell. In general, the ion signals for the analyte elements of these samples stabilize to better than 7% RSD in <20 min, whereas the $^{16}O^+$ signals take as much as 50 min to reach a steady state. The data presented in Table 7.3 illustrate the stability of the elemental ion signals (ratioed to the $^{28}Si^+$ internal standard) over what would be considered a typical 45-min analysis time. Interestingly, only the $^{56}Fe^+$ signal shows a variation over 2.5 RSD. It is expected that this value is elevated as a result of the presence of the isobaric ArO^+ species. Si-referenced RSFs produce elemental concentration accuracies of less than 6% error, except in the case of Fe. The pooled

Table 3 rf-GDMS Analysis of NIST 610 Trace Elements in Glass Standard

			Internal (n = 3)			External (n = 5)		
	Cert. value	RSF	Avg. conc.	%RSD	%Err.	Avg. conc.	%RSD	%Err.
O	50.37%	2.43	50.39	1.5	1.9	52.10	11.3	1.4
Na	5.19	0.658	5.19	0.4	0.1	4.78	13.6	7.9
Al	0.53	0.273	0.55	2.0	3.4	0.52	10.4	2.4
Si	33.66	1.00	33.99	0.4	1.0	32.99	4.9	2.0
Ca	8.58	0.00443	9.07	1.0	5.7	8.95	2.9	4.3
Ti	437 ppm	0.00625	453	0.1	3.7	431	4.7	1.3
Mn	485	1.29	492	0.3	1.5	497	2.7	2.5
Fe	458	0.00262	555	6.6	21.3	546	14.2	19.2
Co	390	1.25	394	0.6	1.1	398	3.2	2.0
Ni	459	0.0971	469	0.7	2.3	466	6.4	1.5
Zn	433	0.168	418	1.2	3.4	408	5.8	5.9
Rb	426	1.28	440	0.9	3.4	435	2.5	2.2
Sr	516	2.08	531	0.7	3.0	517	4.9	0.3
Ag	254	2.54	262	1.8	3.2	243	5.7	4.5
Ce	450	6.68	457	0.7	1.5	437	6.3	3.0
Eu	450	4.21	433	1.3	3.8	434	3.1	3.5
Au	25	1.72	24	0.3	2.2	23	10.6	8.0
Tl	61.8	9.34	65	1.7	5.8	59	10.9	4.5
Pb	426	6.92	429	1.2	0.7	415	6.8	2.7
Th	457.2	51.42	447	2.3	2.3	423	8.9	7.6
U	461.5	66.59	447	1.4	3.1	427	8.3	7.4

Discharge conditions: rf power = 35W, Ar flow rate = 2.00 sccm; orifice diamter = 10 mm; cell = 10 mm.
Source: Ref. 29.

data reflecting the external reproducibility represent five complete analysis cycles with the sample exposed to atmosphere, reintroduced, and sputter-equilibrated for 60 min. In this case, the previously determined RSFs are shown to compensate effectively for differences in sample surface and plasma discharge conditions. The repeatability values presented here are very good and do not differ significantly from those achieved in conventional dc GD-MS analysis of alloys using this instrument. By the same token, limits of detection obtained for trace elements in glass matrix materials are not appreciably different than those for alloys. As an example of this characteristic, Fig. 7.8 depicts the mass spectrum obtained for the lead isotopes present in an NIST 612 Trace Elements in Glass sample generated by a flat-type rf GD-MS source mounted on a VG9000 (Winsford, Cheshire, UK) magnetic sector mass spectrometer. On the basis of the observed signal-to-noise characteristics, the detection limit for the ^{204}Pb isotope (504 ppb in sample) is calcu-

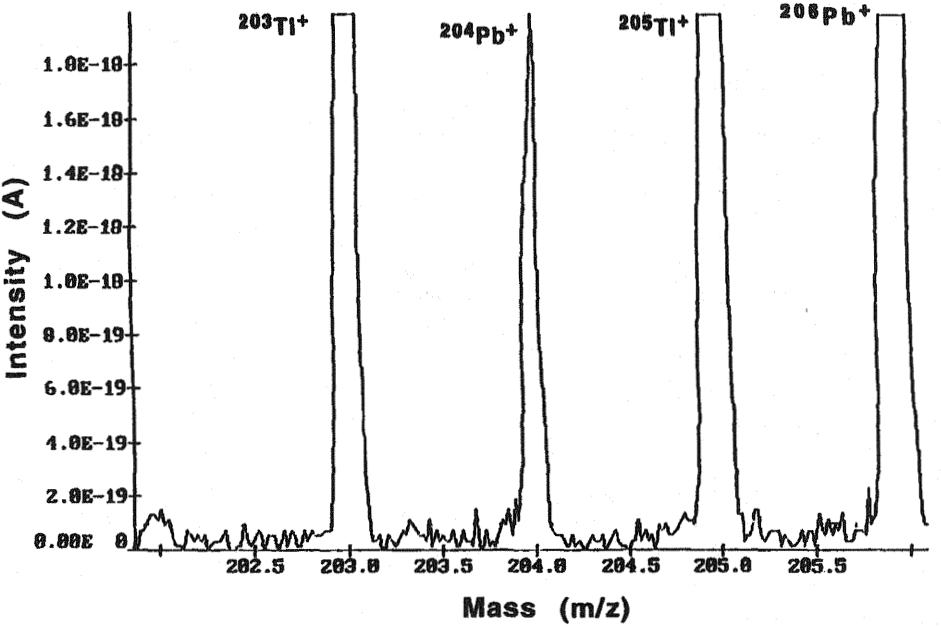

Figure 8 Radio frequency glow discharge mass spectrometry (rf GD-MS) spectrum of the lead components in an NIST 612 Trace Elements in Glass sample; ^{204}Pb concentration, 540 ppb. (From D. C. Duckworth, unpublished results.)

lated to be 16 ppb. This value is very competitive with that achieved in metals analysis under similar acquisition conditions using dc power. Finally, Gibeau and Marcus [67] have shown that the resultant crater shapes produced in the rf sputtering of ceramic materials do not differ appreciably from those of metals, suggesting a number of opportunities in depth profile analyses (albeit at much slower rates).

The analysis of nonconductive (usually oxide) powder samples touches a very diverse set of industrial applications ranging from geological specimens to precious metal containing automotive catalysts. As would be expected from the detailed discussions in Sec. 7.2, the analysis of powders is a great analytical challenge. In fact, the analysis of samples originating in powder form does not benefit to the extent that one might expect from rf powering; the reason is straightforward. Although the use of rf powering permits the analysis of pressed oxide materials without the need for a conductive metal binder (as required for dc GD operation), the much discussed benefits of the use of "gettering" binders is lost. Thus, the mass spectra of directly compacted samples are inherently complicated as a result of adventitious water and trapped gases in the pressing process. In this case, direct comparison with the use of dc powering for getter-bound compacted samples is a reasonable endeavor.

Harrison and coworkers have described in a pair of publications the evaluation of operating characteristics of the rf GD-MS of oxide powders [31] and the comparison of this "direct" method to the use of metal binders for conventional GD-MS analysis [32]. As mentioned, direct compaction of geological materials in this case produces very complex mass spectra consisting of a large range of molecular species related to water and trapped gases. This situation was remedied to a very large extent with the use of a liquid nitrogen cold finger in the plasma region for periods of greater than 30 min prior to mass analysis [31]. The same profound improvement (70%–100% reduction in gaseous ions) was found as well for bulk nonconductors such as Macor. A detailed evaluation of the roles of discharge power and pressure and ion sampling distance on the signal responses of analyte, residual gas, and argon-related species provided very interesting and useful insights into plasma processes and methods of optimizing spectral responses [31]. Although sets of discharge conditions that provide very good sensitivity and high S/N ratios are readily identified, the sensitivity to variations in conditions is quite profound and can cause difficulties. Relative sensitivity factors were compared for a number of analytes and oxide materials, with the span of values for most elements fairly well defined and not out of line with literature values. In fact, semiquantitative analysis, based on simple ion beam ratios, was within a factor of 2 for a firebrick standard. The rf GD-MS of directly compacted oxides produced very stable plasmas (<5% RSD for 1 hr), which are advantageous for quantitative determinations. It should be pointed out that these results are quite comparable to those of Pan and Marcus [68], who evaluated the use of rf GD-AES in the analysis of glass powder samples.

The comparison of rf and dc powering by Harrison and coworkers [32] was carried out at a number of different levels. An NIST iron standard was first used to evaluate the relative characteristics for conducting samples. Discharge conditions that produced similar levels of analyte ion signals were employed for rf and dc, though admittedly these conditions were a compromise relative to the optimum for rf signal intensities. Even so, very few analytical differences existed for the two powering schemes, including relative sensitivity factors, stability (<5% RSD), and sample-to-sample reproducibility (<20%). Interestingly, the rf plasma produced much higher levels of residual water signals than the dc plasma in the case in which cryogenic cooling was not utilized. (This is of no analytical consequence, as cooling is now the norm in all GD-MS analyses.) Trade-offs between conditions yielding high R values ($R = M^+/(M^+ + MO^+)$) and ion signal intensities were seen for the pure La_2O_3 model oxide, with high La^+ signals and R values of ~90% produced for a finite set of compromise conditions. As seen in the earlier study [31], these values were sensitive to changes in plasma and sampling conditions. Comparison of the rf and dc discharges was made for nonconductor analysis using Ag as a very weak getter matrix and again discharge conditions that yielded similar La^+ signals. A relatively low rf power of 8 W was employed as higher powers produced sputtering conditions that tended to clog the sampling orifice. Under such conditions,

the *R* value from dc powering was 98% vs. 75% for the rf. Operation of the rf discharge at higher powers was projected to produce more comparable values. Analysis of a mixture of rare earth elements (REEs) indicated that the degree of atomic ion production was again very sensitive to sampling conditions (i.e., position, pressure/power) in the case of rf, and not so much so for the dc case. In fact, *R* values between the REEs varied with rf conditions, but not for dc, seemingly depending on the M-O bond strengths. Relative sensitivity factors for the rf and dc plasmas were found not to be appreciably different under controlled conditions, as the rf source showed very good stability (~5% RSD) and reproducibility (<15% RSD).

As described in Sec. 7.3, which dealt with the use of the secondary cathode methodology, one of the unexpected areas in which GD-MS may be applied (so long as the sample can be analyzed intact) is the direct analysis of polymeric materials. A simple method providing elemental, end-group, or molecular weight information could have impact in a number of industrial situations. Coburn and coworkers actually reported the production of molecular fragment mass spectra of fluoro- and hydrocarbon polymers by rf GD-MS [69]. Twenty years later, Marcus and coworkers noted a number of unexpected spectral features in the analysis of small glass samples mounted to the DIP via double-sided adhesive tape. On further study, it was shown that these species were in fact representative of the composition of the tape. This observation has opened up an entirely new line of study in the use of rf GD-MS as a tool that provides high-sensitivity determinations of polymer composition.

The first studies by this group involved an evaluation of discharge parameters and their respective roles in the structure and intensity of mass spectra derived from PTFE-based polymers [70]. The spectra were found to be nearly identical to those obtained by SIMS, as shown in Fig. 7.9, but with ion beam currents that were six orders of magnitude more intense (10^{-9} vs. 10^{-15} A). The polymer fragment ion currents are in fact similar to those obtained in metals analysis by rf GD-MS. Plasma stabilization times of less than 5 min were easily achieved, making the analysis very competitive with SIMS. In contrast to those in the work of Schelles and Van Grieken [24], the spectra were rich with molecular fragments as opposed to mainly atomic ions, with the CF_3^+ fragment in the rf spectrum ~1000 times more intense than the C^+ in the dc case. Discharge power was not seen dramatically to change the spectral character, only the ion signal levels. On the other hand, changes in discharge gas pressure, and more correctly the subsequent changes in dc bias, cause substantial variations in the spectral character. Specifically, high Ar pressures (i.e., lower dc-bias values) are less effective in liberating polyatomic species, and so the spectra tend to be more atomic in nature. A depth profile of a metallic layer on a polymer substrate was presented to demonstrate applications such as the analysis of printed circuit boards.

Two additional studies have focused on the area of polymer analysis by rf GD-MS. The problem of sample melting was addressed through the design of a cryogenically cooled sample holder [71]. Just as in the case of Schelles and Van

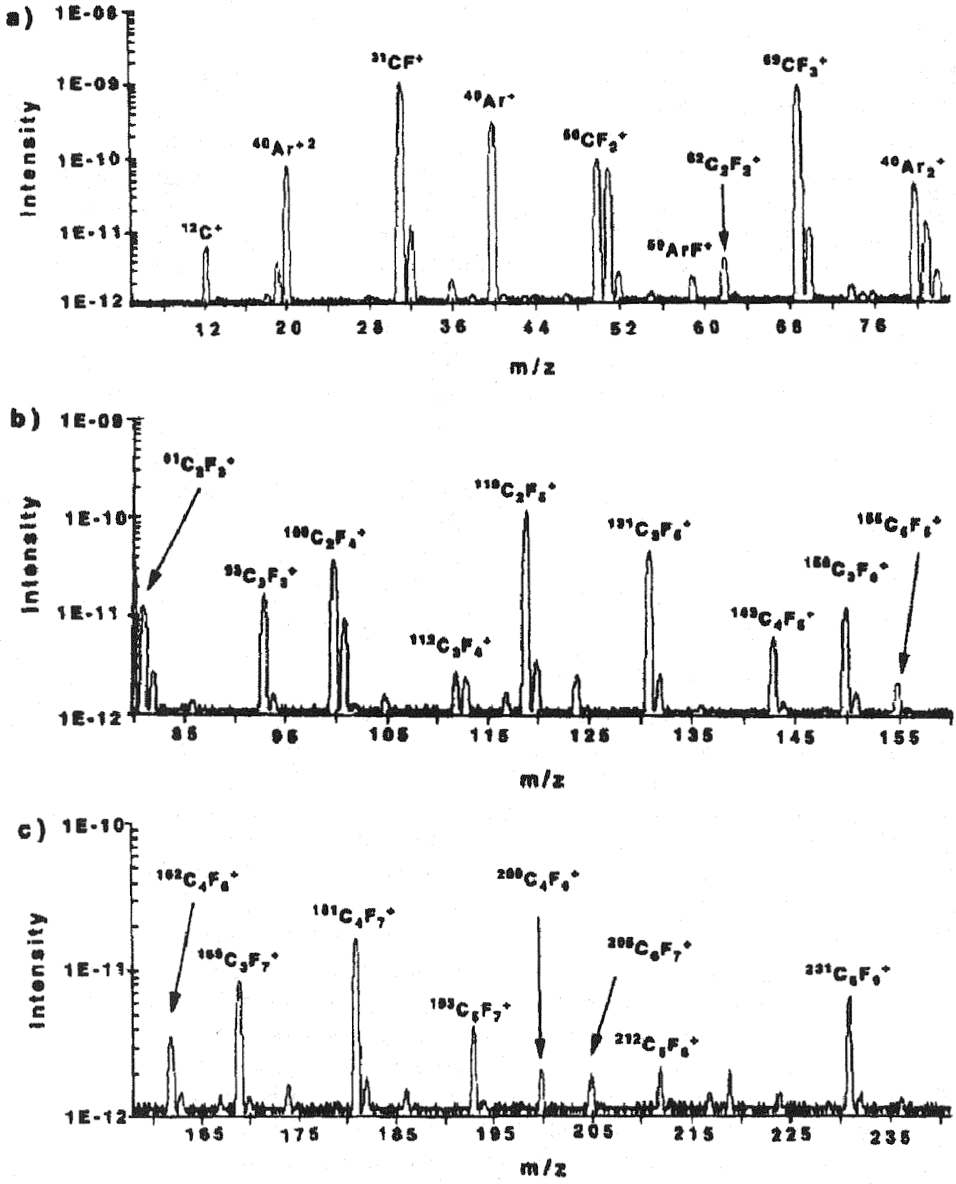

Figure 9 Radio frequency glow discharge mass spectrometry (rf GD-MS) spectrum of a 1.5-mm-thick polytetrafluoroethylene (PTFE) sample (rf power = 20 W, Ar pressure = 0.075 mbar, logarithmic units of ion signal current). (From Ref. 70.)

Grieken, low-melting-point (<100°C) polymers such as polycarbonate decompose readily, even under relatively mild GD sputtering conditions. Marcus and coworkers used a simple plumbing modification of a VG GloQuad system to use the same LN_2 supply for both sample cooling and normal cryocooling of the discharge cell volume. This modification not only allowed effective analysis of low melting point polymers, but also yielded greater temporal stability for all polymer analyses. This assembly has recently been used in a study that has shown that rf GD-MS can be applied to differentiate isomeric fluoro- and hydrocarbon polymers [72]. Ratios of characteristic fragment ion signals were found to be very reproducible and unique for each of the polymers examined. As such, ion ratios in the fingerprint region of the mass spectra can be effectively employed to distinguish polymers of the same (or related) chemical formula. This capability addresses a major point of interest in many industrial laboratories; when coupled with rapid, depth resolved analyses, presents a bright future for rf GD-MS.

7.5 CONCLUSIONS

The power of glow discharge mass spectrometry (GD-MS) in the area of ultratrace analysis of specialty metals and semiconductors is unquestioned. The technique also offers some very positive attributes in the analysis of nonconductive materials such as glasses, ceramics, soils, and polymers. The possible impact of successful analytical developments is immense as it is these sample types that are the most difficult to place into solution. In fact, it is only with new capabilities in these areas that GD-MS will see growth in its user base. The three methods described here all have strengths and weaknesses with regard to sample form, sample preparation complexity, analysis time, analytical figures of merit, and information content. It is hoped that this review has put many of these attributes in a context that will allow persons faced with the challenges of such to make decisions appropriate to their problems at hand.

ACKNOWLEDGMENT

Financial support from the National Science Foundation for work in the Clemson University laboratory is gratefully acknowledged.

REFERENCES

1. Alkemade, C. T. J.; Herrmann, R. Fundamental of Analytical Flame Spectroscopy. Halsted Press: New York, 1979.
2. Koirtyohann, S. R.; Kaiser, M. L. *Anal. Chem.* ***1982***, *54*, 1115A.

3. Fassel, V. A.; Kniseley, R. N. *Anal. Chem.* ***1974***, *46*, 1110A.
4. Houk, R. S. *Anal. Chem.* ***1986***, *58*, 97A.
5. Olesik, J. W. *Anal. Chem.* ***1991***, *63*, 12A.
6. Ahrens, L. H.; Taylor, S. R. Spectrochemical Analysis. Addison-Wesley: Reading, MA, 1961.
7. Sheeline, A. *Prog. Anal. At. Spectrosc.* ***1984***, *7*, 21.
8. Bacon, J. R.; Ure, A. M. *Analyst* ***1984***, *109*, 1229.
9. Boumans, P. W. J. M. Theory of Spectrochemical Excitation. Hilger and Watts: London, 1966.
10. Price, W. J. *Spectrochim. Acta* ***1954***, *6*, 26.
11. Coburn, J. W.; Harrison, W. W. *Appl. Spec. Rev.* ***1981***, *17*, 95.
12. Hess, K. R.; Marcus, R. K., King, F. L., Jr.; Harrison, W. W. *Anal. Chem.* ***1986***, *58*, 341A.
13. Harrison, W. W.; Barshick, C. M.; Klingler, J. A.; Ratliff, P. H.; Mei, Y. *Anal. Chem.* ***1990***, *60*, 943A.
14. King, F. L.; Harrison, W. W. in Glow Discharge Spectroscopies, Marcus, R. K., Ed. Plenum, New York, 1993; Chapter 5.
15. Broekaert, J. A. C. in Glow Discharge Spectroscopies, Marcus, R. K., Ed. Plenum, New York, 1993; Chapter 4.
16. Hocquaux, H. in Glow Discharge Spectroscopies, Marcus, R. K., Ed. Plenum: New York, 1993; Chapter 8.
17. Bengtson, A. *Spectrochim. Acta* ***1994***, *49B*, 411.
18. Dogan, M; Laqua, K.; Massman, H. *Spectrochim. Acta* ***1972***, *27B*, 65.
19. El Alfy, S.; Laqua, K.; Massman, H. Z. *Anal. Chem.* ***1973***, *263*, 1.
20. Caroli, S.; Alimonti, A.; Zimmer, K. *Spectrochim. Acta* ***1985***, *38B*, 625.
21. Milton, D. M. P.; Hutton, R. C. *Spectrochim. Acta* ***1993***, *48B*, 39.
22. Van Grieken, R.; Schelles, W.; De Gendt, S.; Muller, V. *Appl. Spectrosc.* ***1995***, *49*, 939.
23. Van Grieken, R.; Schelles, W.; De Gendt, S.; Maes, K. *Fresenius J. Anal. Chem.* ***1996***, *355*, 858.
24. Schelles, W.; Van Grieken, R. *Anal. Chem.* ***1997***, *69*, 2931.
25. Betti, M.; Rasmussen, G.; Koch, L. *Fresenius J. Anal. Chem.* ***1996***, *355*, 808.
26. Duckworth, D. C.; Marcus, R. K. *Anal. Chem.* ***1989***, *61*, 1879.
27. Duckworth, D. C.; Marcus, R. K. *J. Anal. At. Spectrom.* ***1992***, *7*, 711.
28. Marcus, R. K.; Shick, C. R., Jr.; Raith, A. *J. Anal. At. Spectrosc.* ***1994***, *9*, 1045.
29. Marcus, R. K.; Shick, C. R., Jr. *Appl. Spectrosc.* ***1996***, *50*, 454.
30. Marcus, R. K. *J. Anal. At. Spectrom.* ***1994***, *9*, 1029.
31. De Gendt, S.; Van Grieken, R. E.; Ohorodnik, S. K.; Harrison, W. W. *Anal. Chem.* ***1995***, *67*, 1026.
32. Harrison, W. W.; De Gendt, S.; Van Grieken, R. E.; Hang, W. *J. Anal. At. Spectrom.* ***1995***, *10*, 689.
33. Marcus, R. K.; Duckworth, D. C.; Donohue, D. L.; Smith, D. L.; Lewis, T. A. *Anal. Chem.* ***1993***, *65*, 2478.
34. Saprykin, A. I.; Becker, J. S.; Dietze, H.-J. *J. Anal. At. Spectrom.* ***1995***, *10*, 897.
35. Saprykin, A. I.; Becker, J. S.; Dietze, H.-J. *Fresenius J. Anal. Chem.* ***1995***, *353*, 570.
36. Winchester, M. R.; Duckworth, D. C.; Marcus, R. K. in Glow Discharge Spectroscopies, Marcus, R. K., Ed. Plenum: New York, 1993; Chapter 7.
37. Loving, T. J.; Harrison, W. W. *Anal. Chem.* ***1983***, *54*, 1523.

38. Marcus, R. K.; King, F. L., Jr.; Harrison, W. W. *Anal. Chem.* ***1986***, *58*, 972.
39. Tong, S. L.; Harrison, W. W. *Spectrochim. Acta* ***1993***, *48B*, 1237.
40. Mei, Y.; Harrison, W. W. *Anal. Chem.* ***1993***, *65*, 3337.
41. Mei, Y.; Harrison, W. W. *Spectrochim. Acta* ***1991***, *46B*, 175.
42. Smith, D. H.; Teng, J.; Barshick, C. M.; Duckworth, D. C.; Morton, S. J.; King, F. L. *Appl. Spectrosc.* ***1995***, *49*, 1361.
43. Smith, D. H.; Duckworth, D. C.; Barshick, C. M. *J. Anal. At. Spectrom.* ***1993***, *8*, 875.
44. Wayne, D. M. *J. Anal. At. Spectrom.* ***1997***, *12*, 1195.
45. Stuewer, D. J.; Woo, J. C.; Jakubowski, N. *Anal. At. Spectrom.* ***1993***, *8*, 881.
46. Battagliarin, M.; Sentimenti, E.; Scattolin, R. *Spectrochim. Acta* ***1995***, *50B*, 1995.
47. Barshick, C. M.; Harrison, W. W. *Mikrochim. Acta [Wein]* ***1989***, *111*, 169.
48. Werner, H. W.; Morgan, A. E. *J. Appl. Phys.* ***1976***, *47*, 1232.
49. Jede, R.; Ganschow, O.; Kaiser, U. in Practical Surface Analysis, Briggs, D., Seah, M. P., Eds. John Wiley & Sons: New York, 1992; Chapter 8.
50. Westwood, D. *Prog. Surf. Sci.* ***1976***, *7*, 71.
51. Harrison, W. W.; Bentz, B. L. *Prog. Anal. Spectrosc.* ***1988***, *11*, 62.
52. Van Straaten, M.; Vertes, A.; Gijbels, R. *Spectrochim. Acta* ***1991***, *46B*, 283.
53. Benninghoven, A.; Jaspers, D.; Sichtermann, W. *Appl. Phys.* ***1976***, *11*, 35.
54. Reichlmaier, S.; Hammond, J. S.; Hearn, M. J.; Briggs, D. *Surf. Interface Anal.* ***1994***, *21*, 739.
55. Danis, P. O.; Karr, D. E. *Org. Mass Spectrom.* ***1993***, *28*, 923.
56. Larsen, B. S.; Simonsick, W. J., Jr.; McEwen, C. *J. Am. Soc. Mass Spectrom.* ***1996***, *7*, 287.
57. Chapman, B. Glow Discharge Processes. John Wiley & Sons: New York, 1980.
58. Coburn, J. W.; Kohler, K.; Horne, D. E.; Kay, E.; Keller, J. H. *J. Appl. Phys.* ***1985***, *57*, 59.
59. Paranjpe, A. P.; McVittie, J. P.; Self, S. A. *J. Appl. Phys.* ***1990***, *67*, 6718.
60. Coburn, J. W.; Kay, E. *Appl. Phys. Lett.* ***1971***, *18*, 435.
61. Christopher, S. J.; Ye, Y.; Marcus, R. K. *Spectrochim. Acta* ***1997***, *52B*, 1627.
62. Donohue, D. L.; Harrison, W. W. *Anal. Chem.* ***1975***, *47*, 1528.
63. Hecq, M.; Molle, C.; Springel, S.; Wautelet, M.; Dauchot, J.-P. *Appl. Spectrosc.* ***1995***, *49*, 872.
64. Hecq, M.; Molle, C.; Wautelet, M.; Dauchot, J.-P. *J. Anal. At. Spectrom.* ***1995***, *10*, 1039.
65. Saprykin, Anal. Chem.. I.; Becker, J. S.; Dietze, H.-J. *Fresenius J. Anal. Chem.* ***1996***, *355*, 831.
66. Heintz, M. J.; Myers, D. P.; Mahoney, P. P.; Li, G.; Hieftje, G. M. *Appl. Spectrosc.* ***1995***, *49*, 945.
67. Gibeau, T. E.; Marcus, R. K. *J. Anal. At. Spectrom.*, ***1998***, *13*, 1303.
68. Pan, X.; Marcus, R. K. *Mikrochim. Acta* ***1998***, *129*, 239.
69. Coburn, J. W.; Eckstein, E. W.; Kay, E. *J. Vac. Sci. Technol.* ***1975***, *12*, 151.
70. Shick, C. R., Jr.; DePalma, P. A., Jr.; Marcus, R. K. *Anal. Chem.* ***1996***, *68*, 2113.
71. Gibeau, T. E.; Hartenstein, M. L.; Marcus, R. K. *J. Am. Soc. Mass Spectrom.* ***1997***, *8*, 1214.
72. Jones, M.; Marcus, R. K., *J. Am. Soc. Mass. Spectrom.*, submitted for publication.

8

Multiple-Collector Inductively Coupled Plasma Mass Spectrometry

Alex N. Halliday
ETH Zentrum
Zürich, Switzerland

John N. Christensen, Der-Chuen Lee, Chris M. Hall, and Xiaozhong Luo
University of Michigan
Ann Arbor, Michigan

Mark Rehkämper
Universitaet Muenster
Muenster, Germany

8.1 INTRODUCTION

Within the past 10 years inductively coupled plasma mass spectrometry (ICP-MS) has engendered more effort and excitement within academia and industry than any other area of inorganic mass spectrometry. A few years ago the first papers describing preliminary results from a new kind of double-focusing ICP-MS that incorporates simultaneous measurement with multiple Faraday detectors were published (Walder and Freedman, 1992; Walder et al., 1993a,b). With a prototype instrument, these authors demonstrated that they could accurately measure the isotopic compositions of Sr, Nd, Hf, Pb, and U with the high precision and reproducibility characteristic of thermal ionization mass spectrometry (TIMS), but by nebulizing a solution. The sensitivity (ions detected per atoms utilized) was better than that achievable by TIMS for elements such as Hf, with very high first ionization potential, but comparable or somewhat inferior for other elements. The ease

with which the data could be acquired was remarkable. The same team then went on to demonstrate that they could also determine Pb isotopic compositions at high precision in situ with a laser (Walder et al., 1993c).

Although this instrument was originally marketed in terms of the ease of acquisition with which it could provide isotopic compositions of elements that were already being studied with TIMS and secondary ionization mass spectrometry (SIMS), it quickly became apparent that it was capable of measuring the isotopic compositions of elements that had hitherto proved intractable, as well as providing a new way of measuring in situ at unprecedented precision (Christensen et al., 1995; Halliday et al., 1995, 1997; Lee and Halliday, 1995a; Yi et al., 1995). Thus this field unquestionably represents the most radical breakthrough in high-precision isotope ratio inorganic mass spectrometry in recent years.

In these first 5 years, scientists have used multiple-collector inductively coupled plasma mass spectrometry (MC-ICP-MS) to achieve unprecedented precision in the measurement of Cu, Zn, Ga, Cd, In, Sn, Te, Hf, W, Tl, Pb, Th, and U isotopic compositions at high sensitivity; made the first high-precision isotope dilution measurements of the earth's inventory of many poorly understood elements such as In, Cd, Te, and the platinum group elements; determined the age of the earth's core, the moon, and Mars using a new short-lived chronometer ^{182}Hf-^{182}W; made the first precise Sr, Hf, W, and Pb isotopic measurements in situ; developed a totally new class of high-precision stable isotope measurements of the small, but important fractionations of Zn and Cu in nature; and determined high-resolution Pb isotope stratigraphies for portions of the world oceans. Clearly, this is but the beginning; MC-ICP-MS offers exciting times ahead in fields well beyond the bounds of isotope and trace element geochemistry.

This chapter first presents a review of the rapidly developing range of MC-ICP-MS instrumentation available, then briefly surveys the initial experiments and associated methodologies that have helped to characterize the current and predicted performance of this kind of mass spectrometer, and concludes with a description of the exciting research areas, previously considered to be intractable, that are now developing in the earth sciences, cosmochemistry, oceanography, and the life sciences as a direct consequence of this technique.

8.2 MULTIPLE-COLLECTOR INDUCTIVELY COUPLED PLASMA MASS SPECTROMETRY INSTRUMENTATION

In order to achieve isotopic ratio measurements that are of comparable precision to those acquired by TIMS, but using an ICP source, four difficulties have to be overcome. First, the ICP source is maintained at a high pressure, primarily generated by the Ar used as the plasma support gas, in a similar manner to that commonly deployed in conventional ICP-MS (hereafter referred to simply as *ICP-MS).*

Naturally, one wants to achieve high transmission and extract as many ions from this source as is possible, and in fact the focused $^{40}Ar^+$ ion beam can be as large as a microampere. However, high-precision isotopic measurements require ultrahigh vacuum ($<10^{-8}$ mbar) in order to minimize collisions between analyte ions and atoms in the residual vacuum envelope and preserve good peak shapes. Therefore, all MC-ICP-MS instruments need to be accompanied by a considerable inventory of pumps to achieve efficient near-supersonic extraction at the cone interface, pump away residual Ar, and maintain ultrahigh vacuum in the analyzer.

Second, the source of ions is geometrically broad compared with that in TIMS. Therefore, the extracted ions need to be spatially restricted and directionally focused at the source (defining) slit with minimal loss of transmission, in order for the mass resolved ion beams to fit easily within the openings of the multiple Faraday detectors (buckets) and produce excellent peak shape.

Third, the ions in such an inductively coupled Ar plasma source possess a broad energy spread of up to ~15 V, sometimes as high as 20–30 V—roughly two orders of magnitude greater than in TIMS. Therefore, the ions of interest need to be focused and restricted in their energy spread before entering the magnetic sector; otherwise they will not be focused at the collectors and the peak shape will be greatly degraded. In practice, the energy spread of all components, including the plasma support gas, is too great to provide the same focusing for all ions. This does not matter, however, so long as the ions of interest are focused.

Fourth, all plasma sources are inherently unstable relative to the best TIMS sources. Improving plasma stability assists the task of energy and directional focusing. However, the single-detector system is too slow to respond to the changes in signal size resulting from plasma instability if sequential data collection is deployed. To achieve high precision it is essential to use simultaneous multiple Faraday collection to cancel out the effects of plasma instability. Therefore, all instruments need broad dispersion to incorporate multiple collectors and to produce ion beams that are focused in the z direction with minimal aberrations. Hence extended geometry is the norm for MC-ICP-MS.

The only such multiple-collector ICP-MS proved to operate in a routine manner with a significant track record at the time of writing is manufactured by VG Elemental under the model name Plasma 54 (hereafter P54). However, three new and interesting instruments are being developed and marketed, one by Nu Instruments, the second by Micromass Inc., and the third by VG Elemental. Each of these latter instruments utilizes ICP sources with a large potential difference (±4 to 6 kV) relative to the analyzer region. They all differ from the P54 by including a laminated magnet capable of fast scanning and are accompanied by a range of innovative solutions to the design obstacles discussed. The footprints are smaller. The electronics are greatly simplified and modernized relative to those of the P54, with computerized monitoring and control of nearly all instrument parameters. The data control software suites are relatively accessible. Many programs are written in Vi-

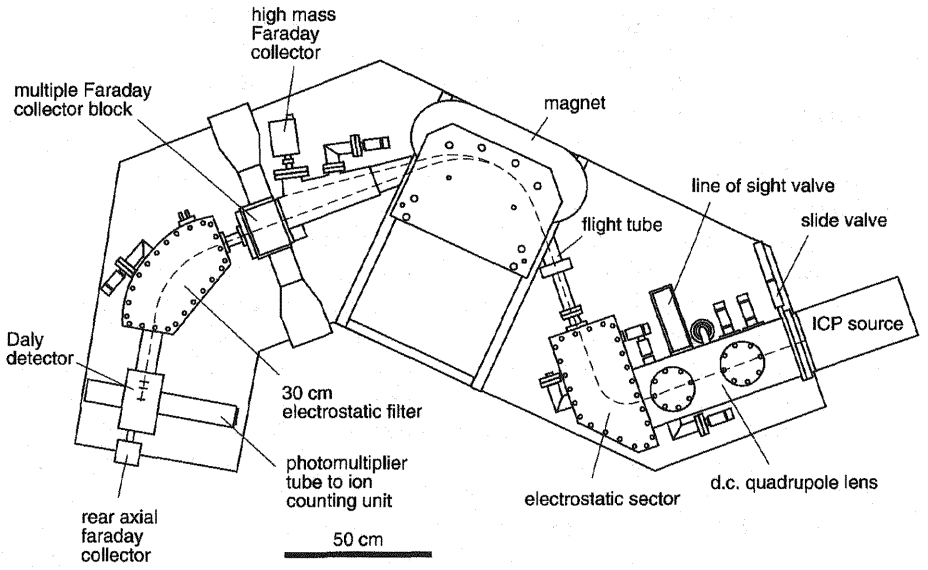

Figure 1 Outline of the multiple-collector inductively coupled plasma mass spectrometer (VG Elemental Plasma 54) at the University of Michigan (U-M). The U-M instrument is equipped with an extra 30-cm energy filter for high-abundance sensitivity measurements. (From Halliday et al., 1998b.)

sual Basic, rather than the more intractable Modula 2, and the latest instrumentation operates from Windows 95, NT, or Unix platforms.

We first describe the P54 and then outline the ways in which the most recent instruments differ from it. Schematics for the instruments are shown in Figs. 8.1 to 8.6.

8.2.1 The VG Elemental Plasma 54

The P54 is a double-focusing forward geometry instrument equipped with an array of mechanically adjustable Faraday collectors (Fig. 8.1). Most of the instrument is at ground, but the source and its associated pumping are floated at high potential. The ions are extracted at high voltage and two quadrupole dc lenses are used to focus the ion beam profile onto the analyzer entrance slit (Fig. 8.1). A small electrostatic analyzer (ESA) is then used to provide energy focusing and match the energy dispersion of the plasma source with that of the magnetic sector analyzer, such that the ions are energy-focused in the directional focal plane at the collectors. To permit effective energy focusing by a small radius (10-cm) ESA with a small voltage offset, the entrance utilizes a deceleration lens. The ions are then reaccelerated

after the ESA with an exit lens. This inverts the image. Therefore, in order to maintain energy focusing at the collector it is necessary for the analyzer to be arranged with an S configuration.

The magnet pole faces are set at an angle that is non-normal to the optic axis, providing double dispersion equivalent to that of a 54-cm-radius magnet. The extended geometry magnet also provides z focusing and sufficient dispersion to permit high transmission of the ions at the source slit at a mass resolution of about 400 (10% valley definition). The exit pole face is adjustable to rotate the ion beams and produce an ion image perpendicular to the optic axis. The University of Michigan (U-M) P54 has a total of 11 Faraday collectors providing true flat-topped peaks. Such peaks, in which each mass-resolved ion beam is entirely collected, are required for high-precision isotope ratio measurements. It is also essential that the transmission through the analyzer region and the detector gains remain constant as the beam is scanned across the interior of the Faraday detector. Unlike with TIMS, the instability of the ICP source prevents the normal measurement of peak flatness. For practical purposes it is currently specified as a static measurement relative to the signal of another isotope measured simultaneously in another detector; it is to be within ±100 ppm over 500 ppm of mass change as the *collector* is moved. The main collector assembly has eight independently adjustable Faraday cups and a fixed axial Faraday cup that can be lowered to allow the ion beam access to a Daly detector with ion counting (Fig. 8.1).

The U-M instrument also has a wide flight tube with an off-axis high-mass Faraday cup for the measurement of U at the same time as Pb is measured with the multiple-collector block (Halliday et al., 1993). This instrument has been further equipped with a second-stage 30-cm energy filter for enhancing abundance sensitivity before the ion beam reaches the Daly detector (Fig. 8.1), permitting highly accurate Th isotopic measurements (Luo et al., 1996, 1997). The abundance sensitivity (relative size of the peak tail at 1 amu) of the U-M instrument in this mode is about 0.3 ppm for Th. An additional Faraday cup is located beyond the Daly detector. This rear cup is normally only used for alignment purposes because the beam is somewhat defocused at this point.

8.2.2 The Nu Instruments Nu Plasma

The Nu Instruments Nu Plasma displays some general similarities to the P54, but critical features are radically different in concept. Most importantly, the instrument deploys novel variable dispersion ion optics that are applied to the ion beams exiting the magnetic analyzer, permitting the use of fixed multiple collectors and rapid peak switching.

Like the P54, the Nu Plasma is a forward geometry double-focusing mass spectrometer with double dispersion, but it has the standard C configuration and defines a smaller footprint (Fig. 8.2). The instrument has a source that is similar to

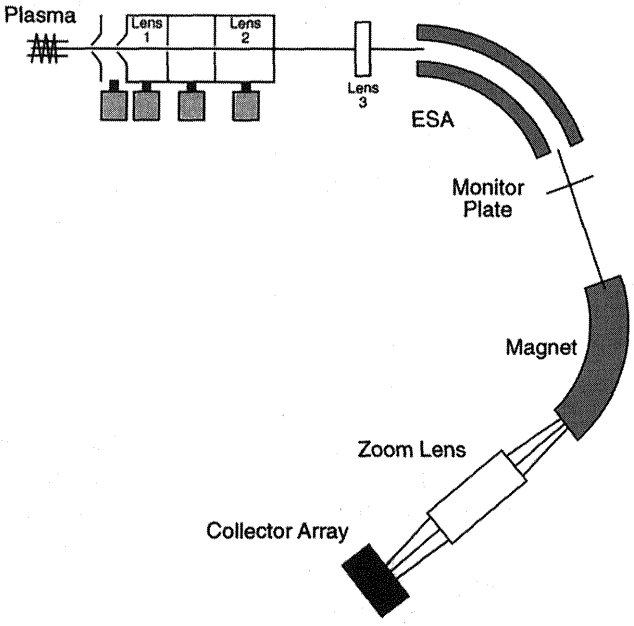

Figure 2 Schematic for the Nu Instruments Nu Plasma.

that used in conventional ICP-MS, and the front end is fitted with a water-cooled nickel sampler (1.0-mm-diameter aperture) and skimmer (0.6-mm-diameter aperture) cones. The extracted 4-kV ions are accelerated immediately behind the skimmer and focused down onto and through an intermediate circular aperture (Fig. 8.3). This circular image is then matched to the rectangular defining slit of the mass spectrometer, using two independent (2-kV) Einzel lenses so as to ensure minimal cross talk between the horizontal (y) and vertical (z) lens actions. Electrostatic beam steering is provided at all necessary points to ensure the ion beam stays on axis (Fig. 8.3). The instrument uses a 35-cm-radius ESA, followed by a 25-cm-radius magnet; the ion optics are designed to allow full transmission of the plasma ions of interest with minimal degradation of peak shape quality. No deceleration and reacceleration of the ions to accomplish energy focusing are used on this instrument. Hence, the standard C configuration is possible and the focused ion beam maintains ~4-kV energy throughout the analyzer. Vertical (z) focusing of the ion beam through the mass spectrometer is achieved by the use of both the Einzel lenses placed in front of the ESA and the non-normal exit pole on the magnet.

Because the spatial separation between ion beams of adjacent isotopes is mass dependent, in nearly all magnetic sector instruments it is necessary to alter the distance between collectors mechanically. This is a particular problem for ICP

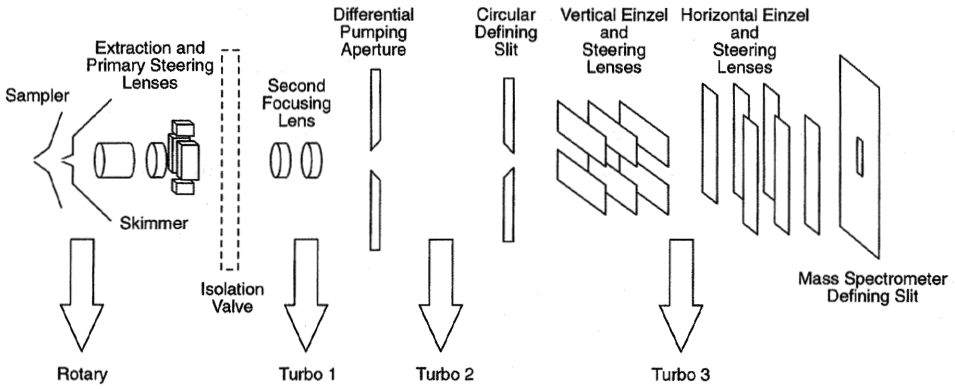

Figure 3 Details of the differential pumping, ion extraction, and focusing for the Nu Instruments Nu Plasma.

sources, where the peak flat can only be measured by moving the collectors. The Nu Plasma utilizes a variable dispersion zoom optic device to overcome this problem, enabling the detectors to remain in fixed positions (Fig. 8.4) (Belshaw et al., 1998). This greatly simplifies the complexity of the detector array, providing greater reliability and more serviceability. Most importantly, since no moving parts are used in the design, fast changes of instrumental configuration are possible, allowing simple multielement isotopic analysis of small quantities of mixed samples. The collectors are a new design of readily replaceable ceramic Faraday buck-

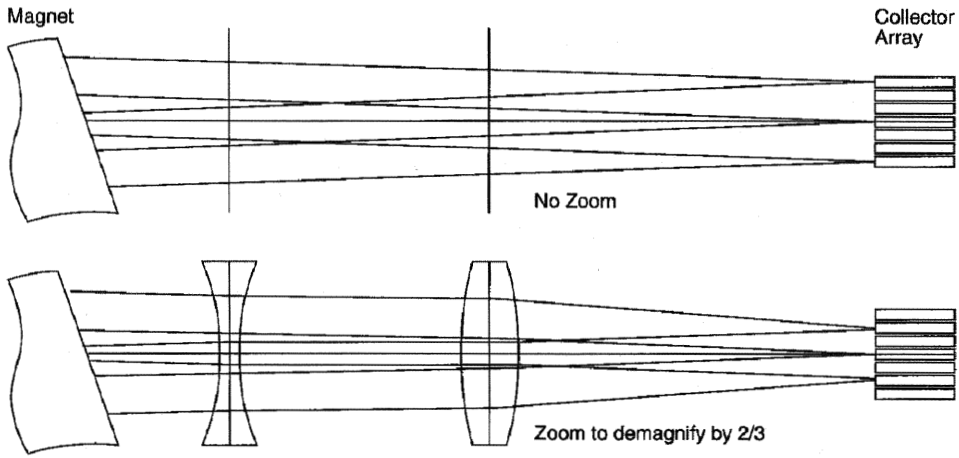

Figure 4 Zoom lens effect with the Nu Instruments Nu Plasma.

ets. Twelve Faraday buckets are provided with the instrument, none of which is required to move because of the use of the zoom ion optics. Unlike with the P54, or the Micromass instrument discussed later, the flight tube does not need to be particularly wide because ions of very different mass can be deflected into the cups of interest. Also unlike the P54, three multipliers with ion counting can be provided as an option, utilizing low-noise discrete dynode multipliers capable of recording signals of greater than 2×10^6 counts per second. The ions are deflected into the multipliers by using electrostatic deflectors located beyond the focal plane. To achieve high abundance sensitivity a small retardation lens is added. This instrument achieves specifications for the low-mass tail comparable to that of the 30-cm energy filter of the P54.

The pumping configuration is also different, with all vacuum pumps and sensors operated at ground potential. The extraction and lens region is divided into three regions differentially pumped with three small turbomolecular pumps (Fig. 8.3). So effective is this arrangement that the vacuum at the second Einzel lens has already achieved 10^{-8} mbar. Therefore the analyzer region is pumped with three ion pumps (Fig. 8.2), in contrast to the heavy-duty turbomolecular pumping used on other MC-ICP-MS instruments (Fig. 8.1). Apart from the acoustic quietness with which the instrument operates, this system has the advantage that if power is lost, the active surfaces still provide pumping, with little loss of vacuum and no risk of contamination. At the time of writing, this instrument provides the most accurate isotopic data of all the commercially available machines.

8.2.3 The Micromass Iso-Plasmatrace

The high temperature of ICP sources (~7000K) inhibits the formation of molecular interferences. Generally, dimers and simple oxides and hydrides are the most complex molecules formed. Combinations of major matrix elements, the solute, and components of the plasma support gas, for instance, oxygen and argon, create the most serious spectral interferences. So, for example, $^{40}Ar^{12}C^+$ on $^{52}Cr^+$, $^{40}Ar^{14}N^+$ on $^{54}Fe^+$, $^{40}Ar^{16}O^+$ on $^{56}Fe^+$, $^{40}Ar^{2+}$ on $^{80}Se^+$, and $^{40}Ar^{35}Cl^+$ on $^{75}As^+$ limit the applicability of the method. The presence of such interferences gives rise to an elevated background at the analyte mass that, at best, raises the achievable detection limits and, at worst, renders the analyte isotope unusable. For this reason most MC-ICP-MS measurements have been restricted to that portion of the mass region ($z > 80$) above which molecular interferences are absent or negligible.

Micromass has developed a potentially powerful new technique that eliminates many of these molecular interferences and also removes ions with an energy that differs from that of the analyte, such as components of the Ar support gas. This has a dramatic effect on the performance of the instrument. The technique deploys a hexapole ion lens (Szabo, 1986) located behind the skimmer cone and surrounded by a gas cell (Fig. 8.5). The hexapole uses a hexagonal array of rods between which a 400-V rf field is applied, confining the ions of interest to stable trajectories be-

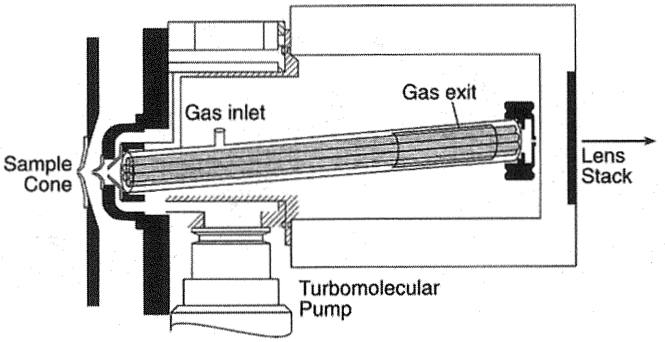

Figure 5 Schematic for the Micromass hexapole lens system.

tween the rods. The hexapole array is enclosed within a jacket into which the collision gas is admitted in the front half. By admission of small amounts of helium (hydrogen, neon, argon, and xenon have also been used, depending on the elements of interest), the pressure over the length of the hexapole is increased. Collisions with the gas break up molecular species and dramatically reduce the energy of the ions to less than 1 V, "thermalizing" the ions to the energy of the gas being used (corresponding to the small energy spread associated with the ambient temperature). This results in a mass spectrum free of certain interferences, allowing analysis of previously difficult or impossible elements at ultratrace levels. Argon, being heavy, is an efficient thermalizer and eliminates hydrides. However, He is preferable as a thermalizer for lighter elements because collisions with Ar can eliminate these elements through collisionally induced aberrations in the flight path. Use of hydrogen eliminates noble gases from the spectrum—the argon ions readily acquire electrons from the hydrogen atoms. The former are pumped away; the latter are eliminated by collisions with the rods. Therefore the use of hydrogen provides the potential to study elements like selenium and iron by MC-ICP-MS, whereas interferences from $^{40}Ar^{16}O^{+}$ on $^{56}Fe^{+}$, or $^{40}Ar^{2+}$ on $^{80}Se^{+}$, would make this difficult. Other oxides are difficult to eliminate with any of these collision cell gases but may be partially removed with xenon. For some elements, hydrides are formed when using hydrogen, and these elements may be better studied with other thermalizers.

Micromass has applied this new hexapole technology to a fast scanning magnetic sector multiple-collector instrument (Fig. 8.6). The source is at ground potential so most of the lens system and analyzer float at -6 kV. The ions are extracted into the hexapole through a sample cone with a 1.1-mm orifice, a 0.8-mm orifice skimmer cone, and finally a 2-mm orifice transfer lens held at -400 V. The hexapole is inclined to prevent line-of-sight transmission and damage to the detectors from the source. A lens system transfers the ions into the mass analyzer.

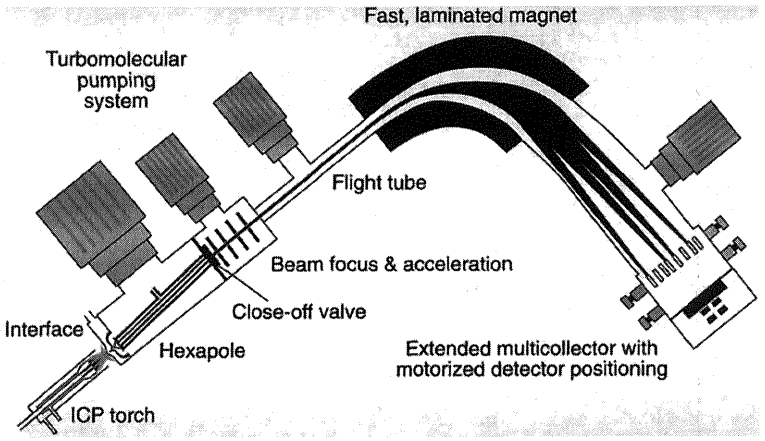

Figure 6 Schematic for the Micromass Iso-Plasmatrace.

The reduction in energy spread means that double focusing is unnecessary. Micromass achieves excellent peak shape and reproducibility with single (directional) focusing. So the lens system is virtually identical to that used in TIMS, accelerating the ions through a stack that starts with an extraction plate at −900 V and ends with a source slit at −8 kV.

The ions travel along a drift length expanding to a z baffle with a 4-mm aperture prior to entering the magnetic field. This ensures that the ion beam is unimpeded as it expands along the 16-mm-high flight tube. The magnet is laminated for fast scanning through the entire spectrum, from mass 6 to mass 238, in 600 ms. The multiple-collector hardware is similar to that of the P54 but uses a very wide (~110-mm) flight tube with a broader array of detectors to take advantage of a wide (~90-mm) linear focal plane (Fig. 8.6).

The Faraday detectors are carbon coated metal, like the P54, but they have demonstrated a particularly long life at high performance (Palacz et al., 1996). Micromass also supplies multiple multipliers, unlike VG Elemental. However, these are small continuous dynode channeltrons, each with a conversion dynode and ion counting, rather than the larger discrete dynode type used by Nu Instruments. This is because with the Micromass instrument there is no provision for electrostatically deflecting the ion beams of interest, and therefore the collectors have to be closely spaced. A total of nine Faraday detectors and eight multipliers with ion counting can be incorporated (including a Daly detector). The abundance sensitivity can be improved with a small deceleration lens that should be extremely effective on this single focusing instrument.

This instrument represents a potentially exciting development in the field of MC-ICP-MS. The hexapole not only eliminates isobars, it generates higher sensi-

tivity, a small energy spread, and remarkably stable focusing and peak shape. We are at the early stages of learning all the possible ramifications for MC-ICP-MS provided by hexapoles.

8.2.4 The VG Elemental Axiom

VG Elemental launched another design of mass spectrometer, the Axiom, a small instrument with extreme dispersion, capable of multiple collection at variable mass resolution. Designed by P. Marriott, the Axiom is very compact yet provides the difficult combination of very high mass resolution (>10,000 when required) with a linear focal plane suitable for multiple collection. The Axiom is a forward geometry double-focusing, C configuration instrument with a 77° electrostatic sector–90° magnetic sector using non-normal incident and exit angles to achieve 580-mm dispersion. Unusually, the instrument is arranged with an upright configuration. As with the P54 and Nu Plasma, the instrument extracts the ions at high voltage (5 kV) onto and through an extraction electrode at ground potential. Turbopumps are used throughout the instrument to create ultrahigh vacuum and to allow reasonable abundance sensitivity. Two Einzel lenses are used to shape the trajectory of the ion beam so that it is partially focused down onto an adjustable source slit. The gradually diverging beam then enters a drift length region in which it is steered, focused, and slightly shaped, before entering the ESA. At this point the pressure has been reduced to 10^{-7} mbar. As the ion beam passes through the magnetic analyzer it broadens to some 15 mm in the nondispersive plane but focuses down to a very small height (1 mm) at the focal plane. This reduced spread in the z direction allows a smaller collector slit height to be used. To achieve high mass resolution, an adjustable collector slit is required. For extremely fast electrostatic scanning over a mass range of 10% Δ m/m, a potential is applied to the rear section of the flight tube itself.

At the time of writing, this instrument is still under development. A prototype has already demonstrated the power of the ion optics in single-collection mode. Also, the beam size has been measured across some 10% Δ m/m of the focal plane, confirming the 90° focal plane and its linearity—endorsing the detailed ion optical modeling used in its design. The instrument is designed for rapid high-precision analytical work, but with the convenient simplicity required by the nonspecialist user.

8.3 PERFORMANCE

The transmission efficiency of MC-ICP-MS is high relative to that of most ICP-MS instruments (>10^8 ions sec^{-1} ppm $^{-1}$ indium using conventional aspiration methods) but is low relative to that of TIMS. This is because the ions in the plasma

source are sampled via a very inefficient assembly of skimmer and sample cones, as in ICP-MS. This "interface" region is where most instrumentation development is clearly needed in the coming years. However, despite the transmission advantage of TIMS it is difficult to obtain high-precision concentration and/or isotopic data for certain elements using such a method simply because they are difficult to ionize. High-precision isotopic composition and concentration isotope dilution (ID) measurements of high-mass elements that are difficult to ionize by other methods are relatively straightforward using MC-ICP-MS (Halliday et al., 1995, 1997).

One of the elements of great interest to isotope geochemists is hafnium (Hf) because of the decay of ^{176}Lu to ^{176}Hf (Patchett, 1983). Of course, Hf has a high first ionization potential (6.65 eV), rendering it a notoriously difficult element to measure at high precision by TIMS. Therefore, the measurement of Hf isotopic compositions has received a great deal of attention from MC-ICP-MS users. The standard method of sample admission utilizes a peristaltic pump or free uptake (the Venturi effect in the nebulizer and capillary action) to deliver dissolved samples to a pneumatic nebulizer. However, desolvating higher-efficiency nebulizers, such as the Mistral, marketed by VG Elemental, or the MCN6000, marketed by Cetac Technologies, yield significant (factor of >10) increases in sensitivity and extremely good reproducibility for small samples (<100 ng of Hf or W) (Walder et al., 1993b; Lee et al., 1997). At the time of writing, the sensitivity of all the instruments described when using the MCN6000 is typically in the range of 0.2% to 0.3% for Hf (total ions detected per atom used), with very good plasma stability. For all of the new instruments discussed, the sensitivity is being worked on as a matter of priority and improvements are expected in the coming years.

The precision and reproducibility of MC-ICP-MS data are comparable to those acquired with modern multiple-collector TIMS for a similar sized ion beam. The values obtained by Walder et al. (1993a,c) are, within uncertainty, identical to recommended values and the accuracy of the method is not in question, provided there are no interferences (such as ^{86}Kr on ^{86}Sr). This is illustrated for Hf in Fig. 8.7. The isotopic composition of Hf standards is reasonably well established and represents an extremely good starting point in terms of establishing the power of MC-ICP-MS for high-precision isotopic measurements of elements that are difficult to ionize. Figure 8.7 shows isotopic data for the JMC-475 standard used by most workers. It yields a mean ^{176}Hf/^{177}Hf of 0.282161 ± 0.000013 (2σ) at the University of Michigan and 0.282163 ± 0.000012 (2σ) at Lyons (Blichert-Toft and Albarède, 1997), in excellent agreement with the value of 0.282154 ± 0.000014 now quoted as the best mean value for TIMS measurements (Nowell, pers. comm., 1996).

High-precision isotopic ratio measurements with MC-ICP-MS have now been made on a large range of elements with high first ionization potential, including Cu and Zn (Blichert-Toft et al., 1996; Maréchal et al., 1997); Ga and Ge (Hirata, 1997); Mo (Lee and Halliday, 1995a); Ru, Pd, and Ag (Rehkämper and

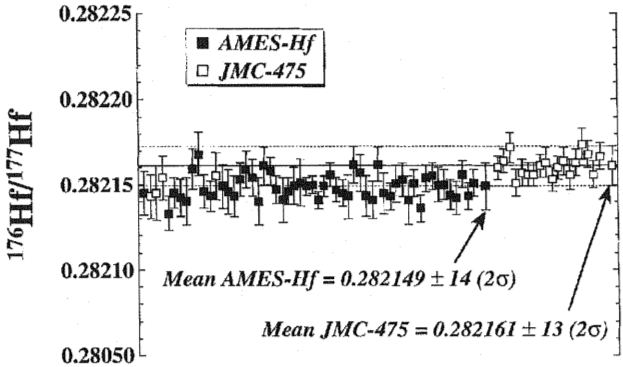

Figure 7 Hafnium isotopic compositions for in-house Ames Hf standard and international standard JMC-475 as measured on the VG Elemental Plasma 54 (P54) at the University of Michigan. (From Halliday et al., 1998b.)

Halliday, 1997; Rehkämper et al., 1997a,b); Cd (Yi et al., 1996, 1998); Sn (Lee and Halliday, 1995a; Yi et al., 1995, 1996); Te (Lee and Halliday, 1995a; Yi et al., 1996, 1998); Hf (Walder et al., 1993b,c; Godfrey et al., 1997; Ballentine et al., 1997; Blichert-Toft et al., 1996, 1997; Nash et al., 1996; Vervoot et al., 1997); W (Halliday et al., 1995; Lee and Halliday, 1995a,b; 1996; 1997; 1998; Lee et al., 1997); Os (T. Hirata, pers. comm., 1996); Re, Ir, Pt (Rehkämper and Halliday, 1997; Rehkämper et al., 1997a,b); Tl (Rehkämper and Halliday, 1999); Pb (Walder and Freedman, 1992; Walder et al., 1993c; Walder and Furutu, 1993; Hirata, 1996; Christensen et al., 1997; Belshaw et al., 1998; Rehkämper and Halliday, 1998); Th (Luo et al., 1996, 1997); and U (Walder and Freedman, 1992; Taylor et al., 1995; Luo et al., 1996, 1997) (Table 8.1).

There is a large mass discrimination (or "bias") in ICP sources reflecting the tendency of heavier ions to be extracted preferentially to light ions. Precise correction for mass bias, which can be difficult in ICP-MS (Ross and Hieftje, 1991; Ketterer et al., 1991; Ketterer, 1992), seems to be relatively straightforward in MC-ICP-MS (Walder et al., 1993b; Halliday et al., 1995; Lee and Halliday, 1995a; Yi et al., 1995). We suspect that this is because many quadrupole mass spectrometers introduce additional artifacts that are hard to distinguish from ionization effects. The consistent mass bias is a highly significant feature of ICP mass spectrometers and contrasts with TIMS, in which mass discrimination is related to work function and, in some instances, poorly understood reactions that occur on the filament during heating. Thus, in MC-ICP-MS using a solution containing a mixture of elements with overlapping mass ranges, the mass discrimination observed in an element of known isotopic composition can, in many cases, be used to determine accurately the unknown isotopic composition of another element. The effect is greater with decreasing mass, and with all the MC-ICP-MS instruments it is about

Table 1 Comparison of Isotopic Compositions Measured by Multiple-Collector Inductively Coupled Plasma Mass Spectrometry and Those Measured by Thermal Ionization Mass Spectrometry

Element	Ratio	Measured	Recommended	Comments	Source
Germanium	70/73	2.6643 ± 3	2.689	Ga normalization	Hirata, 1997
	72/73	3.549 ± 1	3.545		
	74/73	4.703 ± 3	4.653		
Strontium	87/86	0.71032 ± 1	0.71025 ± 2	NIST SRM 987; no corr. for Kr^+	Walder and Freedman, 1992
	87/86	0.70311 ± 2	0.70312 ± 2	C241 feldspar/laser; Kr^+ corr.	Christensen et al., 1995
	87/86	0.70918 ± 2	0.70917 ± 1	Whelk/laser; Kr^+ corr.	
Zirconium	91/90	0.217972 ± 4	0.21799 ± 5	JM	Lee and Halliday, unpubl.
	92/90	0.333373 ± 6	0.33338 ± 6		
	96/90	0.054392 ± 3	0.05439 ± 7		
Molybdenum[b]	94/96	0.55247 ± 1	0.55249	JM12972	Lee and Halliday, unpubl.
	95/96	0.95325 ± 2	0.95324		
	97/96	0.57395 ± 1	0.57393		
Indium	115/113	22.217 ± 7	22.1 ± 2	Pd normalization	Yi et al., 1995
Tin	112/120	0.029812 ± 4	0.02986 ± 5	JM88112	Lee and Halliday, 1995a
	114/120	0.02020 ± 1	0.02022 ± 5		
	115/120	0.010366 ± 7	0.01039 ± 5		
	117/120	0.23531 ± 5	0.23538 ± 8		
	118/120	0.74294 ± 8	0.7430 ± 2		
	119/120	0.26343 ± 5	0.2635 ± 1		
	122/120	0.14209 ± 1	0.14211 ± 7		
	124/120	0.17759 ± 5	0.1775 ± 1		

Tellurium	120/128	0.00292 ± 1	0.00289 ± 3	JM10758	Lee and Halliday, 1995a
	122/128	0.07960 ± 2	0.07949 ± 4		
	123/128	0.02790 ± 1	0.02788 ± 3		
	125/128	0.22204 ± 3	0.22172 ± 5		
	126/128	0.59226 ± 3	0.5915 ± 2		
	130/128	1.07595 ± 3	1.0789 ± 1		
Samarium	144/147	0.20621 ± 8	0.20504 ± 2	Nd normalization	Luais et al., 1997
	148/147	0.74835 ± 7	0.74970 ± 2		
	149/147	0.91813 ± 2	0.92160		
	150/147	0.4892 ± 1	0.49213 ± 3		
Neodymium	143/144	0.5119 ± 1	0.51193 ± 2	CalTech mixed Sm/Nd standard	Halliday et al., 1995
	145/144	0.34842 ± 1	0.348417 ± 7	JM	Luais et al., 1997
	148/144	0.24158 ± 3	0.241578 ± 8		
	150/144	0.23643 ± 4	0.23642 ± 2		
Hafnium	176/177	0.28216 ± 1	0.28216 ± 1	JMC475	Blichert-Toft and Albarède, 1997
Tungsten	180/183	0.0834 ± 1	0.0837 ± 3	NIST SRM 3163	Lee and Halliday, 1995a
	182/183	1.8515 ± 3	1.8513 ± 6		
	184/183	2.1407 ± 1	2.1408		
Lead	206/204	16.937 ± 8	16.94 ± 1	NIST SRM 981; Tl normalization	Walder et al., 1993c
	207/204	15.483 ± 8	15.49 ± 2		
	208/204	36.69 ± 2	36.72 ± 4		
Thorium	230/232	1.0671 ± 5	1.069 ± 4	Activity ratio of Table Mtn. Latite. U normalization	Luo et al., 1997
Uranium	234/238	−34 ± 1	−34 ± 2	δ234 NIST SRM960	Luo et al., 1997

[a]Unless otherwise indicated all data were corrected for mass discrimination by using the normalized value adopted in the recommended reference study.
[b]An earlier result for Mo determined on the prototype Plasma 54 (P54) (Lee and Halliday, 1995a), gives different results that we cannot reproduce with the production P54.

1% per amu at Pb, i.e., an order of magnitude larger than with TIMS. However, this bias is a relatively simple function of absolute mass, following an exponential law (Lee and Halliday, 1995a), and, unlike in the case of a thermal source, is largely independent of time, the chemical properties of the element, or the admixing of other elements (Russ and Bazan, 1987; Walder and Freedman, 1992; Walder et al., 1993c).

There is much that remains to be understood about the mass bias, its control, and artifacts that may be introduced from the sample preparation (Hirata, 1996; Rehkämper and Halliday, 1998, 1999). However, there is no doubt that the implications of such a powerful control on mass discrimination are far-reaching. Normal isotopic compositions, natural fractionations, natural isotopic anomalies, and artificial isotopic enrichments can be measured to higher precision. Elements such as Pb, the isotopic composition of which cannot be normalized with internal normalization, can be corrected for mass discrimination to high levels of accuracy by admixing a standard such as Tl of known isotopic composition and monitoring masses ^{205}Tl and ^{203}Tl (Walder et al., 1993c; Hirata 1996; Christensen et al., 1997). The excellent agreement with recommended values for NIST SRM 981 is shown in Fig. 8.8.

The ability to correct for mass discrimination externally has also proved invaluable in the development of isotope dilution techniques. Since the natural isotopic composition is deliberately changed, the use of a proxy element to define the mass discrimination permits highly accurate concentration measurements to be made. MC-ICP-MS is not suitable for rapid determination of the concentrations of a large range of elements in a single solution, although this is incorporated as a feature of the latest fast scanning versions. However, MC-ICP-MS is ideal for high-precision isotope dilution analysis of separated elements and is very efficient compared with TIMS (Rehkämper and Halliday, 1997; Rehkämper et al., 1997a,b; Yi et al., 1995, 1996, 1998). The technique development required for separating many of the elements of interest is considerable. Isotope dilution data for separated platinum group elements (PGEs) and Re, In, Sn, Te, and Cd in basalts are highly reproducible (Rehkämper and Halliday, 1997; Rehkämper et al., 1997a,b; Yi et al., 1995, 1996, 1998).

In a similar manner, one is able to achieve excellent external reproducibility and precision for Th isotopic measurements by admixing natural U of known isotopic composition and using the 238/235/234 ratios to calibrate the Daly/Faraday gain and the mass discrimination during the analysis (Luo et al., 1996, 1997). These developments are described in detail later. A further important consequence of this simple mass discrimination is that isobaric interferences such as ^{87}Rb on ^{87}Sr, ^{144}Sm on ^{144}Nd, or ^{176}Lu on ^{176}Hf can be corrected for to higher degrees of accuracy than has hitherto been possible (Walder et al., 1993c; Halliday et al., 1995). This is critical for many laser ablation applications in which isobaric interferences cannot be removed by separation techniques (Christensen et al., 1995).

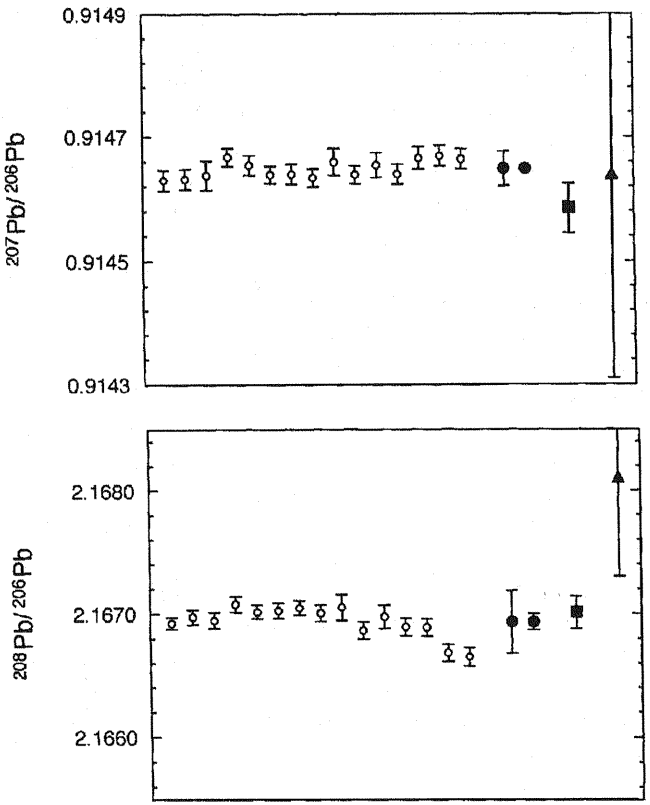

Figure 8 Lead isotopic compositions for NIST SRM 981 as measured on the VG Elemental Plasma 54 (P54) at the University of Michigan, using Tl correction for mass bias. Open dots, individual data ($\pm 2\sigma_{mean}$) from three measurement sessions over a 2-month period; filled dots, our mean ($\pm 2\sigma$ and $\pm 2\sigma_{mean}$; filled square, data from Todt et al. (1996) ($\pm 2\sigma_{mean}$); filled triangle, certified values.

Finally, the simple mass bias is likely to open up a whole arena of previously intractable stable isotope geochemistry. Everybody has known for years that there are small variations in isotopic composition in all elements that are produced by combinations of kinetic and equilibrium processes, especially at low temperatures. For most elements the effects are too small to be reliably measured using conventional mass spectrometry. For low-mass elements that are commonly involved in redox reactions utilizing covalency to form a wide range of compounds (e.g., C, O, N, S), the isotopic effects are often large enough to be highly significant, providing earth scientists with the most powerful tool available for deducing the nature and conditions of low-temperature processes. With all such "stable isotope"

measurements the ability to resolve small isotopic variations is limited, in part, by the need to correct for mass discrimination and mass fractionation during the course of the analysis, normally by alternating the sample with a standard of known composition. Natural isotopic fractionations among heavy elements are typically too small to measure with such techniques. However, Maréchal et al. (1997), using MC-ICP-MS, report success with the measurement of natural fractionations in Cu isotopic compositions using Zn to correct for instrumental mass bias, and vice versa. Similarly, it appears possible to measure natural Ga isotopic variations in meteorites by monitoring instrumental mass bias using admixed Ge (Hirata 1997). Recently, the natural isotopic variations in Tl produced by mass-dependent fractionation have been measured by admixing Pb of known isotopic composition (Rehkämper and Halliday, 1999).

Many of the problems associated with ICP-MS are not relevant to MC-ICP-MS. Most solution work is performed on reasonably pure solutes of separated trace elements, so artifacts associated with the level of total dissolved solids (Williams and Gray, 1988) are negligible. Plasma instability problems (Begley and Sharp, 1994) are not so much of a concern with MC-ICP-MS because of the use of static multiple collection. The effects of plasma instability therefore largely cancel out. The most recent instruments (notably the Micromass instrument) are extremely stable, especially when used in conjunction with the MCN-6000. Polyatomic ion interferences (Date et al., 1987; Gray and Williams, 1987; Marshall and Franks, 1990) are only of concern below about mass 80 and most applications of MC-ICP-MS are used for studying higher masses. The contributions of hydrides and oxides are negligible because a dry plasma is used, either in laser ablation mode or with a desolvating nebulizer. Use of adjustable high resolution, as on all the latest instruments, makes it possible to see which interferences may be present. Use of the hexapole collision cell, as on the Micromass instrument, provides a means to eliminate many of them altogether.

Problems with internal standardization and calibration of signal intensities for concentration measurements with ICP-MS (Walsh, 1992) are irrelevant to MC-ICP-MS because most applications are concerned with isotopic compositions and isotope dilution measurements (Lee and Halliday, 1995b; Yi et al., 1995). Internal standardization is only of significance in the application of laser ablation techniques to the measurement of parent/daughter ratios by MC-ICP-MS. Work has started in this area (Halliday et al., 1998a), and though the results of the first experiments are encouraging, they mandate a great deal of further effort.

8.4 APPLICATIONS

The potential range of application of MC-ICP-MS is enormous. Reviews of some of the geochemical applications can be found in Halliday et al. (1998b). Here we

merely highlight three very different areas of research that illustrate the power of this method.

8.4.1 Very Precise Isotopic Compositions—a Case Study of Tungsten in the Early Solar System

MC-ICP-MS opens up a variety of new fields relating to the basic ability to measure precisely isotopic compositions of elements with high first ionization potential at high sensitivity. A good example of this is found in the element tungsten (W). The time scales over which inner solar system planets and planetesimals accreted and differentiated are unclear because the isotopic systems of many meteorites are disturbed and the more robust long-lived chronometers (such as U-Pb) provide inadequate temporal resolution. Radionuclides with half-lives on the order of 10^6–10^8 years can provide unparalleled insights into the earliest history of the solar system and the nature of the nucleosynthetic events that contributed material to the molecular cloud that collapsed to form the solar nebula. Variations in isotopic abundances in daughter elements in many meteorites are a function of the parent/daughter element ratio, the time at which the object formed, and the abundance of the radionuclide at the start of the solar system (Reynolds, 1960; Lee et al., 1977; Kelly and Wasserburg, 1978; Birck and Allègre, 1988).

The ^{182}Hf-^{182}W chronometer (half-life = 9 Myr) is particularly powerful for constraining the time scales of accretion and metal/silicate differentiation (such as core formation) in planets and planetesimals (Harper et al., 1991a; Lee and Halliday, 1995b, 1996, 1997; Halliday et al., 1996) for the following reasons: Both Hf and W are highly refractory elements and thus are expected to occur in average solar system (= chondritic) proportions in much of the solar system. The effects of the strong heating within the circumstellar disk from friction, accretion, or the T-tauri stage of the sun, all of which may have driven off the volatile elements from the inner solar system, should be negligible. Therefore, we can make reasonable assumptions about the approximate parent/daughter refractory element ratios of planets. However, Hf substitutes into silicates, whereas W prefers to substitute into metals and metallic liquids. So the Hf/W ratio of silicate phases is much higher than that of coexisting metals. If such segregation of metal from silicate occurred during the lifetime of ^{182}Hf, the isotopic abundance of ^{182}W would eventually be greater in the silicate with high Hf/W but be low in the metal with low Hf/W, relative to that found in undifferentiated chondritic material. The magnitude of such an effect in terrestrial W can be used to place constraints on the age of the earth's core (Lee and Halliday, 1995b; Halliday et al., 1996; Harper and Jacobsen, 1996; Jacobsen and Harper, 1996). In a similar manner, the W isotopic compositions of meteorites thought to be derived from the asteroid belt, Martian meteorites, and lunar samples can be used to constrain when their parent planets and planetesimals accreted, melted, and differentiated into silicate/metallic portions (Halliday et al., 1996; Lee and Halliday, 1996, 1997; Lee et al., 1997).

The problem with this technique and the reason why it has been so slow to develop is that it is extremely difficult to measure W isotopic compositions by TIMS because of the very high first ionization potential (7.98 eV). Negative ion techniques have met with some success (Volkening et al., 1991; Harper et al., 1991a; Harper and Jacobsen, 1996; Jacobsen and Harper, 1996). However, W isotopic compositions can be measured relatively easily by using MC-ICP-MS (Halliday et al., 1995; Lee and Halliday, 1995a,b, 1996, 1997; Lee et al., 1997).

The W isotopic compositions of various terrestrial samples, chondrites, iron meteorites, basaltic achondrites, lunar samples, and Martian meteorites are expressed as deviations in parts per 10^4 from the value for the silicate earth (such as the W in a drill bit or chisel), which are the same as those of average solar system materials, represented by carbonaceous chondrites. These values are summarized in Fig. 8.9, from which it can be seen that early segregated metals such as the iron meteorites and metals from ordinary chondrites have only unradiogenic W because they formed early with low Hf/W. The time differences between metal objects segregated from parents with chondritic Hf/W are revealed by the differences in W isotopic compositions between each of the metal objects and chondrites. The Hf-W model ages of all these metals indicate that all of their parent bodies formed within a few million years, implying rapid accretion in the early history of the solar system.

Eucrites are derived from the silicate portions of differentiated bodies, in this case usually considered to be Asteroid 4 Vesta. Two such eucrites yield exceedingly radiogenic W with ε_w of +22 and +33, respectively (Fig. 8.9), correlating with high Hf/W (Lee and Halliday, 1997). These measurements of excess ^{182}W are also explained by differentiation of the meteorite parent bodies during the lifetime of ^{182}Hf, and the W is radiogenic because of high Hf/W ratios. Hf-W model ages for such silicate rocks can be calculated from the differences in Hf/W ratios and W isotopic compositions between the samples and primitive chondritic meteorites. The two eucrites yield very similar model ages of about 8 to 10 Myr after the start of the solar system. Such early ages of differentiation are broadly consistent with studies of other short-lived chronometers including ^{60}Fe-^{60}Ni and ^{53}Mn-^{53}Cr for various eucrites (Shukolyukov and Lugmair, 1993a,b; Lugmair et al., 1994). The absolute ages of many eucrites have yielded much younger, almost certainly erroneous results, using long-lived chronometers such as U-Pb (Wadhwa and Lugmair, 1996; Galer and Lugmair, 1996).

Therefore these data for the short-lived chronometer Hf-W provide a consistent picture of rapid accretion, equilibration, and planetesimal differentiation in the early solar system with only small (10^6-year) time differences resolvable between some events for the parent bodies of chondrites, basaltic achondrites, and iron meteorites.

The W isotopic compositions of Martian meteorites range from chondritic to slightly radiogenic (ε_w = 0 to +3) relative to the mean of carbonaceous chondrites (Fig. 8.9) (Lee and Halliday, 1997). The W isotopic compositions of these

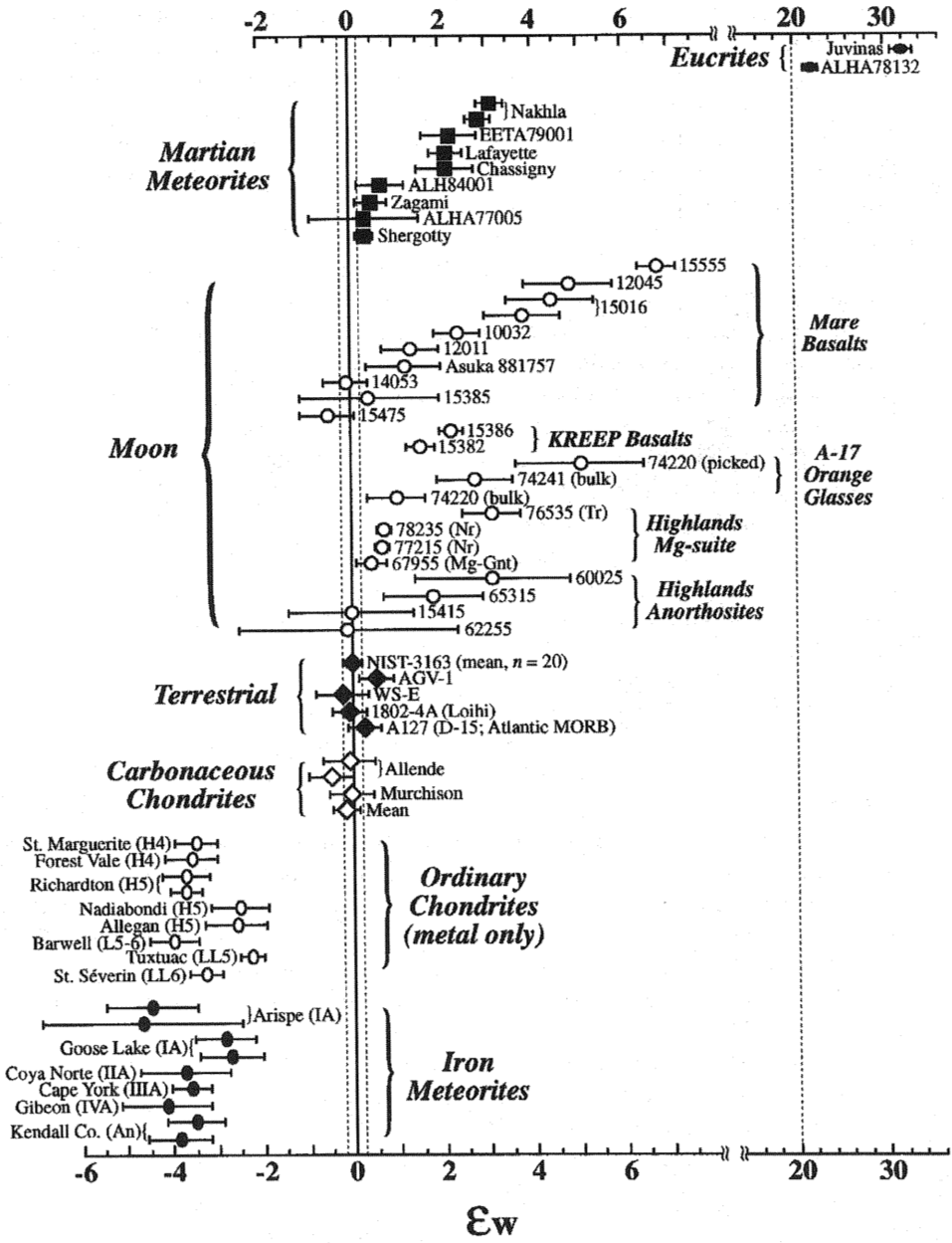

Figure 9 Tungsten isotopic compositions for terrestrial standards, meteorites, and lunar samples expressed as deviations in parts/10^4 from the mean for NIST SRM 3163, as measured by multiple-collector inductively coupled plasma mass spectrometry (MC-ICP-MS). (From Halliday et al., 1998b.)

meteorites reflect the earliest history of their Martian mantle source regions, whereas the measured Hf/W ratios are dominated by the effects of subsequent partial melting, which in most cases is relatively recent. A Hf/W elemental ratio of ~3 is typical for the Martian mantle (Treiman, 1986). Given these low Hf/W ratios the meteorites with radiogenic W, such as Nahkla, must have formed from reservoirs that originally differentiated within the first 10 Myr of the solar system. So the formation and differentiation of Mars also appear to be early and rapid.

The silicate earth would be expected to have excess ^{182}W if terrestrial core formation were early. Lee and Halliday (1995b) used MC-ICP-MS to show that the W isotopic composition of the silicate earth, far from being high because of early core formation, is identical within analytical uncertainties to that of the carbonaceous chondrites Allende and Murchison. The most recent carbonaceous chondrite W isotopic measurements (Lee and Halliday, 1996) now have an uncertainty of just ± 0.5 ε_W, resulting in a mean of -0.17 ± 0.29 ε_W (Fig. 8.9). That is, the W isotopic composition of the silicate earth is now established to be identical to that of carbonaceous chondrites to very high precision. Using a simple two-stage model, core formation on earth, must postdate iron meteorites by 50 Myr, unless accretion was slower than previously considered (Halliday et al. 1996).

Finally, we can determine the age of the moon with this chronometer. The W isotopic compositions and Hf/W ratios of various lunar samples are shown in Fig. 8.9 and display variably radiogenic W ($\varepsilon_W = 0$ to $+6$) (Lee et al., 1997). The moon is thought to have formed in a collision between the early earth and a planet at least the size of Mars. It is difficult to imagine that such W isotopic heterogeneity could have been inherited as debris from earlier planets, given the enormous energy, high temperature and subsequent planetwide differentiation associated with its birth. It is more likely that the radiogenic effects were generated by decay within the moon itself. The moon formed with high Hf/W but then differentiated to produce some mantle reservoirs with extremely high Hf/W. The W isotopic effects are small given these Hf/W ratios, indicating that the moon formed much later than Mars or the eucrite parent body. The Hf-W model ages for the moon cluster around 4.52–4.50 Ga (Lee et al., 1997), in perfect agreement with, but at the upper limit of, existing minimum age constraints of the moon (Carlson and Lugmair, 1988; Shih et al., 1993; Lee and Halliday, 1995b; Halliday et al., 1996).

So the ability to measure W isotopic compositions with MC-ICP-MS has immediately opened up exciting new scientific opportunities of broad significance. In a similar manner the technique could be used to develop other chronometers of early solar system evolution, previously intractable.

8.4.2 U-Th Isotopic Analysis and the Dating of Young Events

An obvious area of application of MC-ICP-MS relevant to the nuclear industry is in the rapid measurement of U enrichment and the isotopic compositions of fission

products (Taylor et al., 1995). Some of these measurements need not be very precise, but the throughput of the instrument at high sensitivity is striking. A more demanding use is high-sensitivity U-Th disequilibrium dating, and in this area MC-ICP-MS promises to be extremely effective. Precise determination of the isotopic compositions of daughter nuclides from the U and Th decay series is difficult but is of great importance in areas such as environmental and earth sciences. The time scales of various geological processes such as melt production, migration, and magma chamber storage (McKenzie, 1985; Condomines et al., 1988; Cohen and O'Nions, 1993; Spiegelman and Elliott, 1993; Qin, 1993; Iwamori, 1994), and recent geological events such as the last interglacial periods (Edwards et al., 1987; Bard et al., 1990; Ivanovich and Harmon, 1992; Ludwig et al., 1992; Stirling et al., 1995), are comparable to the half-lives of several intermediate nuclides from the U and Th decay series, e.g., ^{234}U ($T_{1/2} \sim 0.245$ myr), ^{230}Th ($T_{1/2} \sim 75$ kyr), ^{231}Pa($T_{1/2} \sim 33$ kyr) and ^{226}Ra ($T_{1/2} \sim 1.6$ kyr), but are either too long or inappropriate for ^{14}C $T_{1/2} \sim 5.7$ kyr) dating, or too short to be precisely determined by some of the long-lived chronometers.

The α-particle counting method has been widely used in U-Th disequilibrium series studies (Vdovenko and Dubasov, 1974; Ivanovich and Harmon, 1992). However, recent developments in TIMS have greatly improved the analytical precision and sample size requirements (Chen et al., 1986; Edwards et al., 1987). Certain samples that could not be dated with α counting can now be measured precisely. The use of electrostatic filters or deceleration lenses has greatly improved the abundance sensitivity of TIMS (Cohen et al., 1992), so that ratios of 10^{-5}–10^{-6} for $^{230}Th/^{232}Th$ can now be accurately measured.

Despite the advantages of TIMS over α counting, the very high first ionization potential of Th (~6.97 eV) can still present a problem of low ionization efficiency. In general, the ionization efficiency for Th by TIMS is inversely proportional to the amount of material (Th) used; the more Th on the filament, the lower the ionization efficiency. High sensitivities (of the order of 1%) have been reported by TIMS for carbonates with very little ^{232}Th. However, silicate samples, Fe-Mn oxyhydroxides, and certain carbonates with high ^{232}Th pose more of a problem in terms of the signal sizes of ^{230}Th that can be measured. Ion beam sizes for ^{230}Th of a few hundred counts per second or even worse may severely limit the analytical uncertainty. Sensitivity aside, with high- $^{232}Th/^{230}Th$ samples there are at least three further advantages to using MC-ICP-MS. One can correct for (Faraday/Daly) gain more precisely, measure mass discrimination reliably, and simply use a more concentrated solution to get a larger signal. Such U and Th isotopic measurements have now been developed by using a 30-cm energy filter to improve abundance sensitivity and a Daly detector with ion counting (Luo et al., 1996, 1997).

Isotopic measurements of U standards using MC-ICP-MS have been previously reported by Walder and Freedman (1992) and Taylor et al. (1995) (Table 8.1). For U isotopic analysis the relative Faraday/Daly gain can be best determined by measuring ^{235}U in both detectors. The U separated from a Table Mountain Latite

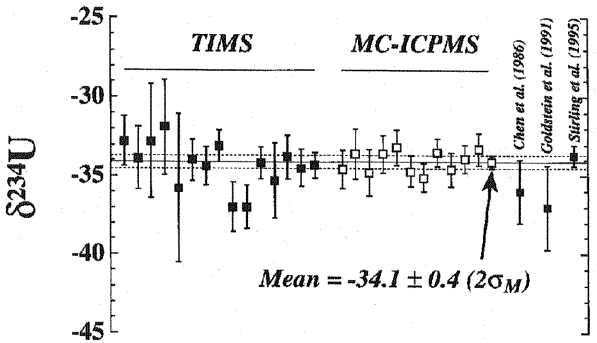

Figure 10 High-precision U isotopic compositions of NIST SRM 960, as measured by thermal ionization mass spectrometry (TIMS) and multiple-collector inductively coupled plasma mass spectrometry (MC-ICP-MS). (From Halliday et al., 1998b.)

(TML #2) is used as our in-house standard, which has been calibrated independently by Williams et al. (1992). The isotopic composition of the U standard NIST SRM-960 has been measured by both TIMS and MC-ICP-MS at U-M, and the results are presented in Fig. 8.10, along with the published TIMS results from other laboratories for comparison. The analytical precision of $^{234}U/^{238}U$ (2 σ) for a typical MC-ICP-MS analysis is about 1 δ unit, comparable to that of the best TIMS measurements; however, the external reproducibility for the MC-ICP-MS appears to be much better (Fig. 8.10). The MC-ICP-MS measurements give a mean $\delta^{234}U$ of -34.0 ± 1.1 ($2\sigma_m$) for the NIST SRM-960, which is identical to the TIMS results of -34.4 ± 2.9 ($2\sigma_m$). Our mean value of MC-ICP-MS is also consistent and among the best in terms of both internal and external precision ($2\sigma_{mean}$) compared to the data reported from other laboratories (Fig. 8.10).

To measure Th at high precision using the P54 we admix U, separated from the same sample for which the $^{234}U/^{238}U$ is already known. Each measurement cycle then involves a combination of static analyses. The $^{230}Th/^{232}Th$ ratio is measured with Daly and Faraday detectors, the predetermined $^{234}U/^{235}U$ ratio of admixed U of known isotopic composition is used to monitor the Daly/Faraday gain during the course of the analysis, and the $^{238}U/^{235}U$ ratio is measured on Faraday detectors for determining mass discrimination. The amount of time spent monitoring the drift in the gain and mass discrimination is kept small relative to the time spent measuring the Th masses. This technique relies on the assumption that the difference in Daly/Faraday gain between U and Th is negligible, as appears to be the case. Our resultant $^{230}Th/^{232}Th$ measurements of the Table Mountain Latite (TML, jar #2) are extremely precise, reproducible, and within uncertainty of previously reported data (Williams et al., 1992) (Fig. 8.11). The analytical precision is typically about 2‰ (2σ) for the MC-ICP-MS measurements, which is a factor

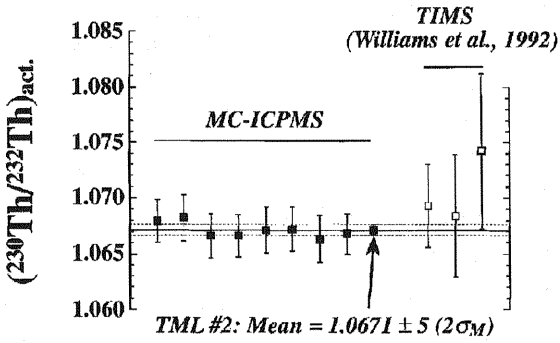

Figure 11 High-precision Th isotopic compositions (activity ratios) for the silicate rock standard Table Mountain Latite, as measured by thermal ionization mass spectrometry (TIMS) and multiple-collector inductively coupled plasma mass spectrometry (MC-ICP-MS). (From Halliday et al., 1998b.)

of 2 better than that of most Th isotopic measurements by TIMS (Fig. 8.11). Perhaps the biggest improvement is in the external precision, which is better than the internal precision, an effect not commonly observed in TIMS measurement. This is thought to be due to the simultaneous corrections for mass fractionation and relative gain between Faraday and Daly detectors during the course of the isotopic analysis.

8.4.3 Laser Ablation Lead Isotopic Measurements Using Multiple-Collector Inductively Coupled Plasma Mass Spectrometry

A number of papers have discussed the use of a Nd-YAG infrared laser with MC-ICP-MS (Walder et al., 1993a; Christensen et al., 1995; Halliday et al., 1995, 1998a; Thirlwall and Walder, 1995). MC-ICP-MS cannot be used for analyzing a very broad range of elements simultaneously by laser ablation. However, laser ablation MC-ICP-MS can provide extremely accurate isotopic ratios in situ (Table 8.2). Furthermore, elemental ratios measured in situ over a restricted mass range are more precise than is possible with ICP-MS and the opportunity exists to characterize and overcome the artifacts associated with laser ablation with greater confidence. Sample preparation is very simple, requiring only that a sample fit in the sample chamber, fall a minimum distance below the top of the sample cell, and be fairly flat. No polishing of the sample is required unless desired to observe textures better.

The Nd-YAG infrared laser beam can be focused down to ~10 μm, producing a microplasma from the sample and the carrier gas (Ar) that ablates the sample surface. The laser can be operated in two different modes with repetitive firing: high magnification that produces a pit diameter of 20–40 μm, and low

Table 2 Comparison of Isotopic Compositions Measured by Laser Ablation Multiple-Collector Inductively Coupled Plasma Mass Spectrometry and Those Measured by Other Methods

Element	Ratio	Measured	Recommended	Comments	Reference
Strontium	87/86	0.70311 ± 2	0.70312 ± 2	C241 Feldspar megacryst	Christensen et al., 1995
	87/86	0.70918 ± 2	0.70917 ± 1	Whelk carbonate	
Hafnium	178/177	1.4671 ± 5	1.4671 ± 1	Zircon megacryst	Thirlwall and Walder, 1995
Tungsten	182/183	1.8470 ± 2	1.8470 ± 1[a]	NIST SRM 611	Halliday et al.,
	184/183	2.1458 ± 6	2.1456 ± 1[a]	glass	1995
Lead	206/204	17.05 ± 2	17.05 ± 1	NIST SRM 610	Walder et al.,
	207/204	15.51 ± 2	15.51 ± 1	glass	1993a
	208/204	36.95 ± 4	36.99 ± 2		

[a]Normalization differs from that reported in Table 8.1.

magnification that produces a pit diameter of about 150–300 μm. The ablated sample material is carried directly to the plasma source by a ~1-L/min flow of Ar. The exact sample material to be ablated is observable at the time of the experiment by using a microscope on line to a camera and monitor and can be viewed with transmitted (plane or polarized) or reflected light. Two modes of sampling have been utilized with the infrared laser. One involves several laser shots lasting a few seconds in different spots on the surface (Walder et al., 1993a). The number of Pb ions detected per number of Pb atoms ablated in NIST SRM 610 glass has been shown to be as high as 1 in 450 in this mode (Walder et al., 1993a). This current *sensitivity* in ions/ppm/unit volume is comparable to that achieved with a SIMS instrument such as the sensitive high-resolution micro probe (SHRIMP) (Compston et al., 1982). The second involves continuous data acquisition from a single spot over several minutes (Halliday et al., 1995; Christensen et al., 1995). This achieves very high stability and precision because the microplasma responsible for the ablation at the sample surface is not strongly dependent on laser focusing. However, the sensitivity is worse (Christensen et al., 1995). The reason better precisions are achievable by MC-ICP-MS than by SIMS despite poorer sensitivity is that laser ablation excavates a far greater volume of material per unit time to produce an ion current that can be measured by simultaneous multiple Faraday collection.

It is necessary to remove the effects of isobaric interferences such as ^{87}Rb on ^{87}Sr, ^{144}Sm on ^{144}Nd (although ^{145}Nd could be used instead), and ^{176}Lu on ^{176}Hf accurately. It has already been shown that, because of the similarity in mass discrimination between elements of similar mass in an ICP source, the isotopic composition of Hf can be determined to high precision in a mixture of Lu and Hf, even with a Lu/Hf ratio of 0.5 (Walder et al., 1993c). Similarly, Nd isotopic composi-

tions can be determined to high precision in mixtures of Sm and Nd (Walder et al., 1993c; Halliday et al, 1995). Christensen et al. (1995) extended this approach to the analysis of Sr isotopic compositions in situ, for which it is necessary to correct for the interference of ^{87}Rb on ^{87}Sr and ^{86}Kr on ^{86}Sr. It has been clearly demonstrated that in situ laser ablation sampling and analysis with an MC-ICP-MS are capable of accurate and precise measurement of Sr isotopic compositions in geological materials (Christensen et al., 1995). The data are very reproducible and memory effects have been shown to be negligible. Similarly Halliday et al. (1995) and Thirlwall and Walder (1995) have shown that W and Hf isotopic compositions can be measured to high precision in situ with a Nd-YAG laser.

For Pb isotopic measurements the data can be corrected for mass discrimination by using Tl isotopes (masses 205 and 203) (Ketterer et al., 1991). Isobaric interferences (such as from Hg) can also be corrected for very precisely. Therefore, the Pb isotope data produced for NIST glass standards SRM 610 and 611 and acquired by using a pulsed Nd-YAG laser and MC-ICP-MS are superior in precision to SIMS results (Walder et al., 1993a). The correction for mass bias in low Tl materials may be achievable by admitting a suitable Tl compound into the source during analysis by using a dual inlet. Although most of the mass spectrum is analyzed by static multiple collection on Faraday detectors, smaller-intensity isotopes (e.g., ^{204}Pb in radiogenic Pb) can be measured on a Daly detector with ion counting. New high-precision laser ablation Pb isotopic data for NIST glasses (Christensen et al., 1997; Halliday et al., 1998a) are well within the uncertainty of previous (less precise) MC-ICP-MS, TIMS, and SIMS data (Walder et al., 1993a).

In order to acquire high-precision isotopic data, even from samples with more than 1000 ppm of the element of interest, the sample utilization with the Q-switched Nd-YAG laser operating in the infrared is at the borderline of what can be achieved with microdrilling and conventional mass spectrometry (Feldstein et al., 1994). This is because a large signal ($>10^{-12}$ A) for each isotope of interest, sustained over several minutes, is necessary to overcome the noise limitations of Faraday detectors. More recently, an ultraviolet-wavelength laser (a frequency-quadrupled Nd-YAG laser) has been used on the U-M instrument (Christensen et al., 1996, 1997; Halliday et al., 1998a). This allows much smaller spot sizes, eliminates heating of the surrounding sample, and, because of smaller particle size, produces greater ionization efficiency within the plasma. The laser can be focused down to 60 μm (a minimum of 10 μm with an aperture in place), allowing fine-scale computer-controlled rastering and very precise isotopic ratios for specific growth zones in minerals. Much of the work on unknowns should be possible using thin sections, cut slightly thicker than normal 50–100 μm). These can be separately studied using other instruments such as a petrographic microscope, an electron probe, or a fluid inclusion stage.

An ideal application of laser ablation MC-ICP-MS is the analysis of ferromanganese crusts from the ocean floor. The isotopic composition of Pb in the oceans should be sensitive to changes in ocean current patterns and sources. Fe-

Mn crusts grow slowly over millions of years, sequestering high concentrations of Pb and providing a long-term record of such changes (Christensen et al., 1997). The analysis of Fe-Mn crusts for Pb isotopic composition using laser ablation MC-ICP-MS has been employed to produce a record of Pb contributions to the central Pacific Ocean (Christensen et al., 1997).

For these analyses, the ultraviolet (UV) laser is set at a 60-μm spot size and moved by computer control to raster out a 100-μm × 150-μm area that is ~400 μm deep after 5 min of analysis. Mass fractionation of Pb isotopic ratios can be corrected by monitoring $^{203}Tl/^{205}Tl$ (there is sufficient natural Tl for this in the sample). ^{202}Hg is monitored to make a correction to mass 204. Typically the calculated ^{204}Hg signal is ~1% of the ^{204}Pb signal. Tl/Pb and U/Pb ratios can also be measured. For a single 5-min analysis, approximately 25 μg of material is ablated from the crust, representing ~30 ng of Pb.

Although very-high-quality Pb isotopic data could be obtained with careful milling and conventional analysis (Burton et al., 1997; Ling et al., 1996; Abouchami et al., 1997), once MC-ICP-MS methods are established, one is able to acquire a considerable quantity of data in just a few weeks. For the 5-min analyses, the average in-run precisions are ±0.09% for $^{206}Pb/^{204}Pb$, $^{207}Pb/^{204}Pb$, $^{208}Pb/^{204}Pb$; ±0.02% for $^{207}Pb/^{206}Pb$; and ±0.03% for $^{208}Pb/^{206}Pb$ and compare well with those of conventional analyses. For longer analysis times, better precisions can be achieved, but with some loss of spatial resolution.

Prior to making such measurements the P54 is tuned, using a desolvating nebulizer with a solution of NIST SRM 981 Pb and Tl. The quality of the laser ablation measurements is then checked by analyzing NIST SRM 611 glass. This operation is facilitated with a dual-inlet system, allowing for rapid switching from nebulizer to laser without shutting down the plasma, which may affect the mass spectrometer focal parameters.

The variations in $^{207}Pb/^{206}Pb$ and $^{208}Pb/^{206}Pb$ along the traverses are displayed in a stacked series of diagrams for two Pacific Fe-Mn crusts in Fig. 8.12. Also shown are the results of the conventional Pb isotopic analyses for one. There is very good agreement between the two methods. During analysis of the traverse, some previously analyzed stratigraphic positions were replicated (Fig. 8.12). One can also return to intermediate positions and produce analyses that are consistent with the adjacent analyses. Day-to-day reproducibility has also been demonstrated. There are resolvable spatial variations in Pb isotopic composition along the traverse that are especially striking for $^{207}Pb/^{206}Pb$ and $^{208}Pb/^{206}Pb$ (Fig. 8.12).

Using the ^{10}Be linear growth rates for these crusts (Ling et al., 1996), the variations can be "remapped" as a Pb isotope stratigraphy (Fig. 8.13). Also shown are the $\delta^{18}O$ values of benthic foraminifera (Miller et al., 1987) and the sea-level curve (Haq et al., 1987). It can be seen that over much of the period the temperature record is matched by changes in $\delta^{18}O$. We are still at the early stages of acquiring extensive amounts of such data for the world's oceans, but the signal is suf-

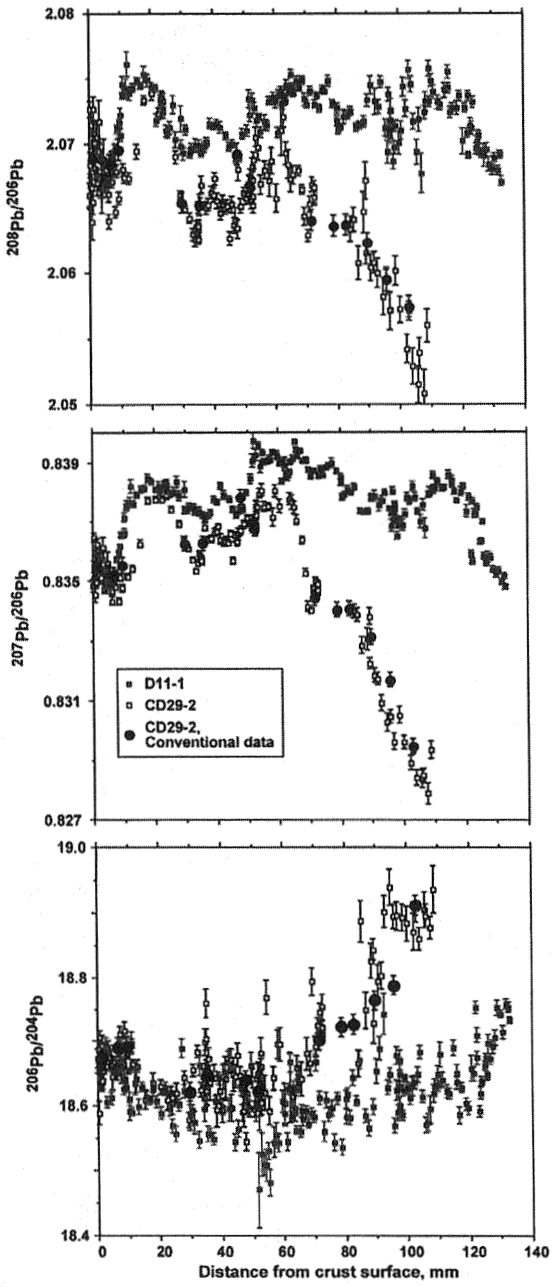

Figure 12 Lead isotopic compositions of two central Pacific Fe-Mn crusts as a function of depth. (From Christensen et al., 1997.)

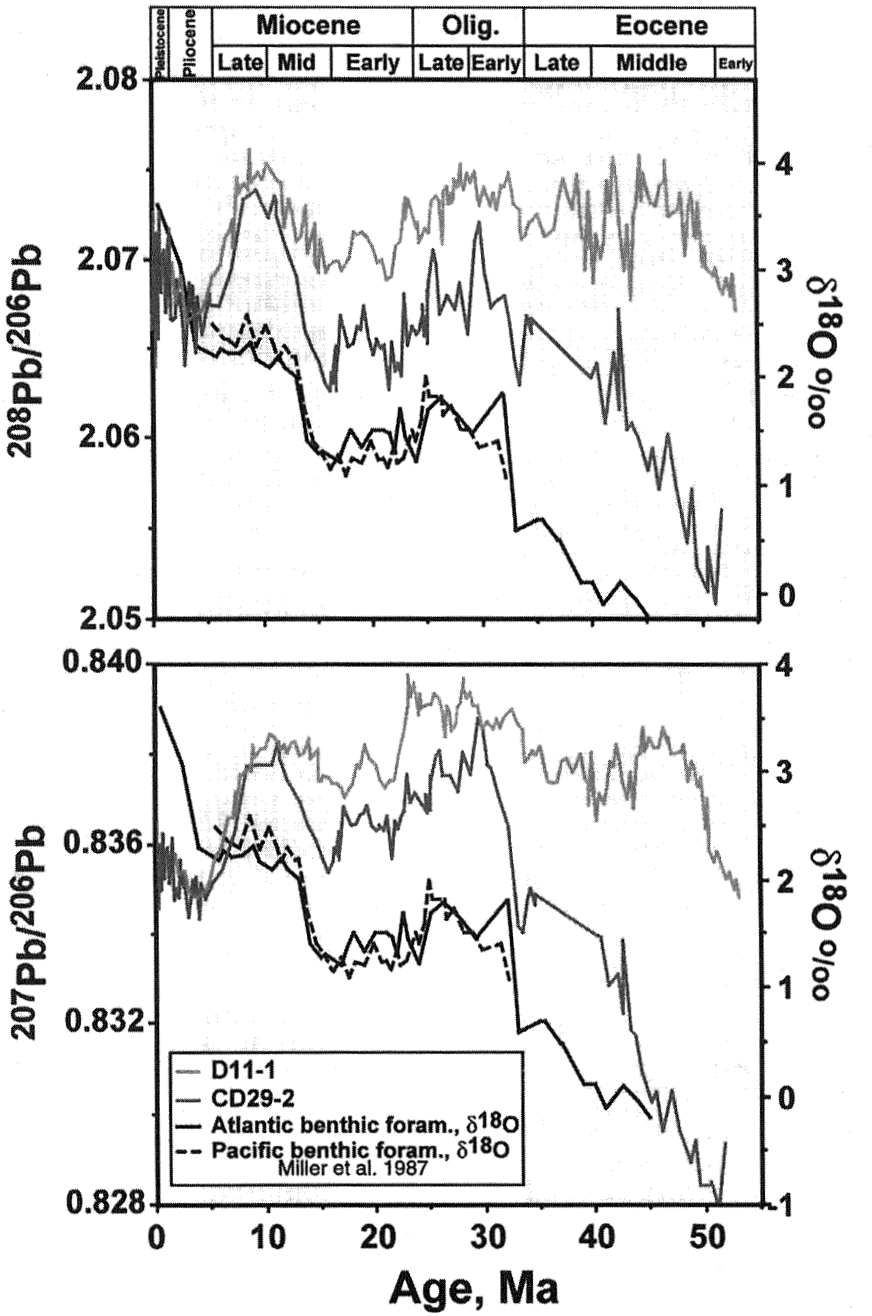

Figure 13 Lead isotopic compositions from Fig. 12 mapped onto an absolute time scale by using ^{10}Be growth rates. (From Christensen et al., 1997.)

ficiently clear and intriguing that it is evident that monitoring the source of Pb with this approach is providing information about changes in ocean circulation that are related to climate change, although not necessarily in a simple manner (Christensen et al., 1997).

The most difficult aspect of laser ablation MC-ICP-MS is the precise measurement of trace element ratios, such as parent/daughter ratios for geochronology in situ, at the same time as the isotopic compositions are determined. Although the P54 is ideally suited for measuring U/Pb, Rb/Sr, Sm/Nd, and Lu/Hf ratios at the same time as Pb, Sr, Nd, and Hf isotopic compositions are determined, and analytical artifacts can be evaluated more easily than with ICP-MS, it is important to characterize fractionation effects generated in both the plasma and the laser ablation process. Obviously, solution aspiration may introduce its own artifacts relative to laser ablation, but demonstrating that the trace element ratio of an unknown can be predicted to high precision by comparison with a solution of known composition, when run under the same conditions, is an important prerequisite to deconvolving artifacts from matrix effects and laser ablation fractionation. We have assessed Rb/Sr and U/Pb measurements in solution without isotope dilution, with this in mind (Halliday et al., 1995). The results convincingly demonstrate that, in the case of simple solutions, the U/Pb and Rb/Sr ratios of an unknown can be determined from the measured/true ratio of a known. Hence, in situ microsampling with the simultaneous measurement of both Pb isotopic composition and U/Pb may be possible by comparing with a standard of known U/Pb, without even a mass bias correction, if matrix effects from the laser ablation and plasma can be minimized or corrected for.

As a follow-up to these experiments, the U/Pb ratios have been measured by using MC-ICP-MS NIST glasses with Nd-YAG infrared and ultraviolet lasers (Halliday et al., 1998a). U/Pb ratios can be measured to within 1% by reference to a standard in at least some simple solutions (Halliday et al., 1995). However, laser ablation analyses with the Nd-YAG laser in infrared mode yield measured/true values that are significantly different from unity and from each other (Halliday et al., 1998a). Therefore, there appear to be significant matrix effects in the infrared laser ablation process. The results for performing the same experiments using frequency quadrupled Nd-YAG in the ultraviolet are more successful. The measured/true ratios are very similar for the two glasses (Halliday et al., 1998a). These results are extremely encouraging and suggest that it will be possible to measure U/Pb ratios with reasonable accuracy in unknowns by comparison with the result for a known.

Although the laser ablation technique is powerful, the extent of the contributions that these methods will make will depend on the degree of success achieved with improvements in transmission and sensitivity. The sensitivity of the P54 for Pb in solution mode is about 0.2%. The best sensitivity achieved with the UV laser at U-M is about 0.1%. However, the sensitivity for Pb in solution and laser ablation mode using some of the more recent instruments is already reported to be ~1%.

Use of a UV laser system at this scale of sensitivity may allow experiments to be conducted directly on thin section material with a far greater spatial resolution (~10 μm) and sample usage (lower ablation rate and more ions/ppm/unit volume ablated). Computer controlled rastering along growth zones in phenocrysts should then be feasible.

REFERENCES

Abouchami, W., Goldstein, S.L., Galer, S.J.G., Eisenhuer, A., and Mangini, A. (1997) Secular changes of lead and neodymium in central Pacific seawater recorded by a Fe-Mn crust. Geochim. Cosmochim. Acta 61, 3957–3974.

Ballentine, C. J., Lee, D-C., and Halliday, A. N. (1997) Hafnium isotopic studies of the Cameroon line and new HIMU paradoxes. Chem. Geol. Hofmann Volume, 139, 111–124.

Bard, E., Hamelin, B., Fairbanks, R. G., and Zindler, A. (1990) Calibration of ^{14}C timescale over the past 300,000 years using mass spectrometric U-Th ages from Barbados corals. Nature 345, 405–410.

Begley, I.S., and Sharp, B.L. (1994) Occurrence and reduction of noise in inductively coupled plasma mass spectrometry for enhanced precision in isotope ratio measurement. J. Anal. Atomic Spectrom. 9, 171–176.

Belshaw, N.S., Freedman, P.A., O'Nions, R.K., Frank, M., and Guo, Y. (1998) A new variable dispersion double-focussing plasma mass spectrometer with performance illustrated for lead-isotopes. Int. J. Mass Spec. Ion Process, 181, 51–58.

Birck, J.-L., and Allègre, C. J. (1988) Manganese-chromium isotope systematics and the developement of the early solar system. Nature 331, 579–584.

Blichert-Toft, J., and Albarède, F. (1997) The Lu-Hf isotope geochemistry of chondrites and the evolution of the mantle-crust system. Earth Planet Sci. Lett. 148, 243–258.

Blichert-Toft, J., Chauvel, C., and Albarède, F. (1997) Separation of Hf and Lu for high-precision isotope analysis of rock samples by magnetic sector-multiple collector ICP-MS. Contrib. Mineral. Petrol. 127, 248–260

Blichert-Toft, J., Luais, B., Maréchal, C., and Albarède, F. (1996) Progress report on the magnetic-sector ICP-MS (Plasma 54). Abstr. Goldschmidt Conference, 65.

Bradshaw, N., Hall, E. F. H., and Sanderson, N.E. (1989) Inductively coupled plasma as an ion source for high resolution mass spectrometry. J. Anal. Atomic Spectrom. 4, 801–803.

Broadhead, M., Broadhead, R., and Hager, J.W. (1990) Laser sampling ICP-MS: semi-quantitative determination of sixty-six elements in geological samples. Atomic Spectroscopy 11, 205–209.

Burton, K.W., Ling, H.-F., and O'Nions, R.K. (1997) Closure of the Central American isthmus and its effect on deep-water formation in the North Atlantic. Nature 386, 382–385.

Cameron, A.G.W., and Benz, W. (1991) Origin of the Moon and the single impact hypothesis IV. Icarus 92, 204–216.

Carlson, R. W., and Lugmair, G. W. (1988) The age of ferroan anorthosite 60025: oldest crust on a young Moon? Earth Planet. Sci. Lett. 90, 119–130.

Chen, J.H., Edwards, R.L., and Wasserburg, G.J. (1986) ^{238}U, ^{234}U and ^{232}Th in seawater. Earth Planet. Sci. Lett. 80, 241–251.

Christensen, J.N., Halliday, A.N., Lee, D-C., and Hall, C.M. (1995) In situ Sr isotopic analyses by laser ablation: Earth Planet. Sci. Lett. 136, 79–85.

Christensen, J.N., Halliday, A.N., Godfrey, L.V., and Hein, J.R. (1996) The lead isotopic record of a central Pacific Fe-Mn crust, in situ measurement by laser ablation. MC-ICPMS Trans. Amer. Geophys. Un. 77, F323.

Christensen, J.N., Halliday, A.N., Godfrey, L.V., Hein, J.R., and Rea, D.K. (1997) Climate and ocean dynamics and the lead isotopic records in Pacific ferromanganese crusts. Science 277, 913–918.

Cohen, A.S., Belshaw, N.S., and O'Nions, R.K. (1992) High precision uranium, thorium and radium isotope ratio measurements by high dynamic range thermal ionization mass spectrometry. Int. J. Mass Spectro. Ion Proc. 116, 71–81.

Cohen, A.S., and O'Nions, R.K. (1993) Melting rates beneath Hawaii: evidence from uranium series isotopes in recent lavas. Earth Planet. Sci. Lett. 120, 169–175.

Compston, W., Williams, I.S., and Clemens, S.W. (1982) U-Pb ages within single zircons using a sensitive high mass resolution ion microprobe. Abstr. 30th Ann. Conf. Am. Assoc. Mass Spectrom. 593–595.

Condomines, M., Hemond, C., and Allègre, C.J. (1988) U-Th-Ra radioactive disequilibria and magmatic processes. Earth Planet. Sci. Lett. 90, 243–262.

Date, A.R., Cheung, Y.Y., and Stuart, M.E. (1987) The influence of polyatomic ion interferences in analysis by inductively coupled plasma source mass spectrometry (ICP-MS). Spectrochimica Acta, 42B, 3–20.

Date, A.R., and Gray, A.L. (1989) Applications of Inductively Coupled Plasma Mass Spectrometry. Chapman & Hall, New York.

Edwards, R.L., Chen, J.H., and Wasserburg, G.J. (1987) ^{238}U-^{234}U-^{230}Th-^{232}Th systematics and the precise measurement of time over the past 500,000 years. Earth Planet. Sci. Lett. 81, 175–192.

Feldstein, S. N., Halliday, A.N., Davies, G.R., and Hall, C.M. (1994) Isotope and chemical microsampling: constraints on the history of an S-type rhyolite, San Vincenzo, Tuscany, Italy. Geochim. Cosmochim. Acta 58, 943–958.

Furutu, N.J. (1991) Optimization of the mass scanning rate for the determination of lead isotope ratios using an inductively coupled plasma mass spectrometer: J. Anal. Atomic Spectrom. 6, 199–203.

Galer, S.J.G., and Goldstein, S.L. (1996) Influence of accretion on lead in the Earth. In: Isotopic Studies of Crust-Mantle Evolution, A.R. Basu and S.R. Hart, eds., 75–98. *American Geophysical Union* (AGU), Washington D.C.

Galer, S. J. G., and Lugmair, G. W. (1996) Lead isotope systematics of noncumulate eucrites. Meteorit. Planet. Sci. 31 (Suppl.), A47–A48.

Godfrey, L.V., Lee, D.-C., Halliday, A.N., Hein, J.R., Salters, V.J.M., and White, W.M. (1996) Hafnium isotope ratios in ferromanganese deposits: a record of ε_{Hf} in seawater? Trans. Amer. Geophys. Un., 77, F323.

Godfrey, L.V., Lee, D-C., Sangrey, W.F., Halliday, A.N., Salters, V.J.M., Hein, J. R., and White, W.M. (1997) The Hf isotopic composition of ferromanganese nodules and

crusts and hydrothermal manganese deposits: Implications for seawater Hf. Earth Planet. Sci. Lett. 151, 91–105.

Gray, A.R., and Williams, J.G. (1987) Oxide and doubly charged ion response of a commercial inductively coupled plasma mass spectrometry instrument. J. Anal. Atomic Spectrom. 2, 81–82.

Halliday, A.N., Christensen, J.N., Jones, C.E., Walder, A.J., and Freedman, P.A. (1993) Precise measurement of parent/daughter ratios and time with an ICP magnetic sector multi collector mass spectrometer equipped with a wide flight tube. Trans. Amer. Geophys. Un. 74, 626–627.

Halliday, A.N., Christensen, J.N., Lee, D-C., Hall, C.M., Ballentine, C.J., Rehkämper, M., Yi, W., Luo, X., and Barfod, D. (1998a) ICP multiple collector mass spectrometry and in situ high precision isotopic analysis. In: Applications of Microanalytical Techniques to Understanding Mineralizing Processes, M.A. McKibben, W.C.P. Shanks, and W.I. Ridley, eds. Reviews in Economic Geology 7, Society of Economic Geologists, 37–51.

Halliday, A.N., Lee, D-C., Christensen, J.N., Rehkämper, M., Yi, W., Luo, X., Hall, C., Ballentine, C.J., Pettke, T., and Stirling, C. (1998b) Applications of multiple collector ICPMS to cosmochemistry, geochemistry and paleoceanography. Geochim. Cosmochim. Acta 62 919–940.

Halliday, A.N., Lee, D-C., Christensen, J.N., Walder, A.J., Freedman, P.A., Jones, C.E., Hall, C.M., Yi, W., and Teagle, D. (1995) Recent developments in inductively coupled plasma magnetic sector multiple collector mass spectrometry. Int. J. Mass Spec. Ion Process. 146/147, 21–33.

Halliday, A.N., Rehkämper, M., Lee, D-C., and Yi, W. (1996) Early evolution of the Earth and Moon: new constraints from Hf-W isotope geochemistry. Earth Planet. Sci. Lett. 142, 75–89.

Haq, B.U., Hardenbol, J., and Vail, P.R. (1987) Chronology of fluctuating sea levels since the Triassic. Science 235, 1156–1167.

Harper, C. L., and Jacobsen, S. B. (1996) Evidence for ^{182}Hf in the early solar system and constraints on the timscale of terrestrial core formation. Geochim. Cosmochim. Acta 60, 1131–1153.

Harper, C. L., Völkening, J., Heumann, K. G., Shih, C.-Y., and Wiesmann, H. (1991a) ^{182}Hf-^{182}W: new cosmochronometric constraints on terrestrial accretion, core formation, the astrophysical site of the r-process, and the origin of the solar system. Lunar Planet. Sci. XXII, 515–516.

Hirata, T. (1996) Lead isotopic analyses of NIST standard reference materials using multiple collector inductively coupled plasma mass spectrometry with a modified external correction method for mass discrimination effect. Analyst 121, 1407–1411.

Hirata, T. (1997) Isotopic variations of germanium for iron and stony iron meteorites. Geochim. Cosmochim. Acta 61, 4439–4448.

Hirata, T., and Nesbitt, R.W. (1995) U-Pb isotope geochronology of zircon: Evaluation of the laser probe-inductively coupled plasma mass spectrometry technique. Geochim. Cosmochim. Acta 59, 2491–2500.

Ivanovich, M., and Harmon, R.S. (1992) Uranium-Series Disequlibrium: Applications to Earth, Marine, and Environmental Sciences. Oxford University Press, New York.

Iwamori, H. (1994) ^{238}U-^{230}Th-^{226}Ra and ^{235}U-^{231}Pa disequilibria produced by mantle melting with porous and channel flows. Earth Planet. Sci. Lett. 125, 1–16.

Jacobsen, S. B., and Harper, C. L., Jr. (1996). Accretion and early differentiation history of the Earth based on extinct radionuclides. In Earth Processes: Reading the Isotope Code, A. Basu and S. Hart, eds. Pp. 47–74. American Geophysical Union, Washington D.C.

Kelly, W. R., and Wasserburg, G. J. (1978). Evidence for the existence of ^{107}Pd in the early solar system. Geophys. Res. Lett. 5, 1079–1082.

Ketterer, M.E. (1992) Assessment of overall accuracy of lead isotope ratios determined by inductively coupled plasma mass spectrometry using batch quality control and the Youden two-sample method. J. Anal. Atomic Spectrom. 7, 1125–1129.

Ketterer, M.E., Peters, M.J., and Tisdale, P.J. (1991) Verification of a correction procedure for measurement of lead isotope ratios by inductively coupled plasma mass spectrometry. J. Anal. Atomic Spectrom. 6, 439–443.

Lee, D.-C., and Halliday, A.N. (1995a) Precise determinations of the isotopic compositions and atomic weights of molybdenum, tellurium, tin and tungsten using ICP source magnetic sector multiple collector mass spectrometry. Int. J. Mass Spec. Ion Process. 146/147, 35–46.

Lee, D.-C., and Halliday, A.N. (1995b) Hafnium-tungsten chronometry and the timing of terrestrial core formation. Nature 378, 771–774.

Lee, D.-C., and Halliday, A.N. (1996) Hf-W isotopic evidence for rapid accretion and differentiation in the early solar system. Science 274, 1876–1879.

Lee, D.-C., and Halliday, A.N. (1997) Core formation on Mars and differentiated asteroids. Nature 388, 854–857.

Lee, D.-C., and Halliday, A.N. (1998) Tungsten isotopes, the initial ^{182}Hf/^{180}Hf of the solar system and the origin of enstatite chondrites. Mineral. Mag. 62A, 868–869.

Lee, D.-C., Halliday, A.N., Snyder, G.A., and Taylor, L.A. (1997) Age and origin of the Moon. Science 278, 1098–1103.

Lee, T., Papanastassiou, D. A., and Wasserburg, G. J. (1977) Al-26 in the early solar system: fossil or fuel? Ap. J. 211, L107–110.

Ling, H.-F., O'Nions, R.K., Burton, K.W., Kamber, B.S., Belshaw, N.S., and Gibb, A. (1996) Nd and Pb isotope history of central Pacific seawater. Goldschmidt Conf. 6, 301.

Longerich, H.P. (1989) The effect of nitric acid, acetic acid and ethanol on inductively coupled plasma-mass spectrometric ion signals as a function of nebulizer gas flow, with implications on matrix suppression and enhancements. J. Anal. Atomic Spectroscopy 4, 665–677.

Luais, B., Telouk, P., and Albarède F. (1997) Precise and accurate neodymium isotopic measurements by plasma-source mass spectrometry. Geochim. Cosmochim. Acta 61, 4847–4854.

Ludwig, K.R., Simmons, K.R., Szabo, B.J., Winograd, I.J., Landwehr, J.M., Riggs, A.C. and Hoffman, R.J. (1992) Mass-spectrometric ^{230}Th-^{234}U-^{238}U dating of the Devils Hole calcite vein. Science 258, 284 –287.

Lugmair, G. W., and Galer, S. J. G. (1989) Isotopic evolution and age of angrite LEW 86010. Meteoritics 24, 140.

Lugmair, G.W., and Galer, S.J.G. (1992) Age and isotopic relationships between the angrites Lewis Cliff 86010 and Angra dos Reis, Geochim. Cosmochim. Acta 56, 1673–1694.

Lugmair, G.W., MacIsaac, C., and Shukolyukov, A. (1994) Small time differences in differentiated meteorites recorded by the ^{53}Mn-^{53}Cr chronometer. Lunar Planet. Sci. XXV, 813–814.

Luo, X., Lee, D.-C., Rehkämper, M., and Halliday, A. N. (1996) High precision Th isotopic measurements by energy-filtered multiple collector ICP mass spectrometry. Trans. Amer. Geophys. Un. 77, F774.

Luo, X., Rehkämper, M., Lee, D-C., and Halliday, A. N. (1997) High precision $^{230}Th/^{232}Th$ and $^{234}U/^{238}U$ measurements using energy-filtered ICP magnetic sector multiple collector mass spectrometry. Int. J. Mass Spectrom. Ion Proc. 171, 105 –117.

Marèchal, C.N., Albarède, F., and Emmanuel, N. (1997) Natural variations in copper and zinc isotopic compositions. In Seventh Annual V.M. Goldschmidt Conference, 131–132, LPI Contribution No. 921, Lunar and Planetary Institute Houston.

Marshall, J., and Franks, J. (1990) Multielement analysis and reduction of spectral interferences using electrothermal vaporization inductively coupled plasma-mass spectrometry. Atomic Spectroscopy 11, 177–186.

McKenzie, D.P. (1985) ^{230}Th-^{238}U disequilibrium and the melting processes beneath ridge axes. Earth Planet. Sci. Lett. 72, 149–157.

Miller, K.G., Fairbanks, R.G., and Mountain, G.S. (1987) Tertiary oxygen isotope synthesis, sea level history, and continental margin erosion. Paleoceanography 2, 1–19.

Nash, W.P. Perkins, M.E., Christensen, J.N., Lee, D-C., and Halliday, A.N. (1996) Temporal variation in $^{143}Nd/^{144}Nd$ and $^{176}HF/^{177}Hf$ in silicic magmas of the Yellowstone hotspot. Trans. Amer. Geophys. Un. 77, F823.

Newsom, H.E., Sims, K.W.W., Noll, P.D., Jr., Jaeger, W.L., Maehr, S.A., and Bessera, T.B. (1996) The depletion of W in the bulk silicate Earth. Geochim. Cosmochim. Acta 60, 1155–1169.

Palacz, Z.A., Haines, C.H., and Turner, P.J. (1996) Performance of a new design of Faraday cup. Abstr. Todai Internat. Symp. Cosmochemistry and Isotope Geochemistry, Tokyo, 194.

Patchett, P.J. (1983) Importance of the Lu-Hf isotope system in studies of planetary chronology and chemical evolution. Geochim. Cosmochim. Acta 47, 81–91.

Qin, Z. (1993) Dynamics of melt generation beneath mid-ocean ridge axes: Theoretical analysis based on ^{238}U-^{230}Th- ^{226}Ra and ^{235}U-^{231}Pa disequilibria. Geochim. Cosmochim. Acta 57, 1629–1643.

Rehkämper, M., and Halliday, A. N. (1997) Separation of Pt, Ir, Pd and other siderophile elements from geological samples with application to trace element geochemistry. Talanta 44, 663–672.

Rehkämper, M., and Halliday, A. N. (1998) Accuracy and long- term reproducibility of lead isotopic measurements by MC-ICPMS using an external method for correction of mass discrimination. Int. J. Mass Spec. Ion Proc., 181, 123–133.

Rehkämper, M., and Halliday, A. N. (1999) The precise measurement of Tl isotopic compositions by MC-ICPMS: application to the analysis of geological materials and meteorites. Geochim. Cosmochim. Acta, 69, 935–944.

Rehkämper, M., Halliday, A. N., Barfod, D., Fitton, J.G., and Dawson, J.B. (1997a) Platinum group element abundance patterns in different mantle environments. Science 278, 1595–1598.

Rehkämper, M., Halliday, A. N., and Wentz, R. F. (1997b) Low blank digestion of geological samples for platinum group element analysis using a modified Carius Tube design. Fresenius J. Anal. Chem. 361, 217–219.

Reynolds, J. H. (1960) Determination of the age of the elements. Phys. Rev. Lett. 4, 8.

Ross, B.S., and Hieftje, G.M. (1991) Alteration of the ion-optic lens configuration to eliminate mass-dependent matrix interference effects in inductively coupled plasma-mass spectrometry: Spectrochim. Acta 46B, 1263–1273.

Russ, G.P. III, and Bazan, J.M. (1987) Isotopic ratio measurements with an inductively coupled plasma source mass spectrometer. Spectrochim. Acta 42B, 49–62.

Shih, C.-Y., Nyquist, L. E., Dasch, E. J., Bogard, D. D., Bansal, B. M., and Wiesmann, H. (1993). Age of pristine noritic clasts from lunar breccias 15445 and 15455. Geochim. Cosmochim. Acta 57, 915–931.

Shukolyukov, A., and Lugmair, G. W. (1992). First evidence for live ^{60}Fe in the early solar system. Lunar Planet. Sci. XXIII, 1295–1296.

Shukolyukov, A., and Lugmair, G. W. (1993a). ^{63}Fe in eucrites. Earth Planet. Sci. Lett. 119, 159–166.

Shukolyukov, A., and Lugmair, G. W. (1993b). Live iron-60 in the early solar system. Science 259, 1138–1142.

Spiegelman, M., and Elliott, T. (1993) Consequences of melt transport for uranium series disequilibrium in young lavas. Earth Planet. Sci. Lett. 118, 1–20.

Stirling, C.H., Esat, T.M., McCulloch, M.T., and Lambeck, K. (1995) High-precision U-series dating of corals from Western Australia and implications for the timing and duration of the last interglacial. Earth Planet. Sci. Lett. 135, 115–130.

Szabo, I. (1986) New ion optical devices utilizing oscillatory electric fields: principle of operation and analytical theory of multipole devices with two dimensional electric fields. Int. J. Mass Spectrom. Ion Process. 73, 197–235.

Taylor, P. D. P., De Bièvre, P., Walder, A. J., and Entwistle, A. (1995). Validation of the analytical linearity and mass discrimination correction model exhibited by a multiple collector inductively coupled plasma mass spectrometer by means of a set of synthetic uranium isotope mixtures. J. Anal. Atomic Spectrom. 10, 395–398.

Thirlwall, M.F., and Walder, A.J. (1995) In situ hafnium isotope ratio analysis of zircon by inductively coupled plasma multiple collector mass spectrometry. Chem. Geol. 122, 241–247.

Todt, W., Cliff, R. A., Hanser, A., and Hofmann, A. W. (1996) Evaluation of a ^{202}Pb-^{205}Pb double spike for high- precision lead isotope analysis. In Earth Processes: Reading the Isotope Code, A. R. Basu and S. R. Hart, eds., pp. 429–437. American Geophysical Union, Washington D.C.

Treiman, A. H., Drake, M. J., Janssens, M.-J., Wolf, R., and Ebihara, M. (1986) Core formation in the Earth and Shergotite Parent Body (SPB): chemical evidence from basalts. Geochim. Cosmochim. Acta 50, 1071–1091.

Vdovenko, V.M., and Dubasov, Y.V. (1974) The analytical chemistry of radium. Wiley, New York.

Vervoort, J.D., Blichert-Toft, J., Patchett, P.J., and Albarède, F. (1997) Hafnium-neodymium isotopic composition of the crust and mantle through time: new directions with hafnium whole rock studies. In Seventh Annual V.M. Goldschmidt Conference, 212, LPI Contribution No. 921, Lunar and Planetary Institute Houston.

Völkening, J., Köppe, M., and Heumann, K. G. (1991). Tungsten isotope ratio determinations by negative thermal ionization mass spectrometry. Int. J. Mass Spec. Ion. Proc. 107, 361–368.

Wadhwa, M., and Lugmair, G. W. (1996). Age of the eucrite "Caldera" from convergence

of long-lived and short-lived chronometers. Geochim. Cosmochim. Acta 60, 4889–4893.

Walder, A. J., Abell, I. D., Platzner, I., and Freedman, P. A. (1993a). Lead isotope ratio measurement of NIST 610 glass by laser ablation inductively coupled plasma spectrometry. Spectrochim. Acta 48B, 397–402.

Walder, A. J., and Freedman, P. A. (1992) Isotopic ratio measurement using a double focusing magnetic sector mass analyzer with an inductively coupled plasma as an ion source. J. Anal. Atomic Spect. 7, 571–575.

Walder, A. J., and Furuta, N. (1993) High precision lead isotope ratio measurement by inductively coupled plasma multiple collector mass spectrometry. Anal. Sci. 9, 675–680.

Walder, A. J., Koller, D., Reed, N. M., Hutton, R. C., and Freedman, P. A. (1993b). Isotope ratio measurement by inductively coupled plasma multiple collector mass spectrometry incorporating a high efficiency nebulization system. J. Anal. Atomic Spec. 8, 1037–1041.

Walder, A. J., Platzner, I., and Freedman, P. A. (1993c). Isotope ratio measurement of Pb, Nd and Sm/Nd mixtures, Hf and Lu/Hf mixtures with a double focusing multiple collector I.C.P.-MS. J. Anal. Atomic Spec. 8, 19–23.

Walsh, J.N. (1992) Use of multiple internal standards for high-precision, routine analysis of geological samples by inductively coupled plasma-atomic emission spectrometry. Chem. Geol. 95, 113–121.

Williams, J.G., and Gray, A.L. (1988) High dissolved solids and ICP-MS: are they compatible? Anal. Proc. 25, 385–388.

Williams, R.W., Collerson, K.D., Gill, J.B., and Deniel, C. (1992) High Th/U ratios in subcontinental lithospheric mantle: mass spectrometric measurement of Th isotopes in Gaussberg lamproites. Earth Planet. Sci. Lett. 111, 257–266.

Yi, W., Halliday, A. N., Langmuir, C., Garcia, M., and White, W.M. (1996) Tellurium and cadmium in MORB and OIB and volatile chalcophile element fractionation in the Earth. Trans. Amer. Geophys. Un. 77, F810.

Yi, W., Halliday, A.N., Lee, D-C., and Christensen, J.N. (1995), Indium and tin in basalts, sulfides and the mantle. Geochim. Cosmochim. Acta 24, 5081–5090.

Yi, W., Halliday, A. N., Lee, D-C., and Rehkämper, M. (1998) Precise determination of cadmium, indium and tellurium using multiple collector ICP-MS. Geostandards Newslett. 22, 173–179.

9

Ion Traps and Their Application to Elemental Analysis

Douglas C. Duckworth
Oak Ridge National Laboratory
Oak Ridge, Tennessee

John R. Eyler and Clifford H. Watson
University of Florida
Gainesville, Florida

9.1 INTRODUCTION

Elemental mass spectrometry has undergone a major expansion in the past 15–20 years. Many new developments in sample introduction systems, ionization sources, and mass analyzers have been realized. A vast array of hybrid combinations of these has resulted from specific analytical needs such as improved detection limits, precision, accuracy, elemental coverage, ease of use, throughput, and sample size. As can be seen from most of the other chapters in this volume, however, the mass analyzers used to date have primarily been magnetic sector and quadrupole mass spectrometers. Ion trapping devices, be they quadrupole ion (Paul) [1] traps or Fourier transform ion cyclotron resonance (Penning) traps, have been used quite sparingly and most work to date has concentrated on proof of principal experiments rather that actual applications.

Many features of ion trapping mass spectrometers (MS) make them arguably the analysis method of choice for coupling to elemental ion sources. This chapter discusses the unique characteristics of both Paul and Penning traps, giving examples of experiments in which these characteristics have been applied with advantage to the mass analysis of ions produced from a variety of elemental ion sources. It also acknowledges some of the inherent analytical limitations of these devices and presents means of dealing with them. For clarity of presentation, we have cho-

sen to divide the chapter into two parts, discussing first Paul traps and then Penning traps.

9.2 QUADRUPOLE ION TRAPS

The application of quadrupole ion traps as mass analyzers in elemental mass spectrometry, although still in its infancy, has already shown great promise. The interest in these devices has arisen largely from their application to organic analysis, in which they have been successfully used as mass analyzers and tandem mass spectrometers for gas [2] and liquid [3] chromatography. Of particular interest to elemental mass spectrometrists are the efficient tandem mass spectrometric (MS/MS) capabilities, viz., collision-induced dissociation and chemical reactions, for dealing with mass spectral interferences. The potential for high mass resolution, the promise of more sensitive detection, and the possibility of reduction of instrument size are also intriguing aspects of this unique analyzer. To date, several of these objectives have been realized, and some unforeseen benefits have resulted as well.

The objectives here are to familiarize the reader with basic fundamentals of quadrupole ion trap operation, as related to elemental analysis, and to present some of the advantages and limitations realized to date. At this early stage of application to atomic mass spectrometry, there are notable limitations that must be addressed; they are primarily due to the finite ion storage capacity of the trap, the effects of higher-order fields (common in the so-called stretched ion trap used in commercial systems), and parametrically dependent nonuniform trapping efficiencies (i.e., differing well depths as a function of m/z, and both the frequency and amplitude of trapping potential). These limitations can affect dynamic range, precision, MS/MS efficiency, and both absolute and abundance sensitivities. For more in-depth treatment of quadrupole ion trap history, operation, and applications, the reader is referred to several books and reviews [4–10].

Quadrupole ion traps, also known as *Paul traps* or *three-dimensional quadrupole traps*, employ quadrupolar electric fields to trap ions in a volume defined by the electrode geometries. The most common geometrical configuration of the quadrupole ion trap, shown in Fig. 9.1a, comprises a ring and two endcap electrodes with hyperbolic surfaces. In most cases the endcaps are grounded and a radio frequency (rf) (usually about 1 MHz) voltage is applied to the ring electrode. When this rf potential is applied to the ring electrode, a quadrupolar (saddle-shaped) field results, as shown in Fig. 9.1b–c. The alternating potential on the ring electrode causes the quadrupole field to invert at a frequency corresponding to the drive frequency on the ring electrode. When the V_{rf} is negative, positive ions are drawn toward the ring electrode and away from the endcaps. Alternatively, a positive V_{rf} results in the opposing motion, effectively trapping the ions.

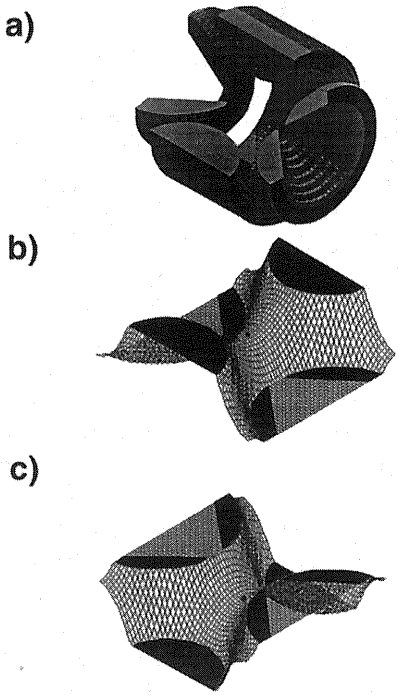

Figure 1 Schematic representation of a quadrupole ion trap showing (a) a cut-away view of the three-dimensional quadrupole ion trap, including two endcap electrodes and the ring electrode, and the (b) positive and (c) negative extremes of the quadrupolar field, alternating as a function of the radio frequency (rf) potential applied to the ring electrode.

A wide range of *m/z* values can be stored in a trap under a given set of conditions (trapping frequency and amplitude and electrode geometry). The low mass limit is defined by

$$\left(\frac{m}{z}\right)_{\min} = \frac{4.44V}{(r_0^2\Omega^2)} \tag{9.1}$$

where V is the amplitude of the trapping potential applied to the ring electrode, Ω is the angular frequency of the oscillating trapping potential, and r_0 is the inscribed radius of the ring electrode. The low mass cutoff is sharply defined, and ions with *m/z* values below it strike the endcap electrodes or are ejected through holes therein. This process is called *mass selective instability*. Thus ions can be scanned out of the trap and detected via a multiplier positioned at an endcap electrode. The upper

mass range is not well defined and depends on the well depth of the trapping potential, which is inversely related to mass. It is generally of little consequence to elemental mass analysis.

The obvious benefit of the quadrupole ion trap is that it is an ion storage device. Therefore, ions can be both accumulated and stored for extended periods. Accumulation can occur over a continuous ionization event or over multiple pulsed ionization periods. When used with pulsed ionization sources, duty cycle, defined in terms of sample utilization, can be as high as 100%. Because a broad range of atomic ions can be stored simultaneously, the quadrupole ion trap is a promising analyzer for transient peak analysis.

Another possible benefit of ion accumulation over extended ionization periods is improved sensitivity for trace elements. This requires that the analyte be selectively accumulated and that trapping efficiencies exceed losses due to scattering and chemical reactions. Although dependent on dimensions and operating parameters, the absolute storage capacity of the quadrupole ion trap is estimated to be approximately 10^6 ions for commercial devices [4]. In practice, however, the storage capacity that results in favorable intensity and mass resolution is ~10^4 ions; beyond this limit the effects of space charge on trapping efficiency and peak shape become detrimental. In the presence of a high concentration of plasma gas ions, such as Ar^+ in inductively coupled plasma (ICP) or glow discharge (GD) ion sources, it is necessary to accumulate the ion(s) of interest selectively while excluding other ions that would fill the trap. A number of approaches have been employed to extend the dynamic range for trace element detection; these are discussed later in this chapter. Though detection limits for plasma-based quadrupole ion trap systems are comparable to those of linear quadrupole systems, improved sensitivity has not been achieved yet, primarily because of inefficiencies in selective ion accumulation (i.e., chemical and scattering losses). That a nominally equivalent level of sensitivity has been achieved at all is remarkable when the limited storage capacity of the trap and the large Ar^+ ion currents produced by such ionization sources are considered.

Extended storage times provide ample opportunity for collisions in the quadrupole ion trap, which may result in collision-induced dissociation (CID) or chemical reactions. Path length and collision frequency are important parameters for CID. As a storage device operating at 1 mtorr, the quadrupole ion trap provides both long path lengths and high collision frequencies. For example, an ion stored in the quadrupole ion trap for 100 msec travels ~770 m. Operating with a bath gas pressure of 1 mtorr He, the ion undergoes more than 2400 collisions during that period. This is a collision rich environment that is difficult to reproduce in other analyzers. Depending on the identity of the ion, the collision energy, and the thermodynamics of the colliding partners, a number of processes can result, including dissociation, charge exchange, adduct formation, and scattering. Examples of these are presented.

Implicit in the preceding discussion is that quadrupole ion traps employ a buffer gas, typically He at 1 mtorr, to cool ions collisionally. A number of publications discuss the benefits of buffer gases for ion trapping, storage, and other mass spectral characteristics [11–14]. The high pressures employed with quadrupole ion traps simplify their interfacing with inorganic ion sources, particularly glow discharge (GD) and inductively coupled plasmas (ICPs). Unlike ion cyclotron resonance (ICR) traps, which utilize image currents for analyte detection and suffer from collisional broadening (presented in the next section) with increasing pressure, the collisional processes in quadrupole ion traps provide focusing (cooling) of the ions toward the center of the trap, which is essential to enhancing mass intensity and resolution.

A vitally important aspect of ion trap operation is the ability to impart translational energy selectively to ions via resonance absorption of alternating current (ac) voltages (10–450 kHz) applied to the endcap. Unlike for linear quadrupole (or other multipole) collision cells, the absorption of energy is *m/z* specific as each *m/z* in the trap precesses at a specific set of frequencies, the most important of which for MS/MS is ω_z, the fundamental frequency of motion in the *z* dimension, which is defined by

$$\omega_z = \frac{\sqrt{2}eV}{(2\pi m r_0^2 \Omega)} \tag{9.2}$$

where V and Ω are the amplitude and angular frequency of the trapping potential, respectively; r_0 is the inscribed radius of the ring electrode; and e and m are the charge and mass of the ion, respectively. When the supplemental ac signal is applied to the endcaps, ions with a corresponding secular frequency acquire additional axial energy that is useful for polyatomic ion excitation (through collisions with the bath gas) or ejection from the trap as a function of the amplitude of resonance excitation signal, bath gas pressure, and trapping potential. Such excitation can be applied as a single-frequency, narrow-band, or broadband waveform, or as a combination of these in tailored waveforms.

Filtered noise fields (FNFs) have been found to be an effective means of tailoring waveforms for resonance excitation and ejection [15,16]. A *filtered noise field* is a digitally synthesized broadband waveform that spans the range of secular frequencies of trapped ions. The waveform is constructed from discrete, equally spaced (by 100, 250, 500, or 1000 Hz in commercial systems) frequency components. The advantage of FNFs is that each frequency component and its amplitude can be modified in near-real time. The limitation lies in the discrete nature of the frequency components and the preset spacing. This can limit the accuracy in matching the applied frequency to the secular frequency and becomes more difficult as the spacing between frequency components increases. This is exacerbated at high *m/z* values, where the inverse relationship between ω_z and *m/z* results in fewer fre-

quency components per mass. With large-frequency components (e.g., 1000 Hz) precise tuning can be difficult, as some frequency components can be slightly off-resonance. This problem can be ameliorated in single-frequency excitation by tuning the rf trapping amplitude while holding the applied excitation signal constant. Accurate tuning for several *m/z* values can be difficult, depending on the frequency resolution, and often results in uneven distribution of excitation energy. This problem is more difficult for resonance excitation than resonance ejection. Unlike in resonance excitation, excess energy in resonance ejection is not often a concern.

Stored waveform inverse Fourier transform (SWIFT) pulses [17] have been applied as a means of broadband ejection of matrix ions generated by Cs^+ desorption [18]. These pulses are generated by taking the inverse Fourier transform of the desired frequency domain spectrum and applying the stored time domain waveform to the endcap electrodes via an arbitrary waveform generator. The magnitude of the SWIFT pulse determines the degree of excitation for ions of specific secular frequencies.

As utilized for selective ion accumulation during trapping or for isolation of trapped ions, the application of resonance frequencies to eject ions from the trap is referred to as *resonance ejection*. Coupled with mass selective instability scans, this process is known as axial modulation and serves to extend the available mass range [19]. Resonance excitation occurs when the translational energy is insufficient to eject the ions from the trap but increases the collision energy with the bath gas, causing an increase in internal energy of the polyatomic ion. As will be shown, high vibrational excitation can be achieved, allowing the dissociation of some of the most strongly bound diatomic species encountered in atomic mass spectrometry.

High-resolution mass spectra, as first demonstrated by groups at Finnigan and Purdue, can be obtained from quadrupole ion traps by combining mass selective instability with resonance ejection (i.e., axial modulation) and reducing the scan speed [20]. Alternatively, high mass resolution can be achieved by slowly scanning the resonance ejection signal [21]. The results of Londry et al., using very slow scans (0.1 amu/sec), showed an extremely high mass resolution of 10^7 at *m/z* 614 and are promising for elemental applications [22]. However, constant peak width over the mass range of the analyzer is a characteristic of quadrupole ion traps, and therefore resolution is poorer in the elemental mass range [unlike in Fourier transform ion cyclotron resonance (FT-ICR) mass spectrometry, in which resolution is inversely related to mass]. Additionally, such extremely low scan rates severely compromise the duty cycle and allow undesirable chemical reactions to occur with reactive atomic ions. Nevertheless, resolving power on the order of a few thousand, which could be obtained at a compromised scan rate, would circumvent many of the common interferences in atomic mass spectrometry. Such resolution was demonstrated by Schwartz et al. using Xe^+ isotopes, formed by electron ionization [23]. By reducing the scan rate from 5550 amu/sec to 55.5 amu/sec, resolution was improved from $m/\Delta m = 400$ at mass 132 to $m/\Delta m = 3800$ (FWHM 0.035 amu). Still, duty cycle is greatly compromised for continuous ionization

sources. For probing small mass ranges that are subject to mass interferences, high resolution could be a valuable tool for atomic mass analysis.

Thus, quadrupole ion traps have a unique combination of features. They are storage devices that operate at relatively high pressure. Ions are afforded a long path length (long resonance times), which results in a high collision frequency, useful for chemical and collisional processes. Resonance specific excitation affords the analyst a high degree of experimental flexibility in selecting which ions are trapped and the amount of energy imparted to each mass-to-charge value. The following applications show how this unique combination of features has been utilized in various applications to elemental mass spectrometry.

9.2.1 Applications of Quadrupole Ion Traps

The 1980s saw a rapid escalation in the number of applications of quadrupole ion traps in organic mass spectrometry and fundamental developments therein. This resulted primarily from the advent and subsequent commercialization of quadrupole ion traps employing mass selective instability [24]. Investigations involving laser desorption [25,26] within the trap volume and the successful interfacing of external ion sources to quadrupole ion traps for the analysis of molecular (via electron impact [13,27], chemical ionization [27], Cs^+ ion sputter ionization [19], and atmospheric sampling glow discharge [12]) and atomic ions (via laser ablation) [13] served as a catalyst for the use of quadrupole ion traps in inorganic mass spectrometry. Developments of quadrupole ion trap mass spectrometry, employing internal and external atomic ion sources, are summarized in the discussion that follows.

Internal Ionization

The quadrupole ion trap is seen as a compact and less expensive alternative to FT-ICR mass spectrometers employed for gas-phase metal ion chemical and mass analysis [28,29]. Although lacking the high mass resolving powers available in Fourier transform ion cyclotron resonance mass spectrometry (FT-ICR-MS), the quadrupole ion trap has been investigated by using nonselective and resonance-selective ionization of ablated metal samples.

A common approach adopted for laser desorption or laser ablation of samples inside the trapping volume has been employed by various investigators [25,26]. An example of this configuration as published by Gill et al. is shown in Fig. 9.2 [30]. Samples were inserted radially through the ring electrode, with the laser aperture located 180° from the sample. A frequency-doubled Nd:YAG laser (532 nm), focused through this aperture, was used to ablate and ionize the sample inside the trap. One advantage of such a configuration is that multiple pulses can be accumulated to improve sensitivity. In practice, however, a high charge density resulted, distorting the quadrupole fields and resulting in degraded mass resolution and storage capabilities. Additionally, the ability to monitor minor components in

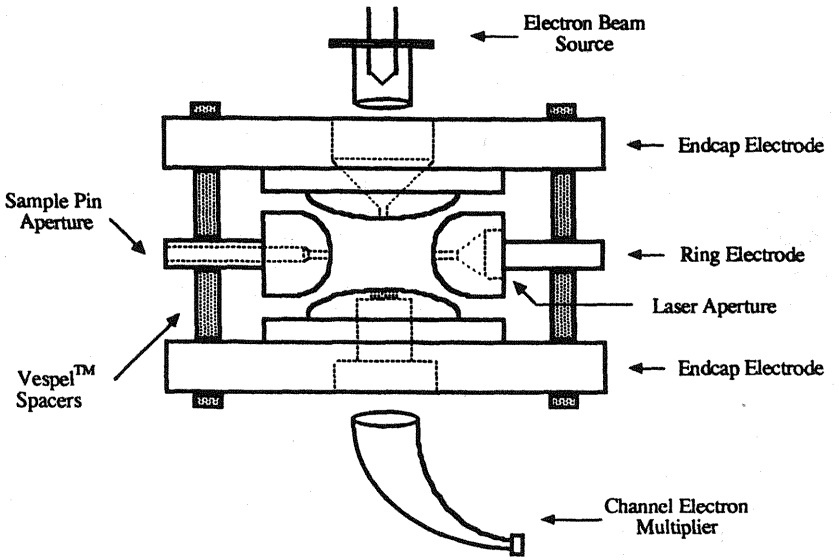

Figure 2 Schematic diagram illustrating the configuration of the quadrupole ion trap for laser ablation inside the ion trap. Samples inserted through the ring electrode are atomized and ionized in the trapping volume by the laser beam, entering the ring electrode from 180° relative to the sample. (From Ref. 30.)

the sample was degraded as the major components filled the trap volume. To prevent this, either laser energy, power density, or helium buffer gas pressure could be adjusted. Doing so caused mass spectral characteristics to improve, but at the expense of sampling or trapping efficiency.

To overcome charge accumulation problems and to extend the sensitivity of quadrupole ion traps for minor components, some means of selectivity is needed to extend the dynamic range. Selectivity in either the ionization event or the trapping technique can be used. Garrett et al., in a similar experimental configuration to that described, employed resonance laser ablation (RLA) to ionize ablated atoms selectively [31]. The leading edge of a tunable laser pulse vaporized near-surface material, resulting in an atomic plume above the surface of the sample. The trailing edge of the laser pulse selectively ionized atoms in the plume. Those atoms with transitions resonant with the incident photons were preferentially excited and subsequently ionized. Doing so achieved selectivities (relative sensitivity) of Cr and Fe of 75 and 50, respectively, by tuning a low-power dye laser into a resonance with these components of the stainless steel sample. Resonant laser ablation schemes, most involving "1 + 1" (photons to resonance + photons to ionize) and "2 + 1" excitations from the ground state, for 15 elements have been reported [32].

Two examples of RLA-IT-MS are shown in Fig. 9.3. Figure 9.3a shows two mass spectra in National Institute of Standards and Technology (NIST) SRM 664

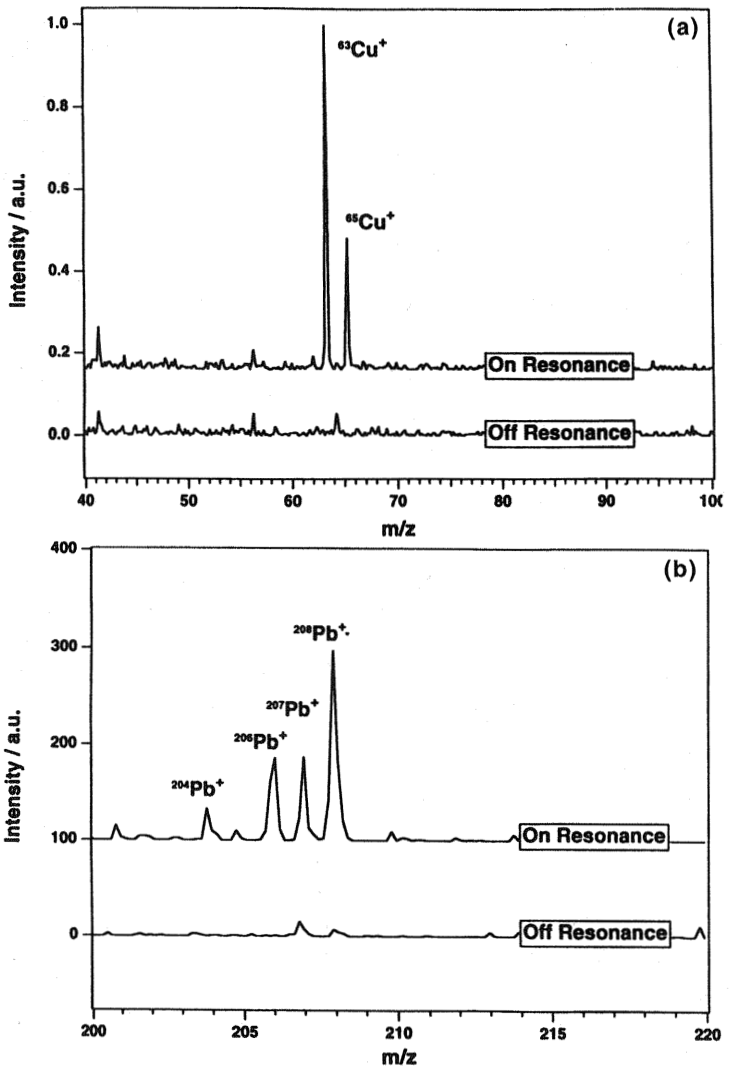

Figure 3 Resonant laser ablation of (a) copper (2500 ppm) in steel and (b) lead (26.5 ppm) in copper. Elemental selectivity is demonstrated for each by the absence of analyte signal when ablating slightly off resonance and by the absence of Fe in (a). (From Ref. 32.)

Modified High Carbon Steel. These two spectra were obtained by tuning the laser to the Cu(2 + 1) transition at 463.507 nm and by tuning the laser just off the resonance transition for Cu (2500 ppm). The selectivity is evident from the lack of a matrix Fe signal. Cu isotopic fidelity is also maintained, with the measured ratio of (0.692 ± 0.005)/(0.308 ± 0.005) comparing favorably with the literature value

of 0.6917/0.3083 [33]. A similar analysis (Fig. 9.3b) of Pb (26.5 ppm) in NIST SRM 494 Unalloyed Copper shows the selectivity of the RLA process and results in a detection limit of about 1 ppm.

In a related work, these authors utilized the selectivity of the RLA process to isolate metal ions (Cr^+, Fe^+, Ni^+, and Cu^+) for investigation of the gas-phase chemical reactions of these reagents with acetone, exploiting the storage capabilities of the ion trap [34]. The RLA process facilitated comparison of metal ion chemical characteristics by allowing multiple elements to be studied without the need to break vacuum. In another work involving the RLA approach, the ability to store both positive and negative ions was utilized to identify both the laser ablated transition element and the transition metal complex [35]. Increasing laser energy caused the decomposition of the complexes. Positive ion mass spectra allowed the determination of the bare transition metal ion, whereas negative ion analysis provided information on the intact acetyl acetonate negative ion.

External Ionization

The ability to inject ions formed in an external ion source (e.g., laser ablation, glow discharge, inductively coupled plasma) greatly extends potential applications of quadrupole ion traps. One of the earliest investigations of factors influencing the injection of externally generated ions used a laser ablation/ionization source to generate metal ions outside the trapping volume [13]. Laser ablated Cs^+, Ta^+, and Au^+ ions were injected via an Einzel lens assembly through an endcap electrode. Two critical parameters were identified—the damping gas pressure and the rf trapping potential.

The externally generated ions had low (~10 eV) kinetic energy entering the trap. Yet, in order to trap the ions, they needed to be collisionally cooled via a bath gas. He, Ne, Ar, and Xe were compared for this purpose, and all promoted trapping of the injected ions. He and Ne were found to be most effective; Ar and Xe produced a 10% to 20% reduction in signal intensity relative to that of He and Ne. Additionally, Xe was found to result in severe (3 amu) peak broadening. In another study, an atmospheric sampling glow discharge ion source was interfaced to a quadrupole ion trap, where H_2 was found to be ~30% more effective than He in ion trapping [12]. However, He has been adopted as the bath gas of choice in most applications, primarily because of the quadrupole ion trap's history as a detector in gas chromatography MS (GC-MS) and handling considerations. As is discussed later, H_2 has useful chemical properties for plasma-based quadrupole ion trap applications.

Another noteworthy observation in the work of Louris et al. [13] was that Ta^+, a strong gettering agent, reacted rapidly with adventitious water in the quadrupole ion trap to form TaO^+ and TaO_2^+. Such reactions are always of concern in the application of quadrupole ion traps to elemental analysis as they produce metal oxides that can interfere with analyte signals of interest. Such oxides form even at low residual gas pressures and have very high bond energies, making them diffi-

cult to dissociate. These are not readily eliminated via ion-neutral chemical processes and therefore have been the subject of investigations using collision induced dissociation [3,37]. Louris et al. also demonstrated the ability to perform metal ion-molecule (benzene) chemical reactions with externally generated Au^+ ions, which resulted in the formation of metal-adduct ions of Au [13].

It is fair to say that much of the impetus for the application of quadrupole ion traps to plasma-based ion sources (glow discharge and inductively coupled plasma) resulted from the possibility of dissociating polyatomic interferences. Additionally, the ability to isolate and accumulate analytes of interest promised to improve sensitivity over that of alternative analyzers. The high mass resolution demonstrated on quadrupole ion traps offered another approach to dealing with polyatomic interferences. Other features of the trap, improved duty cycle and ability to perform ion chemical reactions, were largely secondary issues. MS/MS efficiencies in organic mass spectrometry were noteworthy. A purely atomic mass spectrum, which might be possible with quadrupole ion traps, held much appeal. The reality of quadrupole ion traps as mass analyzers is that ion-molecule reactions are inevitable. These can be either beneficial or detrimental, as will be shown, and are dependent on the rate constants (often very high) for the reactions in the trap and number densities of the reactants (e.g., H_2O and H_2).

Glow Discharge. Although glow discharge mass spectrometry is less prone to spectral interferences than optical emission, it is subject to chemical interferences such as metal argides, metal dimers, and, to a smaller extent, metal oxide ions. It was the ability to dissociate these species, employing the MS/MS capabilities of the quadrupole ion trap, that motivated initial attempts to produce such an interface. Early work involving the use of triple [38] and double [39,40] quadrupole instruments in plasma-source mass spectrometry demonstrated the ability to effect dissociation of diatomic interferences preferentially, relative to atomic scattering losses. The m/z (secular frequency) dependence on ion excitation would allow interferences to be dissociated without scattering losses of concomitant atomic ions. Nevertheless, a trade-off between polyatomic dissociation and atomic ion scattering limited the analytical utility of such approaches.

Several characteristics of the glow discharge ion source facilitate interfacing with quadrupole ion traps. Ion energies, reflecting the low plasma potentials of glow discharge, are only a few electron volts [~3 eV, direct current (dc)-powered; ~18 eV rf-powered). Additionally, the nominal 1-torr operating pressure of the GD facilitates the easy coupling to the ion trap, operating at 1 mtorr. A design similar to that employed in atmospheric sampling glow discharges [12] and adapted for use with a solid sampling glow discharge source is shown in Fig. 9.4 [36]. The rf glow discharge was formed between the sample (cathode), mounted on a direct insertion probe, and the six-way cross, which served as the counterelectrode (anode). Ions were extracted through a 500-μm orifice and were focused with a simple three-element lens system through a hole in the endcap electrode. The second lens element consisted of two half-plates, which were used to deflect the ion beam after

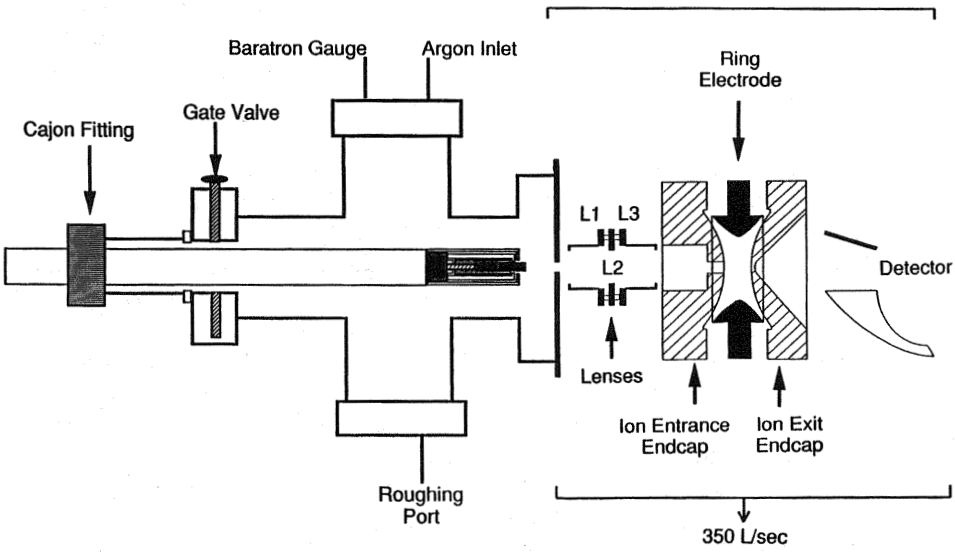

Figure 4 Schematic diagram showing the interfacing of a glow discharge with a quadrupole ion trap. (From Ref. 36.)

injection. Ions were trapped and stored in 1-mtorr He buffer gas, and mass selective instability in conjunction with resonance ejection (i.e., axial modulation) was employed for mass analysis.

The initial experiment demonstrated both beneficial and detrimental ion-molecule reactions with residual gas species (primarily H_2O) in the trap. Beneficial reactions between discharge-gas-related ions and water resulted in the reduction or elimination of the former as a function of ion storage (reaction) time. Figure 9.5 shows mass spectra taken at 30-mS intervals for a brass sample. Cu^+ and Zn^+ ion intensities are unaffected as Ar^+, ArH^+, and Ar_2^+ are depleted via proton and charge transfer reactions with time. Electron transfer from H_2O to Ar^+ is highly exothermic. Subsequent proton transfer from H_2O to H_2O^+ yields H_3O^+, whose intensity grows (only to be lost at 120 msec as a result of its low trapping potential) as Ar-related ions diminish. At 90 msec, Ar^+ is mostly depleted. Ar dimer ions have an ionization potential of 14.5 eV, significantly higher that H_2O (12.6 eV), and can therefore undergo efficient electron transfer too. A predominantly atomic ion mass spectrum (at this sensitivity) results.

Metal argides are a common diatomic interference in GDMS. To date, no metal argides have been observed in glow discharge quadrupole ion trap mass spectrometry. These species have bond energies of only a few tenths of an electron volt [41–43]. Collisions with the He bath gas under standard trapping parameters could effect their dissociation. Alternatively, dissociative charge transfer reactions could also cause their elimination. Metal dimers, such as Cu_2^+ (bond energy ~1.8 eV)

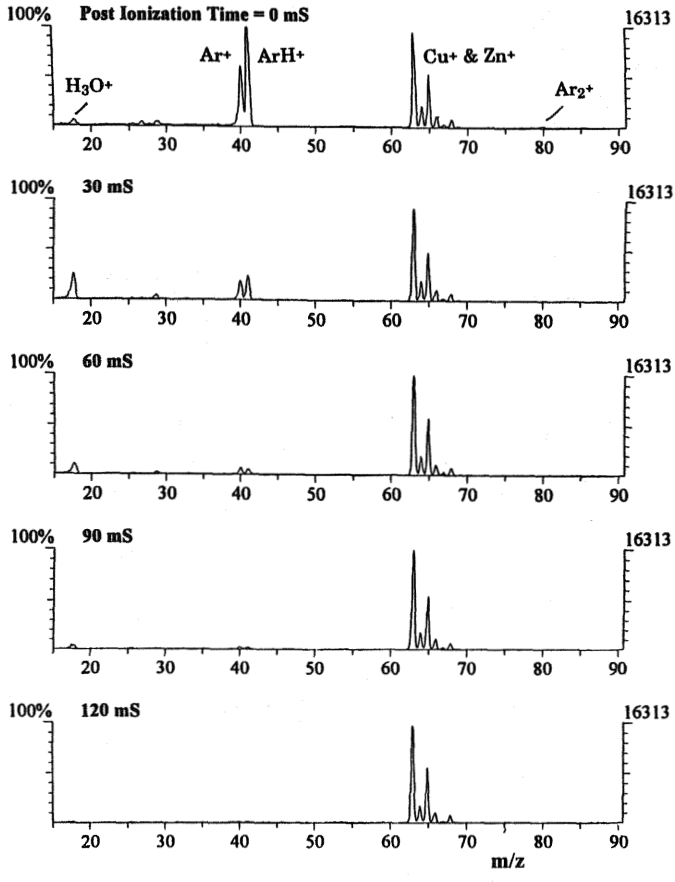

Figure 5 Glow discharge mass spectra of brass acquired after different trapping periods. Proton and charge transfer reactions with adventitious water result in the removal of argon related ions.

[44], have been observed but are easily dissociated in CID experiments (see later discussion and Fig. 9.8).

Chemical reactions in the trap can also be employed to resolve isobaric interferences of atomic ions through a postinjection chemical reaction, which preferentially shifts one of the interfering isobars to higher mass. One such reaction, analogous to that performed by Irikura et al. in FT-ICR experiments [45], is the reaction of Os^+ with CH_4, forming $OsCH_2^+$ and removing the $^{187}Os^+$ isobar from $^{187}Re^+$. This experiment was repeated in the quadrupole ion trap by using glow discharge generated Os^+ and Re^+ ions, which overlap at *m/z* 187, as shown in Fig. 9.6a [10]. With the addition of 2×10^{-4} torr of methane, the Os^+ is efficiently removed from its original mass position. Approximately 53% of the $OsCH_2^+$ product ion is

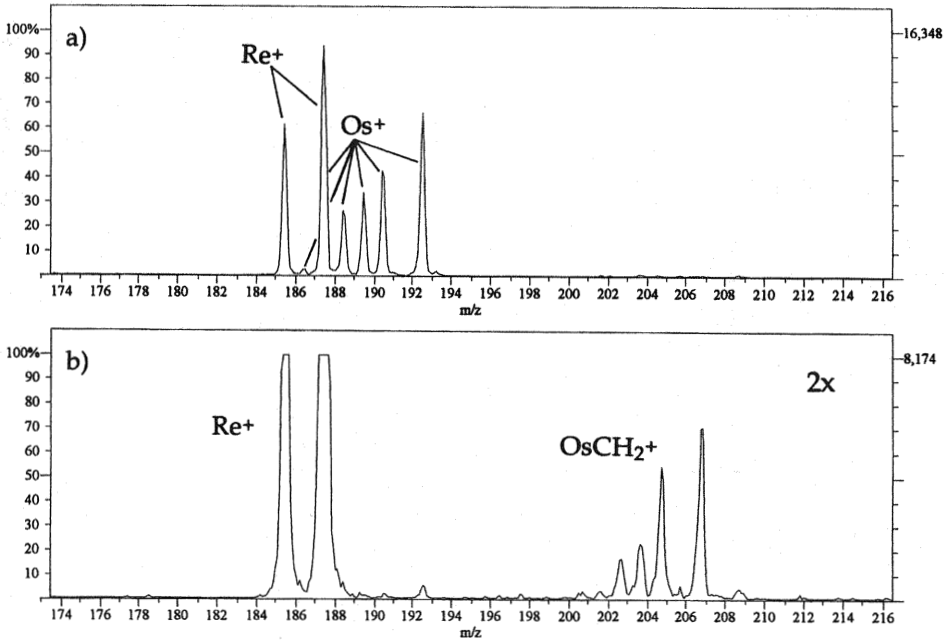

Figure 6 Ion-molecule reactions provide a means of separating atomic isobars as shown in (a) the mass spectrum of ^{187}Os and ^{187}Re. Reaction of CH_4 with Os^+ is highly favored over that of Re^+ and results in (b) the postionization separation of these isobars through the formation of the molecular adduct $OsCH_2^+$.

recovered. Virtually no reaction was observed for Re^+, and, though off-scale in Fig. 9.6b, it appears to have negligible loss in signal intensity.

As reported in the experiments of Louris et al. [13], reactive metal ions, such as Ta^+, in the presence of residual gases can lead to the formation of metal oxides with extended ion injection or storage times. In such cases, CID has been employed to dissociate the polyatomic ions. An example is given in Fig. 9.7, which shows TaO^+ at *m/z* 197 isolated (Fig. 9.7a). TaO^+ has a very high bond dissociation energy (D^o = 8.2 eV), yet with the application of a 0.8-V resonance excitation potential for 14 msec, collisions produced with the 9.3×10^{-5} torr Ar background allow this bond to be dissociated with nearly 100% recovery of the bare Ta^+ ion. The residual TaO^+ results from back-reactions of the Ta^+ product ions, which, if not ejected from the trap after dissociation, react readily with trace residual gases. It has also been demonstrated that the dissociation can occur in a multiple-, stepwise collision process, with collisions resulting in a net increase in vibrational energy, and that the dissociation of TaO^+ can occur at higher rates than scattering losses of atomic ions of the same *m/z* (i.e., Au^+) [46].

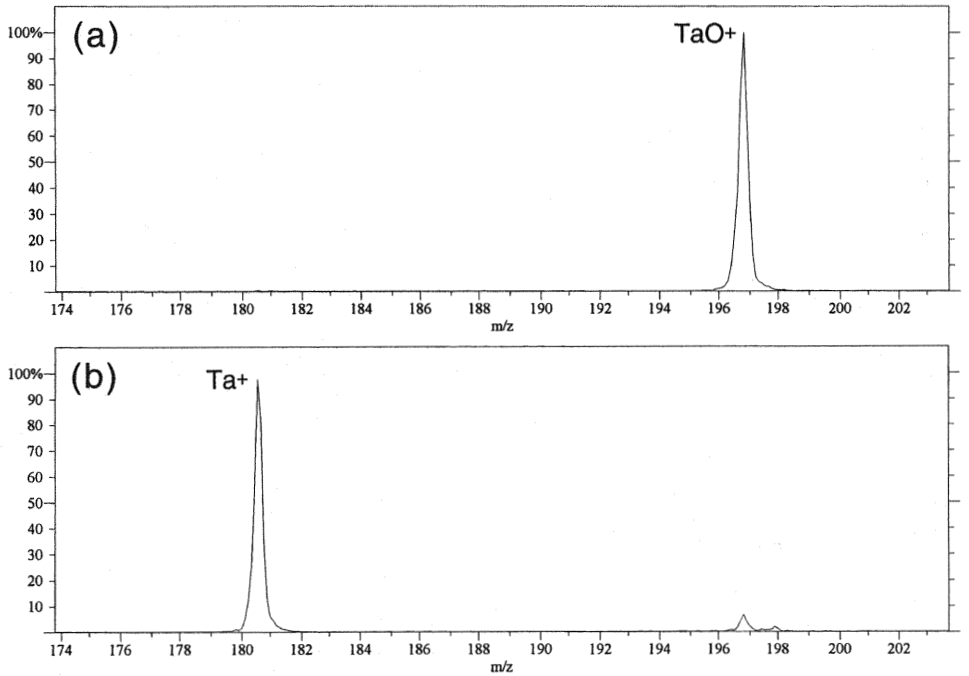

Figure 7 Glow discharge quadrupole ion trap mass spectra showing the dissociation of (a) the strongly bound ($D° = 8.2$ eV) TaO^+ diatomic ion to form (b) Ta^+ with nearly 100% efficiency on collision with background Ar (9.3×10^{-5} torr).

Single-frequency excitation signals can be easily tuned, in both frequency and intensity, for optimal dissociation of polyatomic ions. Alternatively, broadband or tailored waveforms can be employed to excite a range of *m/z* values or can be used in combination to cover several noncontinuous mass ranges. Figure 9.8 shows the use of a tailored waveform (i.e., FNF) [37]. After isolation of the copper dimer ions using mass selective instability (Fig. 9.8a), an FNF was applied. This FNF was constructed from signals of 123, 121, and 119 kHz, corresponding to the resonance frequencies of *m/z* 126, 128, and 130, respectively. As shown in Fig. 9.8b, the bare atomic product ions can be recovered with high efficiency.

Selective ion accumulation is required to extend the dynamic range of the trap beyond $\sim 10^2$ because of its limited storage capacity. Although sophisticated tailored waveforms can be used, it has been demonstrated that several straightforward approaches can extend the dynamic range to 10^5 [47]. These approaches employed various applications of ac and dc potentials to the ring or endcap electrodes to isolate ions of interest over a limited mass range during injection. Ions with unstable trajectories were quickly ejected from the trap and ions of interest were accumulated.

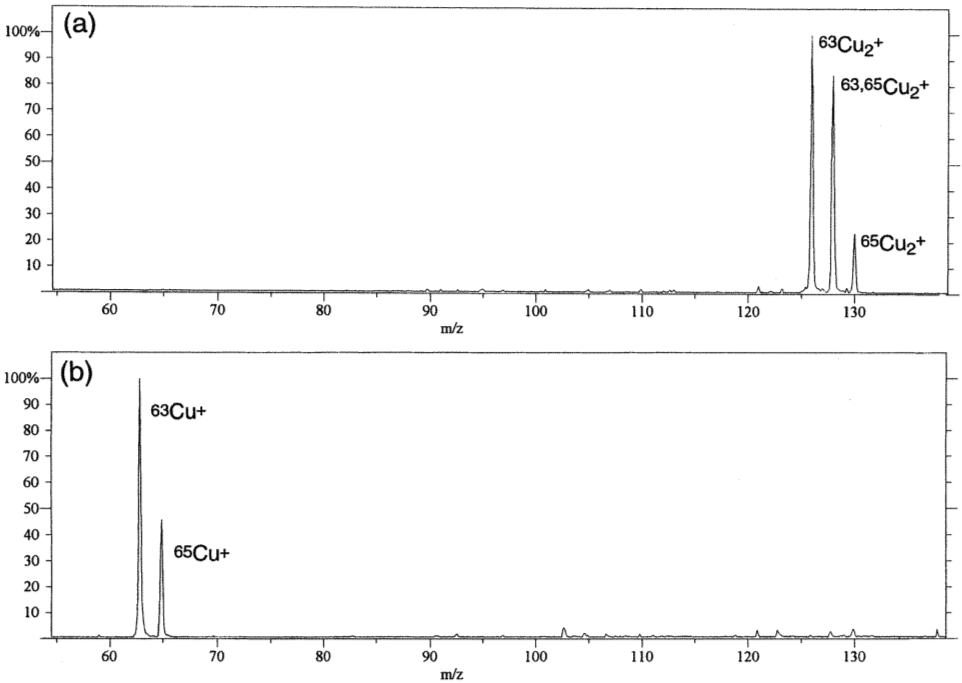

Figure 8 Dissociation of (a) glow discharge generated copper dimer ions using a filtered noise field results in (b) bare copper product ions.

The most common example of selective ion accumulation is mass selective instability, which is shown in Fig. 9.9 for the analysis of National Institute of Science and Technology (NIST) SRM 1103 Free Cutting Brass. Mass selective instability serves as a high-pass filter. When a low mass cutoff of 15 amu is employed (Fig. 9.9a), the trap fills with discharge and residual gas species in an injection period of 0.5 msec. Copper is barely seen above the noise. Increasing the rf amplitude forces the low-mass ions beyond the stability boundary, allowing the Cu^+ and Zn^+ isotopes to be identified at greater intensity for the same injection period (0.5 msec). Signal-to-noise ratio improves 25-fold, and it is possible to accumulate for a longer period as no evidence of space-charge broadening of the peaks is seen. Other means reported include single-frequency resonance ejection (narrow notch filter), combination rf-dc (broad notch filter), and use of a single endcap dc (low-pass filter) potential. These selective ion accumulation schemes can be used alone or in combination within a given scan function. Coupled, such scan functions provide several approaches to multielement analysis in plasma source quadrupole ion trap mass analysis.

Detection limits achieved with the experimental approach described were on the order of 10 ppm. A 40-fold improvement in signal-to-noise ratio was achieved

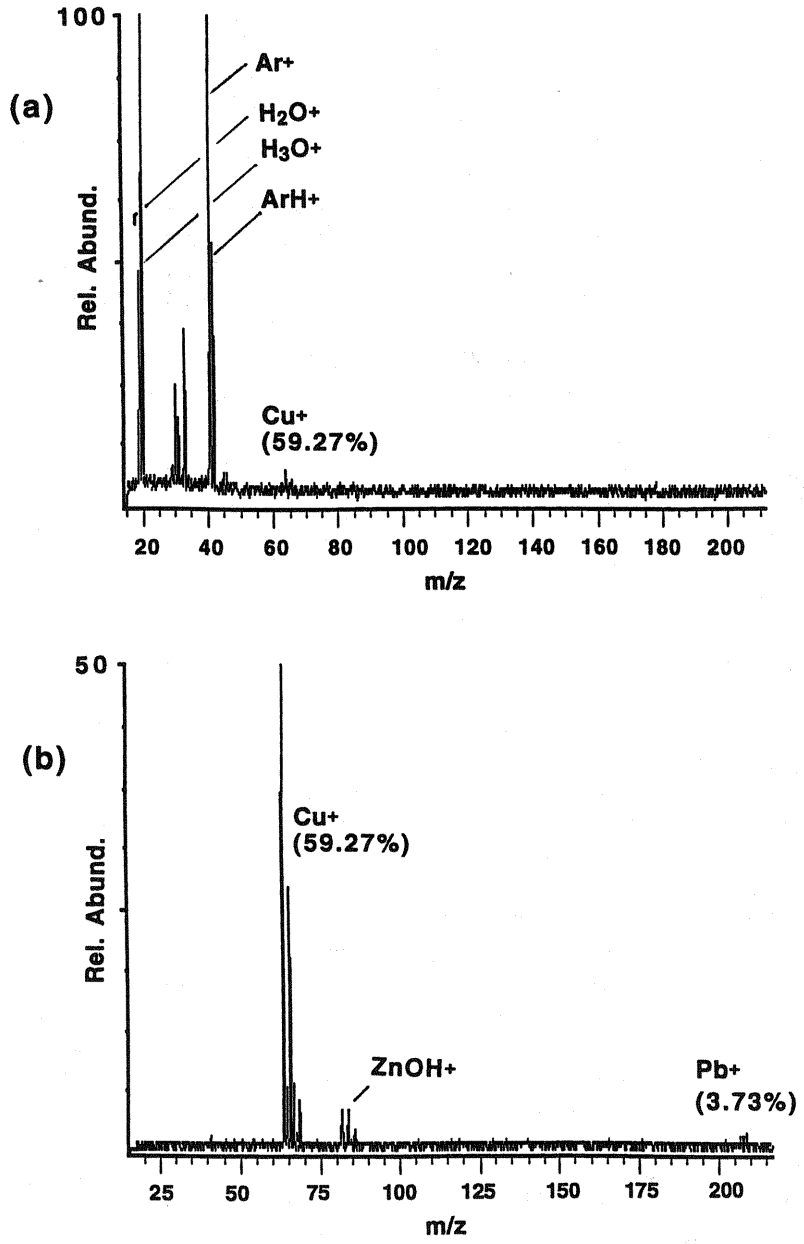

Figure 9 Glow discharge mass spectra of NIST SRM 1103 Free Cutting Brass, demonstrating selective ion accumulation by using mass selective instability: (a) low-mass cutoff, *m/z* 15; (b) low-mass cutoff, *m/z* 45. (From Ref. 36.)

through the use of a pulsed direct current glow discharge [48]. The pulsed discharge was operated in two modes: (1) a high-duty cycle pulse, which allowed continuous injection over the duration of the pulse, and (2) a low-duty cycle pulse with multiple data gates, which allowed gated injections of ions at selected regions of the pulse profile. Both approaches allowed ions to be accumulated during the pulse period and to be detected during the pulse off period. A 20-fold reduction in noise and a 30-fold reduction in background occur when the discharge is "off." Detection limits improve 40-fold by operating with a pulsed discharge and generally range from 0.2 to 0.5 ppm in the solid. It was also shown that operating with a low-duty cycle pulse and a judiciously positioned injection gate afforded another means of selective ion accumulation, with the selectivity based on the temporal dependence on ion formation. Since discharge and residual gas species are formed at different times in the pulse period, the analyte can be accumulated in the absence of ions of Ar and residual gases.

Inductively Coupled Plasma. Because the inductively coupled plasma is an atmospheric pressure ion source with high ion densities, its interfacing to quadrupole ion traps was considered to be a formidable task, requiring some means of matrix ion removal prior to accumulation of the analyte of interest. Without discrimination of the plasma and sample matrix ions, it was thought that the useful capacity of the ion trap ($\sim 10^4$ ions) would be filled with these undesirable ions. Most of the effort in ICP ion trap mass spectrometry has resulted from the work of David Koppenaal, Gregory Eiden, and Charles Barinaga at Pacific Northwest National Laboratory. Early investigations focused on coupling the plasma to the ion trap with a linear quadrupole prefilter. Beneficial ion-neutral reactions that address both atomic and polyatomic interferences have been explored. Other developments include the use of resonance processes to extend abundance sensitivity and to improve the mass resolving power.

Three fundamental instrumental designs have been utilized in coupling ICPs with quadrupole ion traps; the first two are shown in Fig. 9.10 [49–51]. Not shown is a third design, which incorporates a multipole ion guide as a reaction cell prior to the ion trap [52]. Figure 9.10a shows the first plasma source ion trap (PSIT I) tested [49], which for the purpose of analyte selectivity could be operated in the mass resolving (rf + dc), nonresolving (rf only), or notch-filtering ($rf + rf_{aux}$) mode. A commercial linear quadrupole based ICP-MS system was retrofitted with an Einzel lens assembly and a quadrupole ion trap. The central Einzel lens component was used as an injection gate.

Both atomic and metal oxide ions were observed in initial investigations. Ions with low metal oxide or hydroxide bond energies resulted in the detection of only the bare metal ions. For elements with strong oxide bond energies, metal oxides were observed. By utilizing the preselection capability of the linear quadrupole, it was determined that the metal oxides were not originating from the ion

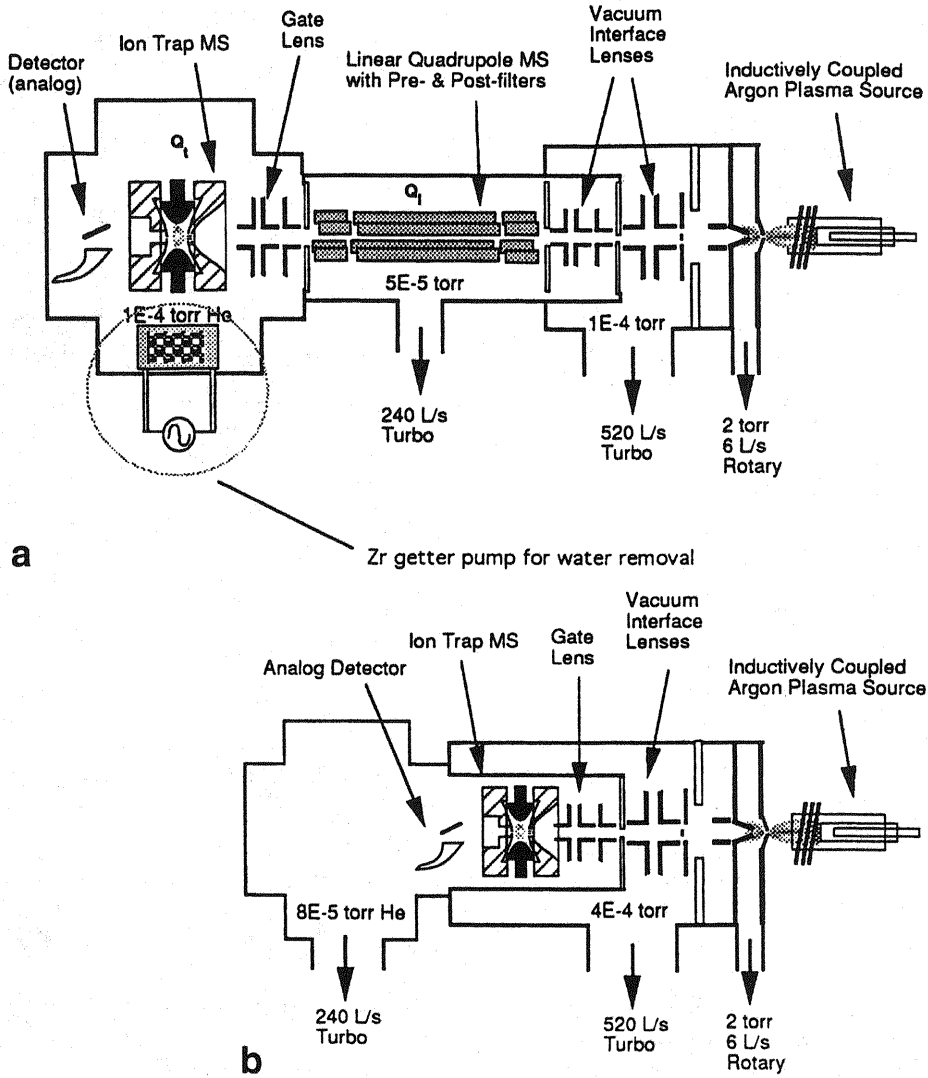

Figure 10 Two instrument configurations of the plasma source ion trap (PSIT): (a) PSIT I utilizes a linear quadrupole for ion transport and mass filtering, (b) PSIT II used direct injection of ions into the trap, eliminating the linear quadrupole transfer/selection optics. (From Ref. 51.)

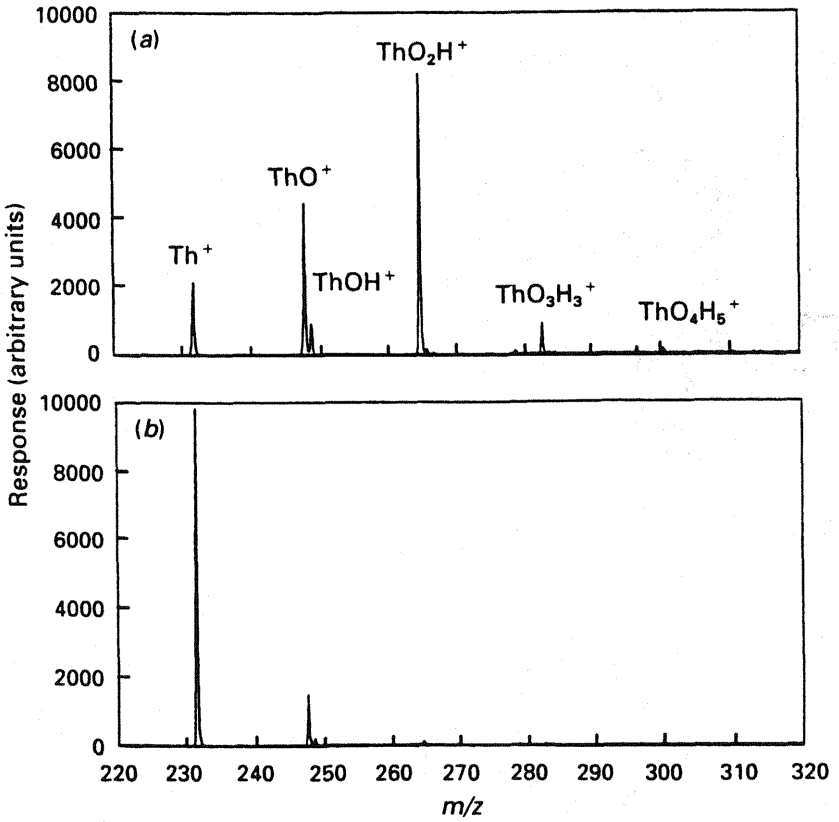

Figure 11 Inductively coupled plasma mass spectra of (a) thorium demonstrates the propensity for metal oxide formation in the quadrupole ion trap. Cryogenic pumping (b) reduces the residual gases, resulting in dramatically reduced oxide formation. (From Ref. 50.)

source, but were instead being formed in the trap via ion-molecule reactions with residual water vapor. Increased pumping of the water vapor via cryogenic or active metal gettering methods resulted in the reduction of metal oxide species. This is demonstrated in the spectra of 1 μg/mL Th in 5% HNO_3 in Fig. 9.11. In the absence of a liquid nitrogen cold finger and a liquid nitrogen trap on the He buffer gas stream, the 2×10^{-6}-torr background pressure resulted a base peak of ThO_2H^+ (Fig. 9.11a). With cryogenic cooling (Fig. 9.11b), a base pressure of 7×10^{-7} torr was achieved, resulting in primarily atomic Th^+ ions. This example shows that even modest amounts of residual gases can have detrimental effects on ion trap mass spectra; great care must be exercised in regard to analyzing reactive species.

Another benefit noted was the absence of common interfering species, including ClO^+, ArO^+, Ar_2^+. Collision-induced dissociation experiments were

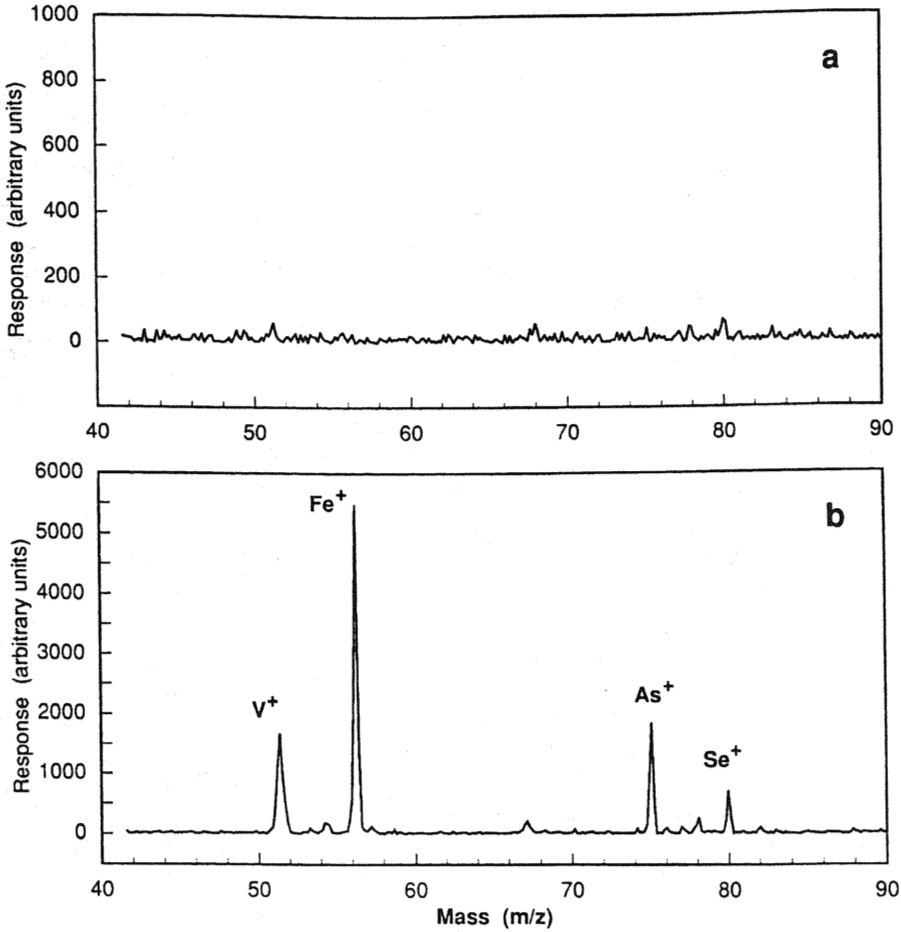

Figure 12 Plasma source ion trap mass spectra of (a) 2% HCl and (b) V, Fe at 1 μg/mL and As, Se at 2 μg/mL in 2% HCl. (From Ref. 51.)

planned for removing these species, but they were reported to dissociate as a result of collision processes during extraction into the high (1-mtorr) trapping environment. Figure 9.12 shows the ICP-MS spectra of the *m/z* 45–85 region, in which the interferences discussed are usually seen in great abundance [51]. As shown in Fig. 9.12a, these interferences are nearly eliminated, allowing difficult elements such as ^{51}V, ^{56}Fe, and ^{75}As (Fig. 9.12b) to be analyzed with minimal or no background interference correction.

As noted in GD-IT-MS applications, Ar^+ was found to be nearly completely neutralized and did not pose the severe space charge limitations that had been anticipated. Two mechanisms for Ar^+ neutralization were proposed: (1) Auger neu-

tralization, in which an Auger electron from the entrance endcap metal neutralizes the argon, and (2) charge exchange neutralization, which involves charge and proton transfer reactions between Ar^+ and ArH^+ and water. The efficiency of Ar^+ neutralization is strongly dependent on H_2O abundance in the trap and indicates that the latter mechanism predominates. This mechanism has allowed K^+ and Ca^+ to be measured by ICP-MS in the absence of the common Ar^+ interference [50].

The efficiency of charge neutralization and the experimental simplicity of design in Fig. 9.10b led to the production of this second configuration (PSIT II), which eliminates the linear quadrupole, allowing ions to be injected directly into the quadrupole ion trap without any prefiltering of the ion beam [51]. Performance was similar to that of the first design, including the reduction of polyatomic interferences (ClO^+, ArO^+, Ar_2^+) and the formation of metal oxides. Limits of detection were similar in both designs. Present instrument detection limits range from 0.3 to 5 pg/mL with method detection limits 2–10 times worse, depending on the degree of interference.

The use of a heated zirconium getter (PSIT I) or a 240-L/sec turbomolecular pump (PSIT II) in the analyzer resulted in reduced base pressures of 2×10^{-7} and 2×10^{-8}, respectively. As base pressure was reduced, metal oxide formation was reduced, but Ar^+ neutralization efficiency was reduced. This observation led to the investigation of H_2 as an alternate means of selective Ar^+ reduction [53]. The reaction between Ar^+ and H_2 was found to proceed at a collision rate that was five to six orders of magnitude faster than that of reactions with other atomic ions. Thirty-three different ions were monitored, and only N^+, O^+, Cl^+, and Ar^+ were found to react. Argon ions were reduced six orders of magnitude via charge and proton transfer reactions. The latter was reported as the dominant mechanism, forming ArH^+, which reacts with H_2 to form H_2^+ and H_3^+ [54]. These ions are not stored under common trapping conditions and serve to shuttle the excess charge out of the trap.

The same chemical reaction was attempted by introducing H_2 behind the skimmer cone in the PSIT I geometry; this has implications for linear quadrupole ICP-MS [53]. The desired chemical reaction was observed, but only a 40-fold reduction in the Ar^+ was seen, as a result of the limited reaction time in this region. The chemical reaction was still selective for Ar^+ and caused only a 5% reduction in the Sc^+ signal as a result of scattering. Subsequent work involved the use of octopole collision cells interfaced with both linear and three-dimensional quadrupoles. Such multipole reaction cells/ion guides provide a sufficient reaction (i.e., "storage") time to effect ion chemical reactions, while minimizing storage time in the trap, which can result in undesirable ion-molecule reactions.

Other gas-phase ion chemical reactions were explored by using oxygen introduced into the octopole collision cell; product ions were injected into and analyzed by the quadrupole ion trap [55]. Reaction of oxygen with Y^+, Zr^+, and Xe^+ was found to proceed rapidly, forming YO^+, ZrO^+, and Xe neutrals, effectively eliminating interferences by the atomic ions. These ions are particularly difficult

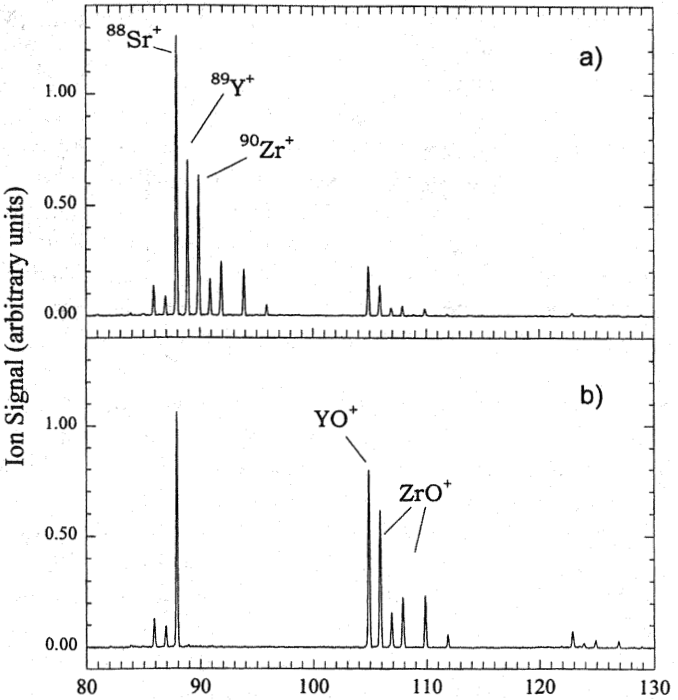

Figure 13 Ion-molecule reactions are used to separate isobaric interferences. Mass spectra of Sr, Y, and Zr are shown (a) without O_2 admitted into the collision cell and (b) with ~10^{-5} torr O_2. (From Ref. 55.)

to work with when analyzing samples containing the fission product ^{90}Sr. Detection of ^{90}Sr often requires chemical separation of the isobars ^{90}Zr and ^{90}Y. The spectrum in Fig. 9.13a shows the mass spectrum for Sr (nonradioactive isotopes were used as surrogates for ^{90}Sr), Y, and Zr before the addition of O_2. A small partial pressure of O_2 (~10^{-5} torr) in the collision cell resulted in a 16-amu mass shift for Y^+ and Zr^+ through the formation of the oxides. $^{90}Y^+$ and $^{90}Zr^+$ were found to react 200 times faster than Sr. The results indicate that ^{90}Sr could be separated from a 100-fold excess of ^{90}Y or ^{90}Zr. Therefore, analysis of the radioactive ^{90}Sr isotope could be done without the need for chemical or chromatographic separations. Other examples include the charge exchange reaction from Xe^+ to O_2 to facilitate the measurement of $^{129}I^+$, a long-lived radionuclide of relevance to environmental monitoring.

One limitation in the addition of reactive gases is the potential for scattering losses of atomic ions. As a general rule, the reactive gas species should be as light as possible and the number density should be optimized, allowing the reaction to proceed rapidly while minimizing scattering and maintaining collisional cooling.

In the Y^+, Zr^+, Sr^+ reaction with O_2 described, the reaction of Y^+ and Zr^+ was approximately 500 times faster than the scattering rate of Sr^+.

The ability to extend the dynamic range via resonance selective (*m/z* selective) ion accumulation processes offers an alternative approach to chemical selection. Filtered noise fields (single-frequency, narrow-band, and wideband) have been used in ICP-IT-MS to remove interfering species, improving dynamic range and sensitivity for neighboring *m/z* species, which for lack of a more precise analogue is termed *abundance sensitivity* (perhaps more accurately described as abundance selectivity) [56]. This abundance sensitivity, demonstrated by the ejection of $^{89}Y^+$ (100 ppb), allowed the measurement of both ^{88}Sr (0.8 ppb) and ^{90}Zr (0.5 ppb) with a selectivity of ~10^5 (i.e., fraction ^{88}Sr or ^{90}Zr lost per fraction of ^{89}Y remaining).

It should be noted that the *m/z* selectivity in such experiments can be affected by the asymmetry of the absorption profiles (signal of a given *m/z* ratio versus frequency of the applied resonance excitation voltage), caused by higher-order fields in the "stretched" geometry of commercial quadrupole ion traps [57]. This asymmetry was also characterized by Eiden et al. [56] as a function of buffer gas, signal amplitude, and signal duration, all of which affect the absorption characteristics as a function of the degree of interaction between a specific *m/z* and the higher-order trapping fields. This interaction increases as ions move away from the center of the trap, as a function of time, amplitude, or collision rate [57]. Absorption tails to low frequencies (high mass) and absorption curves can overlap for adjacent *m/z* values, reducing selectivity. Conversely, the absorption band is found to be sharper on the high-frequency (low-mass) side, allowing greater specificity in the resonance ejection process.

SWIFT excitation affords another method of resonance selection or ejection and has been applied in ICP-IT-MS by C. I. Frum to effect both ion isolation and collision-induced dissociation of ions sampled from an ICP [58]. An example of the isolation of ^{142}Ce from a mixture containing all the lanthanide isotopes is shown in Fig. 9.14. In the absence of SWIFT excitation (Fig. 9.14a) space charge effects on both the lanthanides and Y^+ are evident (space charge for Th^+ is reduced by the prior ejection of lighter ions during the mass scan). Space charge effects are eliminated on application of SWIFT ion isolation.

A final example of the utility of quadrupole ion trap mass spectrometers in atomic mass spectrometry is the ability to generate high-resolution mass spectra through slow scanning techniques. An example is shown in Fig. 9.15, where ^{55}Mn is resolved from $C_4H_7^+$, which can form from charge exchange reactions in the trap [59]. Modest ($m/\Delta m < 500$) resolution is required in this application, but this spectrum demonstrates the improved resolution that can be attained while retaining high sensitivity. Mn is present in solution at 100 pg/mL. Here Δm was measured at half-height. This corresponds to a mass separation of ~0.03 amu (FWHM) and 0.05 amu at 10% of peak height; peaks are slightly asymmetrical, tailing to high *m/z*. (The best quadrupole ion trap resolution noted to date for ICP-MS is about

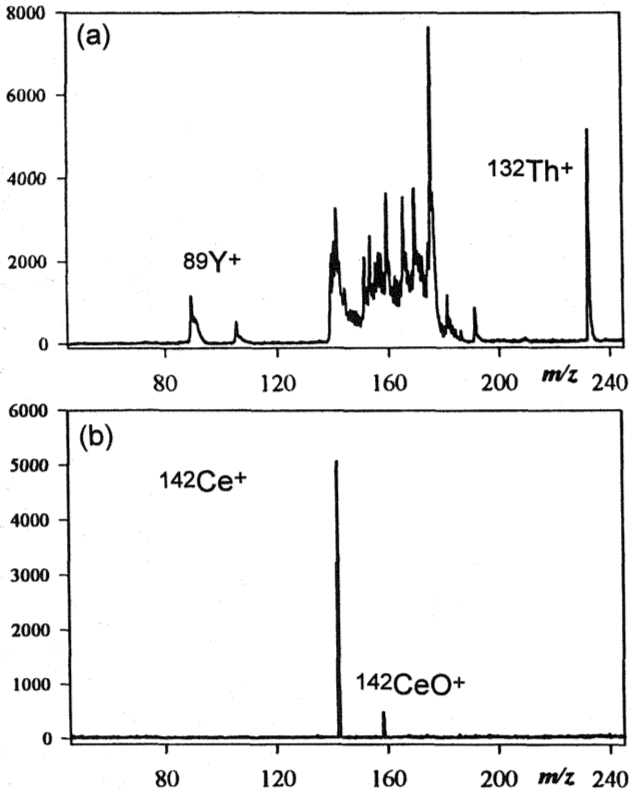

Figure 14 Inductively coupled plasma mass spectra of a mixture of lanthanides, Y, and Th: (a) without stored waveform inverse Fourier transform ion trap (SWIFT) excitation and (b) with the selective accumulation of Ce^+ via SWIFT. (From Ref. 58.)

$m/\Delta m \sim 1000$ for the first-row transition metals [54]). As discussed previously, a trade-off between duty cycle and mass range exists because of the consecutive nature of the ion injection and mass scanning events. Though the limits of mass resolving power have not been fully explored, improved mass resolution is yet another tool available for users of quadrupole ion traps.

9.3 PENNING TRAPS

In this section the use of commercially available devices based on Penning traps, namely, Fourier transform ion cyclotron resonance (FT-ICR) mass spectrometers, is presented. Since its introduction in 1974 [60], the FT-ICR technique has been applied to a plethora of problems in organic, inorganic, and physical chemistry and

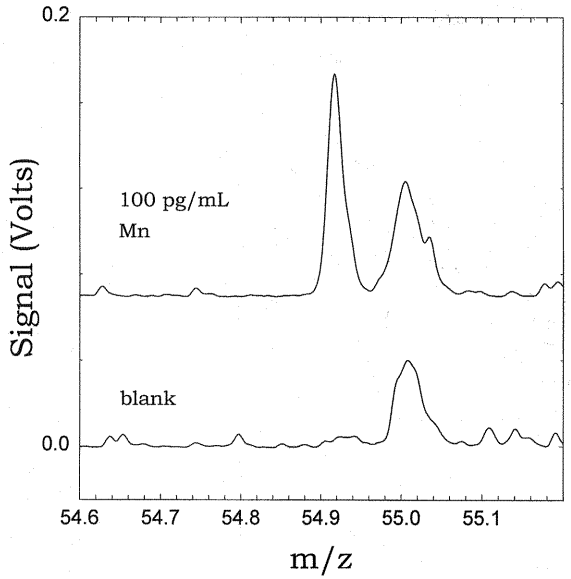

Figure 15 Plasma source ion trap mass spectra of Mn, mass resolved from $C_4H_7^+$.

biochemistry. Numerous reviews [61–66] and several books [67–69] have appeared, so only a brief overview of the important features of the method is given here.

In a Penning trap, ions are constrained spatially by a combination of electric and magnetic fields. In the presence of a homogeneous magnetic field (**B**) ions that have a component of velocity perpendicular to **B** are subjected to the Lorentz force and subsequently follow a circular trajectory [70]. The rotational frequency of this trajectory is proportional to **B** and to the ion charge (q) and inversely proportional to the ion mass (m). When expressed in radians, this rotational frequency is known as the *cyclotron frequency*, ω_c, where

$$\omega_c = qB/m \tag{9.3}$$

Thus the presence of a magnetic field constrains the ion's motion in two dimensions. However, a charged particle is free to drift along the magnetic field lines. To trap ions in the analyzer cell, an electrostatic potential is applied to two parallel electrodes, creating a potential well that confines motion along the magnetic field [71]. This trapping potential (usually only a few volts in magnitude) prevents ions from drifting out of the analyzer cell as they oscillate with simple harmonic motion between the trapping electrodes, as shown in Fig. 9.16. The ions also experience magnetron motion (not shown in Fig. 9.16) as a result of their drift along equipotential surfaces created by the presence of the trapping electrodes. The de-

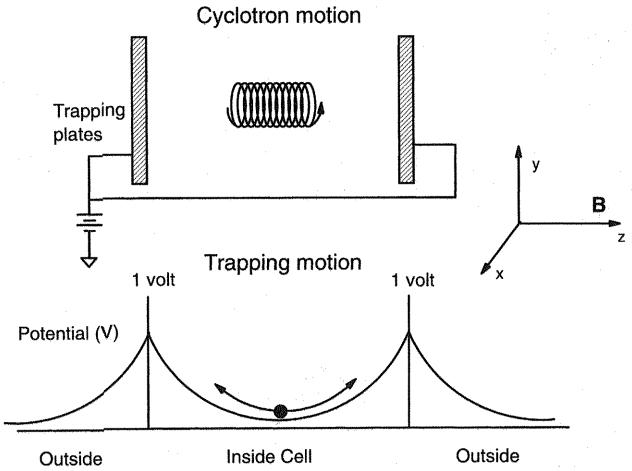

Figure 16 Depiction of two important types of ion motion in Penning traps: cyclotron and harmonic oscillation in the field produced by the trapping potential.

tailed motion of the ions in the FT-ICR trap is described more completely in several of the reviews cited [62,66].

Once the ions are trapped in the analyzer cell, mass analysis is accomplished by applying a resonant rf electric field across the cell by using a set of "excite" electrodes. Ions whose cyclotron frequency matches that of the applied electric field absorb energy and move to larger cyclotron orbits, as depicted in Fig. 9.17. After excitation the coherent ion packet induces an image current in a set of detection electrodes that is converted to a voltage, amplified, digitized with a high-speed analogue-to-digital converter, and stored as a transient response. The transient response (a signal that varies as a function of time) is then subjected to Fourier transformation, yielding a frequency spectrum that is converted to a mass spectrum via Eq. (9.3).

The FT-ICR technique most often operates in a pulsed mode, and the sequential series of events or pulses applied to the analyzer cell during the course of the experiment is characterized by a pulse sequence. Such a sequence usually starts with a quench pulse to remove ions remaining from a previous experiment by applying a positive potential to one trap electrode and a negative potential to the opposite electrode to remove either positive or negative ions. An ionization pulse or accumulation pulse then either creates ions in the cell or allows them to be introduced from an external source (discussed later). A series of high-amplitude (or long-duration) rf ejection pulses or reaction delays can follow the ionization event if it is desired to isolate an ion of a particular m/z or to allow time for ion-molecule reactions. In the FT mode, the Penning trap provides for multichannel detec-

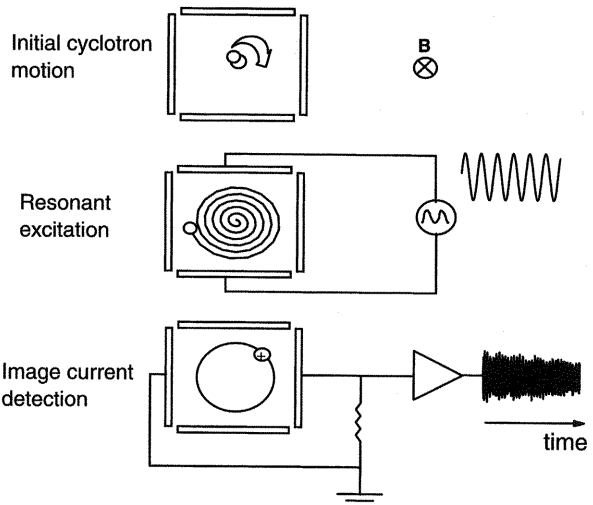

Figure 17 Schematic representation of the Fourier transform ion cyclotron resonance (FT-ICR) excitation and detection process.

tion for all ions of different *m/z* present in the cell. A suitable rf pulse or frequency chirp [72] is applied to the excite electrodes to excite all ions virtually simultaneously to large cyclotron orbits, where their induced image current transients are detected and stored.

Given its basis in frequency measurement (which can be performed with extreme precision and accuracy) and its image current detection scheme, the FT-ICR approach provides a number of advantages over other types of mass spectrometry, most of which can be most useful in elemental analysis. At sufficiently low pressures ($<10^{-8}$ mbar), collisions with background molecules are minimized and the transient response can be measured for increasingly longer times (up to several seconds) to obtain ultrahigh mass resolving power (MRP). For an early report of ultrahigh MRP with electron ionization, see Alleman and colleagues [73]. As will be seen from the examples given, this feature of the FT-ICR technique has been the one most emphasized in work to date. It should also be noted that MRP is inversely proportional to ion mass, and so improves when relatively low-mass elemental ions are analyzed. Ions of a particular mass-to-charge ratio can be isolated in the analyzer cell by applying a series of rf pulses to excite ions of unwanted *m/z* to sufficiently large cyclotron orbits that they are ejected from the cell [74]. Detection of ions in a Penning trap is nondestructive in the sense that the ions remain in the trap after mass analysis. The same packet of ions can be measured multiple times to improve sensitivity by inverting the phase of the excitation waveform by 180° to decelerate ions back to the center of the cell before remeasurement [75].

Alternatively, introduction of a suitable inert collision gas followed by quadrupolar axialization [76] has been used for remeasurement experiments to provide significant improvements in the signal-to-noise ratio. Quadrupolar axialization interconverts any two of the three different motions of ions in the ICR cell (cyclotron, magnetron, and trapping). Since cyclotron and trapping motions are more readily damped by collisions than magnetron motion, and magnetron motion leads most directly to ion loss from the cell, periodic quadrupolar axialization events (accompanied by a pulse of inert collision gas) can bring the same ion population back to the center of the cell (thus axializing it) after either an excitation event or long trapping times that cause the ions to spread out in the cell. This feature could be quite important for detection of trace species from samples that are limited in quantity.

Other FT-ICR advantages include the ease of selectively ejecting unwanted ions (including Ar^+ from glow discharge or inductively coupled plasma sources) from the cell, leaving only analyte ions of interest. Since ions of interest can be trapped for extended periods, they can be subjected to ion-molecule reactions and laser irradiation for diagnostic purposes. The pulsed ion detection method is compatible with pulsed ionization sources. This feature may not be important given the usual operation of GD and ICP sources in a continuous mode, but at least one advantage of pulsed operation is discussed later. The need for low pressures for detection would seem to argue against atmospheric or near-atmospheric pressure sources, but development of external ionization sources coupled with efficient injection schemes has made this coupling quite possible, as is demonstrated at some length later.

9.3.1 Applications of Penning Traps

Internal Ionization

Most analytical studies using FT-ICR mass spectrometry, where ions have been produced inside (or just outside) the analyzer cell, have used lasers as ionization sources. Other than some very limited Cs secondary ion mass spectrometry (SIMS) studies [77], most research utilized direct laser desorption to form various organic [78] and inorganic [79] ions, including metal [80] and semiconductor [81] (including carbon) clusters. More recently matrix assisted laser desorption ionization (MALDI) has been used to form ions of high molecular weight from polymers [82] and many classes of biomolecules [83].

Very few of these studies were directed at elemental analysis. They concentrated on analysis of molecular ions and on study of the structure and reactivity of cluster ions. Another area of investigation, laser microprobe mass spectrometry using FT-ICR mass analysis [84], has most often been concerned with organic impurities on and in materials. However, it can be used to detect elemental ions produced by the laser desorption process.

External Ionization

The vast majority of recent FT-ICR studies have used instrumentation that allows ions to be generated from a number of different ionization sources external to the high magnetic field and then to be transported into the analyzer cell for subsequent mass analysis. A variety of instrumental approaches have been developed to facilitate such ion transport, most involving either electrostatic ion lenses [85] or guides [86] or quadrupole [87] and octopole [88] ion guides. These arrangements utilized several stages of differential pumping so that relatively high-pressure external ion sources were compatible with the FT-ICR detection scheme, which requires quite low pressures in the analyzer cell for optimal ion detection at ultrahigh-mass resolving powers. All of the elemental analysis work with FT-ICR mass analysis reported to date has utilized external ion sources, either glow discharge, inductively coupled plasma, or electrospray. Results for each of these sources are discussed in the following sections.

Laser Desorption. A laser microprobe system has been used for surface analysis to detect both organic and inorganic species [89]. Although this instrument was not developed with elemental analysis in mind, studies of selected inorganic compounds have been carried out, and elemental ions have been and can be detected with the system. One other external source that produces atomic ions should be noted here. A laser vaporization metal ion source [90] has produced a wide variety of reactant ions for use in ion-molecule reactivity studies. In almost all cases, pure metals were used to form the ions, and the intent of the research was chemical reactivity studies and not elemental analysis.

Glow Discharge Sources. Glow discharge (GD) ion sources and some of their applications using different mass analyzers have been discussed in earlier chapters of this volume. Virtually all work that couples these sources to FT-ICR mass analyzers has involved dc discharges (see Chapter 2 for further discussion of the types of GD sources).

The main thrust of our early GD studies was to demonstrate the feasibility of coupling such sources to FT-ICR mass spectrometers, and to explore the mass resolving power and sensitivity that could be obtained. The initial successful experiments [91] utilized a simple coaxial GD ion source [92], and some elementary ion transfer lenses. Improvements in ion transfer optics (such as a conductance limit with adjustable voltages, a flight tube, and a decelerator just before the FT-ICR cell) led to enhanced ion transport and performance with this instrument [93]. At about this time, another group reported coupling an rf discharge to an FT-ICR mass spectrometer [94], using a lensless interface; they obtained mass resolving powers of ca. 40,000 for $^{63}Cu^{+}$.

The next stage in the development of GD-FT-ICR instrumentation involved a collaboration with scientists (primarily Dr. Clifford Watson) at Bruker Instruments, Inc. Using the improved ion injection schemes and differential pumping of

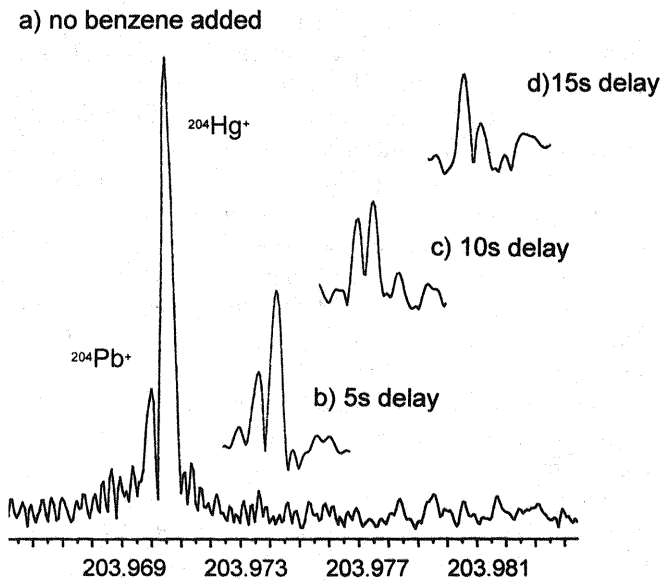

Figure 18 Use of ion-molecule reactions to change relative ion intensities. $^{204}Pb^+$ and $^{204}Hg^+$ were allowed to react with benzene in the Fourier transform ion cyclotron resonance (FT-ICR) analyzer cell for progressively longer periods.

their commercial instrument [95], dramatically improved sensitivity and mass resolving power (MRP) were obtained. Separation of $^{198}Hg^+$ from $^{198}Pt^+$, with MRP of 650,000 (full width at half-height) was reported [96], and many other aspects of the technique were improved and characterized [97]. The ability of FT-ICR to contain ions and subject them to ion-molecule reactions was also exploited. Figure 9.18a shows the GD-FT-ICR mass spectrum of a compacted cathode consisting of lead oxide (10% lead by weight) and mercury oxide (10% mercury by weight) with the balance as silver powder. Mass resolving power of ca. 450,000 is seen. A very simple type of ion-molecule reaction, charge transfer, was used to demonstrate the utility of this approach to modifying (and improving) the relative intensity of analyte ions of interest. The ionization potentials of Hg, Pb, and benzene are 10.44, 7.42, and 9.25 eV, respectively. Thus Hg^+ reacts with benzene, producing the benzene molecular ion, whereas Pb^+ does not react. When benzene was admitted to the FT-ICR analyzer cell at relatively low pressures, and the Hg^+ and Pb^+ ions reacted with it for increasing periods of time after being transferred from the GD source, the ratio of the Pb^+ to Hg^+ was enhanced, as is shown in Fig. 9.18b–d.

Additional studies addressed the advantages of pulsed gas glow discharges coupled to the FT-ICR instrument. The FT-ICR technique requires quite low pressures in the analyzer cell to obtain the highest possible mass resolving power, since

collisions of excited ions with background neutrals damp the ion transient response and this leads to broadened peaks in the mass spectrum after Fourier transformation. Although ions are transferred from the GD source to the analyzer cell by switching several ion transfer elements to appropriate voltages for an "ion injection" time, the GD source is most often operated in a continuous mode, with a constant pressure (ca. 1 torr) of argon present. Despite several stages of differential pumping, some of this gas makes its way to the FT-ICR analyzer cell and contributes to an elevated background there during the ion excitation and detection process. By pulsing the GD discharge gas on and off, and performing mass analysis in the analyzer cell while the discharge gas was off (and thus the pressure in the cell was lower), improved mass resolving powers as high as 1,178,000 (FWHH) for $^{63}Cu^+$ ions were obtained [98].

The advantages of placing the GD source *inside* the magnetic field used in the FT-ICR approach were also investigated, using a probe-mounted GD source [99]. The glow discharge source was found to operate quite satisfactorily in magnetic fields as high as 1.5 tesla, and some enhanced sensitivity resulted from this arrangement. However, the difficulties of observing and monitoring the GD process in a source mounted remotely within the (complicated) differential pumping system and inside the high magnetic field appear to outweigh any advantages gained.

Although the main thrust of our studies has been demonstrating ultrahigh mass resolving power in order to separate polyatomic and isobaric interferences directly, one recent study [100] has examined the precision of isotope ratio measurements with the GD-FT-ICR technique and compared it to that obtained with a commercial reverse Nier geometry mass spectrometer (VG 9000). Precisions of ~0.32% (relative standard deviation) and biases of less than 2.5% were found; they compare favorably with values of ~0.13% and 0.6% on the magnetic sector instrument, particularly when the ultrahigh MRP capabilities that can be obtained by using the same GD-FT-ICR combination are also considered. Figure 9.19 is a schematic representation of the instrumentation in its current form in the authors' laboratory at the University of Florida. A 7-tesla superconducting magnet was used initially with this FT-ICR mass spectrometer, providing even higher mass resolving power. Figure 9.20 shows mass resolving power of 1.7×10^6 (full width at half maximum) for the $^{58}Fe^+$ ion, the highest ever attained in glow discharge mass spectrometry.

Inductively Coupled Plasma Sources. The many advantages (ultrahigh mass resolving power, isolation of ionic species of interest, extended ion trapping for ion-molecule studies, and ion remeasurement) that FT-ICR mass analysis offers to GDMS also hold true for inductively coupled plasma (ICP) mass spectrometry. However, coupling high-temperature, atmospheric pressure ICP sources, rather than cooler GD sources, which generally operate at pressures of ca. 1 torr, to FT-ICR instruments poses some instrumental difficulties. Since 1994

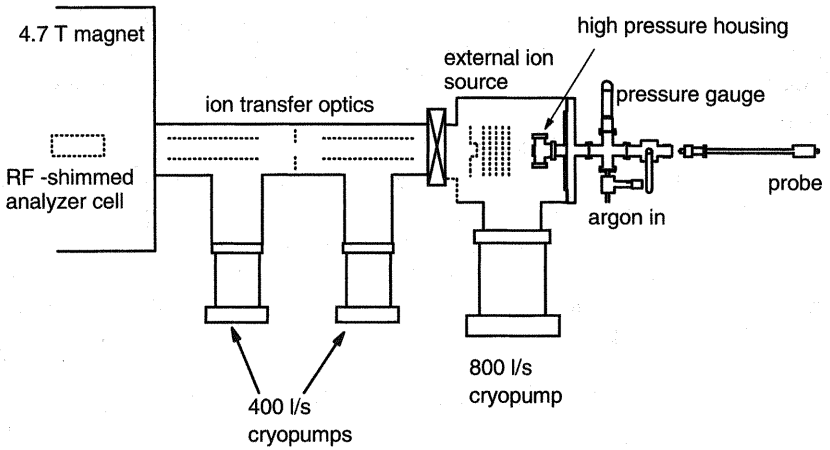

Figure 19 Schematic representation of glow discharge Fourier transform ion cyclotron resonance (GD-FT-ICR) instrumentation currently in use at the University of Florida.

the Eyler group at the University of Florida has been attempting to develop and apply ICP-FT-ICR mass spectrometry to elemental analysis.

Since the ICP source operates at atmospheric pressure, similarly to an electrospray ionization (ESI) source, we initially attempted to modify an existing ESI source housing for use with an ICP torch and sampler, with differential pumping

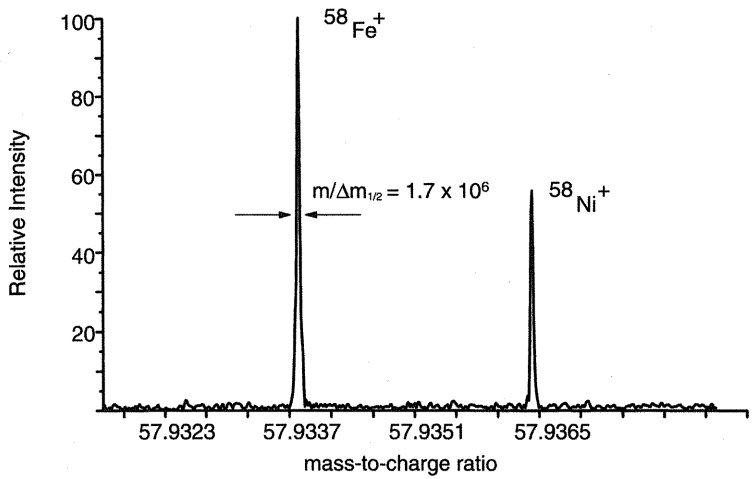

Figure 20 Ultrahigh mass resolving power mass spectrum of $^{58}Fe^+$ from a glow discharge (GD) source obtained with a Fourier transform ion cyclotron resonance (FT-ICR) mass spectrometer equipped with a 7-tesla superconducting magnet.

provided by retaining the metal capillary used for desolvation in the ESI experiment [101]. This approach proved unsuccessful, although valuable insights about the ICP ionization process and interfacing requirements for FT-ICR mass analysis were gained.

A water-cooled sampler-skimmer arrangement from a commercial ICP mass spectrometer (VG Plasma Quad) was next attached to the source housing of a Bruker APEX external source FT-ICR mass spectrometer. Although ions due to argon and ICP plasma impurities were detected, no analyte ion signals could be seen. We believed this resulted from excessive spacing between the extraction lens of the ICP source and the ion transfer optics of our mass spectrometer. This problem was most easily solved by using an instrument [102] in the laboratories of Alan Marshall at the National High Magnetic Field Laboratory that was equipped with a wire-in-cylinder ion guide that could be positioned only a few centimeters from the ICP source extraction lens. Using this instrumentation the first ICP-FT-ICR spectra were obtained in September 1996. The instrumental combination suffered from a need for one additional stage of differential pumping and better shielding of the detection electronics but still achieved sensitivities in the high microgram per liter (μg/L) range and a mass resolving power of 10,000 (10% valley definition), adequate for clearly separating $^{40}ArH^+$ from $^{41}K^+$. The initial stages of our ICP-FT-ICR development discussed in this paragraph have been described in detail in a recent publication [103].

An octopole ion guide was next constructed and added to the Bruker instrumentation at the University of Florida [104] in order to provide an additional stage of differential pumping and to allow the possibility of ion accumulation [88] and ion-molecule reactions, which might selectively remove unwanted ions [53] prior to transfer to the FT-ICR analyzer cell. By using this instrumentation, substantial improvements in ICP-FT-ICR figures of merit have been obtained. Figure 9.21 shows separation of $^{40}Ar^+$ from $^{40}Ca^+$, with a mass resolving power of 260,000 ($m/\Delta m_{10\%\ \text{valley}}$), higher by at least a factor of 5 than any previous ICP-MS results. Figure 9.22 illustrates sensitivities in the very low microgram per liter range for a 140-μg/L sample of In. The $^{113}In^+$ species, present in only 4.3% abundance, exhibits a signal-to-noise (S/N) ratio of ca. 5, thus indicating a limit of detectability better than 5 μg/L. The instrumentation used to obtain the results shown in Figs. 9.21 and 9.22 is shown schematically in Figure 9.23.

The very promising results seen to date with ICP-FT-ICR instrumentation at the University of Florida indicate that elemental analyses with mass resolving powers substantially >100,000 and sensitivities in the mid- to low-microgram-per-liter range are quite attainable. It should also be noted that high levels of Ar^+ ions, which might seriously interfere with the detection of minor analyte ions, are *not* seen in these experiments, and those Ar^+ ions that are present can be ejected from the analyzer cell in a straightforward manner prior to detection and quantitation of the analyte ions present in submicrogram-per-liter concentrations. Improvements to

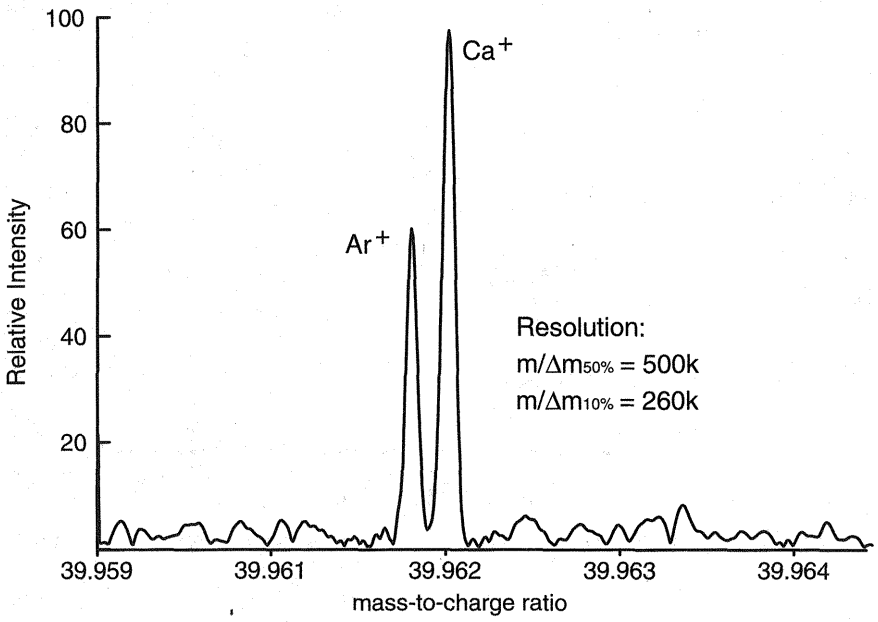

Figure 21 Ultrahigh mass resolving power inductively coupled plasma (ICP) mass spectrum that demonstrates separation of $^{40}Ca^+$ from $^{40}Ar^+$ obtained with a Fourier transform ion cyclotron resonance (FT-ICR) mass spectrometer equipped with a 3-tesla superconducting magnet.

the instrumentation and applications of this powerful elemental method are continuing. In particular, an interface is being constructed that will allow the ICP-octopole ion guide source currently in use at the University of Florida to be coupled with an FT-ICR system utilizing a 6-tesla magnet at the National High Magnetic Field Laboratory in Tallahassee, Florida.

Electrospray Ionization Sources. We have carried out some preliminary studies [105] using electrospray ionization (ESI) sources to demonstrate advantages of the ultrahigh mass resolving power afforded by FT-ICR mass analysis when studying the often complicated spectra produced by ESI of inorganic salts. Figure 9.24 shows the ESI spectrum of a 1×10^{-5} M solution of $Pb(NO_3)_2$, obtained after summing 32 transients of 128,000 data points. A capillary-skimmer voltage difference of 200 V was used, and ions were accumulated in the hexapole ion guide associated with the electrospray source for 1 sec before transfer to the FT-ICR analyzer cell. Both peaks due to elemental Pb^+ and numerous others resulting from adduction of solvent molecules (H_2O and CH_3OH) and counter ions (CH_3O^-) can be seen.

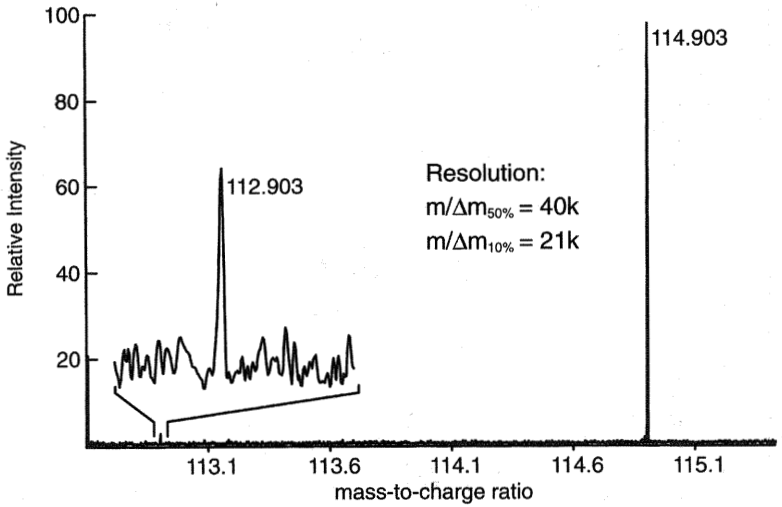

Figure 22 Inductively coupled plasma (ICP) mass spectrum demonstrating better than 5-μg/L limits of detectability.

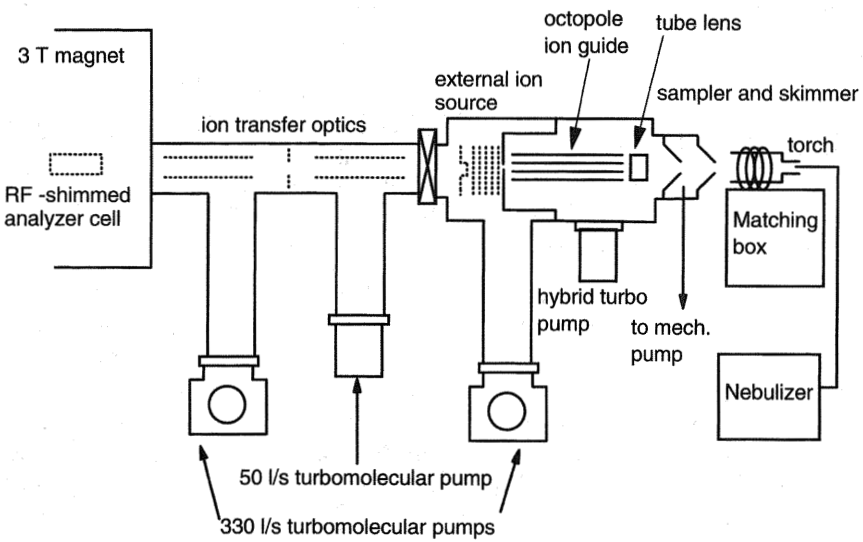

Figure 23 Schematic representation of inductively coupled plasma Fourier transform ion cyclotron resonance (ICP-FT-ICR) mass spectrometer used to obtain spectra shown in Figs. 9.21 and 9.22.

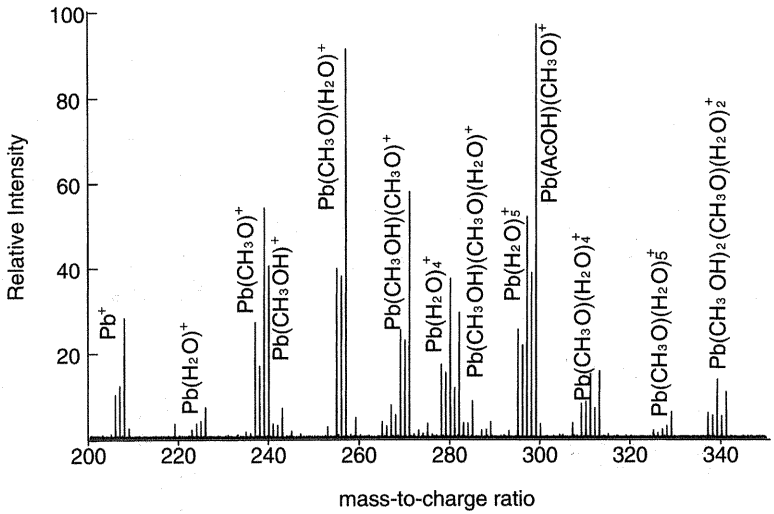

Figure 24 Electrospray ionization Fourier transform ion cyclotron resonance (ESI-FT-ICR) mass spectrum of $Pb(NO_3)_2$ solution.

The advantages of high mass resolving power for studies such as these can be seen in Fig. 9.25, where peaks in the *m/z* 237–*m/z* 240 range from Fig. 9.24 are detected with much higher mass resolving power (100,000 full width at half-height). The $^{207}Pb(CH_3O)^+ - ^{206}Pb(CH_3OH)^+$ and $^{208}Pb(CH_3O)^+ - ^{207}Pb(CH_3OH)^+$ "isobaric" doublets are clearly resolved. Collision-induced dissociation (CID) can be carried out on ions of interest to probe their structures further. Figure 9.26 shows CID results for the $^{208}Pb(CH_3O)(H_2O)^+$ ion at *m/z* 256, which was isolated by a series of correlated sweeps. Loss of both H_2O and CH_3OH from the parent ion is seen, indicating some lability of one of the hydrogen atoms, which can apparently be lost with either water or methanol. The Pb^+ ion, resulting from loss of both ligands, can also be produced in the CID process.

9.4 CONCLUSIONS

In this chapter, both the benefits and the limitations of quadrupole ion trap and ion cyclotron resonance mass spectrometers have been presented. The coupling of each mass analyzer to atomic ion sources is at an early stage of development and largely remains a novelty, being investigated by only a few researchers in inorganic mass spectrometry. Meanwhile, the long-standing utility of traditional sector-based and

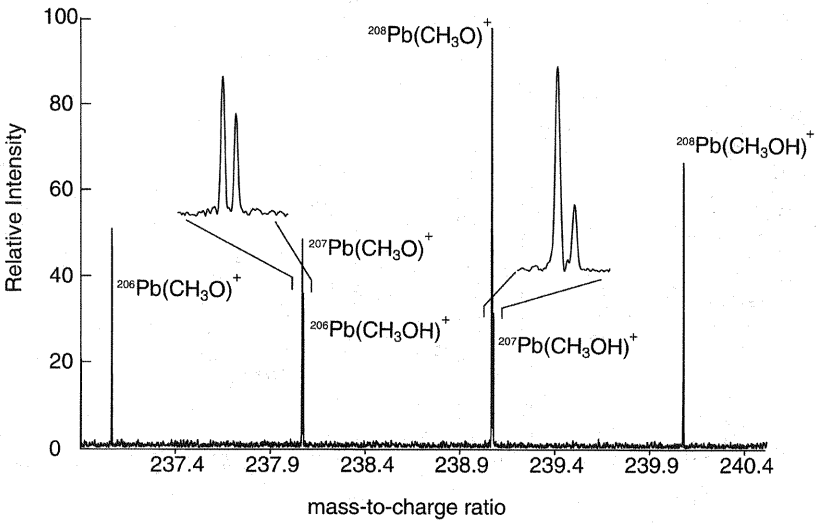

Figure 25 High mass resolving power spectrum of the *m/z* 237–240 range from Fig. 9.24.

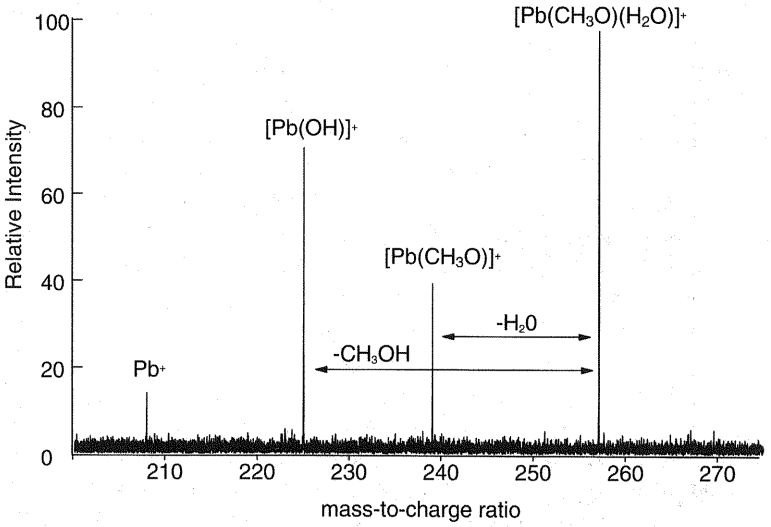

Figure 26 Collision-induced dissociation spectrum of the *m/z* 256 $Pb(CH_3O)(H_2O)^+$ peak from Fig. 9.24.

linear quadrupole-based mass analyzers is clear; most problems can be addressed with these instruments. The rapid data acquisition and simultaneous analysis of time-of-flight mass spectrometry fill many of the needs not addressed by these traditional approaches. So what niche will the trapping techniques fill?

The most obvious niche will be filled by FT-ICR mass spectrometry. The ability to mass resolve spectral interferences is unequivocally the desired analytical approach to mass analysis. There are a few well-known needs for high mass resolution of atomic isobars in which the most abundant or mononuclidic isotope is interfered; however, the greatest impact of FT-ICR may occur in the analysis of nuclear materials, in which fission products of unknown isotopic abundances exist. The single largest impediment to its implementation will likely be instrument costs, but the potential for obtaining the necessary resolution for most interferences in the elemental mass range by using a permanent magnet-based ICR system could reduce such costs, making it an attractive alternative mass analyzer for atomic spectrometry.

Quadrupole ion traps will most likely find their analytical niche in the ability to store and manipulate ions at elevated pressures, affording the possibility of enhanced mass resolution and the ability to integrate transient or weak signals over time. The relatively low costs and small size of quadrupole ion traps are attractive benefits of these analyzers. It is true that many of the advantageous ion-molecule reactions and collisional cooling effects observed in these devices can be produced with multipole collision cells; such cells are extremely effective means of removing many common interferences in plasma-source mass spectrometry. Yet when selective analyte accumulation, ion-molecule chemical reactions, or collision-induced dissociation is desired, the quadrupole ion trap is the preferred approach. The quadrupole ion trap also provides a unique opportunity for fundamental studies of low-energy collisional processes involving metal ions or adducts. CID will most likely remain a less desired approach for removal of spectral interferences in lieu of mass resolving power and charge exchange processes, but the high dissociation efficiency and negligible scattering losses that can be obtained for even strongly bound polyatomic ions do hold promise of analysis free of polyatomic spectral interferences.

REFERENCES

1. Paul, W.; Steinwedel, H.Z. *Naturforsch* **1953**, *8a*, 448.
2. Yates, N.A.; Booth, M.M.; Stephenson, J.L., Jr.; Yost, R.A. in *Practical Aspects of Ion Trap Mass Spectrometry,* Vol. 3, *Chemical, Environmental, and Biomedical Applications*; March, R.E., Todd, J.F.J., eds., CRC Press, New York, 1995, Chapter 4.
3. Kleintop, B.L.; Eades, D.M.; Jones, J.A.; Yost, R.A. in *Practical Aspects of Ion Trap Mass Spectrometry* Vol. 3, *Chemical, Environmental, and Biomedical Applications*; March, R.E., Todd, J.F.J., eds., CRC Press, New York, 1995, Chapter 5.

4. *Quadrupole Storage Mass Spectrometry*; March, R.E., Hughes, R.J., eds., John Wiley & Sons, New York, 1989.
5. *Practical Aspects of Ion Trap Mass Spectrometry*, Vol. 1, *Fundamentals of Ion Trap Mass Spectrometry*; March, R.E., Todd, J.F.J., eds., CRC Press, New York, 1995.
6. *Practical Aspects of Ion Trap Mass Spectrometry*, Vol. 2, *Ion Trap Instrumentation*; March, R.E., Todd, J.F.J., eds., CRC Press, New York, 1995.
7. *Practical Aspects of Ion Trap Mass Spectrometry*, Vol. 3, *Chemical, Environmental, and Biomedical Applications*; March, R.E., Todd, J.F.J., eds., CRC Press, New York, 1995.
8. Cooks, R.G.; Glish, G.L.; McLuckey, S.A.; Kaiser, R.E., Jr. *Chem. Eng. News* **1991**, *69*, 26.
9. a.) McLuckey, S.A.; Van Berkel, G.J.; Goeringer, D.E.; Glish, G.L. *Anal. Chem.* **1994**, *66*, 689A. B.) McLuckey, S.A.; Van Berkel, G.J.; Goeringer, D.E.; Glish, G.L. *Anal. Chem.* **1994**, *66*, 737A.
10. Duckworth, D.D.; Barshick, C.M. *Anal. Chem.* **1998**, *70*, 709A.
11. Stafford, G.C.; Kelly, P.E.; Syka, J.E.P.; Reynolds, W.E.; Todd, J.F.J. *Int. J. Mass Spectrom. Ion Processes* **1984**, *6*, 85.
12. McLuckey, S.A.; Glish, G.L.; Asano, K.G. *Anal. Chim. Acta* **1989**, *225*, 25.
13. Louris, J.N.; Amy, J.W.; Ridley, T.Y.; Cooks, R.G. *Int. J. Mass Spectrom. Ion Phys.* **1989**, *88*, 97.
14. Brodbelt, J.S. in *Practical Aspects of Ion Trap Mass Spectrometry*, Vol. 1, *Fundamentals of Ion Trap Mass Spectrometry*; March, R.E., Todd, J.F.J., eds., CRC Press, New York, 1995.
15. Goeringer, D.E.; Asano, K.G.; McLuckey, S.A.; Hoekman, D.; Stiller, S.W. *Anal. Chem.* **1994**, *66*, 313.
16. Garrett, A.W.; Cisper, M.E.; Nogar, N.S.; Hemberger, P.H. *Rapid Comm. Mass Spectrom.* **1994**, *8*, 174.
17. Marshall, A.G.; Wang, T.-C.L.; Ricca, T.L. *J. Am. Chem. Soc.* **1985**, *107*, 7893.
18. Julian, R.K., Jr.; Cooks, R.G. *Anal. Chem.* **1993**, *65*, 1827.
19. Kaiser, R.E., Jr.; Louris, J.N.; Amy, J.W.; Cooks, R.G. *Rapid Commun. Mass Spectrom.* **1989**, *3*, 225.
20. Williams, J.D.; Cox, K.A.; Schwartz, J.C.; Cooks, R.G. in *Practical Aspects of Ion Trap Mass Spectrometry*, Vol. 2, *Ion Trap Instrumentation*; March, R.E., Todd, J.F.J., eds., CRC Press, New York, 1995, Chapter 1.
21. Goeringer, D.E.; McLuckey, S.A.; Glish, G.L. *Proc. 39th ASMS Conf. Mass Spectrom. Allied Topics*, Nashville, TN, 1991, p. 532.
22. Londry, F.A.; Wells, G.J.; March, R.E. *Rapid Commun. Mass Spectrom.* **1992**, *7*, 43.
23. Schwartz, J.C.; Syka, J.E.P.; Jardine, I. *J. Am. Soc. Mass Spectrom.* **1991**, *2*, 198.
24. Stafford, G.C., Jr.; Kelley, P.E.; Syka, J.E.P.; Reynolds, W.E.; Todd, J.F.J. *Int. J. Mass Spectrom. Ion Processes* **1984**, *60*, 85.
25. Heller, D.N.; Lys, I.; Cotter, R.J.; Uy, O.M. *Anal. Chem.* **1989**, *61*, 103.
26. Glish, G.L.; Goeringer, D.E.; Asano, K.G.; McLuckey, S.A. *Int. J. Mass Spectrom. Ion Processes* **1989**, *94*, 15.
27. Pedder, R.E.; Yost, R.A.; Weber-Grabau, M. *Proceedings of the 37th ASMS Conf. Mass Spectrom. And Allied Topics*, Miami Beach, FL, May 1989, p. 468.
28. Freiser, B.S. *Talanta* **1985**, *32(8)B8*, 1985.

29. Cody, R.B.; Burnier, R.C.; Reents, W.D.; Carlin, T.J.; McCrery, D.A.; Lengel, R.K.; Freiser, B.S. *Int. J. Mass Spectrom. Ion Phys* **1980**, *33*, 37.
30. Gill, C.G.; Daigle, B.; Blades, M.W. *Spectrochim. Acta* **1991**, *46B(8)*, 1227.
31. Garrett, A.W.; Hemberger, P.H.; Nogar, N.S. *Spectrochim. Acta* **1995**, *50B*, 1889.
32. Gill, C.G.; Garrett, A.W.; Hemberger, P.H.; Nogar, N.S. *Spectrochim. Acta* **1996**, *51B*, 851.
33. De Bièvre, P.; Taylor, P.D.P. *Int. J. Mass Spectrom. Ion Processes* **1993**, *123*, 149.
34. Gill, C.G.; Garrett, A.W.; Hemberger, P.H.; Nogar, N.S. *J. Am. Soc. Mass Spectrom.* **1996**, *7*, 664.
35. Alexander, M.L.; Hemberger, P.H.; Cisper, M.E.; Nogar, N.S. *Anal. Chem.* **1993**, *65*, 1609.
36. McLuckey, S.A.; Glish, G.L.; Duckworth, D.C.; Marcus, R.K. *Anal. Chem.* **1992**, *65*, 1606.
37. Duckworth, D.C.; McLuckey, S.A. Unpublished results.
38. King, F.L.; Harrison, W.W. *Int. J. Mass Spectrom. Ion Processes* **1989**, *89*, 171.
39. Rowan, J.T.; Houk, R.S. *Appl. Spectrosc.* **1989**, *43*, 976.
40. Duckworth, D.C.; Marcus, R.K. *Appl. Spectrosc.* **1990**, *44*, 649.
41. Bauschlicher, C.W., Jr.; Partridge, H.; Langhoff, S.R. *J. Chem. Phys.* **1989**, *91*, 4733.
42. Lessen, D.; Brucat, P.J. *Chem. Phys. Lett.* **1988**, *152*, 473.
43. Lessen, D.; Brucat, P.J. *J. Chem. Phys.* **1989**, *91*, 4522.
44. Radzig, A.A.; Smirnov, B.M. *Reference Data on Atoms, Molecules and Ions*, Springer. Berlin, 1985, Chapter 11.
45. Irikura, K.K.; Fowles, E.H.; Beauchamp, J.L. *Anal. Chem.* **1994**, *66*, 3447.
46. Duckworth, D.C.; McLuckey, S.A., *1998 Winter Conference on Plasma Spectrochemistry*, Scottsdale, AZ, January 5–10, 1998, p. 298.
47. Duckworth, D.C.; Barshick, C.M.; Smith, D.H.; McLuckey, S.A. *Anal. Chem.* **1994**, *66*, 92.
48. Duckworth, D.C.; Smith, D.H.; McLuckey, S.A. *J. Anal. At. Spectrom.* **1997**, *12*, 43.
49. Barinaga, C.J.; Koppenaal, D.W. *Rapid Commun. Mass Spectrom.* **1994**, *8*, 71.
50. Koppenaal, D.W.; Barinaga, C.J.; Smith, M.R. *J. Anal. At. Spectrom.* **1994**, *9*, 1053.
51. Barinaga, C.J.; Eiden, G.C.; Alexander, M.L.; Koppenaal, D.W. *Fresenius J. Anal. Chem.* **1996**, *355*, 487.
52. Eiden, G.C.; Barinaga, C.J.; Koppenaal, D.W. *Proceedings of the 45th ASMS Conf. Mass Spectrom. and Allied Topics*, Palm Springs, CA, June 1997, p. 495.
53. Eiden, G.C.; Barinaga, C.J.; Koppenaal, D.W. *J. Anal. At. Spectrom.* **1996**, *11*, 317.
54. Eiden, G.C.; Barinaga, C.J.; Farmer, O.T., III; Koppenaal, D.W. *Proc. Of the 44th ASMS Conference on Mass Spectrometry and Allied Topics*, Portland, OR, 1996, p. 830.
55. Eiden, G.C.; Barinaga, C.J.; Koppenaal, D.W. *Rapid Commun. Mass Spectrom.* **1997**, *11*, 37.
56. Eiden, G.C.; Barinaga, C.J.; Koppenaal, D.W. *J. Am. Soc. Mass Spectrom.* **1996**, *7*, 1161.
57. Williams, J.D.; Cox, K.A.; Cooks, R.G.; McLuckey, S.A.; Hart, K.J.; Goeringer, D.E. *Anal. Chem.* **1994**, *66*, 725.
58. Frum, C.I. *Proc. Of the 44th ASMS Conf. Mass Spectrom. and Allied Topics*, Portland, OR, 1996, p. 831.

59. Eiden, G.C., personal communication, 1998.
60. Comisarow, M.B.; Marshall, A.G. *Chem. Phys. Lett.* **1974**, *4*, 282.
61. Baykut, G.; Eyler, J.R. *Trends Anal. Chem.* **1986**, *5*, 44.
62. Marshall, A.G.; Grosshans, P.B. *Anal. Chem.* **1991**, *63*, 215A.
63. Koster, C.; Kahr, M.S.; Castoro, J.A.; Wilkins, C.L. *Mass Spectrom. Rev.* **1992**, *11*, 495.
64. McLafferty, F.W. *Accts. Chem. Res.* **1994**, *27*, 379.
65. Comisarow, M.B.; Marshall, A.G. *J. Mass Spectrom.* **1996**, *31*, 581.
66. Marshall, A.G.; Hendrickson, C.L.; Jackson, G.S. *Mass Spectrom. Rev.* **1998**, *17*, 1.
67. Buchanan, M.V., ed. *Fourier Transform Mass Spectrometry: Evolution, Innovation, and Applications, ACS Symp. Series*; American Chemical Society, Washington, DC, 1987, 205 pp.
68. Marshall, A.G.; Verdun, F.R. *Fourier Transforms in NMR, Optical, and Mass Spectrometry: A User s Handbook*, Elsevier, Amsterdam, 1990.
69. Asamoto, B.; Dunbar, R.C. *Analytical Applications of Fourier Transform Ion Cyclotron Resonance Mass Spectrometry*, VCH, New York, 1991.
70. Lehman, T.A.; Bursey, M.B. *Ion Cyclotron Resonance Spectrometry*, Wiley, New York, 1976.
71. McIver, R.T., Jr. *Rev. Sci. Instrum.* **1970**, *41*, 555.
72. Comisarow, M.B.; Marshall, A.G. *Chem. Phys. Lett.* **1974**, *26*, 489; Marshall, A.G.; Wang, T- C.L.; Ricca, T.L. *J. Am. Chem. Soc.* **1985**, *107*, 7893; McIver, R.T., Jr.; Baykut, G.; Hunter, R.L. *Int. J. Mass Spectrom. Ion Proc.* **1989**, *89*, 343.
73. Alleman, M.; Kellerhals, H-P.; Wanczek, K.P. *Int. J. Mass Spectrom. Ion Phys.* **1983**, *46*, 139.
74. Comisarow, M.B.; Grassi, V.; Parisod, G. *Chem. Phys. Lett.* **1978**, *57*, 413.
75. Vulpius, T.; Houriet, R. *Int. J. Mass Spectrom. Ion Proc.* **1989**, *88*, 283.
76. Schweikhard, L.; Guan, S.; Marshall, A.G. *Int. J. Mass Spectrom. Ion Proc.* **1992**, *120*, 71; Speir, J.P.; Gorman, G.S.; Pitsenberger, C.C.; Turner, C.A.; Wang, P.P.; Amster, I.J. *Anal. Chem.* **1993**, *65*, 1746.
77. Plesko, S.; Zwinselman, J.J.; Allemann, M.; Kellerhals, H-P. *Helvetica Phys. Acta* **1984**, *57*, 765.
78. Brown, R.S.; Wilkins, C.L. *ACS Symp. Ser.* **1987**, *359*, 127.
79. Spell, T.L.; DeLong, S.E.; Creasy, W.R. *Int. J. Mass Spectrom Ion Proc.* **1993**, *124*, 223.
80. Moini, M.; Eyler, J.R. *J. Chem. Phys.* **1988**, *88*, 5512; Cheeseman, M.A.; Eyler, J.R. *J. Phys. Chem.* **1992**, *96*, 1082; Maruyama, S.; Anderson, L.R.; Smalley, R.E. *Rev. Sci. Instr.* **1990**, *61*, 3686; McElvany, S.W.; Cassady, C.J. *J. Phys. Chem.* **1990**, *94*, 2057; Burnier, R.C.; Byrd, G.C.; Freiser, B.S. *J. Am. Chem. Soc.* **1981**, *103*, 4360.
81. Bach, S.B.H.; Eyler, J.R. *J. Chem. Phys.* **1990**, *92*, 358; Zimmerman, J.A.; Bach, S.B.H.; Watson, C.H.; Eyler, J.R. *J. Phys. Chem.* **1991**, *95*, 98.
82. Easterling, M.L.; Pitsenberger, C.C.; Amster, I.J. *J. Am. Soc. Mass Spectrom.* **1997**, *8*, 195.
83. Castoro, J.A.; Wilkins, C.L. *Anal. Chem.* **1993**, *65*, 2621.
84. Brenna, J.T.; Creasy, W.R.; McBain, W.; Soria, C. *Rev. Sci. Instr.* **1988**, *59*, 873; Cody, R.B.; Bjarnason, A.; Weil, D.A. in *Lasers in Mass Spectrometry*, Lubman, D., ed., Oxford University Press, New York, 1990, 316; Lafargue, P.E.; Gaumett, J.J.; Muller, J.F.; Labrosse, A. *J. Mass Spectrom.* **1996**, *31*, 623.

85. Kofel, P.; Allemann, M.; Kellerhals, H.-P.; Wanczek, K.-P. *Int. J. Mass Spectrom. Ion Proc.* **1985**, *65*, 97; Kofel, P.; McMahon, T.B. *Int. J. Mass Spectrom. Ion Proc.* **1990**, *98*, 1.
86. Limbach, P.A.; Marshall, A.G.; Wang, M. *Int. J. Mass Spectrom. Ion Proc.* **1993**, *125*, 135.
87. Hunt, D.F.; Shabanowitz, J.; McIver, R.T., Jr.; Hunter, R.L.; Syka, J.E.P. *Anal. Chem.* **1985**, *57*, 765.
88. Senko, M.W.; Hendrickson, C.L.; Emmett, M.R.; Shi, S.D.H.; Marshall, A.G. *J. Am. Soc. Mass Spectrom.* **1997**, *8*, 970.
89. Struyf, H.; Van Roy, W.; Van Vaeck, L.; Van Grieken, R.; Gijbels, R.; Caravatti, P. *Anal. Chem. Acta* **1993**, *283*, 139; Struyf, H.; Van Vaeck, L.; Poels, K.; Van Grieken, R. *J. Am. Soc. Mass Spectrom.* **1998**, *9*, 482.
90. Eller, K.; Schwarz, H. *Int. J. Mass Spectrom. Ion Proc.* **1988**, *83*, 23.
91. Barshick, C.M.; Eyler, J.R. *J. Am. Soc. Mass Spectrom.* **1992**, *3*, 122.
92. Harrison, W.W. *J. Anal. At. Spectrom.* **1988**, *3*, 867.
93. Barshick, C.M.; Eyler, J.R. *J. Am. Soc. Mass Spectrom.* **1993**, *4*, 387.
94. Marcus, R.K.; Cable, P.R.; Duckworth, D.C.; Buchanan, M.V.; Pochkowski, J.M.; Weller, R.R. *Appl. Spectrosc.* **1992**, *46*, 1327.
95. Kruppa, G.H.; Caravatti, P.; Radloff, C.; Zurcher, S.; Laukien, F.H.; Watson, C.H.; Wronka J. in *Analytical Applications of Fourier Transform Ion Cyclotron Resonance Mass Spectrometry*, Asamoto, B., ed., VCH Publishers, New York, 1991.
96. Watson, C.H.; Wronka, J.; Laukien, F.H.; Barshick, C.M.; Eyler, J.R. *Spectrochimica Acta* **1993**, *48B*, 1445.
97. Watson, C.H.; Wronka, J.; Laukien, F.H.; Barshick, C.M.; Eyler, J.R. *Anal. Chem.* **1993**, *65*, 2801.
98. Watson, C.H.; Barshick, C.M.; Wronka, J.; Laukien, F.H.; Eyler, J.R. *Anal. Chem.* **1996**, *68*, 573.
99. Goodner, K.L.; Milgram, K.E.; Watson, C.H.; Eyler, J.R.; Dejsupa, C.; Barshick, C.M. *J. Am. Soc. Mass Spectrom.* **1996**, *7*, 923.
100. Barshick, C.M.; Goodner, K.L.; Watson, C.H.; Eyler, J.R. *Int. J. Mass Spectrom. Ion Process.* **1998**, *178*, 73.
101. Milgram, K.E.; Watson, C.H.; Eyler, J.R. *Proc. 43rd ASMS Conf. on Mass Spectrom. And Allied Topics,* Atlanta, GA, May 1995, 1088.
102. White, F.M.; Marto, J.; Marshall, A.G. *Rapid Commun. Mass Spectrom.* **1996**, *10*, 1845.
103. Milgram, K.E.; White, F.M.; Goodner, K.L.; Watson, C.H.; Koppenaal, D. W.; Barinaga, C.J.; Smith, B.H.; Winefordner, J.D.; Marshall, A.G.; Houk, R.S.; Eyler, J.R. *Anal. Chem.* **1997**, *69*, 3714.
104. Milgram, K.E. Ph.D. Thesis, University of Florida, Gainesville, FL, August 1997.
105. Milgram, K.E.; Goodner, K.L.; Watson, C.H.; Eyler, J.R. *Proc. 44th ASMS Conf. on Mass Spectrom. And Allied Topics,* Portland, OR, May 1996, 833.

10

Elemental Speciation by Inorganic Mass Spectrometry

Karen L. Sutton, Kathryn L. Ackley, and Joseph A. Caruso
University of Cincinnati
Cincinnati, Ohio

10.1. INTRODUCTION

Elemental speciation is the identification and quantification of the chemical form of an element. Traditional analytical techniques for trace elemental analysis have focused on determining the concentration of a particular element within a sample. However, knowledge of total element concentration may not provide sufficient information to determine toxicity since the toxicity of many elements is dependent upon their chemical forms. The oxidation state of the element as well as the organic substituents attached to it may have a dramatic effect on the biological properties observed. As a result, researchers have endeavored to develop new and better analytical techniques that are capable of performing elemental speciation.

Elemental speciation is most often required when analyzing biological and environmental samples since the health and ecological risks associated with many elements are related to the chemical forms that are present. All methods devised for speciation comprise two basic parts. The first part involves separation of the various species without altering of their chemical form. This task is usually accomplished through the use of some type of chromatography, although novel separations for speciation have been proposed that do not utilize chromatographic techniques. After separation, a detector must quantify each species. Mass spectrometry has proved to be an excellent method of detection because of its high sensitivity, low detection limits, and element specificity. Reviews detail the use of inductively coupled plasma mass spectrometry as a detection method for speciation

studies [1,2]. The use of microwave induced plasma mass spectrometry (MIP-MS) in speciation studies has also been reviewed [3].

10.2 ELEMENTS OF INTEREST

Elemental arsenic is used in alloys of lead and copper, in semiconductors, and as an additive to the grid metal in storage batteries. Arsenic compounds have been used as pesticides and wood preservatives [4]. Although arsenic is most well known for its use as a poison, some evidence suggests that trace amounts may be essential for good health [5]. Inorganic forms of arsenic are more toxic than the organic forms; arsenite, As (III), is the most toxic form of the element, followed by arsenate, As (V), monomethylarsenate, and dimethylarsenate.

Cadmium is used in electroplating, alloys, and batteries, and in some instances as a stabilizer for certain plastics. Zinc minerals contain cadmium, so elevated environmental levels of cadmium can frequently be attributed to the increased dispersal of zinc and zinc compounds [6]. Cadmium has no known function in the human body, and uncomplexed forms of the element are extremely toxic to the kidneys.

Chromium is used extensively in metal plating and is found as a trace element in natural waters. Chromium is capable of assuming oxidation states ranging from 2^+ to 6^+ with Cr (III) the most stable. Chromium (III) is essential for good health in humans as it plays a role in glucose metabolism. Chromium (III) compounds show little or no toxicity, whereas other chromium compounds, particularly chromium (VI), can be toxic and carcinogenic.

Gold-based drugs are used in the treatment of rheumatoid arthritis, but their mode of action is poorly understood. Gold (I) pharmaceuticals include sodium gold(I)thiomalate, gold(I)thioglucose, and (triethylphosphine)(tetraacetylthioglucose) gold(I) [7]. These compounds are extremely labile and are quickly transformed once they enter the body [8]. Speciation of these drugs and their metabolites in urine and serum samples may offer insight into their mechanistic pathways.

The neutral isotope of iodine is an essential element in the human body; most of the iodine-127 is located in the thyroid gland. Iodine's radioactive isotope, iodine-131, is readily absorbed in the body, where it becomes concentrated in the thyroid gland and may produce cancers. Exposure to radioactive iodine is an increasing concern since it is produced by fission reactions in nuclear reactors and by nuclear weapons tests.

The role iron plays in the lives of humans is significant. Iron is primarily used in the production of steel, and it is an essential element in the human body, where it is part of the protein hemoglobin, which is responsible for carrying oxygen. Iron's two principal oxidation states are Fe (III) and Fe (II), and a complex cycle that is responsible for the conversions between the two forms exists in na-

ture. Iron reaches the water supply in a variety of ways, including through corrosion and industrial waste. Considerable effort is made to remove iron ions from the municipal water supply since they may damage water fixtures.

Health risks associated with exposure to lead are well known. Children are particularly susceptible to exposure. Inorganic lead compounds have been used for paint pigments and ceramic glazes, and organolead compounds such as tetraethyl lead have been used as antiknock agents in gasoline. Organolead compounds act differently in the body than inorganic compounds since they have a strong affinity for lipids and affect the central nervous system [9].

Mercury contaminated foodstuffs and water supplies are a concern because of the extreme toxicity of the element and its compounds. Elemental mercury is used in the production of chlorine gas, and organomercury compounds formerly found use as pesticides and fungicides. Alkyl mercury compounds are of greatest concern since they do not degrade readily, and methyl mercury compounds concentrate in fish lipid tissue [9]. Pregnant women are at greatest risk since methyl mercury readily crosses the placenta, affecting the fetus [6].

Most platinum compounds exist as coordination complexes; the tetravalent compounds typically are more toxic than the hexavalent ones [10]. Certain neutral platinum complexes exhibit antitumor activity and therefore are used in chemotherapy drugs such as cisplatin. Speciation is required to distinguish platinum chemotherapy drugs from their metabolites in patients' blood and serum samples.

Selenium occurs in the earth's crust as metal selenides [5], and the element and its compounds are used in electronic applications and in the production of glass, ceramics, and stainless steel [11]. In trace amounts, selenium is an essential nutrient, but in higher quantities or when certain species are present, the element becomes toxic. The most important forms of selenium are selenate (SeO_4^{2-}), and selenite (SeO_3^{2-}), and selenide (Se^{2-}). Selanates are relatively soluble, whereas selenites and elemental selenium are virtually insoluble [12].

Tellurium usually occurs in nature as metallic tellurides. This toxic element is used in the production of iron, steel, and other alloys. Tellurium can have oxidation states of -2, $+2$, $+4$, and $+6$. Tellurites tend to be more toxic than tellurates [12].

Organotin compounds are regularly utilized for their bactericidal, fungicidal, and insecticidal properties. Tributyltin and triphenyltin compounds in particular are used in antifouling paints, and they are of concern because of the destructive effect they have on nontarget marine organisms. The toxicity of organotin compounds is dependent upon the number and type of organic constituents in the molecule. Speciation of these compounds is vital if environmental risks are to be assessed.

Vanadium is used as an additive to steel and cast iron. This element has been found to be essential for the development of chicks and rats, but its role in humans is more ambiguous [5]. Vanadium has oxidation states ranging from $+5$ to -1, with $+4$ the most stable under normal conditions. The chemistry of vanadium is com-

plex since the ion may exist in solution in a number of different forms, depending on the concentration of the species and the pH of the solution. Some of the forms V (V) may have in solution are $VO_3(OH)^{2-}$, $V_{10}O_{28}^{6-}$, $V_{10}O_{27}(OH)^{5-}$, $V_{10}O_{26}(OH)_2^{4-}$, and VO^{2+}; V (IV) may exist as $VO(H_2O)_5^{2+}$ or $V_{18}O_{42}^{12-}$ [13].

10.3 PLASMA MASS SPECTROMETRIC DETECTION

10.3.1 Inductively Coupled Plasma Mass Spectrometric Detection

By far the most common type of plasma used for speciation analysis is the inductively coupled plasma (ICP) with mass spectrometry (MS) or atomic emission spectrometry (AES) detection. The performance of the ICP-MS system has been well documented since its development in the early 1980s by the Gray and Houk research groups [14,15], and it is now used for a wide variety of applications such as environmental, clinical, geological, food, and industrial analysis.

Figure 10.1 is a schematic diagram of a typical commercial ICP-MS system. The inductively coupled plasma is formed by directing argon gas through a quartz torch, comprised of three concentric tubes that surrounded by a copper load coil connected to a radio frequency (rf) generator. Radio frequency energy (of either 27 or 40 MHz and of 700–1500 W power) is directed to this load coil, and oscillating magnetic and electric fields are induced at the top of the torch. The formation of the plasma occurs when a spark is applied to the tangentially flowing argon gas, causing the formation of argon ions. The free electrons from this process are accelerated by the magnetic field and bombard other argon atoms, causing further

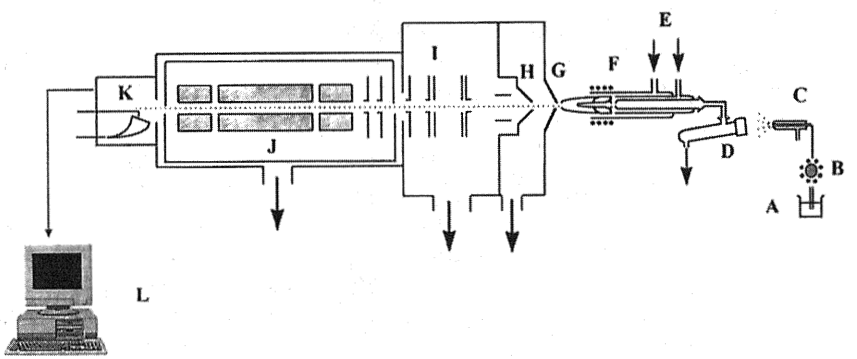

Figure 1 Schematic diagram of a typical commercial inductively coupled plasma mass spectrometry (ICP-MS) instrument: (A) liquid sample, (B) peristaltic pump, (C) nebulizer, (D) spray chamber, (E) argon gas inlets, (F) load coil, (G) sampler cone, (H) skimmer cone, (I) ion lenses, (J) quadrupole, (K) electron multiplier detector, (L) computer.

ionization in an avalanche effect and subsequent plasma formation. The plasma is sustained by continuous application of rf energy to the coil. The appearance of the plasma is an intense, luminous, teardrop-shaped discharge. Samples are introduced to the plasma via the central injector torch tube by means of a carrier gas, commonly argon. Liquid samples are nebulized into an aerosol and are carried to the central channel by this carrier gas, also known as the *nebulizer gas ow*. Once the sample has reached the plasma, desolvation (in the case of liquid samples), vaporization, atomization, and ionization processes occur. Typical ICP-MS operating conditions for aqueous sample introduction are given in Table 10.1.

Ions from the ICP are sampled, using the sampling and skimmer cones, which are usually made of nickel, although platinum cones are used in some instances. The ions pass through the apertures in these cones into chambers sustained at low pressure. The ions are focused into a linear path by using ion lenses, held at varying potential differences, before reaching the quadrupole mass analyzer, where ions of only one mass-to-charge ratio are transmitted at a time. The ions are then detected by using an electron multiplier, where each ion reaching the detector is amplified as an electron pulse.

The ICP-MS has several analytical attractions including very low detection limits [parts per billion to parts per trillion (ppb to ppt) levels], a large linear dynamic range, relatively simple spectra, excellent stability, multielement determination capability, and ability to measure isotopic abundances. Disadvantages are mainly due to the formation of polyatomic interferences from the plasma gas, entrained gases, and matrix elements such as Cl [16].

Table 1 Typical Inductively Coupled Plasma Mass Spectometry Operating Conditions

Parameter	Instrument setting
Radio frequency forward power (W)	1350
Radio frequency reflected power (W)	<5
Plasma gas flow (L/min)	16
Auxiliary gas flow (L/min)	0.8–1.1
Nebulizer gas flow rate (L/min)	0.7–1.0
Liquid sample flow rate (ml/min)	1.0
Sample introduction system	
Nebulizer	Concentric
Spray chamber	Scott-type double-pass
Pump settings	
Expansion stage pressure (mbar)	$<2 \times 10^{0}$
Intermediate stage pressure (mbar)	4×10^{-6}
Analyzer stage pressure (mbar)	0.0×10^{-4}

10.3.2 Microwave Induced Plasma Mass Spectrometric Detection

An alternative ion source for mass spectrometry is the microwave induced plasma. It is used less commonly than the ICP, but it has become more popular since the late 1980s for speciation studies. Olson and Caruso [3] have reviewed the investigations regarding the helium microwave induced plasma. The main advantages for using this alternative plasma source include the requirement for reduced gas and power consumption along with the possibility of utilizing gases other than argon. The argon ICP (ionization potential 15.75 eV) is not an efficient excitation and ionization source for elements of high ionization potential, such as Cl, As, and Se. The helium plasma (ionization potential 24.5 eV) may therefore enhance the degree of ionization for these elements. Isobaric interferences produced by polyatomic species in the argon ICP-MS are also eliminated by the use of helium. Because of heat dissipation requirements, He microwave induced plasmas (MIPs) do not cause marked deterioration of the sampling orifice. There are no commercial MIP-MS instruments available to date, although a gas chromatograph with MIP atomic emission detection has been manufactured [17].

Figure 10.2 is a schematic diagram of a helium MIP-MS system, with gaseous sample introduction, developed by the Caruso group. This is the most popular method of sample introduction to date for MIP-MS analysis as the MIP at low pressures is not tolerant to liquid samples. A commercial ICP-MS system may be modified by mounting an MIP discharge source in place of the ICP source. A Beenakker cavity is commonly used as the microwave source and serves to focus the microwave energy. Cavity construction and dimensions have been described in detail by Evans et al. [18].

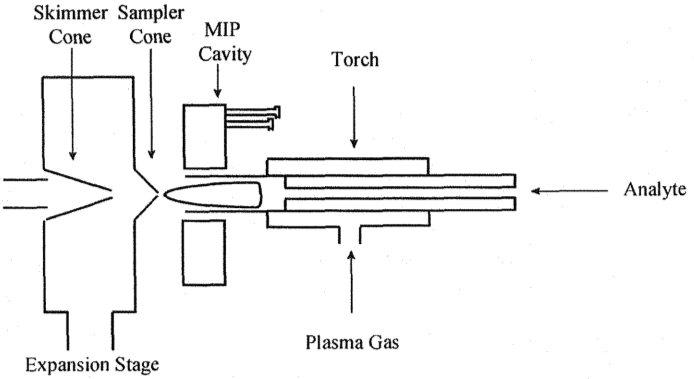

Figure 2 Schematic diagram of a typical microwave induced plasma mass spectrometry (MIP-MS) instrument.

The cavity is connected to a microwave generator and rf energy is applied. This energy is tuned inside the cavity by using tuning stubs, as opposed to a matching network tuning method used with the ICP. The cavity is water-cooled to dissipate heat and to increase longevity. The microwave plasma is initialized by setting the plasma gas flow and inserting a copper wire into the torch. The power is then increased and ignition takes place spontaneously. After ignition, normal operating conditions are set. The optimal operating conditions for low-pressure He-MIP-MS are given in Table 10.2. It should be noted that reduced orifice sampling cones are used for low-pressure He-MIP-MS to minimize air entrainment and background species and to allow easier achievement of necessary vacuum conditions.

10.4 CHROMATOGRAPHIC SAMPLE INTRODUCTION

10.4.1 Liquid Chromatography

Interfacing Liquid Chromatography with Inductively Coupled Plasma Mass Spectrometry

Liquid chromatography (LC) is the most commonly used technique for trace element speciation with ICP-MS detection. The mobile phase flow rates used with most LC techniques (0.5–2.0 mL min^{-1}) are compatible for ICP-MS introduction using conventional sample introduction systems (pneumatic nebulization with cross flow and concentric nebulizers and double-pass spray chambers). An interface, known as a *transfer line*, must be constructed to allow connection between the outlet of the LC column and the nebulizer of the ICP-MS. Inert plastic tubing is commonly used for this purpose with the inner diameter and length kept to 20–50 cm in order to minimize peak broadening.

Conventional ICP-MS sample introduction systems with pneumatic nebulization are inefficient as the amount of sample reaching the plasma is generally less than 2% of the amount of sample actually entering the nebulizer. To obtain im-

Table 2 Microwave Induced Plasma Mass Spectometry Operating Conditions

Parameter	Instrument setting
Radio frequency power (W)	25–500 W
Torch	Tangential flow
Plasma gas flow rate (L/min)	5.0
Intermediate gas flow rate (L/min)	0.12
Sampling orifice (mm)	0.4
Expansion stage	Additional 53 ft^3/min vacuum pump

proved sensitivity and superior detection limits, nebulizers with higher transport efficiencies must be employed. Oscillating capillary nebulizers [19], ultrasonic nebulizers [20], direct injection nebulizers [21], and hydraulic high-pressure nebulizers [22] have all been shown to increase sensitivity and improve detection limits for LC-ICP-MS.

It must be noted that increasing the amount of solvent in the ICP produces a higher load on the plasma and an increase in reflected powers, causing plasma instability. Desolvation of the sample aerosol may overcome this hurdle and is achieved by the use of a cooled spray chamber. In addition, Peltier coolers and membrane dryers [23] have been used for desolvating liquid aerosols and eliminate approximately 90% of the aerosol (Fig. 10.3). Spray chambers may also im-

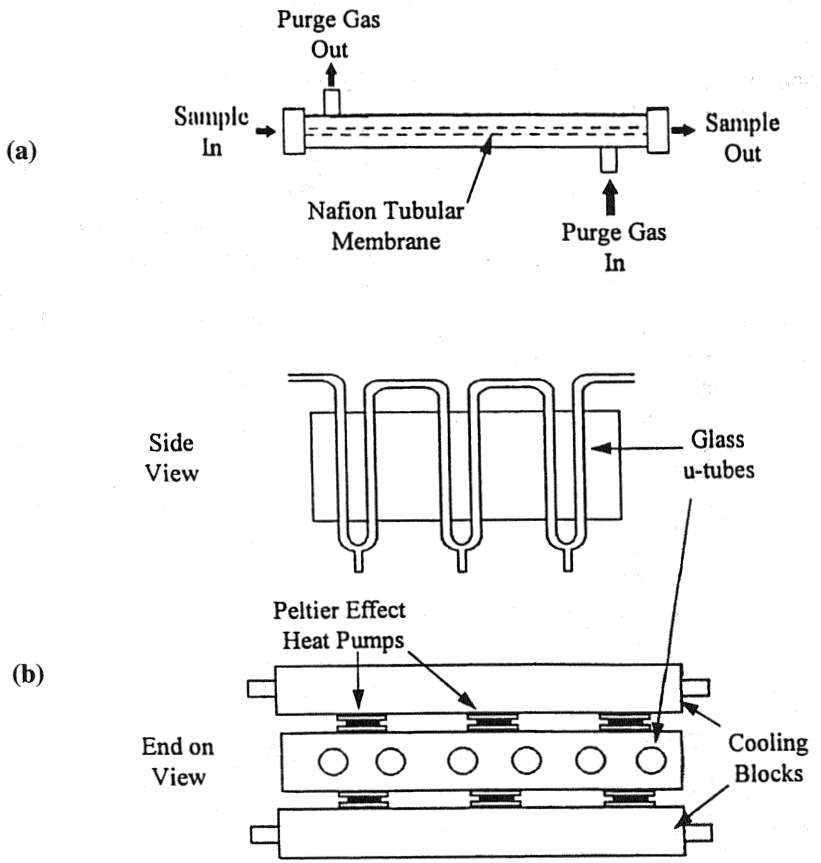

Figure 3 (a) Schematic diagram of Perma Pure Membrane drier. (From Ref. [23]. (b) Schematic of Peltier driven condenser. (From Ref. 23).

prove sample transport efficiency, and their effect has also been examined for LC-ICP-MS [24].

Most LC-ICP-MS hyphenation is performed by using isocratic elution. Gradient elution may be used to improve retention times and partition functions for a chromatographic separation with conventional LC detectors, but difficulties arise when gradients are introduced into the ICP. The changing load on the plasma due to the variations in mobile phase composition often causes plasma instability. In addition, optimal operating conditions evaluated for one mobile phase combination may not be valid when an organic constituent concentration is increased.

Time resolved analysis is essential for monitoring of chromatographic separations. Rapid data acquisition may now be performed, using ICP-MS instruments equipped with software capable of monitoring signal versus time at several different m/z values.

Liquid chromatographic analyses with ICP-MS detection may be divided into categories according to the mode of chromatography used: reversed-phase, ion-pair, micellar, ion-exchange, and size-exclusion chromatography.

Reversed-Phase Liquid Chromatography

Reversed-phase liquid chromatography (RPLC) separates the analytes of interest by using chromatographic columns where the stationary phase surface is less polar than the mobile phase. The solute interacts with the stationary and mobile phases, and separation of the species is thus achieved. The organic modifier or its concentration may be changed in order to change the selectivity of the separation; however, the choice of organic solvent is limited to those that do not significantly affect plasma stability and instrument performance. Methanol and acetonitrile, in combination with water, have been used for such separations.

C_{18}, C_8, or C_1 siloxane stationary phases may be used for reversed-phase separations. Mobile phases of high pH values should be avoided as hydrolysis of the siloxane stationary phase occurs and so the packing material degrades over time. Phosphate or acetate buffers may be used to control the pH of the mobile phase, although the concentration of these salts should be kept to a minimum so that clogging of the torch injector and sampler cone does not occur.

Reversed-Phase Liquid Chromatography—Environmental and General Applications

Reversed-phase liquid chromatography (RPLC) with ICP-MS detection has been used for speciation studies of environmental and more general analytical samples. Butyltin compounds, used in polyvinyl chloride production; and in fungicides and insecticides, have been separated by Dauchy et al. [25] using a methanol/water/acetic acid mobile phase (80:14:6) that had previously been optimized for this separation. Monobutyltin (MBT), dibutyltin (DBT), and tributyltin (TBT) compounds

were separated by using isocratic elution of the mobile phase; detection limits for the three compounds were 0.24 ng, 0.24 ng, and 0.15 ng, respectively (as Sn).

Lead speciation (inorganic lead, trimethyllead chloride, triethyllead chloride, and triphenyllead chloride) has been performed by Al-Rashdan et al. [26]. Despite previous use of a gradient elution (10% to 70% methanol in water) with inductively coupled plasma atomic emission spectrometry (ICP-AES) detection, an isocratic elution was used with ICP-MS detection because gradient elution causes plasma instability. A 30% methanol/water mobile phase was used, along with a C_{18} column, and the pH was optimized by using acetate buffer.

Mercury compounds in tuna samples have been speciated by Bushee et al. [27] and by Huang and Jiang [28] in dogfish muscle and wastewater. Methyl mercury, ethylmercury, and inorganic mercury may be differentiated with picogram detection limits (Fig. 10.4).

Tellurium speciation in water samples from a treatment plant has been performed by Klinkenberg et al. [29]. TeO_3^{2-} and $HTeO_4^-$ were separated along with 11 unidentified organic Te compounds. More structural information was not available as a result of complete decomposition of the compounds in the plasma.

Reversed-Phase Liquid Chromatography—Clinical Applications

The iodide ion, I^-, and five iodo-amino acids, found in thyroid hormones, have been separated by using RPLC-ICP-MS [30]. A 50% methanol eluent was used and the detection limits (35–130 pg) were improved by an order of magnitude compared to that of ultraviolet (UV) absorbance detection.

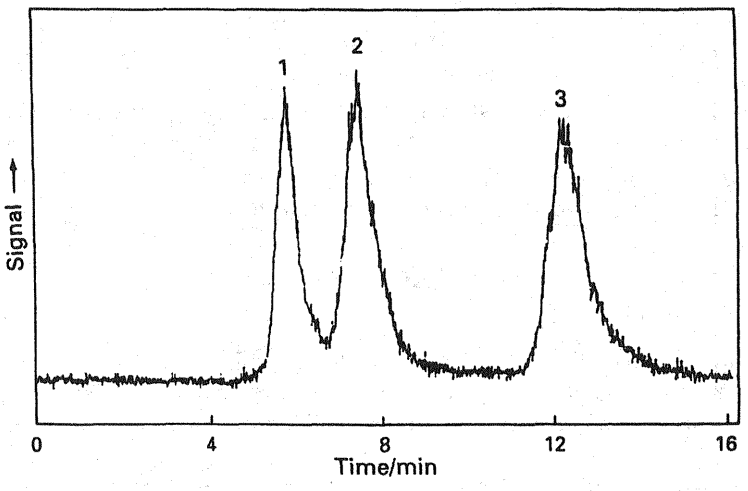

Figure 4 Mercury-selective chromatogram for (1) CH_3HgCl (20 ppb); (2) Hg^{2+} (10 ppb); (3) C_2H_5HgCl (20 ppb). (From Ref. 28.)

The mercury containing compound, thimerosal, has found use as an antimicrobial agent and is employed in biological vaccines and contact lens solutions. The decomposition products, methylmercury chloride, dimethylmercury, and mercury (III) chloride, have been separated by using RPLC with a C_{18} column and a 3% acetonitrile mobile phase [27,31]. Long-term degradation of thimerosal was demonstrated with complete recovery for all species.

Platinum is now used in a variety of chemotherapy drugs that completely metabolize in the human body to a number of platinum containing species. Cairns et al. [23] separated the drug from its metabolites, using a C_{18} column and a 95:5 to 30:70 H_2O/acetonitrile solvent gradient. A desolvation device was used to remove a significant amount of the organic solvent.

Selenium species have been separated by using RPLC with an oscillating capillary nebulizer [19]. A C_{18} column was used along with an optimized mobile phase. Detection limits were found to be in the 30-to 400-pg (as Se) range, depending on the Se species (Fig. 10.5).

Owen et al. [32] used RPLC to speciate Zn compounds in an in vitro gastrointestinal digest of chicken meat. C_8 and C_{18} columns were connected in series to achieve the separation. It was found that time resolved acquisition software needed improvement for peak areas to be determined.

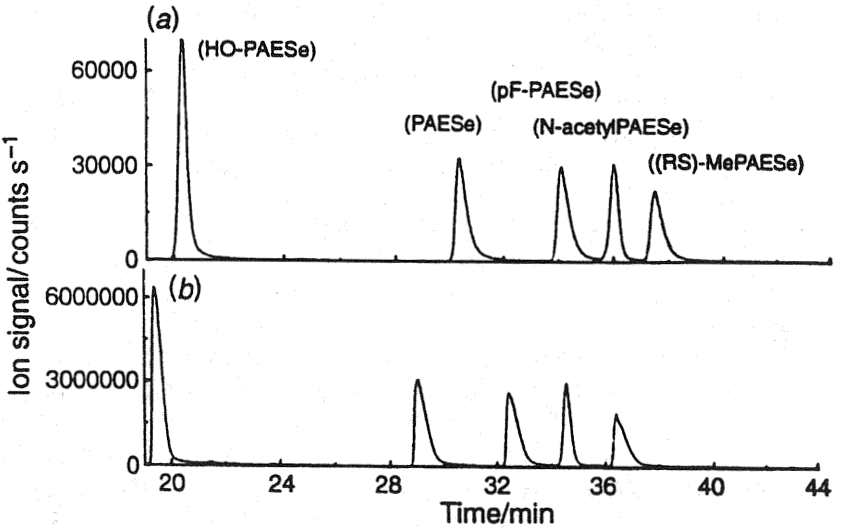

Figure 5 Separation of mixture of five selenides: 166 ng of each species in 1-μL injection, Se m/z = 82: (a) oscillating capillary nebulizer (OCN) at 0.4-ml/min on 25 cm × 3.2 mm i.d. C_{18} column; (b) OCN at 50 μL/min on 25 cm × 1.0 mm i.d. C_{18} column. (From Ref. 19.)

Ion-Pair Chromatography

A variation of reversed phase chromatography, known as *ion-pair chromatography* (IPC), is currently one of the most popular techniques for speciation studies when coupled to ICP-MS. Both ionic and nonionic species may be separated by this technique, and both normal and reversed-phase modes may be used, although only the latter has been successfully interfaced with ICP-MS. The technique employs the same columns used with reversed-phase LC, with a mobile phase containing an organic solvent (usually methanol or acetonitrile), an aqueous buffer, and an ion-pairing reagent. This ion-pairing reagent forms an ion pair with the analyte species and is retained by stationary phase interactions. Alkyl anions (e.g., tetraalkylammonium salts) or cations (e.g., alkylsulfonates) may be used to form ion pairs at a concentration of 0.001 to 0.005 *M*. Separations and selectivities are highly dependent on pH and ion-pair reagent concentration.

Ion-Pair Liquid Chromatography—Environmental, Clinical, and General Applications

The speciation of arsenic compounds, using IPC and ICP-MS as a detector, has received much attention [33–39]. Beauchemin et al. [33,34] used IPC for the analysis of arsenic species in dogfish muscle. The ion-pair reagent was 10 μ*M* sodium dodecylsulfate in a 5% methanol, 2.5% glacial acetic acid mobile phase at pH 2.5 with a C_{18} column. The toxic inorganic species, As (III) and As (V), as well as the less toxic organoarsenic species, monomethylarsenic (MMA), dimethylarsenic (DMA), arsenobetaine (AB), and arsenocholine (AC), were separated. AB was the dominant species and constituted 84% of the total arsenic concentration with a detection limit of 300 pg (as As).

Arsenic (*m/z* 75) is known to suffer from an isobaric interference caused by the presence of $ArCl^+$ (*m/z* 75) during speciation analyses, particularly for samples that contain a high chloride salt content, e.g., sea water and urine. Several groups [37–39] used hydride generation to transform the arsenic compounds into their volatile hydrides before aspiration into the ICP. Selective transportation of the hydrides may thus be achieved by using a gas-liquid separator to eliminate the chloride interference (Fig. 10.6).

In environmental and clinical samples, IPC-ICP-MS may be used for selenium speciation [40–42]. Selenite, selenate, and trimethylselenomium were separated by Yang and Jiang [40], using a mobile phase containing 3% methanol and 5 m*M* PIC-A ion-pairing reagent. An ultrasonic nebulizer was used for improved sample transport, yielding detection limits of 22–74 pg Se for the three species, respectively. Selenite was found to be the most abundant species in urine and unidentified peaks were attributed to selenoaminoacids.

Three such selenoaminoacids were separated and identified in a study by Olivas et al. [42]. Selenomethionine (SeMet), selenocystine (SeCys), and the trimethylselenomium ion ($TMeSe^+$) were separated by using an anionic counter

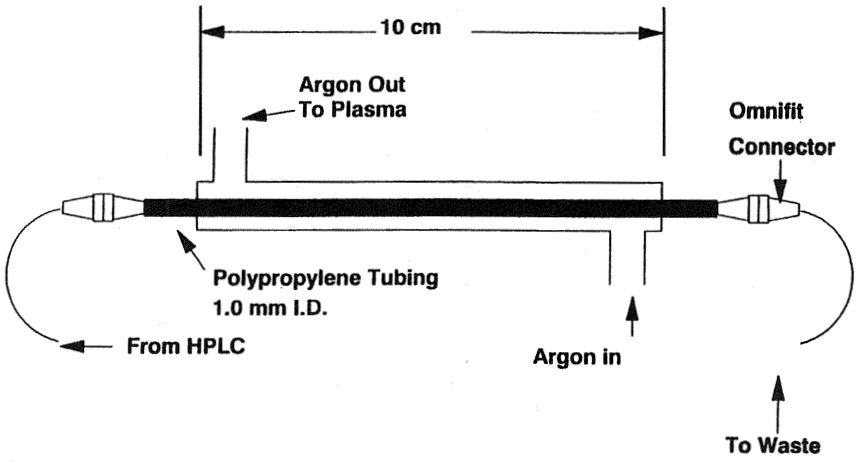

Figure 6 Schematic drawing of a gas-liquid separator. (From Ref. 37.)

ion so that on-column retention was greater for the $TMeSe^+$ species. An optimized methanol water mobile phase was used at pH 4.5 and detection limits were 0.20, 0.10, and 0.20 μg/L for SeCys, SeMe, and $TMeSe^+$, respectively.

A number of studies have been concerned with the separation of lead compounds [26,43–45]. Al-Rashdan et al. [26] compared reversed-phase, ion-pairing, and ion-exchange LC modes for the separation of inorganic lead (Pb^{2+}), trimethyllead chloride (TML), triethyllead chloride (TEL), and triphenyllead chloride (TPhL). Each LC mode was optimized for pH and organic modifier concentration. It was found that the best separations were obtained by using the isocratic reversed-phase LC mode (Fig. 10.7). A gradient elution would have been desirable but was unfeasible because of plasma instability. A further study [44], however, used IPC with PIC-B5 ion-pair reagent and methanol/water mobile phase for the successful separation of inorganic lead, TEL, TPhL, and TEL with detection limits in the range 0.17–3.9 ng of Pb, respectively.

Both lead and mercury speciation has been performed by Shum and coworkers [43]. Direct injection nebulization and an ion-pair separation with a microbore LC column were used with ICP-MS detection. A mobile phase of 20:80% v/v acetonitrile/water with 5 m*M* ammonium pentanesulfonate ion pairing reagent at pH 3.4 was used to separate inorganic lead, inorganic mercury, and three organomercury species. Detection limits, based on peak area calculations, were 0.2 pg of Pb for all the lead compounds and 7–18 pg of Hg for the mercury compounds. Spiked urine samples were analyzed to evaluate the performance of the method.

IPC has been used by the Caruso group for organotin speciation [46–49]. The effect of inorganic tin chloride on the separation of TMT, TBT, and TPhT has been investigated [46]. A PRP-1 column was used to achieve baseline separation at pH 6 using IPC. Further work [47–49] used supercritical fluid extraction to ex-

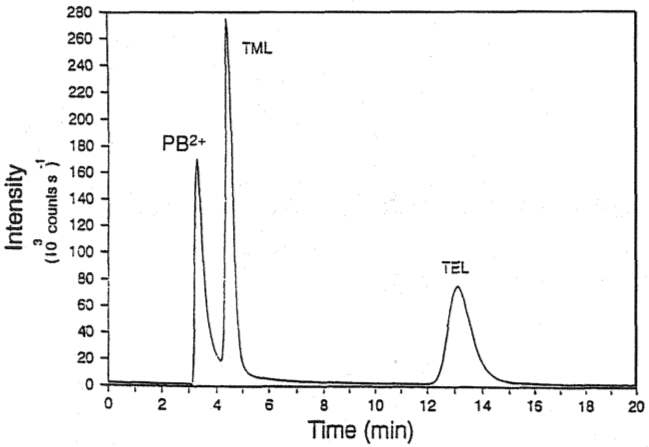

Figure 7 Liquid chromatography inductively coupled plasma mass spectrometry (LC-ICP-MS) chromatogram of a standard mixture of organolead and inorganic lead compounds (Pb^{2+}, TML, and TEL) using reversed-phase HPLC. Mobile phase, 0.1 *M* ammonium acetate, and 0.1 *M* acetic acid at pH 4.6, 30% ethanol. Flow rate 1 mL/min. (From Ref. 26.)

tract TBT and TPhT from biological samples before separation. Optimization of extraction temperature, pressure, and modifier was performed to increase extraction efficiency.

The speciation of Cr (III) and Cr (VI) has been performed by Jakubowski et al. [22] with IPC-ICP-MS and hydraulic high-pressure nebulization. A mobile phase of 25% methanol, ammonium acetate, and an ion-pair reagent (tetrabutylammonium acetate) was used. Oxygen addition was used to reduce carbon interferences from the high organic content in the mobile phase, along with desolvation.

Platinum speciation using IPC-ICP-MS has been achieved by Zhao et al. [50]. An ODS C_{18} column and 1-heptanesulfonate ion-pairing reagent at pH 2.6 were used to separate the metabolites of cisplatin and cisplatin hydrolysis products. The low pH was required in order to retain thiol containing complexes. All complexes were resolved and urine and blood samples were analyzed by the speciation method.

Micellar Liquid Chromatography

Micellar liquid chromatography (MLC) is another variation on reversed-phase and ion-pair chromatography. In this mode, the counter ion is a surfactant of high concentration and a long-chain hydrocarbon. Micelles form when the concentration of the surfactant is increased to the point at which aggregation occurs and spherical particles are formed. The hydrophilic parts of the long-chain hydrocarbon are oriented toward the outside of the sphere with the hydrophobic end in the center of the sphere. A mixture of compounds of varying polarity partitions between the

stationary phase, the micellar hydrophobic phase, and the micellar hydrophilic phase so that ionic and nonionic compounds may be separated.

Micellar Liquid Chromatography—Applications

There are few applications of MLC with ICP-MS for speciation studies to date. Alkyltin speciation has been performed by Suyani and coworkers [51]. Trimethyltin chloride (TMT-Cl), triethyltin chloride (TET-Cl), and tripropyltin chloride (TPT-Cl) were separated by using a C_{18} Spherisorb column and 0.01 *M* sodium dodecylsulfate (SDS), a negatively charged surfactant, to form the micelles. Detection limits for the three alkyltin species were in the range 27–111 pg (Sn). The concentration of SDS was increased to 0.02 *M* for the separation of monoethyltin chloride (MET-Cl), dimethyltin chloride (DMT-Cl), and TMT-Cl with detection limits in the range 26–126 pg (Sn). It should be noted that the capacity factor (k') of an analyte during a separation should be kept to a minimum. Increasing the micelle concentration lowers k', but care must be taken to prevent excess salt buildup. It is important that, with MLC, the concentration of the surfactant is kept below 0.1 *M* to prevent clogging of the torch injector and sampling cone.

Further work by the Caruso group [52] used MLC for arsenic speciation studies with detection by ICP-MS. As (III), As (V), dimethylarsenic (DMA), and monomethylarsenic (MMA) were separated (Fig. 10.8). Cetyltrimethylammonium bromide (0.05 *M*) was used to form the micelles along with a mobile phase of 10% propanol and 0.02 *M* borate as buffer. "Dirty samples" such as urine were analyzed easily by this method of LC.

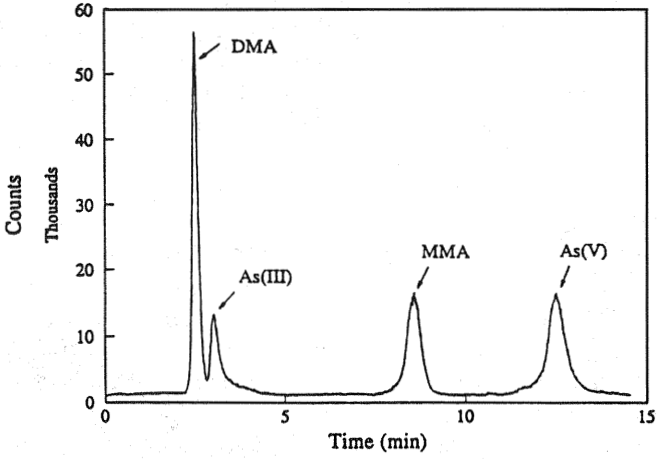

Figure 8 Chromatogram of mixture of four arsenic standards, Hamilton PRP-1 column; chromatographic conditions 0.05*M* CTAB, 10% propanol, pH 10.2, column temperature 40°C, $m/z = 75$. (From Ref. 52.)

Ion-Exchange Chromatography

Ion-exchange chromatography (IEC) employs the mechanism of exchange equilibrium between stationary phase surface ions and oppositely charged ions in the mobile phase. Analyte counter ions compete for the ion son the stationary phase and the relative afiniites of the solute ions determine the extent of the retention. Ion-exchange chromatogrphy may be performed in two modes–cation exchange chromatogrphy, in which the stationary phase resin contains sulfonic acid groups or carboxylic acid groups, and anion exchange chromatography, in which the resin contains primary or quaternary amine functionalities. Styrene and divinylbenzene are used to form the ion-exchange packing materials, and the cationic or anionic groups are bonded to this surface.

Neutral and charged species may be separated by using IEC. In addition, the introduction of an organic modifier to the mobile phase may influence a separation, as do the ionic strength of the solute, the pH, the temperature, the buffer concentration, and the liquid flow rate.

Anion-Exchange Chromatography—Applications

The majority of work performed by anion-exchange chromatography (AEC) with ICP-MS detection has been developed for arsenic speciation studies [53–60]. As mentioned previously, the analysis of As by ICP-MS is inherently affected by the isobaric interference for $ArCl^+$. In the analysis of urine, this is significant, as the concentration of NaCl in urine is commonly five orders of magnitude higher than that of any arsenic species present. Anion-exchange chromatography has been successfully used to separate Cl^- chromatographically from the arsenic species [53]. A Wescan anion-exchange column was used with a phthalic acid mobile phase. Dilution of the urine samples was performed. In addition, nitrogen addition has been used in an attempt to remove the $ArCl^+$ interference [60]. Steps must be taken to ensure that the speciation of compounds in a sample is not affected by sample pretreatment. Harsh sample preparation may cause oxidation of arsenic species, particularly of As (III) to As (V) [58], which results in inaccurate speciation quantification and identification.

Anion-exchange chromatography (AEC) has been used extensively for Se speciation studies [41,61]. Selenate and selenite have been separated by using preconcentration steps to improve detection limits. Preconcentration steps are sometimes essential for LC-ICP-MS analyses as ultratrace levels found in some environmental samples are undetectable by ICP-MS. Organoselenium compounds have also been separated from the inorganic forms, using anion exchange chromatography and a salicylate mobile phase at pH 8.5 [41,61].

Chromium speciation by using anion-exchange chromatography has also received much attention in recent years because the element is both essential to humans and toxic in large doses [62–66]. Cr (III) and Cr (VI) may be separated by

anion-exchange LC, but the Cr (III) species had to be stabilized in this study. This is commonly achieved by a chelation procedure with ethylene diamine tetraacetic acid (EDTA) [63,64] or another complexing agent. Byrdy et al. [63] used an ammonium sulfate/ammonium hydroxide mobile phase with an IonPac As7 mixed mode column. Because of a polyatomic interference from SO^+ formation the *m/z* 53 isotope may be monitored instead of the *m/z* 52 isotope; however, the *m/z* 53 isotope may also suffer from a possible chloride interference (Fig. 10.9). Absolute detection limits for Cr (III) and Cr (VI) were 40 and 100 pg, respectively.

Heumann et al. [67] used anion-exchange chromatography to speciate iodide and iodate in mineral water samples. Iodate concentrations were in the range 0.5–20 mg/mL and iodide concentrations were 0.1–5 ng/mL.

The metabolic pathway and degradation of gold based drugs in the human body are not completely understood. Gold drug metabolites, as well as Zn and copper species, in human blood have been separated by using AEC-ICP-MS [68]. A mobile phase liner gradient was successfully used, starting with 20 m*M* aqueous Tris buffer at pH 6.5. Two Au species as well as three Zn and four Cu containing species were separated.

Cation-Exchange Chromatography—Applications

There have been few elemental speciation studies in the literature involving cation-exchange chromatography (CEC) coupled to ICP-MS. A cation-exchange column was used by Larsen et al. [57,69] for arsenic speciation in several seafood sample extracts. The chromatography was optimized for the separation of arsenocholine, trimethylarsinic, trimethylarsine oxide, inorganic As, and two unknown cationic arsenic compounds. A mobile phase of 20 m*M* pyridinium ion, at pH 2.65, was used to perform the separation (Fig. 10.10).

Organotin compounds have also been separated by this mode of chromatography [48,70]. In the former study [48], cation exchange was compared to IPC and was found to give a superior linear dynamic range for the separation of tetramethyltin chloride, tetrabutyltin chloride, and tetraphenyltin chloride. In the latter study [70] a mobile phase of 0.30 *M* ammonium acetate in 60:40 methanol/water with a pH gradient of 6 to 3 in 1 min was used successfully to resolve tetrabutyltin and dibutyltin.

The speciation of vanadium (IV) and (V) has been performed by Tomlinson et al. [71], using an Alltech Adsorbosphere cation-exchange column and ICP-MS detection. Single-ion monitoring at *m/z* 51 was used for data acquisition. The mobile phase was 7 m*M* 2,6-pyridine carboxylic acid and 9.6 m*M* lithium hydroxide at pH 4.0 (Fig. 10.11).

Size-Exclusion Chromatography

Size-exclusion chromatography (SEC), or gel permeation chromatography (GPC), separates species on the basis of molecular size. Molecular interactions between

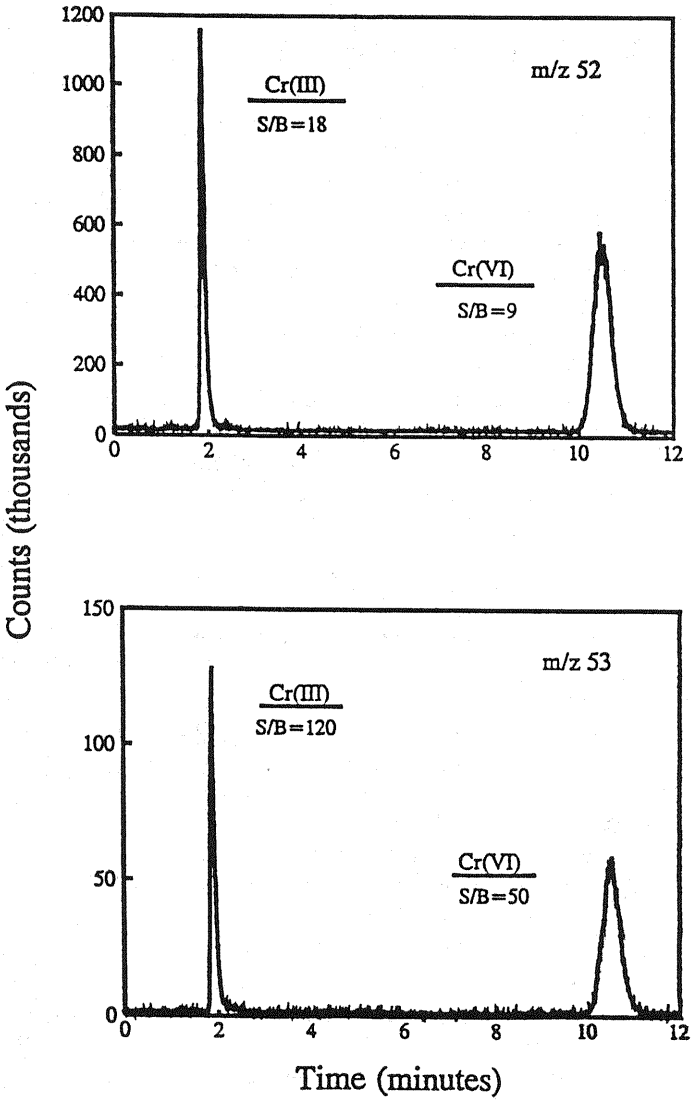

Figure 9 Chromatograms of a mixture of Cr (III) (60 ng) and Cr (VI) (100 ng) with single-ion monitoring at *m/z* 52 and *m/z* 53 showing signal-to-background ratio at the latter *m/z* value. Conditions: pH 9.2, flow rate 2 mL/min, 35 m*M* $(NH_4)_2SO_4$. (From Ref. 63.)

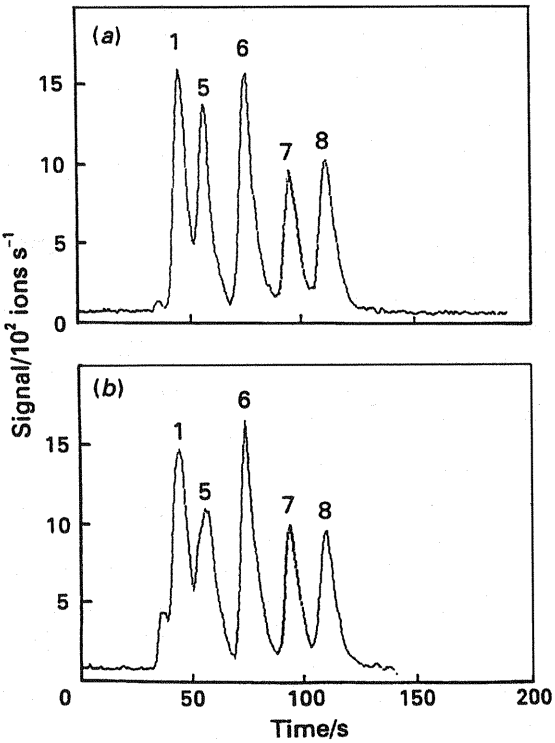

Figure 10 Cation exchange liquid chromatography inductively coupled plasma mass spectrometry (LC-ICP-MS) of arsenic species spiked in (a) aqueous solution and (b) urine diluted (1 + 3). Amount of each species injected 0.44 ng. Peaks: (1) DMA; (2) As (III); (3) MMA; (4) As (V); (5) AsB; (6) TMAO; (7) AsC; (8) TMAs. (From Ref. 69.)

the analyte and the stationary phase control the retention of the species. Large molecules are eluted before smaller molecules as the latter sample a greater pore volume: i.e., their path through the column is longer. Solvent molecules are eluted at the end of the separation, in contrast to the LC methods mentioned, in which the components are eluted after the "deadtime."

Size-Exclusion Chromatography—Applications

Reports of SEC with ICP-MS detection in the literature have principally concerned the separation of metalloproteins [32,72–78]. Dean and coworkers [73] used SEC with a Tris HCl mobile phase in an attempt to determine the cadmium content in two metalloproteins. A further study used this technique for the speciation of Cd in pig kidney samples [77]. The majority of cadmium was associated with a pro-

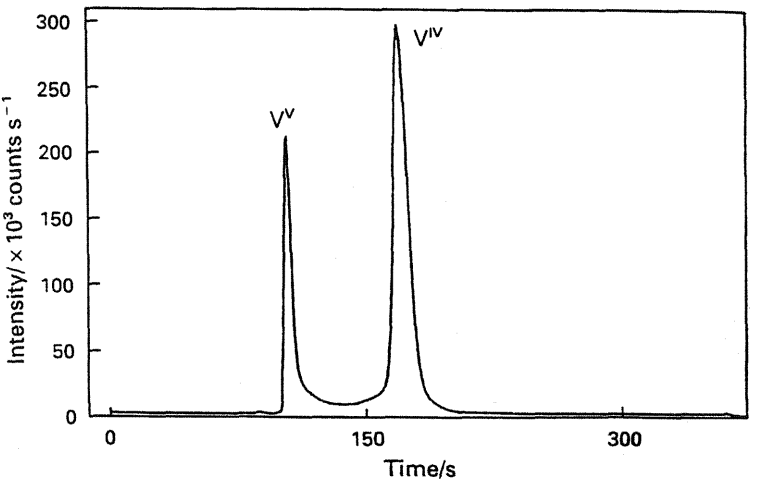

Figure 11 Speciation of V using an Alltech Adsorbosphere 5-μm SCX column and inductively coupled plasma mass spectrometry (ICP-MS) detection using single-ion monitoring at *m/z* 51: eluent, 2,6-pyridinedicarboxylic acid (7.0 mmol/L) and lithium hydroxide (9.6 mmol/L) at pH 4.0; flow rate, 1.5 mL/min and injected amount 12.5 ng. (From Ref. 71.)

tein of similar structure to that of metallothionein that survived cooking and simulated digestion.

SEC has been used extensively to separate proteins containing different elements such as Zn (II), Cd (II), Cu (II), and Hg (II) in metallothionein [78–80]. These studies show the potential of SEC-ICP-MS for metalloprotein separations but are not specifically concerned with elemental speciation.

Rottmann and Heumann [81] used this separation technique to examine interactions of humic substances with Co and Mo in water. After interaction, three Mo species and two Cu species were identified and the total species concentration corresponded with the total elemental levels.

10.4.2 Gas Chromatography

Introduction

Gas chromatography (GC) is a technique that has received particular interest for speciation studies when coupled to ICP-MS as a detector. Samples must be volatile in nature to be separated by using this mode of chromatography, and if the samples are not readily volatilized, derivitization of the samples must be performed.

Gas-liquid and gas-solid chromatography are the two common modes of GC; however, only the former has been used, to date, for speciation studies with ICP-MS detection. Here, a liquid sample is injected onto a GC column that is held at a

temperature high enough to vaporize the sample (50°C higher than the boiling point of the least volatile analyte). The sample is then eluted by a gaseous mobile phase, commonly helium, argon, nitrogen, or carbon dioxide. The mobile phase should ideally be inert to the sample and only serve to carry the analytes through the column. Separation of analytes occurs by interactions with a liquid phase that is retained on an inert solid support. This liquid phase should be involatile and also chemically inert.

Both packed and capillary-type GC columns have been used for speciation studies and are normally between 2 and 50 m long. Columns are coiled and mounted inside the oven.

Peters and Beauchemin [82] described in detail the advantages of using GC-ICP-MS for volatile species separation. The primary advantage is the near-ideal (100%) sample transport efficiency of the analytes into the plasma, which results in excellent recoveries and limits of detection. As no energy from the plasma is required to desolvate and vaporize the gaseous analyte, ionization of the analyte is more efficient. In addition, isobaric interferences are reduced as a result of the absence of an aqueous mobile phase. The lack of an aqueous mobile phase also causes less of a load to be applied to the plasma so plasma stability is greater and noise levels are reduced. Also, as high ionic strength buffers are not required with GC, clogging and erosion of the torch injector and sampler cones do not occur.

Interfacing Gas Chromatography with Inductively Coupled Plasma Mass Spectrometry

As with LC-ICP-MS coupling, the hyphenation of GC with plasma detection also requires the construction of a transfer line to connect the outlet of the gas chromatograph to the ICP-MS sample introduction system. In most instances of GC-ICP-MS, coupling [83–93] has been performed by construction of a stainless steel transfer line less than 1 m long to the base of the ICP torch (Fig. 10.12). This transfer line is then heated (to approximately 250°C), using thermocouples or heating tape, to prevent condensation of the analytes in the transfer process. Several modifications have been suggested in the literature to increase sample throughput. Van Loon et al. [83] introduced oxygen gas into the midpoint of the transfer line to prevent carbon deposition on the torch and cones when introducing organometallic compounds. Other workers [84,90] have suggested using a glass [84] or quartz [90] lined stainless steel transfer line to provide a more inert surface to prevent analyte adsorption and condensation. To improve sample transport, the GC column may be actually inserted into the transfer line [85,86]. In addition, the outlet of the transfer line may be positioned to just below the injector of the torch so that a more stable plasma may be obtained [84]. This distance has been found to be important for ideal sample recoveries along with the length of the transfer line and alignment of the torch and transfer line [85,86].

To improve some separations, it has been found that heating the argon carrier gas through the transfer line may improve GC separations [88,91] (Fig. 10.13).

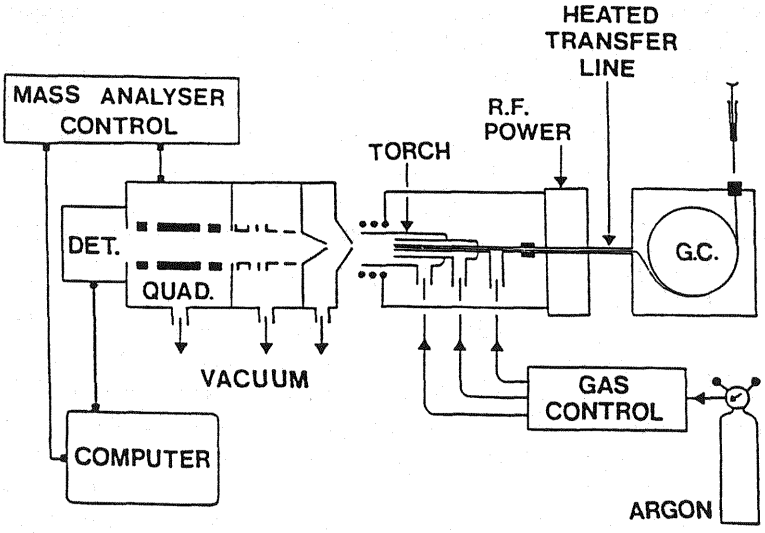

Figure 12 Schematic diagram of a coupled capillary gas chromatography inductively coupled plasma mass spectrometry (GC-ICP-MS) system. (From Ref. 86.)

This may be achieved by using an argon heater constructed from nichrome wire inside a silica tube that is heated to "red heat." The argon gas flows through the silica tube and is subsequently heated.

Gas Chromatography Inductively Coupled Plasma Mass Spectrometry—Applications

GC-ICP-MS has been used primarily for the speciation of volatile organometallic compounds. Van Loon and coworkers [83] described one of the first instance of GC-ICP-MS for speciation studies. Several organotin compounds were separated, using a Chromasorb GC column and a carrier gas flow of 8 mL/min Ar and 2 mL/min O_2 at 250°C. A 0.8-m stainless steel transfer line, also at 250°C, was used. Detection limits for the compounds were in the range 6–16 ng (as Sn). Organotin compounds were also separated by the De Smaele group [91,92], using a "bent" transfer line to facilitate coupling of GC with ICP-MS. A 30-m capillary column was used (Fig. 10.14).

Alkyllead compounds in a naphtha hydrocarbon mixture were separated in two studies by Kim et al. [85,86]. Helium was used as the carrier gas in these studies with argon added to allow efficient sample transport into the plasma. Various column and temperature gradients were used with an aluminum transfer line,

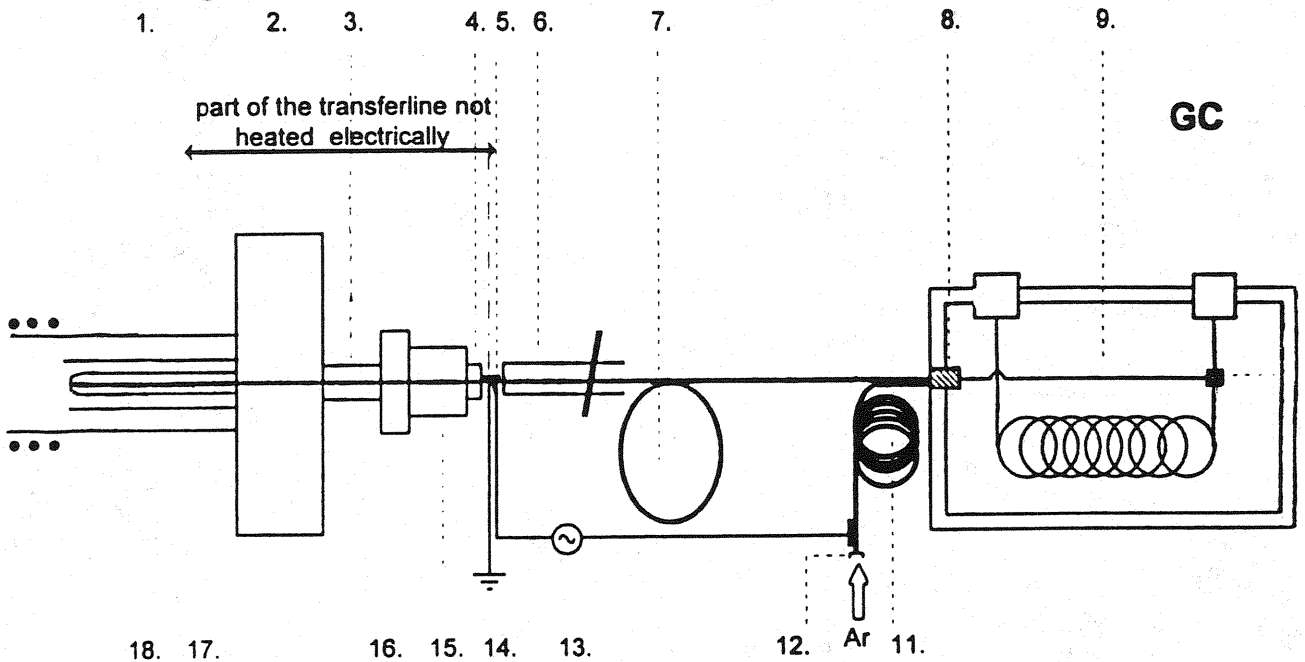

Figure 13 Scheme of coupling of the gas chromatograph (GC) with the inductively coupled plasma mass spectrometry (ICP-MS) instrument: (1) torch; (2) injector supply; (3) Teflon piece + Teflon Swagelok adapter; (4) Swagelok T-joint; (5) commercial transfer line; (6) stainless steel transfer tube; (7) transfer capillary. (From Ref. 91.)

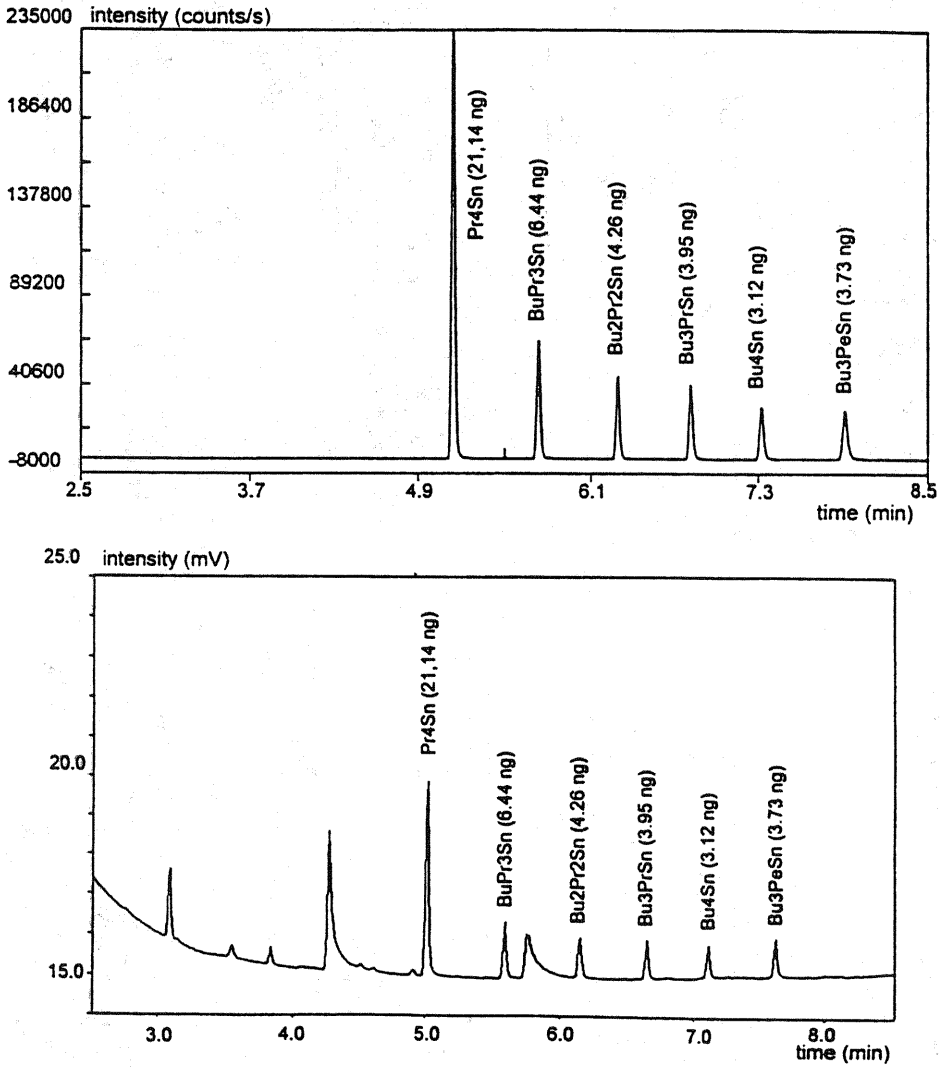

Figure 14 Chromatogram of a mixture of organotin compounds, recorded with the inductively coupled plasma mass spectrometer (ICP-MS) coupled to the gas chromatograph (GC) with custom-made transfer line. Injection temperature, 240°C; split, 1/20; detector, ICP-MS. Transfer line temperature 250°C; carrier gas, Ar. (b) Chromatogram of a mixture of organotin compounds, recorded with the FID detector. Injection temperature, 240°C; detector FID; carrier gas Ar. (From Ref. 91.)

through which the column was inserted. Ferrocene and nickel diethyldithiocarbamate were also separated.

Peters and Beauchemin [82] separated three chlorinated hydrocarbons by GC with ICP-MS detection. Dichloromethane, 1,1,1-trichloroethane, and trichloroethylene were separated by monitoring the $^{35}Cl^+$ ion. Detection limits were in the range 2.2–2.6 ng.

Methylmercury species in sediment samples were speciated in a study by Hintelman et al. [89]. Detection limits were 1 pg (as Hg) in dry sediment samples. Organomercury compounds, along with organotin and organolead compounds, were also separated in another study by Prange and Jantzen [90]. Detection limits were three orders of magnitude lower than those reported previously in the literature. A quartz transfer line was used in this study.

10.4.3 Supercritical Fluid Chromatography

Introduction

An increasingly popular alternative to liquid chromatography and gas chromatography is supercritical fluid chromatography (SFC). When a substance is heated above its critical pressure and temperature, it may exist in a supercritical fluid state. Carbon dioxide is an example of a supercritical fluid. At temperatures above 31°C and pressures exceeding 73 atmospheres, the individual molecules of the compound are able to overcome restrictive intermolecular forces and move in a manner more similar to that of a gas.

There are a number of advantages of using SFC rather than LC or GC for speciation studies. SFC elutes compounds faster than LC as the viscosity of the mobile phase is lower and analyte diffusion coefficients are higher. Resolution of complex mixtures may therefore be improved. GC with ICP-MS often yields broad peaks that may be sharpened by using SFC. SFC is also able to separate compounds that are nonvolatile, labile, and of high molecular weight, compared to GC. To achieve an ideal separation it is possible to change more variables with SFC than with LC or GC. Gradient elution is possible by making pressure adjustments and by using mobile phase gradients and temperature gradients. As with GC, both packed and capillary columns may be utilized; however, capillary columns have better efficiencies. These columns are around 10–20 m in length, which is midway between column lengths for LC and GC. The stationary phase is constructed from fused silica coated with polysiloxane. Carbon dioxide, ethane, pentane, dichlorodifluoromethane, diethyl ether, and tetrahydrofuran are all used as supercritical fluid mobile phases. In instances in which comparatively polar compounds are to be separated, modifiers are added to the mobile phase to adjust the solvent strength. Commonly used modifiers are acetonitrile, methanol, chloroform, and water. The addition of these polar modifiers does not seriously affect plasma stability so resolution and sensitivity are not affected.

Interfacing Supercritical Fluid Chromatography with Inductively Coupled Plasma Mass Spectrometry

The principal methods of interfacing SFC with ICP-MS have been discussed by Carey and Caruso [94]. Where packed SFC columns are used, the SFC restrictor is connected to a heated cross flow nebulizer and the nebulizer gas flow carries the sample to the plasma. For the more commonly used capillary columns, the SFC restrictor is passed through a heated transfer line that is connected directly to the torch of the ICP-MS. For optimal resolution of peaks, the restrictor should be positioned so that it is level with the injector of the ICP torch. This position may be varied slightly (Fig. 10.15). Heat is applied where the transfer line and torch connect to prevent freezing of the mobile phase when it decompresses after exiting the restrictor. To transport the analyte to the plasma efficiently, a gas flow of approximately 0.8–1.0 mL/min is used. This gas flow may also be heated to improve peak resolution.

Supercritical Fluid Chromatography Inductively Coupled Plasma Mass Spectrometry–Applications

Shen et al. [95] reported the first instance of SFC coupled to ICP-MS for tetraalkyltin speciation. The mobile phase used was CO_2. Tetramethyltin (TMT), tetrabutyltin (TBT), thetraphenyltin (TPT), tributyltin acetate (TBTA), and dibutyltin diacetate (DBTDA) were all resolved. CO_2 was also used as the auxiliary gas flow for ICP-MS. The Sn signal was optimized by adjusting the CO_2 flow and the rf forward power. The compounds were found to interact poorly with the stationary phase; thus only TBT and TPT could be separated. No organic modifiers were added, however. Further organotin speciation studies by the same group

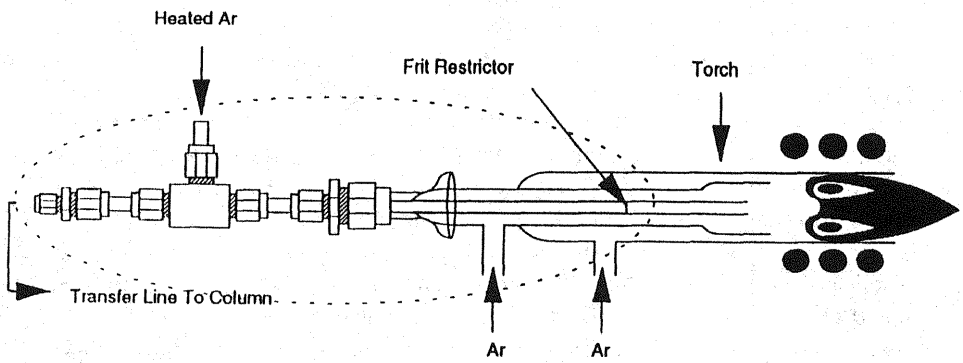

Figure 15 Supercritical fluid chromatography inductively coupled plasma mass spectrometry (SFC-ICP-MS) instrument diagram showing a SFC-ICP interface. (From Ref. 116.)

[96] examined interface temperature (Fig. 10.16), oven temperature, supercritical fluid pressure, column length, and mobile phase composition. An additional nebulizer gas flow was not required to introduce the sample into the plasma. The use of longer columns gave broader peaks for TBT, tributyltin chloride, triphenyltin chloride, and TPT.

The speciation of organoarsenic, organoantimony, and organomercury compounds was performed by Kumar and coworkers [47]. Trimethylarsine (TMA), triphenylarsine (TPA), triphenylarsenic oxide (TPAO), triphenylantimony (TPSb), and diphenylmercury (DPHg) were separated during the same chromatographic run. To improve As detection limits, a mixed-gas He/Ar plasma was used, along with methanol as the modifier. It was found that TMA was distinguished from the solvent peak; that did not occur when flame ionization was used for the same separation. Speciation of organotin, organoarsenic, and organoiron compounds was also achieved by the Raynor group [97,98].

Chromium speciation has also been successfully achieved by using SFC [99]. Two β-ketonate chromium compounds and an organochromium dimer were separated initially, using CO_2 as the mobile phase. However, as a result of an isobaric interference at m/z 52 (the major chromium isotope) from the formation of $^{40}Ar^{12}C^+$, nitrous oxide was used instead.

10.4.4 Capillary Electrophoresis

Introduction

Capillary electrophoresis (CE) with ICP-MS detection is a technique that first started to receive attention in 1995 [100–102]. There are several modes of CE, including capillary zone electrophoresis (CZE), capillary gel electrophoresis (CGE), micellar electrokinetic chromatography (MEKC), capillary isoelectric focusing (CIEF), and capillary isotacophoresis. Capillary zone electrophoresis is the most common mode of CE to be used with ICP-MS detection to date, although coupling of other modes with ICP-MS may have significant potential.

Capillary electrophoresis separations are dependent on the relative mobilities of analytes under the influence of an electric field and do not depend on mobile phase/stationary phase interactions. A fused silica capillary is filled with a buffer and both ends submerged into two reservoirs of the buffer. A platinum electrode is immersed in each reservoir and a potential difference (5–30 kV) is applied across the electrode. An aliquot of sample of a few nanoliters is injected onto the capillary by either hydrostatic or electrokinetic injection, and the components migrate to the negative electrode. Separations of analytes arise from differences in the electrophoretic mobilities, which are dependent on the mass-to-charge ratio of the components, physical size of the analyte, and buffer/analyte interactions. An electro-osmotic flow (EOF) of the buffer occurs in the capillary and arises as a result of interactions of the buffer with dissociated functional groups on the surface of the capillary. Positive ions from the buffer solution are attracted to negative ions

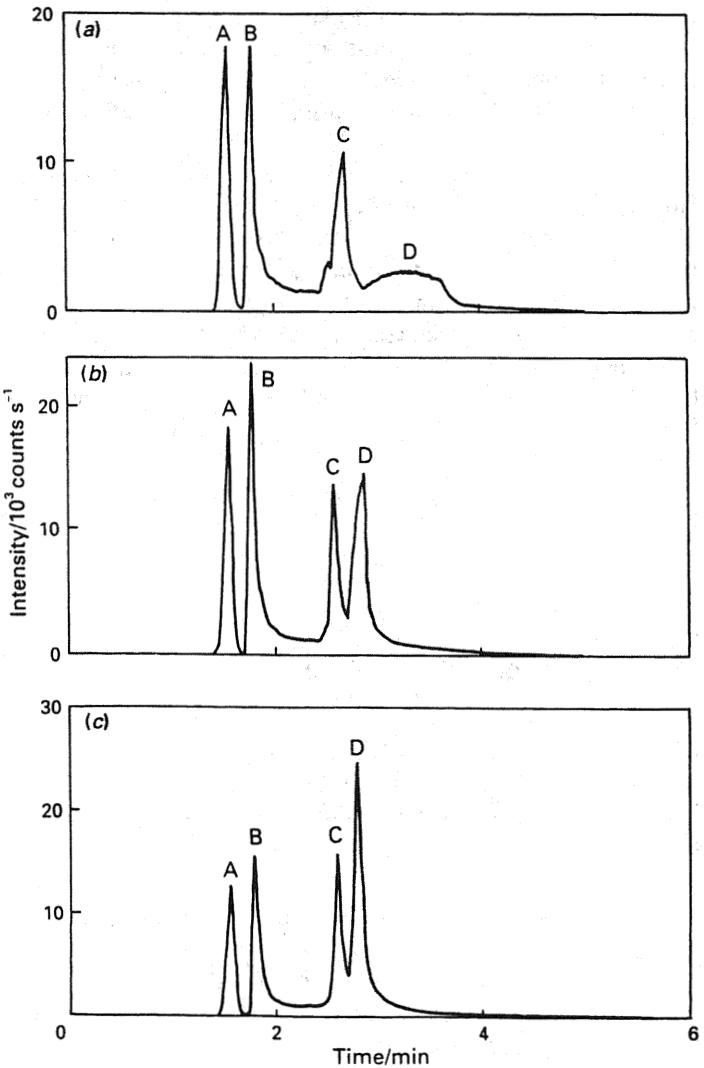

Figure 16 Effect of interface temperature (a) 215°C, (b) 300°C, and (c) 350°C for supercritical fluid chromatography (SFC) chromatograms of a mixture that contains (A) TBT, (B) TrBT-Cl, (C) TrPT-Cl, (D) TPT. (From Ref. 96.)

on the capillary surface, resulting in a double-layer effect. These positive ions are attracted to the negative electrode and transport the analyte molecules at the same time, resulting in flat flow profiles and minimizing peak broadening.

Common detectors used with CE are essentially the same as those used with high-pressure liquid chromatography (HPLC). These detectors, however, are not normally very specific or sufficiently sensitive. ICP-MS may fulfill these criteria; however, coupling the two systems is not as straightforward as LC-ICP-MS coupling. An initial problem lies with the extremely low flow eluted from the CE, which is usually of the order of less than a microliter per minute. Most nebulizers used with ICP-MS are not suitable for such flows so "low-flow" nebulizers such as the high-efficiency nebulizer (HEN) [103], direct injection nebulizer (DIN) [101], oscillating capillary nebulizer (OCN) [104], and ultrasonic nebulizer [20] may be used. Further, when CE is coupled to a system such as ICP-MS, the detector end of the capillary is no longer immersed in the buffer solution and so the electrode must be "grounded."

Capillary Electrophoresis Inductively Coupled Plasma Mass Spectrometry–Interfaces and Applications

The first CE-ICP-MS coupled system was described by the Olesik group [100] for potential speciation studies. The need for an interface, with low dead volume to minimize peak broadening, was identified. In this interface, the capillary was grounded by coating 5 cm of the end with a controlled thickness of silver paint. The EOF was approximately 0.05 $\mu L/min^{-1}$; however, the liquid flow rate increased, as a result of a vacuum effect from the nebulizer gas flow, which, in turn, resulted in a parabola-shaped velocity profile. This caused beak broadening to occur.

A direct injection nebulizer has been used for CE-ICP-MS [101] with the capillary actually inserted through the central sample introduction capillary of the DIN (Fig. 10.17). This nebulizer is very well suited to the very low flow rates associated with CE and also offers approximately 100% sample transport efficiency. A platinum grounding electrode was used, situated in a three-port connector, which also accommodated the DIN capillary and a makeup buffer flow. The makeup buffer was used so that the DIN operation was independent of the EOF, and the two flows were combined at the capillary exit. The system was used for feasibility studies for As and Se speciation.

A recent study [103] described the use of a HEN nebulizer with a conical spray chamber to improve sample transport for low flows in CE (Fig. 10.18). A stainless steel tee was used with the capillary threaded through the collinear ends of the tee. A makeup buffer, termed a *sheath electrolyte*, was also introduced through the lower arm of the tee. The effect of sheath electrolyte flow on the *laminar ow* (flow in the direction of the detector) was investigated, and it was found that improved peak resolution was possible by increasing the sheath electrolyte

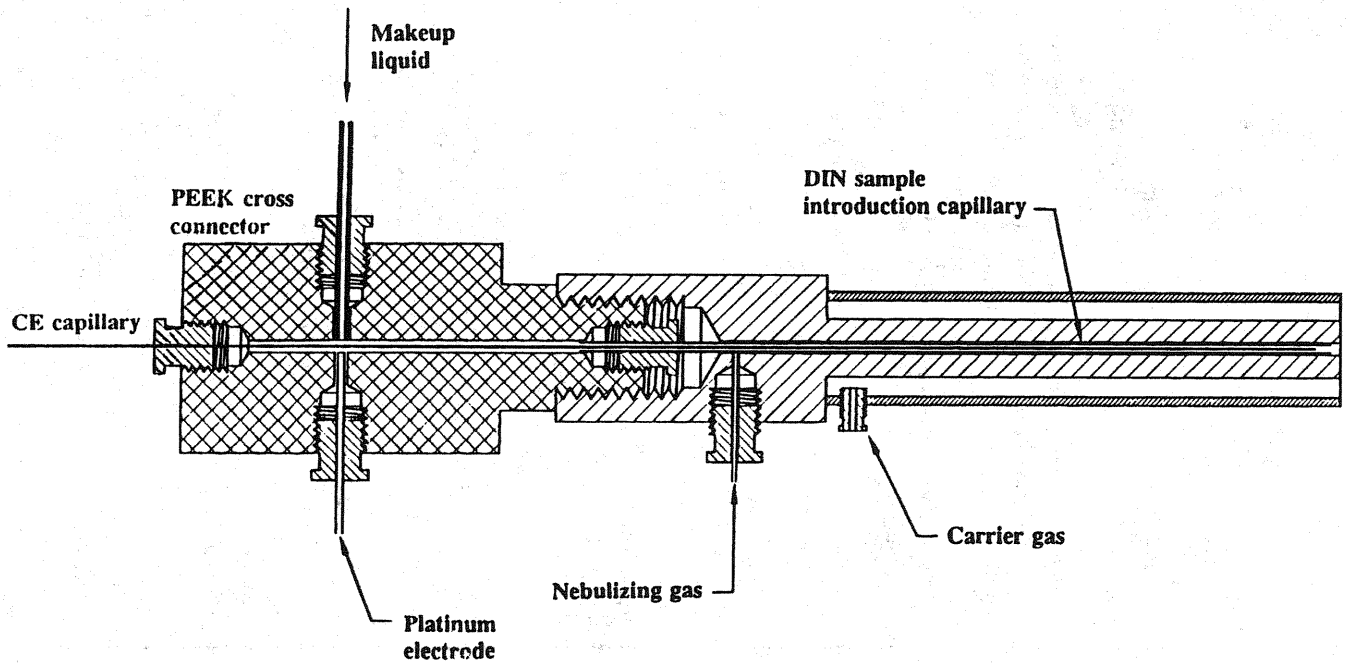

Figure 17 Block diagram of a direct injection nebulizer capillary electrophoresis inductively coupled plasma mass spectrometry (DIN CE-ICP-MS) interface. (From Ref. 101.)

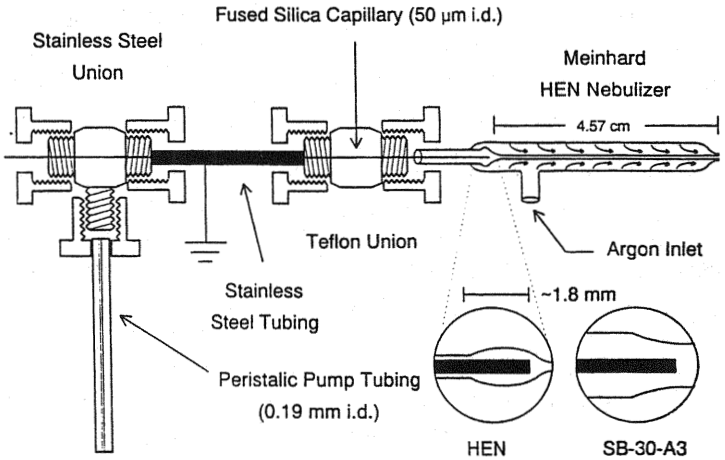

Figure 18 Diagram of interface between electrophoresis capillary and high-efficiency nebulizer (HEN). (From Ref. 103.)

flow rate so that the laminar flow was eliminated. This flow rate should be optimized to obtain ideal resolution.

An ultrasonic nebulizer (USN) has been found to be amenable to CE-ICP-MS interfacing [102]. The ground path was again provided by a sheath electrolyte, and separations were superior to those obtained by using a concentric nebulizer. It should be noted that the noisy background obtained by the USN may not give better detection limits than other nebulizers.

Magnuson et al. [105] described the use of CE with a hydrodynamically adjusted EOF with hydride generation for arsenic speciation and ICP-MS detection. Hydrodynamic pressure was applied in the opposite direction to the EOF so that large quantities of the analyte could be injected without significant peak broadening. Four arsenic species were separated with detection limits in the range 6–58 ppt.

10.5 OTHER PLASMA MASS SPECTROMETRIC TECHNIQUES FOR SPECIATION STUDIES

10.5.1 Use of the Helium Microwave Induced Plasma for Speciation Studies

Work performed by the Caruso group [3,106–109] has encompassed several studies of the use of a He-MIP with mass spectrometric detection for chromatography, with particular application to speciation studies. As mentioned previously, the helium microwave induced plasma offers several advantages over conventional ICP-

MS, including reduced gas flow and power consumption requirements. In addition, ionization conditions are more favorable when using He as a plasma gas.

The main method of sample introduction into the helium MIP is in the form of a gas [3,106–109]. The coupling of gas chromatography to He-MIP for speciation has been well documented for both metals and nonmetals [3,106–109]. Both atmospheric [109,110] and reduced-pressure [106–108,111,112] systems have been described. Mohamad et al. [110] used GC coupled to atmospheric pressure MIP-MS for the speciation of chlorinated hydrocarbons. Figure 10.19 shows a schematic of the atmospheric pressure helium MIP torch used in MIP-MS sampling for capillary GC detection. A tangential flow torch is used to provide a larger plasma and thus minimize sampling air entrained regions of the plasma. A stainless steel insert may be employed to heat the capillary column and minimize sample condensation. A stainless steel line must also be constructed and wrapped with heat tape so that the temperature of the transfer line may be maintained at 250°C. Figure 10.20 shows a chromatogram of chlorobenzene, *p*-chlorotoluene, and *o*-chlorophenol obtained by such an interface. Suyani et al. [109] used atmospheric pressure MIP-MS successfully for organotin speciation.

Reduced pressure helium MIP-MS has also been used as a GC detector for the separation of phosphorus, sulfur, and halogenated compounds [106–108]. This plasma is particularly well suited to these applications as air entrainment and subsequent high background signals are minimized. Again, heated stainless steel transfer lines are commonly used to connect the GC column to the ICP torch.

Microwave induced plasma mass spectrometry has also been used as a detector for supercritical fluid chromatography (SFC) [113] for the separation of halogenated hydrocarbons. The design of an SFC-MIP interface must ensure that the frit restrictor temperature remains at a high temperature to prevent condensation of analytes. Stainless steel transfer lines may be used. The frit restrictor should be connected to a length of deactivated fused silica capillary, inserted through the transfer line, and positioned flush with the aluminum MIP torch inset (Fig. 10.21).

10.5.2 The Use of Low-Pressure Helium Inductively Coupled Plasma Mass Spectrometry for Speciation Studies

Low-pressure He-ICPs have been used as chromatographic detectors for mass spectrometry [111,112,114]. Organotin compounds [112] were speciated by using a plasma operated at 100 W. A low-pressure torch must be constructed from a quartz tube of dimensions approximately 150 mm long and 6 mm outer diameter to sustain such a plasma. This torch is connected at one end to the GC interface and to the sampler cone at the other. Heated transfer lines must be used for reproducible transfer of the GC analytes. As the low-pressure system may not completely at-

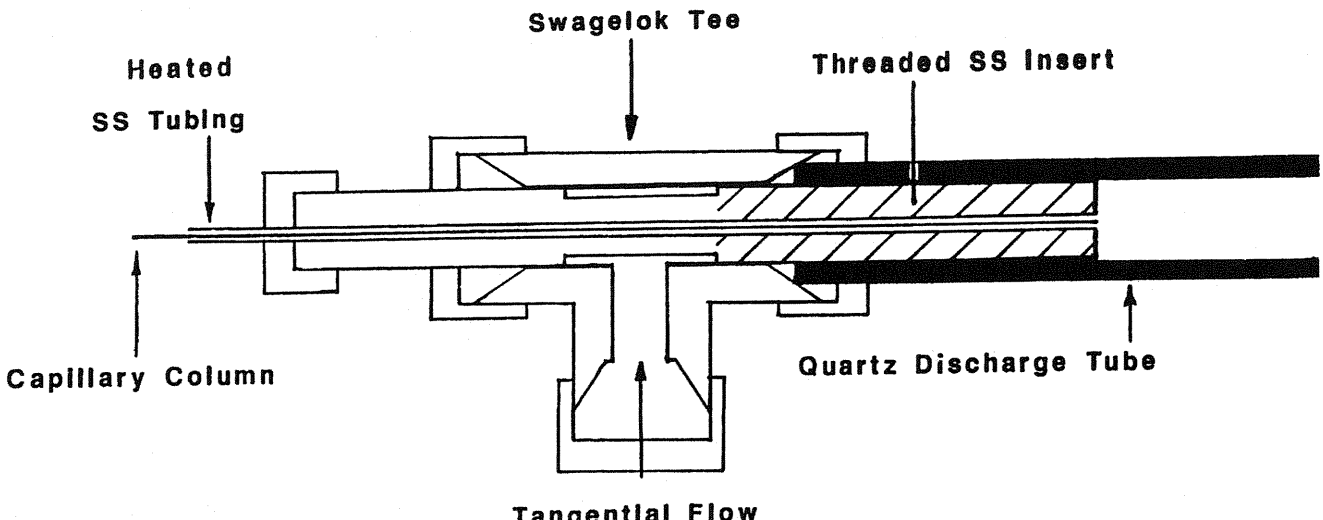

Figure 19 Helium microwave induced plasma (MIP) torch used in MIP mass spectrometry (MIP-MS) sampling for capillary gas chromatography (GC) detection. (From Ref. 110.)

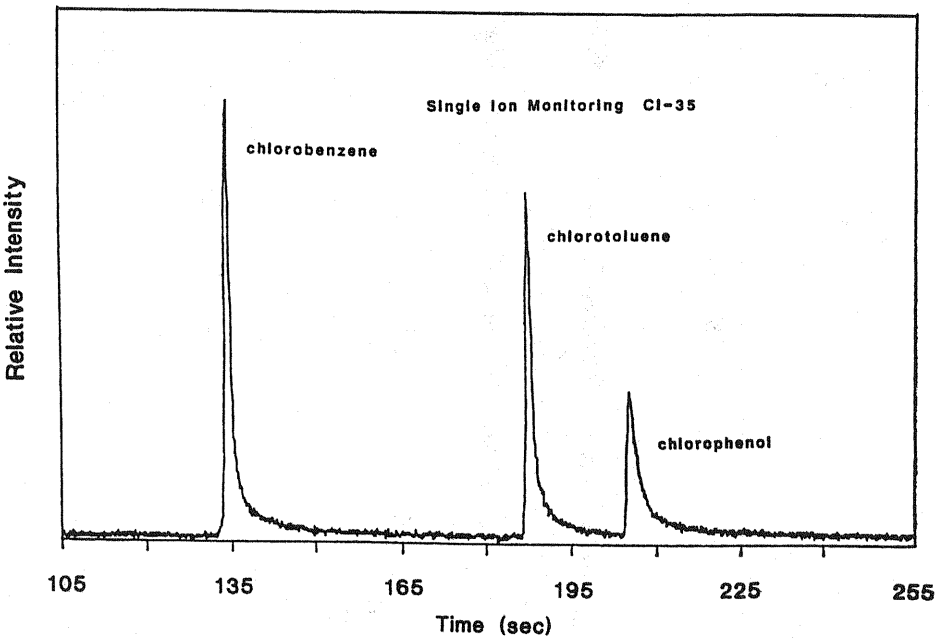

Figure 20 Chromatogram of chlorobenzene, *p*-chlorotoluene, and *o*-chlorophenol; 5 ng of each component injected. (From Ref. 110.)

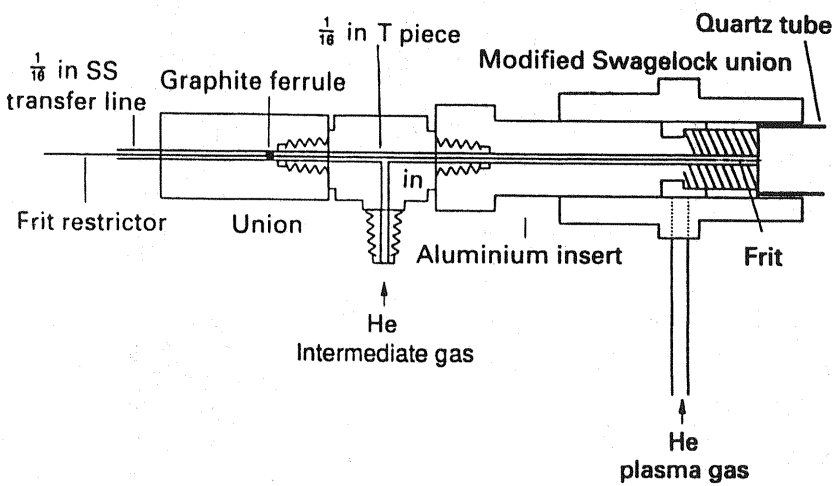

Figure 21 Supercritical fluid chromatography microwave induced plasma mass spectrometry (SFC-MIP-MS) torch interface. (From Ref. 113.)

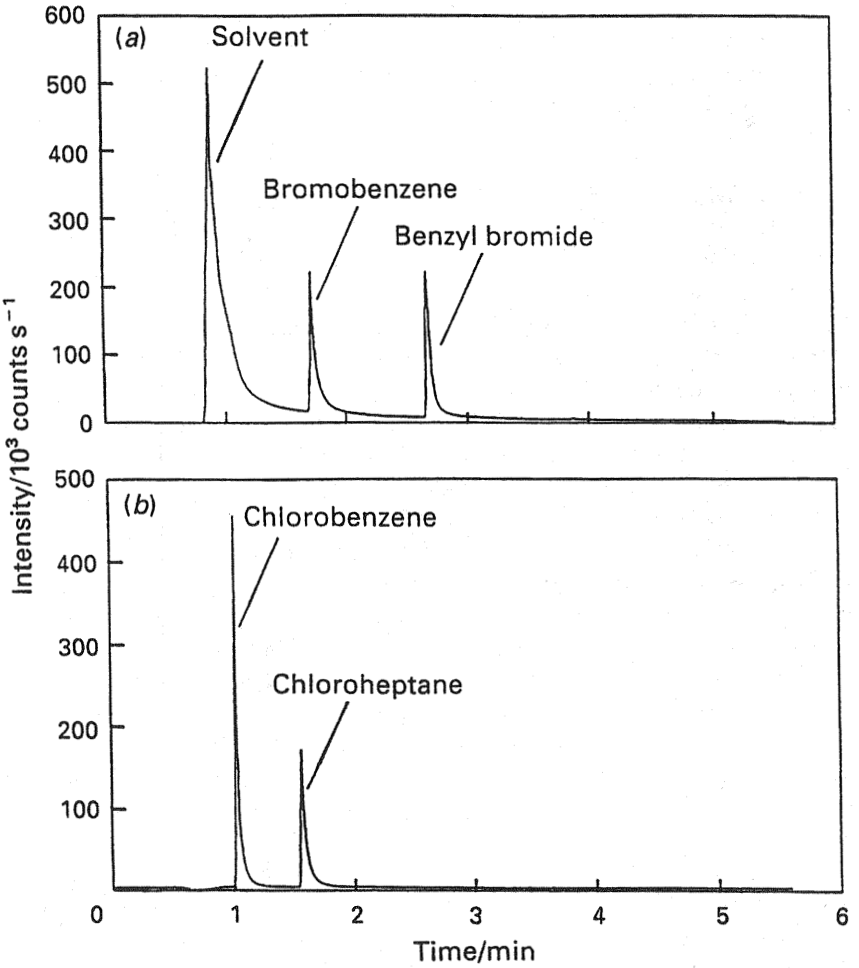

Figure 22 Chromatograms of 10-ng injection of (a) bromine- and (b) chlorine-containing compounds without venting the solvent, using single-ion monitoring at $m/z = 79$ and $m/z = 35$, respectively. (From Ref. 114.)

omize compounds, fragment ions may be sampled from such a low-pressure ICP, potentially allowing more structural information to be evaluated.

Halogenated gas chromatographic effluents have also been separated successfully by using LP-He-ICP-MS [114] (Fig. 10.22). The effect of venting solvents has been discussed [114], and it appears that shorter analysis times are attainable under no-venting conditions although limits of detection (LODs) are slightly higher.

The introduction of liquid samples into the LP-ICP-MS has been shown to be feasible [115]. A glass frit nebulizer may be used along with desolvation to improve analyte signal stability. To date, however, no speciation studies using such a system have been performed.

10.6 CONCLUSIONS

It is clear that ICP-MS is increasingly becoming a popular method for elemental chromatographic detection. All modes of chromatography may be hyphenated with ICP-MS, including liquid chromatography, gas chromatography, and supercritical fluid chromatography. In addition, the use of ICP-MS as a detector for CE is rapidly gaining popularity although the majority of papers describe the hyphenation of the two techniques. Table 10.3 shows some representative figures of merit for the different chromatographic techniques and for capillary electrophoresis with ICP-MS detection. In addition, some of the advantages and disadvantages of the hyphenated techniques are given.

The potential of CE-ICP-MS for use in speciation studies offers the analyst a useful alternative for the separation of compounds of environmental and clinical importance. Detection limits for CE-ICP-MS are often superior to those achieved with traditional detection methods such as refractive index and uv spectroscopy. The use of low-flow nebulizers, such as the direct injection nebulizer and the high-efficiency nebulizer, which can accommodate the low electroosmotic flow of CE, offers significant advantages in terms of improved sensitivity.

Speciation information for both metals and nonmetals may be obtained by ICP-MS and MIP-MS detection, thereby offering a method for the speciation of more difficult to analyze elements such as the halogens.

Microbore LC offers potential for speciation studies with ICP-MS detection. The lower liquid flow rates associated with the technique cause less mobile phase to reach the plasma. Often the mobile phases used in LC contain organic solvents that cause plasma instability at high flow rates and pressures. Microbore LC is therefore promising for separations using reversed-phase and ion-pairing chromatographic techniques.

Commercial ICP-MS instruments currently used in laboratories are computer controlled and employ time resolved acquisition software to present chromatograms. Software may often determine the ease of chromatographic acquisition, and, in many cases, the software does not allow the acquisition of chromatograms of high enough resolution. It is clear that the demands of the chromatographer must now be met when instrument manufacturers design software packages, so that improved methods for rapid data acquisition are available.

Finally, there is now obviously a need for development of certified materials that contain quantitative information regarding not only total elemental con-

Table 3 Figures of Merit for Techniques Utilized in Speciation

Technique[a]	Absolute detection limits	Comments	Selected references
LC-ICP-MS			
Reversed-phase	pg	High concentration of organic solvents that may cool the plasma are usually required.	30, 117
Ion-pair	pg	High concentrations of organic solvents are usually required.	40, 43, 118
Micellar	pg	Surfactants may clog the sample introduction system. Smaller concentrations of organic solvents are required.	48, 52
Ion-exchange	pg	Ions such as Cl^-, which could cause interferences, may be separated from the analyte.	53, 62, 119
Size exclusion	pg	Smaller concentrations of organic solvents are required.	72, 74, 80, 119
GC-ICP-MS	pg-fg	This technique has high resolving power but requires a heated transfer line.	85, 89, 90, 92
He-MIP-MS	pg	These instruments are not commercially available, but the He-MIP is a more efficient excitation/ionization source for some nonmetals.	3
Low-pressure He-MIP-MS	pg-fg	These instruments are not commercially available.	106, 107, 109
Low-pressure He-ICP-MS	pg	This technique may provide information on both elemental composition and molecular structure. These instruments are not commercially available.	112, 115, 111
SFC-MIP-MS	fg	Compounds are eluted faster. Nonvolatile, labile, and high-molecular-weight compounds may be separated. A heated restrictor is required.	49, 94, 95, 116
SFC-ICP-MS	—	A heated restrictor is required.	94
CE-ICP-MS	fg	Low detection limits are possible, but low-flow nebulizers are required	20, 102

[a]LC-ICP-MS, liquid chromatography inductively coupled plasma mass spectrometry; GC, gas chromatography; MIP, microwave induced plasma; SFC, supercritical fluid chromatography; CE, capillary electrophoresis.

centration but individual species concentration. A few standards that contain information regarding the speciation of the constituent elements are currently available, but many more are required so that accurate speciation methods for a wide range of elements may be developed.

ACKNOWLEDGMENTS

The authors are grateful to the National Institute of Environmental Health Sciences for the partial support of this work through grant number ESO490E.

REFERENCES

1. Tomlinson, M. J.; Lin, L.; Caruso, J. A. *Analyst* **1995**, *120*, 583–589.
2. Vela, N. P.; Olson, L. K.; Caruso, J. A. *Analytical Chemistry* **1993**, *65*, 585A–597A.
3. Olson, L. K.; Caruso, J. A. *Spectrochimica Acta Part B* **1994**, *49*, 7–30.
4. Greenwood, N. N.; Earnshaw, A. *Chemistry of the Elements*, 1st ed.; Pergamon Press: Oxford, 1984.
5. Massey, A. G. *Main Group Chemistry*, 1st ed.; Ellis Horwood: New York, 1990.
6. O'Neill, P. *Environmental Chemistry*, 2nd ed.; Chapman & Hall: London, 1993.
7. Elder, R. C.; Eidsness, M. K. *Chemical Reviews* **1987**, *87*, 1027–1046.
8. Elder, R. C.; Jones, W. B.; Zhao, Z.; Dorsey, J. G.; Tepperman, K. *Metal-Based Drugs* **1994**, *1*, 363–374.
9. Manahan, S. E. *Environmental Chemistry*, 6th ed.; Lewis Publishers: Boca Raton, FL., 1994.
10. Pollutants, Committee on Medical and Biologic Effects of Environmental Pollutants *Platinum-Group Metals*, 1st ed.; National Academy of Sciences: Washington, DC, 1977.
11. Pollutants, Committee on Medical and Biologic Effects of Environmental Pollutants *Selenium*, 1st ed.; National Academy of Sciences: Washington, DC, 1976.
12. Klaassen, C. D.; Amdur, M. O.; Doull, J. *Casarett and Doull s Toxicology: The Basic Science of Poisons* Macmillan: New York, 1986, pp 974.
13. Cotton, F. A.; Wilkinson, G. *Advanced Inorganic Chemistry*, 5th ed.; John Wiley: New York, 1988.
14. Houk, R. S.; Fassel, V. A.; Flesch, G. D.; Svec, H. J.; Gray, A. L. *Analytical Chemistry* **1980**, *52*, 2283.
15. Date, A. R.; Gray, A. L. *Analyst* **1981**, *106*, 1255.
16. Evans, E. H.; Giglio, J. J. *Journal of Analytical Atomic Spectrometry* **1993**, *8*, 1–18.
17. Fior, R. L. *American Laboratory* **1989**, *21*, 40.
18. Evans, E. H.; Giglio, J. J.; Castillano, T. M.; Caruso, J. A. *Inductively Coupled and Microwave Induced Plasma Sources for Mass Spectrometry*, 1 ed.; The Royal Society of Chemistry: Cambridge, 1995.
19. Wang, L.; May, S. W.; Browner, R. F.; Pollock, S. H. *Journal of Analytical Atomic Spectrometry* **1996**, *11*, 1137–1146.

20. Lu, Q.; Barnes, R. M. *Microchemical Journal* **1996**, *54*, 129–143.
21. Shum, S.C.K.; Neddersen, R.; Houk, R. S. *Analyst* **1992**, *117*, 577–582.
22. Jakubowski, N.; Jepkens, B.; Stuewer, D.; Berndt, H. *Journal of Analytical Atomic Spectrometry* **1994**, *9*, 196–201.
23. Cairns, W. R. L.; Ebdon, L.; Hill, S. J. *Fresenius Journal of Analytical Chemistry* **1996**, *355*, 202–208.
24. Rivas, C.; Ebdon, L.; Hill, S. J. *Journal of Analytical Atomic Spectrometry* **1996**, *11*, 1147–1150.
25. Dauchy, X.; Cottier, R.; Batel, A.; Jeannot, R.; Borsier, M.; Astruc, A.; Astruc, M. *Journal of Chromatographic Science* **1993**, *31*, 416–421.
26. Al-Rashdan, A.; Heitkemper, D.; Caruso, J. A. *Journal of Chromatographic Science* **1991**, *29*, 98–102.
27. Bushee, D. S. *Analyst* **1988**, *113*, 1167–1170.
28. Huang, C.-W.; Jiang, S.-J. *Journal of Analytical Atomic Spectrometry* **1993**, *8*, 681–686.
29. Klinkenberg, H.; Wal, S. v. d.; Frusch, J.; Terwint, L.; Beeren, T. *Atomic Spectroscopy* **1990**, *11*, 198–201.
30. Takatera, K.; Watanabe, T. *Analytical Chemistry* **1993**, *65*, 759–762.
31. Bushee, D. S.; Moody, J. R.; May, J. C. *Journal of Analytical Atomic Spectrometry* **1989**, *4*, 773–775.
32. Owen, L. M. W.; Crews, H. M.; Hutton, R. C.; Walsh, A. *Analyst* **1992**, *117*, 649–655.
33. Beauchemin, D.; Siu, K. W. M.; McLaren, J. W.; Berman, S. S. *Journal of Analytical Atomic Spectrometry* **1989**, *4*, 285–289.
34. Beauchemin, D.; Bednas, M. E.; Berman, S. S.; McLaren, J. W.; Siu, K. W. M.; Sturgeon, R. E. *Analytical Chemistry* **1988**, *60*, 2209–2212.
35. Thompson, J. J.; Houk, R. S. *Analytical Chemistry* **1986**, *58*, 2541–2548.
36. Shibata, Y.; Morita, M. *Analytical Sciences* **1989**, *5*, 107–109.
37. Story, W. C.; Caruso, J. A.; Heitkemper, D. T.; Perkins, L. *Journal of Chromatographic Science* **1992**, *30*, 427.
38. Thomas, P.; Sniatecki, K. *Journal of Analytical Atomic Spectrometry* **1995**, *10*, 615–618.
39. Hwang, C.-j.; Jiang, S.-J. *Analytica Chimica Acta* **1994**, *289*, 205–213.
40. Yang, K.-L.; Jiang, S.-J. *Analytica Chimica Acta* **1994**, *307*, 109–115.
41. Cai, Y.; Cabañas, M.; Fernández-Turiel, J. L.; Abalos, M.; Bayona, J. M. *Analytica Chimica Acta* **1995**, *314*, 183–192.
42. Olivas, R. M.; Donard, O. F. X.; Gilon, N.; Potin-Gautier, M. *Journal of Analytical Atomic Spectrometry* **1996**, *11*, 1171–1176.
43. Shum, S. C. K.; Pang, H.-m.; Houk, R. S. *Analytical Chemistry* **1992**, *64*, 2444–2450.
44. Al-Rashdan, A.; Vela, N. P.; Caruso, J. A.; Heitkemper, D. T. *Journal of Analytical Atomic Spectrometry* **1992**, *7*, 551–555.
45. Brown, A. A.; Ebdon, L.; Hill, S. J. *Analytica Chimica Acta* **1994**, *286*, 391–399.
46. Kumar, U. T.; Dorsey, J. G.; Caruso, J. A.; Evans, E. H. *Journal of Chromatography A* **1993**, *654*, 261–268.
47. Kumar, U. T.; Vela, N. P.; Caruso, J. A. *Journal of Chromatographic Science* **1995**, *33*, 606–610.
48. Suyani, H.; Creed, J.; Davidson, T.; Caruso, J. *Journal of Chromatographic Science* **1989**, *27*, 139–143.

49. Vela, N. P.; Caruso, J. A. *Journal of Analytical Atomic Spectrometry* **1996**, *11*, 1129–1135.
50. Zhao, Z.; Tepperman, K.; Dorsey, J. G.; Elder, R. C. *Journal of Chromatography A* **1993**, *615*, 83–89.
51. Suyani, H.; Heikemper, D.; Creed, J.; Caruso, J. *Applied Spectroscopy* **1989**, *43*, 962.
52. Ding, H.; Wang, J.; Dorsey, J. G.; Caruso, J. A. *Journal of Chromatography A* **1995**, *694*, 425–431.
53. Sheppard, B. S.; Shen, W.-L.; Caruso, J. A.; Heitkemper, D. T.; Fricke, F. L. *Journal of Analytical Atomic Spectrometry* **1990**, *5*, 431.
54. Sheppard, B. S.; Caruso, J. A.; Heitkemper, D. T.; Wolnik, K. A. *Analyst* **1992**, *117*, 971.
55. Branch, S.; Bancroft, K. C. C.; Ebdon, L.; O'Neill, P. *Analytical Proceedings* **1989**, *26*, 73–75.
56. Heitkemper, D.; Creed, J.; Caruso, J.; Fricke, F. L. *Journal of Analytical Atomic Spectrometry* **1989**, *4*, 279–284.
57. Larsen, E. H.; Pritzl, G.; Hansen, S. H. *Journal of Analytical Atomic Spectrometry* **1993**, *8*, 1075–1084.
58. Wang, J.; Tomlinson, M. J.; Caruso, J. A. *Journal of Analytical Atomic Spectrometry* **1995**, *10*, 601–607.
59. Demesmay, C.; Olle, M.; Porthault, M. *Fresenius Journal of Analytical Chemistry* **1994**, *348*, 205–210.
60. Branch, S.; Ebdon, L.; O'Neill, P. *Journal of Analytical Atomic Spectrometry* **1994**, *9*, 33–37.
61. Crews, H. M.; Clarke, P. A.; Lewis, D. J.; Owen, L. M.; Strutt, P. R.; Izquierdo, A. *Journal of Analytical Atomic Spectrometry* **1996**, *11*, 1177–1182.
62. Zoorob, G.; Tomlinson, M.; Wang, J.; Caruso, J. *Journal of Analytical Atomic Spectrometry* **1995**, *10*, 853–858.
63. Byrdy, F. A.; Olson, L. K.; Vela, N. P.; Caruso, J. A. *Journal of Chromatography A* **1995**, *712*, 311–320.
64. Inoue, Y.; Sakai, T.; Kumagai, H. *Journal of Chromatography A* **1995**, *706*, 127–136.
65. Pantsar-Kallio, M.; Manninen, P. K. G. *Analytica Chimica Acta* **1996**, *318*, 335–343.
66. Ding, H.; Olson, L. K.; Caruso, J. A. *Spectrochimica Acta Part B* **1996**, *51B*, 1801–1812.
67. Heumann, K. G.; Rottmann, L.; Vogl, J. *Journal of Analytical Atomic Spectrometry* **1994**, *9*, 1351–1355.
68. Matz, S. G.; Elder, R. C.; Tepperman, K. *Journal of Analytical Atomic Spectrometry* **1989**, *4*, 767.
69. Larsen, E. H.; Pritzl, G.; Hansen, S. H. *Journal of Analytical Atomic Spectrometry* **1993**, *8*, 557.
70. McLaren, J. W.; Siu, K. W. M.; Lam, J. W.; Willie, S. N.; Maxwell, P. S.; Palepu, A.; Koether, M.; Berman, S. S. *Fresenius Journal of Analytical Chemistry* **1990**, *337*, 721–728.
71. Tomlinson, M. J.; Wang, J.; Caruso, J. A. *Journal of Analytical Atomic Spectrometry* **1994**, *9*, 957–964.
72. Takatera, K.; Watanabe, T. *Analytical Sciences* **1992**, *8*, 469–474.

73. Dean, J. R.; Munro, S.; Ebdon, L.; Crews, H. M.; Massey, R. C. *Journal of Analytical Atomic Spectrometry* **1987**, *2*, 607–610.
74. Mason, A. Z.; Storms, S. D.; Jenkins, K. D. *Analytical Biochemistry* **1990**, *186*, 187–201.
75. Lyon, T. D. B.; Fell, G. S. *Journal of Analytical Atomic Spectrometry* **1990**, *5*, 135–137.
76. Mason, A. Z.; Storms, S. D. *Marine Environmental Research* **1993**, *35*,19–23.
77. Crews, H. M.; Dean, J. R.; Ebdon, L.; Massey, R. C. *Analyst* **1989**, *1989*, 895–899.
78. Takatera, K.; Watanabe, T. *Analytical Sciences* **1993**, *9*, 19–23.
79. Takatera, K.; Watanabe, T. *Analytical Sciences* **1993**, *9*, 605–609.
80. Gercken, B.; Barnes, R. M. *Analytical Chemistry* **1991**, *63*, 283–287.
81. Rottmann, L.; Heumann, K. G. *Fresenius Journal of Analytical Chemistry* **1994**, *350*, 221–227.
82. Peters, G. R.; Beauchemin, D. *Journal of Analytical Atomic Spectrometry* **1992**, *7*, 965–969.
83. Van Loon, J. C.; Alcock, L. R.; Pinchin, W. H.; French, J. B. *Spectroscopy Letters* **1986**, *19*, 1125–1135.
84. Chong, N. S.; Houk, R. S. *Spectroscopy Letters* **1987**, *41*, 66–74.
85. Kim, A. W.; Foulkes, M. E.; Ebdon, L.; Hill, S. J.; Patience, R. L.; Barwise, A. G.; Rowland, S. J. *Journal of Analytical Atomic Spectrometry* **1992**, *7*, 1147–1149.
86. Kim, A.; Hill, S.; Ebdon, L.; Rowland, S. *Journal of High Resolution Chromatography* **1992**, *15*, 665–668.
87. Peters, G. R.; Beauchemin, D. *Analytical Chemistry* **1993**, *65*, 97–103.
88. Pretorius, W. G.; Ebdon, L.; Rowland, S. J. *Journal of Chromatography* **1993**, *646*, 369–375.
89. Hintelmann, H.; Evans, R. D.; Villeneuve, J. Y. *Journal of Analytical Atomic Spectrometry* **1995**, *10*, 619–624.
90. Prange, A.; Jantzen, E. *Journal of Analytical Atomic Spectrometry* **1995**, *10*, 105–109.
91. Smaele, T. D.; Verrept, P.; Moens, L.; Dams, R. *Spectrochimica Acta Part B* **1995**, *50B*, 1409–1416.
92. Smaele, T. D.; Moens, L.; Dams, R., Sandra, P. *Fresenius Journal of Analtyical Chemistry* **1996**, *355*, 778–782.
93. Pritzl, G.; Stuer-Lauridsen, F.; Carlsen, L.; Jensen, A. K.; Thorsen, T. K. *International Journal of Environmental Analytical Chemistry* **1996**, *62*, 147–159.
94. Carey, J. M.; Caruso, J. A. *Trends in Analytical Chemistry* **1992**, *11*, 287–293.
95. Shen, W.-L.; Vela, N. P.; Sheppard, B. S.; Caruso, J. A. *Analytical Chemistry* **1991**, *63*, 1491–1496.
96. Vela, N. P.; Caruso, J. A. *Journal of Analytical Atomic Spectrometry* **1992**, *7*, 971.
97. Raynor, M.W.; Blake, E.; Cornell, D. *Journal of Chromatography A* **1994**, *683*, 223–231.
98. Blake, E.; Raynor, M.W.; Cornell, D. *Journal of High Resolution Chromatography* **1995**, *18*, 33–37.
99. Carey, J. M.; Vela, N.P.; Caruso, J. A. *Journal of Analytical Atomic Spectrometry* **1992**, *7*, 1173–1181.

100. Olesik, J. W.; Kinzer, J. A.; Olesik, S. V. *Analytical Chemistry* **1995**, *67*, 1–12.
101. Liu, Y.; Lopez-Avila, V.; Zhu, J. J.; Wiederin, D. R.; Beckert, W. F. *Analytical Chemistry* **1995**, *67*, 2020–2025.
102. Lu, Q.; Bird, S. M.; Barnes, R. M. *Analytical Chemistry* **1995**, *67*, 2949–2956.
103. Kinzer, J. A.; Olesik, J. W.; Olesik, S. V. *Analytical Chemistry* **1996**, *68*, 3250–3257.
104. Wang, L. Q.; May, S. W.; Browner, R. F.; Pollock, S. H. *Journal of Analytical Atomic Spectrometry* **1996**, *11*, 1137–1146.
105. Magnuson, M. L.; Creed, J. T.; Brockhoff, C. A. *Journal of Analytical Atomic Spectrometry* **19967**, *12*, 689–695.
106. Story, W. C.; Caruso, J. A.; *Journal of Analytical Atomic Spectrometry* **1993**, *1993*, 571–575.
107. Story, W. C.; Olson, L. K.; Shen, W.-L.; Creed, J. T.; Caruso, J. A. *Journal of Analytical Atomic Spectrometry* **1990**, *5*, 467–470.
108. Creed, J. T.; Davidson, T. M.; Shen, W.-L.; Caruso, J. A. *Journal of Analytical Atomic Spectrometry* **1990**, *5*, 109.
109. Suyani, H.; Creed, J.; Satzger, R. D.; Caruso, J. A. *Journal of Analytical Atomic Spectrometry* **1989**, *4*, 777–782.
110. Mohamad, A. H.; Creed, J. T.; Davidson, T. M.; Caruso, J. A. *Applied Spectroscopy* **1989**, *43*, 1127–1131.
111. Evans, E. H.; Pretorius, W.; Ebdon, L.; Rowland, S. *Analytical Chemistry* **1994**, *66*, 3400–3407.
112. O'Connor, G.; Ebdon, L.; Evans, E. H.; Ding, H.; Olson, L. K.; Caruso, J. A. *Journal of Analytical Atomic Spectrometry* **1996**, *11*, 1151–1161.
113. Olson, L. K.; Caruso, J. A. *Journal of Analytical Atomic Spectrometry* **1992**, *7*, 993.
114. Castillano, T. M.; Giglio, J. J.; Evans, E. H.; Caruso, J. A. *Journal of Analytical Atomic Spectrometry* **1994**, *9*, 1335–1340.
115. Castillano, T. M.; Giglio, J. J.; Evans, E. H. *Journal of Analytical Atomic Spectrometry* **1997**, *12*, 383–385.
116. Carey, J. M.; Vela, N. P.; Caruso, J. A. *Journal of Chromatography A* **1994**, *622*, 329–340.
117. Kumar, U.; Dorsey, J. G.; Caruso, J. A. *Journal of Chromatographic Science* **1994**, *32*, 282–285.
118. Jiang, S.; Houk, R. S. *Spectrochimica Acta* **1988**, *43B*, 405–411.
119. Shum, S. C. K.; Houk, R. S. *Analytical Chemistry* **1993**, *65*, 2972–2976.

11

Geological Applications of Secondary Ion Mass Spectrometry

Lee R. Riciputi
Oak Ridge National Laboratory
Oak Ridge, Tennessee

11.1 INTRODUCTION

Geochemical analysis is a major subset of secondary ion mass spectrometry. Among microanalytical techniques, its versatility makes it unique in the geochemical community, as no other method provides both the capability for analysis of a wide variety of trace elements at the part per billion (ppb) to part per million (ppm) level and the ability to measure both stable (H, Li, B, C, N, O, S, plus Si, Mg, Ca, Ti) and radiogenic (U-Pb, Re-Os) isotope ratios with precision sufficient for geochemical applications. Compared to that of most laser sampling techniques, the spatial resolution of secondary ion mass spectrometry (SIMS) is superior, particularly in the third dimension (depth). Interest in this technique is reflected in a doubling in the number of SIMS facilities devoted principally to geochemistry and cosmochemistry since 1990, and rapid growth in application over the past 10 years (Fig. 11.1). Compared to many other SIMS applications, geochemical analysis is characterized by a number of features, including (1) predominantly insulating matrices; (2) complex, chemically variable matrices; (3) requirements for both high precision and high accuracy, particularly for isotope ratio analysis, in which precision of 1000 ppm or better is often required; and (4) demand for analysis of a wide range of elements and isotope ratios. Although most geochemical work has been focused on elemental and isotopic spot analysis, there is a significant subset of depth profiling work focused on experimental determination of diffusion rates, as well as work utilizing SIMS imaging capabilities.

This chapter is intended to provide an overview of recent technical SIMS developments and applications relevant to geo- and cosmochemistry, and to supple-

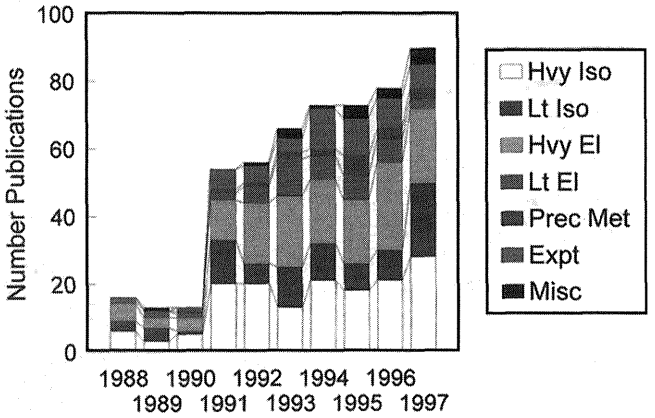

Figure 1 Studies published between 1988 and 1997 reporting use of secondary ion mass spectrometry (SIMS) in geochemistry and cosmochemistry. Papers are subdivided according to theme: Hvy Iso, studies of heavy isotope ratios, principally for U-Pb dating; Lt Iso, studies of light stable isotope ratios (H, B, C, O, S); Hvy El, studies primarily focused on analysis of elements >40 amu (e.g., rare earth elements); Lt El, studies primarily focused on analysis of elements <40 amu (e.g., water content); Prec Met, analysis of precious metal contents (e.g., Au, Ag, Pt); Expt, analysis of experimental run products; Misc, other miscellanous studies utilizing SIMS.

ment the general chapter in this volume, in which the history and fundamentals of SIMS are discussed (Chapter 4). Three main analytical challenges dominate application of SIMS in geochemistry: (1) sample surface charging on insulators; (2) presence of a wide variety of isotopic, molecular, and multicharged ions as isobaric interferences; and (3) dependence of secondary ion yields on the chemical properties of the sample being analyzed. The first part of the chapter is focused on a brief overview of the these problems, and the instrumentation and techniques that are used in various geochemical applications. The latter part of the chapter attempts to provide brief summaries of a variety of different types of SIMS applications in geochemistry. Given the rapid growth of geochemical SIMS literature over the past few years (Fig. 11.1), it is impossible to provide a comprehensive review of SIMS applications. As the technique has rapidly matured in recent years, more recent developments and applications are emphasized. Readers are referred to several excellent overview articles that already exist in the literature both for additional details on analytical techniques and for reviews of older geochemical SIMS literature (MacRae, 1995; Hinton, 1995; Reed, 1989; Zinner, 1989; Shimizu and Hart, 1982; Shimizu et al., 1978).

11.2 INSTRUMENTATION AND ANALYTICAL METHODS

In part as a result of the demands for high precision and accuracy and the abundance of isobaric molecular interferences arising from complex matrix chemical processes, almost all geochemical SIMS work has employed magnetic sector SIMS instruments. Time-of-flight (TOF) SIMS holds promise, particularly in the area of analysis/imaging of mineral surfaces, but its potential in geochemistry is only beginning to be explored. The instrumentation overview presented concentrates on factors controlling analytical procedures for magnetic sector SIMS instruments; further detail can be found in Chapter 4, as well as reviews such as Benninghoven et al. [1987] and the geochemical SIMS reviews mentioned earlier.

11.2.1 Primary Beam

Although a variety of bombarding ions can be employed (see Chapter 4), most geological applications use either an oxygen (O^- or O_2^+) or a cesium (Cs^+) primary ion beam. Secondary ion yields are strongly influenced by the bombarding species, so that the desired application often dictates the choice of primary ion beam. Oxygen (O^-) is often used, as sample charging problems on insulating specimens are minimized with a negative charged primary ion beam. However, much higher current densities are possible when using Cs^+ and O_2^+ primary ion beams, allowing better spatial resolution. Additionally, use of a Cs^+ primary beam enhances the ion yield (sensitivity) for electronegative elements. For most geological applications, the primary ion beam is focused to a fine spot, using a series of lenses and apertures or Kohler illumination (see Chapter 4). Because of sensitivity and precision requirements, almost all geological applications utilize dynamic SIMS, where the sample surface is actively eroded by the primary ion beam. The potential for static SIMS, wherein the primary ion current is low enough that the surface layers survive for long periods, is very promising for the study of reactions occurring at mineral surfaces, particularly by utilizing time-of-flight secondary ion mass spectrometry, but is just beginning to be explored [e.g., Ingram et al., 1998].

11.2.2 Secondary Ion Analysis

A wide variety of positive and negative charged secondary ions and neutral species are sputtered from the sample surface, including elemental, molecular, and multiply charged ions. These ions have a range of kinetic energies, trajectories, and spatial origin within the sputtered surface. Typically, either positive or negative charged secondary ions are analyzed, although molecular species and multiply charged ions have also been used for quantitative analysis [e.g., Compston et al., 1984; Riciputi et al., 1993]. To maximize sensitivity, it is important that secondary ions be efficiently extracted into the secondary ion mass spectrometer, as ion-

ization efficiency of most elements is typically <5%. In addition, the secondary mass spectrometer must be capable of discriminating between elemental ions and molecular isobaric interferences.

As mentioned earlier, almost all geochemical work has used magnetic-sector instruments. Because of the large range in energy of secondary ions emitted from the sample surface, a double-focusing geometry using both an electrostatic analyzer and a magnet is employed to achieve both high mass resolution and transmission. The sample is typically held at a high potential (1–10 keV) to extract secondary ions from the sample surface, although in some instruments (e.g., VG Isolab), a two-stage process is used, in which ions are extracted by utilizing low energies (<200 eV) and then further accelerated. The ions are focused onto the entrance slit of the mass spectrometer by a transfer lens. In the typical geometry, ions then pass through an electrostatic filter, where they are dispersed on the basis of energy. The amount of energy filtering can be controlled by an energy slit: Decreasing the energy spread increases the focus of the ions but decreases transmission and can also affect the relative ion intensities both of different elements and among isotopes of the same element. The ions then pass through the secondary magnet, which disperses them on the basis of momentum. Most instruments are equipped with a single-exit slit through which the ion beam passes before entering the detector system; different masses are monitored sequentially by slewing the magnetic field to select masses of interest. Closing the entrance and exit slits and improving the shape of the secondary ion beam allow smaller mass differences between peaks of interest and molecular interferences to be resolved. However, this is achieved at the expense of ion transmission, and hence sensitivity.

The magnetic sector SIMS instruments can be subdivided into two groups, those possessing magnets with a small radius (Cameca f series) and those possessing large-radius magnets [sensitive high-resolution ion microprobe (SHRIMP, Cameca 1270)]. For the small-radius instruments, transmission begins to drop off rapidly once mass resolution exceeds about 2000 and decreases by over 90% when mass resolution of 5000 is reached. Physical separation of masses is increased if the magnetic radius is enlarged, allowing improved transmission at high mass resolution. Driven principally by the need for high mass resolution coupled with high transmission for analysis of U-Pb ratios in geological samples, a number of large-magnetic-radius instruments have been built, including the SHRIMP and Cameca 1270 instruments. In these instruments, transmission does not begin to decrease significantly until mass resolution exceeds 5000.

Secondary ion currents are typically detected by using a Faraday cup if intensities are high enough (>1 MHz or 10^6 counts per second). For most geological applications count rates are so low that an electron multiplier (or other single-ion counter), in which each ion impact is converted to a charge pulse that is counted by the detector system, is used. The efficiency of the ion-to-charge conversion ratio varies between both elements and isotopes of the same element, generally be-

coming less efficient with heavier masses; particularly for heavier ions, the conversion efficiency can be increased by using higher secondary ion accelerating potentials [e.g., van der Heide and Fitcher, 1998]. Relative variations among elements and isotopes also change as the multiplier ages, requiring careful calibration of the instrument for high-precision applications. At higher count rates multiple pulses can arrive at the detector essentially simultaneously. If the counting system is unable to resolve the two pulses electronically, they are counted as a single pulse, and one count in the pair is not recorded by the counting system. The loss of these counts can be corrected by using the equation

$$C_{\text{measured}} = C_{\text{true}} \exp(t^* C_{\text{true}})$$

where C is the count rate and t is the deadtime. Therefore, for precise and accurate results, the "deadtime" of the counting system must be well known, particularly for isotope ratio measurements [Hayes and Scholler, 1977; Zinner et al., 1986]. The deadtime, and the precision with which it is known, typically limit the maximum count rate at which isotope ratio measurements can be made with an electron multiplier. Multiple-detector systems consisting of Faraday cups and electron multipliers are a potential solution, but difficulties with drift between different detectors must be overcome before significant increases in precision become possible.

11.2.3 Isobaric Interferences

The overlap of molecular peaks with the elemental ion peak of interest is a major problem, particularly in complex geological matrices. For molecular species arising from contamination from vacuum gases (e.g., MH, MOH), maintaining good vacuum conditions can help to minimize the size of interfering peaks. In many cases, with knowledge of the matrix composition, a particular isotope of an element of interest can be selected to minimize potential interferences. When interferences cannot be prevented, one of two major techniques is used to separate or eliminate interferences: high mass resolution or some form of kinetic-energy filtering.

For high mass resolution, the exit slits of the mass spectrometer are closed down; narrowing the slits, when coupled with collimating the secondary ion beam by using entrance slits and apertures, allows small differences in mass between elemental and nearby isobaric peaks to be resolved. For example, a mass resolution ($M/\Delta M$) of 4735 is required to resolve the mass difference between ^{16}OH (17.002700 D) and ^{17}O (16.999131 D). The mass resolution required to separate MO species from elemental peaks generally increases from ~1000 for light masses (^{7}Li^{16}O on ^{23}Na) to ~5000 around mass 60. Above this mass range, transmission losses become prohibitive for small-radius instruments. Although required mass resolution is high for intermediate masses ($M/\Delta M$ typically >10,000 for amu 90–150), required resolution decreases to 7000–9000 for amu > 150, so that large-radius instruments can be used to resolve most interferences on heavy elements

such as Pb, allowing precise measurement of isotope ratios. It should be noted that if samples are sufficiently old, geologically useful differences in Pb isotope ratios in zircons can be measured by using a small-radius instrument [Wiedenbeck and Goswami, 1994; Wiedenbeck et al., 1996]. Resolution of hydride peaks is feasible for light masses; it requires $M/\Delta M$ of 1000 to 5000 for masses between 2 and 40. Above this mass range, the required resolution increases rapidly to values above 10,000, with resolution of almost 50,000 required to resolve UH peaks from other U species, a process that is beyond the capabilities of even the large-radius SIMS instruments. Fortunately, with good vacuum conditions and with the exception of light isotope analysis, hydrid interferences are typically less of a problem than oxide interferences.

Sputtered ions leave the surface with a range of kinetic energies. As the kinetic energy distribution of most molecular species is narrower than that of the elemental ions, kinetic energy filtering can be used to suppress the intensity of molecular ions relative to elemental ions [e.g., Shimizu et al., 1978]. In *conventional energy ltering* [e.g., Shimizu et al., 1978; Zinner and Crozaz, 1986], the accelerating potential of the sample surface is offset by 80–100 eV relative to the acceptance energy of the electrostatic analyzer. Assuming an offset voltage of 100 eV is applied, and the energy slits have a bandpass of ±20 eV, only sputtered ions having an initial kinetic energy of 100 ± 20 eV are transmitted through the mass spectrometer. An energy offset of this magnitude is sufficient to suppress trimers and many dimers. In some cases, such as the interference of light rare earth oxides on heavy rare earth peaks (e.g., $^{142}Ce^{16}O$ on ^{158}Gd), significant interferences persist, and energy filtering must be coupled with mathematical peak deconvolution [e.g., Zinner and Crozaz, 1986].

Almost complete suppression of molecular species can be achieved by utilizing high offset energies, although there is a severe reduction in overall ion signal. In the specimen isolation (SI) technique, uncoated samples are allowed to charge, producing an offset energy of 400–600 eV [e.g., Metson et al., 1983; McIntyre et al., 1985], and analyses such as determination of rare earth element (REE) abundances can be done without concern for interfering oxide species. This technique requires a much higher primary beam intensity, however, to compensate for the decrease in sensitivity, resulting in loss of spatial resolution. In addition, the degree of charging (energy offset) cannot be precisely controlled. Similar effects can be achieved by offsetting the sample accelerating voltage by several hundred electron volts relative to the acceptance energy of the mass spectrometer (with more precise control of the kinetic energy of the secondary ions), although older (Cameca 3f and 4f) instruments must be modified to have this capability. This capability, termed *extreme energy filtering*, has been primarily exploited for the analysis of light stable isotope ratios (O, C, S) in insulating matrices [e.g., Hervig et al., 1992; Riciputi and Paterson, 1994; Valley et al., 1997; Riciputi et al., 1998]. Typically at offset energies of 300–350 eV, hydride species are suppressed to in-

significant levels [e.g., Schauer and Williams, 1990; Hervig et al., 1992]. Therefore, the instrument can be operated at low mass resolution, which partially offsets the loss in secondary ion signal due to the use of high-energy secondary ions. Riciputi [1996] and Paterson et al. [1997] demonstrated that when compared to that of high mass resolution, instrumental mass bias was more reproducible from sample to sample using the extreme energy filtering technique, presumably as a result of minimization of surface effects due to the higher initial kinetic energy of the analyzed ions.

11.2.4 Matrix Effects

A second challenge in ion microprobe analysis is calibration, as the secondary ion yields for each element (and isotope) can vary by orders of magnitude, depending on both the primary beam that is used to sputter the sample and the chemical composition of the sample. Choice of primary beam allows increased sensitivity for the target elements (typically use of oxygen enhances ion yields of electropositive elements, and cesium enhances yields of electronegative elements) and can be controlled by the operator. The chemical composition of the target substrate, however, cannot be operator controlled. At present, sputtering theory cannot accurately predict most matrix effects. Therefore, to obtain accurate analyses, ion yields must be empirically quantified by using standards that have major element compositions that are closely matrix-matched to the unknown samples, a major task, given the wide variety of minerals and solid solutions in many chemical series. For trace element analysis, two different methods have been used. In one, a known quantity of a labeled isotope of the element of interest is implanted into a mineral, and the ion yield is determined by measuring the yield of this isotope relative to the known (implanted) concentration. The major drawback with this method is expense, as a separate implant has to be performed for each element of interest, and the number of implants required can rapidly multiply, especially if a variety of mineral compositions are of interest. The more common method to determine ion yield in geological matrices involves use of natural minerals that have been characterized by bulk methods. The biggest problem is finding materials that are (1) homogenous on the micrometer scale, (2) free of inclusions that could compromise the bulk analyses, and (3) available in sufficient quantities for bulk determination. Most natural materials are heterogeneous, making the search for suitable mineral standards a difficult one. For at least some compositions and analytical conditions, ion yields between crystalline minerals and glasses of identical chemical composition are similar, allowing the use of synthetic standards [e.g., MacRae et al., 1993; Bottazzi et al., 1992; Hinton, 1990].

Absolute ion yields can vary during the course of an analytical session as a result of a variety of factors. However, these variations affect ion yields of different elements in a similar manner, so that by ratioing the ion yield of an element of

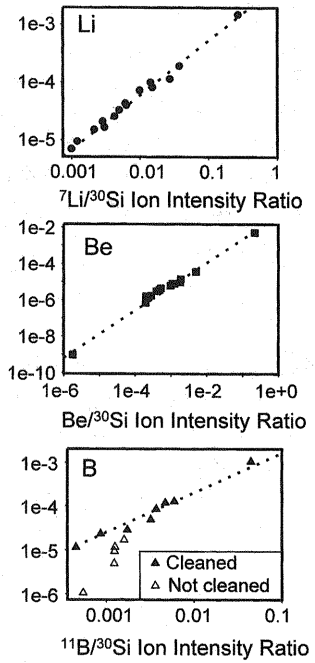

Figure 2 Examples of calibration curves for silicate glasses and minerals for Li, Be, and B. Note the linear behavior over several orders of magnitude. The B example illustrates the strength of using several standards; a standard mount that was not properly cleaned [e.g., Chaussidon et al., 1997] shows the effect of sample contamination in elevated B counts relative to the actual sample concentration.

interest to that of a major element of known concentration (typically Si or Ca), these effects can be minimized. This ratio of ion yields is converted to concentration by a *relative sensitivity factor*, which for most geological applications is determined from the slope of the ion yield ratio compared to the concentration ratio from a set of standards (Fig. 11.2; see Chapter 4). Analysis of multiple standards allows the possibility of a nonzero intercept, indicative of either an interfering species or surface contamination, to be evaluated.

Matrix effects (termed *instrumental mass bias*) also present problems in isotope ratio analysis as the measured isotope ratio is almost always light isotope enriched relative to the accepted ratio, and the degree of this enrichment depends on the matrix composition. Although mass bias variations between different mineral compositions are relatively minor for most elements (a few percentage points at most), the high accuracy required in isotope analysis (often 1% or better) demands careful calibration. For isotope ratio measurements in essentially isochemical

phases [e.g., oxygen isotopes in quartz (SiO_2), lead isotopes in zircon ($ZrSiO_4$)], the mass bias can be simply calibrated using an appropriate standard. However, many minerals consist of chemical solid solutions, so that some means of correlating mass bias to chemical composition must be developed. A variety of empirical mass bias relations that have been developed (e.g., Riciputi et al., 1998; Eiler et al., 1997; Hervig et al., 1992; Deloule et al., 1992] allow prediction of isotopic mass bias for some elements in some minerals to be made with accuracy that approaches precision, but a universal model has yet to be developed.

11.2.5 Sample Charging

With the exception of some sulfides and oxides, geological materials are electrically nonconductive, so that sputtering by a charged primary ion beam leads to surface charging. As absolute ion yields, as well as relative ion yields, between different elements and isotopes of the same element vary with secondary ion energy, sample charging can severely compromise the analysis. Surface charging is dominated by the charge of the primary ion beam, so that during analysis by a negatively charged primary ion beam (e.g., O^-) an excess negative charge develops, and bombardment by a positively charged primary ion beam (e.g., O_2^+, Cs^+) produces an excess positive charge. An additional effect is caused by the polarity of secondary ions that are analyzed: Analysis of negative secondary ions accentuates positive charge buildup as secondary electrons generated during sputtering are extracted from the sample surface.

Negative charge build-up can be dealt with relatively easily by coating the sample surface with a thin layer of a conductive material (e.g., Au or C). Excess electrons can migrate away from the analysis location through this conductive layer, preventing charge build-up, as long as the sputtered area is not so large that the electrons cannot "jump" to the conductive layer. Therefore, analysis using an O^- primary ion beam circumvents most sample charging problems and is typically chosen for most trace element (and Pb isotope) analyses. However, as discussed earlier, yields of electronegative elements (e.g., C, O, S) are enhanced by orders of magnitude by using a Cs primary ion beam and extracting negative charged secondary ions. This produces a large excess positive charge build-up, particularly under bombardment by the relatively intense primary ion beams required for precise stable isotope analysis. Efforts to compensate for charge build-up have focused on using an electron gun to deliver electrons to the sample surface and thus neutralizing positive charging [Migeon et al., 1990]. Even with an electron gun, however, if surface charging is not controlled to within a few electron volts the mass bias of light elements can vary significantly during the course of the analysis if secondary ions with kinetic energies near zero are analyzed (Fig. 11.3). Under extreme energy filtering conditions, however, mass bias is stable over a range of tens of electron volts, so that perfect charge compensation is not necessary for stable

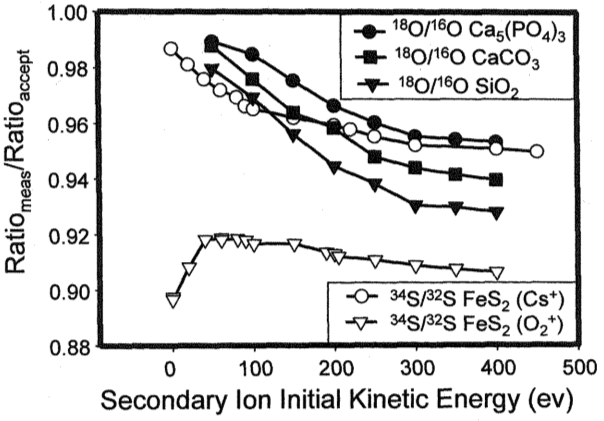

Figure 3 Illustration of the effect of changing secondary ion energies on instrumental mass bias for light isotope ratios. Ratio$_{meas}$ is the isotope ratio (either $^{18}O/^{16}O$ or $^{34}S/^{32}S$) measured on a particular mineral by secondary ion mass spectrometry (SIMS), Ratio$_{accept}$ is the accepted value for the same mineral. Results for $^{18}O/^{16}O$ utilizing a Cs primary ion beam and negative secondary ions for phosphate, silicate, and carbonate have very similar shapes. Results for $^{34}S/^{32}S$ measurements on the mineral pyrite (FeS_2) also illustrate the effect of the primary ion beam; the shape of the curve measured by a Cs primary ion beam is similar to the results obtained for oxygen isotope ratios (using a Cs beam), whereas the mass bias dependence is very different when sputtering with an oxygen primary ion beam.

analytical conditions. Development of the extreme energy filtering technique has allowed precise measurement of oxygen, carbon, and sulfur isotope ratios on insulators using negative charge secondary ions [e.g., Hervig et al., 1992; Riciputi and Paterson, 1994; Riciputi et al., 1998]. Recent improvements in the design of electron guns have enhanced charge-compensation capabilities to the point where it is feasible to utilize the much more abundant population of low- energy secondary ions, potentially improving both sensitivity and precision [e.g., Lyon et al., 1995; Leshin et al., 1997; Leshin et al., 1998].

11.3 APPLICATIONS

11.3.1 Trace Element Analysis

The ion microprobe has been widely applied to the analysis of trace elements in a variety of geological materials, as the excellent spatial resolution provides the ability to study either elemental zoning patterns in a large mineral or to analyze phases that are too fine-grained (or are too limited in quantity) to make separation and bulk analysis practical. In comparison to other techniques, the ion probe also of-

fers the ability to analyze a wide variety of elements at part per billion to part per million concentrations. Major applications of SIMS for trace element analysis include (1) light elements (e.g., Li, Be, B, F, H_2O contents); (2) the lanthinide, or rare earth, elements (REEs); (3) precious metals (e.g., Au, Ag, Pt); and (4) a variety of other heavy trace elements. The greatest application of SIMS in elemental analysis has been in the area of igneous petrology, but use in other areas of geochemistry is increasing.

Melt Inclusions

In recent years, the ion microprobe has been extensively used to evaluate the chemical composition of a magma prior to its eruption. This information is exceedingly difficult to obtain by using bulk samples, as degassing during eruption and posteruption typically obscures the record of primary magma chemistry. However, small melt inclusions are often trapped during the growth of a mineral (phenocryst) in the magma prior to eruption and are thus isolated from subsequent alteration. Typically, SIMS analyses of trace element and volatile contents (particularly water) of melt inclusions are coupled with electron microprobe determinations of major element contents. Analysis of multiple melt inclusions in zoned phenocrysts can yield information on the evolution of a magma body through time and the components involved in its generation. As the studies to be described here have demonstrated, the ion microprobe has opened up a new area of research, providing information on primary magmatic compositions that have hitherto only been speculative.

Melt inclusion studies have been carried out on a range of igneous rock compositions, some of them focusing on silicic rocks associated with explosive volcanism. Webster et al. [1994] utilized glass inclusions in quartz phenocrysts to determine the original composition of highly altered air-fall ash deposits. Hervig and Dunbar [1992] examined glass inclusions from the Bishop and Bandolier tuffs and concluded that compositional zoning in both units is the result of mixing between two different rhyolitic magmas in the magma chamber. Wilding et al. [1993] found that glass inclusions in quartz phenocrysts from peralkaline rhyolites from the Kenyan rift had relatively high water content (>3%), in contrast to low values (<0.5%) in the matrix glass. This indicates that significant degassing of the magma occurred during or immediately before eruption. The authors suggested that this degassing could have been a driving force for eruption. However, Barclay et al. [1996] found no correlation between eruptive style and volatile (H_2O, CO_2, F, and Cl) contents in melt inclusions from New Zealand peralkaline rhyolites and concluded that magma supply was the major factor controlling eruptions. Some studies have focused on determining the composition of silicic magmas associated with the formation of economic deposits, such as tin mineralization associated with the Taylor Creek rhyolite [Webster & Duffield, 1994] and rare-metal deposits associated with granites [Kovalenko et al., 1995].

Primary magma compositions, especially water contents, have been the focus of a number of studies on igneous rocks associated with arc magmatism. Roggensack et al. [1997] found that water and carbon dioxide contents in melt inclusions from the explosive 1992 eruptions of Cerro Negro volcano were elevated compared to those in the nonexplosive 1995 eruptions and argued that this increase could be related to the level of magma ascent in the crust. Portnyagin et al. [1996] studied glass inclusions in olivine from bonitite and concluded that at least four different components were involved in magma generation. Sobolev and Chaussidon [1996] studied glass inclusions from Mg-rich olivine in basalts and other ultramafic magmas. Their results suggested that water contents in ocean-ridge magmas are low (0.1 to 0.5 wt%) but are much higher (1–3 wt%) in more evolved bonitites and other arc-related magmas. Ohnenstetter and Brown [1996] carried out a detailed investigation of bonitites and suggested that water contents in more evolved magmas could be explained by fractional crystallization processes. However, analysis of glass inclusions in phenocrysts from arc-related magmas from the Cascades led Sisson and Layne [1993] to conclude that fractional crystallization alone could not generate the range of water contents observed. They suggested that assimilation of a water-rich component was required during generation or crustal modification of these magmas. Rampone et al. [1997] utilized glass inclusions to study the process of melt impregnation and peridotite-melt interaction in ophiolites. Gurenko and Chaussidon [1995] found both enriched and depleted primitive melt compositions from melt inclusions in olivine from Icelandic tholeiites; they suggested that continuous melting of a mantle column could generate the observed range in compositions.

Mantle Xenoliths and Related Samples

Along with studies of melt inclusions, the study of mantle *xenoliths* (samples of mantle material entrained and brought to the surface in eruption magmas) and exhumed mantle rocks is one of the most common applications of SIMS for trace element analysis. SIMS is ideally suited to this task, as there is no need to try to make mineral separates from what are often limited amounts of sample, alteration can be prevented, and zoning easily studied.

Taylor et al. [1996] examined REE patterns from inclusions of the minerals garnet and clinopyroxene in diamonds and compared them to REE patterns found in garnets and clinopyroxenes of the eclogitic rocks hosting the diamonds. They found no simple relation between the two sets of data, indicating that the diamonds formed under different conditions from those recorded in the host eclogite xenoliths. Tribuzio et al. [1996] examined REE distributions in blueschists and eclogites to determine their fate during subduction of sediments and the resulting high-pressure, low-temperature metamorphism. They found that the light REEs (LREEs) were partitioned into stable minerals such as lawsonite and epidote, and

thus LREEs could be subducted deep into the mantle without necessarily being released in a fluid. Vannucci et al. [1995] examined amphiboles from orogenic peridotites and lherzolitic xenoliths. The amphibole had been thought to form by metasomatism during infiltration of LREE-enriched fluid, but they found that the amphiboles were typically LREE depleted and suggested that these values could result from either reequilibration during cooling or some type of unidentified chromatographic process. Zanetti et al. [1996] also found that REE and trace element patterns in hornblende and pyroxene around a hornblendite vein from a sample of the subcontinental lithosphere were consistent with chromatographic fractionation of elements from the vein into the wallrock, coupled with the effects of crystallizing phases in the vein. Studies of REE in samples of oceanic mantle xenoliths have included those of Sen et al. [1993], who examined mineral REE patterns in mantle xenoliths from Hawaii, and Sobolev and Baanova [1995], who studied REE patterns in clinopyroxene in mantle lherzolites from the Troodos ophiolites. Other studies focused on trace element behavior in mantle rocks include those of Nimis and Vannucci [1995], Rhoden and Shimizu [1993], and Matthews et al. [1992]. SIMS REE analysis has also been applied to extraterrestrial materials, including lunar samples [e.g., Snyder et al., 1993; Papikke, 1996], shergottitite (Martian) meteorites [Wadhwa et al., 1994], and eucritic meteorites [Pun et al, 1997].

Although much less common, SIMS has also been used to study magmatic processes in silicic rocks; examples include that by Sevigny [1993], who used REE patterns in garnets to demonstrate that Nd/Sm dating of leucogranites could be effected by monazite fractionation. Dorais and Macrae [1994] studied trace and REE element zoning patterns in amphibole from a syanite complex and found that they were consistent with those expected for fractional crystallization.

Analysis of Precious Metals

In studies of economic deposits, SIMS has been increasingly used for analysis of precious metal contents (e.g., Ag, Au, Pt) in sulfide minerals. Many of these studies have coupled both quantitative spot analyses (maximizing precision and detection limits) with imaging of individual grains to determine better the spatial distribution of the precious metals. These studies have often resulted in revision of preexisting concepts of precious metal sourcing and mineralization timing. An excellent summary of technical considerations and application of the ion microprobe to the study of precious metals in sulfides can be found in Larocque and Cabri [1998]. Cabri and McMahon [1995] demonstrated that detection limits for Au and Pt were in the range of 0.01 to 0.25 ppm in pyrite, pyrrhotite, and chalcopyrite, and Larocque et al. [1995a] demonstrated 60-ppb detection limits for Ag in pyrite and chalcopyrite. These calibrations were applied in a study of Ag and Au mineralization in the metamorphosed Mobrun volcanogenic massive sulfide deposit in Canada, where Larocque et al. [1995a] demonstrated that metamorphic recrystal-

lization released "invisible" Au and Ag from pyrite, which was then deposited in easily exploitable tectonic veins [Larocque et al., 1995a,b]. Tarnocai et al. [1997] studied Au distributions in sulfides from the Campbell mine in Canada. They found that Au was concentrated in arsenopyrite zones and that Au distributions were zoned in coarse grains and concluded that Au mineralization coincided with the peak of metamorphism. Santanguida and Hannington [1996] conducted a survey of Au in massive sulfide deposits in central Newfoundland and demonstrated that up to 50% of the Au was "invisible," occurring at the single part per million to hundreds of parts per million level in pyrite and arsenopyrite. Neumayr et al. [1993] utilized SIMS in their study of lode-gold deposits in Western Australia. Although previous consideration of native Au textures suggested that Au mineralization occurred during retrograde metamorphism, they concluded that it was actually deposited before metamorphism in the mineral lollingite and was then remobilized during retrograde metamorphism. Additional studies of precious metal mineralization utilizing SIMS include lode-gold deposits from the Ashanti gold belts in Ghana [Mumin et al., 1994], studies of modern Au mineralization along the Mid-Atlantic Ridge [Hannington et al., 1995], Pt mineralization in the Duluth Complex [Ripley and Chryssoulis, 1994], and those on sediment-hosted disseminated gold deposits in Nevada, utilizing SIMS analysis of both precious metal contents and sulfur isotope compositions [Arehart et al., 1993a,b].

These studies have demonstrated the utility of SIMS in understanding the concentration and distribution of precious metals in a number of different ore-deposit types and have often resulted into new insights into the formation of the deposits. This improved understanding can be applied both to search for new deposits and to improve the efficiency of extraction techniques in currently exploited deposits. Given these strengths, it is likely that the use of SIMS in the study of precious metal deposits will continue to grow.

Studies of Diagenesis and Other Low-Temperature Geochemical Processes

Although most ion microprobe trace element work has focused on igneous and metamorphic petrology, applications to processes occurring at lower temperatures have been steadily increasing. Probably the biggest single area of study has focused on trace elements in carbonate minerals. Early studies evaluated the potential of the ion microprobe for analysis of Sr, Mn, Fe, and Mg in calcite and dolomite [Mason, 1987; Swart, 1990; Veizer et al., 1987] and demonstrated sensitivities of 1 to 10 ppm. Mason [1987] used this method to evaluate potential correlations between chemical composition and cathodoluminescence in calcite cements from a Lower Carboniferous limestone in Wales and showed that Mn was the main activator and Fe a suppressor. Savard et al. [1995] confirmed these results, demonstrating that ~ 20 ppm of Mn is required to activate luminescence, and that Fe con-

centrations above 1400 ppm quench it. However, they also showed that at Mn concentrations between 20 and 225 ppm, a wide range of luminescence types could occur, suggesting additional controls on luminescence behavior. Riciputi et al. [1994a] examined B, Na, Mg, Fe, Mn, Sr, and Ba contents in carbonate cements from Devonian reefal carbonates in the Western Canada Sedimentary Basin. They demonstrated that primary compositional variations over scales <100 μm were preserved through later diagenesis, suggesting that trace element compositions can be used for early diagenetic interpretations even in old and deeply buried carbonates. The nature of fluids responsible for alteration of carbonaceous chondrite meteorites was studied by trace element analysis of carbonate [Riciputi et al., 1994b]. They suggested that the increasingly brinelike nature of the fluids calculated to be in equilibrium with these carbonates could have been formed by membrane filtration, low-pressure boiling, or addition of components to the fluid during formation of phyllosilicates.

Recently, SIMS analysis of rare earth elements has been applied to diagenetic problems. Srinivasan et al. [1994, 1995] examined REE contents in Cambrian and Ordivician calcite cements in platform carbonates from Tennessee, demonstrating that the rare earth element patterns might be used to determine the maturity of the fluid source rocks and that rare earth contents could be used to determine paleofluid flow direction. REE zoning in fracture-filling calcite cement from Yucca Mountain was suggested to reflect variations in water table levels during calcite precipitation [Denniston et al., 1997]. SIMS has also been used to analyze REE contents in individual conodont fossils from the upper Devonian period [Grandjeanlecuyer et al., 1993]. The researchers found that the REE patterns in these conodonts do not resemble those of post-Cretaceous biogenic phosphates and suggested that REE contents in pre-Cretaceous seawater were controlled by desorption-adsorption processes rather than being nutrient controlled.

11.3.2 Isotope Ratio Analysis

SIMS has been used increasingly to measure isotope ratios for a variety of elements in geological materials. In the 1980s, two different domains were major research areas using SIMS. The first is *isotopic astrophysics*, the use of SIMS to analyze anomalous isotope ratios of elements such as C, N, O, Mg, Si, Ca, and Ti in tiny inclusions from meteorites and stellar dust that record information on both stellar nucleosynthesis processes and formation of the early solar system. The second is the use of large-radius SIMS instruments to obtain ages of igneous and metamorphic events by dating zircons by using the U-Pb isotope system. Improvements in precision and accuracy since the early 1990s have led to increasing application of SIMS for the analysis of light stable isotope ratios (e.g., D/H, B, C, O, S) in both extraterrestrial and terrestrial systems.

Isotope Ratios in Extraterrestrial Materials

There is an extensive literature of SIMS isotope analysis of a variety of light elements in meteorites and other samples of extraterrestrial matter such as dust particles gathered from the upper atmosphere, stretching back over 15 years. Most of these studies have focused on studies of primitive particles such as interplanetary dust particles (IDPs), silica carbides (SiCs), calcium-aluminum rich inclusions (CAIs), and graphite grains. Analysis of the isotope ratios of various elements from these materials allows the nuclear processes occurring in different star types to be modeled, and a number of different stellar classes have been developed on the basis of this information. For instance, Amari et al. [1995] analyzed C, N, O, Mg, Si, Ca, and Ti isotopes in graphite grains from the Murchison meteorite. They found large excess ^{18}O, suggesting that the particles originated in either Wolf-Rayet stars of a type II supernova, and used Si isotope ratios to suggest that a supernova origin was more likely. Another example is that of Huss et al. [1997], who examined Si, C, N, and Mg isotope ratios in SiC grains from Orgueil to constrain stellar nucleosynthesis. In addition to analyzing stellar nuclear processes, studies of meteorite inclusions often provide insight into early evolution of the solar system. Sahijpal et al. [1998] found correlations between ^{41}K and ^{26}Mg in primitive meteorites. These isotopes are the decay products of the short-lived nucleids ^{41}Ca and ^{26}Al, and the correlation suggests that they have a similar origin, possibly in a single stellar source, which constrains the duration of the collapse of the protosolar cloud to a period <1 million years. Srinivasan et al. [1996] examined K and Mg isotopes in CAIs in Eframovka. Although unable to constrain thoroughly the source of the ^{26}Al and ^{41}Ca (they suggested that an asymptotic giant branch star was most likely), their results also indicate that the timing between injection and formation was <1 million years.

Improved precision in light isotope ratio measurement has led to the examination of more subtle isotopic variations in meteorites in recent years. Although the primary igneous minerals were almost completely altered, Leshin et al. [1997] were able to determine that the oxygen isotope compositions of relict olivine and pyroxene grains from carbonaceous Ivuna (CI) chondrites lie along a 1:1 $^{17}O-^{18}O$ mixing line. This is in contrast with terrestrial and most other solar system oxygen isotope systematics, which lie along a 2:1 slope line reflecting normal mass-dependent fractionation processes. The olivine and pyroxene grains are thought to have crystallized from a melt, indicating that the oxygen isotope trend is primary and due to nebular processes, rather than the product of interaction with the fluid responsible for altering the pyroxene and olivine in the meteorite. Deloule and Robert [1995] used SIMS to determine where hydrogen phases containing anomalous D/H ratios were sequestered within the Renasso and Semarkona meteorites. Contrary to expectations, they found that it was contained in phyllosilicate (alteration) minerals. This rules out thermal production of the anomalous ratio in the dense solar nebula, indicating that it was inherited from interstellar space or that

it was formed in the outer regions of the nebula at temperatures between 110K and 140K. McSween et al. [1997] documented isotopically light sulfide in the Kaidun meteorite, which contrasts to the heavy $\delta^{34}S$ values found in other carbonaceous chondrites, and suggested that these light values were acquired during hydrothermal alteration of the meteorite.

Recently, SIMS has been used to analyze secondary minerals in the Martian meteorite ALH 84001, to help constrain whether these features could have formed as a result of biological activity. Valley et al. [1997] found that $\delta^{18}O$ values of carbonate concretions ranged from +9.5 to +20.5‰ and suggested that this range of values indicated that the carbonates formed under nonequilibrium processes at low temperatures, consistent with biological activity. Leshin et al. [1998] observed an even larger range in $\delta^{18}O$ values [+5.4 to +25.3‰) and noted that the range in values correlated with major element compositions. In contrast to Valley et al. [1997], they interpret the data as indicating that the carbonates were formed by inorganic processes. They suggested that these observations were consistent with either formation in a water-rich environment with temperatures fluctuating in the 125–350°C range or formation from a limited amount of CO_2–rich fluids at higher temperatures. Greenwood et al. [1997] used SIMS to determine that $\delta^{34}S$ values ranged from −2 to +3‰ in six igneous Martian meteorites. SIMS analyses of secondary pyrite in crush zones of ALH 84001 were on average isotopically heavier (+2.0 to +7.3‰) than sulfides from other Martian meteorites, similar to the range (+4.8 to +7.8‰) measured in three grains by Shearer et al. [1996]. Greenwood et al. were also able to measure the $\delta^{34}S$ value of a fine-grained sulfide aggregate within a carbonate globule and found that the value [+6‰] was indistinguishable from that of the pyrite in the crush zones. Typically, biogenic activity produces very light $\delta^{34}S$ values, so Greenwood et al. [1997] argued that the heavy $\delta^{34}S$ values of ALH84001 suggest that all the sulfides formed by inorganic processes and did not support the presence of sulfate-reducing bacteria.

Analysis of Light Stable Isotopes in Terrestrial Settings

Application of the ion microprobe to the study of light stable isotopes in terrestrial settings has historically been limited by the need for both high precision and accuracy. However, since 1990 SIMS measurements have improved to the point where precision and accuracy are within two to five times those of conventional techniques, while utilizing orders of magnitude less sample. The ability to measure isotopic variations at the tens of micrometers scale has led to increased interest in the technique in the past few years. Most work has focused on analysis of oxygen, boron, and sulfur isotopes, but the ion microprobe has also been used for relatively high-precision analysis of hydrogen and carbon isotope ratios as well.

Sulfur Isotopes. Because of the large range of δ34S values found in natural systems, favorable minor isotope abundances (34S is ~4% of total sulfur), and

the property that many sulfide minerals are conductive, sulfur isotopes were the first light isotope system explored in terrestrial systems utilizing SIMS, with literature dating back into the mid-1980s [see McKibben and Riciputi, 1998, for a review]. SIMS has been used extensively to analyze sulfur isotope fractionations in economic deposits and to investigate sulfur isotope systematics in the mantle. More recently, SIMS has also been applied to study sulfur isotope systematics in a lower-temperature diagenetic setting where biological activity can play a more direct role. The ion microprobe has proved invaluable for discerning microscale isotopic zonations associated with different paragenetic events that would be impossible to discern utilizing conventional techniques.

Lu et al. [1996] used the SHRIMP to investigate microscale sulfur isotope systematics in slate-belt Au deposits from New South Wales, Australia. They found systematic temporal shifts in $\delta^{34}S$ values, which they attributed to mixing of fluids, sampling two different sulfur isotope reservoirs with $\delta^{34}S$ values of +7 and 0‰, suggesting a shift from local sourcing of sulfur in a reduced fluid to a more oxidized fluid derived from deeper in the crustal sequence. McKibben and Eldridge [1995] found evidence for two sources of sulfur in the pyrite and chalcopyrite from the Pb-Zn deposits of the Viburnam Trend in Missouri, in the United States. Although all sulfides were zoned with isotopically light cores and heavier rims, early pyrite had $\delta^{34}S$ values (−10 to +10‰) distinct from later chalcopyrite (0 to +25‰). They suggested that the zoning and temporal shifts originated either by mixing of two sulfur sources or by poorly understood in situ sulfur isotope fractionations. Eldridge et al. [1995] conducted an elegant study of diamond formation using a variety of SIMS analytical applications. SIMS U-Pb dating and REE analysis revealed that two different populations of zircons were found in kimberlites. Sulfur isotope analysis on sulfide inclusions in the diamonds suggested two different sources, one "pristine" mantle and one that was more variable and whose $\delta^{34}S$ values were consistent with a more oxidizing, lower-temperature crustal source. Using these data, they suggested that kimberlite formation and diamond growth were due to the introduction of crustal material into the mantle.

Studies of sulfur isotope variations in Fe sulfides from lower-temperature diagenetic settings have revealed large variations in sulfur isotope ratios. The ion microprobe was used to investigate the potential interplay of bacterial and thermochemical sulfate reduction in Devonian reefal carbonates of the Western Canada Sedimentary Basin [Riciputi et al., 1996]. Isotopic compositions correspond with Fe sulfide textures: early-formed sulfide had light (−30 to −20‰) and late sulfides had heavier (+10 to +20‰) $\delta^{34}S$ values. These ranges were interpreted to reflect sulfide formation in two distinct events. The first, diagenetically early, was caused by bacterial sulfate reduction. The second was associated with deep burial and thermochemical sulfate reduction. Riciputi and Hendry [1997] documented complex temporal zonations in sulfides from the North Sea Basin, zoned Fe sulfides revealing an initial decrease in $\delta^{34}S$ values from ~+15‰ to ~−10‰, and then increasing to very heavy values (+50‰) toward the rims. These zonations were in-

terpreted to reflect the input of multiple fluid sources during rapid burial associated with hydrocarbon generation, coupled with the effects of Rayleigh fractionation. Kohn et al. [1998] investigated sulfur isotope zoning in foram casts during initial burial diagenesis (0–20-cm depth) in Monterey Bay. The light isotopic values indicate that sulfide was formed by bacterial sulfate reduction, and Kohn et al. [1998] suggested that, if the system were closed to input of additional sulfate, isotopic zoning could be used to map the temporal growth of bacterial colonies.

Boron Isotopes. SIMS inherent sensitivity, and lack of a matrix effect on instrumental mass bias (contrary to other isotope systems), suggest that precision of ±5‰ δB is possible for minerals with boron concentrations in the 0.1- to 1-mg/g range, with precision improving as B concentrations increase [Chaussidon et al., 1997]. Chaussidon and Appel [1997] used boron isotope analyses of 3.8-billion-year-old tourmalines from Greenland to constrain the isotope composition of ancient seawater to a δB value of +27 ± 13 ‰. Measurement of the boron isotope ratio in glass inclusions from olivine phenocrysts in Icelandic basalts allowed Gurenko and Chaussidon [1997] to estimate that the underlying mantle was homogeneous with a δB value of −11‰, similar to that proposed for primitive mantle. Smith and Yardley [1996] found a +0.6 to −12.7‰ range in δB values in magmatic tourmaline from southwest England, and attributed the variation to fractionation between aqueous and melt species. Chaussidon and Jambon [1994] measured B contents and isotope ratios in a variety of oceanic basalt glasses. They found a range of values between −7 and +1‰ δB, suggesting limited enrichment of 11B in the upper mantle, which constrains boron recycling into the mantle to ~2% of the amount in the subducted slab.

Hydrogen Isotopes. Hydrogen isotope studies have been relatively limited, but the ability to measure D/H ratios on the <50-μm scale with 3–10‰ precision has great potential. Deloule et al. [1991] found δD values of −80 to −125‰ in mantle-derived hornblendes from Salt Lake Crater, Hawaii. The presence of low (−125‰ δD) rims suggests an isotopically light hydrogen reservoir in the suboceanic mantle, and the preservation of 50‰ variations suggests that hydrogen isotope compositions in the mantle are heterogeneous. Even larger intragrain variations in δD values (110‰) of mantle amphiboles were documented by Graham et al. [1994].

Carbon Isotopes. To date, carbon isotope studies on terrestrial samples utilizing the ion microprobe have been limited. Compared to the expected values of ~− 6‰, Mathez et al. [1995] found very light δ13C values in microdiamond (−30.7‰) and moissanites (SiC, −22 to −29‰) from a kimberlite in Yakutia, Russia. They suggested that these light values might reflect incorporation of crustally-derived carbonaceous sediment that had been subducted, and the low oxygen fugacity required for moissanite stability indicated that it might be stored in a very reduced area of the mantle. Mojzsis et al. [1996] found isotopically light carbon in apatite from 3.8-billion-year-old rocks from Greenland. They argued

that the presence of light carbon indicated that metabolic pathways (life) were established by this time in earth's history.

Oxygen Isotopes. As a result of technical development allowing measurement of δ18O values with precision of 1‰ or better in insulating phases, use of SIMS for oxygen isotope analysis in terrestrial samples has grown rapidly over the past 5 years. A number of studies have focused on processes occurring during diagenesis in basinal settings, and in particular, in the study of isotope variations in quartz overgrowths. Hervig et al. [1995] documented 10‰ within-sample variations in δ18O values in authigenic quartz overgrowths in the Kiskatinaw Sandstone and suggested that they precipitated from meteoric fluids at low (15°–35°C) temperatures. Analysis of authigenic quartz overgrowths from the Travis Peak Formation (Texas) indicated a range of δ18O values from 22 to 35‰ [Williams et al., 1997]. Zoning patterns were interpreted to indicate that early overgrowths (δ18O > 29‰) formed from meteoric fluids (δ18O < 0‰) at temperatures <50°C, with most of the cement formed between 60°C and 90°C from an isotopically heavier fluid. Graham et al. [1996] documented differences in the oxygen isotope composition between samples of the St. Peter Sandstone in the deep basin of Michigan (buried at ~3 km depth, δ18O 12 to 22‰) and those that were formed at more shallow depths on the Wisconsin Arch (δ18O values 18 to 32 ‰). Spotl et al. [1999] examined authigenic quartz formed at higher temperatures (~200°C) from the Spiro Sandstone in the Arkoma Basin. They were able to distinguish two quartz cements, each with relatively limited compositional variation (20.4‰ ± 1.4‰, 22.1‰ ± 1.7‰) compared to that observed in quartz cements formed at lower temperatures. Compared to conventional methods for analyzing quartz overgrowths, which utilize mechanical separation, all of these SIMS studies have documented both a larger range and heavier δ18O values due to lack of contamination by isotopically light detrital quartz.

SIMS has also been applied to other authigenic phases. Chen et al. [1998] utilized SIMS to examine the oxygen isotope compositions of authigenic potassium feldspar cements from the Mount Simon Sandstone in the Illinois Basin. They documented an increase of 10‰ in $\delta^{18}O$ values of feldspar northward along a 600-km transect across the Illinois Basin. Coupled with constraints suggesting a relatively constant temperature of formation for quartz and feldspar cements across the basin, they suggested this trend was consistent with fluid migration from south to north. Ripperdan et al. [1998] utilized SIMS analyses of oxygen isotopes in authigenic magnetite from the Belden formation to constrain authigenic fluids to $\delta^{18}O$ values ~0‰, consistent with formation from meteoric rather than basinal fluid. Paleomagnetic measurements on authigenic magnetite are often used to date the time of basinal fluid migration; these results demonstrate that formation of authigenic magnetite is not necessarily linked to migration of basinal fluid.

Several studies have utilized SIMS to examine higher-temperature fluid-rock interaction in a hydrothermal setting. Single garnets from the Dalnagorsk borosil-

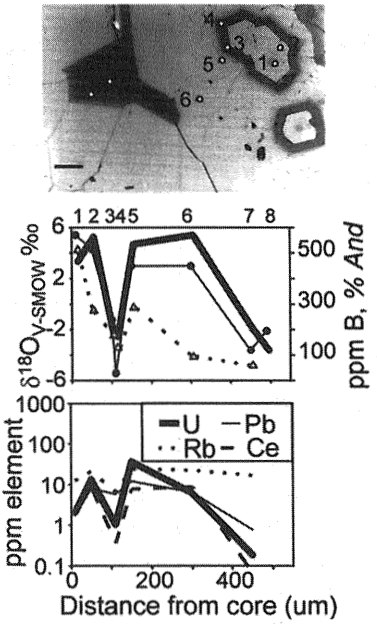

Figure 4 Results of analysis of a zoned garnet (Fe-Al solid solution) from the Dalnagorsk borosilicate deposit. Top, backscatter image; lighter areas have higher Fe content. Scale bar = 100 μm. Middle, plot of the variation in oxygen isotope ratio (solid circle and narrow solid line), B content (open triangle and dashed line), and percentage Fe garnet component (Andradite; $Ca_3Fe_2Si_3O_8$, wide solid line). Analysis numbers are plotted across the top. Bottom, plot of the variation of other trace element contents as a function of distance from the core of the garnet (analysis 1). Note the strong covariation between oxygen isotope composition and trace element contents.

icate deposit in Kamchatka, Russia, were found to preserve complicated zonations of up to 12‰ in $\delta^{18}O$ values over a few hundred micrometers (Fig. 11.4) [Crowe et al., 1999; Benezak et al., 1995]. These variations, which are correlated very well with trace element variations, are interpreted to be due to large fluctuations in percentages of meteoric and magmatic components in the fluid during growth of the garnet; repeated cycling is interpreted to be due to repeated overpressuring of the magmatic fluid. Mora et al. [1998, 1999] were able to use microscale zonations in oxygen isotopes to determine that alteration of the Boehls Butte Anorthosite, Idaho, which has bulk $\delta^{18}O$ values ranging from +6 (igneous) to −6‰, occurred after the peak of metamorphism at 60 Ma. SIMS analysis revealed $\delta^{18}O$ values as light as −15‰, and modeling of steep gradients in oxygen isotope ratios in single thin sections indicates that large-scale alteration took place very rapidly (~10 ky) at high (>500°C) temperatures. This indicates relatively deep penetration (5–10 km) of

meteoric fluid during detachment faulting. Valley and Graham [1996] examined hydrothermal alteration in granites from the Isle of Skye, Scotland. They found that $\delta^{18}O$ values in quartz were heterogeneous, varying by up to 13‰ over scales <1 mm, with low values corresponding to healed cracks. They suggested that quartz and feldspar interacted in contrasting styles, with quartz reacting along microfractures, and feldspar exchanged principally along grain rims.

Age Determination (Heavy Isotope Ratios)

Over the past 15 years, one of the major applications of SIMS in earth sciences has been in the analysis of Pb isotope ratios in the mineral zircon, to obtain age information from the U-Pb isotope decay system; as seen in Fig. 11.1, at least 20% of the geoscience papers published annually involve heavy isotope analysis. In fact, the requirement for high sensitivity at high mass resolution in these analyses has been the driving force behind the development of the large-magnetic-radius instruments (SHRIMP I, II, RG; Cameca 1270). SIMS studies have revealed complex age information contained in single zircon grains that is nearly impossible to resolve by conventional techniques. Given the proliferation of SIMS in this area of research, the few recent examples that follow cannot do justice to this particular area of research. Readers are referred to an excellent overview for further information [Williams, 1998]. Whitehouse et al. [1997] investigated the discrepancy in ages of the Archean Lewisian gneisses using Sm-Nd and Pb-Pb bulk techniques, as both methods yielded ages of ~2.8 Ga using whole rock isochrons. However, mineral separates of trondhjemite yield ages of ~2.4 Ga, whereas mineral separates from the hornblendite give an age of 3.3 Ga. SIMS U-Pb ages on zircons from both rock types gave ages similar to the whole rock isochrons (~2.8 Ga), and Whitehouse et al. [1997] suggested that the anomalous mineral separate ages resulted from resetting during regional metamorphism (trondhjemite) or postcrystallization open-system behavior (hornblendite). The capability to analyze different areas within a zircon, each possibly formed during a different geological event, is particularly powerful when coupled with other techniques such as cathodoluminescence imaging. This was elegantly illustrated by Vry et al. [1996] in their investigation of the timing of metamorphism in the Reynolds Range, Australia. Although earlier U-Pb zircon work suggested that the final episode of low-pressure, high-temperature metamorphism occurred at ~1780 Ma, dating of narrow zircon overgrowths [identified by cathodulumiuescence (CL)] and zircons in rocks associated with partial melting or metasomatism reveals that the granulite metamorphism occurred at 1580 Ma. Collins and Williams [1995] also used ion microprobe U-Pb dating to discern that high-temperature, low-pressure metamorphism in the Arunta Inlier (Australia) consisted of a series of distinct ~10-Ma-duration episodes between 1820 and 1600 Ma, rather than a single long-duration (>100-Ma) event. The potential pitfalls in ion microprobe analysis of some zircons was illustrated by Wiedenbeck [1995], who found zircons with very low U/Pb ratios that yielded

SHRIMP $^{238}U/^{206}Pb$ ages as old as 7.2 Ga, much older than the $^{207}Pb/^{206}Pb$ concordia age of 2.68 Ga. Isotope dilution thermal mass spectrometry analysis of the same zircons demonstrated that the ion microprobe U/Pb ratios were too low. This was attributed to the presence of a labile Pb component within amorphous microdomains that had an anomalously low U/Pb ion yield, which invalidated the SHRIMP U-Pb ion yield calibration.

Recently, SIMS dating techniques have been extended to very young rocks, using both "traditional" U-Pb zircon techniques and recently developed methods of U-Th disequilibria. Gebauer et al. [1997] examined zircons in the ultrahigh-pressure rocks of the Dora Maria Massif in the western Alps and determined the age of metamorphism at 35.4 ± 1 Ma; fission track ages in apatite indicate that the rocks had cooled below 290°C by 29.9 Ma. These results indicate that vertical displacement of 120 km occurred very rapidly over 5–6 Ma. Baldwin [1995] utilized SHRIMP of zircons in gneisses and granodiorites in Papua New Guinea to investigate the timing of recent magmatism and metamorphism during metamorphic core complex formation; they determined that the granodiorites crystallized in the period 1.65 to 1.98 Ma and that peak metamorphism occurred slightly earlier (~2.6 Ma). The decay of ^{232}Th to ^{208}Pb was used to date monazite in leucogranite to help constrain the timing of activity on the North Himalayan Fault [Harrison et al., 1995]. They detected both inherited monazite (~600 Ma), casting doubt on earlier bulk studies, and a major population yielding dates of 22.4 Ma, which they interpreted as the crystallization age, indicating that the fault was active by this time. Reid et al. [1997] used U-Th disequilibria in zircon to investigate the residence time of young rhyolites in the Long Valley Caldera, with results indicating that the zircon remained suspended in the magma for at least 100,000 years. These results indicate that even small magma reservoirs can remain molten for relatively long periods, presumably as a result of regular recharge by more mafic magma.

Another area of recent interest has been the use of the ion microprobe to date zircons in sediments to determine sediment sources. Goldstein et al. [1997] found three distinct age populations (2.8, 2.1, 1.1 Ga) in detrital zircons from the Orinoco River, Venezuela. These ages coincide with periods of active crustal growth in South America and suggest that sediments are being sourced from areas containing all three crustal ages. In contrast, Sm-Nd model ages of the fine silicate sediment give an age of 1.9 Ga, which does not correspond to a single crust-forming event but can be used to obtain a "weighted average" of the crustal ages of the sediment sources. Pell et al. [1997] utilized U-Pb dating of zircons from three Quaternary dunefields from Australia to determine that the sands are deriving material both locally and from sources up to 850 km distant, with significant changes in sourcing suggesting recent shifts in climate and sediment transport patterns. Additional studies of detrital sourcing using U-Pb dating of zircons include those of Gray and Zeitler [1997], who examined clastic wedges in the Appalachian foreland, and Morton et al. [1996], who investigated zircons from the Statfjord Formation, North Sea and determined that two of three zones distinguished by differ-

ences in heavy mineral content were sourced from the same area, whereas the third zone had a different source area.

Support of Experimental Studies

SIMS has become one of the most important tools for the characterization of experimental products because of its minimal sample requirements, high spatial resolution, excellent sensitivity, and unsurpassed ability for depth-profile measurements. Most of the experimental work can be split into two different areas. The first consists of studies examining diffusion rates of different elements in minerals or melts under a variety of pressure, temperature, and fluid conditions, typically by using an isotopically enriched tracer. These analyses are done either by cutting a surface parallel to the diffusion direction and taking a traverse of spot analyses (for conditions in which profiles in the tens to hundreds of micrometers are expected) or by depth-profiling in from the mineral surface to depths of as much as 5–10 micrometers. In the latter mode, depth resolution on the tens of nanometer scale is possible (see Chapter 4). The second area is focused on determining partition coefficients for trace elements between different minerals and fluids/melts at specific temperatures, pressures, and fluid conditions, to provide the data needed to interpret trace element contents measured in natural minerals. This type of analysis typically involves spot analysis of mineral run products.

Diffusion experiments can be split into several general areas. Studies of diffusion in melts have included investigations of cation diffusion in haplobasaltic melts [LaTourette and Wasserburg, 1997; LaTourette et al., 1996], Si and O self-diffusion in basaltic liquid [Lesher et al., 1996], and B diffusion in haplogranitic melts [Chakraborty et al., 1993]. Most anion diffusion studies have focused on oxygen diffusion in a variety of minerals, including sanidine [Freer et al., 1997], titanite [Morishita et al., 1996], grossular (Ca-bearing) garnet [Wright et al., 1995], calcite [Farver, 1994], and ankermanite, anorthite, diopside, and spinel [Ryerson and McKeegan, 1994]. Examples of cation diffusion studies include alkali diffusion in feldspar [Gilletti and Shanahan, 1997], Ca and Mg in garnet [Schwandt et al., 1996, 1995; Chakraborty and Rubie, 1996], and Sr in amphibole [Brabander et al, 1995] and plagioclase feldspar [Gilletti and Casserly, 1994]. Diffusion along grain boundaries between minerals has been investigated in a number of systems, including Ca in calcite [Farver and Yund, 1996] and O and K in K− feldspar/quartz aggregates [Farver and Yund, 1995].

Because of a variety of factors, including strong interest in the igneous petrology community and rapid rates that allow relatively simple and short experiments, most equilibrium partitioning studies have focused on trace element distributions between silicate melts and various minerals. Examples of these types of studies include amphibibole and quartz-diorite to tonalitic melts [Klein et al., 1997], paragasite and andesitic melt [Brenan et al, 1995], amphibole and phlogopite in

basanitic melt [Latourette et al, 1995], clinopyroxene and melt [Gaetani and Grove, 1995; Hart and Dunn, 1993], garnet and clinopyroxene in basaltic melt [Hauri et al., 1994], and hornblende and melt [Sisson, 1994]. Experiments have also examined the partitioning of high-field-strength elements between rutile and aqueous fluids under conditions expected during subduction [Brennan et al., 1994]. SIMS has been used to measure water contents in water solubility studies in albite [Paillat et al., 1992] and along the albite-orthoclase mineral join and in rhyolite melts [Miyagi et al., 1997].

A more recent development has been the application of SIMS to examine isotopic behavior in different geological systems. Hammouda et al. [1996] discovered that Sr isotope compositions in the liquid formed during melting of a feldspar and fluorphlogopite mixture were zoned; that suggests that partial melts are not in isotopic equilibrium with bulk values in the source area. With advances in the precision and accuracy of light stable isotope analyses, SIMS is also beginning to be used to determine equilibrium partitioning coefficients of light stable isotopes between minerals and coexisting fluids. Fortier et al. [1995] used SIMS to determine oxygen isotope compositions in small grains of magnetite grown in water at 350°C, demonstrating excellent agreement between SIMS analysis of single grains and laser ablation gas source spectrometry on bulk samples of grains. In addition, the SIMS analyses demonstrated isotopic equilibrium was present at a fine scale, minimizing concerns about possible kinetic or other nonequilibrium effects. Another recent novel experimental technique involves developing diffusion profiles between isotopically labeled water and single mineral crystals so that the isotopic composition of the outer 1- to 2-μm rim is very close to equilibrium with the fluid [Riciputi et al., 1998a; Chacko et al., 1999]. By analyzing the composition of this rim using shallow craters sputtered into the face of the mineral and running two experiments using fluid compositions that are isotopically lighter and heavier than the mineral, the equilibrium fractionation factor can be tightly bracketed, as demonstrated for hydrogen isotope partitioning between water and epidote. This technique allows differing reaction mechanisms (diffusion versus solution/reprecipitation) to be distinguished and promises to open new avenues of experimental investigation using SIMS to determine isotope fractionation factors in mineral systems that are difficult to address by conventional methods.

11.4 CONCLUSIONS

In the past 10 years, SIMS has become an important instrument in geochemistry. The period has witnessed a rapid expansion in the types of SIMS analyses that are being conducted, and in the types of rocks and geological settings/processes that are being investigated. In many ways, the potential applications of SIMS in geology are just beginning to be explored, but already the microscale information that

SIMS has provided has led to important new insights into the processes that are occurring in a wide variety of geological settings, and the fundamental mechanisms responsible for the macroscale features that are observed. SIMS instrumentation and analytical techniques continue to evolve rapidly, promising even greater capabilities in the near future, capabilities that will certainly be exploited in an ever-increasing variety of geochemical investigations.

ACKNOWLEDGMENTS

Preparation of this chapter was supported by the Office of Science, Basic Energy Research, U.S. Department of Energy, under contract DE-AC05-96OR22464 with Oak Ridge National Laboratory, managed by Lockheed Martin Energy Research Corp, and the National Science Foundation (EAR 97-06072). I would like to thank Steve Cristy and Dave Smith for helpful reviews, and Chris Barshick. Without his persistence, this chapter (and book) would not have been realized.

REFERENCES

Amari, S.; Zinner, E.; Lewis, R.S. *Astrophys. J.* **1995**, 2, L147.

Arehart, G.B.; Chryssoulis, S.L.; Kesler, S.E. *Econ. Geol.* **1993a**, 88, 171.

Arehart, G.B.; Eldridge, C.S.; Chryssoulis, S.L.; Kesler, S.E. *Geochim. Cosmochim. Acta* **1993b**, 57, 1505.

Baldwin, S.L. *Geology* **1995**, 23, 1023.

Barclay, J.; Carroll, M.R.; Houghton, B.F.; Wilson, C.J.N. *J. Volcanol. Geotherm. Res.* **1996**, 74, 75.

Evidence of protracted growth history of skarn garnet using SIMS oxygen isotope, trace element, and rare earth element data. *Geol. Soc. Amer.* Abstr. Prog. **1995**.

Benninghoven, A.; Rüdenauer, F.G.; Werner, H.W. *Secondary Ion Mass Spectrometry: Basic Concepts, Instrumental Aspects, Applications, and Trends*, John Wiley & Sons: New York, **1987**.

Bezenek, S.R.; Crowe, D.E.; Riciputi, L.R. *Geol. Soc. Amer. Abstr. Prog.* **1995**.

Bottazzi, P.; Ottolini, L.; Vannucci, R. *Scanning Electron Microsc.* **1992**, 14, 160.

Brabander, D.J.; Hervig, R.L.; Jenkins, D.M. *Geochim. Cosmochim. Acta* **1995**, 59, 3549.

Brenan, J.M.; Shaw, H.F.; Ryerson, F.J.; Phinney, D.L. *Earth Planet. Sci. Lett.* **1995**, 135, 1.

Brenan, J.M.; Shaw, H.R.; Phinney, D.L.; Ryerson, F.J. *Earth Planet. Sci. Lett.* **1994**, 128, 327.

Cabri, L.J.; McMahon, G. *Can. Mineral.* **1995**, 33, 349.

Chacko, T.; Riciputi, L.R.; Cole, D.R.; Horita, J. *Geochim. Cosmochim. Acta* **1999**, in press.

Chakraborty, S.; Rubie, D.C. *Contrib. Mineral. Petrol.* **1996**, 122, 406.

Chakraborty, S.; Dingwell, D.B.; Chaussidon, M. *Geochim. Cosmochim. Acta* **1993**, 57, 1741.

Chaussidon, M.; Appel, P.W.U. *Chem. Geol.* **1997**, 136, 171.
Chaussidon, M.; Robert, F.; Mangin, D.; Hanon, P.; Rose, E.F. *Geostandards Newslett.* **1997**, 21, 7.
Chaussidon, M.; Jambon, A. *Earth Planet. Sci. Lett.* **1994**, 121, 277.
Chen, Z.; Riciputi, L.R.; Mora, C.I.; Fishman, N.S.; Driese, S.G. *Geol. Soc. Am. Abst. Prog.* **1998**.
Collins, W.J.; Williams, I.S. *Precamb. Res.* **1995**, 71, 69.
Compston, W.; Williams, I.S.; Meyer, C. *J. Geophys. Res.* **1984**, 89, B525.
Crowe, D.E.; Riciputi, L.R.; Bezenek, S.; Ignatiev, A. in review.
Deloule, E.; Allègre, F.; Sheppard, S. M. F. Earth Planet. Sci. Lett. *1991*, 105, 543.
Deloule, E.; France-Lorand, C.; Allègre, F. in *Stable Isotope Geochemistry*, H.P. Taylor et al. (Eds.), Geochemistry Society Special Publication 3, **1992**.
Deloule, E.; Robert, F. *Geochim. Cosmochim. Acta* **1995**, 59, 4695.
Denniston, R.F.; Shearer, C.K.; Layne, G.D.; Vaniman, D.T. *Geochim. Cosmochim. Acta* **1997**, 61, 1803.
Dorais, M.J.; MacRae, N.D. *Contrib. Mineral. Petrol.* **1994**, 117, 76.
Eiler, J.M.; Graham, C.; Valley, J.W. *Chem. Geol.* **1997**, 138, 221.
Eldridge, C.S.; Compston, W.; Williams, I.S.; Harris, J.W.; Bristow, J.W.; Kinny, P.D. *Econ. Geol.* **1995**, 90, 271.
Farver, J.R. *Earth Planet. Sci. Lett.* **1994**, 121, 575.
Farver, J.R.; Yund, R.A. *Contrib. Mineral. Petrol.* **1996**, 123, 77.
Farver, J.R.; Yund, R.A. *Geochim. Cosmochim. Acta* **1995**, 59, 3697.
Fortier, S.M.; Cole, D.R.; Wesolowski, D.J.; Riciputi, L.R.; Paterson, B.A.; Valley, J.W.; Horita, J. *Geochim. Cosmochim. Acta* **1995**, 59, 3871.
Freer, R.; Wright, K.; Kroll, H.; Gottlicher, J. *Philos. Mag. A* **1997**, 75, 485.
Gaetani, G.A.; Grove, T.L. *Geochim. Cosmochim. Acta* **1995**, 59, 1951.
Gebauer, D.; Schertl, H.P.; Brix, M.; Schreyer, W. *Lithos* **1997**, 41, 5.
Giletti, B.G.; Casserly, J.E.D. *Geochim. Cosmochim. Acta* **1994**, 58, 3785.
Giletti, B.J.; Shanahan, T.M. *Chem. Geol.* **1997**, 139, 3.
Goldstein, S.; Arndt, N.T.; Stallard, R.F. *Chem. Geol.* **1997**, 139, 271.
Graham, C.M.; Valley, J.W.; Winter, B.L. *Geochim. Cosmochim. Acta* **1996**, 60, 5101.
Graham, C.M.; Kinny, P.D.; Harte, B.; Valley, J.W. *Mineral. Mag.* **1994**, 58A, 345.
Grandjeanlecuyer, P.; Feist, R.; Albarede, F. *Geochim. Cosmochim. Acta* **1993**, 57, 2507.
Gray, M.B.; Zeitler, P.K. *Tectonics* **1997**, 16, 151.
Greenwood, J.P.; Riciputi, L.R.; McSween, H.Y. Jr. *Geochim. Cosmochim. Acta* **1997**, 61, 4449.
Gurenko, A.A.; Chaussidon, M. *Chem. Geol.* **1997**, 135, 21.
Gurenko, A.A.; Chaussidon, M. *Geochim. Cosmochim. Acta* **1995**, 59, 2905.
Hammouda, T.; Pichavant, M.; Chaussidon, M. *Earth Planet. Sci. Lett.* **1996**, 144, 109.
Hannington, M.D.; Tivey, M.K.; Larocque, A.C.L.; Petersen, S.; Rona, P.A. *Can. Mineral.* **1995**, 33, 361.
Harrison, T.M.; McKeegan, K.D.; Lefort, P. *Earth Planet. Sci. Lett.* **1995**, 133, 271.
Hart, S.R.; Dunn, T. *Contrib. Mineral. Petrol.* **1993**, 113, 1.
Hauri, E.H.; Wagner, T.P.; Grove, T.L. *Chem. Geol.* **1994**, 117, 149.
Hayes, J.M.; Schoeller, D.A. *Anal. Chem.* **1977**, 49, 306.
Hervig, R.L.; Dunbar, N.B. *Earth Planet Sci. Lett.* **1992**, 111, 97.

Hervig, R.L.; Williams, P.; Kirkland, I.K.; Longstaffe, F.J. *Geochim. Cosmochim. Acta* **1995**, 59, 2537.
Hervig, R.L.; Williams, P.; Thomas, R.M.; Schauer, S.N.; Steele, I.M. *Intl. J. Mass Spectrom. Ion Proc.* **1992**, 120, 45.
Hinton, R.W. in *Microprobe Techniques in the Earth Sciences*; Potts, P.J. et al. (eds.), Chapman and Hall: London, **1995**, 235.
Hinton, R.W. *Chem. Geol.* **1990**, 83, 11.
Huss, G.R.; Hutcheon, I.D.; Wasserburg, G.J. *Geochim. Cosmochim. Acta* **1997**, 61, 5117.
Ingram, J.C.; Groenwold, G.S.; Olson, J.E.; Gianotto in *Secondary Ion Mass Spectrometry, SIMS XI*, G. Gillen et al. (eds.), John Wiley & Sons: New York, **1998**, 863.
Klein, M.; Stosch, H.G.; Seck, H.A. *Chem. Geol.* **1997**, 138, 257.
Kohn, M.J.; Riciputi, L.R.; Stakes, D.; Orange, D.L. *Am. Min.* **1998**, 83, 1454.
Kovalenko, V.I.; Tssaryeva, G.M.; Goreglyad, A.V.; Yarmolyuk, V.V.; Troitsky, V.A.; Hervig, R.L.; Farmer, G.L. *Econ. Geol.* **1995**, 90, 530.
Larocque, A.C.L.; Cabri, L.J. *Rev. Econ. Geol.* **1998**, 7, 155.
Larocque, A.C.L.; Jackman, J.A.; Cabri, L.J.; Hodgson, C.J. *Can. Mineral.* **1995a**, 33, 361.
Larocque, A.C.L.; Hodgson, C.J.; Cabri, L.J.; Jackman, J.A. *Can. Mineral.* **1995b**, 33, 378.
LaTourrette, T.; Wasserburg, G.J. *Geochim. Cosmochim. Acta* **1997**, 61, 755.
LaTourrette, T.; Wasserburg, G.J.; Fahey, A.J. *Geochim. Cosmochim. Acta* **1996**, 60, 1329.
LaTourrette, T.; Hervig, R.L.; Holloway, J.R. *Earth Planet. Sci. Lett.* **1995**, 135, 13.
Lesher, C.E.; Hervig, R.L.; Tinker, D. *Geochim. Cosmochim. Acta* **1996**, 60, 405.
Leshin, L.A.; McKeegan, K.D.; Carpenter, P.K.; Harvey, R.P. *Geochim. Cosmochim. Acta* **1998**, 62, 3.
Leshin, L.A.; Rubin, A.E.; McKeegan, K.D. *Geochim. Cosmochim. Acta* **1997**, 61, 835.
Lu, J.C.; Seccombe, P.K.; Eldridge, C.S. *Chem. Geol.* **1996**, 127, 229.
Lyon, I.C.; Saxton, J.M.; McKeever, P.J.; Chatzitheodoridis, E.; Van Lierde, P. *Intl. J. Mass Spectrom. Ion Proc.* **1995**, 9, 1.
MacRae, N.D. *Can. Mineral.* **1995**, 33, 219.
MacRae, N.D.; Bottazzi, P.; Ottolini, L.; Vannucci, R. *Chem. Geol.* **1993**, 103, 45.
Mason, R.A. *Chem. Geol.* **1987**, 64, 209.
Mathez, E.A.; Fogel, R.A.; Hutcheon, I.D.; Marshintsev, V.K. *Geochim. Cosmochim. Acta* **1995**, 59, 781.
Matthews, M.; Harte, B.; Prior, D. *Geochim. Cosmochim. Acta* **1992**, 56, 2633.
McIntyre, N.S.; Fichter, D.; Metson, J.B.; Robinson, W.H.; Chauvin, W. *Surface Interface Anal.* **1985**, 7, 69.
McKibben, M.A.; Riciputi, L.R. *Rev. Econ. Geol.* **1998**, 7, 121.
McKibben, M.A.; Eldridge, C.S. *Econ. Geol.* **1995**, 90, 228.
McSween, H.Y.; Riciputi, L.R.; Paterson, B.A. *Meteor. Planet. Sci.* **1997**, 32, 51.
Metson, J.B.; Bancroft, G.M.; McIntyre, N.S.; Chauvin, W.J. *Surface Interface Anal.* **1983**, 5, 181.
Migeon, H.N.; Schumacher, H.; Slodzian, G. *Surface Interface Anal.* **1990**, 16, 13.
Miyagi, I.; Yurimoto, H.; Takahashi, E. *Geochem. J.* **1997**, 31, 57.
Mojzsis, S.J.; Arrhenius, G.; McKeegan, K.D.; Harrison, T.M.; Nutman, A.P.; Friend, C.R.L. *Nature* **1996**, 384, 55.
Mora, C.M.; Riciputi, L.R.; Cole, D.R. *Geol. Soc. Amer. Abstr. Prog.* **1998**.
Mora, C.M.; Riciputi, L.R.; Cole, D.R.; Walker, K. **in sub**.
Morishita, Y.; Giletti, B.J.; Farver, J.R. *Geochim. J.* **1996**, 30, 71.

Morton, A.C.; ClaoueLong, J.C.; Berge, C. *J. Geol. Soc.* **1996**, 153, 915.
Mumin, A.H.; Fleet, M.E.; Chryssoulis, S.L. *Mineral. Deposita* **1994**, 29, 445.
Neumayr, P.; Cabri, L.J.; Groves, D.I.; Mikucki, E.J.; Jackman, J.A. *Can. Mineral.* **1993**, 31, 711.
Nimis, P.; Vannucci, R. *Chem. Geol.* **1995**, 124, 185.
Ohnenstetter, D.; Brown, W.L. *Contrib. Mineral. Petrol.* **1996**, 123, 117.
Paillat, O.; Elphick, S.C.; Brown, W.L. *Contrib. Mineral. Petrol.* **1992**, 112, 490.
Papike, J.J. *Am. Mineral.* **1996**, 81, 525.
Paterson, B.A.; Riciputi, L.R.; McSween, H.Y., Jr. *Geochim. Cosmochim. Acta* **1997**, 61, 601.
Pell, S.D.; Williams, I.S.; Chivas, A.R. *Sed. Geol.* **1997**, 109, 233.
Portnyagin, M.V.; Magakyan, R.; Schmincke, H.U. *Petrology* **1996**, 4, 231.
Pun, A.; Papike, J.J.; Layne, G.D. *Geochim. Cosmochim. Acta* **1997**, 61, 5089.
Rampone, E.; Piccardo, G.B.; Vannucci, R.; Bottazzi, P. *Geochim. Cosmochim. Acta* **1997**, 61, 4557.
Reed, S.B.J. *Mineral. Mag.* **1989**, 53, 3.
Reid, M.R.; Coath, C.D.; Harrison, T.M.; McKeegan, K.D. *Earth Planet. Sci. Lett.* **1997**, 150, 27.
Rhoden, M.F.; Shimizu, N. *J. Geophys. Res.* **1993**, 98, 14091.
Riciputi, L.R. *Rapid Comm. Mass Spectrom.* **1996**, 10, 282.
Riciputi, L.R.; Paterson, B.A. *Am. Mineral.* **1994**, 79, 1227.
Riciputi, L.R.; Machel, H.G.; Cole, D.R. *J. Sed. Res.* **1994a**, A64, 115.
Riciputi, L.R.; McSween, H.Y., Jr.; Johnson, C.A.; Prinz, M. *Geochim. Cosmochim. Acta* **1994b**, 58, 1343.
Riciputi, L.R.; Christie, W.H.; Cole, D.R.; Rosseel, T.M. *Anal. Chem.* **1993**, 65, 1186.
Riciputi, L.R.; Cole, D.R.; Machel, H.G. *Geochim. Cosmochim. Acta* **1996**, 60, 325.
Riciputi, L.R.; Hendry, J.P. in *Geo uids II 97: Contributions to the Second International Conference on Fluid Evolution, Migration, and Interaction in Sedimentary Basins and Orogenic Belts*, Hendry, J.P. et al. (eds.), Anthony Rowe: Chippenham, U.K., **1997**, 331.
Riciputi, L.R.; Paterson, B.A.; Ripperdan, R.L. *Intl. J. Mass Spectrom. Ion Proc.* **1998**, 178, 81.
Riciputi, L.R.; Chacko, T.; Cole, D.R.; Horita, J. *Secondary Ion Mass Spectrometry, SIMS XI* G. Gillen et al. eds., John Wiley & Sons: New York, **1998a**, 79.
Ripley, E.M.; Chryssoulis, S.L. *Econ. Geol.* **1994**, 89, 201.
Ripperdan, R.L.; Riciputi, L.R.; Cole, D.R.; Elmore, R.D.; Banerjee, S.; Engel, M.H. *J. Geophys. Res.* **1998**, 103, 21015.
Roggensack, K.; Hervig, R.L.; McKnight, S.B.; Williams, S.N. *Science* **1997**, 277, 1639.
Ryerson, F.J.; McKeegan, K.D. *Geochim. Cosmochim. Acta* **1994**, 58, 3713.
Sahijpal, S.; Goswami, J.N.; Davis, A.M.; Grossman, L.; Lewis, R.S. *Nature* **1998**, 391, 559.
Santaguida, F.; Hannington, M.D. *Can. J. Earth Sci.* **1996**, 33, 316.
Savard, M.M.; Veizer, J.; Hinton, R. *J. Sed. Research* **1995**, A65, 208.
Schauer, S.N.; Williams, P. *Intl. J. Mass Spectrom. Ion Proc.* **1990**, 103, 21.
Schwandt, C.S.; Cygan, R.T.; Westrich, H.R. *Am. Mineral.* **1996**, 81, 448.
Schwandt, C.S.; Cygan, R.T.; Westrich, H.R. *Am. Mineral.* **1995**, 80, 483.
Sen, G.; Frey, F.A.; Shimizu, N.; Leeman, W.P. *Earth Planet. Sci. Lett.* **1993**, 119, 53.

Sevigny, J.H. *Geochim. Cosmochim. Acta* **1993**, 57, 4095.
Shearer, C.K.; Layne, G.D.; Papike, J.J.; Spilde, M.N. *Geochim. Cosmochim. Acta* **1996**, 60, 2921.
Shimizu, N.; Hart, S.R. *Ann. Rev. Earth Planet. Sci.* **1982**, 10, 483.
Shimizu, N.; Semet, M.P.; Allègre, C.J. *Geochim. Cosmochim. Acta* **1978**, 42, 1321.
Sisson, T.W. *Chem. Geol.* **1994**, 117, 331.
Sisson, T.W.; Layne, G.D. *Earth Planet Sci. Lett.* **1993**, 117, 619.
Smith, M.P.; Yardley, B.W.D. *Geochim. Cosmochim. Acta* **1996**, 60, 1415.
Snyder, G.A.; Taylor, L.A.; Crozaz, G. *Geochim. Cosmochim. Acta* **1993**, 57, 1143.
Sobolev, A.V.; Batanova, V.G. *Petrol.* **1995**, 3, 440.
Sobolev, A.V.; Chaussidon, M. *Earth Planet Sci. Lett.* **1996**, 137, 45.
Spotl, C.; Houseknecht, D.W.; Riciputi, L.R. in *Quartz Cement: Origin and Effects Upon Hydrocarbon Reservoirs*, R. Worden; S. Morad (eds.), International Association of Sedimentologists Special Publication, **1999**, in press
Srinivasan, G.; Sahijpal, S.; Ulyanov, A.A.; Goswami, J.N. *Geochim. Cosmochim. Acta* **1996**, 60, 1823.
Srinivasan, K.; Walker, K.R.; Steinhauff, D.M.; Goldberg, S.A.; Riciputi, L.R. *Geol. Soc. Amer. Abstr. Prog.* **1995**.
Srinivasan, K.; Riciputi, L.R.; Walker, K.R. *Geol. Soc. Amer. Abstr. Prog.* **1994**.
Swart, P.K. *Anal. Chem.* **1990**, 62, 722.
Tarnocai, C.A.; Hattori, K.; Cabri, L.J. *Can. Mineral.* **1997**, 35, 805.
Taylor, L.A.; Snyder, G.A.; Crozaz, G.; Sobolev, V.N.; Yefimova, E.S.; Sobolev, N.B. *Earth Planet. Sci. Lett.* **1996**, 142, 535.
Tribuzio, R.; Messiga, B.; Vannucci, R.; Bottazzi, P. *Geology* **1996**, 24, 711.
Valley, J.W.; Graham, C.M. *Contrib. Mineral. Petrol.* **1996**, 124, 225.
Valley, J.W.; Eiler, J.M.; Graham, C.M.; Gibson, E.K.; Romanek, C.S.; Stolper, E.M. *Science* **1997**, 275, 1633.
Van der Heide, P.A.W.; Fitcher, D.A. in *Secondary Ion Mass Spectrometry, SIMS XI*, G. Gillen et al. (eds), John Wiley & Sons: New York, **1998**, 747.
Vannucci, R.; Piccardo, G.B.; Rivalenti, G.; Zanetti, A.; Rampone, E.; Ottolini, L.; Oberti, R.; Mazzucchelli, M.; Bottazzi, P. *Geochim. Cosmochim. Acta* **1995**, 59, 1763.
Veizer, J.; Hinton, R.W.; Clayton, R.N.; Lerman, A. *Chem. Geol.* **1987**, 64, 225.
Vry, J.; Compston, W.; Cartwhight, I. *J. Metamorph. Geol.* **1996**, 14, 335.
Wadhwa, M.; McSween, H.Y., Jr.; Crozaz, G. *Geochim. Cosmochim. Acta* **1994**, 58, 4213.
Webster, J.D.; Duffield, W.A. *Econ. Geol. Soc. Bull.* **1994**, 89, 840.
Webster, J.D.; Congdon, R.D.; Lyons, P.C. *Geochim. Cosmochim. Acta* **1995**, 59, 711.
Whitehouse, M.J.; Claesson, S.; Sunde, T.; Vestin, J. *Geochim. Cosmochim. Acta* **1997**, 61, 4429.
Wiedenbeck, M. *Chem. Geol.* **1995**, 125, 197.
Wiedenbeck, M.; Goswami, J.N.; Roy, A.B. *Chem. Geol.* **1996**, 129, 325.
Wiedenbeck, M.; Goswami, J.N. *Geochim. Cosmochim. Acta* **1994**, 58, 2135.
Wilding, M.C.; MacDonald, R.; Davies, J.E.; Fallick, A.E. *Contrib. Mineral. Petrol.* **1993**, 114, 264.
Williams, I.S. *Rev. Econ. Geol.* **1998**, 7, 1.
Williams, L.B.; Hervig, R.L.; Dutton, S.P. in *Basin-wide Diagenetic Patterns: Integrated Petrologic, Geochemical, and Hydrologic Considerations*, Montanez, I.P. et al. (eds.), SEPM Special Publication 57, **1997**, 269.

Wright, K.; Freer, R.; Catlow, C.R.A. *Am. Mineral.* **1995**, 80, 1020.
Zannetti, Z.; Vannucci, R.; Bottazzi, P.; Oberti, R.; Ottolini, L. *Chem. Geol.* **1996**, 134, 113.
Zinner, E. *US Geol. Surv. Bull.* **1989**, 1890, 145.
Zinner, E.; Crozaz, G. *Intl. J. Mass Spectrom. Ion Proc.* **1986**, 69, 17.
Zinner, E.; Fahey, A.J.; McKeegan, K.D. in *Secondary Ion Mass Spectrometry, SIMS V*, Benninghoven, A. et al. (eds.), Springer-Verlag: New York, **1986**, 170.

12

Inorganic Time-of-Flight Mass Spectrometry

David P. Myers
Leco Corporation
St. Joseph, Michigan

Steven J. Ray and Gary M. Hieftje
Indiana University
Bloomington, Indiana

12.1. INTRODUCTION

The time-of-flight mass spectrometer (TOF-MS) shows a great deal of promise in becoming a valuable tool for inorganic mass analysis. In a number of applications and in conjunction with myriad ionization schemes TOF-MS is being used with great success. Recently a number of investigators have attempted to exploit the unique attributes of this versatile mass spectrometer for inorganic mass analysis.

Among the many important features of a TOF-MS is its ability to determine simultaneously all mass-to-charge values within a mass range of interest, and without moving parts or scanning fields. As a result, the TOF-MS is freed from many of the constraints faced by sequentially scanning instruments and enjoys precision, sensitivity, and resolution that are independent of mass coverage. Time-of-flight (TOF) mass analyzers are also recognized for their unsurpassed speed of analysis, producing full mass spectra in tens to hundreds of microseconds and generating thousands of complete mass spectra every second when coupled to continuous ionization sources. Such high spectral generation rates make TOF-MS very well suited to provide complete mass spectral characterization of transient events, and with high temporal resolution. This same attribute also makes TOF instruments capable of providing high sample throughput on a masses/sample/hour basis when utilized for routine analysis.

The TOF-MS is physically the simplest of the common mass spectrometers, consisting conceptually of little more than an evacuated hollow tube. The lack of restrictive architecture (e.g., slits) allows such spectrometers to be assembled at reasonable cost and with little complication but more importantly endows a TOF with high transmission efficiency. Also unique among its attributes is the theoretically unlimited mass range of a TOF-MS, allowing spectrometers of similar design to mass-analyze species from protons to large biomolecules merely by utilizing a number of alternative ionization sources. Undoubtedly, utilization of a TOF-MS for inorganic mass analysis can provide a number of advantages.

It bears noting that TOF, first demonstrated by Cameron and Eggers in 1948 [1], is enjoying a resurgence of interest in recent years. In part, this renaissance can be traced to a number of key advances that have changed the way TOF-MS is accomplished, but perhaps the trend is more accurately associated with an improved ability to capture, store, and analyze the enormous wealth of information produced by such spectrometers. As this ability matures through the application of more advanced electrical engineering, and as additional advances and refinements are made within the field, we are sure to see even greater exploitation of the unique attributes of the TOF-MS.

In this chapter, the principles of operation of TOF-MS are first reviewed, with an emphasis on how those principles relate to inorganic mass analysis. Methods of interfacing continuous ion sources with a TOF-MS are then considered, since most conventional inorganic ion sources (e. g., plasmas) are continuous. The advantages of TOF-MS for inorganic analysis are then outlined. Alternative successful designs of TOF-MS for inorganic analysis are next examined and the performance of the two dominant designs compared. Components of typical TOF-MS instruments are reviewed, including ion optics, detectors, and electronic systems. Sample-introduction and processing options, such as laser ablation, electrothermal vaporization, and other steady-state and transient methods, are covered next. We conclude with a projection of what the future might bring in the area of inorganic TOF-MS.

12.2 TIME-OF-FLIGHT MASS SPECTROMETRY

12.2.1 Principles

All time-of-flight mass spectrometers operate on the basis of the same straightforward physical principle: ions of different mass (m), given the same kinetic energy (KE), achieve different velocities (v) according to

$$KE = 1/2\, mv^2 \tag{12.1}$$

Thus, accelerating a population of ions across a chosen potential drop U, allows them all to achieve the same kinetic energy eU, where e is the electronic charge.

Because of this differential acceleration and the consequently disparate velocities, a mass spectrum can be obtained by measuring the time required for each mass to traverse a field-free drift region of known length. The time-dependent output of a suitable ion detector placed at the end of this field-free region reflects the relative abundances of ions of increasingly greater mass-to-charge ratio with greater flight time, the latter, it should be noted, quadratically related to mass-to-charge ratio according to Eq. (12.1). Although all TOF instruments rely on this simple physical principle, several key advances in the field have extended the utility of TOF mass spectrometry well beyond the simple instrument introduced in 1948 [1]. The great challenges within the field remain in compensating for the initial spatial distribution, velocity distribution, and temporal formation of the ions being sampled.

Compensating for the Spatial Distribution of Sampled Ions

The technique of compensating for the initial finite spatial width of the sampled ion population is termed *space focusing*. The concept behind space focusing and its experimental demonstration were first offered by Wiley and McLaren in 1955 and have proved among the most valuable in TOF mass spectrometry [2]. The basic idea can be illustrated with a simple TOF instrument depicted in Fig. 12.1. This simple instrument consists of a two-field acceleration region in which ions are accelerated to the final kinetic energy, and a field-free drift region wherein mass separation takes place. In the case of Fig. 12.1 the two electric fields (E_1 and E_2) are separated by a mesh or grid, G_0, and the entrance to the flight tube is also defined by a grid, G_1. In this arrangement a positive pulsed field, E_1, can be applied to push

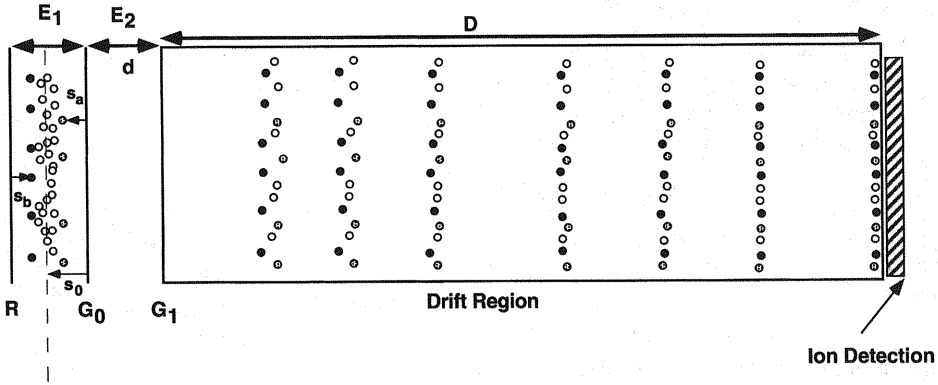

Figure 1 General diagram of a time-of-flight mass analyzer. R, repeller electrode; G_0, entry grid; G_1, acceleration grid, E_1 and E_2, electric fields; s_0, distance to the midpoint of the first acceleration field; s_a and shaded circles, ion starting position closer to G_0; s_b and closed circles, ion starting position more distant from G_0; D, total drift length.

ions into the negative, static acceleration field E_2, which is maintained between G_0 and G_1.

Differences in the arrival time of isomass ions at the detector can arise from the finite spatial width of the ion packet within the first acceleration region. If a cloud of ions of the same mass with significant spatial width are given the same accelerating energy, they will achieve the same velocity and will strike the detector surface at times that are dictated by their initial starting position. It can be said that each ion experiences a flight-time error that is due to its initial position within the first acceleration region; the resolution of the TOF-MS is then limited by the finite dimensions of the ion beam being sampled.

In some instances the magnitude of such flight-time error is minimized as a consequence of the geometry of the ionization source; for example, ions extracted from a planar surface possess a relatively small distribution of initial spatial positions. Unfortunately, many of the ionization sources utilized within inorganic mass spectrometry, such as the inductively coupled plasma (ICP), do not give this luxury. Another solution to this problem lies in the application of an acceleration gradient within the acceleration region, and in the realization that ions located at different positions within the region are accelerated through different potentials. For the TOF instrument in Fig. 12.1, if a positive extraction pulse E_1 were applied to the repeller electrode, ions located at different positions (s_a and s_b) within the region would experience different accelerating fields and would therefore attain slightly different velocities. At some point after extraction has occurred, the ions located nearer the repeller electrode, which experience a larger potential drop and therefore achieve slightly greater velocities, overtake the more slowly traveling ions that begin farther from the repeller electrode. The location where the ions overtake each other is known as the *space-focus plane*.

By considering the TOF equations for a given instrument geometry, and evaluating the first derivative of the flight time with respect to initial position within the first acceleration region(s), Wiley and McLaren showed that for this simple acceleration scheme the following equation must be satisfied to produce optimal space-time focusing [2].

$$D = (L^{1/2}(1 - d/(k_0 + k_0^{1/2})s_0) \tag{12.2}$$

where s_0 is a point halfway inside the first acceleration field, d is the length of the second acceleration region, $L = 2s_0k_0^{3/2}$, $k_0 = (s_0E_1 + dE_2)/s_0E_1$, and E_1 and E_2 are the field strengths in the first and second field regions, respectively (see Fig. 12.1). Here, the initial energy of the ions is assumed to be zero. From this equation, the flight length, D, at which ions with different initial position have the minimum flight-time spread can be determined.

The second derivative of the flight time with respect to initial position represents an inflection point; the derivations show that for a two-field source (such as that shown in Fig. 12.1) it has greatest value for an ion starting at s_0. This is desirable because a longer flight time leads to better resolving power [2]. Derivations

also show that a single-field extraction source has an optimal space focus at a flight length of $2s_0$, which is so short that it would yield very poor resolution for the instrument [3].

It is interesting to note that perfect space focusing cannot be achieved within any TOF-MS that utilizes linear extraction and acceleration fields. This is a consequence of the fact that the kinetic energy each ion receives upon extraction is directly proportional to its location within the extraction region and is therefore quadratically related to the velocity it attains. Since there exists no simple analytical solution to such equations, mathematical calculation of optimal TOF-MS instrument conditions is often accomplished by seeking to minimize changes in flight time resulting from small differences in initial position by means of a series expansion. By solving the first term of such a series expansion, one arrives at a first-order space-focusing condition. Recently, several investigators have demonstrated solutions to both the first and second terms of the expansion, attaining second-order space-focusing conditions that provide a space-focus plane of much higher fidelity.

Because the geometric parameters of the TOF-MS (s, d, and D)are usually fixed, adjustment of the fields within the two-step acceleration zones (E_1 and E_2) is the usual means of achieving space-time focusing at the detector surface. This approach works well to resolve masses up to about 300 amu in a linear instrument provided that the spatial distribution is a small percentage of the first field.

Compensating for the Velocity Distribution of Sampled Ions

If space-time focusing is optimized, much of the remaining flight-time error is attributable to differences in the magnitude and direction of the ion's initial velocity. As might be expected, the energy distribution due to these initial velocities is superimposed on the final energy they obtain in the TOF-MS, so a flight-time error is incurred. If a significant portion of these velocity vectors are oriented away from the direction of acceleration, a serious problem known as *turn-around time* occurs. This effect is due to the time that is required to eliminate this initial velocity component before an ion is accelerated back toward the flight tube. As a result, two ions, one with no initial velocity and the other traveling away from the flight tube, may achieve the same final energy and leave the extraction region at different times. One solution to this problem, called *time-lag focusing* [2], involves inserting a delay time between the formation of the ions and their acceleration to ensure that all ions are moving toward the detector surface before they are accelerated. Since there is usually a trade-off between time-lag focusing and space-time focusing, this strategy is often reserved for cases in which turn-around time is the dominant cause of error.

Provided that the initial ion energy distribution is not large with respect to the acceleration potential, a much more common approach is the incorporation of a device known as an *ion mirror* or *re ectron* [4,5]. This concept, first introduced

by Karataev, Mamyrin, and Shmikk in 1972 [5], has proved to be of equal importance to the concept of space focusing.

For the current discussion, an ion mirror can be described qualitatively as a potential ramp used to reflect ions back along their original flight path. The higher-energy ions travel farther up the potential ramp than those of slightly lower energies and therefore spend more time within the reflecting fields. The overall effect is to provide an energy-dependent detour of correct duration such that ions of higher energy, following a longer path length than those of lower energy, arrive at the detector at the same time as the lower-energy ions. The ion mirror maintains space-time focusing by reflecting the space-focus plane back to a plane that is opposite the ion mirror position. A suitable ion detector is then placed at this plane (see Fig. 12.2). In this mode of operation E_1 and E_2 are chosen so that the primary space-focus plane is at a minimum drift length, D, i.e., a short distance from the second field E_2. This space-time plane can then be reflected back to the detector surface (secondary space-focus plane).

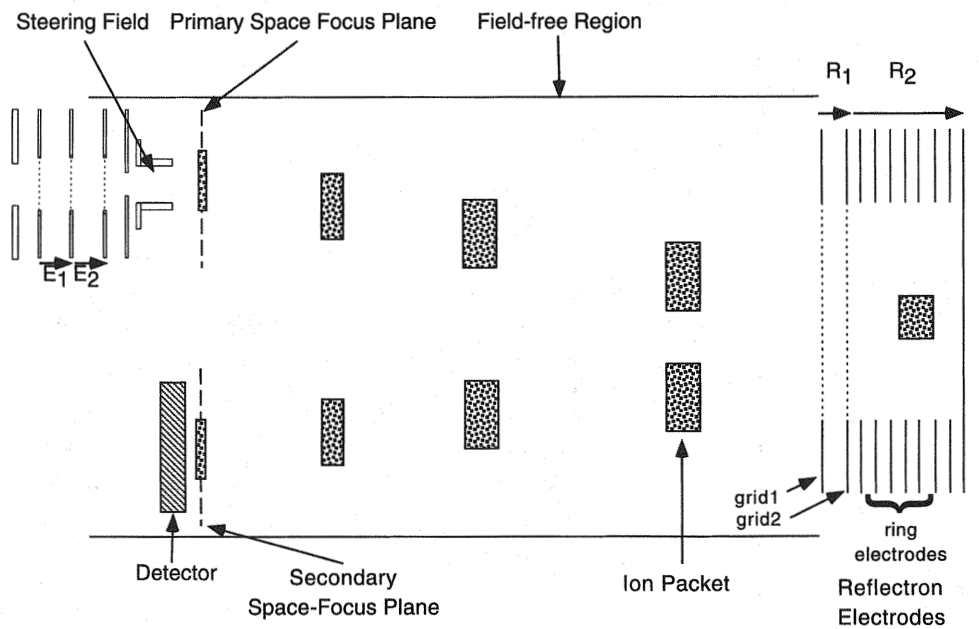

Figure 2 Schematic diagram of ion mirror illustrating the reflection of the primary space-focus plane to a secondary space-focus plane at the detector surface. Shaded blocks represent ion packet dimensions at different points during flight. R_1, first retarding field; R_2, reflecting field defined by concentric rings each joined by equal resistance; E_1 and E_2, electric fields in acceleration regions.

Experimentally, the ion mirror is often constructed from a group of concentric rings stacked one atop another with specific spacing to achieve optimal performance. Often the reflectron contains two electrostatic field regions (R_1 and R_2 in Fig. 12.2) in a so-called dual-stage arrangement. These fields are then defined by grids placed on the concentric rings and maintained by connecting resistors between adjacent rings to produce a linear potential drop in the region. By adjustment of the reflecting fields, the time spread at the detector space-focus plane can be minimized.

In this manner an isomass time spread can be reduced quite effectively, especially for energy distributions that are less than 10% of the total acceleration potential. Predicted resolving powers (FWHM) of 10^3 can be achieved with this device and such a distribution, with higher values possible at kinetic-energy distributions below 10% [4]. Resolving power (R) as high as 35,000 has been reported with a two-stage reflectron and a laser-ionized Cs neutral beam [6]. In addition, a grid-free ion mirror has been described that achieved a resolving power of 10,000 to 20,000 and an ion transmission of 90% [7]. Recently, an ion mirror that employs nonlinear fields and a different geometry to correct for larger initial ion-energy distribution has been described [8].

The preceding discussion has been provided to give the reader a general understanding of some of the concepts utilized within TOF mass analyzers but is by no means exhaustive. The interested reader is encouraged to investigate a number of excellent reviews on the subject [9–11].

12.2.2 Use of Continuous Ion Sources with Time-of-Flight Mass Spectrometry

Much of the work in the early development of the preceding techniques incorporated pulsed electron-impact ionization sources or any of several types of laser ionization techniques. In almost all of these cases the ions were created in a pulsed fashion in vacuum and formed in or sent into the acceleration region of the mass spectrometer, where a static acceleration field present there injected them into the mass spectrometer. Such ion sources use the TOF-MS very efficiently because the repetition rate of the spectrometer is limited by the frequency of the ionization event itself. This arrangement allows the TOF-MS to mass analyze of all of the ions formed completely. However, many of the most popular ionization techniques being used in inorganic analysis today are continuous in nature.

Although some early research did focus on introducing a pulsed external ion beam from a plasma jet into the acceleration region of the TOF-MS [12], it has not been until recently that continuous ion sources such as plasmas, electrospray devices, and other atmospheric-pressure discharges have been coupled with TOF-MS. Unfortunately, the inherently pulsed nature of the spectrometer can cause this marriage to be quite inefficient. The primary challenge in using the TOF-MS with

a continuous ion source is the loss of ions during the mass analysis cycle, as the spectrometer is unable to examine any ions while the previous mass analysis is under way. If the time required to complete a repetition cycle is significant compared to the time required for the continuous ion beam to refill the extraction region, losses will occur. The relative degree of inefficiency can be quantified in a measure known as the *duty factor*, which can be broadly defined as

$$\text{Duty factor} = ft = f(x/v) \tag{12.3}$$

where f represents the repetition frequency and t is the time during which the continuous beam is sampled. For example, if a particular TOF analyzer has a repetition rate of 10 kHz (i.e., a mass-analysis period of 100 μsec), and a 100-ns portion of the continuous ion beam is pulsed into the mass spectrometer, then the duty factor of the instrument is 10^{-3} or 0.1%. Alternatively, one can use x, the physical length of the extracted ion beam, and v, the mean velocity of the ion beam, to calculate the time of sampling. The limiting duty factor of a TOF-MS when utilized for a specific application with a continuous ion source lies in all three of the parameters (f, x, and v).

The repetition rate (f) of the TOF analyzer is limited by factors such as the heaviest mass to be measured, the requirement of adequate resolving power, data-acquisition speed, detector response time, flight tube length, and acceleration potentials. The amount/volume of ions that can be used from the continuous ion beam is dictated primarily by the geometry of the ion acceleration region and by the method of pulsing ions into the TOF-MS. The length of the ion beam extracted with each analysis, (x), is limited by resolution-influencing factors such as space-time focusing and energy focusing, as well as by the fact that longer initial ion volumes may require larger-area detectors. Finally, the mean velocity of the incoming ion beam, (v), is often limited by the characteristics of the ion source itself. For example, the sampling of atmospheric-pressure ionization sources creates continuous ion beams whose limiting mean velocity is dictated by the characteristics of the extraction process, pressure differentials, and bath-gas identity. A variety of instrument designs have been used to maintain duty factors that approach 10%–20%. These designs are discussed in detail in Sec. 12.3. It should also be noted that there is no reason that the coupling of the correct TOF geometry and continuous ion source could not lead to a duty factor of 100%, as many of the limitations noted are experimental in nature.

12.2.3 Time-of-Flight Mass Spectrometer Benefits for Elemental Mass Spectrometry

In order to justify the use of a TOF-MS as a viable alternative to those mass spectrometers already utilized for inorganic mass spectrometry, one must realize some additional capabilities. The TOF-MS possesses a number of unique attributes that

extend the utility of methodologies already in use, as well as create new possibilities by virtue of those methodologies.

Perhaps the greatest attribute that TOF-MS may apply to elemental mass spectrometry is the ability to provide simultaneous multielemental analysis. Of course, a TOF-MS does not *record* all the masses in the spectrum simultaneously; the time difference between adjacent masses is typically in the nanosecond regime. However, all masses are sampled into the mass spectrometer simultaneously and an entire spectrum is generated from each injected ion pulse. Because successively recorded mass spectra are obtainable in short periods in a TOF-MS, especially in instances in which there is a small, well-defined mass range of interest, thousands of mass spectra can be obtained each second.

Many of the benefits attributable to the use of the TOF-MS are a result of what the TOF-MS does not do—scan. Most of the instruments in use within inorganic mass spectrometry are scanning in nature and as such are only capable of monitoring one mass-to-charge ratio at any given time. Thus, there must necessarily be a trade-off between the sensitivity, resolution, and precision of a measurement and the mass coverage. In the limiting case, a mass scanning instrument such as the quadrupole filter must hop from one mass to the next for maximum speed in multielement determinations.

Assuming a 200-msec dwell time at each mass of a 15-element measurement, an analysis time of 3 sec would be required for one repetition. Investigation of the entire atomic mass range utilizing a 1-meter TOF-MS with an acceleration voltage of 2000 V would take approximately 25 μsec; thus the spectral or multielement-acquisition speed of TOF-MS exceeds that of a quadrupole by approximately two orders of magnitude. In this example, if the TOF-MS is also allowed to integrate for 3 sec, it achieves a better signal-to-noise ratio, assuming the instruments have equal sensitivity.

If we consider the case of ICP-MS, instruments typically achieve sensitivities of about 10,000 ion counts/sec/ppb; thus, at the specified dwell time, a quadrupole mass spectrometer generates about 2000 counts at each mass for a 1-ppb solution. A TOF-MS with the same sensitivity generates 30,000 counts at each mass. In the scanned instrument, lower concentrations obviously yield fewer counts and require longer dwell times. Therefore, for analyses that require many elemental signals to be measured for either more sample information, internal standardization, or isobaric corrections the TOF-MS has the potential to deliver complete analysis with no loss in speed or sensitivity.

The rapid spectral acquisition rates and multielemental and isotopic coverage of the TOF-MS are important when investigating transient signals. Pulsed sampling techniques such as laser ablation, electrothermal vaporization, flow injection techniques, and pulsed discharges all benefit from the ability to investigate the entire mass range of interest with high temporal resolution. The mass coverage per unit time obviates the need to dilute or reach a steady-state condition so that mul-

tielemental analysis can be completed. This is of particular importance when analyzing samples of limited quantity, or in cases in which each transient event possesses an additional dimension of information, such as in the case of glow discharge analysis for depth resolution. In the future, as measurement techniques are applied to situations of decreasing sample dimensions, the ability of the TOF-MS to provide the maximum amount of information is likely to be exploited to an even greater degree.

Additionally, chromatographic techniques such as ion chromatography, gas chromatography and capillary electrophoresis are of increased utility. In part this is because the addition of a mass spectrometric detection system allows for an increased tolerance of nonideal separations. If two eluents are not completely separated at the time of elution, the added dimension of *m/z* detection often allows the two to be separated on the basis of differences in their mass spectra. The utility of this approach is directly related to the number of mass spectra available during the period of elution.

Second, and specific to the use of a TOF-MS, is the lack of spectral skew. As a chromatographic peak elutes, it has a changing concentration profile with time. If a scanning instrument is utilized to provide mass spectrometric analysis, the mass analyzer, unable to look at more than a single *m/z* at any given time, must scan the mass range as the concentration of the eluent is changing. This sequential detection then causes a skewing of the relative intensities of different masses. Because a TOF-MS simultaneously extracts all masses from the incoming beam, and does so very rapidly, the changing concentration of the eluent does not affect the measured signal intensities of different *m/z* ratios.

One additional benefit of the simultaneous extraction of all masses from the primary ion beam is the capability for improved precision. Because the ions are sampled from the ion beam simultaneously, any fluctuations from the ion source should be reflected in changes in the intensities of all masses. Thus, internal standardization and isotope ratioing techniques should theoretically increase precision by compensating for these fluctuations. Conversely, a scanning instrument must investigate the different *m/z* at different times, making it susceptible to errors due to these source fluctuations that cannot be corrected for in a similar manner. Indeed, when the peak hopping time of a quadrupole instrument is reduced to a minimum, the precision of the ratio has been observed to improve correspondingly [13]. Workers using a twin-quadrupole device were able to achieve ratios limited by counting statistics by measuring two masses simultaneously with each quadrupole [14]. Of course, the best isotope ratios from a plasma ion source are obtained on sector-based multicollector instruments, with which the continuous, simultaneous observation of the masses of interest can be achieved [15]. Although the TOF is not capable of continuously monitoring these masses of interest, it is capable of monitoring all of the masses at a very high rate. It has been shown that isotope ratios can be obtained with precision limited by counting statistics on a plasma-source TOF instrument, for all of the elements and isotopes simultaneously, and

without instrumental modification. By choosing the proper internal standard, ratioing has been shown to improve the signal stability in TOF-MS [16]. Moreover, adding more elemental signals will not sacrifice speed or sensitivity.

Certainly the most publicized attribute of the TOF mass analyzer is the unlimited mass range of which the analyzer is capable. Although certainly underutilized within most inorganic applications, this attribute may offer a degree of added flexibility and may prove valuable in applications such as elemental speciation. Since instruments very similar in design can be utilized with a wide range of ionization sources, different mass range applications may be investigated with the same instrument just by changing the ionization source. This may broaden the role of a single instrument from dedicated inorganic analysis to provide a much wider range of analytical information.

The TOF mass analyzer also offers experimental advantages such as its architectural simplicity, lack of moving parts or scanning fields, and propensity for economical construction. Because the TOF possesses such an open, nonrestrictive flight path these mass analyzers are capable of very high transmission efficiency. The transmission efficiency of a TOF-MS is typically estimated at 0.5–1 for the entire mass range at once. Scanned quadrupole mass analyzers operating at slightly less than unit mass have similar transmission. The important difference is the rejection of all other masses by scanned instruments during analysis of mass.

Discussion of the benefits that TOF-MS may yield when applied to inorganic analysis is incomplete without also considering some of the current disadvantages of the approach. Perhaps the most noteworthy is the low duty factor of the TOF-MS.

The discussion in Sec. 12.2.2 touched on the origins of the low duty factors often encountered when coupling TOF-MS with continuous ionization sources. The pulsed operation of the TOF-MS may reduce the duty factor because a scanning instrument is capable of monitoring a single m/z continuously, whereas a TOF-MS must always examine the whole mass range of interest regardless of the analysis being conducted. Thus, whereas the duty factor of the conventional TOF-MS is a fixed quantity dependent upon instrumental and source parameters, the duty factor of the scanned instrument is a function of the number of masses being investigated. Therefore, sensitivity must then be recovered somewhere to achieve the performance of continuous sampling mass spectrometers. This recovery can be accomplished by taking advantage of the speed and high transmission efficiency of the TOF-MS.

The speed of the TOF-MS requires fast readout systems that can be expensive, data-intensive, and elaborate. Additionally, one of the most valuable techniques within trace analysis, ion counting, is of less utility when utilized with TOF-MS. These are unavoidable effects of the pulsed nature of the TOF-MS, and of the wealth of information that the TOF-MS is capable of producing.

Designing and using a TOF-MS with plasma sources are not without challenges, many of which can be overcome with proper design of the instrumentation. One example is the removal of the large densities of plasma gas ions such as argon,

oxygen, and molecular species that can cause detector saturation, thereby blinding the detector to ions that may arrive after these peaks. Additionally, when utilizing a source such as the glow discharge, matrix ions must be deflected as well. By deflecting these species out of the flight path of the TOF, the lifetime of the detector is extended, and coulombic effects that may occur inside the flight tube can be lessened.

The design of the TOF-MS interfaced to the plasma ion source is the most important issue in its development. In the next section the merits of differing designs are explored; then the implementation of these designs is reviewed.

12.3 ELEMENTAL TIME-OF-FLIGHT MASS SPECTROMETRY

12.3.1 Design Considerations

Orthogonal and Axial Geometries

A plasma source was coupled to a TOF-MS as early as the 1960s, when workers at Bendix [12] used such an arrangement to analyze the chemical species in a plasma jet. The instrument utilized a pulsed supersonic inlet probe similar to that found in current inductively coupled plasma mass spectrometry (ICP-MS) quadrupole instruments and employed a TOF-MS that was oriented at a 90° angle to the input ion beam. More importantly, however, it used a pulsed extraction field to extract ions from the plasma source and accelerate them into the flight tube. It is this concept of injecting discrete ion bunches into the TOF-MS analyzer that has been almost ubiquitously employed by workers using continuous ion sources [17,18].

Although the right-angle or orthogonal geometry does have benefits for duty factor and resolving power, it is also instructive to consider on-axis and linear designs. As each geometry and pulsing scheme has its strengths and weaknesses, each should be evaluated on the basis of its estimated sensitivity, resolution, and duty factor. Of course, analytical figures of merit such as precision, dynamic range, and detection limits ultimately determine the usefulness of the instrument for plasma-based elemental analysis.

In an on-axis arrangement, the drift tube of the TOF-MS is located coaxial with the incoming continuous ion beam, and thus modulation of the ion beam is required in order to create a time-of-flight mass spectrum. One such modulation scheme, depicted in Fig. 12.3, involves continually accelerating ions into the flight tube while sweeping this high-kinetic-energy beam across a slit located in front of the detector [19,20]. After the continuous ion beam is accelerated into the drift tube, the ions pass between two plates to which a voltage pulse is applied to create a deflection field. This sweeping action creates a "kink" in the beam, of small spatial width, which is then allowed to traverse the drift length and is extracted

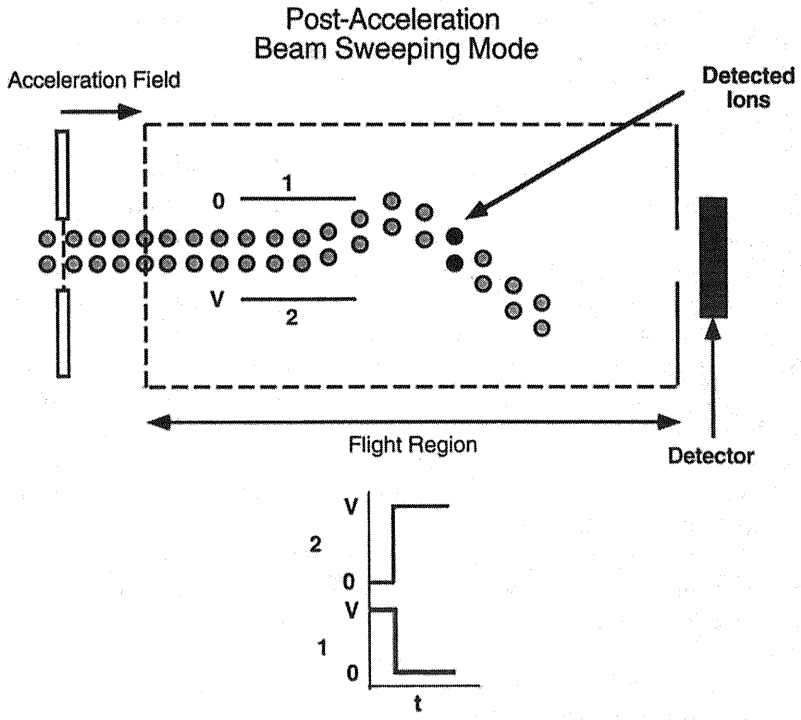

Figure 3 Postacceleration beam sweeping mode for continuous ion-beam modulation in an on-axis time-of-flight mass spectrometry (TOF-MS) geometry. 1, 2, deflection plates; V, deflection voltage; t, time; ●, ions reaching detector; ❁, ions not reaching detector.

through the slit located prior to the detector. As one deflection event corresponds to the creation of a single time-of-flight spectrum, when the heaviest ion of interest has reached the detector, the deflection can be carried out again.

In this beam-sweeping scheme the effective spatial distribution of the ions sampled is defined by the characteristics of the sweeping action and the detector slit parameters [20]. Maintaining the fast rise time of the deflection pulse is critical in maintaining spatially small ion packets at the detector surface, and thus adequate resolution. The overall resolution for the differential impulse-sweeping mode in Fig. 12.3 can be estimated with the following equation developed by Bakker [20]:

$$R = \frac{L^2 V_0}{2DU(B + S)} \tag{12.4}$$

Here, the variable L is the drift length in meters, V_0 is the deflection potential in volts, D is the distance between the deflection plates in meters, U is the acceleration potential in volts, B is the beam diameter in meters, and S is the slit width at the detector surface in meters. If we consider an example using $L = 1.14$ m, $V_0 = 100$ V, $B = 1.0$ mm, $S = 3.0$ mm, $D = 10.0$ mm, and $U = 2000$ V, the approximate resolution is calculated to be ~800. This resolution is comparable to that obtainable on quadrupole systems (~500) and should be adequate for routine ICP-MS measurements.

However, as the initial kinetic energy distribution of the ions in the continuous beam also affects the flight time of isomass ions, and thus instrumental resolution, we must consider this estimated resolution to be somewhat higher than might be observed. One limitation of this instrumental design is that it does not employ space-focusing techniques to compress the spatial width of the extracted ion kink; nor does the fundamental design allow for the simple incorporation of energy focusing techniques such as the reflectron. Nonetheless, a safe assumption is that a beam-sweeping TOF-MS could provide unit-mass resolution for all elements by application of the appropriate fields.

In an orthogonal geometry (Fig. 12.4) the ions within the incoming continuous ion beam are focused into an extraction region, which is defined between the repeller electrode and the initiation of the acceleration region. The electric field within the extraction zone is controlled by this repeller plate and the opposing grid. At a set repetition frequency a linear electrostatic field is established within the region, by application of either a positive potential to the repeller or a negative potential to the grid. Those ions within the region are extracted into the static acceleration field of the TOF-MS. Within this field the ions attain their final drift energies before entering the field-free region where mass separation takes place. Thus, as long as this extraction zone is allowed to refill with ions before the next pulsed field occurs, a complete sample of the region enters the TOF-MS with each repetition event.

The attainable resolution within the right-angle TOF-MS benefits greatly from the ability to utilize techniques to compensate for the initial spatial distribution of ions within the extraction region, as well as for the distribution in their initial energies. Through application of the space-focusing techniques outlined in Sec. 12.2.1, the initial spatial width of the ion beam can be compressed such that differences in flight time due to the differences between the ions' initial starting position are minimized. Additionally, ion optical elements applied to the incoming ion beam can be used to collimate the ion beam, giving it a well-defined width within the region and further decreasing this effect.

The effect of the initial kinetic energy distribution upon resolution is also lessened within this approach. Partly, this is due to the ability to incorporate easily methods of compensation, such as the reflectron, within this design. Additionally, the ions are extracted at a 90° angle from the primary beam. As the kinetic

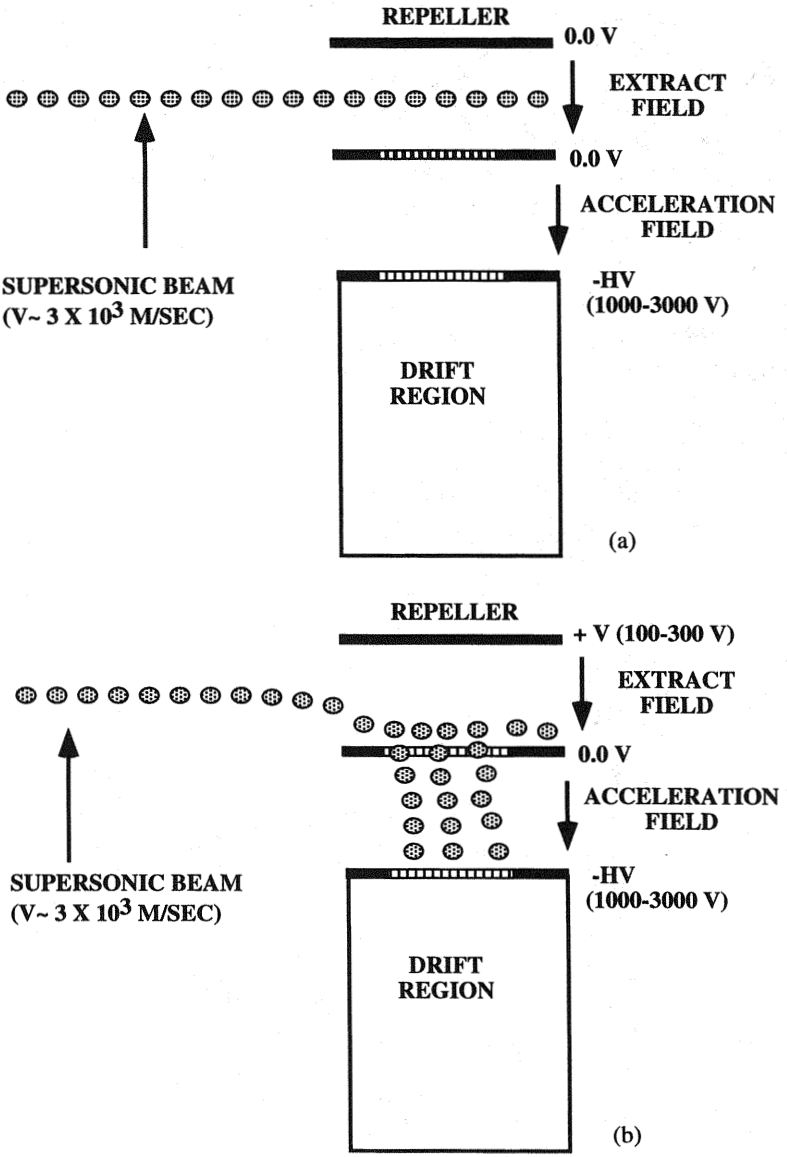

Figure 4 Orthogonal time-of-flight mass spectrometry (TOF-MS) in a nonextraction mode (top) and extraction mode (bottom).

energy spread is greatest along the axis of beam propagation, the act of extracting ions perpendicularly samples the beam along the direction where the distribution is minimal, and thus degradation of mass resolving power is minimized. Unlike in the beam-sweeping TOF-MS, there is no simple quantitative way to estimate the resolution of the right-angle geometry, but previous workers have demonstrated much better than unit-mass resolution across the elemental mass range [17,18,21]. Although this design is susceptible to flight time error due to turn-around time, the judicious application of space- and velocity-focusing techniques should allow for resolution at least equal to, if not greater than, that attainable with the beam-sweeping design.

The last geometry to be considered here is depicted in Fig. 12.5 and is also an on-axis design. It has, however, more in common with the orthogonal extraction geometry than the beam-sweeping method. It also relies upon space- and velocity-focusing techniques and utilizes a two-stage acceleration geometry. Indeed, the operating principles of this design are identical to those of the right-angle geometry, except that the ions enter the extraction region through a gridded repeller electrode. Here, however, similarities end because of the requirement for an additional

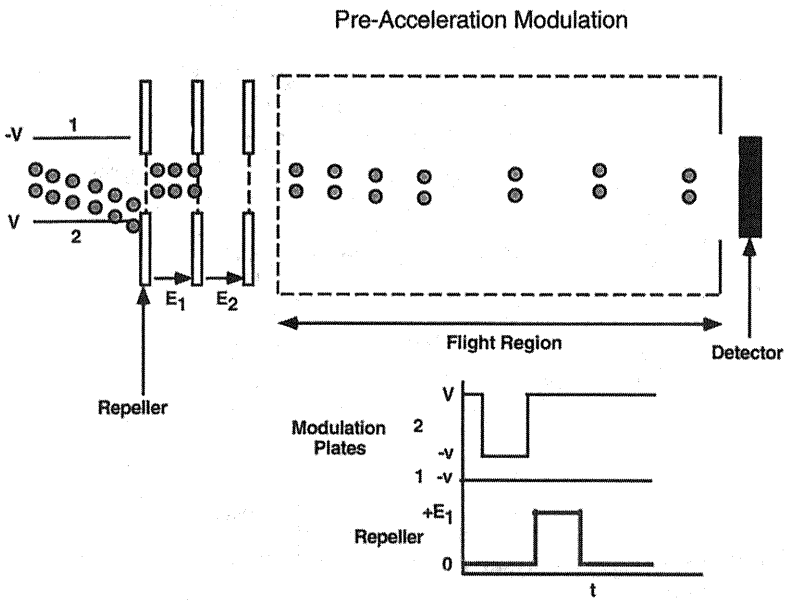

Figure 5 Preacceleration continuous ion-beam modulation in an on-axis time-of-flight mass spectrometry (TOF-MS) geometry. 1, 2, deflection plates; V, deflection voltage; V, transmission voltage; t, time; E_1 and E_2, electric fields in acceleration region.

modulation step because of the coaxial propagation of the bulk beam and the extracted ion packets.

This modulation can be achieved by preacceleration modulation, that is, by the formation of ion packets prior to extraction. A portion of the ion beam that is similar in length to that extracted in the right-angle design is "selected" by a set of parallel plates and allowed to travel into the extraction region, where the ions are extracted for mass analysis. In theory, any optical device that would allow a portion of the ion beam to enter the extraction region would work in this case.

Alternatively, the difference in the energies of those ions present within the extraction region at time of a repeller event from those ions not selected for mass analysis can be exploited. By applying a potential barrier of the appropriate dimensions immediately prior to the detector, ions within the continuum that do not have sufficient energy do not pass this barrier, and those ions contributing to signal are detected. The different means of modulation are examined in more detail in a later section.

The resolving power of this on-axis approach is questionable. Although space focus considerations between the two designs are quite similar, the fact that the ion beam now propagates coaxially with the flight tube axis places the axis of greatest kinetic energy dispersion along the direction of extraction. This, in comparison with the orthogonal extraction geometry, makes the effects of the ions' initial kinetic energy quite pronounced, and the use of some velocity compensation scheme is required. However, this design does not suffer from the effects of ion turn-around time noted, and experimental evidence presented later in this discussion suggests that a half-meter TOF-MS based on this fundamental principle is capable of resolving powers adequate for elemental mass spectrometry.

Duty Factor A low duty factor when coupling continuous ionization sources with TOF-MS is a disadvantage in comparison to the continuous operating nature of sequentially scanning instruments. Obviously, a TOF-MS that samples more of the continuous beam is desirable, as it more efficiently utilizes those ions presented to the mass analyzer. For a beam-sweeping geometry, the mechanism of modulation relies on sampling a very small portion of the total ion beam, and thus the duty factor is greatly limited by the need for adequate resolution. In addition to the fact that only a fraction of those ions located between the deflection plates during a sweeping event are finally detected, all of the ions that are deflected as the mass separation is taking place are lost as well. Since the ion beam is traveling at an accelerated velocity, the result is an inherently poor duty factor.

The two-stage acceleration geometries have a significant advantage in this regard. Because the ion packets are pulsed out of the incoming beam before acceleration takes place, there exists a large difference in the velocities of the incoming primary ion beam and the ions undergoing mass separation within the flight

tube. While mass separation takes place, the relatively slow-moving primary beam is allowed to refill the extraction region before the next repetition. The difference in velocities may be two orders of magnitude or more, allowing these designs to enjoy a much higher duty factor.

If we again consider the example of ICP-MS, the ion beam travels at an approximate velocity of 2.3×10^3 m/sec and fills the 1-inch extraction zone in approximately 11 μsec. If the mass spectral repetition rate is 20 kHz, then 50 μsec is required to generate a mass spectrum, translating to a duty factor of 22%. Under similar conditions, we might expect a duty factor of 0.007% from a swept-beam approach.

Sensitivity The overall sensitivity attainable with a TOF-MS is a function of the transmission efficiency, duty factor, and extraction method utilized with that particular mass analyzer. Since the on-axis beam-sweeping TOF-MS traverses only a small portion of the continuous ion beam across the detector surface, one can intuitively appreciate that the two-stage acceleration designs, sampling a larger portion of the continuous ion beam, should offer better sensitivity. This can be illustrated numerically by considering ion-beam densities that have been observed in ICP-MS quadrupole instruments. For a 1-ppm solution of a typical analyte element, a quadrupole system produces 1×107 counts/sec ($1.6 \times 10-14$ A). For the sake of the following illustrative calculations, we can use this as a rough estimate of the analyte ion concentration within the incoming primary ion beam.

Within a beam-sweeping instrument, all ions are continuously accelerated as they enter the drift tube. Their velocity after acceleration can be calculated with the following equation

$$v = \sqrt{\frac{2eU}{m}} \tag{12.5}$$

where e is the electronic charge (1.6×10^{-19} C), m is the ion mass in kilograms, and U is the acceleration field in volts. Using the heaviest element typically analyzed, uranium (238 amu), and an acceleration potential of 2000 V, one calculates that the uranium ions attain a velocity of 2.8×10^4 m/sec. For a 1-ppm solution, assuming the same analyte concentration of 10^7 analyte ions/sec/ppm, there are then 350 ions/m in the accelerated beam. If 1-cm deflection plates are utilized, then there are an average of 3.5 analyte ions between the plates at any instant in time. Bakker has developed an equation to estimate the fraction of ions resident between the plates that will be detected [20]:

$$\text{Fraction} = \frac{(B + S)\mathrm{D}(UU_1)^{1/2}}{V_0 pL} \tag{12.6}$$

where U_1 represents the initial energy of an ion before acceleration, and p denotes the length of the deflection plates. Utilizing the parameters defined previously, p = 1 cm, and U_1 = 9 eV [22], the fraction of detectable ions is calculated to be 0.01, and thus there should be 0.035 ions/modulation for a 1-ppm solution of analyte. Even for solution concentrations as high as 1 ppm, a single TOF spectrum likely does not contain any analyte ions, and ion counting or some form of spectral integration is clearly needed. If one considers that the current ICP-MS instruments are capable of detection limits (10s, 3σ) of 0.1 part per trillion (at 1 cps of background noise), a beam-sweeping instrument would only achieve 3.5×10^{-9} ion/modulation at this concentration. If the TOF-MS could acquire spectra at 20 kHz, this means that no more than 7×10^{-5} ions/sec might reach the detector with no losses; in other words, one would have to wait an average of almost 4 hours before observing a single ion count! Obviously, the sensitivity of this on-axis design is inherently poor, and the low population of analyte to total ion density in the ICP ion source afflicts this geometry tremendously.

Estimation of the sensitivity for the orthogonal extraction and alternative on-axis instruments is quite straightforward. The velocity (v) of the ion beam formed by skimming the supersonic expansion within the ICP-MS interface can be calculated as

$$v = (5kT_0/m)^{1/2} \tag{12.7}$$

where m is the mass of the bath gas, T_0 denotes the mean gas temperature, and k represents the gas constant. An argon ICP with a gas temperature of 5000K produces an ion beam with a mean velocity of 2.3×10^3 m/sec [23], at which analyte ions achieve the same velocity as the bath gas. For the same analyte concentration of 10^7 cps/sec/ppm, a 1-ppm solution should yield approximately 5000 analyte ions/m or 100 ions within a 1-inch-wide extraction region of the mass spectrometer at any given time. Here, 100 ions can enter the TOF-MS for each cycle of the pulsed extraction; thus the sensitivity of these instruments exceeds that of the beam-sweeping design by a factor of 2000.

For a 1-ppt solution, an average of 1×10^{-4} ion counts per extraction pulse would be expected. At a repetition rate of 20 kHz, a 10-sec integration would then yield 20 ion counts, as long as no losses occurred within the mass spectrometer, and with a background of 1 cps, a detection limit of less than 1 ppt. More importantly, the 2 counts/sec would be measured for all elements in the periodic table that can be determined by ICP-MS. In contrast, the quadrupole ICP-MS would integrate 100 counts over the same 10-sec period, yielding a 0.1-ppt detection limit with similar background. This analysis will have been completed for one analyte only, and thus conducting a similar analysis for only 10 m/z values would require 100 sec. Although these calculations are of a somewhat qualitative nature, they are effective in highlighting the differences between these TOF-MS designs, and in il-

lustrating the slight trade-off between the continuous monitoring of a single mass and multielemental mass coverage.

Ion Optics

The efficient transport of ions through any mass spectrometer is vital, but it is perhaps of special concern within TOF-MS because of the duty factor issues and the excellent transmission efficiencies of which these spectrometers are capable.

Since the flight tube itself is an open field-free region, the ion throughput of a TOF analyzer is quite high and can approach 100% in some designs. However, fields in the analyzer are usually defined with metallic grids, typically 70 lines per inch, which are predicted to have 90% transmission, the number of which can quickly add up to reduce the transmission of the device. For example, a typical two-step acceleration source contains two grids and the typical two-stage reflectron another two, which the ions actually travel through twice. This reduces the transmission to 53, assuming no other losses.

Gridded ion electrodes are usually intended to present a electrostatic plane; however, the fact that they are constructed of wire segments may compromise this goal. If placed too closely, potential wells formed within the spaces between adjacent wires convert the grid into a series of small focusing or defocusing elements, causing beam divergence and adding to the losses in transmission efficiency. It should be noted that some gridless designs of reflectrons do exist, although the currently discussed ion acceleration regions require the use of grids.

Transmission efficiency and resolving power may also be compromised by a divergent incoming ion beam. Focusing elements must be utilized to collimate the incoming ion beam, as angular divergence certainly limits transmission efficiency, and may also result in spherical aberrations that may limit mass resolving power. Focusing devices such as Einzel lenses and steering plates can be used in the flight tube to direct the ions in the proper path. The detailed construction of these optical devices in the TOF-MS depends upon the TOF geometry at issue.

An optical consideration specific to the use of the TOF-MS with high-intensity sources is the removal of background ions, plasma gas ions, and matrix ions to prevent detector saturation. To date, this has been accomplished with parallel-plate deflection in the flight path, which is depicted in Fig. 12.6. Removal of specific m/z ions is accomplished by the application of a time-dependent potential to one, or both, of the plates at some time delayed with respect to the repeller pulse. In this way, those ions between the plates at the time of the pulse experience a field transverse to the flight axis and are removed from the flight path. The voltage pulses employed here must have fast rise and fall times (<10–20 nsec), and be applied at precise delay intervals to ensure that mass resolution is not compromised, and to allow for the unimpeded passage of the previous and subsequent masses. Also, the

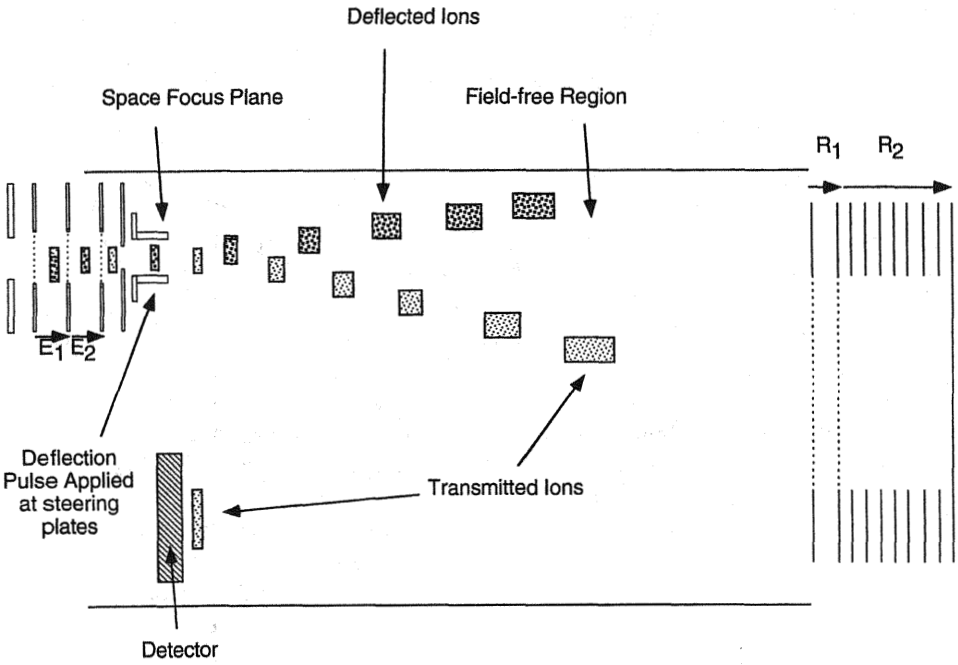

Figure 6 Parallel plate ion deflection. E_1 and E_2, electric fields in acceleration region; R_1, first retarding field; R_2, reflecting field.

length of the plates should be optimized for maximum deflection without introducing large fringing fields, which could hinder resolution [17].

For efficient removal, these plates should ideally be placed at the point at which ions attain their tightest temporal and spatial focus prior to detection. Although deflection of this type would be challenging with a swept-beam geometry, the space focus plane of the two-stage acceleration design offers an excellent opportunity to deflect the maximum number of ions over the shortest distance in the shortest time. This placement also ensures the most resolution of mass deflection. For an ICP-TOF-MS, the efficiency of removal for this parallel-plate scheme was promising [24].

When dealing with a large number of matrix ion species, as is the case in glow-discharge (GD) mass spectrometry, a greater number of different masses must be ejected over a broader mass range. This task is made more difficult by the decreasing temporal dispersion between adjacent masses with increasing flight times. Workers in GD-TOF-MS have investigated the deflection of ions close to the detector surface [25]. By employing a baffle device to prevent the deflected

ions from scattering further into the TOF-MS detector region, good deflection efficiencies and single atomic mass unit (amu) mass resolution have been demonstrated [25]. The only disadvantage of the technique is in the high fields required to deflect ions so close to the detector surface, which may make design of the pulsing system difficult.

Perhaps the most attractive alternative to the use of deflection plates in the literature is the combed ion deflector, which has been described by Enke et al. [26]. This design relies upon an architecture of parallel wires located within the ion path. At the appropriate times, voltage pulses of equal potential and of opposite polarity are applied to alternating wires, creating electrostatic fields of alternating polarity between adjacent wires. A collimated ion beam incident upon such a device experiences a large defocusing effect in the dimension parallel to the wires and is thus removed from the flight path. With a technique such as this, deflection can be accomplished over a short distance, and thus with high temporal and mass resolution. Although promising, the use of such a deflector in elemental TOF-MS has not yet been reported.

Ion transport from a continuous ion source to the extraction/acceleration region of the TOF-MS presents many of the challenges also associated with other mass spectrometers. Specifically, a means of efficiently focusing incoming ions into a beam of well-defined energy and spatial characteristics is required in order to achieve optimal performance for any mass analyzer.

As the resolution of the TOF-MS is partially determined by the success of space-focusing techniques, investigators utilizing an orthogonal extraction instrument with the ICP have found that limitation of the spatial width of the ion beam within the extraction region can lead to greatly improved resolving power [27,28]. This is accomplished by placing a slit electrode, typically 1 to 3 mm in width, immediately prior to the extraction region. The presence of this spatially restrictive device confines the beam to a fraction of the full width of the extraction region, enhancing the capability of the spectrometer to compensate for the finite dimensions of the beam, and thus enhances resolution. A cylindrical lens system, however, produces an ion beam of circular cross section, and thus its application here produces significant losses. These losses can be reduced substantially by changing the ion beam image from circular to oval in shape, an end accomplished by utilizing the dc quadrupole system depicted in Fig. 12.7. Researchers found that the use of a quadrupole singlet improved signals by a factor of 4; moreover, the use of a quadrupole doublet raised ion currents 25 times [28,29].

One class of optical components that holds significant promise for inorganic TOF-MS is the radio frequency (rf) multipole device. This device has already been employed with great success with TOF-MS in a number of organic mass spectrometric applications, as well as with other mass analyzers within inorganic mass spectrometry. Certainly, TOF-MS may also enjoy the advantages offered to all mass analyzers such as the removal of matrix ion species by selective ejection or

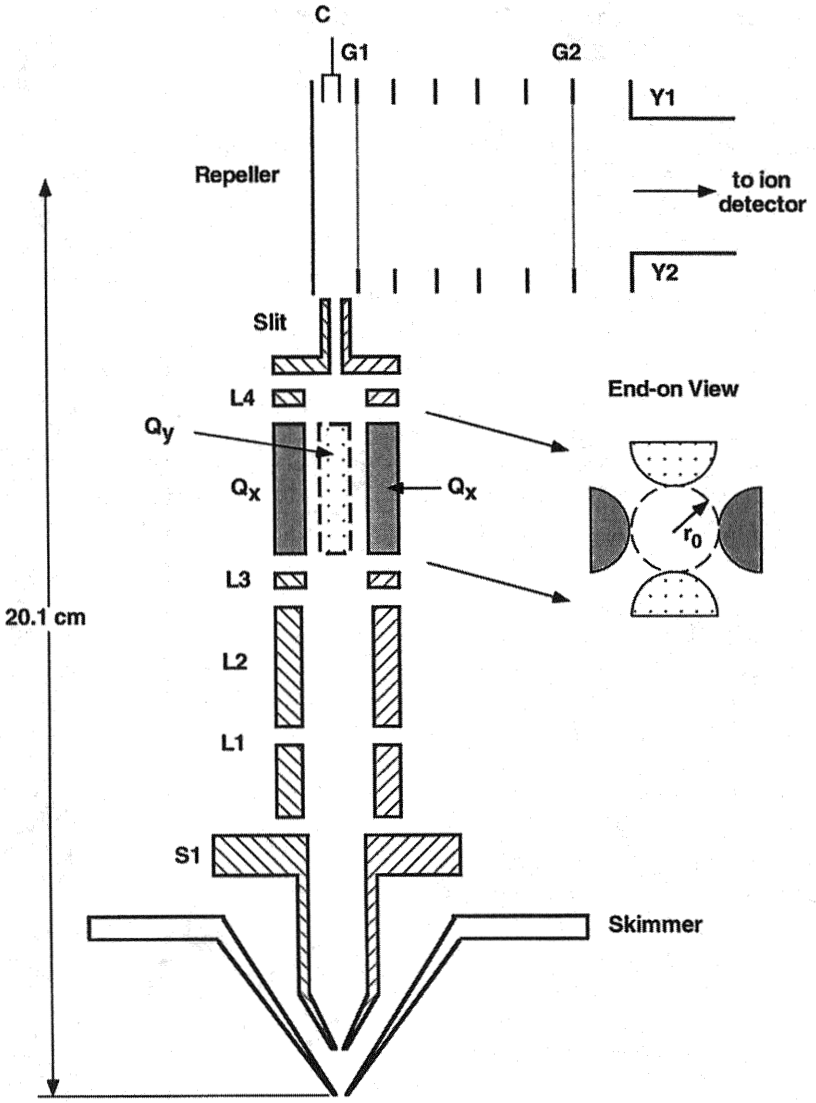

Figure 7 Quadrupole lens system tested for inductively coupled plasma time-of-flight mass spectrometry (ICP-TOF-MS). L1–L4, cylinder lenses; Q_x, *x* dimension poles, Q_y, *y* dimension poles; r0, radius of quadrupole open aperture (0.5 cm); S1, second-stage extraction optic; C, Faraday cup; G1, grounded entry grid; G2; acceleration grid; Y1, Y2, steering plates. (From Ref. 28.)

charge-exchange reaction, the ability to accomplish ion chemical reactions, as well as an added capability for the dissociation of polyatomic species [30–32]. Specifically, however, the TOF-MS has been shown to benefit greatly from the ability to control the incoming energy distribution and spatial confinement of the ions precisely. Since the resolution and sensitivity of the TOF-MS are dependent on both of these characteristics, the use of multipole devices in inorganic TOF-MS may allow for greater resolving power and an increased duty factor. Although promising, the use of such a device within inorganic TOF-MS has not yet been reported.

Another intriguing combination is the ion trap-TOF-MS, which can be used on the front end of the TOF-MS to improve its duty factor. Lubman and coworkers have interfaced an atmospheric plasma discharge to a reflectron TOF-MS [33]. The instrument performed well on a sensitivity basis with trapping times from 10 μsec to 10 sec with higher resolutions obtained at longer trap times. The challenge of such an approach for use with a high-intensity plasma ion source is the necessity to trap the entire elemental mass range while ejecting plasma gas ions. To achieve a 100% utilization of the incoming ion beam in supersonic beam sources the trapping times are in the 10-μsec range.

Detectors

In considering detector requirements for use with TOF-MS, it is instructive to consider first some of the important attributes that an ideal detector might possess. Foremost, a detector for TOF-MS must have excellent temporal resolution in order to distinguish between peaks that may be nanoseconds in width and separated by flight times that are measured in the tens of nanoseconds. In addition to offering high gain, making the detection of single ions possible, the detector should offer a significant dynamic range to extend detection from a single ion to the realm of continuous current. This dynamic range should be available on a measurement-to-measurement basis as well as within a single mass spectrum, allowing single-ion detection to be accomplished at a mass adjacent to the most intense peak. The detector should also have minimal mass bias, giving equal conversion efficiency to ions of greatly different momentum. Moreover, the detector should have attractive physical characteristics such as a large format and flat surface in order to minimize flight-time errors that could result from curvature. Finally, a number of experimental characteristics such as less stringent vacuum requirements, a resistance to poisoning by atmospheric and vacuum contaminants, and a long detector lifetime are important.

The microchannel plate (MCP) remains the detector of choice for many TOF-MS applications because of its large, flat active area; high gain; and excellent time response. Typical rise times of MCP devices are unparalleled; transitions from 10% to 90% of peak intensity are routinely on the order of picoseconds [34]. Often, two microchannel plates are oriented back to back in what is termed a chevron arrangement to achieve gains of 10^6 or greater, each plate contributing about 10^3. Mi-

crochannel plates are also capable of good dynamic range, some providing coverage from the single-ion level to 10^{-4}-A output current. The detectable mass range of MCPs can be extended through a technique known as *post acceleration*. By biasing the plates at a potential 2–5 kV more negative than the flight-tube potential while fixing the potential dropped across the plates to a constant, nominally 1 kV potential, additional acceleration is imparted to incoming ions. This additional acceleration step greatly increases the detection efficiency of heavier ions, allowing their routine use in applications requiring the detection of large biomolecules. Microchannel plates are also available in large formats and in a wide range of sizes and shapes. This flexibility can be important when designing TOF-MS around an orthogonal extraction geometry, in which beam dimensions often dictate that detectors of large area be employed. Unfortunately, these formidable detectors do have some drawbacks for use in elemental TOF-MS.

Because of the high field strengths present within the channels of the MCP, residual gas molecules in the vacuum chamber can be ionized, creating an avalanche effect that can destroy portions of the MCP. To prevent this "ion feedback," the bias angles of the channels are oriented to prohibit the ions from having a direct path to the detector cathode [34], and the vacuum is maintained at or below 10^{-6} torr for the optimal lifetime and performance of the chevron system. Additionally, MCP devices have a hygroscopic nature, necessitating that they be stored in an inert environment or in vacuum [34]. Disadvantages specific to their use with elemental TOF-MS are their saturation properties. Although the temporal response of a single channel to an ion hit is outstanding, microchannel plates have a significant ohmic resistance that prevents the channels from recharging quickly. These recovery times are often in the millisecond range. This effect not only limits the gain available immediately after the detection of a very intense mass-spectral peak, but also limits the gain of the detector when it is utilized in applications in which succeeding spectra are being obtained at high repetition rates [35].

Another option for ion detection is the discrete-dynode electron multiplier. These detectors do not suffer the saturation problems of the MCP, and recently manufacturers have been producing multipliers specially designed for TOF-MS. Such devices offer rise times of 1–2 nsec and possess larger active areas than do conventional discrete-dynode detectors. Gains for these detectors can be as high as 10^7, and their dynamic range, stability, and single-ion detection capability are similar to those of the MCP. Detectors of this sort have the added advantage of being quite stable at atmosphere and can tolerate ambient pressures up to 10^{-5} torr more reliably. The primary disadvantage to date has been the unavailability of electron multipliers with active areas as large as those available in MCP detectors.

Time-of-Flight Data Systems

Perhaps the greatest limiting factor in the development of the TOF-MS for elemental analysis has been the lack of appropriate data-acquisition systems. The re-

cent resurgence of interest in the technique can be traced, in part, to the dramatic increase in the capabilities of technology over recent years.

The difficulty in data capture arises from the rapid spectral-generation rates of TOF-MS, the requirement of high temporal resolution, and the desire for high measurement precision. The problem becomes clear if we consider an ICP-TOF-MS application. A typical mass spectrum may be collected over 50 μsec wherein mass-spectral peaks possess temporal widths of 10–20 nsec measured at FWHM. Thus, one needs to acquire measurements every 2 nsec, or at a rate of 500 MHz, in order to ensure an average of 5–10 samples across a mass peak of interest. Such a system then produces 25,000 points per mass spectrum and, at a minimal analog-to-digital converter resolution of 8 bits per point, generates 25 kbytes of information per mass spectrum or 500 Mbytes every second. As this is well beyond the capabilities of even the fastest current system, the solution must then be to sacrifice single-spectrum acquisition, complete mass spectral coverage, measurement or temporal resolution, or acquisition rate in a way that minimally impairs the application at hand. The most attractive solution is through spectral summing or averaging wherein sequential mass spectra are combined before being stored, thus reducing the acquisition load to a fraction of what it could otherwise be. Although single-spectrum acquisition and real-time resolution are limited, many applications do not require such high temporal resolution, and a very acceptable compromise can be reached.

Acquisition systems of this type are usually based on fast digital oscilloscopes or flash analog-to-digital converter (ADC) computer boards. By means of a flash-ADC it is currently possible to acquire analog data at a sampling rate of 1 GHz with 12-bit resolution; recent progress in the design of systems for gas chromatography (GC) TOF-MS has demonstrated the capability of acquiring up to 1000 complete summed spectra per second [36,37]. These systems may be limited in applications requiring the mass analysis of extremely fast transient signals as a result of the massive amount of data they generate but on balance are sure to be valuable tools for elemental TOF-MS.

Alternatively, the ability to conduct single-spectrum intensity measurements might be appropriately sacrificed and classical ion-counting techniques used. In comparison to the situation in sequentially scanning mass spectrometers, the application of ion counting to TOF-MS is an exceedingly inefficient process. Because a scanning instrument is capable of monitoring a single m/z continuously, the maximum obtainable count rate is limited only by the ability of the detector and acquisition system to distinguish between the arrival of two ions and the statistical probability that two will arrive within that time. This allows such instruments to register millions of counts per second. Because mass spectral information is encoded within the time domain in a TOF mass spectrum, ions of the same mass arrive at the detector within nanoseconds of each another, clearly exceeding the ability of the detector or acquisition system to differentiate between events caused by

single or multiple ions. To reduce this "pulse pile-up" error, the TOF-MS is restricted to utilizing ion counting in a concentration regime in which the probability of a single ion hit is much less than unity: that is, in which there is an average of less than one ion of a specific *m/z* detected in every spectrum. This restriction limits the acquisition rate to less than about 10^4 counts per second, corresponding to solution concentrations of 1 to 10 ppb.

The use of a multistop time-to-digital ion-counting converters (TDCs) allows real-time digitization of an entire mass spectrum with excellent (picosecond) temporal resolution. Additionally, electronic measurement error within the system is virtually eliminated, as the precision of ion counting measurements is a function of the source noise, the number of integrated events, and the degree of pulse pile-up error. Although the restraints of counting statistics limit the dynamic range, ion counting remains extremely valuable as a tool for trace analysis and may be most valuable when utilized in conjunction with an analog technique.

In some instances, the design of the data acquisition system may be driven by the requirements of a specific application. In ICP-MS, for example, the masses of the elemental isotopes are well known, so only those masses need to be investigated. In such a situation, an attractive technique is the use of a number of single-channel devices, such as boxcar integrators [38], each of which is responsible for continually monitoring a specific mass of interest. At the expense of complete mass spectral coverage, a simple, inexpensive system that generates relatively small amounts of data with real-time temporal resolution can be utilized.

Modern boxcar integrators can be programmed under computer control to accumulate signal at a predetermined delay time after a trigger pulse, and with gate widths adjustable to less than 1 nsec. The boxcar integrator recovers signal from noise by integration or averaging; the signals, being correlated with some trigger pulse (here, the pulse that sends ions into the flight tube of the TOF-MS), accumulate directly with the number of input pulses, whereas the noise integrates only as the square root of that number. This principle of operation limits its utility at low signal levels, as the boxcar-integrator begins to integrate noise a greater portion of the time and signal pulses only occasionally. To overcome this limitation, workers have used a discriminator-boxcar integrator system that triggered the boxcar integrator only when signal was present in the window of interest [39]. Alternatively, ion counting can be employed in a similar gated manner (see Fig. 12.8). Here, ions are counted in an adjustable-width gate delayed with respect to the repeller pulse to record an ion peak of interest [16,40].

Clearly, in order to realize the broadest dynamic range, the total data acquisition system for a TOF-MS is likely to remain a composite of both analog and counting systems. As associated technologies advance in speed, through highly parallel system architecture, application of information encryption strategies, and use of fast storage systems, the capabilities of the TOF-MS will also be extended.

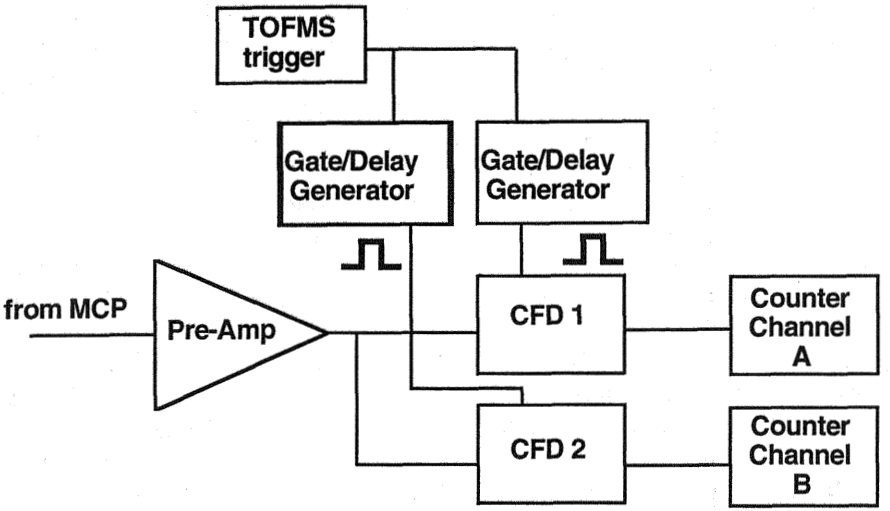

Figure 8 Layout of the gated ion-counting detection system. CFD, constant-fraction discriminator. (From Ref. 27.)

12.3.2 Orthogonal Time-of-Flight Mass Spectrometer

The advantages resulting from the use of a TOF-MS with a technique such as ICP-MS have been touched upon. In the following sections, it is our aim to highlight some illustrative applications, touching on aspects of instrumental performance and notable design considerations.

Inductively Coupled Plasma Time-of-Flight Mass Spectrometry Performance

The coupling of an ICP ionization source to a TOF-MS was first reported by Myers and Hieftje [24]. A schematic diagram of their instrument is provided as Fig. 12.9. Similarly to other ICP-MS instruments, it utilized a three-stage differentially pumped interface in order to realize the microtorr pressures required for TOF-MS from mean-free path considerations. This instrument was based on an orthogonal-extraction geometry and utilized a 1.6-m total flight path, which, at a 2-kV acceleration potential, dictated a maximum spectral repetition frequency of 20 kHz.

Notable among the instrumental design characteristics is the use of direct current (dc) quadrupole lenses to limit ion-beam width spatially within the extraction region. These lenses, along with the use of an ion reflectron, provided resolving powers of approximately 1600 (FWHM) [40]. An illustrative spectrum of Pb and Bi obtained with this instrument is provided as Fig. 12.10.

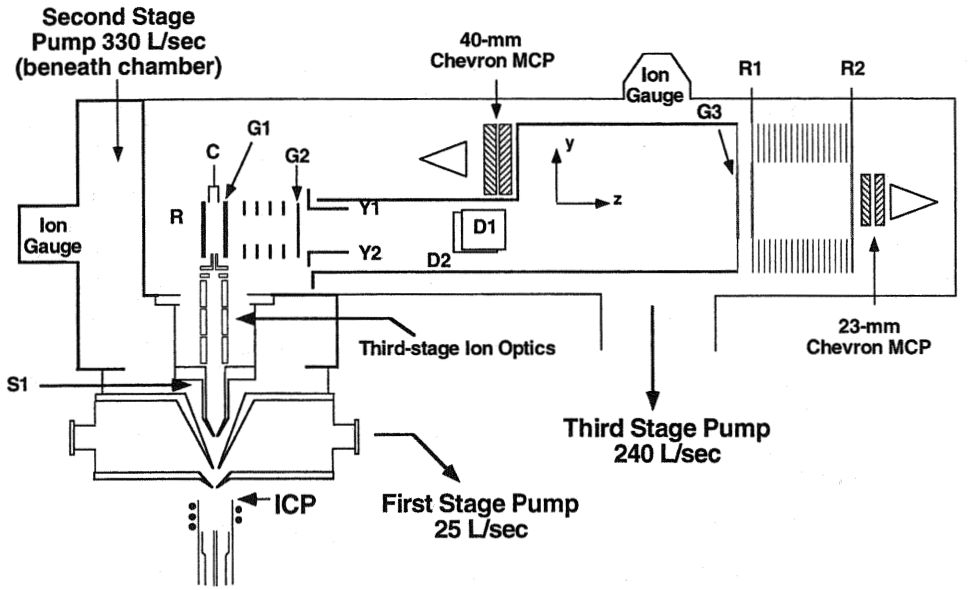

Figure 9 Layout of the inductively coupled plasma time-of-flight mass spectrometer (ICP-TOF-MS) with improved vacuum chamber and ion optics. *S*1, second-stage extraction lens; *R*, repeller; *C*, Faraday cup; *G*1, *G*2, TOF-MS entry grids; *Y*1, *Y*2, steering plates; *D*1, *D*2, deflection plates; *G*3, reflectron entrance grid; *R*1, deceleration grid; *R*2, reflecting grid; MCP, microchannel plate. (From Ref. 27.)

This design also utilized two sets of beam steering plates. One set, labeled D1 and D2 in Fig. 12.9, constitute a pair of deflection plates employed to remove Ar^+ from the extracted ion packets. A 230-V pulse of variable duration delayed from the repeller pulse eliminated more than 99% of these ions and prevented detector saturation.

The second set of plates, labeled *y* plates in Fig. 12.9, were utilized to give the extracted ions the correct trajectory to enter the reflectron, and thus strike the detector. Because the incoming ion beam is oriented at a right angle to the flight-tube axis, the extracted ions possess a component of their velocity oriented in their original direction. In order for the ions to traverse the flight path successfully, this original velocity vector must be eliminated or compensated for. The degree of steering required is determined by the directed kinetic energy of the incoming ion beam and thus by the ion source employed. Since the extraction of ions from this atmospheric-pressure source involves the formation of a supersonic expansion, all masses possess the same velocity and therefore a mass-dependent energy [16]. This then necessarily leads to a mass-dependent steering plate potential. Additionally, dispersion within the energies of isomass ions leads to differences in ion trajec-

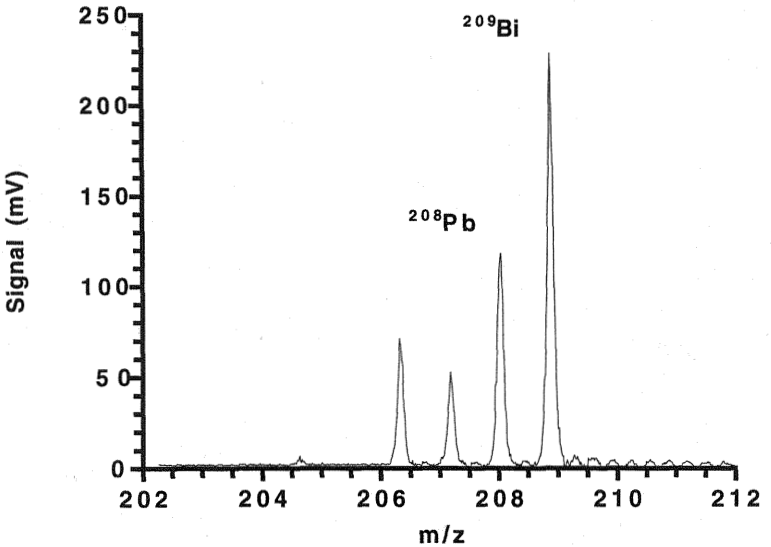

Figure 10 Inductively coupled plasma time-of-flight mass spectrometry (ICP-TOF-MS) spectrum for a 4-ppm solution of both Pb and Bi using the ion reflectron (average of 1000 shots). (From Ref. 40.)

tory, and thus to an angular beam divergence that limits transmission efficiency. These workers calculated that a 5-eV energy spread within the energies of incoming ions would limit the transmission efficiency of the mass analyzer to approximately 20% [27].

Figure 12.11 shows this mass-dependent steering bias for a group of elements ranging in mass from Li to Bi. Since one of the attributes of the TOF-MS is simultaneous multielemental coverage, this mass bias represents a significant limitation. Myers et al. demonstrated that this mass-dependent steering voltage can be overcome by application of a voltage ramp to the steering plate, since ions of increasing mass, and therefore increasing energy, are passing the plates with increasing flight time [16]. This technique was applied in the orthogonal ICP-TOF-MS successfully; however, a linear ramp is only an approximation of the quadratic ramp that would be ideal [16].

Coles and Guilhaus have shown that the use of steering plates in the flight path to compensate for the perpendicular velocity component degrades resolving power [41]. They have proposed an alternative approach that they have termed *spontaneous drift* [41]. This strategy makes no attempt to compensate for the perpendicular velocity component but rather tailors the angle of the flight tube to the energy of the perpendicularly accelerated ions such that the ions finally strike the

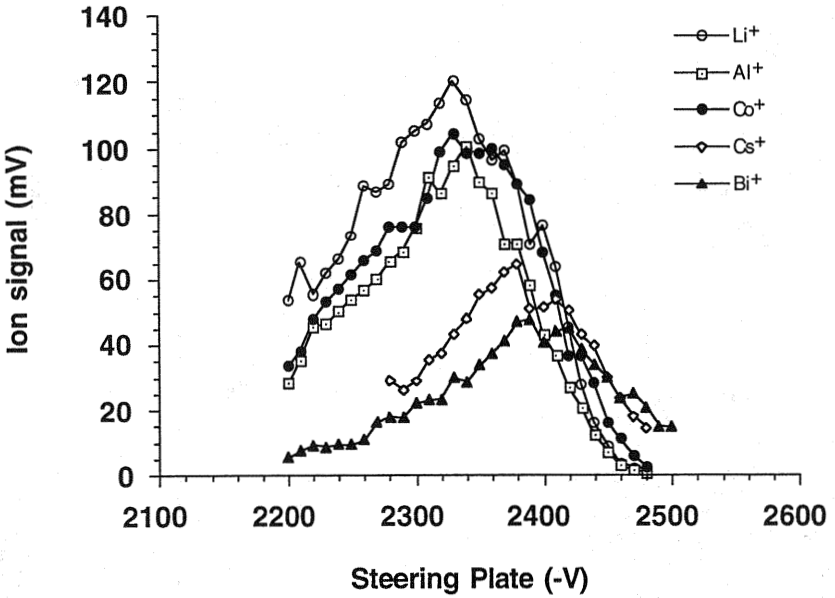

Figure 11 Ion signals vs. steering potential (*Y2*) for ions of differing mass. (From Ref. 27.)

detector. This design eliminates the need for steering plates; however, to detect the entire elemental mass range, a larger reflectron and detector would be required.

In the first instrument, sensitivity and limits of detection were constrained by the total ion beam current measured after the extraction region of the TOF-MS [42]. Although pulser circuitry limited the repetition rate to 7.1 kHz and a duty factor of 3.5%, detection limits ranged from 0.03 to 3 ppb using ultrasonic nebulization [16]. Mahoney et al. later reported on improvements to the same orthogonal ICP-TOF-MS [29]. The use of a commercial skimmer cone and quadrupole doublet in the extraction optics led to an increase in primary ion current from 2 nA to 50 nA [29]. This, along with electronic improvements allowing a 16-kHz spectral-repetition rate, dropped limits of detection to 1–10 ppt when ultrasonic nebulization was utilized.

The authors reported that these detection limits were compromised by the presence of a significant continuum background of 1000 cps per 50-nsec window [29]. The sources of this noise were hypothesized to be the leakage and scattering of ions into the mass spectrometer, the mechanism of which is depicted in Fig. 12.12 [42]. Since the duty factor of the mass analyzer was approximately 10%, the majority of a repetition cycle saw the ion beam passing through the extraction region unimpeded. During this time, fringing fields or off-axis ion trajectories allow ions to pass though grid G_1 to be accelerated into the drift region. As these ions

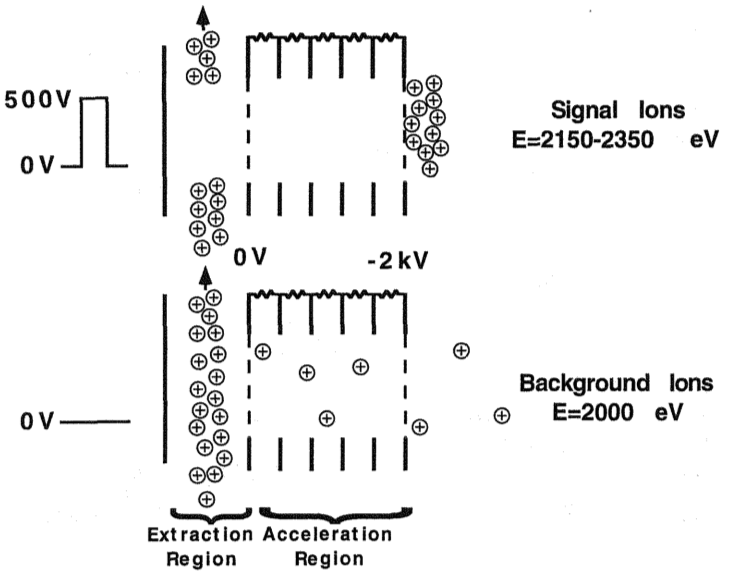

Figure 12 Schematic diagram illustrating properly extracted signal ions (top) and "leakage" ions that contribute to the continuum background (bottom) in an orthogonal-acceleration time-of-flight mass spectrometry (TOF-MS) with continuous ion sources. The energies of the two types of ions are shown at the right. The signal ions receive a distribution of energies resulting from their original starting positions along the potential gradient in the extraction region formed by the repeller pulse (left). While the repeller pulse is off, no gradient exists and the maximum energy of the "leakage" ions is 2000 eV. (From Ref. 42.)

have no defined "start" time, when they strike the detector they appear as a noise that clutters the entire mass spectrum.

Several strategies were employed in order to reduce this effect. Myers et al. described the use of a pulsed ion optic to limit the access of ions to the extraction region [28]. By application of a voltage pulse to one of the quadrupole optics, the ion beam was swept across the slit at the end of the primary optic chain. By correct choice of delay parameters, the extraction region was filled with ions only immediately prior to a repeller event. Mahoney et al. described a different approach that relied on differences in the energies of "signal" and continuum background ion populations [42].

As the ions responsible for the continuum background enter the acceleration region without the aid of the extraction pulse, they possess only the energy they gain within the acceleration region (see Fig. 12.12). The extracted ions, in contrast, are subjected also to the linear extraction field created by the repeller pulse and therefore possess slightly greater energies. By placing a potential barrier some-

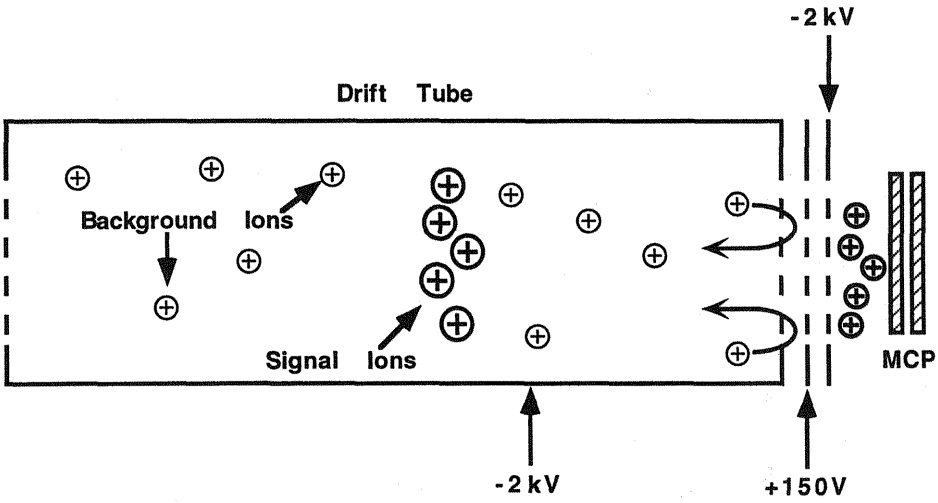

Figure 13 Pictorial representation of energy discrimination (ED). Lower-energy (2000-eV) background ions are repelled by the barrier formed by the three grids in front of the detector. Higher-energy (2150- to 2350-eV) signal ions pass through the barrier and are detected. MCP, microchannel-plate detector. (From Ref. 42.)

where within the flight path, one can discriminate against the lower-energy continuum background [43–45].

Experimentally, this is accomplished by placing a three-grid assembly (shown in Fig. 12.13) immediately in front of the detector surface, the middle grid of which is maintained at an elevated potential. As is evidenced by Fig. 12.14, a potential of 160 V is adequate to reduce the continuum background noise in order of magnitude, while the signal from a 1-ppb Rh solution remains relatively unchanged [42]. Consequently, limits of detection were observed to improve by an order of magnitude in accordance with counting statistics. The remaining background noise was studied and determined to arise from neutrals that are formed via charge exchange with the background gas [42]. A disadvantage to this energy discrimination (ED) approach is that the energy focusing of the reflectron is compromised, and the resolving power with ED grids falls to 1230 from 1520 [42].

The full dynamic range of the technique remained undemonstrated because a detection system that employs ion counting for trace determinations and analog measurement for the higher concentrations was not available. Assuming that such a system existed, Mahoney et al. reported a dynamic range of ICP-TOF-MS $>10^6$ [42]. Detection limits were measured by using gated ion counting, in which a 50-nsec window is located at the mass of interest and ions arriving within this period are counted.

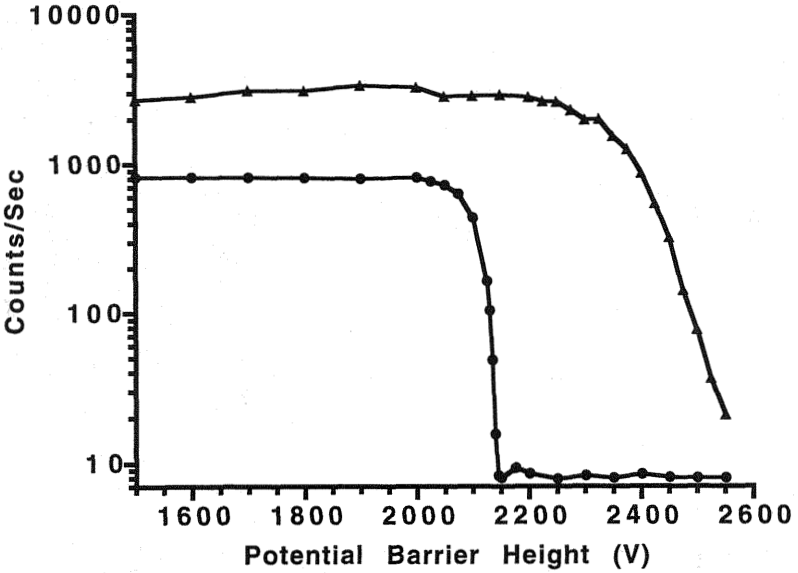

Figure 14 Signal (triangles) and adjacent background (circles) count rates as a function of potential-barrier height for a 1-ppb ^{103}Rh solution. (From Ref. 42.)

Inductively Coupled Plasma Time-of-Flight Mass Spectrometry Applications

Isotope Ratios and Internal Standardization The ability to extract all ions from an incoming ion beam simultaneously allows the TOF-MS to provide better precision than sequentially scanned ICP-MS instruments. Provided that the dominant source of noise is multiplicative in nature, all elements and isotopes should experience the same perturbations. Therefore, ratioing techniques such as isotopic dilution should allow compensation for drift and source noise, and isotope-ratio measurements should improve in precision.

Past work has shown the attainable isotope-ratio precision to be affected to a great extent by the data acquisition scheme. Measurements conducted with a digital oscilloscope, boxcar averager, or gated boxcar integrator have yielded a limiting isotope ratio precision of about 0.5%. The error sources, it was found, were associated with the imprecision of the data acquisition system itself, in factors such as gate drift and jitter, electronic drift, and readout errors [46]. The use of a multistop TDC ion counting scheme has proved more successful, as the method discriminates against electronic noise sources and benefits from the ability to examine the entire mass spectrum. It was shown that the limiting precision with which ratios could be measured was determined by counting statistics [46]. Figure 12.15

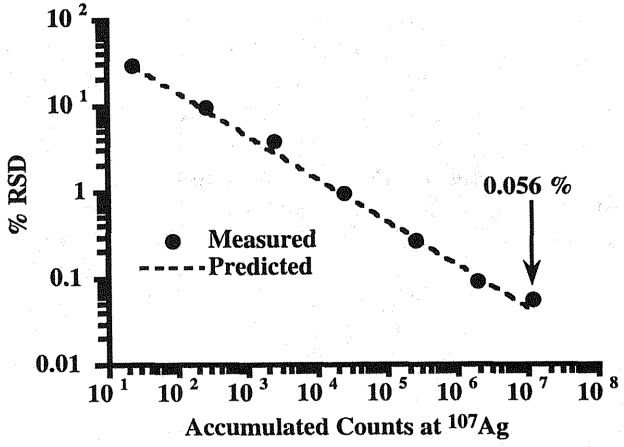

Figure 15 Isotope-ratio measurement precision as a function of the number of accumulated counts. Each measured value (circles) represents the relative standard deviation of 10 repetitions. The dotted line represents the precision predicted by counting statistics for a given number of accumulated counts. Because the measured values match the predicted values closely, it is confidently expected that longer integration times will yield even better precision (<0.01%). (From Ref. 47.)

illustrates the dependence of ratio RSD on the number of integrated events (n) and displays the characteristic $1/n^{1/2}$ dependence predicted by counting statistics. The integration of 10^7 ion counts yielded a limiting precision of 0.0056% for the ratio of $^{107/109}$Ag [47]. The inefficiency of ion-counting techniques with TOF-MS requires that low count rates be used, greatly extending analysis times and limiting the concentration range over which these results were obtainable. It is worth noting, however, that all of the elemental isotopes are available for study during the analysis and that the use of an analog averaging approach of the appropriate fidelity may hold promise for precise ratio determination over a significant dynamic range.

The success of ratioing techniques is entirely dependent upon the proper choice of an internal standard or ratio reference. Certainly, another isotope of the same element under study is the best choice; indeed, it has been shown that lead signals temporally varying with 17% RSD can be radioed to yield 1.9% RSD, with this limitation imposed by the data acquisition system. In some cases, such as the monoisotopic elements or expense considerations, isotopic dilution may not be attractive and thus alternative elements must be utilized for ratioing. Here, it was found that improvements in precision were greatly dependent upon the choice of internal standard, with best results obtained for elements of close mass and ionization energy.

Laser Ablation The ability to provide simultaneous multielemental mass coverage at high spectral generation rates makes a TOF-MS particularly well suited for the analysis of signals from transient sample introduction sources. Typical laser ablation ICP-MS techniques use a 10-Hz laser repetition rate to generate a steady-state signal in order to accommodate the scanning of the mass spectrometer. In this mode of operation much of the spatial resolution of which laser ablation is capable is lost. Further, the scanning nature of the mass spectrometer makes determinations susceptible to error induced by shot-to-shot laser power variation, and the large amount of ablated material may lead to deposition on the sampling cones of the instrument. An ICP-TOF-MS offers complete multielemental and isotopic coverage at mass spectral generation rates of 20 kHz or greater, and therefore can produce 20,000 complete spectra from the 1-sec transient produced by a single laser shot. Additionally, the simultaneous extraction of all masses affords the opportunity to employ ratioing techniques to compensate for the shot-to-shot variations in laser ablation events. The attractiveness for the determination of multielemental spatial distributions in solids is obvious.

Mahoney et al. described the coupling of a laser ablation sample-introduction system to the orthogonal ICP-TOF-MS instrument described in Sec. 2.2.1.1 [16,29]. They utilized a free-running non-Q-switched ruby laser operating at 694 nm with an energy of 100 mJ/pulse, and with a manual repetition rate of 0.1 Hz that was limited by the charging time of the flash-lamp capacitors [29]. Nevertheless, the TOF system, operating at a repetition rate of 10 kHz, produced 3000 complete spectra from the 0.3-sec transient laser ablation signal. By utilizing the gated-ion counting approach (see Sec. 2.1.4) and integrating the transient signal generated in this period. a detection limit of 10 ppb was achieved for lead in cast iron [29]. The authors note that the detection capabilities are likely better than calculated because the signal levels used for the determination were in the pulse pile-up regime.

By employing a digital oscilloscope with the same system, complete multielement spectra were acquired for single laser pulses. A spot-by-spot analysis of a lava sample that contained plagioclase crystals within the matrix was also performed. A multielemental spectrum of both the crystal site and background lava matrix is shown in Fig. 12.16 [29]. By sweeping the laser beam along an 11-mm section and sampling every millimeter, the distribution of elements as a function of spatial location was accomplished. A plot of selected elemental signals as a function of spatial location is reproduced in Fig. 12.17 [29]. The positions where crystal inclusions were sampled are evidenced by increases in the Al, Na, and Ca signals; the lava matrix was found to contain significant concentrations of Fe, Mg, P, K, and Mn [29].

Allen et al. have also reported the coupling of a laser ablation sample introduction to a commercial ICP-TOF-MS [48]. The authors illustrated the true multielemental capability of such a system when equipped with an improved data-ac-

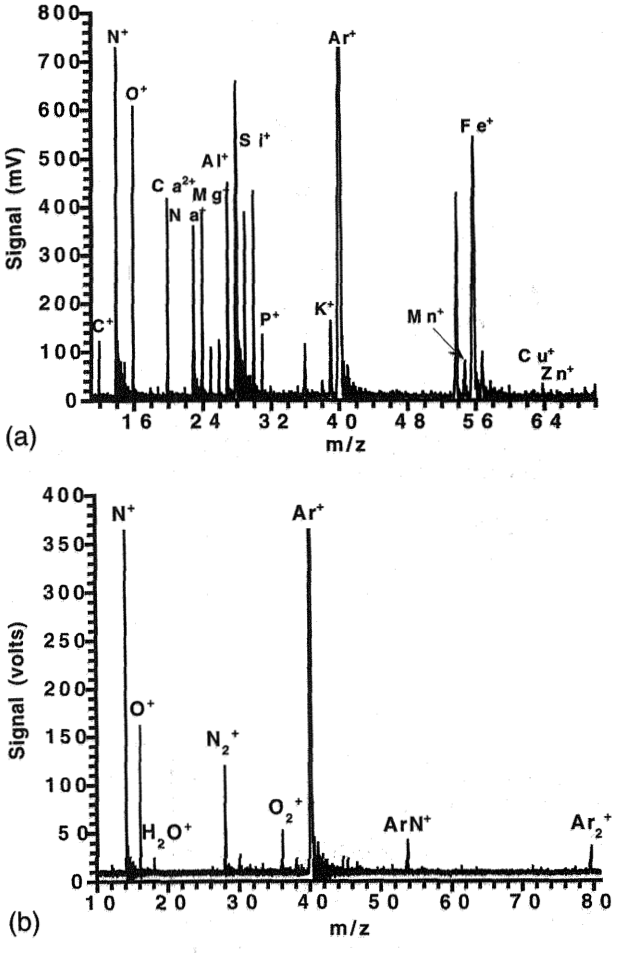

Figure 16 (a) Spectrum obtained from the average of 20 cycles (repeller pulses) after a single ruby-laser pulse incident on a plagioclase crystal contained in a lava sample. The ringing that follows abundant peaks is due to detector saturation. (b) Background spectrum obtained under the same conditions as in (a) but in the absence of a laser pulse. (From Ref. 29.)

quisition system. Several of the advantages of single-shot analysis, as compared to the sequential dilution of many laser ablation events where demonstrated by the determination of elemental segregation within NIST steel standards by single-shot multielemental analysis [48].

Although a detection system that could acquire the counting and analog-domain signals simultaneously would improve the dynamic range and utility of spot

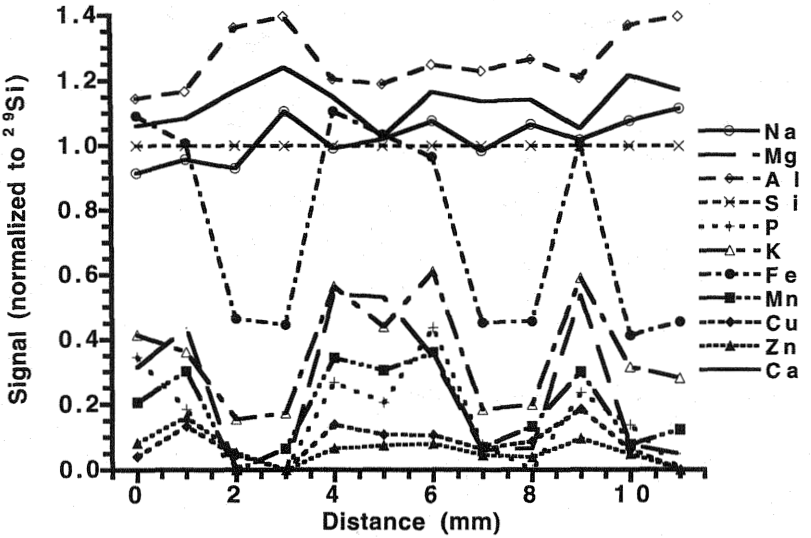

Figure 17 Relative distributions of 11 elements (normalized to ^{29}Si) across the 11-mm distance. Visual inspection under a microscope supports the distributions suggested in the plot. Laser shots on the lava matrix occurred at 0, 1, 4, 5, 6, and 9 mm, whereas laser shots on the plagioclase crystals occurred at 2, 3, 7, 8, 10, and 11 mm. (From Ref. 29.)

analysis with laser ablation (LA), this past work illustrates the promise of the LA-ICP-TOF-MS for spatial mapping and multielement transient analysis.

Electrothermal Vaporization Like laser ablation, electrothermal vaporization (ETV) sample introduction techniques also benefit from the talent of TOF-MS for the analysis of transient signals. Utilizing a 250-MHz flash ADC data acquisition system, investigators were able to investigate 32 different elements during the vaporization of a single 10-μL aliquot of sample solution [49]. Although the capability to examine all masses during a single ETV event is impressive, perhaps more important is the ability of the TOF-MS to provide added dimensionality to the analysis. In a sense, the use of a laser ablation system with TOF-MS adds the dimension of spatial characterization on a single-shot basis. In the same sense, the addition of the electrothermal atomizer provides the added dimension of thermal characterization.

Figure 12.18 depicts such an analysis wherein *m/z* ratio is plotted as a function of volatilization time (proportional to temperature) for a single ETV event. The high temporal resolution of TOF-MS allows the complete mass spectral characterization of the event and allows observation of the different appearance times

of the different elements present on the basis of their volatilization characteristics. This strategy has been widely employed for the separation of isobaric interferences of species having different vaporization characteristics, such as the elimination of ArO^+ interference on ^{56}Fe. Moreover, the addition of a TOF-MS facilitates the resolution of isobaric overlaps even between elements, such as Sn and Cd at m/z = 112, on the basis of their different volatilization characteristics. Such a separation can be accomplished only with a mass-spectral resolution of 100,000 but has been accomplished here with a mass spectrometer with resolving power of about 1800 and the added dimensionality of thermal characterization.

Other Applications The applications described have highlighted the ability of TOF-MS for the analysis of transient signals, a definition that encompasses many sample introduction schemes and transient events. One important application is the coupling of chromatographic techniques with TOF-MS, as the mass analyzer is capable of providing fast multielemental analysis free of spectral skew. Such a coupling has already been successfully employed with GC systems utilizing electron-impact (EI) ionization sources but has yet remained largely uninvestigated in association with ICP-TOF-MS.

Pack et al. described the coupling of GC separations to TOF-MS by utilization of a microwave plasma torch (MPT) [50]. This low-power microwave plasma source has exhibited excellent limits of detection for halogenated species. When such species are separated by GC, the simultaneous capabilities of TOF-MS allowed the monitoring of ^{12}C and ^{35}Cl simultaneously, thereby facilitating the determination of empirical formulas. Presumably, ion chromatographic separations, FIA systems, and other separations might also benefit from the capabilities of TOF-MS.

Although electrospray ionization (ESI) sources have long been employed with TOF-MS for the analysis of large biomolecules, Mahoney et al. utilized ESI for the measurement of elemental species [51]. Similarly to previous investigations by Horlick et al. [52], Mahoney et al. found that variations in the interface potentials could effect the transition from a "bare-metal" ion spectrum to a mass spectrum composed of clustered or molecular species. These investigators demonstrated the utility of such an approach in the analysis of ferrocene, wherein molecular fragments or atomic iron species were selected by adjustment of these same interface potentials. This result is perhaps most valuable as a demonstration of the principle of a modulated, tandem, or switched source that can be employed for the acquisition of both atomic and molecular information. In such a scenario, a single source or a pair of sources operating in tandem would be operated in such a manner as to produce sequentially fragmentation, or EI-like, spectra under one condition and atomic information under another. Further, if accomplished in a rapidly switched manner in conjunction with a TOF-MS, such a system would be capable of the unambiguous identification of rapidly eluting chromatographic peaks.

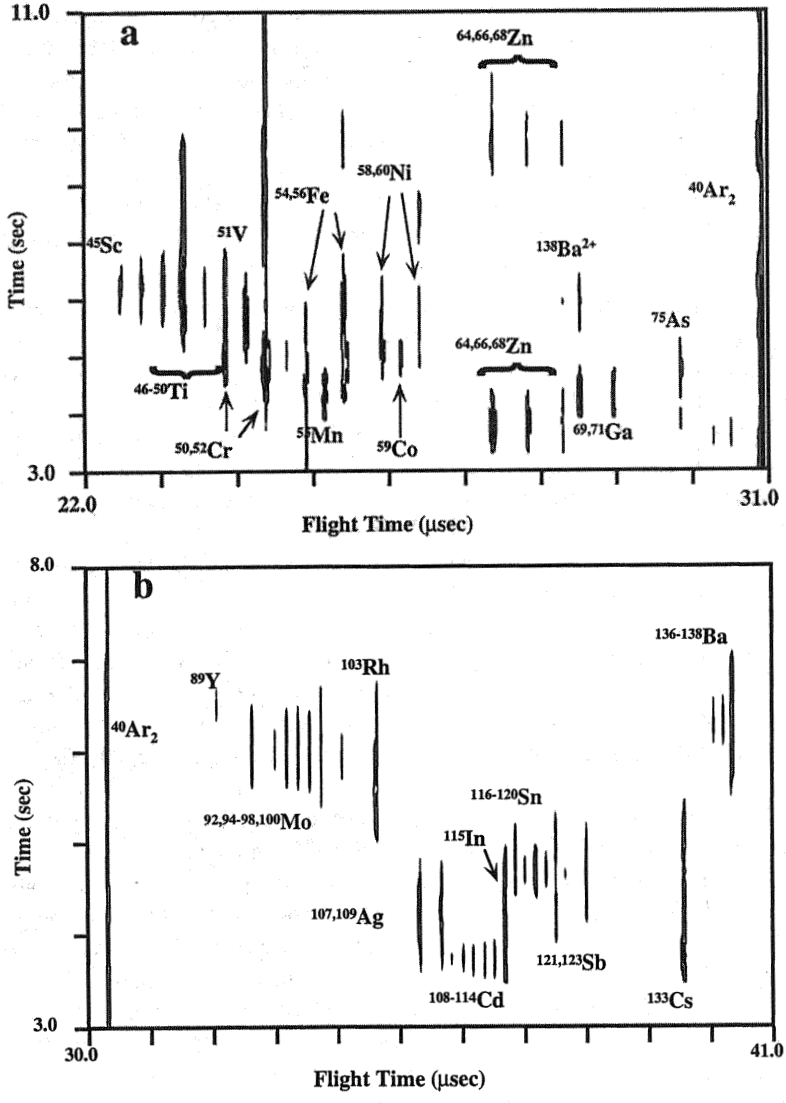

Figure 18 (a) Sequential elemental inductively coupled plasma (ICP) mass spectra obtained during the atomization step of an electrothermal vaporization (ETV) cycle after the injection of a multielement solution containing 34 elements, each at 100-ppb concentration. Flight time (x axis) denotes time-of-flight (TOF) drift time. Larger values on the y axis correspond to higher furnace temperature (time = 0 is the end of the ashing stage). Gray scale value corresponds to signal level. For clarity, the spectra are separated into three sections for m/z: (a) 43–81; (b) 79–144; and (c) 160–212. (From Ref. 55.)

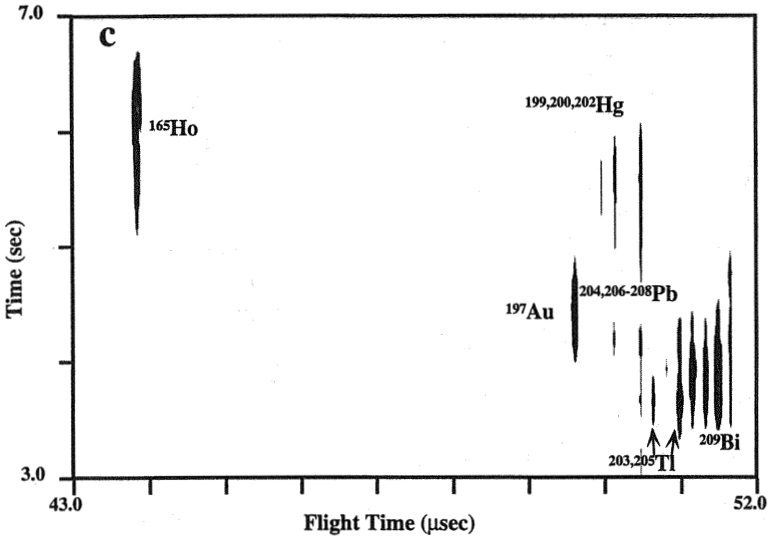

Glow Discharge Time-of-Flight Mass Spectrometric Performance

The ICP has not been the only elemental ion source coupled to a TOF-MS; nor is it the only ion source to derive benefits from the use of a simultaneous mass spectrometer. In 1994, Myers et al. described the use of a pin-type radio-frequency (rf) glow discharge with the TOF-MS [53]. Although the instrument did not yet utilize direct current (dc) quadrupole lenses, the use of an ion reflectron provided unit-mass resolution at mass 208. Interestingly, ion signals for differing masses did not vary as a function of the steering plate potential in the instrument, as had occurred when it was utilized with the ICP. This difference can be attributed to the fact that the ions possess the same energies, rather than velocities, an expected result at the operating frequency and pressure of this rf discharge. Reported detection limits for trace elements in brass and steel samples were in the single-part-per-million range [53].

Later, Heintz et al. investigated a planar rf-magnetron glow discharge coupled to the same orthogonal instrument [54]. Sampler-to-skimmer spacing was set at 18 mm, and a sliding gate valve allowed easy sample removal [54]. The RF-GD-MS ran optimally at 30–40 W of power and a pressure of 0.2 torr, producing detection limits of 7–20 ppm in MACOR and 0.1–0.7 ppm in aluminum samples [54]. Primary beam currents from the glow discharge were quite high (20–50 nA). One drawback presented by the magnetron discharge was the observed signal drift, a drawback that can be overcome by the choice of proper internal standards [54].

Although the coupling of steady-state discharges to the TOF-MS has proved successful, the TOF-MS is perhaps better suited for the investigation of pulsed GD sources. Here, the high temporal resolution and multielement capabilities of the TOF-MS can be fully exploited, with the coupling of a pulsed source to a pulsed

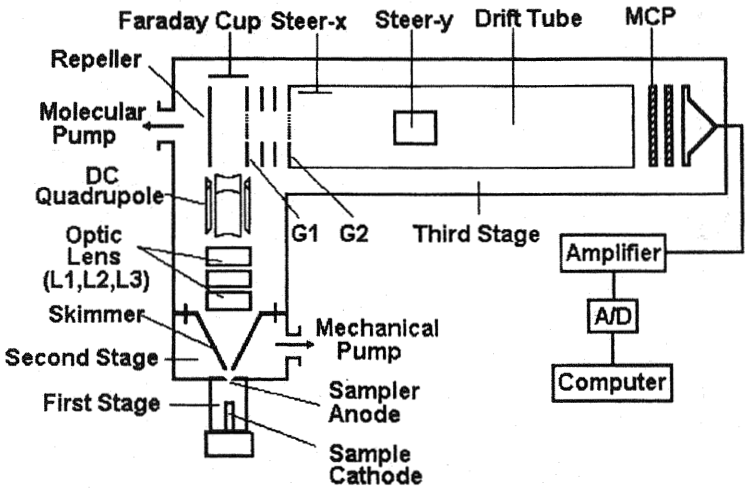

Figure 19 Schematic diagram of the microsecond pulsed glow discharge time-of-flight mass spectrometry (GD-TOF-MS) system. (From Ref. 55.)

mass spectrometer to improve resolution. Hang et al. reported the coupling of a pin-type pulsed GD to an orthogonal TOF-MS [55]. This instrument employed a linear geometry (1.25-m flight length), orthogonal extraction, and two-step acceleration (see Fig. 12.19). The pulsed glow discharge source operated over an adjustable frequency range of 500 Hz to 5 kHz and a pulse duration of 0.2 to 9 μsec (pulse height of 600 or 1100 V) [55]. Peak ion currents measured at the exit of the orthogonal extraction zone were over 100 nA when using this discharge (600 V, 3-μsec pulse, 3 kHz) [55]. A dc operating discharge at this voltage produced only 0.2 nA of continuous current.

In addition to high ion current and instantaneous powers, the use of a TOF-MS in conjunction with a pulsed source allows the realization of much higher duty factors. On the basis of the drift time required for ions to reach the Faraday cup at the end of the extraction region, Hang calculated that ions require about 1.25 μsec to traverse the orthogonal extraction zone, facilitating analysis of about 25% of the pulsed-current transient from the discharge [55]. An appropriate delay time from glow discharge pulse to TOF-MS repeller pulse (5 μsec) was chosen to analyze the sputtered species. Using the same linear TOF-MS a resolution of more than 500 was achieved for ^{63}Cu with a 100-MHz bandwidth readout [55]. In this early study ion deflection in the flight tube was inefficient as a result of limitations in pulsing circuitry, and MCP detector saturation occurred after the Ar^+ ion appeared (removal of 50%) [55]. Nevertheless, the results were quite promising with this pulsed GD ion source, especially the high ion currents obtainable, in addition to the surprisingly high resolving power of the linear TOF-MS.

The compatibility of the pulsed glow discharge source with TOF-MS continued to drive the research in developing a GD-TOF-MS. Harrison and Hang presented work at the 1996 Winter Conference on Plasma Spectrochemistry on an orthogonal TOF-MS with a reflectron; however, in this preliminary study the mass spectrometer was operated in a linear mode only [56]. They utilized a stable and versatile pulse generator for the microsecond discharge and adjusted time delay to the repeller pulse of the TOF-MS. With this approach, the separation of gas species and sputtered species was possible. Figure 12.20 shows a plot of a group of mass spectra obtained as a function of repeller delay for a copper sample [56]. The TOF-MS offers the time resolution to separate sputtered species from the discharge gases. Here, the time lag between the two is related to diffusion of the sputtered species to the sampling orifice and to the long lifetime of the metastable argon that can ionize sputtered atoms after the pulsed discharge is off [56]. The design of the TOF-MS is similar to that described in the previous paragraphs, with the exception of the replacement of a dc quadrupole lens with two steering plates to focus ions through a slit prior to the extraction region (see Fig. 12.21). Peak ion currents in this instrument were 8 nA, with a 900-V discharge pulse of 4-sec duration used [57]. The resolving power of the instrument measured at ^{100}Mo (peak width of 50 nsec) was 300. The authors estimated a transmission of 10% for the TOF-MS but point out uncertainties in their predictions due to inaccuracies in the pulsed current measurement. A spectrum produced from a steel sample is displayed in Fig. 12.22.

Hang et al. followed the preceding work with investigation of a reflectron mode of operation. The resolution of this instrument at that time was 1600 (FWHM) [57]. Figure 12.23 shows a spectrum from the instrument obtained in linear and relectron modes. Detection limits were in the low-part-per-million range and limited by the data acquisition electronics. Signal stability of the pulsed discharge was 10% over 1 hour, comparable with that reported for other GD sources [57]. Besides improvements in the data collection system, the authors also planned improved pumping in the third stage of vacuum to lower background noise and reduce ion scattering.

Pulsed discharges may be utilized to analyze nonconductive samples. Steiner et al. described the use of a pin-type pulsed rf-GD in conjunction with a linear orthogonal extraction TOF-MS [58]. Figure 12.24 depicts differences in the spectra obtained 4.0 msec after the power plateau and 7.0 msec after the plateau. As expected, the sputtered species (Si) in the discharge are found in the afterpeak at 7.0 msec (see Fig. 12.24). The resolution and sensitivity of this early system were limited and improvements were planned in the input optical system of the instrument.

Su and coworkers developed a design similar to the Grimm-type discharge to alleviate the need for pin samples [59]. This discharge was coupled to an improved version of the instrument previously described by Hang. Ion throughput was increased through better pumping and improved ion optics. In addition, some

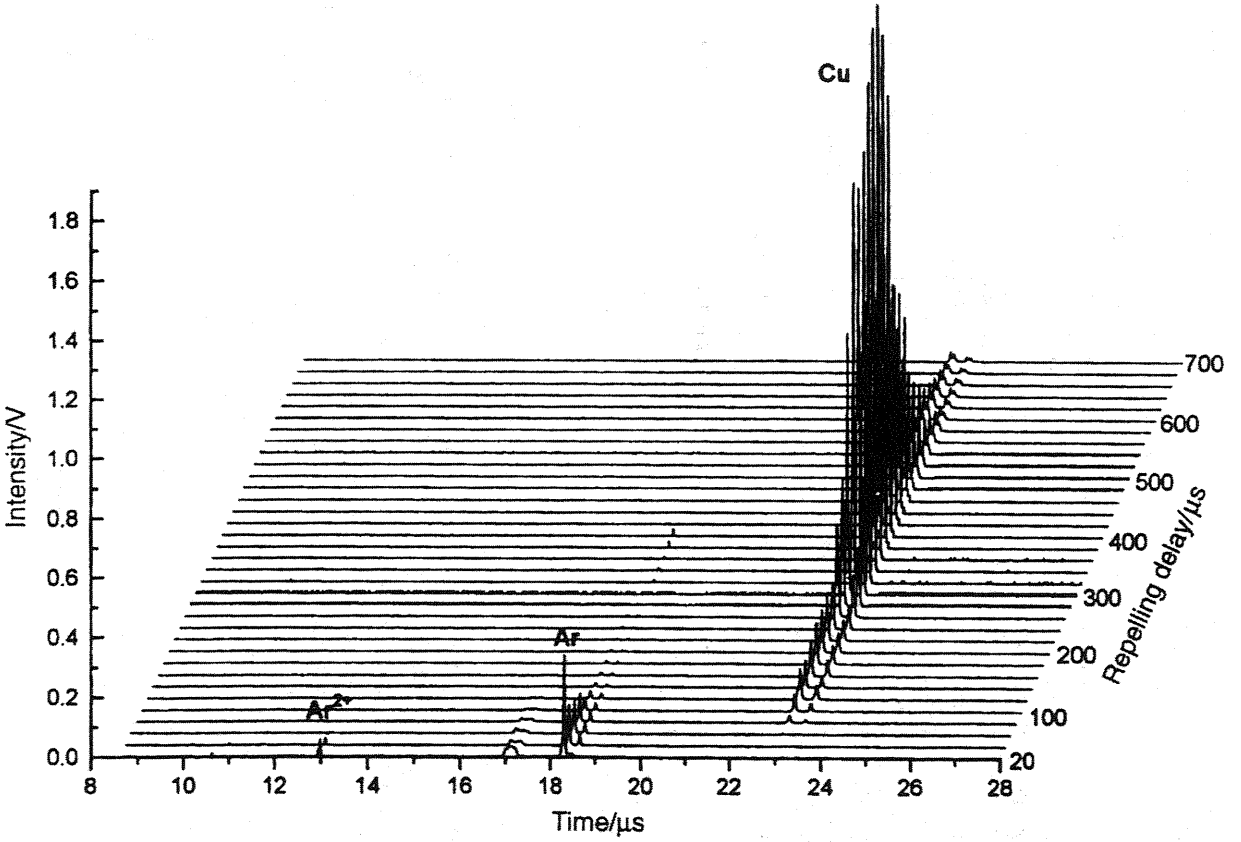

Figure 20 Microsecond pulsed mass spectra of copper in an argon glow discharge (GD) showing spectra taken at different delay times. Operating conditions: cathode-orifice distance, 5 mm; argon pressure, 1.0 torr; pulse width, 15 μsec; pulse magnitude, 3.0 kV; frequency, 100 Hz. (From Ref. 56.)

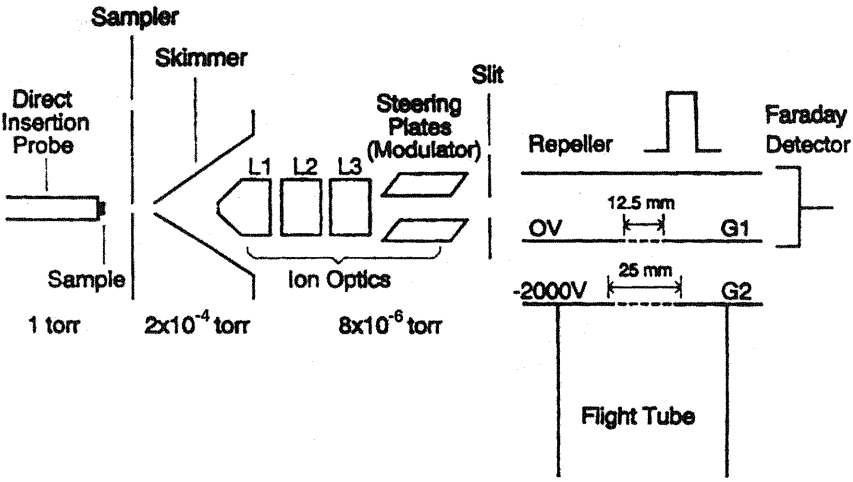

Figure 21 Ion optics for glow discharge time-of-flight mass spectrometry (GD-TOF-MS) (From Ref. 56.)

parametric studies revealed the optimal frequency for the pulsed discharge. Figure 12.25 shows a plot of Cu signal vs. discharge pulse frequency; the authors point out that results above 2 kHz should yield more signal, but the power supply could not provide enough power at these higher frequencies [59].

One application of great interest is depth profiling by means of GD-TOF-MS. Particularly in conjunction with pulsed GD sources, the simultaneous multi-elemental capabilities of TOF-MS permit the analysis of solid samples as a function of depth (or time) as the discharge operates. In such a case, one might envision complete trace elemental analysis of solid materials with resolution on the nanometer scale.

Overall, it is clear that as in ICP-TOF-MS, in GD-TOF-MS instruments are still improving. However, as in ICP-TOF-MS, the analysis of transient signals, like the pulsed GD ion source, has proved successful. The pulsed GD offers many advantages over conventional discharges. The discrimination against gaseous species and the high ion currents and instantaneous powers obtainable are two major strengths of the GD-TOF-MS combination and should be the future of the technique.

12.3.3 Axial Time-of-Flight Mass Spectrometry

Instrument Principles and Performance

Section 12.3.1.1 highlighted two different on-axis TOF-MS geometries that might find use with an elemental ion source such as the GD or ICP. A design incorporat-

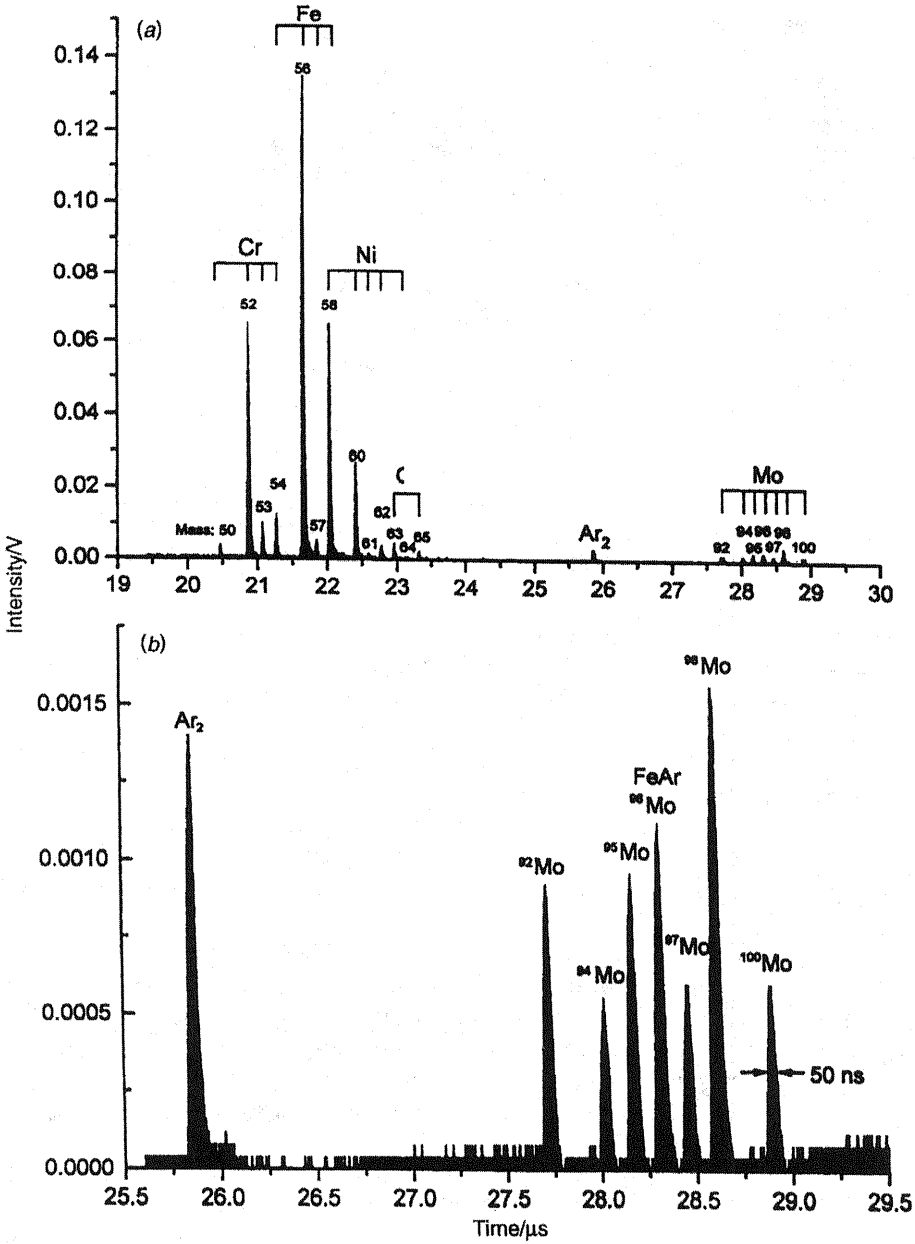

Figure 22 (a) Glow discharge time-of-flight mass spectrometry (GD-TOF-MS) spectrum of steel sample. (b) Magnification of Mo section of the spectrum. Operating conditions: argon pressure, 1 torr; cathode-orifice distance, 4 mm; repelling pulse delay, 220 μsec; pulse magnitude, 2 kV; frequency, 100 Hz; detector voltage, 1.6 kV; 100 pulses averaged. (From Ref. 56.)

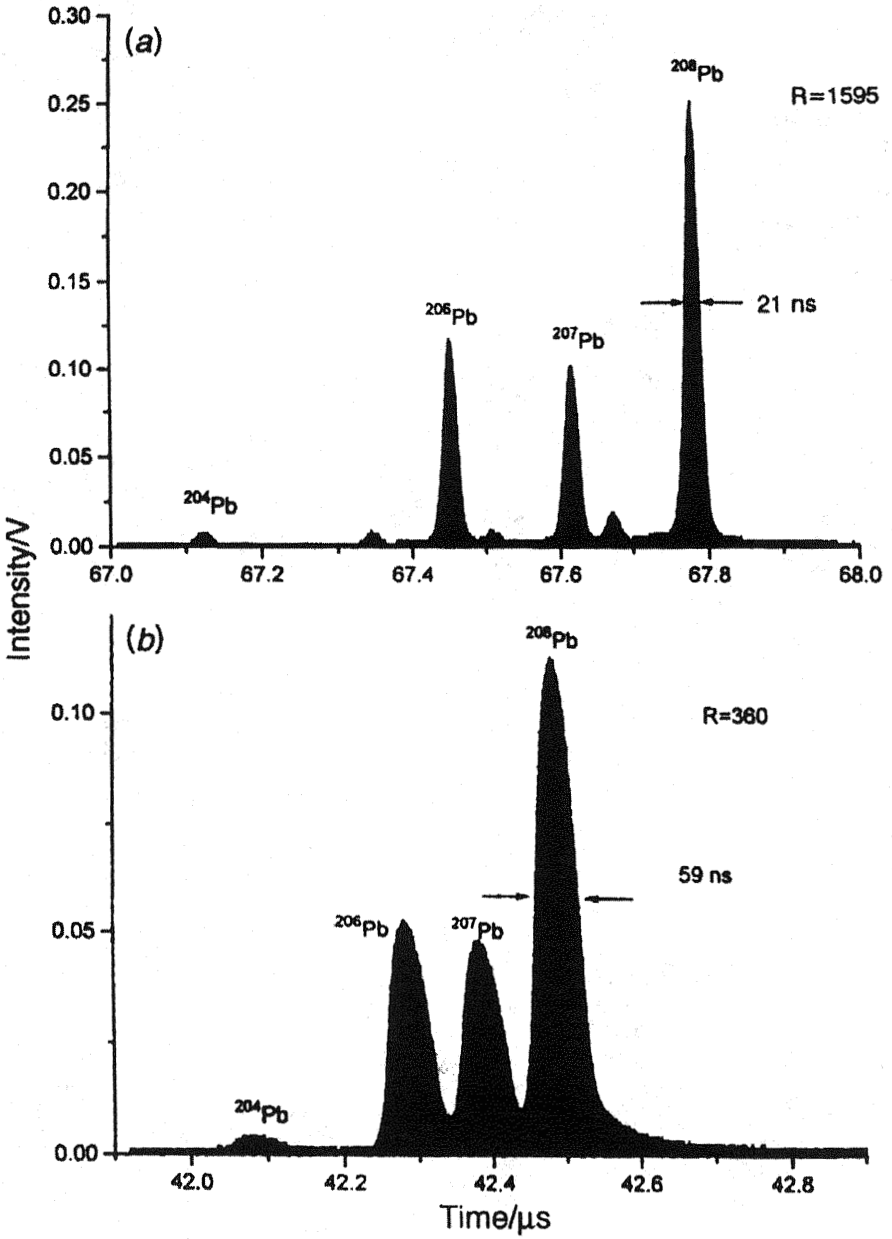

Figure 23 Mass spectra of lead disc: (a) reflectron mode, (b) linear mode, Source, 1 torr, 5 mm; pulse, 100 Hz, 15 μsec; pulse width, 10 μsec; 2.8 kV. (From Ref. 57.)

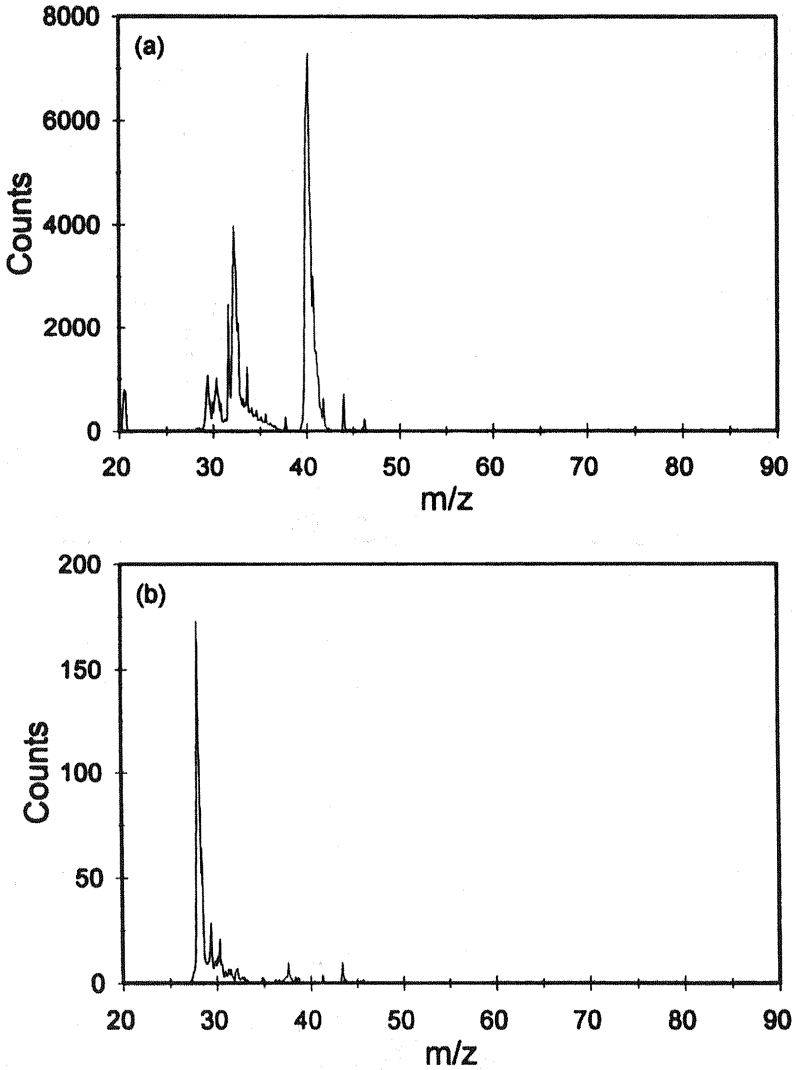

Figure 24 Radio frequency glow discharge time-of-flight mass spectrometry (GD-TOF-MS) spectra of silica glass at (a) 4.0 msec after power onset (plateau) and (b) 7.0 msec after power onset (afterpeak). (From Ref. 58.)

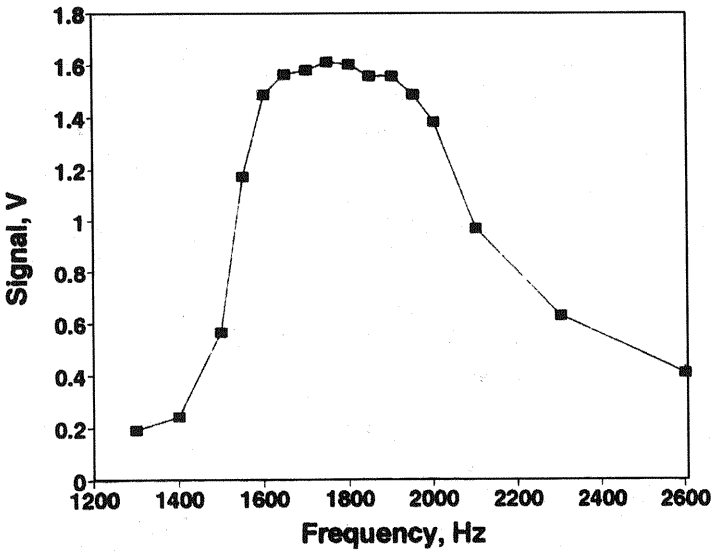

Figure 25 Effect of the pulse frequency on the $^{63}Cu^{+}$ signal (discharge pressure, 180 Pa; discharge current, 3 A; discharge pulse duration, 2 μsec). Each point was an average value based on 1000 pulses. (From Ref. 59.)

ing postacceleration modulation (Fig. 12.3) has not yet seen use in that field. Presumably, this is due to the low duty factors, and therefore sensitivities, that such an instrument would probably deliver. An instrument based on premodulation acceleration (Fig. 12.5), in contrast, should offer analytical figures of merit similar to those obtainable with an orthogonal-extraction geometry and is therefore more attractive.

To date, two groups have reported on the development of an on-axis ICP-TOF-MS utilizing preacceleration modulation [60–62]. The latter is a commercially available ICP-TOF-MS instrument, manufactured by LECO Corp [63]. Both designs utilize the basic geometry patented by Li and Hieftje, a schematic diagram of which is included as Fig. 12.26 [63]. The design can be visualized as an orthogonal extraction instrument, part of which has been rotated through an angle of 90°, and whose repeller plate has been replaced with a gridded ring electrode. In this way the continuous incoming ion beam enters the extraction region through the repeller electrode, as opposed to between the repeller plate and first acceleration grid (see Fig. 12.9). The instrument also differs from the orthogonal extraction design in the use of simple cylindrical lenses as extraction optics, but perhaps more importantly in the incorporation of a modulation region.

Because the continuous ion beam and extracted ion packets follow the same path after extraction, some additional means of separating the two is required. In

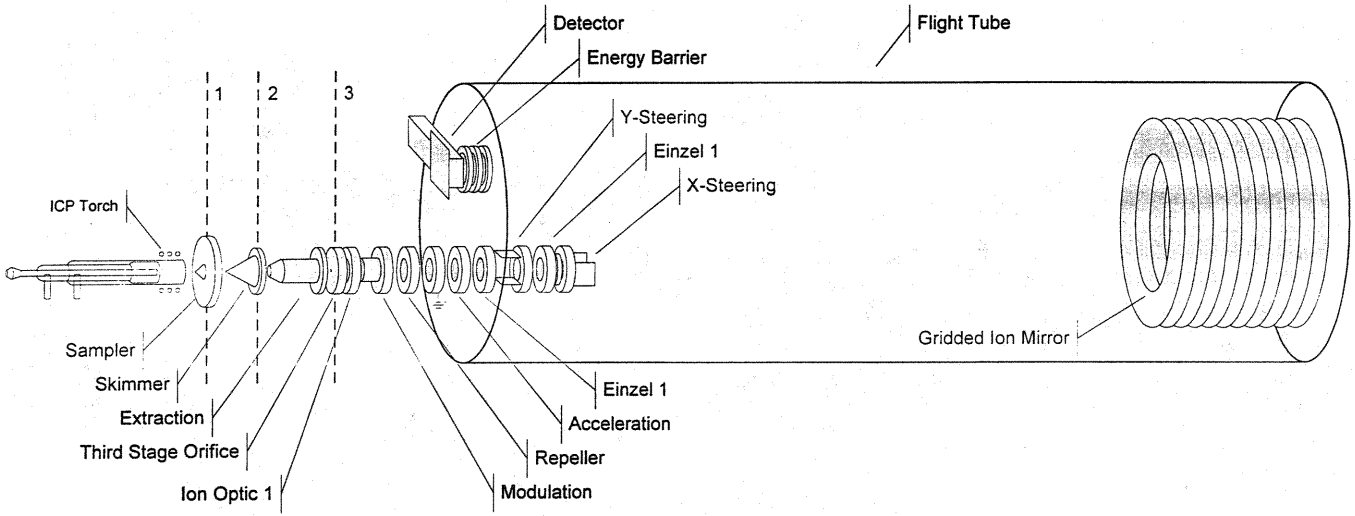

Figure 26 Schematic diagram of the LECO on-axis time-of-flight mass spectrometer. 1, 2, 3, first, second, and third stages of vacuum, respectively.

one case, this is accomplished by the use of a set of parallel deflection plates located immediately in front of the repeller electrode. Prior to extraction, a portion of the ion beam is selected by application of a voltage pulse of the appropriate magnitude, nominally 15-V magnitude and 5-μsec duration prior to the repeller pulse. The selected ion packet is then allowed to propagate into the extraction region, where it is selected for mass analysis by the repeller pulse. Although this arrangement is conceptually simple, proper pulse delay and width are critical to ensure a representative sampling of the incoming ion beam. This strategy is thus dependent upon the energy of the incoming ion beam, and a slight overfilling of the extraction region in front of the repeller is often necessary in order to ensure unbiased analysis. One related aspect worthy of note is the use of a shielded load coil to reduce ion energies in the beam [63].

This instrument has also been operated without the aid of preacceleration modulation, by relying upon the repeller pulse alone to generate a mass spectrum [63]. In a manner analogous to the noise attenuation technique, the so-called energy discrimination TOF-MS exploits the differences in energy between signal and background in order to differentiate between the two. With a potential barrier placed in front of the detector (see Fig. 12.26), ions that are continually accelerated into the TOF-MS are prevented from striking the detector. In contrast, ion packets that are intentionally extracted into the flight tube are given an extra kick, enabling them to surmount the barrier. Although this approach is simple to implement, its disadvantage with a high-current source such as the ICP lies in the large background that is observed. Because the ion beam is continuously allowed to enter the flight tube, the number of neutral species generated by charge exchange is much higher than in the orthogonal geometry, resulting in a continuum background approaching 2000 cps per 50-nsec portion of the mass spectrum [63]. In practice, the use of both preacceleration modulation and the energy discrimination greatly reduce the background noise [60–62].

Although similar in a number of ways, such as in the use of two-stage acceleration, the simple geometric difference between the orthogonal and on-axis designs produces several additional advantages and challenges. Indeed, the development of the on-axis instrument resulted in part from a desire to eliminate the mass-dependent steering and low transmission efficiency observed in the orthogonal-extraction design of Fig. 12.9. By placing the incoming ion beam and flight tube on the same axis, the need for compensatory steering is lessened, thus restoring the capability of multielemental analysis under a single set of instrumental conditions. Figure 12.27 illustrates a study analogous to that portrayed in Fig. 12.11, wherein the behavior of different masses is monitored as a function of steering potential. Although a very slight mass bias exists in the on-axis instrument, the maximum signal from different elements occurs over a significantly smaller steering-voltage range.

The attainment of mass-independent steering and a smaller beam cross section is achieved at the cost of placing greater demands on the instrument to com-

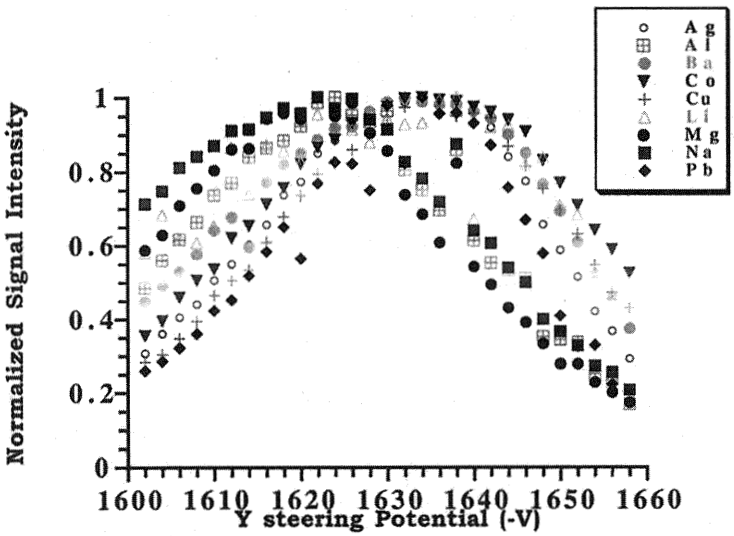

Figure 27 Plot of signals vs. steering plate (Y) potential for differing masses in the LECO on-axis time-of-flight mass spectrometer. Compare to Fig. 12.9, obtained with an orthogonal-extraction, time-of-flight mass spectrometer (TOF-MS).

pensate for energy dispersion in the incoming ion beam. Because the vector of greatest energy dispersion now lies along the flight axis, the reflectron must compensate for a much broader distribution of energies, and thus resolving power might be sacrificed. Experimentally the success of this compensation is verified by the achievement of adequate resolving power. Myers et al. demonstrated typical resolutions of 1300 (FWHM), an example of which is included as Fig. 12.28 [62]. This resolution is only slightly less than that obtained with the orthogonal extraction instrument of Fig. 12.9, and with an instrument having approximately half the flight length.

In terms of analytical performance, the on-axis instrument has exhibited figures of merit similar to those obtained with orthogonal-extraction geometries. Using modulation, initial results reported by Myers et al. [62] and Ray et al. [60,61] include detection limits in the 1- to 10-ppt range for most elements, using pneumatic nebulization. The sensitivity of the on-axis instrument is typically 1000–2000 cps/ppb (midmass range, monoisotopic element) with pneumatic nebulization, which appears to indicate slightly higher ion throughput than in the previous orthogonal ICP-TOF-MS instrument. A plot of background noise as a function of mass is shown in Fig. 12.29. The pressure in the analyzer region of the instrument in these measurements was 1.5×10^{-6} torr, and the remaining continuum ion background is presumably from the charge exchange mechanism.

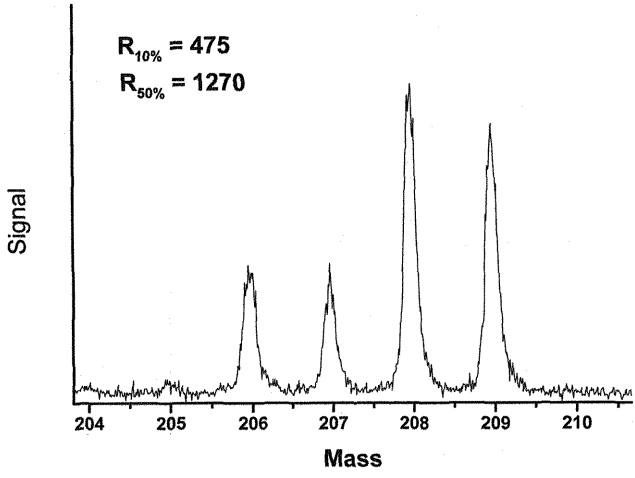

Figure 28 Mass range from 204 to 210 amu for a 10-sec integration while nebulizing a 1-ppb Pb and Bi solution into the on-axis time-of-flight mass spectrometer.

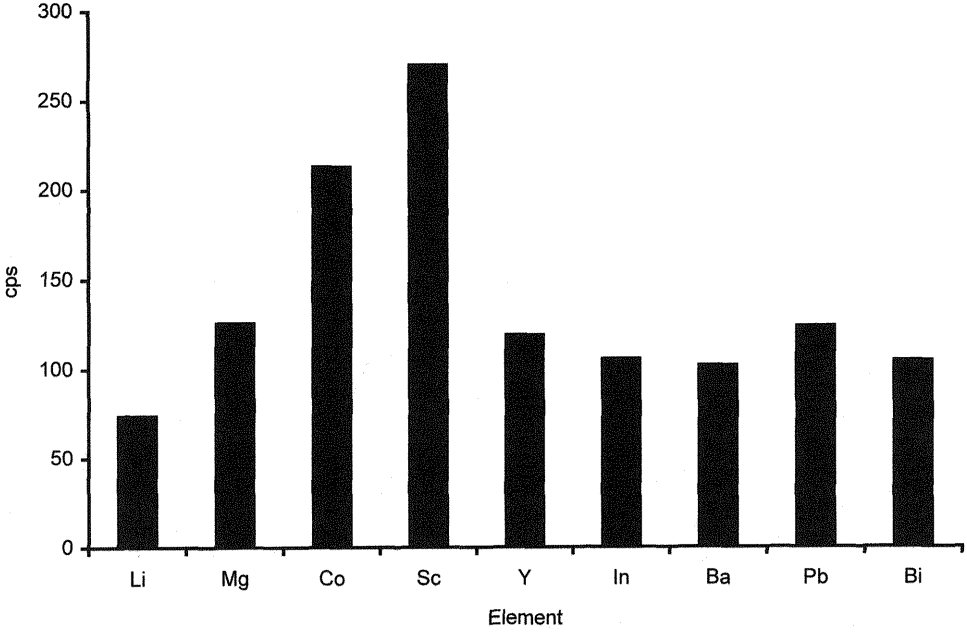

Figure 29 Background (counts/second) in mass windows for indicated elements obtained on the LECO on-axis time-of-flight mass spectrometer.

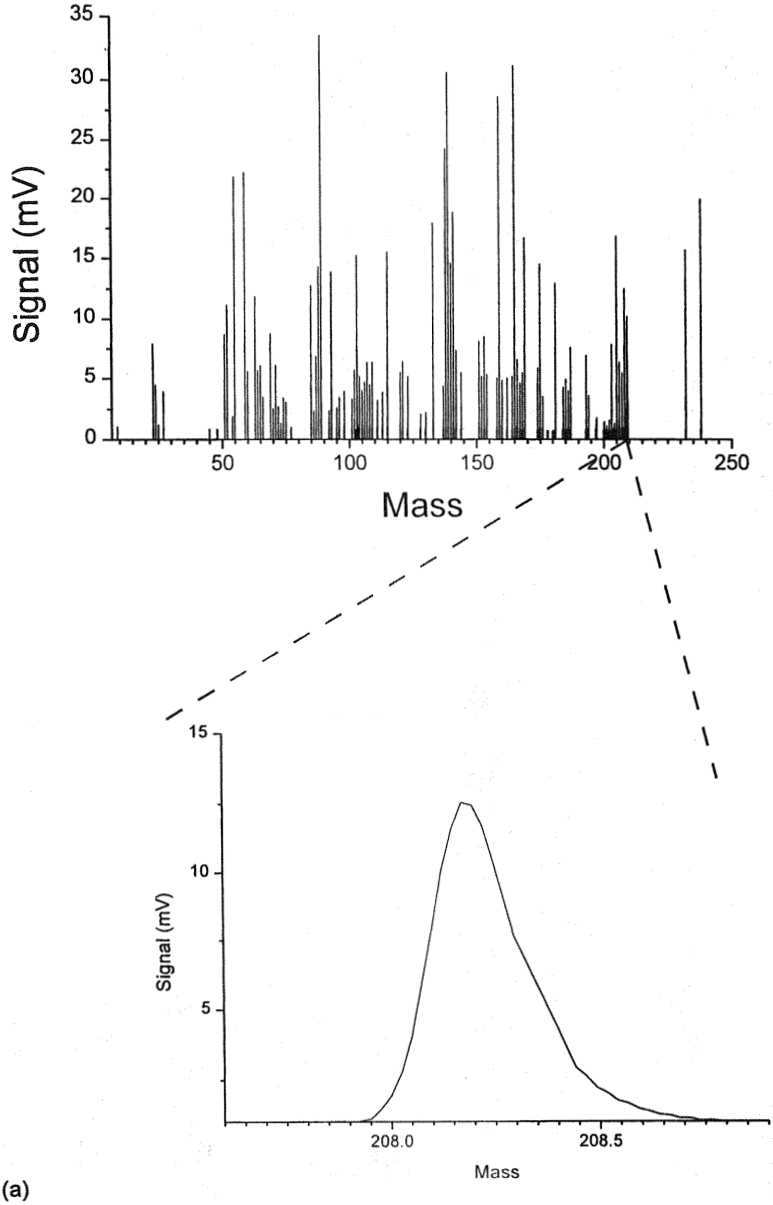

(a)

Figure 30 (a)Analog multielement spectrum consisting of 100 isotopic windows, each a 1-sec integration 19 bins in width (or 38 nsec), for a 100-ppb solution of 62 elements obtained with the patented LECO data acquisition system. (b) Counting domain spectrum obtained for the same solution and acquisition parameters with a 10-ppb solution.

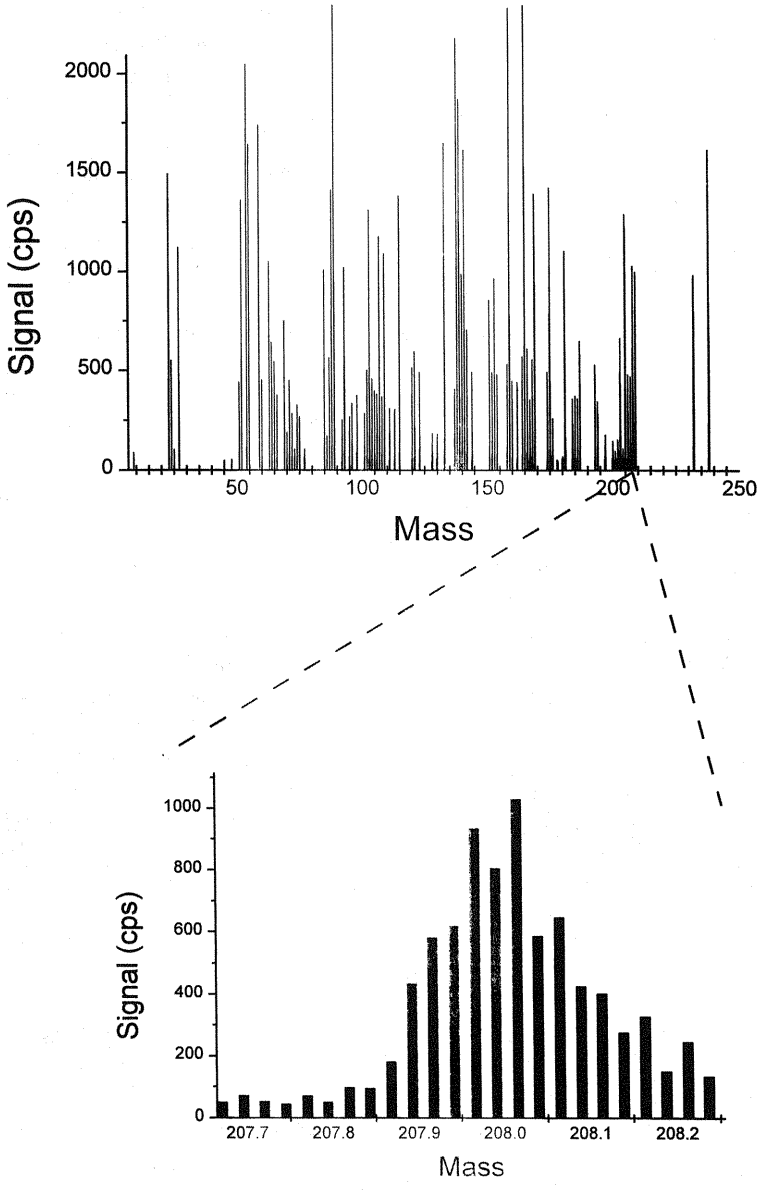
Signal (cps)
2000
1500
1000
500
0
50
100
150
200
250
Mass
Signal (cps)
1000
800
600
400
200
0
207.7
207.8
207.9
208.0
208.1
208.2
Mass

(b)

As stated throughout this chapter, the heart of an elemental TOF-MS is a detection system that can deliver an excellent dynamic range for the multielement analysis of broad concentration ranges at once. With its new on-axis instrument, LECO has introduced a detection system that can collect ion counting and analog signals simultaneously from the same detector. This patented system uses a 500-MHz analog-to-digital converter in conjunction with a 100-MHz discriminator/counter [62]. By using "binned" acquisition of the spectra and accumulation circuitry the amount of information generated by a 20 to 30-KHz TOF-MS is handled much more easily. This acquisition concept allows the user to place 2000 2-nsec bins at any spectral location desired in order to view the mass spectral peaks of interest. In this mode, more than 100 elemental isotopes can be acquired simultaneously with bins having counting and analog output [62]. Figure 12.30 shows a spectrum obtained on this commercial instrument of a solution containing 62 elements with the instrument acquiring 100 isotopes of interest in a 1-sec integration.

Transient Analysis

Just as with the orthogonal TOF-MS, the on-axis instrument is well suited for the analysis of transient signals. With the data acquisition system employed in the LECO in-axis ICP-TOF-MS, multielement analysis of fast transient signals is possible for a selectable number of isotopes. The exceptional speed of the TOF-MS will no doubt be exploited extensively in future applications with this instrument. Further development of software to ensure the integrity of the time-domain transient signals is a necessity. As the number of isotopic signals increases, the data analysis becomes a more daunting task for both the computer and the analyst. With this commercial instrumentation results similar to those achieved in the previously described LA-ICP-MS and ETV-ICP-MS can be realized over a large range of signal levels.

12.4 CONCLUSIONS

Judging from the degree of apparent interest and the number of papers published in the field of elemental TOF-MS over the last 3–4 years, it appears that this marriage is one full of promise for the future of elemental analysis. Perhaps the primary reason for such a trend is the need for a truly simultaneous mass spectrometer capable of extending capabilities beyond current instrumentation. The fields of ICP and GD atomic emission spectroscopy have been revolutionized by the incorporation of simultaneous array detectors. This revolution is just now beginning in the mass spectrometry field.

The time-of-flight mass spectrometer is an instrument capable of increasing the amount of information obtained from a sample per unit time. Multielemental

and isotopic measurements accomplished with greater precision and increased speed will drive more efficient sample utilization. With the capability for rapid semiquantitative analysis of the entire periodic table, and a talent for the characterization of transient signals, the TOF-MS is capable of increasing the amount of information gleaned from progressively smaller sample quantities. In addition, the number of elemental signals can be increased for internal standardization purposes, isobaric corrections, or ratioing without loss in sensitivity or increase in analysis time.

Significant challenges and opportunities remain in the use of TOF-MS for elemental analysis. One recurrent theme recognized in inorganic TOF-MS thus far has been the need for a detection system capable of high speed, high resolution, and wide dynamic range. Although the aforementioned data-acquisition system developed for ICP-TOF-MS fulfills many of these requirements, the further refinement of such systems represents a key to the future of inorganic TOF-MS. It is an interesting juxtaposition of the simplest of mass spectrometers and a data system that is truly complex, and as digital electronics become faster and more affordable the performance of the elemental TOF-MS will certainly improve correspondingly.

Another significant challenge remains in further increasing the efficiency with which sample species are utilized through increased ion throughput and duty factor. Currently many of the ions generated by continuous ionization sources are lost because of the pulsed nature of the instrument. Realization of higher duty factor and the unit transmission efficiency of which TOF-MS is capable could propel the TOF-MS into a sensitivity realm well beyond that of current mass analyzers.

Whatever the future holds for time-of-flight instruments in the inorganic mass spectrometry field, they have certainly shown the power of simultaneous readout of the entire elemental mass spectrum.

REFERENCES

1. Cameron, A. E.; Eggers, D. F. *Rev. Sci. Instrum.*, **1948**, *19*, 605.
2. Wiley, W. C.; McLaren, I. H. *Rev. Sci. Instrum.*, **1955**, *26*, 1150.
3. Sanzone, G. *Rev. Sci. Instrum.*, **1970** *41*, 741.
4. Mamyrin, B. A.; Karataev, V. I.; Shmikk, D. V.; Zagulin, V. A. *Sov. Phys. JETP*, **1973**, *37*, 45.
5. Karataev, V. I.; Mamyrin, B. A.; Shmikk, D. V. *Sov. Phys. Tech. Phys.*, **1972**, *16*, 1177.
6. Bergmann, T. P.; Martin, P.; Schaber, H. *Rev. Sci. Instrum.*, **1989**, *60*, 792.
7. Grix, R.; Kutshcer, R.; Li, G.; Gruener, U.; Wollnik, H. *Rapid Commun. Mass Spectrom.*, **1988**, *2*, 83.
8. Vlasak, P. R.; Beussman, D. J.; Qinchung, Ji; Enke, C. G. *J. Am. Soc. Mass Spectrom.*, **1996**, *7*, 1002.
9. Cotter, R. J., Ed., *Time of Flight Mass Spectrometry*, American Chemical Society, Washington, DC, 1994.

10. Cotter, R. J., Ed., *Time of Flight Mass Spectrometry: Instrumentation and Applications in Biological Research, ACS Professional Series*, American Chemical Society, Washington, DC, 1997.
11. Wollnik, H. *Mass Spectrom. Rev.*, **1993**, *12*, 89.
12. O'Halloran, G. J.; Walker, L. W. Technical Document no. ASD TDR 62-644, Parts I and II, Nov. 1964, prepared under Contract No. AF 33(657)-1108 by the Bendix Corporation, Research Laboratories, Southfield, MI.
13. Begley, I. S.; Sharp, B. L. *J. Anal. Atom. Spectrom.*,**1994**, *9*, 171.
14. Warren, A. R.; Allen, L. A.; Pang, H. M.; Houk, R. S.; Janghorbani, M. *Appl. Spectrosc.*, **1994**, *48*, 1360.
15. Walder, A. J.; Koller, D.; Reed, N. M.; Hutton, R. C.; Freedman, P. A. *J. Anal. Atom. Spectrom.*, **1993**, *8*, 1037.
16. Myers, D. P.; Li, G.; Mahoney, P. P.; Hieftje, G. M. *J. Am. Soc. Mass Spectrom.*, **1995**, *6*, 411.
17. Dawson, J.H.J.; Guilhaus, M. *Rapid Commun. Mass Spec.*, **1989**, *3*, 155.
18. Sin, C. H.; Lee, E. D.; Lee, M. L. *Anal. Chem.*, **1991**, *63*, 2897.
19. Yefchak, G. E.; Schultz, G. A.; Allison, J., Enke, C. G.; Holland, J. F. *J. Am. Soc. Mass Spectrom.*, **1990**, *1*, 440.
20. Bakker, J.M.B. *J. Phys. E.*, **1973**, *6*, 785.
21. Opsal, R. B.; Owens, K. G.; Reilly, J. P. *Anal. Chem.*, **1985**, *3*, 743.
22. Chambers, D. M.; Hieftje, G. M. *Spectrochim. Acta B*, **1991**, *46B*, 761.
23. Douglas, D. J.; French, J. B. *J. Anal. Atom. Spectrom.*, **1988**, *3*, 743.
24. Myers, D. P.; Hieftje, G. M. *Microchem. J.*, **1993**, *48*, 259.
25. Hang, W; Harrison, W. W. "Time-of-Flight Mass Spectrometry for a Glow Discharge Source." Presentation 1089 at Pittcon '97, Atlanta, GA, March, 1997.
26. Enke, C. G.; Vlasak, P. R.; Beussman, D. J.; Davenport, M. R. *Rev. Sci. Instrum.*, **1996**, *67*, 68.
27. Myers, D. P.; Li, G.; Yang, P.; Hieftje, G. M. *J. Am. Soc. Mass Spectrom.*, **1994**, *5*, 1008.
28. Myers, D. P.; Li, G.; Mahoney, P. P.; Hieftje, G. M. *J. Am. Soc. Mass Spectrom.*, **1995**, *6*, 400.
29. Mahoney, P. P.; Li, G.; Hieftje, G. M. *J. Anal. Atom.*, **1996**, *11*, 401.
30. Eiden, G. C., Barinaga, C. J.; Koppenaal, D. W. *J. Anal. Atom.*, **1996**, *11*, 317.
31. Eiden, G. C., Barinaga, C. J.; Koppenaal, D. W. *Rapid Comm. Mass Spectrom.*, **1997**, *11*, 37.
32. Tanner, S. D.; Baranov, V. I. *At. Spectros.*, *20*(2), **1999**, 45.
33. Chien, B. M.; Michael, S. M.; Lubman, D. M. *Anal. Chem.*, **1993**, *65*, 1916.
34. Wiza, J. L. *Nucl. Instrum. Methods*, **1979**, *162*, 587.
35. Gulcicek, E. E.; Boyle, J. G. *Rev. Sci. Instrum.*, **1993**, *64*, 2382.
36. Holland, J. F.; Newcombe, B.; Tecklenburg, R. E., Jr.; Davenport, M.; Allison, J.; Watson, J. T.; Enke, C. G. *Rev. Sci. Instrum.*, **1991**, *62*, 69.
37. Arataev, V. B.; Burrill, P. H.; McNitt, K. L.; Schmitz, D. A.; Enke, C. G.; Holland, J. F. "High-Speed GC/MS Analysis of Complex Mixtures Using Time-of-Flight Mass Spectrometry with Time-Array Detection." Poster TP186 presented at the 42nd ASMS Conference on Mass Spectrometry and Allied Topics, Chicago, Illinois, May 29 - June 3, 1994.

38. Smith, B. K.; Delaney, P. A.; Passler, M. A. *Rev. Sci. Instrum.*, **1988**, *59*, 2079.
39. Yang, P.; Myers, D. P.; Li, G.; Hieftje, G. M. *Appl. Spectrosc.*, **1995**, *49*, 945.
40. Myers, D. P.; Li, G.; Mahoney, P. P.; Hieftje, G. M. *J. Am. Soc. Mass Spectrom.*, **1995**, *6*, 920.
41. Coles, J.; Guilhaus, M. *Trends Anal. Chem.*, **1993**, *12*, 203.
42. Mahoney, P. P.; Ray, S. J.; Li, G.; Hieftje, G. M. *J. Am. Soc. Mass Spectrom.*, **1997**, *8*, 125.
43. Ferguson, R. E.; McCulloh, K. E.; Rosenstock, H. M. *J. Chem. Phys.*, **1965**, *42*, 100.
44. Ryan, P. W.; Futrell, J. H.; Vestal, M. L. *Chem. Phys. Lett.*, **1973**, *18*, 329.
45. Chait, B. T.; Field, F. H. *Int. J. Mass Spectrom. Ion Phys.*, **1981**, *41*, 17.
46. Myers, D. P.; Li, G.; Mahoney, P. M.; Hieftje, G. M.; *J. Am. Soc. Mass Spectrom.*, **1995**, *6*, 920.
47. Mahoney, P. P.; Ray, S. J.; Hieftje, G. M. *Appl. Spectrosc.*, **1997**, *51*, 16A.
48. Allen, L. A.; Georgitis, S. T.; Myers, D. P. *Phys. Stat. Sol. (a)*, **1998**, *167*, 357.
49. Mahoney, P. M.; Ray, S. J.; Li, G.; Hieftje, G. M. *Anal. Chem.*, **1999**, *71*, 1378.
50. Pack, B. P.; Broekaert, J.A.C.; Guzowski, J. P.; Hieftje, G. M. *Anal. Chem.*, *70,* 3957.
51. Mahoney, P. P.; Guzowski, J. P., Jr.; Ray, S. J.; Hieftje, G. M. *Appl. Spectrosc.*, **1997**, *51*, 1464.
52. Horlick, G.; Stewart, I. *Trends Anal. Chem.*, **1996**, *15*, 80.
53. Myers, D. P.; Heintz, M. J.; Mahoney, P. P.; Li, G.; Hieftje, G. M. *Appl. Spectrosc.*, **1994**, *48*, 1337.
54. Heintz, M. J.; Myers, D. P.; Mahoney, P. P.; Li, G.; Hieftje, G. M. *Appl. Spectrosc.*, **1995**, *49*, 945.
55. Hang, W; Yang, P.; Wang, X.; Yang, C.; Su, Y.; Huang, B. *Rapid Commun. Mass Spectom.*, **1994**, *8*, 590.
56. Harrison, W. W.; Hang, W. *J. Anal. Atom. Spectrom.*, **1996**, *11*, 835.
57. Hang, W.; Baker, C.; Smith, B. W.; Winefordner, J. D.; Harrison, W. W. *J. Anal. Atom. Spectrom.*, **1997**, *12*, 143.
58. Steiner, R. E.; Lewis, C. L.; King, F. L. *Anal. Chem.*, **1997**, *69*, 1715.
59. Su, Y.; Zhen, Z.; Yang, P.; Wang, X.; Huang, B. *Spectrochim. Acta B*, **1997**, *52*, 633.
60. Ray, S. J.; Hieftje, G. M. *J. Am. Soc. Mass Spectrom.*
61. Ray, S. J.; Guzowski, J. P., Jr.; Myers, D. P.; Hieftje, G. M., *J. Anal. Atom. Spectrom.*62. Myers, D.; Brushwyler, K.; Allen, L.; Georgitis, S. "Elemental Analysis with ICP-TOFMS." Presentation #3 at the 24th Annual Conference of the Federation of Analytical Chemistry and Spectroscopy Societies, Providence, RI, October, 1997.
63. Li, G.; Hieftje, G. M. U.S. Patent # 52 614, 711, March 25, *1997.*

Index